Numerical modelling of bond behaviour of FRP bar reinforced concrete beam under high strain rate impact load

By

Golnoush Heidarzadeh

A dissertation submitted in conformity with the requirements for

The degree of

Doctor of Philosophy

In the

Department of Mathematics, Computer Science and Engineering

City university of London

2022

Declaration

This thesis entitled “Numerical modelling of bond behaviour of FRP bar reinforced concrete beam under high strain rate impact load” is submitted to the City University of London for the degree of Doctor of Philosophy.

The research presented in this thesis is solely work of Golnoush Heidarzadeh, under supervision of Dr. Feng Fu, except where otherwise accredited in the context. Full references are provided where other sources were used and fully attributed.

Golnoush Heidarzadeh

July 2022

Abstract

Since 1980s, the use of fibre-reinforced polymer (FRP) has been introduced as reinforcement or retrofitting measures to concrete structures. The FRP material features in high strength to weight ratio, high flexibility, ease of installation and energy absorption, higher corrosion resistance, made this material a viable option for strengthening RC members in high strain rate events such as impact and blast.

One of the most dominant failure modes in FRP reinforced concrete structures is the debonding failure, which happens near or at FRP interface to concrete. Extensive research has been made on the bond behaviour of FRP RC structures under static loading. However, the influence of high strain rate on bond behaviour of FRP reinforced concrete under dynamic load is still not well understood as limited studies are investigated on the influence of high velocity impact load on bond of FRP to concrete. In addition, the results do not represent the real bond behaviour of FRP to concrete as factors such as strain rate was not included in the investigations.

This thesis undertakes an exploration into the bond behaviour of reinforced concrete beams, specifically reinforced with Fiber Reinforced Polymer (FRP) bars, when subjected to high-velocity impact loads characterized by varying strain rates. Employing ABAQUS, a commercially available finite element software, a comprehensive three-dimensional finite element model was meticulously constructed. The reliability of this model was meticulously ascertained for both static and dynamic scenarios, with a particular focus on the local reinforcement strain distribution. The initial stage of this investigation involved a thorough analysis of variables influencing the bond between FRP and the concrete interface. These variables encompassed concrete compressive strength, bar diameter, the type of fibres utilized, and the variation in applied impact loads, which were collectively examined using a dataset of 255 distinct beam models. It was conclusively determined that both the diameter of the FRP bars and the strength of the concrete matrix exert a significant influence on the bond behaviour exhibited by FRP-reinforced concrete beams. Notably, this study unveiled a groundbreaking revelation,

demonstrating that the strain rate directly impacts the bond mechanism governing the behaviour of beams subjected to impact loading.

Furthermore, this research effort culminated in the identification and reporting of optimized parameters for FRP bar diameter, concrete strength, and the type of fibre, all tailored to the specific requirements of reinforced concrete beams exposed to high-impact loading conditions. These findings represent a valuable contribution to the body of knowledge in the field of structural engineering and materials science.

In the subsequent phase of the study, an innovative multi-way regression analysis was undertaken, marking the first instance in which equations were derived through a parametric study to forecast slip, maximum bond strength, and mid-deflection in Fiber Reinforced Polymer (FRP) reinforced concrete beams. To assess the accuracy of these prognostic equations, validation was carried out through the creation of novel models.

This research effort yielded significant outcomes, notably the formulation of a concrete Dynamic Increase Factor (DIF) model, which exhibited a strain rate dependency. This development stemmed from an exhaustive numerical examination of bond slip behaviour between FRP bars and the adjacent concrete matrix under varying loading rates. Additionally, a dynamic slip rate-dependent model for FRP-reinforced concrete beams was introduced for the first time. The finite element predictions stemming from the bond-slip DIF model were accurately compared and corroborated against established guideline codes, founding their reliability and applicability in engineering practice.

Acknowledgement

I would like to express my gratitude to my supervisor Dr. Feng Fu for his enlightening guidance, his enthusiasm, motivation and patience throughout this course and during all the phases of completion of this thesis. I am deeply grateful for his generous support and continued guidance to carry out and producing this thesis.

I would like to thank my friends and colleagues in City University for their moral support and useful suggestions, making many dark days brighter throughout the period.

Finally, I would like to express my deepest appreciation to my family for their true love, support and care during the past years. My family worked diligently to support my studies financially and morally, for which I cannot be grateful enough. The last phases of this journey were rigorous and would have been unmanageable to complete without believing in myself and reflecting on my strength.

What is to give light must endure burning-

Viktor Frankl

Contents

Nomenclature

Acronyms

ABAQUS	Computer program
AFRP	Aramid fibre reinforced polymer
BFRP	Basalt fibre reinforced polymer
CFRP	Carbon fibre reinforced polymer
CDP	Concrete damage plasticity
DIF	Dynamic increase factor
FE	Finite element
FEA	Finite element analysis
FRPs	Fibre reinforced polymers
GFRP	Glass fibre reinforced polymer
LVDTs	Linear variable differential transducers
RC	Reinforced concrete
Rebar	Reinforcement bars
3D	Three dimensions

Notations

$A_{f,bar}$	Area of bar
A_t	Area of transverse reinforcement
b	Width of rectangular cross section
b_p	Width of FRP plate;
C	The lesser of the cover to the centre of the bar or one-half of the centre-to-centre spacing of the bars being developed;
c	*Lesser of the cover to the centre of the bar*
d	Distance from extreme compression fibre to centroid of tension rebar
d_s	Diameter of spiral
d_t	Scalar damage variable in tension
$E_\circ$	*Available maximum energy*
E_b	*Bending energy*
E_f	FRP modulus of elasticity
E_{ker}	*Rotational kinetic energy*
E_s	Young's modulus of steel;
E_{sec}	Stress-strain behaviour of outside the confined core concrete
E_t	Young's modulus of transverse reinforcement
f_c	*Specified concrete strength*
f'_{co}	Unconfined concrete strength
f'_{cc}	Compressive strength of confined concrete
f_{cr}	Cracking strength of concrete
f_y	Yield strength of transverse reinforcement
f'_c	*Concrete compressive strength*
f_{bod}	Design bond strength of concrete
f_f	Stress in FRP reinforcement in tension

$f_{r,frp}$	FRP rupture strength
g	*Gravitational acceleration*
h_d	*Drop height*
K_1	Bar location factor
K_2	Concrete density factor
K_3	Bar size factor
K_4	Bar fibre factor
K_5	Bar surface profile factor
K_{tr}	Transverse reinforcement index
k_e	Confinement coefficient
$L(t)$	*Length of object at time*
$L_0(t)$	*Original length*
l_d	*Development length of reinforcement*
M	*Mass of the impact object*
M_u	*Ultimate moment*
n	Number of bars being developed along the plane of splitting
P_u	Ultimate load at the FRP end from the load slip curve
S	Centre to centre spacing of the transverse reinforcement
s	Slip
s_1	Slip at the peak bond stress
s_r	Parameters based on curve-fitting resulted from test data
s'	Clear spacing between spiral or hoop bars
w_l	*Concrete width*
w_f	*FRP width*
R_r	*Rib area*
τ_f	*Average bond stress*
τ_{max}	*Maximum bond strength*

$\emptyset_b$	*Diameter of reinforcement bar*
ε	*Strain rate*
ε_t	Total strain in tension
ε_{cu}	Ultimate strain in concrete
ε_t^{pl}	Equivalent plastic strain in tension
ε_t^{ck}	Cracking strain
$\partial\varepsilon$	*Immediate strain*
∂t	*Time interval*
$\Delta E_\circ$	*Change in kinetic energy*
v_i	*Impact velocity*
v_f	*Velocity of falling object*
α	*Curve fitting parameter*
φ	Parameters based on curve-fitting resulted from test data
Δ	Standard deviation with the same unit as the sample x
δ_{mid}	Mid Deflection
t_p	Thickness of FRP plate
s_f	Final slip of bond-slip curve
τ_{max}^d	Dynamic maximum local bond stress under different strain rate
$\hat{\bar{\sigma}}$	Maximum principle effective stress
σ_{c0}	Initial axial compressive yielding stress
σ_{b0}	Initial equibiaxial compressive yielding stress
σ_m	Maximum stress under static condition
$\overline{p}$	Effective hydrostatic pressure
$\overline{q}$	Mises equivalent effective stress
ρ_f	FRP reinforcement ratio

List of Figures

List of Tables:

Chapter 1: Introduction

1.1 Background

Reinforced concrete (RC) structures are widely used as structural material in construction. Yet, there are steel disadvantages such as corrosion under changed environments, heavy weight and difficulties in handling the steel structures can cause failure in structural elements, which leads to high maintenance cost and major repair. For many years, engineers tried to prevent the corrosion and high cost of rehabilitation of steel by replacing it with different materials for structural members, nonetheless the results happen to be unsuccessful [5]. In contrast, properties of fibre reinforced concrete (FRP) made this material a viable option for replacing and strengthening the RC structural members, [6]. Benefits of using FRP includes high strength, light weight, high energy absorption, high electrochemical corrosion resistance, excellent tensile strength that makes insignificant amount of FRP in structure to increase resistance of members to resist large extent of tensile load and bending moment, without considerably increase in weight of the members. Consequently, throughout the past 20 years, use of FRP to strength and replace steel reinforcement increased in concrete structures. Due to certain properties of FRP such as high electrochemical corrosion resistance, FRP reinforcements are used in harsh weather and chemical environments that steel cannot be applicate. These structures include sea walls, magnetic resonance imaging rooms (MRI) in hospitals, Laboratory that needs elements with electromagnetic neutrality, floating piers and many other civil infrastructure [7].

Meanwhile, mechanical properties of FRP such as high tensile strength, low young's modulus and linear stress-strain diagram until the rupture point are different from Steel mechanical properties. Therefore, same method of calculation for steel reinforcement cannot be used for FRP reinforcement. Mechanical properties of FRP can cause wide cracks and large deflection under different loads due to high tensile strength and low modulus of elasticity of FRP that makes structures stiffer without significantly enhance the ductility of the members. This behaviour leads the structure

to brittle failure [8] [9]. FRP properties varies between different types of FRP. In civil structures Carbon fibre reinforced polymer (CFRP), Glass fibre reinforced polymer (GFRP), Basalt fibre reinforced polymer (BFRP) are widely used as strengthening and reinforcement application. There are numbers of different fabrication processes reported for FRP bars in different guidelines including ACI committee 440 reports [10] [11]. Pultrusion is one of the most common fabrication process that allows production to complex shapes. This method is used in different industries including civil engineering and automotive. The reinforcement bars are pulled into resin matrix bath in order to saturated with a resin with a low viscosity in pre-shaping station with a temperature of 110°to 160˚C to make the final product. During this stage of process, curing happen and fibres eternally tensioned in the axis direction. At the end, the profile pulled through "moving-cut off-saw" section for sawing, then cut into specified lengths.

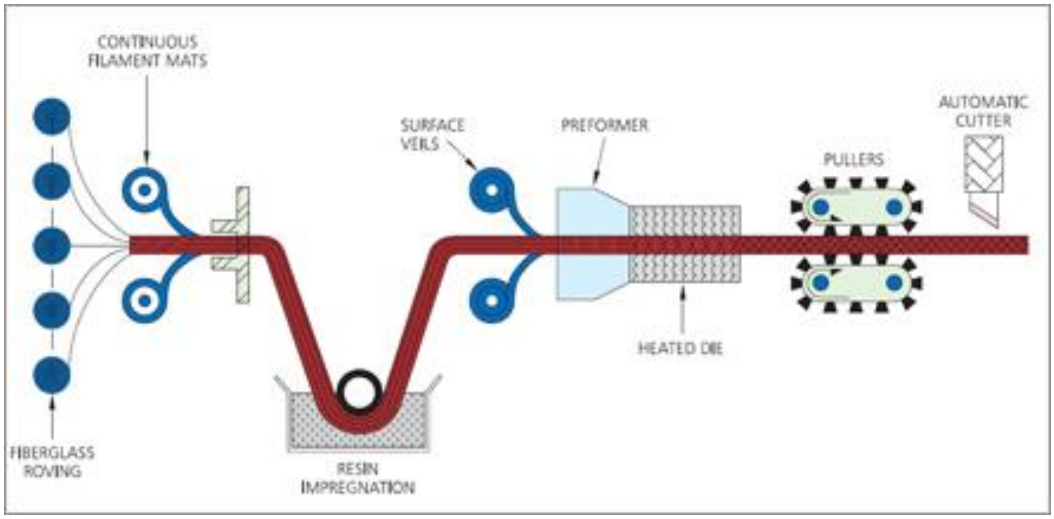

Figure 1: Different stages of Pultrusion manufacturing process, [12].

Different types of FRP have been used in existing studies including Carbon, Glass, Basalt and aramid fibre reinforced polymer. These FRPs are used in shape of bar, rebar, sheet and wraps for different members of RC structures. Figure (2) demonstrate number of FRP bars in tension that do not yield before failure and reveal higher strain tolerance compare to steel bars.

The FRPs have linear stress-strain relationship until the failure point that can be result of fragile rupture, as FRP bars have low elastic modulus and stiffness. The

mechanical properties of FRP bars such as young's modulus, ductility and even bond potentials are considerably vary between different FRP bars depending on the capacity of fibres and nature of FRPs. Thus, determined values for mechanical properties of FRP cannot be established and indicative standards can be specified as mechanical properties for different FRPs bars.

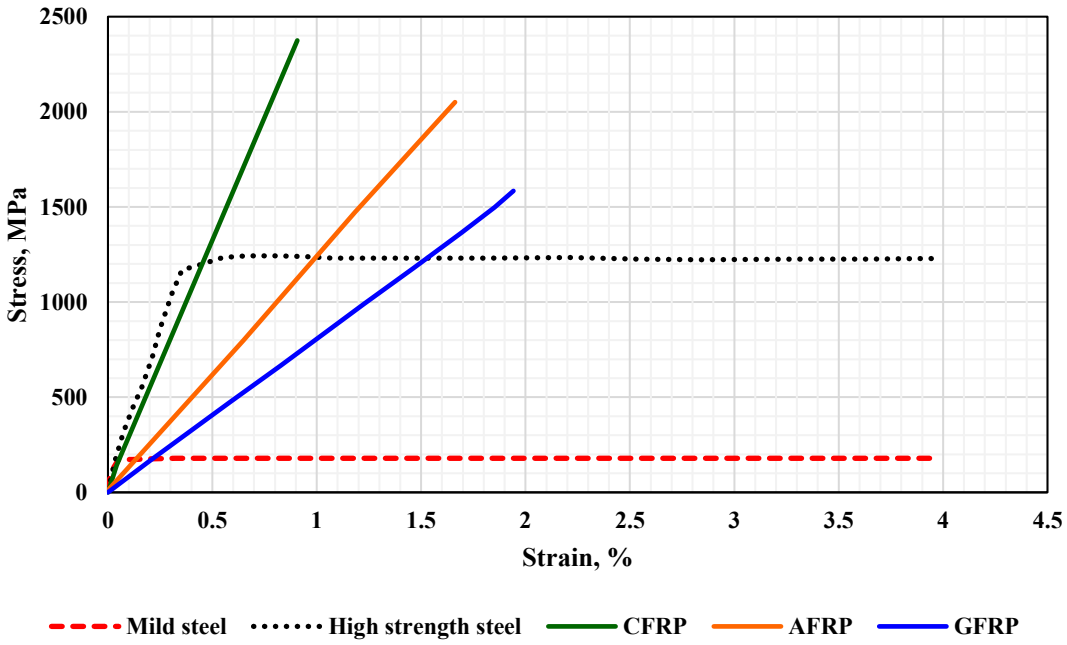

Figure 2: stress-strain relation of FRP bars compared to steel in tension, [13]

Different shapes and forms of FRP can be produced and used for structural members. However, circular shape of FRP bars is one of the most common option for RC structures. Furthermore, different methods are used to improve FRP bond features in concrete including: surface texture, sand coating, surface deformations such as ribbed deformed, helical wrapping and indented grooves [14] [15].

FRP RC structures have complex behaviour such as post cracking, failure modes under different loading, interaction effect between FRP and concrete interface and etc. this complex behaviour would increase if the structure is subjected to dynamic loading such as explosion or impact of dropped weights. FRP RC structures subjected to impact loading suffer deformation in both locally and globally. This deformation may occur by projectile impact as scabbing, crushing or plug formation locally or as bending failure globally. Impact loads can be divided into two categories: natural and

unnatural event. The natural events are such as rock avalanches, fall of objects, and moving debris from tornados. Unnatural events are terrorist attacks, and collision of vehicles into structure members. Impact loads are either high velocity, (exceeding $10\ {}^{m}/_{S}$), or low velocity impact load, [16] [17].

There are different ways to determine the reaction of members subjected to impact loading. These approaches include experimental tests, analytical investigation and numerical solutions. Experimental test result in finding empirical equations that consider the local response of global independent members subjected to impact load. Analytical investigation such as mass-spring system or vibration may consider the global formation with avoiding the influence of local response of the members. Consequently, the results would not show real behaviour of FRP RC members under impact loading. Numerical solutions such as finite element methods provide sufficient tools to investigate the behaviour of FRP RC structures under impact loading with considering both local and global responses. Many studies involved numerical models of FRP RC members in two-dimensions in case of static loading. Yet, tow-dimensions model cannot show accurate results under the dynamic loading such as explosion or impact load. Hence, three-dimensional models can be a more practical option for dynamic loading since the member modelled closer to the real-life ones. There are numbers of three-dimensional models of FRP RC members under impact loading, but these studies either did not consider effect of high strain rates on behaviour of FRP RC members or assumed perfect bonds between FRP and surrounding concrete.

1.2 Motivation

To establish Fiber Reinforced Polymer (FRP) as a viable choice for concrete structures, a comprehensive comprehension of their properties and behaviour is imperative. While various guidelines exist for the use of FRP materials in composite structures, the insufficiency of information regarding FRP behaviour, coupled with the inapplicability of existing steel Reinforced Concrete (RC) codes to FRP RC structures, necessitates extensive research and studies on FRP structural behaviour. This

research aims to augment existing guidelines and formulate specific codes tailored to FRP RC structures [18].

An essential aspect in understanding the structural behaviour of FRP RC is the enhancement of bond strength between FRP reinforcement and the concrete member. The bond between FRP and concrete is pivotal as it maintains the connection between reinforcement and the adjacent concrete interface, facilitating the transfer of loads. Consequently, bond strength significantly influences the formation of cracks and the occurrence of failures under applied loads. Although extensive studies have explored the bond behaviour of steel RC structures under both static and dynamic loading, as well as FRP RC structures under static loading, limited research has delved into the bond behaviour of FRP RC structures under dynamic loading, particularly with regard to high strain rates induced by high-velocity impact loads.

Despite numerous studies on the bond behaviour of FRP RC structures under dynamic loads, particularly impact and blast loads, most of these investigations have concentrated on the overarching debonding failure of FRP RC structures, often simplifying the failure mechanisms and material characteristics of FRP. As a result, the performance of FRP in FRP RC structures may not be accurately represented under high-loading rate conditions [19] [20]. Therefore, it is crucial to consider the influence of strain rate effects and bond failures in the analysis of impact and blast scenarios.

1.3 Research gap

Several studies have explored the impact of strain rate on the bond behaviour and effective bond length of Fiber Reinforced Polymer (FRP) reinforced concrete members,[1] [21] [22]. These investigations have specifically considered the influence of strain rate and dynamic loading on the bond behaviour between FRP sheets or rebars and the concrete interface. However, one significant area that has received limited attention is the response of internal FRP-reinforced concrete structures when subjected to high impact loads. Furthermore, existing design

guidelines predominantly focus on steel-reinforced concrete structures under impact loading conditions, [23] [24] [25]. As of the present day, there are no established guidelines or recommendations for the design of FRP RC structures exposed to impact loading. Additionally, only a handful of studies have explored the behaviour of FRP RC beams under impact loads, [2] [26] [27]. These studies have primarily concentrated on glass FRP RC beams subjected to low-velocity impact loads, considering factors such as reinforcement ratio and concrete compressive strength.

Notably, no study to date has investigated the response of Carbon Fiber Reinforced Polymer (CFRP), Aramid Fiber Reinforced Polymer (AFRP), and Glass Fiber Reinforced Polymer (GFRP) RC beams to high-velocity impact in a large-scale context. Furthermore, there is a dearth of research examining the behaviour of FRP RC beams under conditions of high strain and high-velocity impact loads.

This thesis contributes by presenting numerical simulations of AFRP, CFRP, and GFRP RC beams subjected to high-strain, high-impact loads. Additionally, it explores the impact response and its influence on the bond behaviour of carbon, aramid, and glass FRP RC beams using modelling techniques within the ABAQUS software platform.

1.4 Aim and Objectives of the research

The primary objective of this research is to investigate the bond behaviour of Fiber Reinforced Polymer (FRP) bar reinforced concrete beams under conditions of high-strain dynamic loading. To accomplish this overarching goal, the study is structured around the following specific objectives:

- Conduct a comprehensive review of the existing literature pertaining to the bond behaviour between FRP and the concrete interface. This review will encompass both static and dynamic loading scenarios, encompassing pull-out

and direct beam tests. The aim is to identify various variables and mechanisms governing bond transfer in FRP RC structures.

- Develop a numerical model capable of examining the principal factors influencing bond behaviour. These factors include the type of fibres, bar diameter, Young's modulus of the FRP material, concrete compressive strength, and strain rate. Based on the numerical outcomes, the study seeks to elucidate the influence of these variables on bond-slip and bond failure in FRP models. The research aims to formulate equations for predicting the bond behaviour of FRP RC beams and validate these predictions by comparing them with numerical results on parameters such as slip, maximum bond strength, and deflection.
- Create a numerical model that accounts for slip rate dependency, enabling the simulation of bond behaviour in FRP RC beams while considering concrete Dynamic Increase Factor (DIF). This model should be flexible enough to accommodate variations in the bond behaviour of different types of available FRP materials through the incorporation of user-defined bond-slip laws. Additionally, the model should offer versatility to adjust material properties. The final model will be utilized to analyse how bond and mechanical variables impact the bond behaviour of FRP RC beams under varying impact loading conditions.

The research methodology employed in this study strives to closely emulate the actual behaviour of beams and the impact events they experience. Furthermore, three-dimensional models of the beams have been constructed to account for non-symmetry effects, including variations in support conditions. Additionally, the FRP bars have been individually modelled to consider the influence of strain rate and reinforcement on the localized response of beams, incorporating rate dependency into the analysis.

1.5 Research Significance

Over the past decade, numerous experimental and numerical investigations have been undertaken to gain insights into the bond behaviour under both static and dynamic loading conditions. These studies have yielded various design recommendations. However, it is important to note that only a limited number of studies have addressed the bond behaviour of Fiber Reinforced Polymer (FRP) Reinforced Concrete (RC) members under dynamic loading, and there is a notable absence of publications that examine the influence of specific parameters, such as the Young's modulus of FRP bars, on the bond behaviour of FRP RC beams subjected to high strain-rate, high-velocity impact loading.

This study holds significant importance for several reasons:

- The outcome from this study will deliver valuable numerical results for concrete beams reinforced with CFRP, AFRP and GFRP bars and would provide a better understanding of performance of different FRP types on bond behaviour of FRP RC beams under high strain rate loading.
- The numerical investigation provided the effect of high strain rate, high velocity impact loading on bond behaviour of FRP RC beams including different variables: FRP bar's Young's modulus, concrete compressive strength, bar diameter, and high velocity impact load. The results will determine the load transfer and bond-slip behaviour of FRP RC beam under high velocity impact loading.
- Regression analysis provided equations with specific coefficients to predict slip, maximum bond strength, and mid-deflection for FRP RC beams under impact loading. The study will determine design stress and DIF for FRP RC beams. The presented information in this thesis is valuable for designers using FRP bars as reinforcement and also for the expansion of design guidelines.

1.6 Innovation and Contributions

The investigation conducted in this study has resulted in several notable accomplishments and contributions in the field of innovation and engineering. These findings are presented in a more detailed narrative form as follows:

One significant achievement of this study involves the effective modelling of Fiber Reinforced Polymer (FRP) reinforced concrete beams within a beam test simulation. This modelling incorporates a rate-dependent bond-slip model and is capable of simulating both static and dynamic scenarios. The outcomes of these simulations were meticulously validated against existing experimental tests, demonstrating a high degree of concordance between the simulated and observed results.

A key contribution of this research is the development of an equation derived from a comprehensive examination involving 225 detailed finite element analyses of FRP reinforced concrete beams. This equation serves to predict slip, reaction forces, and deflection in relation to four distinct parameters and their corresponding coefficients, which are presented in Chapter 5.8. These coefficients were derived through a multi-way analysis of variance (ANOVA) for each specific scenario.

Furthermore, the study introduced a novel strain rate-dependent model aimed at achieving Design Impact Factor (DIF) objectivity in finite element modelling of FRP reinforced concrete beams under high-strain impact loads. This model represents a significant advancement in the field.

An interesting observation emerged from the research findings, specifically concerning the dynamic increasing factor. It was noted that this factor is approximately 5.3-8% higher in Aramid Fiber Reinforced Polymer (AFRP) bars when compared to Carbon Fiber Reinforced Polymer (CFRP) and Glass Fiber Reinforced

Polymer (GFRP) bars under impact loading conditions, shedding light on material-specific behaviour.

The study went further to comprehensively compare all local and global responses of FRP reinforced concrete beams with data from existing experimental works. This comprehensive analysis revealed a robust coordination and agreement between the model results and experimental observations.

The development of a strain-load dependent 3D model marks a noteworthy contribution to the field. This model is designed to simulate FRP bond-slip behaviour, pull-out, and de-bonding failure, particularly under high impact loads. It represents a pioneering effort in the simulation of these complex behaviours.

In addition to the above, a novel equation was derived to predict slip, reaction forces, and deflection of FRP reinforced concrete beams, and due consideration was given to the coefficients developed in the process, adding a valuable tool to the field of engineering analysis.

Finally, a significant milestone was achieved by determining the design stress for FRP reinforced concrete beams under the influence of high strain rates and impact loads. This determination was based on an extensive dataset obtained from simulating FRP reinforced concrete beam models and providing DIF values for AFRP, CFRP, and GFRP bars under various loading durations, contributing to the advancement of structural design practices in this context.

1.7 Outline of the work

This study consist of seven subsequent chapters that is arranged as follow:

Chapter 1 presents a general background of FRP material and discussion of the problems, the aim and objectives of this study, research significance and the brief outline of this research.

Chapter 2 presents a precise review of FRP bars as materials, their mechanical properties and use in structures, the bond of FRP bars to concrete interface and bond mechanisms, the behaviour of FRP RC under impact loading, impact resistant design, and the solution of using FRP as reinforcement for RC beams under impact loads. This chapter provides a review on evolution of finite element models of FRP RC members.

Chapter 3 presents an overall description of finite element methods to simulate FRP RC beams including static and dynamic finite element model of FRP RC beams and validating results by comparing to experimental test results, [3] [28]. Moreover, it includes constitutive models for concrete and FRP, interfacial interaction between FRP bar and surrounding concrete, finite element meshing and boundary condition approach, and loading and increment size scheme applied in simulation.

Chapter 4 presents a detailed description of the finite element models of FRP RC beams. Each phase of developing the numerical model was presented, importantly, the bond-slip model, material properties, beam geometry, and other functions used in this simulation.

Chapter 5 the results from numerical investigation of FRP RC beams under different type of loading presented. The bond behaviour and FRP RC beam response under high velocity impact load captured and extensive discussion provided. In addition, a parametric study was considered to examine the influence of various parameters on bond behaviour and response of FRP RC beams under impact loading. A regression analysis conducted based on numerical results to predict behaviours of FRP RC beams under high velocity impact loads.

Chapter 6 additional FE models developed to investigate strain rate dependency of FRP bars under impact loads. A DIF table produced for FRPs based on conditions in this thesis to calculate design flexural strength for FRP reinforced concrete beams and compare with design codes.

Chapter 7 reviews the entire thesis, thus provides conclusions from the study. Recommendations on future works are made to emphasis areas of further investigations and help better understanding of behaviours of FRP RC beams under impact loads.

Appendix A contains the extra tables and figures for Chapter one to three.

Appendix B provides tables and figures for Chapter four.

Appendix C provides tables and figures for Chapter five to six.

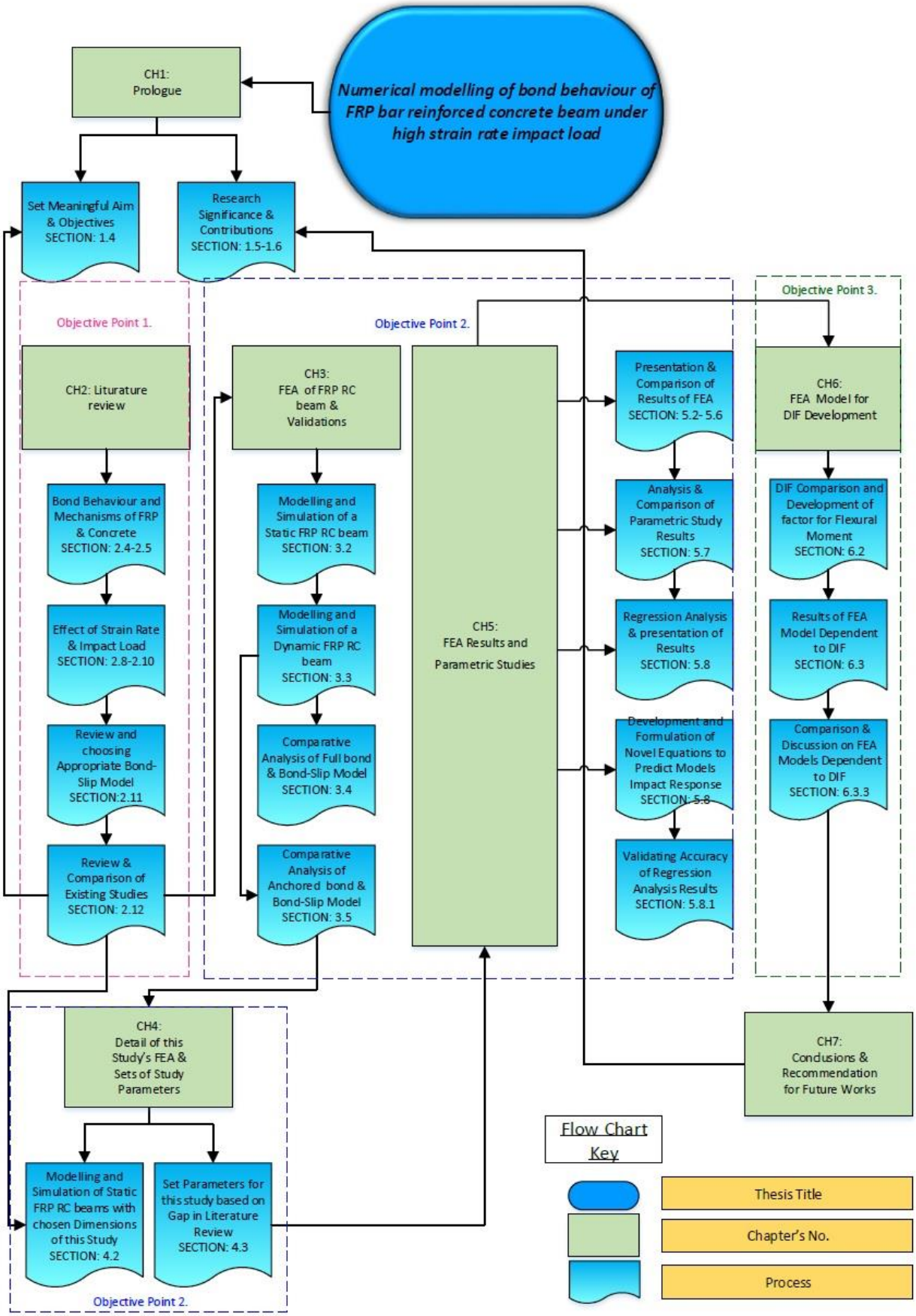

Figure (I): Flow Chart for Thesis work.

Chapter 2: Literature review

2.1 Introduction

Before the 1840s, concrete was employed in construction for substantial structures like robust walls, foundations, and bridges owing to its high resistance to compression forces. However, concrete's inherent weakness in tension led engineers in the early 19th century to innovate a novel approach: incorporating internal steel bars within concrete. This combination, known as reinforced concrete (RC), bolstered the material's tensile strength. Nonetheless, utilizing steel bars as reinforcement in concrete presented challenges, particularly related to corrosion. Even concrete it could not prevent the corrosion of embedded steel bars, resulting in structural deterioration induced by moisture penetration into the concrete. Engineers experimented with various methods to mitigate steel bar corrosion, including techniques such as galvanized coating, power resin coating, and polymer-impregnated concrete epoxy coating., [29].

In the mid-19th century, Fiber Reinforced Polymer (FRP) bars emerged as an alternative to steel bars in concrete structures. They became a feasible choice for internal reinforcement in concrete, particularly when industries sought non-ferrous reinforcement for applications requiring non-magnetic composite materials. The increasing interest in FRP bars for structural use prompted extensive research into their properties and behaviour in various environments.

However, despite the growing body of research on FRP bars, there remain certain factors related to concrete reinforced with FRP bars under specific conditions that have not received adequate investigation. The literature review provided in this chapter offers an overview of prior studies concerning the overall behaviour of FRP materials and the impact of high strain rates on the bond behaviour of FRP RC beams. In this chapter, we delve into the specifics of FRP bars, their material properties, concrete and its material characteristics, and the influence of various factors on the bond behaviour between FRP and concrete.

2.2 Fibre-reinforced polymer

2.2.1 General

Fiber Reinforced Polymer (FRP) comprises fibrous materials enveloped within a polymer matrix. The synergy of these two constituents offers several advantages to structural elements. The fibrous component of FRP contributes stiffness and strength to the structure while effectively transferring the majority of the applied load. Simultaneously, the surrounding polymer matrix serves a protective role by safeguarding the fibres and bearing the applied stresses [30].

In the early 1950s, conventional materials fell short of meeting the rigorous demands of the aerospace industry, prompting researchers to explore novel approaches. After numerous endeavours, scientists succeeded in developing a composite material composed of robust fibres encased within a polymeric matrix. This innovative composite was termed "fibre reinforced polymer" (FRP) and brought several advantages compared to traditional metallic reinforcement. These merits encompassed corrosion resistance, reduced weight, high tensile strength, electromagnetic transparency, and the capacity to tailor mechanical properties by selecting various fibre types, orientations, and constituent compositions. These attributes positioned FRP as a viable and versatile option across a myriad of applications in diverse industries, [31].

Fiber Reinforced Polymer (FRP) emerged as a pivotal material in the aerospace industry, renowned for its lightweight properties coupled with exceptional strength and stiffness. Its success in the aerospace sector paved the way for its adoption across diverse industries including naval, sports goods, and military applications, [32]. The utilization of FRP for reinforcing concrete materials dates back to the 1960s and 1970s, with notable advancements in the United States, Europe, and Japan, [33] [34] [35]. However, it was in the late 1980s that FRP truly gained prominence in research, industry, and commercial applications. Various types of fibres, such as Carbon, Glass,

aramid, and recently Basalt, have been employed in FRP bars as alternatives to traditional glass fibres. These fibres are bound together by a matrix that provides protection and coverage. The matrix effectively transfers applied shear stresses from one fibre to another, facilitating load distribution and reinforcement within the material, [30].

Matrices in Fiber Reinforced Polymer (FRP) are typically composed of resins like epoxies, vinyl esters, or polyesters that have undergone thermosetting processes. Among these, epoxy stands out as the most commonly employed matrix, particularly in conjunction with carbon fibres.

The manufacturing techniques for FRP encompass pultrusion, weaving, and braiding, yielding a variety of cross-sectional shapes, including solid profiles. Nevertheless, the most prevalent cross-sectional shape for FRP remains circular. During the manufacturing process, FRP bars are bent and tested, as once the resin cures, these bars become rigid and lose their flexibility. To enhance the mechanical bond between FRP bars and concrete, the surface of FRP bars undergoes deformation or texturing through methods such as sand coating or fibre winding.

One of the notable advantages of FRP is its high tensile strength. Research has indicated that the size of FRP bars directly influences their longitudinal tensile strength due to the phenomenon of shear lag, [36].

In an effort to mitigate uncertainties regarding the performance of FRP, various test methods have been developed to characterize and assess the properties of FRP reinforcements. These test methods are informed by insights gleaned from extensive research endeavours. Table (1) provides an overview of the documents that have introduced diverse test methods on a global scale.

Year	Title	Country	Description
1996	JSCE- Recommendation for design and construction of concrete structures using continuous fibre reinforcing materials	Japan	First guidelines introduced test methods for quality control and inspection of FRP-rebar
1999	ASTM- ISO composite materials handbook	US	Test methods for FRP composites for civil structures
2002	CSA- Design and construction of building components with fibre-reinforced polymers	US	Methods of model test for FRP bars
2004	ACI 440-3R: Guide test methods for FRPs for reinforcing or strengthening concrete structures	Canada	Testing procedures for FRP composites

Table 1: documents for test methods of FRP composites for civil structures, [31].

Over the past 20 years, studies and experimental investigations showed that FRP is a viable option to be used particularly as inner reinforcement in concrete structures. Fibre reinforced polymer bars are produced with different manufacturing techniques and mechanical properties from steel bars that are explained in more details in following sections.

2.2.2 FRP bar

An FRP bar is composed of continuous fibres known for their elasticity and brittleness, coupled with remarkable strength. These fibres are enveloped by a matrix crafted from thermosetting resins. The fabrication of FRPs offers a spectrum of options, with various types of fibres and resins available for selection. When external loads are applied to FRP bars, the fibres bear the brunt of these forces. Concurrently, the resin performs the crucial role of holding the fibres together, safeguarding them, and facilitating the transmission of stresses from one fibre to another while lending lateral support to prevent buckling. The combination of factors including the volume of employed fibres relative to the overall composition of the FRP and the specific type of fibre chosen profoundly influences the bar's strength and stiffness. Additionally,

the type of resin utilized in the FRP formulation significantly impacts fracture toughness and the mechanisms governing failure in the material.

FRP bars represent anisotropic materials and can be manufactured using various methods, with pultrusion being the most prevalent. In FRP composites, the fibres, which are notably stronger than the resin material, impart crucial mechanical properties, including Young's modulus and strength. The ultimate mechanical characteristics of the resulting FRP bars are influenced by a range of factors. These encompass the chosen manufacturing techniques, the orientation of the fibres, the degree of resin curing, and the effectiveness of quality control and inspection measures implemented throughout the manufacturing process.

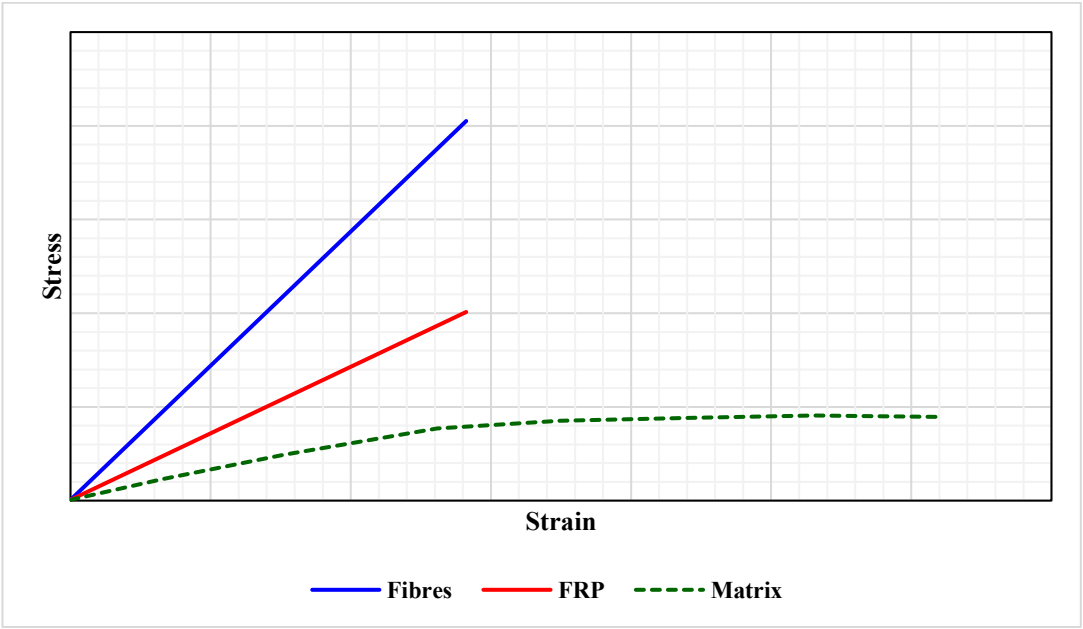

Figure 3: Stress-strain relationships for fibres, FRP and matrix, re-produced from, [37]

2.2.3 Fibres

Most common fibres used in FRP composites are Carbon, Glass, Aramid and basalt. Carbon fibres have higher strength compare to Glass fibres, but most of the structural works use glass fibre because of economic cost of it over carbon fibre. Recently basalt fibres are used as alternative option for glass fibres. Typical material properties of different fibres and comparison with steel bar is presented in Table (2).

Glass fibres

Glass fibres, readily available in the industrial sector, are primarily derived from silica sand and can be manufactured in the form of continuous strands or filaments with varying diameters. They are offered in diverse grades, such as E-glass (electrical), C and S-glass (high strength), AR-glass (alkali- resistance). These distinct grades are distinguished by their specific attributes; for instance, E-glass fibres exhibit significant electrical insulation properties, while S-glass fibres excel in composite materials, particularly in terms of strength, [38] [39]. In comparison to other fibre types, glass fibres boast notable characteristics, including high chemical resistance, minimal flammability, and strong resistance to fire. They exhibit impressive strength, ranging from 483 to 1600 MPa, and, in the event of thermal degradation, Glass Fiber Reinforced Polymer (GFRP) materials produce reduced quantities of carbon monoxide and smoke. These exceptional properties have positioned glass fibres as a preferred choice for applications in ceiling panels and structural flooring. Moreover, they serve as an alternative to carbon fibres, enhancing construction safety and cost-effectiveness, [40] [41] [42].

Carbon fibres

Carbon fibres, which are derived from either Polyacrylonitrile fibres (commonly referred to as PAN) or pitch-based fibres, can be manufactured in various formats, including continuous filaments, mats, and chopped fibres. These carbon fibres possess an impressive modulus of elasticity ranging from 120 to 580 Giga Pascals (GPa) and exhibit high tensile strength, typically falling between 600 and 3690 Mega Pascals (MPa). They also boast a range of additional exceptional properties, including a high strength-to-volume ratio, resistance to corrosion and fatigue, effective vibration damping, low thermal expansion, and electrical conductivity, [45]. The remarkable attributes of carbon fibres have resulted in their utilization in multiple applications, such as earthquake-resistant materials in reinforced concrete, aerospace industry components, and sporting goods, [46]. It's worth noting that carbon fibres are crafted from high-quality materials, contributing to their relatively elevated cost. However, their high stiffness can render them more brittle when

subjected to loads in comparison to other fibres like Glass, aramid, or basalt fibres, [42].

Property	CFRP	GFRP	AFRP	BFRP	Steel
Density, (g/cm^3)	1.50 to 1.60	1.25 to 2.10	1.25 to 1.40	2.7	7.90
Longitudinal CTE, α_L ($\times 10^{-6}/°C$)	-9.0 to 0.0	6.0 to 10.0	-6 to -2	*	11.7
Transverse CTE, α_T ($\times 10^{-6}/°C$)	74 to 104	21.0 to 23.0	60.0 to 80.0	*	11.7
Nominal yield stress, (MPa)	N/A	N/A	N/A	N/A	276 to 517
Tensile strength, (MPa)	600 to 3690	483 to 1600	1720 to 2540	2800 to 4800	483 to 690
Elastic modulus,(GPa)	120 to 580	35 to 51	41 to 125	86 to 90	200
Yield strain, %	N/A	N/A	N/A	N/A	0.14 to 0.25
Ultimate tensile strain,%	0.5 to 1.7	1.2 to 3.1	1.9 to 4.4	3.1	15 to 20

Table 2: Properties of steel and different fibres, [43] [44]

Basalt fibres

Basalt fibre, a relatively recent addition to the Fiber Reinforced Polymer (FRP) landscape in comparison to glass and carbon fibres, is derived from basalt rock. The

manufacturing process for basalt fibres mirrors that of glass fibres, beginning with the excavation, crushing, washing, and subsequent melting of basalt rock at 11500℃, [47]. Following this, molten basalt rocks are extruded through small nozzles to produce continuous filament basalt fibres. An important cost advantage is realized in the production of basalt fibre as it does not require the addition of any other substances. Basalt fibre exhibits a tensile strength ranging from 2800 to 4800 Mega Pascals (MPa), surpassing that of glass fibre. This remarkable strength, coupled with its resistance to high temperatures, excellent fire resistance, and capacity to withstand impact loads, positions basalt fibre as a promising candidate for use in FRPs and composite structures. Additionally, since basalt fibres are derived from basalt rock, they can be considered a sustainable material. Nevertheless, the application of basalt fibres in civil engineering contexts within FRPs remains less widespread compared to carbon, glass, and aramid fibres.

Aramid fibres

Aramid fibres represent a class of synthetic organic fibres that were initially introduced under the trademark names Kevlar and Nomex. When combined with resins, aramid fibres yield high-performance composites characterized by a remarkable fracture energy, making them particularly well-suited for applications in which energy absorption by the fibres, such as during impact loads or blast events, is critical. Aramid fibres exhibit tensile strength and modulus values that surpass those of glass fibres by approximately 50% [48]. These fibres possess a low density within the range of 1.2 to 1.4 (g/cm^3) and exhibit favourable thermal and electrical insulation properties. However, it's important to note that aramid fibres are comparatively lacking in compressive strength. One of their notable attributes is their high fire resistance, especially when compared to inorganic fibres like carbon and glass fibres, owing to the fact that aramid fibres do not conduct heat into the matrix. To provide specific figures, the tensile strength of aramid fibres typically ranges from 1720 to 2540 (MPa), with a Young's modulus between 41 and 125 (GPa), [39] [49].

2.2.4 Matrices resin

Resin matrices in composite materials are typically categorized into two main classes: thermoplastic resins and thermoset resins. Thermoset resins are either low-melting-point solids or exist in liquid form. They undergo curing through a combination of heat and a catalyst. Once thermoset resins have completed their curing process, they cannot revert to their original liquid state under the influence of heat or pressure. In contrast, thermoplastic resins possess the unique ability to return to their original liquid or low-melting-point solid state when subjected to heating and pressure. Thermoset resins offer several advantages, including excellent viscosity control at handling temperatures and minimal shrinkage during the curing process, [50]. Among the most commonly employed thermosetting resins in composite applications are Epoxies, Polyesters, and vinyl esters. Throughout the manufacturing process, additives and fillers may be incorporated into the resin mixture to enhance composite performance, modify specific characteristics, and reduce production costs, [43].

Epoxy resin

Epoxy resins are widely favoured for their exceptional mechanical properties, minimal shrinkage during processing, ease of handling, and their ability to form strong bonds with a wide range of fibres. They exhibit excellent resistance to both heat and water, boast high corrosion resistance, and can be effectively combined with other adhesives to tailor specific performance attributes. However, it's important to note that the relatively high cost of epoxy resins and their propensity to absorb moisture during the curing process and afterward can pose challenges for long-term performance, [39] [43].

Polyester resin

Polyester resins, on the other hand, offer a well-rounded combination of mechanical, chemical, and electrical properties. Their advantages include cost-effectiveness, favourable electrical and mechanical performance, and the capacity for chemical modification to fine-tune performance characteristics and dimensional stability. Consequently, polyesters stand out as a viable resin choice. However, they are not particularly adept at forming strong bonds with carbon and aramid fibres, making

them less suitable for use in FRP bars due to their comparatively lower chemical resistance when compared to other resin options, [39].

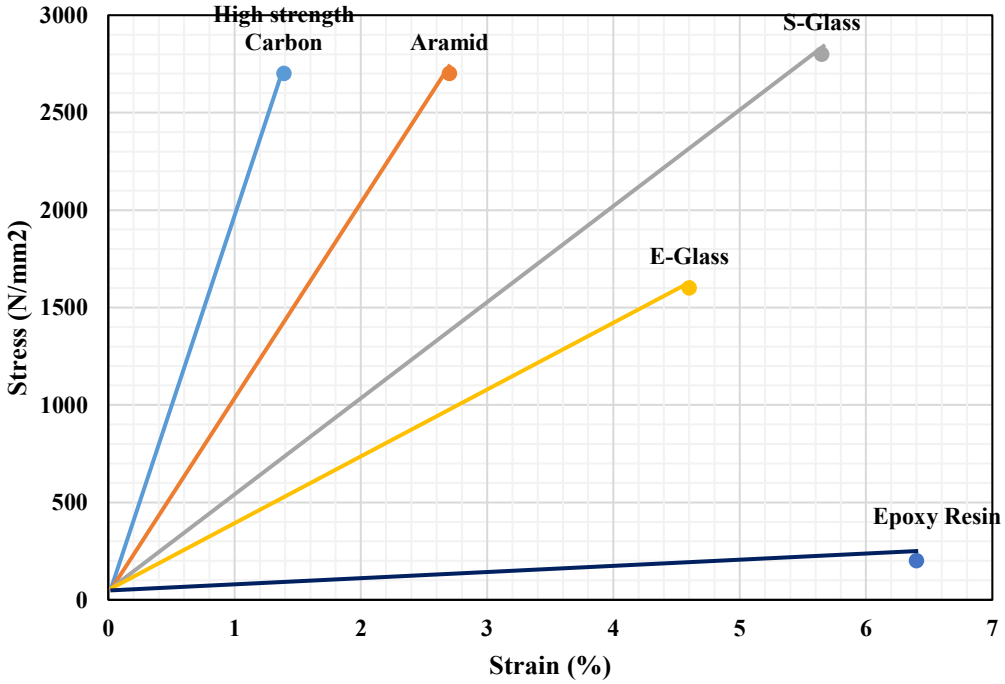

Figure 4: Relationship of stress and strain of selected fibres t their failure, [51]

Vinyl esters

Vinyl esters have fast curing time same as Polyester and high strength and chemical resistance as epoxy resins. Vinyl esters have excellent adhesion with glass fibres and consequently this resin made a primary choice for glass-FRP manufacturing. Alkali resistance and good wet-out are other advantages of Vinyl esters resin, [43].

Property	**Resin matrices**		
	Epoxy	Polyesters	Vinyl-ester
Density, (Kg/m3)	1200-1400	1200-1400	1150-1350
Tensile strength, (MPa)	55-130	34.5-104	73-81
Poisson's ratio	0.38-0.40	0.35-0.39	0.36-0.39
CTE, (10-6/C)	45-65	55-100	50-75

Table 3: Properties of thermosetting resins, [52]

2.3 Manufacturing and Characteristics of Fibre Reinforced Polymer

Despite the numerous advantages offered by FRP reinforcement, it cannot serve as a direct replacement for conventional steel bars due to distinct differences in their physical and mechanical properties. The reasons behind the limited adoption of FRP bars as internal reinforcement in structural composites can be classified as follows:

- Ductility and Failure Behaviour: FRP materials exhibit low ductility, displaying linear elastic behaviour when subjected to tensile forces in the direction of the fibres until the point of failure is reached. Consequently, FRP materials lack a yield point before failure.
- Young's Modulus: The Young's modulus of FRP bars, such as AFRP and GFRP, is lower compared to steel bars. This necessitates the use of a larger number of FRP bars within a structure to control crack width and deflection effectively.
- Bond Behaviour: The bond behaviour between FRP and concrete differs from that between steel and concrete due to variations in surface texture and the anisotropic material properties of FRP bars.
- Economic Factors: The cost of steel is generally more economical than that of FRP. Additionally, a lack of comprehensive knowledge regarding the behaviour of FRP in structures, coupled with incomplete incorporation of FRP as a reinforcement in design codes, has hindered the widespread adoption of FRP as a new reinforcement material in concrete structures, [53].

The geometric cross-section of FRP reinforcing bars plays a significant role in their performance, as does the surface texture of these bars. FRP bars and one-dimensional FRP reinforcements are typically manufactured through processes such as pultrusion or other similar methods like pull-forming. Pultrusion is a continuous melding process that combines fibre reinforcement and resins. This process is particularly suitable for composites with a need for continuous fabrication and a consistent cross-sectional shape, such as bars. In this process, fibres are drawn through a liquid resin bath to ensure thorough impregnation of all the fibres. Prior to this stage, the fibres are carefully separated to guarantee uniform mixing with the thermoset resin. The impregnated fibres with resin are then directed through a metal

die to define the bar's size and to apply surface textures, such as sand coatings, in preparation for the subsequent stage - curing in an oven. In the curing oven, controlled heat is applied to transform the resin from a liquid to a solid state. The resulting bar emerges from the curing oven at the desired size and is cut into the specified lengths, [43].

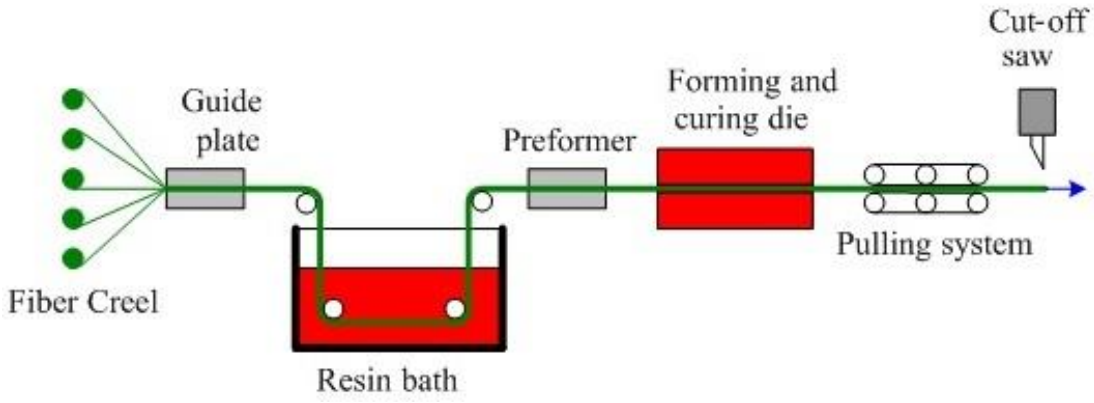

Figure 5: pultrusion process of manufacturing FRP bars, [54].

Duration of pultrusion process depends on the length of FRP bar. Different size of final bar can change the time of this procedure and normally it would take about 0.91m per minute. In order to applicate FRP bars in structural applications, FRP bar must be produced and used to its full possible performance. That means FRP bars must be able to take loads fully to their breaking point under ultimate state conditions and place correctly in composite member. As if FRP bars replace directly instead of steel bars in concrete, they are not have the same performance because of concrete low tensile strain capacity approximately around 0.35%, whereas FRP high tensile strain capacity of around 1.5%, [55].

Advantages of different FRP bar's surface texture and geometry of cross-sections are as presented below. Table (5) consider in more details about circular cross section as it is chosen for research in the present paper. Typical physical properties of FRP bars are mentioned in table (2). Density of FRP bars is about quarter to one-sixth of steel bar's density that results in lower transportation costs and easy-handling of FRP bars on project site, [44]. The coefficients of thermal expansion (CTE) of FRP bars alter in transverse and longitudinal directions and get influence by types of fibre, resin type and volume fraction of elements.

Type of Fabrication	Advantages	Products
Casting	Flexibility in Design, (Shape, Colour)	Sinks
	Usually chosen for non-structural parts	Tubs
	Suitable for small-run parts, Low-Priced Molds	Counter Tops
Lay-up/ Spray up	Suitable for small-run parts	Tanks
	Chosen for Complex Designs	Building Facades
Infusion/ RTM	Suitable for Mid to high Volume	Furniture
	Chosen for Complex Designs	Building Facades
	for Consistent parts	
Continuous Panel	Suitable for High Volume	Building Cladding
	Restriction on Physical Design	Light Panels
	Special Fabrication for Continuous Panels	
Pultrusion	Suitable for Continuous, Linear parts	Bars
	High volume	Window Lineal
	Moderately Flexibility in Design	Hand Rails
Press Molding	Very High Volume	Door Surface
	Suitable for Complex Designs	Appliance Bodies

Table 4: Different types of Fabrication for FRP Material, [56]

Table (2) provides a comprehensive overview of various mechanical properties associated with FRP bars, including ultimate tensile strain and tensile strength. Notably, when subjected to tension, FRP bars do not exhibit yielding behaviour before failure occurs. Consequently, the tensile behaviour of FRP bars is distinguished by a linearly elastic stress-strain relationship that persists until rupture. In direct comparison with steel bars, FRP bars exhibit a higher tensile strength but possess a lower modulus of elasticity and ultimate tensile strain, primarily attributable to the absence of yielding behaviour. It's important to note that the tensile strength of FRP bars undergoes alterations with variations in bar diameter, although this does not influence the longitudinal modulus due to the presence of the shear lag phenomenon.

A good composite is the one that effectively transfer applied loads from reinforcements to concrete. Therefore, the most important mechanical property for FRP bars is bond behaviour to concrete.

Geometry of Cross-section	Surface Texture	Feature
Circular	Roughed surface; (grained covered, sand-coated, etc.)	Improve bond adhesions and friction between FRP and concrete.it leads to increase bond strength.
Circular	Ribs and Grooves	Increase mechanical interlock.
Non-Circular	Rough and Smooth surface	increase the cross-sectional area of outer surface in order to improve ratio of bond and tensile strength by mechanical interlock

Table 5: Patents of FRP bars in three groups, [15] [53]

2.4 Mechanical Properties of Fibre-Reinforced Polymers

An important consideration in applications involving the use of fibre-reinforced polymers (FRP) as reinforcement lies in understanding the impact of high strain rate loading on the mechanical properties of FRP. There has persistently been concern that composite material properties might exhibit subpar performance under conditions of high strain rate loading. Consequently, extensive research endeavours have been undertaken to investigate how the mechanical properties of FRPs may be influenced by strain rate. This research aims to ensure the design of structures that do not prematurely or unpredictably fail under high-rate loading conditions. Furthermore, characterizing the dynamic mechanical properties of FRP reinforcement serves to validate the feasibility of using FRPs as weight-efficient reinforcements for applications subjected to high-rate dynamic loads. In the following section, we present a review of published studies that examine the effects of strain rates on various mechanical properties of FRP composite materials, encompassing tensile, dynamic modulus, shear, compressive, and flexural properties, as detailed in Table (47) in appendix (A).

Davies and Magee [57] conducted a study to examine the impact of strain rate on the ultimate tensile strength of glass/polyester composites. Their findings revealed that the glass/polyester combination exhibited rate sensitivity, with an increase in the strain rate resulting in a 55% increase in the magnitude of ultimate tensile strength. Rotem and Liftshitz [58] investigated the strain rate effect on the tensile strength

properties of unidirectional glass fibre-reinforced polymer (GFRP) with an epoxy mixture. Their results demonstrated that dynamic tensile strength exceeded static strength by a factor of three, and the dynamic modulus was 50% greater than the static value.

In a separate study by Liftshitz [59], which focused on angle-ply glass/epoxy laminates, it was found that the elastic modulus remained unaffected by strain rate, and dynamic stress failure exceeded the static value by only 20 to 30%. Okoli and Smith [60] [61] delved into the effect of strain rate on the tensile properties of glass/epoxy composites, noting that tensile strength was influenced by strain rate, and the increase in tensile strength was attributed to the enhanced strength of glass fibres with increasing strain rate. Another study by Okoli and Smith [62] examined the effect of strain rate on the tensile, shear, and flexural behaviour of glass/epoxy laminates. They observed a 9.3% increase in tensile strength and a 1.82% increase in tensile modulus for each decade increase in the logarithm of the strain rate.

Armenakas and Sciamarella, [63] conducted an experimental study that aligned with the above observations. Their results demonstrated a linear variation of the tensile modulus of unidirectional glass/epoxy fibre-reinforced polymer with the logarithm of the strain rate. Furthermore, they indicated a change in failure modes with increasing strain rate, with a noticeable increase in energy absorption.

Harding and Welsh [64] [65] employed a dynamic tensile technique to assess various composites, including graphite/epoxy, glass/epoxy, graphite/polyester, glass/polyester, and Kelvar/polyester, over a strain rate range of 10^(-4) to 1000 s^(-1). For graphite/epoxy, properties such as modulus, failure stress, and failure mode were found to be insensitive to strain rate. In contrast, dynamic modulus and strength for glass/epoxy were twice the static values. The same trend was observed for glass/polyester, graphite/polyester, and Kelvar/polyester, where the elastic tensile modulus increased with an increase in strain rate.

Shim [66] investigated the effect of strain rate on the tensile properties of short carbon fibre-filled liquid crystalline composites under static loading at 10^(-2) s^(-1) and dynamic loading at 400 s^(-1). The study revealed that the Young's modulus and

fracture strain of the composite were significantly influenced by variations in strain rate.

Bai [67] explored the strain rate effect on the tensile properties of glass bead/high-density polyethylene (HDPE) composites. Their results indicated that both Young's modulus and tensile strength of glass bead/HDPE increased with an increase in strain rate.

Daniel [68] examined the impact of high strain rate on the dynamic response of carbon/epoxy composites using three different test methods. In longitudinal loading, the modulus increased by 20% compared to the static value, with no significant changes in ultimate strain and strength. In transverse loading, both modulus and strength increased significantly, while ultimate strain showed a marginal increase. In in-plane shear loading, the modulus and strain increased by 30%.

Additionally, Hayes and Adams [69] conducted an experimental study involving pendulum impact testing to investigate the strain rate effect on the tensile properties of unidirectional glass/epoxy and graphite/epoxy mixtures. They found that the modulus and strength of glass/epoxy composites remained insensitive to strain rate, whereas the modulus and strength of graphite/epoxy composites decreased with increasing impact speed.

Daniel and Liber [70] [71] explored the effect of strain rate on the mechanical properties of unidirectional composites, including glass/epoxy, boron/epoxy, and Kelvar/epoxy. Their results showed a 20% increase in tensile modulus and failure strength of Kelvar/epoxy in the fibre direction over a strain rate range of 10^(-4) to 27 s^(-1). Under transverse and shear loading, modulus and failure strength of Kelvar/epoxy increased by 40% and 60%, respectively. However, glass/epoxy and boron/epoxy were found to be insensitive to changes in strain rate.

Kawata [72] [73] investigated the effect of strain rate ranging from 10^(-3) to 2000 s^(-1) on the tensile properties of glass/epoxy, glass/polyester, graphite/epoxy, and graphite short fibre-reinforced nylon composites. The results indicated that the

strength of graphite/epoxy and graphite nylon composites increased with increasing strain rate, while the strength of glass/epoxy and glass/polyester decreased.

Peterson [74] examined the tensile properties of chopped glass-reinforced composites over a strain rate range of 10^(-3) to 10 s^(-1). An increase in strain rate led to a 50% to 70% increase in elastic modulus and strength for the composites.

Tzeng and Abrahamian [75] [76] [77] investigated the dynamic response of fibre composites in ballistic applications, specifically examining the dynamic effects on graphite/epoxy composites under projectile strain rates. Their experiments, employing an air gun system, showed a 10% increase in compressive strength at impact speeds ranging from 2.7 to 4.9 m/s. The ultimate strain under impact failure was measured at 1.5%, which exceeded the static ultimate strain of 1.1%.

Cazeneuve and Maile [78] examined the effect of strain rate ranging from 10^(-3) to 600 s^(-1) on the compressive strength response of unidirectional graphite/epoxy composite materials. They observed a 30% increase in compressive strength in the transverse direction and a 50% increase in longitudinal strength with increasing strain rate.

Numerous other studies have also investigated the effect of strain rate on the mechanical properties and dynamic response of fibre composite materials, as detailed in Table (47) in the appendix (A).

In order to establish FRP materials as widely accepted reinforcements in the structural industry, it is imperative to gain a comprehensive understanding of the bond between FRP bars and concrete. Further details regarding the bond behaviour of FRP and the influencing factors are expounded upon in section (2.5).

2.5 Bond Interaction between FRP bars to Concrete

2.5.1 General

The acceptance of FRP applications in large composite structures hinges upon a comprehensive comprehension of FRP's role as reinforcement and its interaction with the encompassing concrete. A secure composite structure is one where applied force are effectively transmitted from the reinforcements to the concrete, and this hinges predominantly on the bonding process between FRP and concrete. The bond performance between FRP bars and concrete exhibits variations compared to conventional steel bars. These disparities are a result of differences in interaction mechanisms and distinct material properties between FRP and steel. Several critical parameters influence the bond behaviour of FRP bars with surrounding concrete, notably the Young's modulus, shear stiffness, and resin matrix shear strength, all of which dictate the deformations' strength on the surface of the FRP bar.

2.5.2 Bond behaviour of FRP bar and concrete

Bond performance of FRP bar and concrete defers for different FRP bar surface configurations. Therefore, the bond behaviour alters for case of deformed, plain or surface treated bars, [79].

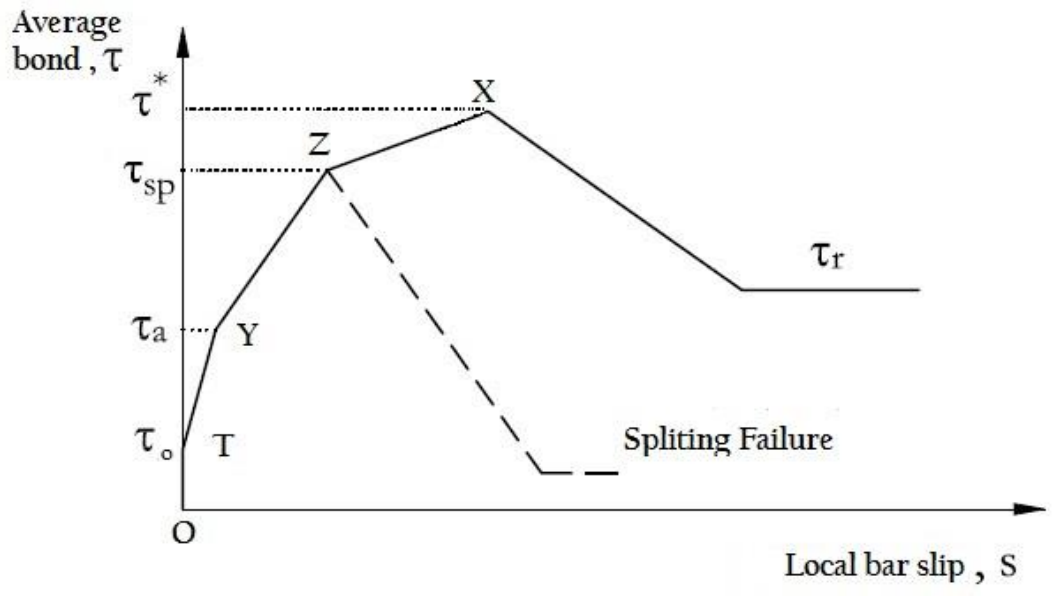

Figure 6: Typical local bond stress-slip curve of an FRP.

Scientists elucidate the interaction mechanisms between FRP bars and concrete through a pull-out test encompassing four distinct stages, as delineated by previous research [80], and visually represented in Figure (6).

Stage O-T: in this initial stage, characterized by low bond stress not exceeding the point τ_o, no measurable slip occurs between the bar and the encompassing concrete. During this phase, the dominant resistance mechanisms originate from the chemical adhesion between the bar and concrete, ensuring the bond's efficacy under external loads.

Stage T-Y: the escalation in bond stress triggers a breakdown in the chemical adhesion between the bar and concrete, giving rise to various mechanisms contingent on the surface configuration of the reinforcing bar. Deformations in the bar introduce bearing stresses within the adjacent concrete. As the principal tensile stress surpasses the tensile strength of the concrete, transverse microcracks form on the deformed bar's surface, initiating bar slippage.

Stage Y-Z: the increasing prevalence of microcracks characterizes the concrete's response to loading. Consequently, the concrete's stiffness decreases, resulting in more pronounced slip of the bar and heightened bearing stresses. The radial component emanating from the bar's surface deformation interacting with the surrounding concrete balances against concentric rings of tensile stresses developed within the concrete, as illustrated in Figure (7).

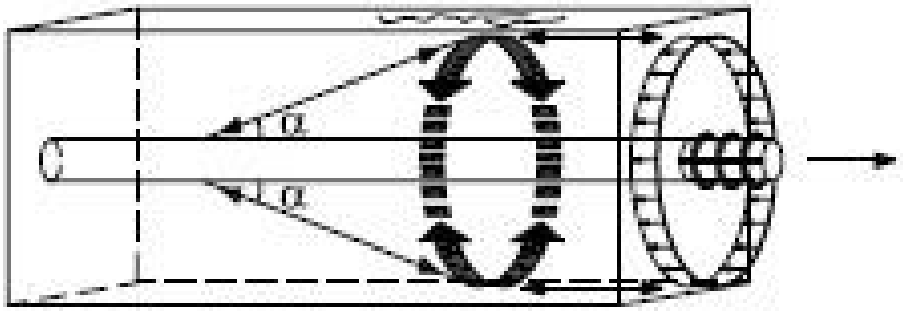

Figure 7: simplified portrayal of how radial component of the bond forces are balanced against tensile stress rings in the concrete, [81].

When the tensile hoop stress surpasses the tensile strength of the concrete, it initiates the formation of splitting cracks along the length of the reinforcing bar.

Stage Z-Y: in situations where the concrete exhibits high resistance to splitting, the bond stress can elevate to its maximum value, denoted as τ^*. During this phase, shear cracks commence, affecting either a portion or the entire length of the concrete ribs.

The final stage encompasses a solitary mechanism: frictional resistance between the reinforcement bar and the adjacent concrete surface, ultimately leading to shear failure, as detailed in prior research [81] [79].

The previous chapter presented the factors influencing bond behaviour of FRP RC members. The subsequent comparison of bond behaviour between Fiber Reinforced Polymer (FRP) and surrounding concrete under both static and dynamic loading conditions highlights the significance of recognizing these differences.

Under static loading conditions, the bond strength between FRP and concrete exhibited consistent and predictable behaviour. The gradual and sustained application of load enabled effective stress transfer across the interface, resulting in stable bond strength values through various test setups.

In contrast, under dynamic loading, bond strength displayed a wider range of variation. The rapid and instable nature of dynamic loads introduced stress concentrations and localized failures at the bond interface, making the bond performance less predictable.

About slip behaviour, static loading conditions led to slow and moderately even patterns. The onset of slip and the rate of slip development were distinct and consistent across various tests.

On the contrary, dynamic loading conditions resulted in abrupt and unpredictable slip behaviour. Slip in the specimens occurred more rapidly, and the rate of slip progression changed considerably across different tests. Dynamic loading often yielded higher peak slip values compared to static loading, indicating more pronounced slip behaviours under dynamic conditions.

Bond failure exhibited distinct characteristics under static and dynamic loading. In static loading, bond failure typically occurred within the adhesive layer or the FRP material itself, frequently displaying cohesive failure modes, such as de-bonding or delamination within the adhesive or FRP material.

Under dynamic loading, bond failures were more intricate, combining cohesive and adhesive failure modes. Rapid and cyclic loading induced fatigue-related damage at the bond interface, resulting in a mixture of cohesive and adhesive failures. This complexity made it challenging to predict the precise failure mode.

The observed differences in bond behaviour were influenced by several factors. Loading rate, particularly pronounced under dynamic conditions, significantly impacted bond strength, slip behaviours, and failure modes. Additionally, the duration and amplitude of dynamic loads played a critical role, with short-duration, high-amplitude loading tending to induce more severe bond failures and higher slip values compared to longer-duration, lower-amplitude loading.

2.5.3 Bond mechanisms between Concrete and FRP

As previously discussed, the bond mechanism governing the interaction between reinforcement bars and concrete is discernible through the bond stress-slip curve at distinct stages. In essence, three distinct mechanisms come into play: (I) Chemical adhesion, facilitating the connection between the bar and the surrounding concrete, (II) the mechanical interlock generated by the surface deformation of the bar, and (III) the development of frictional forces resulting from surface irregularities between the bar and the adjacent concrete.

In order to mitigate the risk of bond failure, it is imperative that the reinforcing bar is adequately anchored within the concrete or possesses adequate concrete cover and transverse reinforcement. Consequently, the tangential and radial stresses that manifest along the reinforcement bar remain within the capacity of the concrete, ensuring that the bar can attain and maintain its designed tensile strength. Through

the implementation of sufficient confinement or anchoring measures, the failure mode may manifest in alternative forms such as concrete crushing, shear failure, or bar rupture, as established by prior research [82].

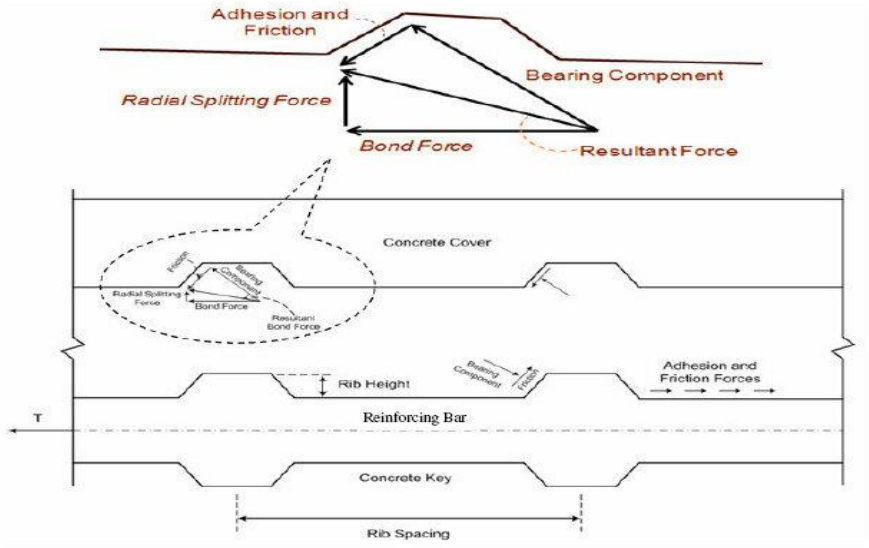

Figure 8: Bond between FRP bar surface and concrete with radial forces, [83]

Bond failures can be categorized into two distinct types: splitting and pull-out failure.

Pull-out failure**:** Pull-out failure specifically occurs when the reinforcing bar withdraws from the surrounding concrete, devoid of any concurrent splitting in the concrete or rupture in the bar, as depicted in Figure (9). The root cause of this failure mode lies in the fact that the radial forces acting on the bar are insufficient to surpass the concrete's capacity, while the tangential stresses exceed the concrete's load-bearing capacity, rendering the concrete unable to withstand these forces. Consequently, shear forces emerge around the upper section of the bar's ribs.

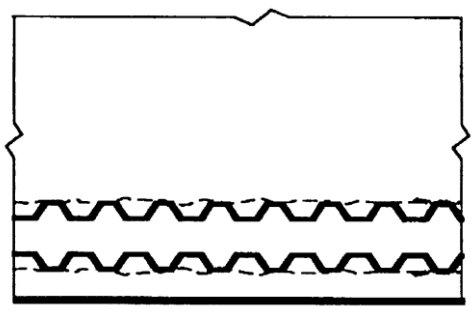

Figure 9: shear crack and/or local concrete crushing caused by bar pull-out in side view, [83]

Splitting failure: This type of failure occurs when concrete splitting takes place without any rupture in the reinforcement bar, as illustrated in Figure (10). When a load is applied to the reinforcement bar, it exerts radial pressure onto the surrounding concrete. If the concrete is inadequately reinforced or the transverse bars cannot effectively counteract this pressure, it results in the formation of a splitting crack between the bar and the adjacent concrete. This crack propagates either parallel or perpendicular to the reinforcement, extending towards the surface and ultimately leading to a splitting failure in the concrete.

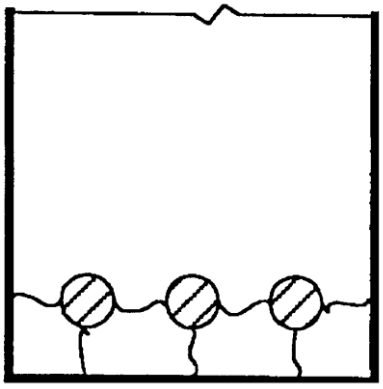

Figure 10: concrete splitting cracks between FRP bars and concrete cover in cross-sectional view.

Both of the mentioned bond failures are correlated with slip of the bar in relation to the surrounding concrete. Yet, concrete with higher bond strength more likely have pull-out failure than splitting failure as the radial pressures need more energy to split the concrete and reach the outer surface of the concrete.

2.5.4 Bond test specimens

Beam tests and pull-out tests are utilized to measure the bond strength of reinforcing bars, as illustrated in Figure (11) The values obtained from these tests differ from each other, with bond strength typically being lower in beam tests compared to pull-out tests, as indicated by [82]. This discrepancy arises because beam tests tend to avoid concrete splitting, mainly due to the absence of local bending on the bar and the presence of a thicker concrete cover. In contrast, in pull-out tests, the surrounding concrete is subjected to compression. However, in beam tests, the

concrete surrounding the reinforcing bars is placed under tension, which varies along the span length and leads to cracking, consequently reducing the bond strength. Consequently, pull-out tests often yield overly optimistic but unrealistic bond stress values, which can be considered as upper limits rather than realistic values for the bond stress-slip efficiency of FRP reinforcing bars. Therefore, beam tests are considered more accurate than pull-out tests in simulating the actual behaviour of reinforced concrete members, as noted in [84].

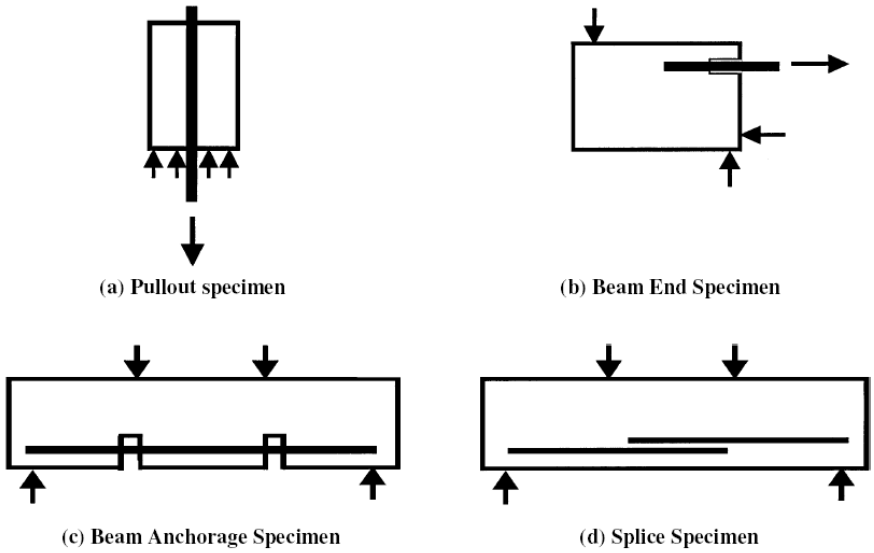

Figure 11: Schematic of bond test; a: pull-out test, b, c, d: beam tests.

2.5.5 Bond behaviour of steel rebars

When the adhesive bond between a steel reinforcing bar and the surrounding concrete is lost, the steel bar begins to move in relation to the concrete. During this process, various forces come into play, including friction forces acting on the ribs and barrel of the bar and bearing forces acting on the ribs. Studies have indicated that after the initial slip of the steel bar, a significant portion of the force is transferred through bearing. Compressive bearing forces on the ribs lead to an increase in friction forces. However, as slip continues to increase, there is a reduction in friction on the barrel of the steel bar, which affects the forces at the interface between the ribs and the adjacent concrete, which are the primary mechanisms of force transfer, as discussed in [82].

Nonetheless, it's essential to emphasize that friction plays a crucial role in transferring force between the ribs of the bar and the surrounding concrete. This principle also applies to bars without ribs, where friction arises due to transverse stresses caused by slip at the surface of the bar.

Numerous studies have delved into the mechanics of bond stress transmission from FRP reinforcement to concrete. Some of these investigations involved experimental tests on FRP bars used as reinforcement in beam specimens made of GFRP, AFRP, and CFRP, each with different surface textures. These tests were specifically designed to induce failure in a concrete splitting mode. The primary objective was to elucidate the bond mechanisms, including frictional resistance for smooth bars and bearing resistance for deformed bars (ribbed). Kanakubo presented all the results and data in their paper but did not provide specific design equations or recommendations, as outlined in [85].

A comprehensive study conducted on the pull-out test of GFRP rebars embedded in concrete is detailed in reference [86]. The results presented in this paper reveal that, under the same test conditions, the average nominal bond stress for steel rebars exceeded that of GFRP rebars during failure. Additionally, it was observed that the anchorage design method typically employed for steel rebars is not directly applicable to GFRP bars. In summary, the relative slip between the GFRP bar and the concrete surface was more pronounced when compared to steel rebars.

Further investigation into the bond strength of FRP rebars was carried out, with results being compared to those of steel rebars. This study considered two different types of FRP, three different embedment lengths, and four nominal diameters for both FRP and steel rebars. The findings indicated that the bond strength of steel bars exceeded that of GFRP bars, with variations observed in rebar diameters and embedment lengths. Ultimately, the authors concluded that friction and adhesion were identified as the primary factors influencing bond strength, as described in [87].

The impact of surface treatment on the bond behaviour of FRP bars was explored in another investigation. Various surface configurations of CFRP, GFRP, and AFRP bars, coated in epoxy resin, were subjected to bond tests. The results revealed that bars

subjected to sand coating exhibited an enhanced chemical bond, resulting in increased bond strength. However, it was noted that during the tests, sand-coated bars experienced sudden separation between sand grains and the bar interface, leading to brittle bond failure, as documented in [88].

A thorough examination of interface bond behaviour was conducted within the EUROCRETE project. This project explored the influence of embedment length, bar type, and cross-sectional area. The findings indicated that the bond behaviour of FRP bars with a smooth surface is primarily influenced by the type of matrix and fibres used, with the effect of concrete being negligible. Moreover, it was established that the pull-out mechanism of FRP reinforcement differs from that of deformed steel bars, with the bond of FRP being dependent on a broader range of variables, as detailed in [89] [90].

2.5.6 Influencing factors on bond behaviour of FRP

To understand behaviour of bond between FRP and concrete under different conditions, factors that influence bond behaviour of FRP need to be recognized These experiments include specimens with different types of FRP and surface configuration bars, [91] [92] [93] [94] [95] [96] [88] [97] [98] [15] [99]; [100] [101] [102] [103] [104] [105] [106] [107] [4]. Studies show different factors influence the bond behaviour of FRP bar reinforced concrete members. Numbers of significant factors that have high influence on bond behaviour of FRP bars in concrete are mentioned in the following segments.

Surface Configurations: due to anisotropic nature of the FRP and lower strength of resin in comparison with concrete compressive strength, different bond interaction forms than that of steel bond to concrete and failure in FRP reinforcement is due to destruction of ribs instead of cracking of concrete. Thus, stress and strain failures in both transverse and longitudinal directions are directly influence on bond behaviour. As one of the factors that bond behaviour depend on is surface texture of FRP bars, many researchers separate FRP bars into straight bars, including smooth, grain covered and sand blasted, and deformed bars, including ribbed, indented and braided, to understand the bond mechanisms of these bars separately. Researchers

concluded that during pull-out test for smooth bars two different bond components appears in different phases: first phase- adhesion and second phase- friction.

In a test by [108] load transfer behaviour between FRP and concrete were studied. Test was a conventional pull out test for FRP with both 5 and 10 embedment lengths and bars with different fibre and resin configuration including glass-vinyl ester, carbon-vinyl ester and carbon-epoxy and concrete compressive strength of 42.7 to 66.1 MPa. Test results showed smooth bars had very low bond strength and deformed glass-vinyl ester and carbon-vinyl ester developed bond stresses of 13 and 14 MPa correspondingly. All specimens in this test failed by shearing off of lugs and sliding showing in case of smooth bars bond strength is not influenced by concrete strength and friction occur to be the major cause of pull-out resistance since adhesion disappear as soon as the bars slips. Another conclusion was that the friction component of bond strength mostly influenced by the different smoothness of resin.

In other test demonstrated by ([109] about effect of smooth bar surface on bond resistance. The results showed bond strength of glass-vinyl ester increase 5 times higher after removing resin layer caused by skin-removed effect. This result proved surface condition of FRP bars influence bond components of adhesion and friction and bond strength. Similar experiment conducted by [110] on smoothness of FRP bar surface on Bond behaviour of FRP. Results showed sand coated FRP bars have better chemical bond and increase in bond strength but brittle failure occurred due to detach of sand grains and bar interface.

Same results of effect of smooth FRP rod surface confirmed by [111] by using specimens prepared according to [112] with embedment length being four times the rebar diameter and concrete compressive strength range from 25.2 MPa to 93.2 MPa. Bars with nominal diameter of 12.7 mm were subjected to surface treatment of sand coated and helical wrapping for bond improvement. Results showed GFRP bars with only sand coating quickly dropped in bond stress but GFRP bars with sand coated and helical wrapping revealed steady drop in bond stress. At the end author concluded improvement rate of GFRP bars bond strength with regard to concrete strength depend on the ratio of the delaminated area.

[113] Performed a more in detail study on effect of surface pre-conditioning on bond behaviour between CFRP rods and concrete. The pull-out test consists of smooth bar and surface treated bars with three different sand grain sizes, Figure (12).

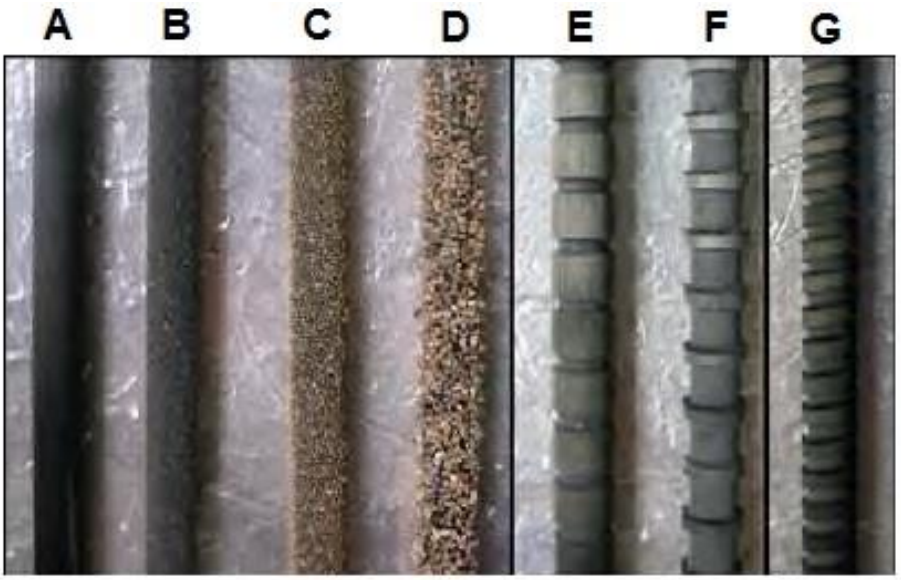

Figure 12: A-Smooth, B, C, D-Sanded, E, F, G-Machined bars in pull-out test, [18]

The results of FRP bars were compared with smooth and deformed surface steel bars. As smooth FRP bars do not make mechanical interlock with concrete, smooth steel bars presented greater bond strength in comparison with smooth CFRP bars. Author defined a formula to show influence of different surface configuration of rebars on bond behaviour:

$$Concrete\ Lug\ Ratio(CLR) = \frac{Concrete\ Width}{(Concrete+CFRP)Width} = \frac{\omega_c}{(\omega_c+\omega_f)} \quad (2.1)$$

According to [113], a CLR of 35% for CFRP shows same result of ribbed steel bars in bond strength and bond failure due to shearing off of lugs in the concrete. Yet, a CLR of 78% was discovered to be necessary for FRP bars to have better bond strength and failure due to shearing off of lugs in FRP.

Studies on deformed FRP bars established for indented bars in pull-out test. Two different phase of transverse compression and shear deformation in a plane including longitudinal and radial directions must form during the test. In this situations longitudinal shear modulus of FRP rods are the ruling fundamental parameter. Therefore, interlocking interaction between deformed FRP bar and concrete,

geometry of surface configuration of FRP bar and most importantly mechanical characteristic of reinforcement are influencing the bond behaviour of deformed FRP bars.

A test by [114] showed in some cases deformed FRP bars do not form mechanical interlock with surrounding concrete. In the test, deformed rebars were glued by spiral on the outer surface of rebars. Results showed the deformed rebars have same bond behaviour as straight FRP bars with no mechanical interlock. Failure of specimens was due to separation of spiral from interface of rebars without cracking in concrete. It means confinement pressure and concrete compressive strength is not affecting bond performances.

Similar results found by [115] were surface of concrete is not cracked considerably, but outer surface of twisted strand CFRP rebar is strongly damaged.

A study on the rib geometry influence on bond slip behaviour of GFRP ribbed bars was recommended an optional ratio of rebar ribs to rebar diameter by:

$$Rib\ Area\ (R_r) = \frac{Projected\ rib\ area\ normal\ to\ bar\ axis}{Nominal\ bar\ perimeter \times Center{-}toCenter\ rib\ spacing} \quad (2.2)$$

Experimental results showed increase in rib spacing of FRP bars would cause decrease in peak bond strength and initial stiffness, whilst increase the loaded end slip value at the peak load. In addition, in crease of rib height from 4% to 6% helped and increases in peak bond strength and initial stiffness. However, ribbed spacing of 50% of the bar diameter did not confirm the result on increasing initial stiffness and peak bond strength. At the end, it suggested that best rib spacing is equivalent to bar diameter and best rib height is 6% of the bar diameter. Therefore, optimal relative rib area is equal to 0.06, [116].

Different experiments on GFRP deformed rods, braided rebars and spiral indented bars showed friction on bond behaviour were concrete cracked observed and concluded that adhesion and friction are the component of bond between FRP bars and surrounding concrete, [96] [117] [97].

In an experiment on GFRP bars with indented outer surface and ribbed deformation author observed both friction and mechanical interlock in bond mechanisms. Results from specimens have shown wide cracks in concrete and damage to outer surface of rebars that indicates a bearing mechanisms was initiated, [114]. A comparable result reported by [115] on spiral wounded on outer surface of aramid FRP bars. Author noticed mechanical property of resin and concrete compressive strength influenced maximum bond stress. Therefore, it proved the pull-out mechanism of FRP reinforcements contrast from that of deforms steel bars, where bond performance is only affected by concrete strength.

[118] Noticed difference from bond behaviour of FRP bar to deformed steel bars. They reported that bond strength of GFRP bar surrounded by high strength concrete is similar to GFRP bar embedment in low strength concrete. This result imply that bond strength in FRP reinforcements does not change linearly with the square root of concrete compressive strength (f_c) as it does in conventional steel reinforcements. Such a bond behaviour is result of deformed surface of FRP rod is not able to deliver enough lateral confinement through rib bearing.

Concrete compressive strength: As mentioned before, shear and tensile strength of concrete have effect on causing pull-out and splitting failure in bond between FRP and surrounding concrete, which is also pertain to the compressive strength of concrete. ACI committee, [ACI Committee 408, 1992] reported that concrete tensile strength is almost proportional to the square root of concrete compressive strength($\sqrt{f_c'}$). However, experimental studies on bond behavior of FRP bars in concrete showed different results. Researchers concluded based on regression analysis that better correspondence is between bond strength and concrete compressive strength, [119] [120] [95] [121] [10] [107]. The effect of concrete strength on bond behaviour of FRP rebars in concrete conducted by Ehsani, [94]. Researcher concluded with increase in concrete strength, bond stress of FRP rebars and first stiffness of bond stress-slip curve increased. Meanwhile the slip decreased with increase in concrete strength. In a study by Hattori, [115], on bond behaviour of AFRP bars, the maximum bond stress showed dependency on the concrete

compressive strength. Other studies investigated the bond behaviour of FRP rebars in concrete under effect of concrete strength in beam bond tests and the results showed increase in concrete strength with proportion to the square root of concrete compressive strength, [110] [97] [84].

Based on pull-out tests results on the mode of failure of FRP reinforced concrete, bond strength of FRP bars has independency from concrete compressive strength when concrete strength is higher than 30 MPa, ($f_c' > 30\ MPa$). Thus, in these cases failure happens at the FRP bars surface. On the other hand, concrete compressive strength has direct effect on the bond behaviour of FRP bars when concrete strength is lower than 15 MPa, as failure interface occurs in concrete matrix, [122] [100] [90] [4].

Bar diameter: effect of bar diameter on bond performance of FRP bars has been examined by [108] and [97]. In the test carried out by Nanni et al. 1995 smooth rods of glass-vinyl ester, carbon-vinyl ester and carbon epoxy with 12.7 and 6.3 diameter and constant embedment length of 63 mm were subjected to pull-out test. The results showed the average bond resistance of FRP rods rises as bar diameter decreases. Similar results found by Benmokrane et al. 1996 while test included GFRP rods with 12.7, 15.9, 19.1 and 25.4 mm in diameter and result of bond strength for these rods were 10.6, 7.3, 6.6, and 6.4 MPa respectively.

Bar Position in the Cast: an experiment investigated the position of bar in the cast for smooth and sand coated bars. In the pull-out tests on specimens bars had orthogonal and parallel positions relative to the cast. Results showed bars in orthogonal position performed between 1.5 to 2 times lower bond strength in comparison to bars in parallel position in the cast, [123].

Transverse Reinforcement: Using transverse reinforcement in concrete cause increase in bond strength of reinforcing bars in RC composite as it confines the concrete. Research on bond performance of steel reinforcement in concrete presented that transverse reinforcement confines concrete and interlocks bars by reducing the development of cracks, [124] [125] [126] [127]. Yet, there is not enough

work on influence of confinement caused by transverse reinforcements on the bond performance of FRP bar reinforcement in concrete. Wambeke and Shield, [128], study the bond performance of FRP rebars in concrete on 269 beam-type specimens, which just 19 specimens had transverse reinforcements. Results of the experiment indicated the bond strength of FRP rebars in concrete is independence from transverse reinforcement.

Top-bar: [93], [118] and [97] investigated the influence of top-bar on bond performance of FRP rebars. Explicitly, [93] directed a test with two different specimens. First specimen has bars with estimated cover of 19 mm from bottom of the cast. In the second specimen, FRP bars were cast with 280 mm of concrete below the bar and a clear cover of 19 mm from the top of the specimen. The results specified that the allowable bond stress in the top bar was 66% of that for the bottom bar. In an experiment by Chaallal and Benmokrane a new factor introduced as a pull-out strength ratio between the bottom rods and top rods. The results showed the average ratio for normal-strength concrete was 1.23 and for high-strength concrete was 1.18. It means the top cast modification factor is dependent on small degree of concrete strength. Furthermore, a value introduced for the top cast modification factor as 1.1 for pull-out tests with concrete average compressive strength of 52 MPa.

Embedment Length: a study conducted the effect of embedment length of glass-vinyl ester bar. The study included two different cases of embedment of 10 dimeters and embedment of 5 diameters. Results showed there was higher nominal bond strength developed for specimens with shorter embedment length, [108] . Same observation reported by [88] on a test that included carbon, aramid, glass and vinyl rebars with different surface configuration and ratio of embedment length to diameter of 10, 20 and 40.

An inclusive study of embedment length, concrete strength and concrete cover done by [128]. The variables in this study are taken as influencing parameters on bond strength of FRP in concrete composite and following formula presented:

$$\frac{u}{0.083\sqrt{f_c'}} = 4.0 + 0.3\frac{c}{\emptyset_b} + 100\frac{\emptyset_b}{l_b} \qquad (2.3)$$

In this equation u is average bond stress (MPa), f_c is specified compressive strength of concrete (MPa), c is the lesser of the cover to the centre of the bar, $\emptyset_b$ is diameter of reinforcement bar, l_d is the development length of the reinforcement. However, [128] did not include surface characteristics as an influential factor on bond strength and authors such as [129] and [4] showed in their test that the bond strength developed by the rebars were significantly influenced by the type of surface configuration on the embedded rebars.

Confinement pressure: The influence of confinement pressure on the interface between FRP rebars and concrete was investigated in a study conducted by [114]. This study involved E-glass FRP rebars, some of which had deformed surfaces, while others were stressed and spiral-glued to the outer surface. The rebars were subjected to five different levels of radial-confining pressure. The results obtained from the deformed and stressed rebars revealed a significant impact of confinement pressure on bond strength. In contrast, the bond behaviour of spiral FRP rebars appeared to be largely unaffected by confining pressure.

In the case of spiral FRP rebars, it was observed that the spiral structure broke and separated from the bar during the tests. Interestingly, there was no rupture of the concrete cylinder in any instance. Consequently, the concrete cylinder was able to withstand most of the confining stress without transferring it to the bar and the interface between the bar and concrete. Consequently, the resistance to bond was primarily provided by the frictional interaction between the FRP bar and the surrounding concrete.

2.6 Available guidelines for FRP RC members

Over the past two decades, significant efforts have been undertaken worldwide to incorporate FRP (Fiber-Reinforced Polymer) bars into structural design codes and guidelines. These guidelines have been developed across various regions, including Asia, Europe and North America, with four primary sets of historical and design guidelines emerging from Japan, [130] [131] Canada [132] [37] [112] [133], United States [134] [135] [136] [137] [44] and Europe [138]. The low modulus of elasticity exhibited by FRP has rendered it a brittle material, resulting in a linear-elastic

behaviour for FRP reinforcement. This characteristic has had a profound impact on all the existing guidelines, [139].

These existing guidelines have been adapted from conventional steel Reinforced Concrete (RC) design codes and primarily employ limit state design methods. They encompass fundamental principles that are heavily influenced by the mechanical properties of FRP reinforcement and are supplemented by empirical equations derived from experimental studies conducted on FRP RC members globally.

It is worth noting that the International Federation of Structural Concrete (FIB) recently published a report addressing the use of FRP reinforcement in RC composites. However, this report does not include specific design codes, leaving a gap in the provided technical guidance by FIB [140].

As a result of unreliable experimental results, current ACI 440 guideline recommended reduction in characteristic value of tensile strength of GFRP, CFRP and AFRP by 80%, 45% and 70%to ensure the serviceability limit state of the existing structure. In addition, Italian design guideline provided an empirical expression with a multiplier factor in deformation analysis if FRP RC structures. The empirical expression is based on Eurocode 2 [141] that makes value of deformation cracked element greater, [142]. Recent investigation have revealed method such as the one mentioned is exaggerated result as deformations mostly influenced by the bond characteristics of FRP bars and surrounding concrete, [143] [144].

Gudonis [52] Recommended that design guidelines of RC composite reinforced with FRP bars should be based on the result of experiments of bond properties of FRP bars embedded in concrete and structural stiffness. Other factors, such as concrete cover and strength, bar location and diameter are considered in all guidelines. Thus, bar surface configuration only considered in Canadian standards. The CSA S806-12 includes factor K_5 to specify the influence of surface characteristics. K_5 value for rough, sand coated or braided surface is equal to 1.0 and for spiral pattern or ribbed surfaces is 1.05, and 1.8 for indented surface. It also shows that bond strength is inversely proportional to K_5 factor, where sand coated, roughed, and braided surfaces deliver higher bond strength compare to bars with indented surface. CSA S6-

06 also includes K_4 to provide influence of surface characteristics, which is the ratio of the bond strength of FRP bar to steel deformed bar with similar cross section area but smaller than 1.0. CSA S6-06 suggested value of 0.8 for factor K_4 for the cases with no experimental data. In case of CSA S806-1 and ACI 440.1R-15 the surface characteristics was counted into the study based on where the formula for bond strength was defined. Thus, the result of study showed that the bar surface did not affect the outcome. Table (6) shows list of existing guidelines from different countries.

Region	*Country*	*Year*	*Title*	*Publisher*
Asia	Japan	2007	Recommendation for Design and Construction of Concrete Structures Using Continuous Fibre Reinforced Materials	JSCE
Europe	United Kingdom	1999	Interim Guidance on the Design of Reinforced Concrete Structures Using Fibre Composite Reinforcement	The Institution of Structural Engineering
	Norway	2002	SINTEF report STF22 A98741, Modifications to NS3473 When Using Fiber Composite Reinforcement 2.24	NBR
	Italy	2006	CNR-DT 203/2006, Guide for the Design and Construction of Concrete Structures Reinforced with Fiber-Reinforced Polymer Bars	CNR
North America	Canada	2007	Reinforcing concrete Structures with Fibre-Reinforced Polymers Design Manual	ISIS
		2002-2012	CAN/CSA-S806-12 Design and Construction of Building Structures with Fibre-Reinforced Polymers	CSA
		2006-2010	CAN/CSA-S6-06; CAN/CSA S6S1-10 Canadian Highway Bridge Design Code	CSA
		2010	CAN/CSA-S807-10 Specification for Fibre Reinforced Polymers	CSA
	United States	2009	AASHTO LRFD Bridge Design Guide Specifications for GFRP Reinforced Concrete Bridge Decks and Traffic Railings	AASHTO
		2004-2012	ACI 440.3R-04 Guide Test Methods for Fiber-Reinforced Polymers for Reinforcing or Strengthening Concrete Structures	ACI
		2001-2015	ACI 440.1R guide for the Design and Construction of Structural Concrete Reinforced with FRP Bars	ACI

Table 6: Existing guidelines for FRP RC structures from different countries.

2.7 Application of FRP in Retrofitting Civil Engineering Structures

Environmental conditions, including factors such as chloride exposure, humidity levels, temperature fluctuations, and structures subjected to marine and chemical environments, significantly accelerate the deterioration of reinforced structures, ultimately leading to concrete degradation. In certain cases, the cost of repairing these damaged structures can surpass the initial construction expenses. For instance, in 2002, it was estimated that the cost of repairing concrete structures exceeded 59 billion pounds in Canada. Repair costs for existing highway bridges alone amounted to over 40 billion pounds, and for all concrete structures in the United States, the range was estimated at 80 billion to 2 trillion pounds. Additionally, the annual cost of addressing steel corrosion in Europe was approximately 2.4 billion pounds [145].

The exceptional physical and mechanical properties of FRP have positioned this reinforcement as a versatile solution for various applications within civil engineering, serving as an alternative to traditional steel reinforcement. There exist diverse methods for employing FRP composites in either new construction projects or the strengthening and repair of existing structures. The application of FRP in civil engineering can be broadly categorized into two groups: internal reinforcement utilizing FRP bars, rods, and tendons, and external reinforcement involving FRP sheets, laminates, and wraps.

Typically, concrete structures are reinforced with steel bars or plates. However, a notable shift is occurring. Andrew McNaughton, the Chief Engineer of the railway network, discussed the composition of the UK's network rail's bridges in a conference report. He noted that many of these bridges are constructed from various materials, including timber, concrete, cast iron, brick, masonry, and steel, with ages exceeding 100 years. There is a growing inclination to employ more advanced composites for these structures, such as fibre-reinforced polymers, which are already being used for reinforcement to enhance the strength and durability of these aging bridges [146].

FRP materials have demonstrated their effectiveness, particularly as longitudinal reinforcement in concrete composites, with benefits such as corrosion resistance and primary engagement in resisting bending forces. Therefore, structures such as bridge

decks, floor slabs, wall structures, and beams are excellent candidates for longitudinal FRP reinforcement. A list of FRP composite structures in the UK is provided in Table 7.

Year	Structure	Location
1974	Mondial House- The GPO Headquarters	North Bank of the Thames, London
1974	Primary School In Thornton Clevelys	Lancashire
1993	Aberfeldy Footbridge	Scotland
1994	The Bonds Mill Single Bascule Lift Road Bridge	Oxfordshire
2001	Halgavor Bridge	Cornwall
2002	The Road Bridge over the River Cole at West Mill	Oxfordshire
2003	The Wilcott Footbridge	A5-Nesscliffe
2007	Networl Rail Footbridge cross Paddington-Penzance	St Austell

Table 7: Examples of FRP application in composite structures in UK, [147]

2.8 Effects of Strain rate

The applied forces acting on structures can be categorized into two distinct groups: static and dynamic, and this classification is based on various factors including the duration of force application, the magnitude of inertial forces, and how these forces evolve over time. Static loads represent long-term forces that exhibit minimal changes over time. Conversely, dynamic loads are characterized by short-term applications that vary over time, leading to the generation of inertial forces. Additionally, dynamic loads can be further classified into two subcategories: periodic and non-periodic, with the distinction based on the temporal characteristics of the load variation. Periodic loading involves a consistent time duration for each load cycle, which repeats for a number of successive cycles. On the other hand, non-periodic loading exhibits an asymmetrical time duration for the loads and may have either a lengthy time history, such as seismic events, or a brief time history, as seen in cases of explosions or impact loads [148].

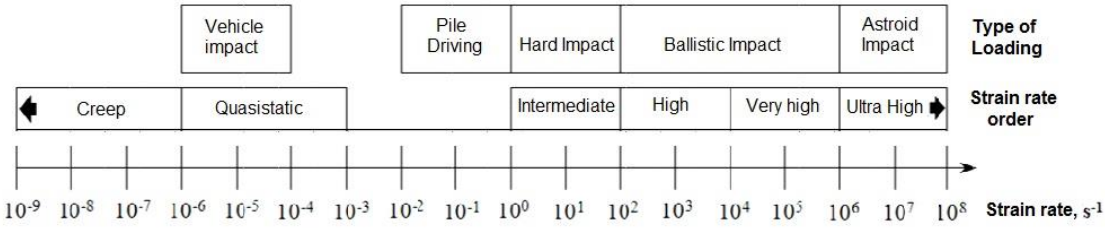

Figure 13: strain rate for different loading types, [149] [150]

The dynamic loads effects can be classified with respect to time domain in the strain rate terms. The rate that strain deformation happen under impact loading is called strain rate,$\dot{\varepsilon}$ with unit of strain per second, s^{-1}:

$$\dot{\varepsilon} = \frac{\partial \varepsilon}{\partial t} \tag{2.4}$$

$$\partial \varepsilon = \frac{[L(t) - L_0(t)]}{L_0(t)} \tag{2.5}$$

Where $\partial \varepsilon$ is immediate strain, ∂t is time interval, $L(t)$ is length of the object at time t, $L_0(t)$ is the original length.

Strain rate in contrariwise proportional to time-history of applied load. For example, high strain rate in explosion or impact events happen over short period of time, [151]. Strain rate for various types of loading demonstrated in Figure (13). It can be seen that impact loads yield loads associated with strain rate in the range of 10^0 to 10^2 s^{-1}, while blast pressure is located in the range of 10^2 to 10^4 s^{-1}.

2.8.1 Test Methods for Assessing the Influence of Strain Rate:

Since strain rate changes in differ load scenario, different methods used for study the effect of strain rate on dynamic material properties of composite concrete under impact loading. These tests include:

- Split Hopkinson bar, [152] [153] [154]
- Drop-weight tests, [59]
- Pendulum, [155]
- Charpy pendulum, [156] [69]
- Izod impact testing, [157]
- Servo-hydraulic testing apparatus, [158]

- Explosively driven hammers, [159]

Among the previously mentioned tests, the Split Hopkinson bar test, Charpy pendulum test, and drop-weight test stand out as the most widely utilized. In the Split Hopkinson bar test, a solid bar serves as a striker to apply dynamic loads to a structural member sample. Multiple strain gauges are strategically positioned on both the incident bar and the transmission bar to enable the measurement of stress-strain behaviour in both compression and tension regions, particularly under high strain rates. The drop-weight test, conversely, involves a sequence of specimens subjected to a free-falling weight, resulting in induced damage or cracking, which is then quantified through the assessment of visible damage. In the Charpy pendulum test, a pendulum hammer is employed to strike the specimen, with the primary objective being the determination of the energy absorbed by the specimen during the fracture process.

Numerous experiments and analytical models have delved into the phenomenon of debonding failure at the interface between FRP and concrete, aiming to understand factors such as maximum bond strength and ultimate load. However, it is noteworthy that a substantial portion of these prior investigations has tended to employ simplified FRP modelling approaches.

Additionally, their primary emphasis has often revolved around the broader response characteristics of FRP-reinforced concrete members subjected to impact and blast loads [160] [161] [162] [163]. Failure to comprehensively account for material characteristics and failure mechanisms can potentially lead to inaccurate outcomes when analysing FRP-reinforced concrete structures under high-load conditions. Therefore, it is crucial to address critical factors such as the impact of strain rate and the occurrence of debonding failure in the assessment of FRP-reinforced concrete structures subjected to impacts and blasts [164]. It's worth noting that existing analytical models have addressed the strain rate effect on concrete and steel materials, yet they have often overlooked the influence of strain rate on FRP in high-strain rate scenarios [165] [166] [167] [168] [169].

It is stablished that structural material such as steel and concrete have performed differently under dynamic load than static condition. [170] Reported Dynamic Increase Factor, DIF, for concrete and steel to gain higher strengths as strain rate increases under blast and impact load. DIF for concrete starts to rise quickly above 1.2 as soon as the strain rate go above $0.1s^{-1}$. The grade of steel is effective as for steels with higher grades show less strain rate effect and DIF for the yield strength is higher in comparison to DIF for the ultimate strength. Strain rate might influence FRP materials but, different manufacturing methods will make FRPs to have different material properties and hence dissimilar behaviour under strain rate.

Number of studies investigated the viscous nature of fibre reinforced composites including GFRP and CFRP. Researchers documented occurrence of creep in composites due to the matrix supporting stresses in shear deformation under long term loading, [171] [172] [173]. A study presented the effect of strain rate on material characteristics on different forms of composites using different test methods. Results showed behaviour of composites are dependent on strain rate, composite type, mode of loading and fibre orientation, [174]. During hydraulic/pneumatic tests, it is noticed due to inertial of the load cell and wave propagation effects, strain rate were limited to 10 to $100s^{-1}$. A study on effects of strain rate on polymer material composites reported inconsistent results due to specimen sizes and different testing measures, [175].

Investigation on high strain rate effect on different composites using a tension bar configuration conducted by [65]. The tests utilized carbon, Kevlar and glass reinforced polyester resins. It has concluded ultimate strength of materials affected by strain rate. Tensile strength of CFRP sample increased by 50% at strain rate of $10s^{-1}$. Other observation was the appearance of specimens fracture differed during different loading rate. In similar test by [176], it noticed at strain rates around $20s^{-1}$ the tensile strength were almost similar to static strength. However, tensile strength was increased by 70% for strain rates around$100s^{-1}$. In addition [177] studied glass/epoxy composite under servo-hydraulic test. The specimens in this test were subjected to strain rates from 0.001 to $100s^{-1}$. The results showed the tensile

strength of GFRP increased at strain rate of $8s^{-1}$. Another study on effect of strain rate on GFRP resulted in increase of tensile strength by approximately 5% to 15% starting at strain rate of $10s^{-1}$, [178].

In general, studies showed the bond stress and interfacial fracture energy of FRP and concrete increase with strain rate as a logarithmic function, and type of adhesion and FRP composites have no effect on strain rate, [179] [180]. Yet, there is not enough understanding about the effect of dynamic loading on the bond-slip relationship of FRP bar and concrete. Furthermore, strain rate effect on GFRP starts at around $8s^{-1}$ and for CFRP to affect tensile strength starts around 10 to $20s^{-1}$. It should be considered these tests were not applied on same type of CFRP and GFRP therefore there may or may not be strain rate effect at very high load.

2.9 Characteristics of Impact loading

Dynamic loads characterized by short cycles are commonly referred to as impact loads. These dynamic loads can take the form of either concentrated point loads or distributed loads [181]. For example, field experiments involving explosions typically result in distributed loads, whereas laboratory-based impact tests are often conducted by applying a single point load [182]. In the context of reinforced concrete elements, attributes like moment, axial capacity, and shear traditionally define the static resistance. However, in situations where loads are applied over a brief duration, parameters indicative of energy absorption capacity are typically prioritized as the fundamental variables [182] [183].

When a rigid falling object strikes a beam, a quick transfer of momentum will occur while there is reduction in kinetic energy of the impact object, [182] [181]. From equation (2.6) the energy loss of impacting object at any time after initial contact can be determined:

$$\Delta E_{\circ} = \frac{1}{2} M(v_i^2 - v_f^2) \tag{2.6}$$

$\Delta E_{\circ}$ is the change is kinetic energy, M is the mass of the impact object, v_i is the impact velocity and v_f is the velocity of the falling object at interested point in time. Part of the energy from the falling object will be transferred to the beam and some will be

lost due to heat and friction. The energy absorbed by the beam at any point of time can be calculated from the equation below, only with ignoring the translational kinetic energy and vibrational energy of the beam:

$$\Delta E_{\circ} = E_{ker} + E_b \quad (2.7)$$

Where E_{ker} is the rotational kinetic energy and E_b is strain or bending energy. Meanwhile the maximum energy from impact object ready to transfer to the beam can be determined by the equation (8):

$$E_{\circ} = Mgh_d = \frac{1}{2}Mv_i^2 \quad (2.8)$$

Where $E_{\circ}$the available maximum energy, g is gravitational acceleration and h_d is the drop height, [181].

Most of studies on concrete beams strengthened with FRP showed different bond behaviour under impact loading to those under static tests. This difference in behaviour caused as impact loading is a very intense loading specified by a force from extreme severity in a brief time period. Structure behaviour under impact loading consist of two reaction forms, local and overall response. When the falling object strike the structure stress wave occur after impact at the loading point in an extremely short magnitude of time. In this case, the structure has local response.

The overall response of structure includes free vibration that continues lengthier period after the impact load. Loading rate and dynamic characteristics of the structural member are the main two dominant factors that govern overall response of structure, [184] [185]. These two response phases may lead to double-impact on the bonding which can cause decrease in the bond strength.

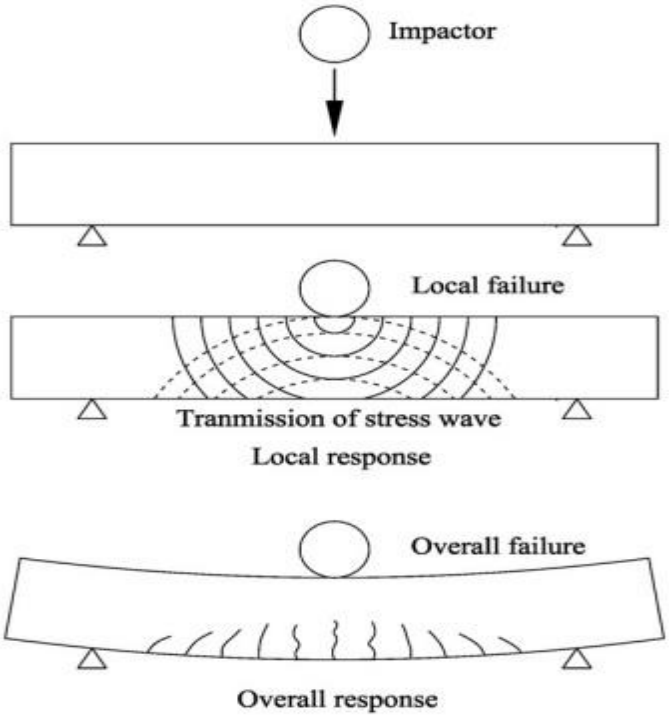

Figure 14: Dynamic response of RC structure under impact load, [184]

2.5.5 Behaviour of RC beams under impact load

Unlike FRP reinforced concrete elements, there are many studies on behaviour of reinforced concrete under impact load, [186] [185] [187] [188] [189]. RC beams that subjected to impact load have three different responses: local response, global response or combination of both.

Thabet and Haldane reported following mechanisms for concrete response under impact load [191]:

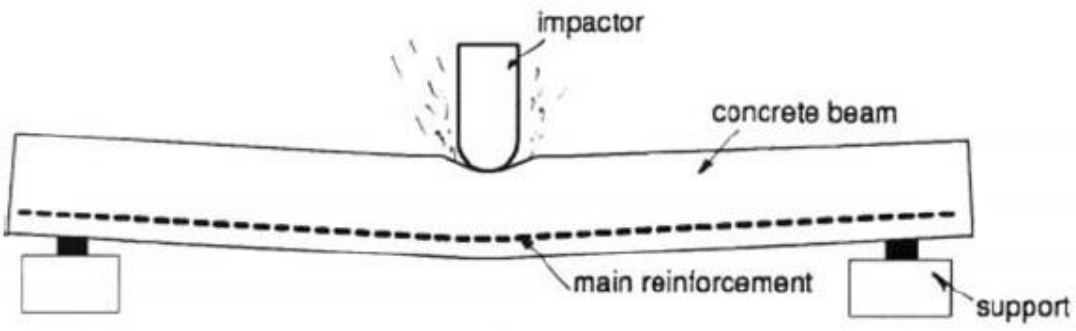

Figure 15: Global response of beam subjected to impact load, [190]

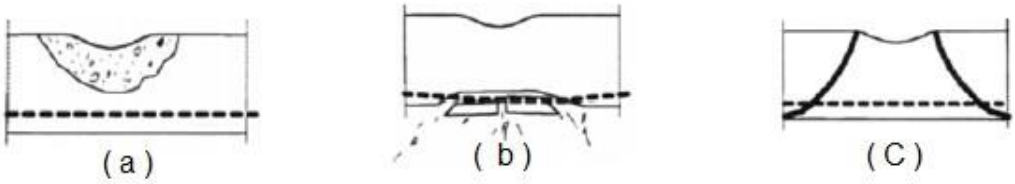

Figure 16: Contact area failure involving steel reinforced concrete beam: (a) Local crushing and spalling in the contact zone, (b) Local effect of scabbing, (c) Formation of the concrete plug, [190].

Surface crushing: when the falling object strike the beam, stress waves are transferred into the beam at contact area in short period of time. On this contact area concrete is crushed and forms a crater on the surface, Figure (16-a).

Concrete Plug: as the stress waves transmitted through the element, a large number of internal wave reflectors occur and encounter with stress waves. These internal wave reflectors formed by collision of stress waves to aggregate particles, cement paste and voids. As the stress wave start to decompose, momentum is became more and denser within the concrete. Presuming that the momentum under the contact area is large, a local punching shear failure arise earlier than the beam has time to react to flexure. This phenomenal is known as concrete plug and often cause cracks in the concrete element, Figure (16-b).

Scabbing: tension failure occur in concrete normal toward its free surface due to the reflection of compressive stress waves within the concrete. this limited detachment of a region of concrete that generally is along with the flexural reinforcing bars with right angles to the direction of impact load is known as scabbing and it occur on the other side of impact area, Figure (16-c), [192].

2.9.2 Dynamic Characteristics of Reinforced Concrete under High Strain Rates Loading

Numerous researchers have investigated the dynamic characteristics of both conventional concrete and fibre-reinforced concrete when subjected to various loading rates. The findings have indicated that, in the case of high strain rate events such as impact and blast loading, concrete exhibits increased fracture energy and strength without a concurrent rise in its susceptibility to break, [193]. The Dynamic Increase Factor (DIF), or Dynamic Amplification Factor, is a dimensionless parameter

that quantifies the ratio of deflections or stresses at any given time to the product of static deflections or stresses resulting from the application of dynamic loads to a structure. DIF serves to elucidate alterations in material properties of structural elements under static and dynamic loading conditions.

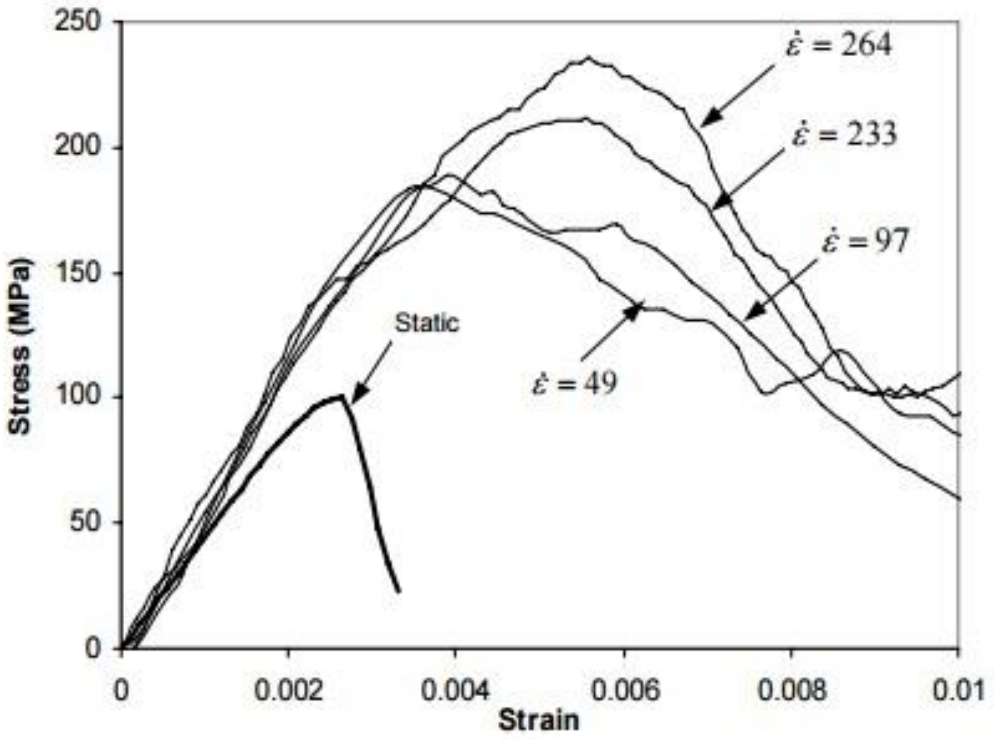

Figure 17: Stress-strain curves of concrete under different strain rate loading [194]

In Figure (17) stresses gained higher value under compressive impact loading than the ones under static loading for a period of time.

Grote, [195] Reported increase in strength magnification factor as great as 4 in compression and about 6 in tension under strain rates of 10^2 to 10^3 per second. CEB-FRP model introduced a DIF for increase in peak compressive stress of concrete (f_c') under strain rate loading, [196]:

$$DIF = (\frac{\dot{\varepsilon}}{\dot{\varepsilon_s}})^{1.026\alpha} \quad \text{for} \quad \dot{\varepsilon} \leq 30s^{-1} \tag{2.9}$$

$$DIF = \gamma(\frac{\dot{\varepsilon}}{\dot{\varepsilon_s}})^{1/3} \quad \text{for} \quad \dot{\varepsilon} > 30s^{-1} \tag{2.10}$$

Where:

$\dot{\varepsilon}$: Strain rate;

$\varepsilon_s^{\cdot}$: $30 \times 10^{-6} s^{-1}$ (quasi-static strain rate)

$log\ \gamma = 6.156\alpha - 2$

$\alpha = 1 / (5 + 9\ f_c' / f_{c0})$

f_c' = The static cube uniaxial compressive strength of concrete, MPa

$f_{c0} = 10MPa = 1450\ psi$

In the comprehensive design code for concrete, DIF for tension stress of concrete under high strain rates:

$DIF = 1.0$ for $\varepsilon^{\cdot} < 10^{-4} s^{-1}$ (2.11)

$DIF = 2.06 + 0.26\ log\ \varepsilon^{\cdot}$ for $10^{-4} s^{-1} \leq \varepsilon^{\cdot} \leq 1 s^{-1}$ (2.12)

Figure (18) shows the peak compression stress of DIF of concrete:

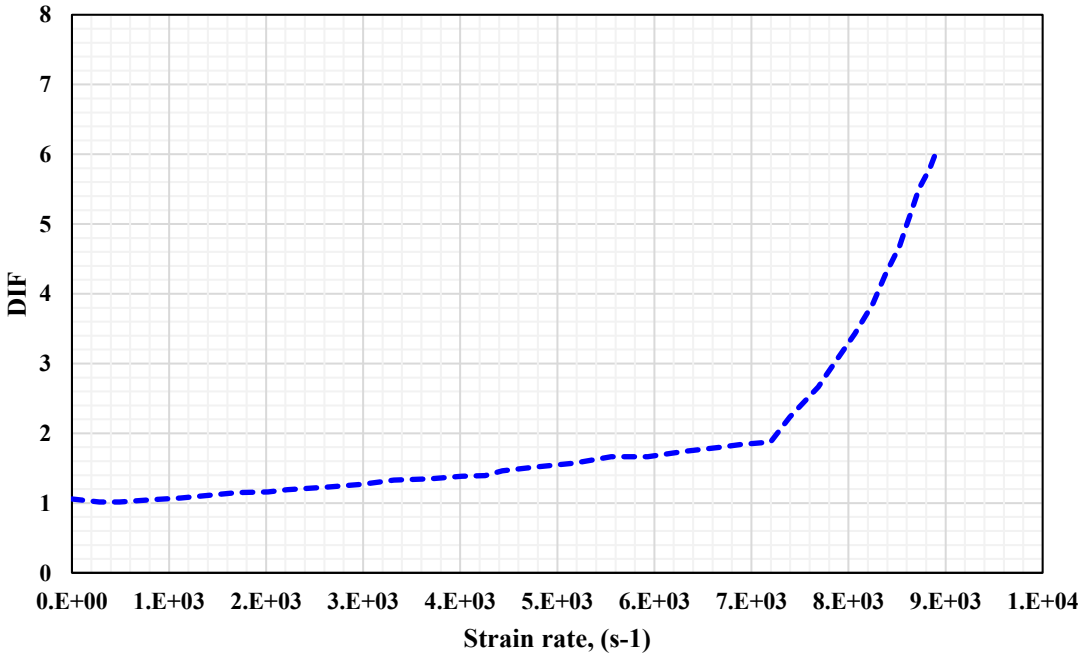

Figure 18: Dynamic Increase Factor for compression concrete, [193]

Lok [197] Investigated DIF of steel fibre reinforced concrete by using 75 mm diameter split Hopkinson pressure bar with different strain rates ranged between 20 and $100 s^{-1}$. Results showed two different equations for compression steel fibre-reinforced concrete response under different strain rates:

$DIF = 1.080 + 0.017 \log(\varepsilon^{\cdot}) \quad 0 \leq \varepsilon^{\cdot} \leq 20 s^{-1}$ (2.13)

$DIF = 0.067 + 0.796 \log(\varepsilon^{\cdot}) \quad 20 \leq \varepsilon^{\cdot} \leq 100 s^{-1}$ (2.14)

2.10 Comparative Evaluation of Bond Strength Codes

The capacity to withstand localized horizontal shear forces per unit surface area of the concrete surrounding a reinforcing bar is termed as bond strength. The bond strength for a reinforcing bar embedded within concrete can be defined as follows, while maintaining an equilibrium condition. We assume that the stress distribution is consistent throughout the length of the reinforcing bar, and the forces acting on the bar's surface are counteracted by the average bond stress, denoted as τ_f, as illustrated in Figure (19):

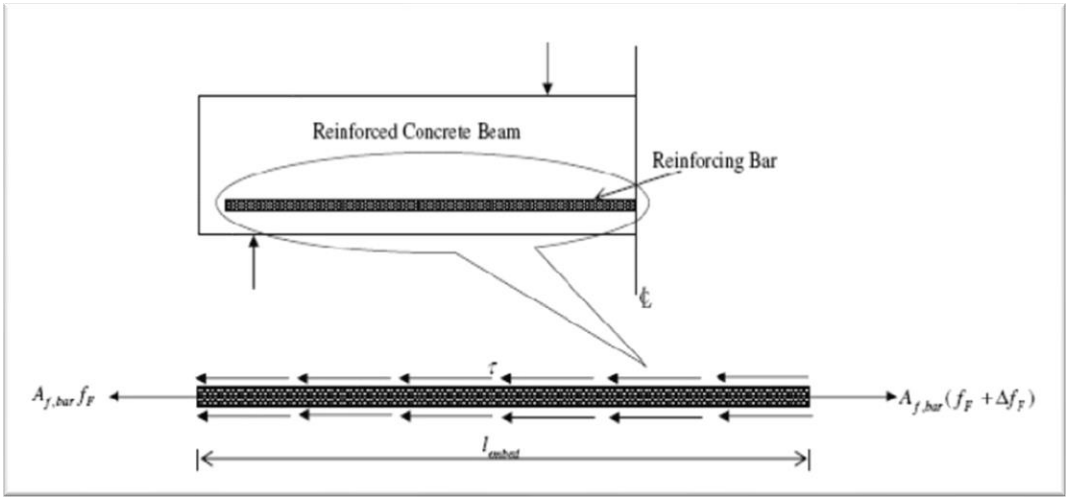

Figure 19: transfer of a force acting on surface of reinforcing bar through bond, [83]

$$\tau_f \pi d_b l_{embed} + A_{f,barf} f_F = A_{f,bar}(f_F + \Delta f_F) \quad (2.15)$$

$$\tau_f = \frac{A_{f,bar}\Delta f_F}{\pi d_b l_{embed}} = \frac{d_b \Delta f_F}{4 l_{embed}} \quad (2.16)$$

where,τ_f = average bond stress (MPa);

d_b = diameter of the bar (mm);

l_{embed}= embedment length of the bar (mm);

f_F = tensile stress of the bar (MPa);

$A_{f,bar}$ = area of one bar (mm^2).

There is not a direct bond strength equation presented in design codes. In other hand, all design codes state the require embedment length to develop the design stress in

the bar. Therefore by substituting embedment length equations provided in design codes into equation (2.16), chosen parameters can be related to the bond strength.

CSA S806-02:

The equation to determine the development length for the FRP bars in Canadian Standards Association [112] is:

$$l_d = 1.15 \frac{K_1 K_2 K_3 K_4 K_5}{d_{cs}} \times \frac{f_F}{\sqrt{f_c'}} \times A_{f,bar} \quad (2.17)$$

l_d= development length of FRP bar (mm);

$A_{f,bar}$= rebar cross-sectional area (mm2);

d_{cs}= smallest of the distance from the closest concrete surface to the centre of the bar being developed or two-thirds the c-c spacing of the bars being developed (mm) $d_{cs} \leq 2.5 d_b$ (d_b has been mentioned above);

f_F= required tensile stress in the rebar (MPa);

f_c'= compressive strength of concrete (MPa);

K_1 = bar location factor (1.3 for horizontal reinforcement placed so that more than 300 mm of fresh concrete is cast below the bar; 1.0 for all other cases);

K_2 = concrete density factor (1.3 for structural low-density concrete; 1.2 for structural semi-low-density concrete; 1.0 for normal density concrete);

K_3 = bar size factor (0.8 for ≤ 300 mm^2; 1.0 for A_b > 300 mm^2);

K_4 = bar fibre factor (1.0 for CFRP and GFRP; 1.25 for AFRP);

K_5 = bar surface profile factor (1.0 for surface roughened or sand coated or braided surfaces; 1.05 for spiral pattern surfaces or ribbed surfaces; 1.8 for indented surfaces).

The average bond strength equation yields from replacement of equation (2.17) into equation (2.16):

$$\tau_f = \frac{d_{cs}\sqrt{f_c'}}{1.15(K_1 K_2 K_3 K_4 K_5)\pi d_b} \quad (2.18)$$

As mentioned in CSA S806-02, [112], Equation (2.18) shows that bond strength is influenced by the fibre type, bar surface configuration, concrete cover, concrete strength, concrete density and bar position.

ACI 440.1R-15:

Equation of bond strength for FRP bars in concrete represented in ACI 440.1R-15 as follows:

$$\frac{\tau}{0.083\sqrt{f_c'}} = 4.0 + 0.3\frac{C}{d_b} + 100\frac{d_b}{l_{embed}} \quad (2.19)$$

Where τ = is bond strength between FRP reinforcing and surrounding concrete;

f_c' = is concrete compressive strength;

C = is the lesser of the cover to the centre of the bar or one-half of the centre-to-centre spacing of the bars being developed;

d_b = is the bar diameter;

l_{embed} = is the embedment length of the bar in concrete.

This equation was mainly developed based on GFRP rebars and the experiment supported this equation was not included the effect of transverse reinforcement on bond strength. Thus, it is required to re-examine this equation with use of different types of fibres and usage of transverse reinforcement.

JSCE:

The development length of FRP bar in concrete for splitting failure is reformed by the Japanese Design Code [131] [83]. The modified expression is as follow:

$$l_d = \alpha_1 \kappa \frac{f_d}{4f_{bod}} d_b \quad (2.20)$$

Where f_d= is the design tensile strength of the reinforcement;

κ = is the a top bar modification factor that takes a value of 1 if there is less than 300mm of concrete cast below the bar;

d_b = is diameter of the bar (mm);

f_{bod} = is the design bond strength of concrete and it is given as:

$$f_{bod} = \frac{0.28\alpha_2 f_c'^{2/3}}{1.3} \leq 3.2 \ {}^{N}/_{mm^2} \quad (2.21)$$

Where f_c' = is the concrete compressive strength (MPa);

α_2 = is the bond strength modification factor (it is equal to 1 when bond strength is equal to or greater than the deformed steel bar, or else α_2 shall be reduced according to the test results);

α_1 = is confinement modification factor defined as listed below:

α_1 =1.0 (where $k_c \leq 1.0$);

α_1 =0.9 (where $1.0 < k_c \leq 1.5$);

α_1 =0.8 (where $1.5 < k_c \leq 2.0$);

α_1 =0.7 (where $2.0 < k_c \leq 2.5$);

α_1 =0.6 (where $k_c > 2.5$);

And k_c equation is:

$$k_c = \frac{c}{d_b} + \frac{15A_t}{sd_b} \times \frac{E_t}{E_s} \quad (2.22)$$

Where c= is the smaller of the bottom clear cover of main reinforcement or half of the clear space between reinforcement being developed;

A_t = is the area of transverse reinforcement;

E_t = is the Young's modulus of transverse reinforcement;

E_s = is the Young's modulus of steel;

CSA S6-06:

The modified expression for development length of FRP bar in the Canadian Highway Bridge Design Code [198] is presented as follow:

$$l_d = 0.45 \frac{k_1 k_4}{[d_{cs} + K_{tr} \frac{E_{FRP}}{E_s}]} [\frac{f_F}{f_{cr}}] A_{f,bar} \quad (2.23)$$

Where l_d= is the development length for FRP bar, (mm);

$A_{f,bar}$= is cross-sectional area for bar, (mm^2);

d_{cs}= smallest of the distance from the closest concrete surface to the centre of the bar being developed or two-thirds the c-c spacing of the bars being developed (mm);

K_1 = bar location factor;

K_4 = bar surface factor;

K_{tr}= is transverse reinforcement index (mm), which is defined as follow:

$$K_{tr} = \frac{A_{tr} f_y}{10.5sn} \tag{2.24}$$

Where A_{tr}= is area of transverse reinforcement normal to the plane of splitting through the bars, (mm^2);

f_y= is the yield strength of transverse reinforcement, (MPa);

S= is centre to centre spacing of the transverse reinforcement, (mm);

n= is the number of bars being developed along the plane of splitting;

E_{FRP} = modulus of elasticity of FRP bar (MPa);

E_s = modulus of elasticity of steel (MPa);

f_F = specified tensile strength of FRP bar (MPa);

f_{cr} = cracking strength of concrete (MPa).

By implementing equation (2.24) into equation (2.16) provides expression for average bond strength related to Young's modulus of FRP bar and steel as follow:

$$\tau_f = \frac{f_{cr}(d_{cs} + K_{tr}\frac{E_{FRP}}{E_S})}{0.45\pi d_b k_1 k_4} \tag{2.25}$$

Among different bond strength equations, CSA S806-12 code is including the most parameters influencing FRP concrete bond. The factors includes bar location k_1, density of concrete k_2, bar size k_3, bar fibre k_4, and bar surface k_5. In case of CSA S6-10, equation of bond strength is also considered young's modulus of FRP and steel, the area of transverse reinforcement, the spacing between reinforcement and flexural strength of concrete. The mentioned equations in codes are identified to yield over conventional approximations. Table (8) shows following existing equations for the FRP concrete bond stress.

Guideline & Experimental work	Bond strength equation
ACI 440 1R-15	$\tau = \frac{\sqrt{f_c'}(0.332 + 0.025\frac{c}{d_b} + 8.3\frac{d_b}{l_e})}{\alpha}$
CSA S6-10	$\tau = \frac{\left[d_{cs} + Ktr\frac{E_{frp}}{E_s}\right] f_{cr}}{0.45(k_1 k_4)\pi d_b}$
CSA S806-12	$\tau = \frac{d_{cs}\sqrt{f_c}}{1.15(k_1 k_2 k_3 k_4 k_5)\pi d_b}$
JSCE	$\tau = \frac{f_{bod}}{\alpha_1}$
Okleo and Yuan	$\tau = 14.7\frac{\sqrt{f_c'}}{d_b}$
Lee et al	$\tau = 3.3(f_c')^{0.3}$

Table 8: Existing bond strength equations.

Numerous researchers have conducted experiments and compared their findings with the values derived from established code equations, leading to similar conclusions. For instance, Newman [199], scrutinized 48 specimens of GFRP and CFRP reinforced concrete beams against the equations from ACI 440.1R-06 and found them to be reliable. Similarly, Hossein [200], arrived at a comparable conclusion after conducting bond tests on 96 specimens and comparing the results to CSA S6-06, CSA S806-12, and ACI 440.1R-06. In another study, Ametrano [201], compared the results of 72 pull-out tests and 32 beam tests with equations from ACI 440.1R-06, CSA S6-06, and JSCE, reporting a substantial safety margin. However, Okleo and Yuan [121] conducted tests on 151 specimens with concrete compressive strengths ranging from 29 to 60 MPa and GFRP bars measuring 6 to 19mm. They found that the equation for bond strength suggested by ACI 440.1R-06 was applicable, while the JSCE code did not account for all the variables affecting the bond between FRP and concrete. In a separate investigation, Lee et al. tested 54 specimens with concrete compressive strengths ranging from 25 to 92 MPa and sand-coated GFRP rebars [111].

Despite a consensus among researchers regarding the safety of code equations, there are differing opinions on which equation best approximates real-life experimental results. Yan [202], reported that the experimental results of pull-out tests closely

aligned with the values predicted by the ACI 440.1R-15 equation, diverging further from other code equations. In the study by [203] the results of a pull-out test on GFRP bars were compared to the bond strength values predicted by the ACI 440.1R-15 equation, and a strong agreement was observed. Conversely, CSA S6-06 and CSA S806-12 deviated further from the values obtained through experimental testing. On the contrary, Makhmalbaf [204], concluded that the equation from ACI 440.1R-15 is overly conservative, and other code equations provide predictions that are closer to the experimental values.

These differing viewpoints regarding the adequacy of code equations underscore the need for potential modifications to the bond strength equations within the guidelines, based on the outcomes of existing experimental studies.

2.11 Models of Bond-slip behaviour of FRP Reinforced Concrete

To delve into the numerical analysis of the bond interaction between FRP reinforcement and concrete, it is imperative to establish an analytical model representing the bond stress-slip constitutive relationship. Over time, a multitude of such models for FRP reinforcement in concrete have been proposed. In the subsequent section, we will provide a concise overview of the most prevalent models for FRP bars, offering a comparative analysis to delineate their respective advantages and limitations.

2.11.1 Malvar Model

The initial modelling of the bond phenomenon for FRP rods was developed by Malvar, drawing from data derived from pull-out tests [114]. In his experimental investigation, GFRP bars were utilized, featuring three distinct surface configurations (indented surface, deformed surface, and a combination of deformed and indented surfaces). The study encompassed a spectrum of confinement pressure values and indentation depths, with the tensile strength of the concrete being held constant. Malvar formulated two empirical relationships grounded in the observed bond stress-slip curves. These relationships are expressed in equations (2.26) and (2.27):

$$\frac{\tau_1}{f_t} = A + b\left(1 - e^{-c\tau_1/f_t}\right) \quad (2.26)$$

$$s_1 = D + E\sigma_1 \tag{2.27}$$

Where:

f_t : Is tensile concrete strength

A, B, C, D and E: are empirical constants for different types of bar

The subsequent formulation, denoted as $\tau = \tau\,(s, \sigma_r)$ in equation (2.28), represents a refined model capturing the comprehensive bond behaviour. In this model, a total of seven empirical constants were introduced to elucidate the relationship between bond stress and the slip at the loaded end.

$$\frac{\tau}{\tau_1} = \frac{F\left(\frac{s}{s_1}\right)+(G-1)\left(\frac{s}{s_1}\right)^2}{1+(F-2)\left(\frac{s}{s_1}\right)+G\left(\frac{s}{s_1}\right)^2} \tag{2.28}$$

Where:

F, G: are empirical constants determined for different bar

τ_1: Is the peak bond stress

s_1: is slip at the peak bond stress.

Malvar's experimental investigation was limited to GFRP rebars featuring only two distinct surface configurations. Consequently, the influence of parameters like rebar diameter and various types of fibres on the empirical constants used in the model were not explored. Furthermore, a study by Consenza [205] compared various bond-slip behaviour models, revealing that while Malvar's model could describe the complete stress-slip curve using a single relationship, it was less dependable in modelling the ascending segment of the bond stress-slip curve compared to other existing analytical models.

2.11.2 Eligehausen, Popov, and Bertero Model (BPE Model)

The bond-slip analytical law first proposed by Eligehausen in 1983, [206] for conventional deformed steel rods and then successfully applied to FRP rebars to show bond stress-slip relationship by Faoro, [207], Alunno Rossetti [123] and Cosenza [205]. BPE model has an ascending curve branch that characterizes the bond

mechanisms of chemical adhesion where ($s \leq s_1$), then the model presents constant maximum bond stress ($\tau = \tau_1$) up to a slip $s = s_2$; a linear descending branch from slip and stress of (s_2, τ_1) to (s_3, τ_3); and finally a horizontal branch $s > s_3$ and value of τ due to constant frictional response ($\tau = \tau_3$), figure (20).

Following equations defines the bond-slip curve of BPE model that the bond stress is a function of the bond-slip curve relation:

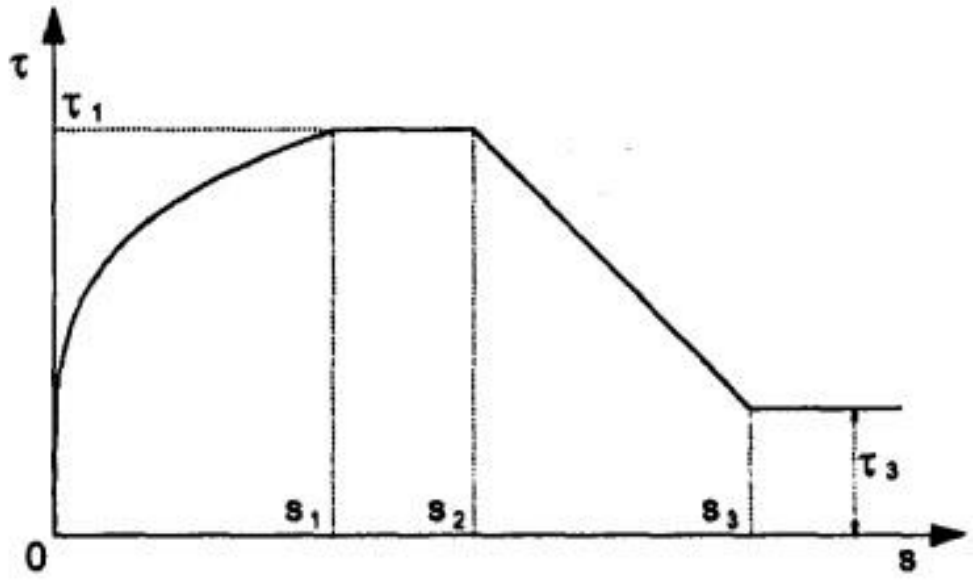

Figure 20: BPE model

$$\frac{\tau}{\tau_{max}} = \left(\frac{s}{s_1}\right)^{\alpha} \qquad for \qquad 0 \leq s \leq s_1 \tag{2.29}$$

$$\tau = \tau_{max} \qquad for \qquad s_1 < s \leq s_2 \tag{2.30}$$

$$\tau = \tau_{max} - \left(\tau_{max} - \tau_f\right)\left(\frac{s - s_2}{s_3 - s_2}\right) \qquad for \qquad s_2 < s \leq s_3 \tag{2.31}$$

$$\tau = \tau_f = \beta\tau_{max} \qquad for \qquad s_3 < s \tag{2.32}$$

In equation (29), in order for graph to be physically meaningful α, which is a curve-fitting parameter, must be equal or less than 1. Eligehausen, [206], proposed α value of 0.40 for case of steel bars. The model is extracted properties and developed based on CEB-FIP analytical model that was for conventional steel reinforcements with specific series of parameters including peak bond stress τ_{max}, slip at peak bond stress s_1 and other parameters such as α and β, which related to the amount of concrete strength and bond conditions. In research carried out by Cosenza, [205], parameters

of s_2, s_3 and β and α were determined for FRP re-bars with different types of fiber, surface configurations and confinement pressures as variables. Results from the tests consisting of indented and grain covered rebars showed good conformity in terms of bond strength, however, the test for the spirally wounded rebars were in various directions.

2.11.3 BPE Modified Model

Consenza introduced a revised model based on the BPE model. This modified model accounts for the influence of both FRP bond strength and various surface configurations. Following a thorough comparison between experimental and analytical curves, the BPE modified model excludes the second branch, characterized by a constant maximum bond stress, present in the original BPE model.

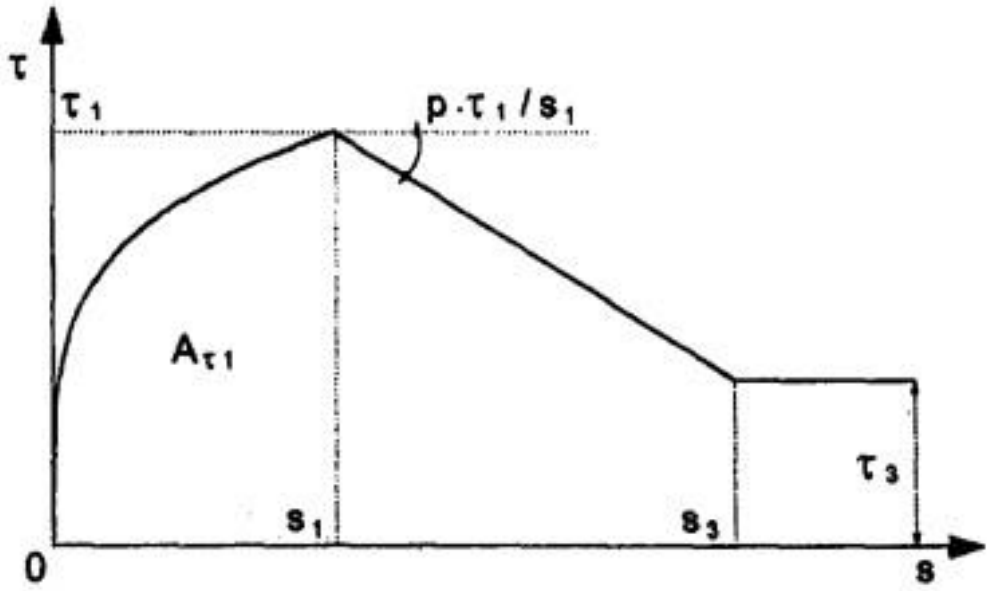

Figure 21: BPE modified model

Although in this model the overall bond slip curve for FRP bars given, but effects of different fibre types and bar diameter have not been covered. Following equations represent the segments for curve in Figure (21):

$$\frac{\tau}{\tau_1} = (\frac{s}{s_1})^{\alpha} \qquad for \qquad 0 \leq s \leq s_1 \tag{2.33}$$

$$\frac{\tau}{\tau_1} = 1 - p\left(\frac{s}{s_1} - 1\right) \qquad for \qquad s_1 < s \leq s_3 \tag{2.34}$$

$$\tau = \tau_3 \qquad for \qquad \tau_3 < s \tag{2.35}$$

2.11.4 CMR Model

Consenza proposed another model for only the ascending branch of the bond slip curve at serviceability level.

$$\frac{\tau}{\tau_1} = (1 - \exp\left(-\frac{s}{s_r}\right))^{\varphi} \tag{2.36}$$

Where:

s_r, φ: are parameters based on curve-fitting resulted from test data.

In the experiment, effects of factors such as different surface configurations and various fibre types were investigated. Thu, some of the test included scattered results.

To ensure accurate predictions of bond-slip behaviour, it is crucial to select an appropriate bond-slip model that reflects the overall shape of the curve. Figure (22) illustrates bond-slip models for typical adhesive FRP-to-concrete joints sourced from [208] [209] [210] [163] which are grounded in experimental data. Notably, the Nakaba linear-brittle model differs from the other three bond-slip models. Previous research has indicated that a realistic bond-slip curve should exhibit both ascending and descending branches, similar to the B.P.E modified model. However, Neubauer's linear-brittle model does not align well with actual results. Beyond the general shape of the bond-slip model, critical parameters such as slip at peak stress, peak bond stress, and maximum slip at zero bond stress play a vital role in determining the accuracy of the bond-slip model.

It is important to note that the models proposed by Nakaba, Monti, Savioa, and the B.P.E modified model exhibit significant alignment and are specifically tailored to represent the occurrence of failure in the models. After reviewing the existing literature, the B.P.E modified model has been selected for the present study. A table containing bond-slip models and equations from these mentioned authors can be found in Appendix (A).

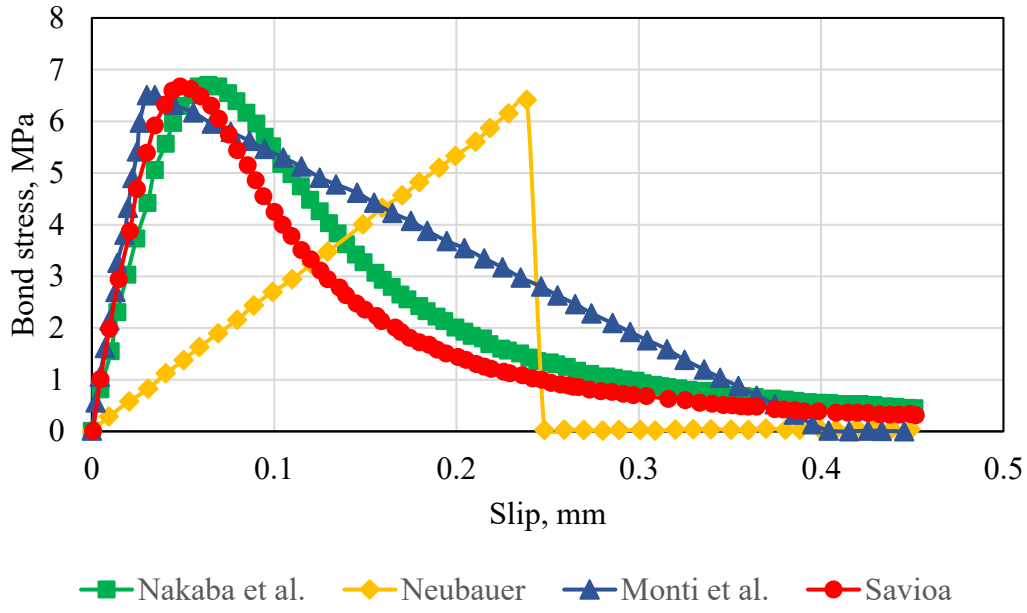

Figure 22: Bond-slip curves of existing bond-slip model.

2.12 Existing works on bond behaviour of FRP RC members under static and dynamic loading

In order to assess the response of FRP RC beams under varying loads and to comprehend the overall behaviour of the structure, it is imperative to employ a suitable bond-slip model that defines the bond behaviour within FRP RC beams. Understanding the deformation within reinforced concrete structures necessitates an in-depth investigation into the interaction between the reinforcing elements and the concrete matrix. This investigation becomes particularly significant in the context of bond strength, as bond behaviour plays a pivotal role in the design of reinforced concrete components. While numerous guidelines exist for the formulation of steel-reinforced concrete members, their direct applicability to FRP reinforcements has often proven inadequate. The dearth of precise information and accuracy in some of the existing methods has prompted researchers to conduct experimental studies aimed at comprehending how the material properties of reinforcement impact the characteristics of bond behaviour. Additionally, a substantial volume of experimental work has been undertaken to assess the effects of impact and impulse loading on reinforced concrete members, supported by numerical studies utilizing finite element methods, which have been corroborated by experimental data.

2.12.1 Static Experimental Investigations on FRP RC members

Murugan [211] conducted tests on four concrete beams reinforced with GFRP bars: two of them were reinforced with sand-coated GFRP bars with a reinforcement ratio of 0.73%, and the other two were reinforced with grooved GFRP bars with a reinforcement ratio of 1.24%. These tests subjected the beams to monotonic loading. The results demonstrated that the ultimate load-bearing capacity of the sand-coated and grooved GFRP bars was 15% and 5% lower, respectively, when compared to steel-reinforced beams. Furthermore, an increase in the reinforcement ratio of GFRP to 1.08% led to a 25% increase in the ultimate load for sand-coated GFRP beams and a 40% increase for grooved GFRP bar beams. Additionally, an increase in the reinforcing ratio resulted in smaller maximum deflections for the grooved bar beams when compared to the sand-coated bar beams. The moment-curvature behaviour of all beams is depicted in the following Figure (23).

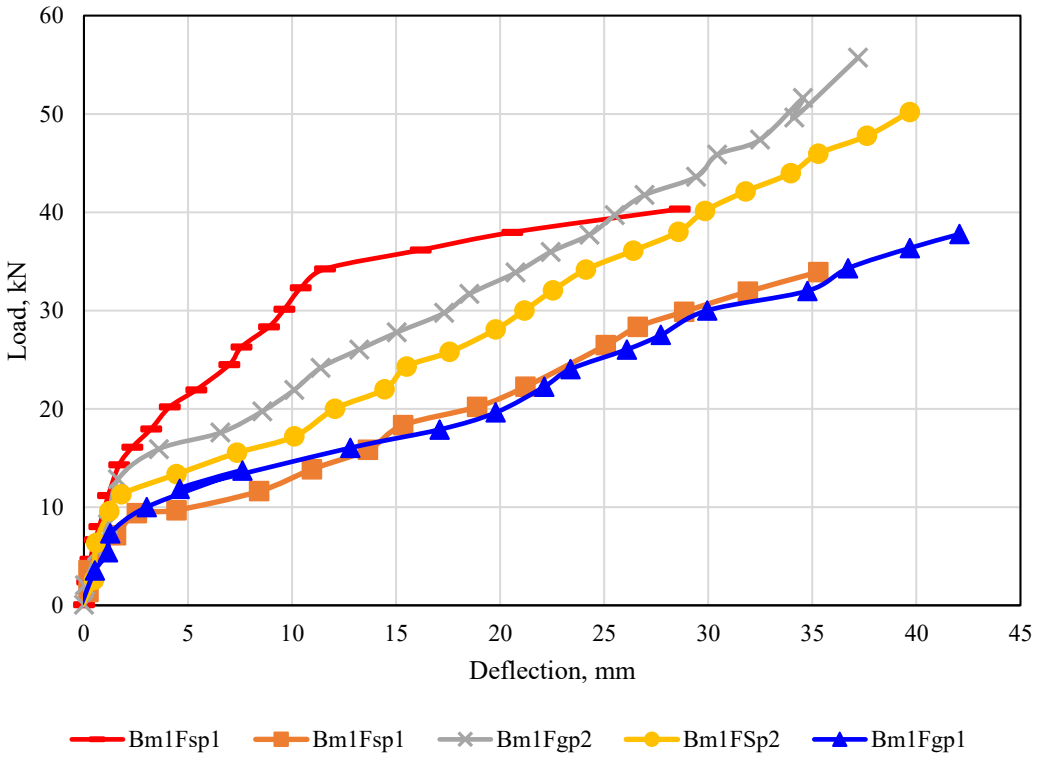

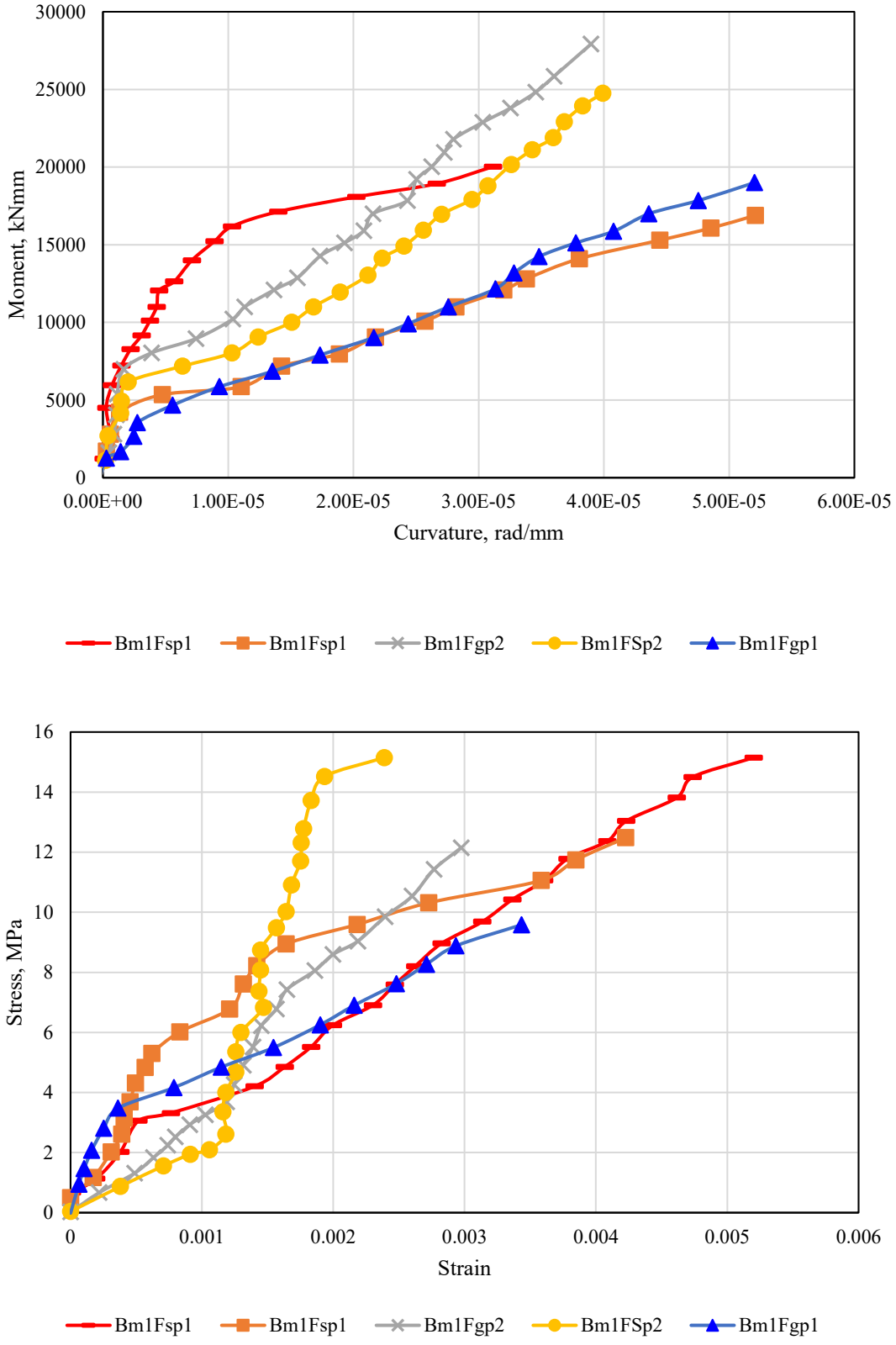

Figure 23: Results from Murugan experimental tests.

Beam	GFRP type	Reinforcement ratio
$Bm_1F_eP_1$	Steel	0.73
$Bm_1F_sP_1$	Sand coated	0.73
$Bm_1F_sP_2$	Sand coated	1.08
$Bm_1F_gP_1$	Threaded	0.73
$Bm_1F_gP_2$	Threaded	1.08

Table 9: Detail of beam Specimens from Murugan experiment.

Al-Allaf [212] conducted a series of pull-out tests on lightweight concrete prisms reinforced with CFRP sheets. The experimental results revealed that the use of lightweight concrete substantially reduced the bond strength and had a minor influence on bond slip failure compared to the normal weight concrete specimens. Interestingly, increasing the length of the CFRP sheets beyond 75 mm did not lead to a reduction in slip failure or an increase in load capacity.

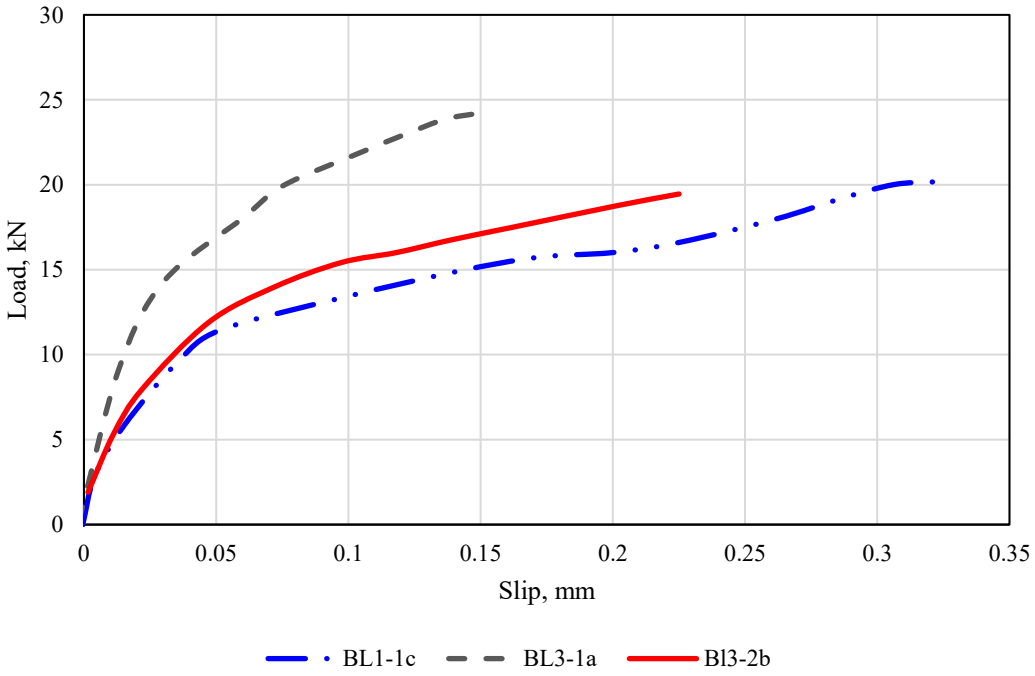

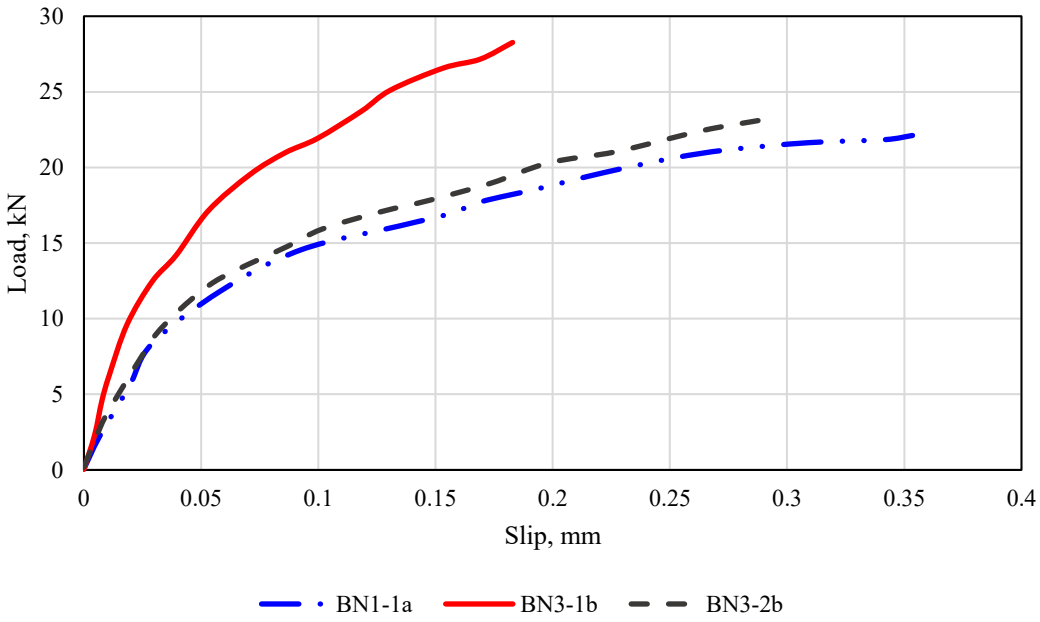

Figure 24: Influence of CFRP bond thickness of lightweight and normal weight concrete specimens on slip from AL-Allaf experimental test.

Zhang [213] conducted 4-point bending test to investigate the flexural and bond-slip characteristics of RC beams reinforced with CFRP, GFRP, and BFRP, considering various bar diameters and surface configurations. The test outcomes revealed that specimens with smooth surface bars exhibited inferior performance in bond-slip behaviour. Additionally, FRP bars with grain-covered surfaces exhibited superior bonding compared to other specimens.

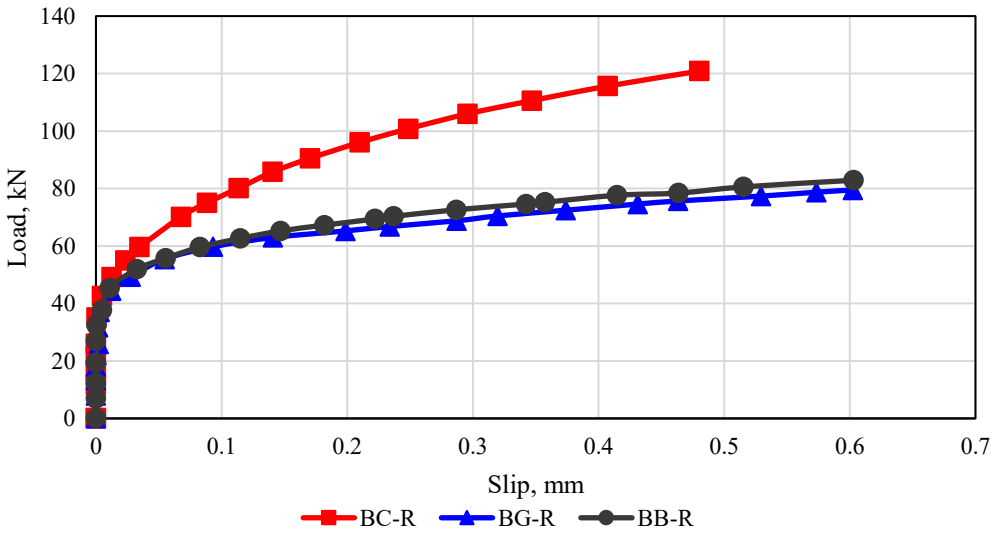

Figure 25: Load-Slip curvature for different FRP bar types in RC beams with ribbed surface from Zhang experimental test.

Pan [214] conducted an analytical investigation into the failure mechanism of the bond between FRP plates and concrete joints. For this study, a straightforward bond-slip model with a linear ascending segment was employed. The results revealed that the stiffness of the FRP plates was significantly affected by the effective bond length of the FRP.

Lu [215] compiled a comprehensive test database and compared the test results with existing bond models by Neubauer [209]and Chen and Teng [216]. This comparison considered various parameters, including concrete strength, the influence of bond length, width ratio, and FRP plate stiffness. Chen's model [216] was found to provide accurate predictions for bond strength and ultimate loads when compared to a substantial body of experimental data. However, it lacked a suggested bond-slip relationship suitable for numerical applications. The static bond-slip model proposed by Lu [215] was primarily built upon Chen's work [216].

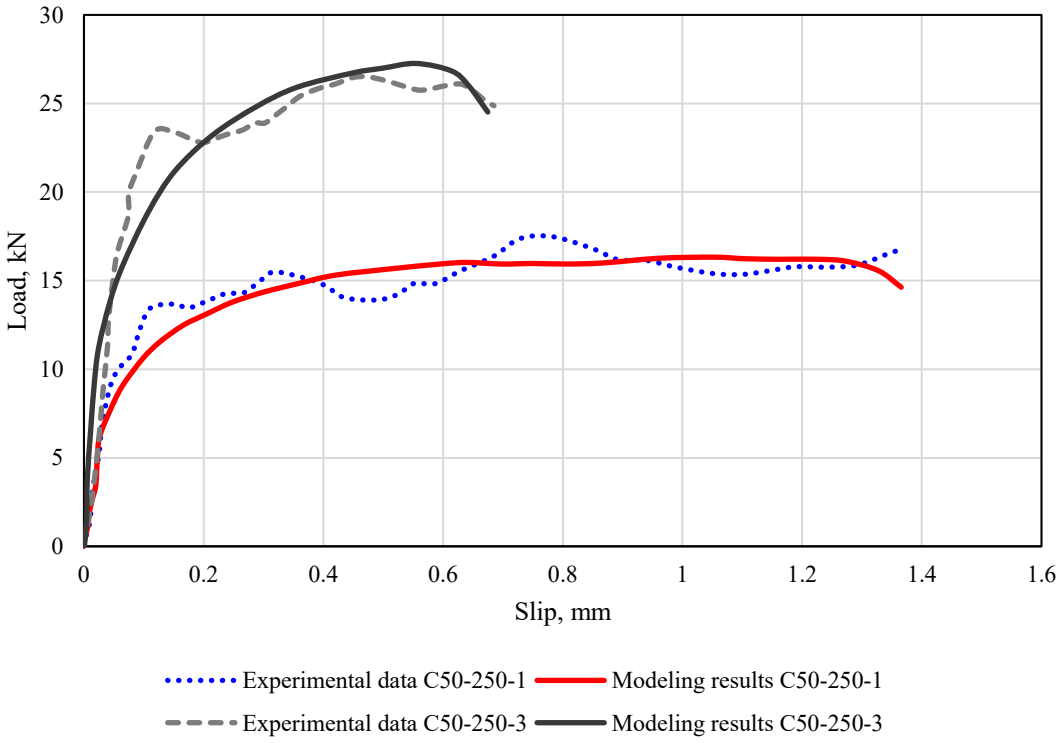

Figure 26: Load-Slip relationship of CFRP plate reinforced concrete from analytical and experimental work by Pan.

The author presented data of 118 test specimens and set of predictions of bond strength models that shown in Figure (27).

The standard deviation, Δ in statics is implemented to verify which static bond-slip model is more appropriate as the basis for the dynamic bond-slip model.

$$\Delta = \sqrt{\frac{\sum_{i=1}^{n}(x-\bar{x})^2}{n}} \tag{2.37}$$

Δ is standard deviation with the same unit as the sample x;

$\bar{x}$ is average value;

x is normalised ultimate load, that is equal to the value of analytical ultimate load from Equation (2.38) divided by the ultimate load from test data.

$$\tau_{max} = \frac{P_u^2}{E_p t_p b_p^2 s_f}$$

τ_{max} is the maximum value of bond stress;

P_u is the ultimate load at the FRP end from the load slip curve;

E_p is young's modulus of FRP;

t_p Is the thickness of FRP plate;

b_p is width of FRP plate;

s_f is the final slip of bond-slip curve.

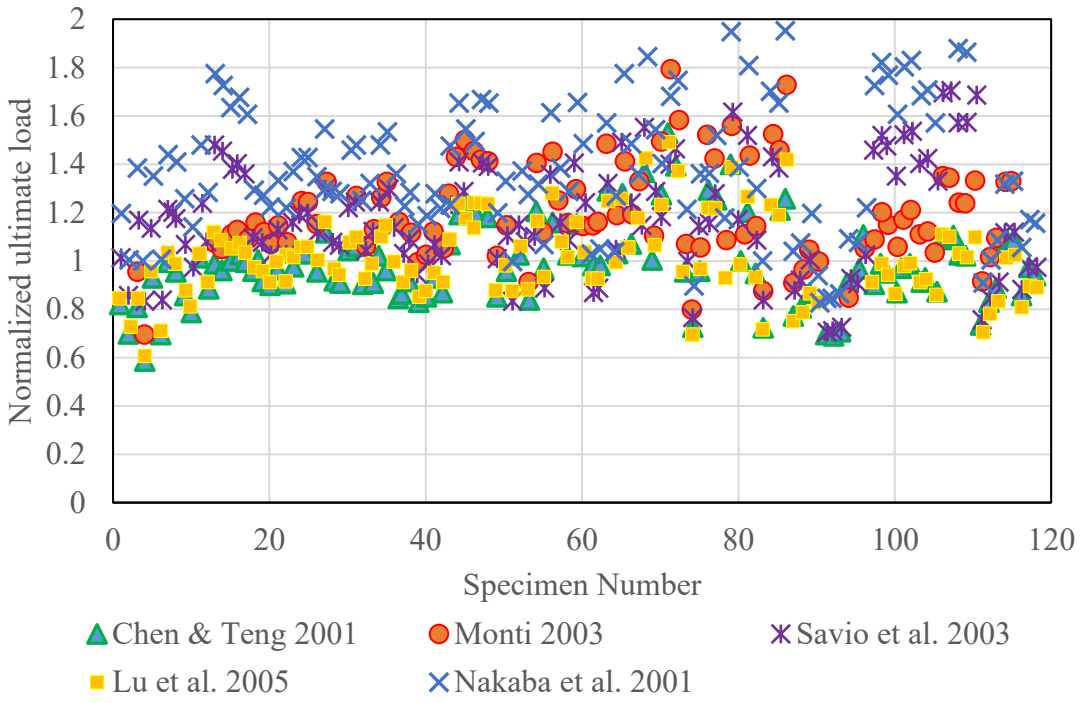

Figure 27: Normalized maximum load predictions from existing bond strength models.

Figure (27) clearly illustrates a strong concurrence between the findings of Chen [216] and Lu [215]. Lu [215] elucidated in his research that two distinct approaches could be employed for modelling de-bonding in FRP RC members using nonlinear finite element models.

The first approach involves the utilization of an interface element, incorporating a layer of interface between the FRP element and concrete, to simulate de-bonding failure. This method is grounded in the existing bond-slip model.

The second approach recommends circumventing the interface element and instead directly simulating de-bonding failure by modelling concrete cracking at a short distance from the adhesive layer.

2.12.2 Experimental investigations on FR PRC members

The subsequent section provides an account of investigations into FRP-concrete debonding and the behaviour of reinforced concrete beams subjected to impact loads, utilizing a combination of numerical, experimental, and analytical techniques.

Several researchers have delved into the dynamic characteristics of FRP materials, focusing on parameters like tensile strength and elastic modulus under dynamic loading conditions. For instance, Eskandari [217] conducted tensile split Hopkinson bar tests on five specimens of quasi-isotropic graphite/epoxy composites with a nominal thickness of 1.4 mm. The tests featured pulse durations ranging from 200 to 250 microseconds and peak strain rates of$350s^{-1}$.

Armenakas and Sciammarella [159] explored the mechanical properties and failure modes of glass/epoxy-reinforced plates under high strain rates of 3×10^4in./in./min applied in the direction of the fibres. Shokrieh and Omidi, [177], investigated the tensile failure properties of unidirectional glass/epoxy composites using high-speed servo-hydraulic testing, with test speeds ranging from 0.001 to 2000 mm/s and strain rates from 8×10^{-5} to $160s^{-1}$.

Hou [152] conducted a comprehensive investigation involving experimental and finite element analysis of 3-D orthogonal woven fabric (3DOWF) subjected to high strain rate impulse loading, with a specific focus on understanding the tensile behavior of these specimens. The experimental setup featured a specially designed split Hopkinson tension bar, enabling testing across a wide range of strain rates, from 0.003 to$2308s^{-1}$. The stress-strain data derived from these tests were employed to assess how 3DOWF responds to variations in strain rate, thereby establishing its tensile sensitivity to such dynamic loading conditions.

In the numerous experimental studies mentioned earlier, including those by Lifshitz, [59] and Daniel [223], which are just a subset of the extensive research in this field [218] [219] [220] [221] [222], it has been consistently observed that the dynamic properties of FRP materials are sensitive to the loading rate, and this sensitivity varies with different loading rates. However, Lifshitz [59] specifically examined the tensile strength of seven glass/epoxy fibre unidirectional laminas under impact loading,

employing a drop weight apparatus with strain gauges to measure strain rates and an impact velocity of $4.2\,m/s$. This study concluded that the failure mechanism of laminates is contingent upon fibre orientations, and the tensile strength of FRP material does not exhibit sensitivity to strain rate variations. Building upon this work, Daniel [223] delved into the influence of strain rate on graphite/epoxy unidirectional laminates and ring specimens exposed to strain rates ranging $100 - 500s^{-1}$.

with specimens loaded through internal pressure generated explosively by a liquid. The author concluded that FRP materials did not demonstrate dependencies on modulus, tensile strength, or strain failure rate in relation to strain rate variations. It's important to acknowledge that these conflicting findings might arise from variations in material fabrication, potential experimental errors, or the different ranges of loading rates examined across these studies.

Jadhav, [221], conducted an investigation into the influence of fibre orientation on the dynamic properties of angle-ply graphite/epoxy composites, focusing on aspects such as modulus, ultimate strain, and strength. This study employed the split Hopkinson pressure bar test, subjecting the specimens to varying strain rates ranging from $500 - 1500s^{-1}$. The results of this research indicated that, as the applied strain rate increased, the stress-strain characteristics of FRP materials generally exhibited an upward trend. Specifically, the ultimate strain of FRP materials showed a continuous increase with rising strain rates, while the stress remained relatively constant as the ultimate stress reached a specific peak value.

Among these investigations, Lifshitz [224], Hayes [69], Gilat [222], Barre [225], Niak [226] did not report significant strain failure in their respective studies. In contrast, Armenakas, Eskandari, Shokrieh, and Hou reported an increase in strain failure in their experimental work [159] [227] [158] [152]. Additionally, some other studies indicated a decrease in strain failure [228] [218] [219], while Liftaz observed no significant alteration in strain failure in his experiments [59]. It is important to note that the observed variations in strain failure outcomes across these studies could be attributed to factors such as differences in experimental methodologies, material variations, or the specific range of strain rates investigated.

Goldston, [23] conducted an experimental investigation to examine the behaviour of concrete beams reinforced with GFRP bars subjected to both static and impact loading conditions. This study involved a total of 12 rectangular concrete beams, each with cross-sectional dimensions of 100×150 mm and a length of 2400 mm. These beams were reinforced with internal FRP bars. Two different levels of average concrete compressive strength were considered: 40 MPa and 80 MPa. Furthermore, three distinct GFRP bar diameters of 6.35 mm, 9.53 mm, and 12.7 mm were employed to achieve varying reinforcement ratios of 0.5%, 1.0%, and 2.0%.

The experimental program was divided into two series. The first series encompassed six specimens that were subjected to four-point static loading. In contrast, the second series included six beams that were subjected to impact loading using a drop hammer apparatus. All six beams in the second series were simply supported and subjected to dynamic three-point loading. The primary objective of the second series was to investigate dynamic GFRP tensile strain, dynamic mid-span deflections, the impact force's influence, and dynamic reaction forces.

The test parameters under consideration included the concrete compressive strength and the longitudinal reinforcement ratio. The beams were designed with double reinforcement, featuring two GFRP bars in the compression zone and two in the tension zone. The results revealed that beams subjected to impact loading experienced shear plug failure, with cracks appearing on both sides of the impact points, approximately in parallel. A limited number of flexural cracks were observed, and the beams remained within the elastic range even after being impacted by the drop hammer. This behaviour was attributed to the energy absorption capacity of the beams. Additionally, it was found that higher concrete compressive strength played a dominant role in reducing mid-span deflection and increasing post-cracking bending stiffness.

In study conducted by Elgabbas [229], an experimental investigation was carried out to examine the structural performance of Basalt FRP (BFRP) bars in concrete beams subjected to four-point bending. The primary objective of this research was to

characterize the flexural behavior of the bars under both service and ultimate limit conditions while assessing the bond-dependent coefficient (k_b), which quantifies the bond between the FRP bars and the concrete.

The specimens consisted of six concrete beams with cross-sectional dimensions measuring 200×300 mm and a length of 3100 mm. The concrete used in this experiment exhibited a compressive strength of 40 MPa. For tension reinforcement, three different BFRP bar diameters of 10 mm, 12 mm, and 16 mm, all with a sand-coated surface, were employed. Steel bars were utilized for the top and transverse reinforcements within the beams. These simply supported beams were subjected to monotonic loading in a four-point bending configuration until failure occurred.

The results revealed a characteristic bilinear relationship between tensile strains in the FRP and the average compressive strain in the concrete, especially in beams with low reinforcement ratios, up to the point of failure. Neither pre-cracking nor cracking load was affected by the reinforcement ratio. However, after cracking, an increase in stiffness or a decrease in reinforcement strains exhibited a proportional relationship with the reinforcement ratio. Furthermore, an increase in the reinforcement ratio led to higher energy absorption during the initial crack formation, resulting in increased strain and the initial crack width.

Lin and Zhang, [230], conducted an extensive investigation into the bond-slip relationship of glass, carbon, and basalt FRP (Fiber Reinforced Polymer) rebars in concrete beams under four-point bending, employing both experimental and numerical methods.

In the experimental phase, four-point bending tests were employed on FRP-reinforced beams to elucidate the physical behavior of these composite concrete beams, focusing on their flexural and bond-slip characteristics. Additionally, numerical studies utilizing Finite Element methods were conducted to delve into the behavior of these FRP concrete beams, considering variables such as rebar surface treatment and rebar type.

Each specimen was fortified with three FRP rebars in the tension zone and two steel rebars in the compression zone. The test specimens consisted of six concrete beams, with cross-sectional dimensions measuring 100×200 mm, a length of 1060 mm, and a compressive strength of 40 MPa.

The results stemming from the experimental study unveiled a suboptimal bond between FRP bars with smooth surface treatment and the surrounding concrete. Consequently, this inadequate bond resulted in a substantial increase in deflection with only a marginal increase in load-bearing capacity. Conversely, concrete beams reinforced with BFRP (Basalt Fiber Reinforced Polymer) bars exhibited a superior load-bearing capacity and demonstrated enhanced bond performance in comparison to the other two types of FRP bars. The bond-slip relationship exerted a significant influence on the flexural behavior of the specimens. Despite GFRP (Glass Fiber Reinforced Polymer) and CFRP (Carbon Fiber Reinforced Polymer) bars possessing superior mechanical properties compared to BFRP, concrete beams reinforced with BFRP bars displayed superior structural behavior due to the robust bond formed between the surface-treated BFRP bars and the surrounding concrete beams.

Similar models were explored numerically using Finite Element methods, with the outcomes strongly supporting the efficacy of different surface configurations of the bars and aligning well with the experimental findings.

Shen and Shi [22] conducted an empirical investigation focusing on the dynamic behaviour of basalt FRP (Fiber Reinforced Polymer) sheets in conjunction with concrete, with specific attention to varying strain rates. The primary objective of this study was to assess the impact of strain rate variations on dynamic factors including the dynamic ultimate load, dynamic maximum bond stress, and dynamic bond slip occurring between BFRP sheets and concrete under dynamic loading conditions.

The concrete specimens employed in this study possessed an average compressive strength of 37.5 MPa. BFRP sheets, measuring 0.121 mm in thickness and 50 mm in width, were affixed to both sides of concrete blocks using epoxy resins in the axial

direction. These concrete blocks had cross-sectional dimensions of 100×100 mm and a length of 510 mm.

A servohydraulic testing machine was utilized to apply an initial load of 3.5 kN at a rate of 3.5 (kN)/min. Subsequently, dynamic loading was applied to the specimens until they reached the point of failure, at displacement rates of 0.07, 0.7, 7, and 70 mm/s. Three specimens were tested for each specific load history.

Based on the results obtained, the authors concluded that the dynamic maximum bond stress occurring between BFRP sheets and concrete increases as the strain rate escalates. The author presented the following equation to estimate the dynamic maximum bond stress under varying strain rates:

$$\tau = \tau_{max}^{d}[\frac{s}{s_0} \times \frac{n}{(n-1)+(s/s_0)^n}] \quad (2.37)$$

Where:

τ= The local bond stress- MPa;

s= the local slip- mm;

τ_{max}^{d}= the dynamic maximum local bond stress under different strain rate- MPa;

s_0= the slip at $\tau_{max}^{d} = 0.115mm$;

n= constant equal to 3.09.

Park and Lim [231] conducted an experimental investigation focusing on the bond performance of concrete members reinforced with FRP (Fiber Reinforced Polymer) rebars, with particular emphasis on the influence of various factors including the type of FRP, the position of concrete casting, and the location of the rebars within the concrete structure.

The experiment involved a total of 63 specimens, each incorporating seven distinct types of rebars. These rebars included zinc-coated deformed steel, deformed steel, spiral-wrapped GFRP (Glass Fiber Reinforced Polymer), sand-coated GFRP, braided CFRP (Carbon Fiber Reinforced Polymer), CFRP strand, and deformed AFRP (Aramid Fiber Reinforced Polymer). The specimens were subjected to vertical and horizontal

concrete casting positions, with rebars placed in two positions within horizontally casted concrete, corresponding to the top and bottom of the cross section. All the rebars employed in this experiment had a length of 810 mm.

For the vertically casted specimens, the dimensions were 150×150×150 mm^3, with the rebars aligned along the central axis. In contrast, the horizontally casted specimens had dimensions of 150×150×300 mm^3. The arrangement of all specimens adhered to the CSA S806-02 standard. A universal testing machine with a capacity of 1000 kN was utilized to conduct pull-out tests. The test was conducted under displacement control, with a loading rate applied to the rebars of approximately 0.9 mm/min.

The findings revealed that the bond performance of FRP rebars was significantly influenced by their external surface configurations. Notably, the average bond strength of FRP rebars measured 54% that of steel deformed rebars. Among the various types of FRP rebars, those with sand-coated surfaces exhibited the most favourable bond behaviour, while strand-type and spiral rebars displayed the least desirable performance. To optimize bond performance, the authors recommended the use of sand-coated surface rebars for reinforcement.

In analysing the bond stress-slip characteristics of deformed steel and GFRP rebars, it was observed that the bond stress rapidly decreased after reaching its peak value. Conversely, for AFRP, CFRP strand, and CFRP braided rebars, the bond stress progressively decreased after reaching its maximum, and the associated slip was moderately significant.

Furthermore, the test results indicated that bond strength varied in response to variations in concrete casting positions and rebar locations. Specifically, the average bond strengths of horizontally cast specimens were found to be 40% and 91% of those for vertically cast specimens for top and bottom rebars, respectively.

Baena and Torres [4] conducted an extensive investigation aimed at assessing the bond behaviour between concrete and FRP (Fiber Reinforced Polymer) bars through pull-out tests. The study adhered to the standards set by ACI 440.3R-04 and CSA S806-

02. The research involved a total of 88 specimens, with the primary objective of elucidating the influence of various factors, including rebar surface characteristics, fibre type, rebar diameter, and concrete strength.

The FRP bars incorporated in this study encompassed several types, namely CFRP (Carbon Fiber Reinforced Polymer) and GFRP (Glass Fiber Reinforced Polymer) bars with sand-coated surfaces, CFRP bars with textured surfaces, GFRP bars with helical wrapping and sand coating, GFRP bars with grooved surfaces, GFRP bars solely with helical wrapping, and, for the sake of comparison, steel rebars.

To encompass a wide range of scenarios, two distinct concrete compressive strengths were employed, corresponding to values of 28.63 MPa and 52.19 MPa. The experimental findings were analysed with respect to changes in bond strength and failure modes, highlighting the variations in concrete compressive strength and the surface characteristics of FRP bars. The results underscored the presence of distinct bond mechanisms associated with different bar surface configurations.

However, it was observed that the effect of bar surface characteristics was less pronounced in concrete with low compressive strength when compared to concrete with high compressive strength. Moreover, the experimental results indicated that bars with larger diameters exhibited lower bond strength. It is important to note that the early stiffness of the specimens was not significantly influenced by the diameter of the bars.

2.12.3 Analytical Investigation on FRP RC members

The analytical expressions describing the bond-slip relationship of FRP bars, as mentioned, have been widely referenced in various literature sources to assess their ability to replicate experimental outcomes, [232] [113] [233] [234] [235] [103] [205]

[15] [236]. or instance, in the work conducted by Al-Mahmoud [113], the B.E.P analytical model was employed to complete the study. The model's unknown parameters were tailored to align with machine and sand-coated surface CFRP rods.

In another experimental investigation by Aiello [235], three theoretical approaches were considered, and the experimental results were scrutinized using bond stress-slip relationships. These theoretical approaches were based on equations (2.29) and (2.36), representing the B.E.P, C.M.R, and modified B.E.P models. The first phase of this investigation involved analyzing each type of rebar and gathering data from pull-out and modified pull-out tests. The primary aim was to explore the impact of these tests on bond properties. The second phase focused on evaluating the influence of rebar surface configurations. The results led to the conclusion that not only does the surface texture of the rebars affect the bond stress-slip relationship, but the mechanical properties of the individual rebars also exert a significant influence on bond properties. However, it's important to note that this study has limitations, particularly the absence of various surface textures and configurations, which represents a notable drawback.

Conversely, several researchers have delved into the relationship between the bond strength of FRP bars and the compressive strength of the surrounding concrete [111] [84] [121].

The researcher, Okelo [121], conducted an extensive experimental investigation involving pull-out tests on straight FRP reinforcing bars. This comprehensive study comprised 151 specimens featuring a variety of rebars, including steel, CFRP, GFRP, and AFRP, each with varying diameters ranging from 6mm to 19mm and employing five distinct surface configurations (sand-coated, textured, deformations, grooves, and helical wrapping with sand coating). The embedment lengths were set at 5 to 7 times the diameter of the rebars. Three different types of concrete were utilized, each with compressive strengths ranging from 29.7 MPa to 60.4 MPa. Several assumptions were made to establish a new relationship between bond strength and concrete compressive strength. These assumptions included assuming a normal distribution of the average bond strength, asserting that the average bond strength

was proportional to $(f_c')^{0.5}$, and observing a decline in the average bond strength of rebars as the diameter of the reinforcing bars increased. As a result of this comprehensive experimental study, the author proposed Equation (2.38):

$$\tau_{b,max} = 14.7\frac{\sqrt{f_c'}}{d_b} \tag{2.38}$$

The equation mentioned above was subjected to validation by Ehsani [95]. However, this validation was exclusively conducted for GFRP bars, utilizing constants of 14.7 and 14.25. The table below provides a compilation of equations derived from various studies that establish the relationship between bond strength and concrete compressive strength.

Author	Equation
ACI Design Code	$\tau_{b,max} = 20.23\frac{\sqrt{f_c'}}{d_b}$
Lee & Kim, [111]	$\tau_{b,max} = 4.1(f_c')^{0.5}$; $\tau_{b,max} = 3.3(f_c')^{0.3}$
Tighiouart & Benmokrane, [84]	$\tau_{max} = 4.97\frac{\sqrt{f_c'}}{d_b}$

Table 10: equations of bond strength of FRP reinforced concrete related to concrete compressive strength.

2.12.4 Numerical Investigation on FRP RC members

The analytical methodologies presented here offer valuable insights into describing bond behaviour. Nonetheless, it's important to note that these constants cannot be readily adapted to predict outcomes in tests conducted under varying conditions. Consequently, numerical approaches have been introduced to encompass a broader spectrum of bond mechanisms. Numerous research endeavours have employed

simulations to gain a deeper understanding of the interaction between FRP and concrete interfaces. These studies categorize modelling methods into four main divisions: the interface approach, smeared crack approach, discrete crack approach, and a hybrid approach that combines smeared crack and discrete crack methodologies.

Author Achillides, [237] introduced a model for an FRP concrete cube using two-dimensional elements. Concrete behaviour was represented by 4-noded plane elements, while the FRP material was depicted with 2-noded square elements. To simulate the bond interaction between FRP and concrete, spring elements were employed. The spring parameters were derived from experimental data obtained through short embedment length pull-out tests. Numerical simulations were conducted for longer embedment lengths, and the results, which indicated a reduction in bond strength as embedment length increased, were validated against analytical solutions. The numerical study revealed that the decrease in bond strength occurred at a higher rate for smaller embedment lengths compared to longer ones.

In another numerical model [238] the surface configurations of the bar and the one-dimensional geometry of the bar were considered. This model incorporated bar truss elements, bond elements, concrete elements, and an optional bond-slip law. The authors concluded that the results obtained from any finite element model assuming perfect bonding are highly dependent on the mesh size.

Author Tvergaard [239] proposed a debonding model that initially neglected friction, ensuring there was no damage to the interface. Friction was introduced only when discontinuity occurred in this model. In contrast, Chaboche [240] presented a model in which friction was introduced right from the beginning of the process. Both models were rooted in cohesive-zone models and incorporated mechanisms of accumulated damage from plasticity theory. They aimed to simulate a gradual debonding process with flexibility.

Interface approach

This approach, as indicated by previous research [215], is the most time-efficient method for simulating debonding between FRP and concrete. In this approach,

material properties for both concrete and FRP members are considered linear elastic, and the debonding phenomenon is represented using an interfacial layer that employs springs or cohesive elements. Numerous bond-slip models have been put forth by various researchers [241] [215] [210] [208] [163].

The interfacial approach is cost-effective because it confines the nonlinear mechanical behaviour to a limited number of elements between the FRP and concrete interface, while the remainder of the elements is modelled as linear elastic.

Discrete model

In this approach, the reinforcements are represented as bar or beam elements, which are linked to the nodes of the concrete mesh, as noted in a previous study [267]. Consequently, there is node sharing at the interfaces between the concrete and reinforcement elements. Furthermore, the reinforcement is positioned within the concrete mesh, resulting in the concrete and reinforcement coexisting in the same spatial region, as illustrated in Figure (28). However, it's worth noting that a drawback of employing this discrete model is that the placement of the reinforcement imposes constraints on the concrete mesh.

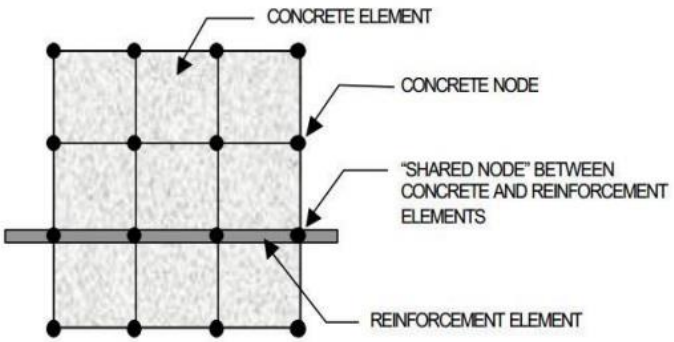

Figure 28: Distributed nodes between reinforcement and concrete element in discrete model, [267].

Smeared model

In this approach, it is assumed that the reinforcement is uniformly distributed within specific regions of the finite element mesh for the concrete. Consequently, the material properties within these regions are modelled by considering both the properties of the concrete and the reinforcement, following a composite material concept. This methodology is typically employed in models of large-scale structures

where the reinforcements have a relatively minor impact on the overall structural response, as depicted in Figure (29).

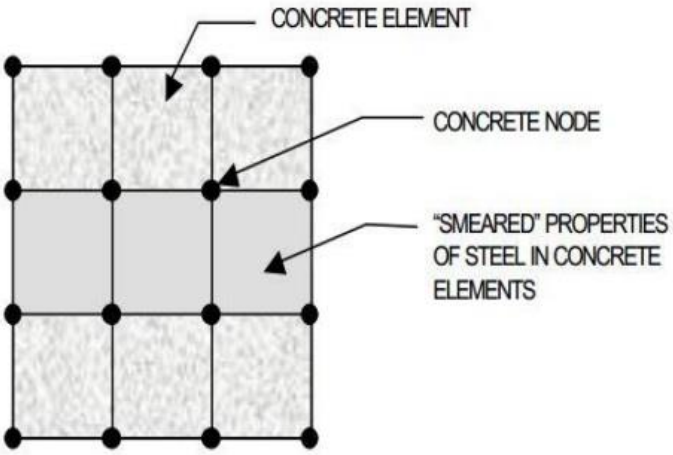

Figure 29: Reinforced concrete distributed evenly in concrete region by smeared model.

Embedded Model

In In the embedded modelling approach, the assessment of the stiffness of the reinforcement is conducted independently of the concrete elements.

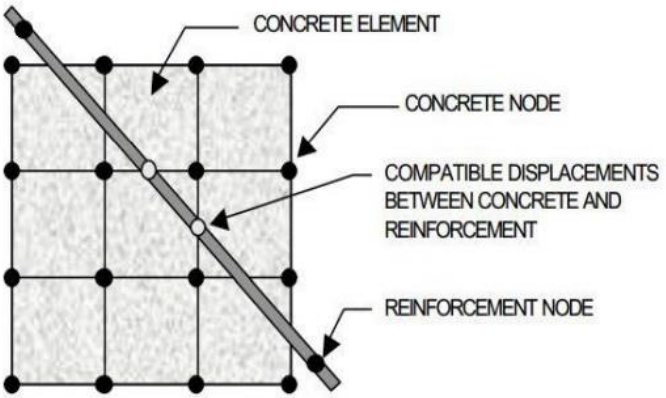

Figure 30: Reinforced concrete modelled by embedded method.

Furthermore, the displacement of the reinforcement is made to correspond with the displacement of the adjacent concrete.

Due to these arrangements, this modelling method addresses the limitations associated with smeared and discrete models, as illustrated in Figure (30). In this

study, the embedded method was employed to simulate the behaviour of FRP bars within concrete.

2.13 Conclusion

This section provides a comprehensive review of the literature pertaining to the behaviour of FRP-reinforced concrete structures under both static and dynamic loads. Researchers have explored various parameters, including FRP diameter, embedment length, types of FRP, and concrete compressive strength. Comparisons between the behaviours of FRP RC members under static and dynamic loads have revealed the following:

Under static loading, the primary mechanism for load transfer from FRP to concrete is adhesion and friction at the interface between the FRP reinforcement and the concrete. The bond-slip behaviour of specimens under static loading tends to be more stable. However, under dynamic loading, the bond strength of specimens generally decreases compared to static loads. This reduction is attributed to the rapid loading, including fatigue effects, which impact the bond between FRP and concrete, leading to microcracking.

Specimens subjected to dynamic loading also experience time-dependent effects, such as creep, which affect the bond-slip behaviour of the members over time. Consequently, specimens may undergo progressive debonding or a reduction in bond strength.

Results indicate that strain rate has a less pronounced effect on the bond-slip behaviour of FRP-reinforced concrete members under static loads compared to dynamic loading. Failure modes under static loads are typically dominated by gradual debonding or concrete crushing, whereas under dynamic loading, failure modes often involve catastrophic debonding and extensive cracking due to the reduction in bond strength.

Overall, the comparison of the effects of static and dynamic loading on the bond behaviour of FRP RC members reveals significant differences, particularly in the types of failure modes and the load-carrying capacity of the members.

Based on the findings presented in the literature review, the following conclusions can be drawn:

- The behaviour of FRP-reinforced concrete structures differs markedly from steel-reinforced structures.
- It is evident that the bond strength of FRP bars is significantly lower than that of steel reinforcing bars. Parameters such as concrete compressive strength, embedment length, and bar diameter directly influence bond failure modes in FRP RC members.
- Several bond-slip models have been proposed, and the comparison suggests that the B.P.E modified model is the most suitable choice for this study.
- Areas such as different load cases, strain rates, and types of FRP materials still require further investigation.
- Computational research on the analysis of bond behaviour in FRP RC members under impact loading appears to be lacking.
- There is a need for numerical studies to explore the impact of different parameters on the bond behaviour of FRP RC beams under high-velocity impact loading.

The present thesis will address research areas that have not received sufficient attention in the application of composite materials in structural engineering. Nevertheless, despite the numerous studies in these fields, there has been no investigation into the bond behaviour of CFRP, AFRP, and GFRP RC beams under high strain rate, high-velocity impact loading. This represents a crucial area that requires further exploration and investigation. Additionally, other areas with limited research include the effect of the Young's modulus of FRP bars, concrete compressive strength, FRP bar diameter, impact velocity, and impact load on the performance of FRP RC beams under high-strain-rate impact loading. Thus, the current study aims to fill these knowledge gaps and contribute to a deeper understanding of these less-explored fields, primarily focusing on the high-strain-rate impact responses of CFRP, AFRP, and GFRP bars in RC beams.

Chapter 3: Application of Finite Element Analysis and validation for FRP-RC Beams

As previously alluded to, the modelling of the bond between Fiber-Reinforced Polymer (FRP) materials and the surrounding concrete presents a range of intricate challenges. Within this chapter, we delve into the meticulous selection and implementation of constitutive models, interfacial bond formulations between FRP bars and concrete, meshing techniques, and boundary conditions. These choices are meticulously crafted to construct static and dynamic finite element models, meticulously executed with the ABAQUS finite element software. These models serve as a critical foundation for conducting accurate nonlinear finite element analyses of FRP-reinforced concrete beams subjected to high-strain-rate impact loading.

To comprehensively explore the bond performance of FRP bar-reinforced concrete beams under high-strain-rate impact loading, a series of numerical beam tests have been meticulously simulated. The geometrical parameters and boundary conditions for these simulations have been thoughtfully derived from authoritative references, specifically Ali Nadjai's static calibration model [3] and Saleh's dynamic calibration experiment [241], [2] [1]. By employing these meticulously calibrated models, we aim to evaluate a set of influential factors that collectively contribute to the precision and reliability of predicting the bond performance of FRP-reinforced concrete beams under the rigorous conditions of high-strain-rate impact loading.

3.1 Introduction:

Engineers and researchers commonly employ finite element simulations to prototype the behaviour and performance of structures under various loading scenarios. In order to accurately model FRP bar-reinforced concrete beams, with particular attention to capturing the phenomenon of slip between the FRP bar and the concrete, it is imperative to comprehensively characterize and correctly model the bond interaction between the FRP bars and the surrounding concrete. This modelling should also account for the rate dependency of this bond interaction.

In the forthcoming sections, we undertake a rigorous effort to calibrate the behaviour of a composite beam within the ABAQUS finite element software. Our goal is to replicate the same load-displacement behaviour observed in both the static testing conducted by Ali Nadjai [3] and the dynamic loading testing carried out by Zein Saleh [2]. This endeavour is critical in ensuring that our finite element model accurately reflects the real-world behaviour of FRP bar-reinforced concrete beams under a range of loading conditions, including both static and dynamic scenarios.

3.2 Nonlinear Finite Element Modelling of FRP RC Beam Under Static Load:

A substantial body of analytical research has been dedicated to the finite element analysis of concrete beams reinforced with Fiber-Reinforced Polymer (FRP) under static loading conditions, yet many of these studies have overlooked the critical consideration of incorporating an accurate representation of the bond-slip behaviour between the FRP and concrete interfaces. In this regard, our static finite element model, denoted as FEM-S, is meticulously crafted based on the experimental investigations conducted by Ali Nadjai [3] and Marta Baena [4].

The FEM-S model is meticulously developed within the ABAQUS finite element software to facilitate precise nonlinear finite element analyses of concrete beams reinforced with FRP bars under static loading conditions. Notably, this model mirrors the material properties and geometry of the experimental tests conducted by Ali Nadjai [3], while crucially avoiding the assumption of a perfect bond and instead accounting for the bond-slip phenomenon between the FRP bars and the concrete interface.

To accurately model the bond-slip interaction between FRP and concrete, we have incorporated data from Marta Baena's experimental work [4]. This data provides essential parameters such as the bond strength,τ_{max}, the slip value at the bond strength, S_m, and a curve fitting parameter, α, that must remain less than 1. Furthermore, a set of connectors has been introduced between the nodes

representing the FRP and the concrete, effectively serving as springs to replicate the bond behaviour while accommodating any potential slip.

The concrete component of the model is represented as a solid and homogeneous material, whereas the FRP bars and stirrups are modelled as truss elements. An appropriate bond-slip law is meticulously applied to the model to capture this intricate interaction. The model's robustness is further validated through mesh convergence studies, and an explicit dynamic approach is employed to ensure the accurate representation of the complex behaviour exhibited in FRP-reinforced concrete beams subjected to static loading conditions.

3.2.1 Constitutive models for simulations

3.2.1.1 Modelling of concrete

There exists a plethora of guidelines designed to facilitate the simulation of the mechanical behaviour of concrete within finite element models, as documented in numerous references, [242] [243] [244] [245] [246] [247] [248] [249]. Among these guiding principles, one that stands out for its capacity to enable finite element modelling to accurately capture essential characteristics of concrete is the concept of "Concrete Damage Plasticity," a feature readily available in ABAQUS.

Concrete damage plasticity proves highly efficient in modelling concrete's inherent asymmetric behaviour in tension and compression. It allows for the degradation of material properties due to damage accumulation, as well as accurately representing concrete's sensitivity to pressure-induced yielding and stiffness variations. Throughout the course of this thesis, we extensively discuss and apply this constitutive modelling approach to ensure a comprehensive and precise representation of concrete behaviour under various loading conditions.

Yield Criterion

Concrete damage plasticity model present in ABAQUS is using the yield function that initially recommended by Lubliner, [250] and improved by Lee and Fenves [251]. The

yield function is employed to form the estimation of concrete strength in different multifaceted stress states. The formula for yield is set as

$$F(\bar{\sigma}, \tilde{\varepsilon}^{pl}) = \frac{1}{1-\alpha}\left(\bar{q} - 3\alpha\bar{p} + \beta(\tilde{\varepsilon}^{pl}) < \hat{\bar{\sigma}}_{max} > -\gamma < -\hat{\bar{\sigma}}_{max} >\right) - \bar{\sigma}_c(\tilde{\varepsilon}_c^{pl}) \leq 0 \quad (3.1)$$

Accompanied by

$$\alpha = \frac{\sigma_{b0} - \sigma_{c0}}{2\sigma_{b0} - \sigma_{c0}} \quad (3.2)$$

$\hat{\bar{\sigma}}$ is the maximum principle effective stress; The quantities σ_{c0} and σ_{b0} represent initial axial compressive yielding stress, and initial equibiaxial compressive yielding stress respectively, where typically σ_{b0} is equal to $1.16\sigma_{c0}$. The parameter β can be calculated by

$$\beta(\tilde{\varepsilon}^{pl}) = \frac{\bar{\sigma}_c(\tilde{\varepsilon}_c^{pl})}{\bar{\sigma}_t(\tilde{\varepsilon}_t^{pl})}(1-\alpha) - (1+\alpha) \quad (3.3)$$

The quantities $\bar{\sigma}_t$ and $\bar{\sigma}_c$represent the effective tensile and compressive cohesion stresses sequentially and γ is given by

$$\gamma = \frac{3(1-K_c)}{2K_c - 1} \quad (3.4)$$

K_c represent the ratio of the second stress invariant on the tensile meridian to that of the compressive meridian. The value of The $K_c$is set to 0.666 as suggested by users guide, [252] γ parameter merely interpose in equation (3.1) when $\hat{\bar{\sigma}}_{max}$ is less than zero.

The $\bar{p}$, which represent effective hydrostatic pressure, is given by

$$\bar{p} = -\frac{1}{3}\bar{\sigma}: I \quad (3.5)$$

The $\bar{q}$, which represent Mises equivalent effective stress, is given by

$$\bar{q} = \sqrt{\frac{3}{2}\bar{S}: \bar{S}} \quad (3.6)$$

Where, $\bar{S}$ represent the deviatotric part of the effective stress tensor $\bar{\sigma}$ and is equivalent of

$$\bar{S} = \bar{p}l + \bar{\sigma} \tag{3.7}$$

Concrete in compression

In explaining the stress-strain behaviour of concrete under uniaxial compression, this thesis adopts the modelling approach proposed by Kent and Park, as outlined in reference, [253] Specifically, for unconfined concrete, the Kent and Park model is employed. This model enhances our understanding of post-peak concrete stress-strain behaviour by extending and generalizing Hognestad's equation [254].

The Kent and Park model introduces modifications to Hognestad's second-degree parabolic representation. Notably, it sets the parameter f_c, equal to f_{ck}, and shifts a specific portion of the curve to the uppermost region. This adjustment is made to more accurately capture the ascending branch of the stress-strain curve, providing a refined depiction of concrete behaviour beyond the point of peak stress.

$$\sigma_c = f_c{}'[\frac{2\varepsilon_c}{\varepsilon_{c0}} - \left(\frac{\varepsilon_c}{\varepsilon_{co}}\right)^2] \qquad \text{For} \qquad \varepsilon_c \leq \varepsilon_{co} \quad \varepsilon_{co=0.002} \tag{3.8}$$

The straight line is an assumption to occur after peak brunch and its slope was defined mainly as a concrete strength function

$$\sigma_c = f_c{}'\{1 - Z(\varepsilon_c - \varepsilon_{co})\} \qquad \text{For} \qquad \varepsilon_{co} \leq \varepsilon_c \leq \varepsilon_{20c} \tag{3.9}$$

Where

$$\varepsilon_{50u} = \frac{3+0.285f_c{}'}{145f_c' - 1000} \tag{3.10}$$

ε_{50u} represents the strain that corresponds to the stress level equivalent to 50% of the ultimate strength of unconfined concrete.

$$\varepsilon_{50h} = \frac{3}{4}\rho_s\sqrt{\frac{h^{"}}{s}} \tag{3.11}$$

$$Z = \frac{0.5}{\varepsilon_{50u} + \varepsilon_{50h} - \varepsilon_{co}} \tag{3.12}$$

In these equations, the variables are defined as follows; σ_c denotes concrete stress; f_c' represents concrete cylinder strength (MPa); $h^{"}$ stands for width of confined core

concrete (Stirrups inside area); s is stirrup spacing; ρ_s is stirrup percent spacing that is presented as follow

$$\rho_s = \frac{A_{s0}(a^{"}+h^{"})^2}{s(a^{"})(h^{"})} \tag{3.13}$$

Where $a^{"}$ is small size of the core concrete. From point C to D

$$f_c = 0.2f_c' \qquad \text{For} \quad \varepsilon_c \geq \varepsilon_{20c} \tag{3.14}$$

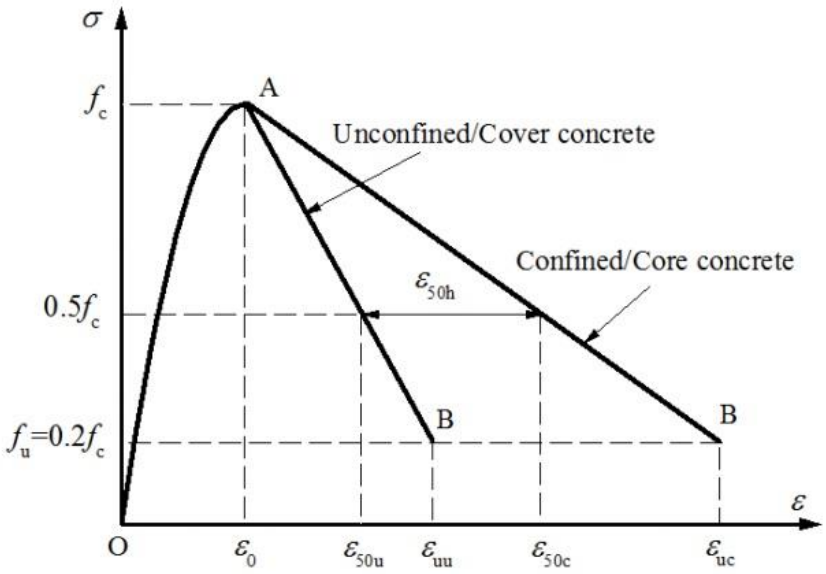

Figure 31: Stress-Strain curve for confined and unconfined concrete, [255]

In this thesis, the Mander model, which describes the stress-strain behaviour of confined concrete under compression, has been incorporated into the various models. The Mander model takes inspiration from the failure criteria proposed by William and Warnke [256], supplemented by data sourced from Schickert and Winkler [257], to formulate a comprehensive multiaxial confinement model. To delineate the complete stress-strain curve, a three-parameter equation derived from the Popovics model [258] has been adopted. These equations are presented as follows:

$$\frac{f_c}{f_{cc}'} = \frac{r\left(\frac{\varepsilon_c}{\varepsilon_{cc}}\right)}{(r-1)+\left(\frac{\varepsilon_c}{\varepsilon_{cc}}\right)^r} \tag{3.15}$$

$$r = \frac{E_c}{(E_c - E_{sec})} \tag{3.16}$$

$$E_{sec} = \frac{f'_{cc}}{\varepsilon_{cc}} \tag{3.17}$$

$$E_c = 5000\sqrt{f'_{co}} \tag{3.18}$$

Where E_c is the modulus of elasticity of the unconfined concrete in MPa, f'_{co} is the unconfined concrete strength, E_{sec} to define the stress-strain behaviour of outside the confined core concrete where descending branch, ($\varepsilon_c > 2\varepsilon_{co}$). ε_{cc} is the strain at the maximum compressive strength of confined concrete, f'_{cc} is compressive strength (peak stress) of confined concrete that are given as

$$\varepsilon_{cc} = \varepsilon_{co}\left[1 + 5\left(\frac{f'_{cc}}{f'_c} - 1\right)\right] \tag{3.19}$$

$$f'_{cc} = f'_c\left[-1.254 + 2.254\sqrt{1 + \frac{7.94f'_l}{f'_c}} - 2\frac{f'_l}{f'_c}\right] \tag{3.20}$$

Where f'_l is given by

$$f'_l = \frac{1}{2}k_e\rho_s f_{yh} \tag{3.21}$$

ρ_s is ratio of volume of transverse confining steel to volume of confined concrete core, f_{yh} is yield strength of transverse reinforcement and k_e is confinement coefficient, where equations for circular hoops and circular spirals are given respectively;

$$k_e = \frac{\left(1 - \frac{s'}{2d_s}\right)^2}{1 - \rho_{cc}} \tag{3.22}$$

$$k_e = \frac{1 - \frac{s'}{2d_s}}{1 - \rho_{cc}} \tag{3.23}$$

ρ_{cc} is ratio of area of longitudinal reinforcement to area of core of the section, s' is clear spacing between spiral or hoop bars, and d_s is diameter of spiral. Mander model for confined and unconfined concrete is shown in Figure (32).

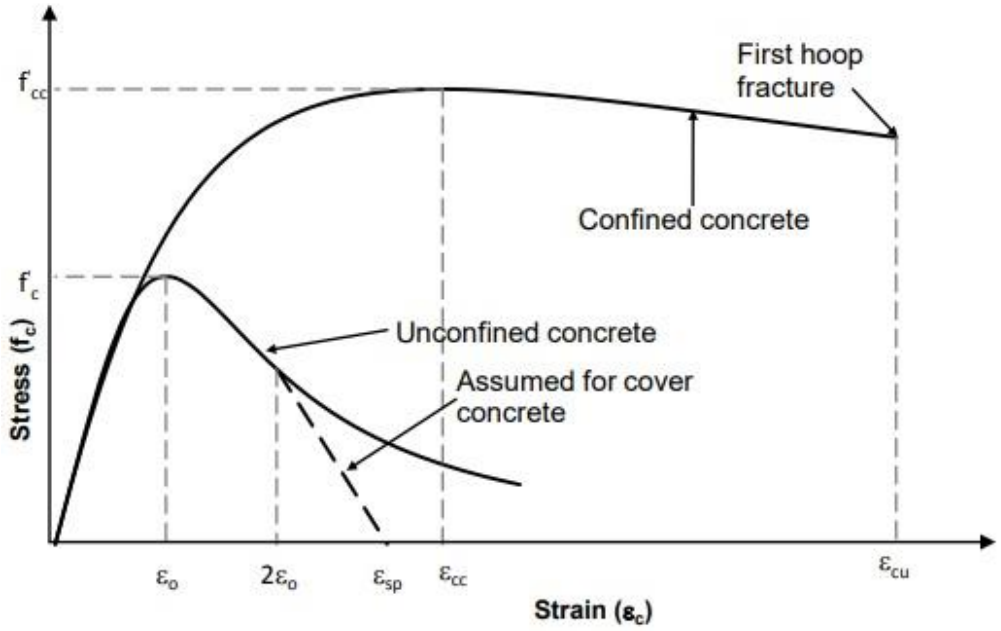

Figure 32: stress-stain relation proposed for monotonic loading of confined and unconfined concrete [259].

In order to accurately depict the stress-strain characteristics of both confined and unconfined concrete, whether of normal or high strength, it is imperative to employ a robust model that effectively captures concrete behaviour. In this pursuit, two distinct models have been incorporated into the finite element simulations: the Mander stress-strain relationship for confined concrete and the Kent & Park stress-strain model.

For unconfined concrete, the Kent & Park model is employed to define the curves for the ascending branch, while bilinear straight-line equations are employed to characterize the post-peak behaviour. This approach has proven to be particularly suitable for representing concrete behaviour within the scope of the current study.

The proposed stress-strain relationships for both confined and unconfined concrete have demonstrated their effectiveness in faithfully replicating concrete behaviour when compared to existing experimental data. This represents a significant advancement as the proposed models address a major limitation of previous concrete stress-strain models. Unlike previous models that either inadequately capture the descending portion of the stress-strain relationship or pose challenges in

terms of inversion or integration within finite element software, the proposed models in this study provide a robust and accurate representation that closely aligns with experimental observations.

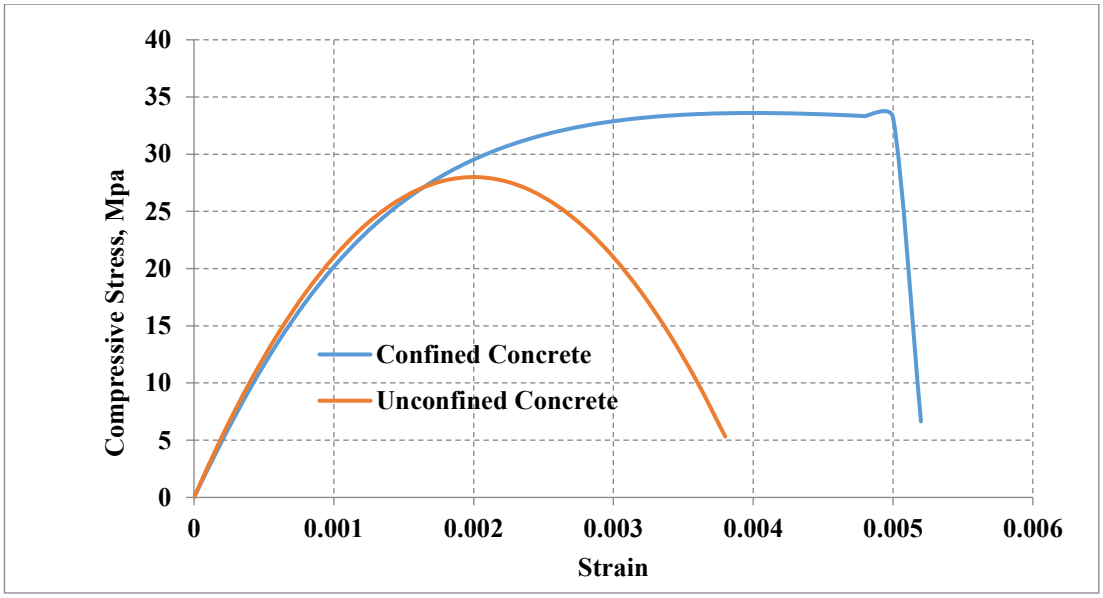

Figure 33: Stress-strain relation for confined and unconfined concrete used for this study based on Kent & Park and Mander model.

Concrete in tension

As elucidated in earlier sections, the Concrete Damage Plasticity model (CDP) has been employed to emulate the nonlinear behaviour of concrete in this study. The CDP model utilized in ABAQUS is founded on a sequence plasticity-based damage concept, which accounts for the uniaxial tensile and compressive responses by incorporating damage plasticity. Specifically, in the context of this research, the model describing concrete behaviour under tension is employed.

Under uniaxial tension, the stress-strain relationship exhibits a linear elastic behaviour up to the point where it reaches the failure stress denoted as σ_{t0}. The occurrence of micro-cracking within the material is closely linked to this stress failure. Subsequent to stress failure, the microcracks that form are meticulously characterized at a microscopic level, and their response is represented through a softening stress-strain behaviour.

When at any point along the strain softening branch, the material's unloading response is determined by a reduction in its elastic stiffness. It's noteworthy that this degradation of elastic stiffness behaves differently in tension and compression. In both tension and compression, as plastic strain accumulates, this effect becomes more pronounced. The degree of degradation in elastic stiffness in tension is quantified by d_t, which is a progressively increasing function of plastic strain. Its value ranges from zero, signifying an undamaged state, to one, indicating a fully damaged state.

The following relationship express the uniaxial tensile stress, σ_t

$$\sigma_t = (1 - d_t)E_0\left(\varepsilon_t - \varepsilon_t^{pl}\right) \tag{3.24}$$

E_0 is the initial modulus of elasticity, d_t is the scalar damage variable in tension, ε_t is total strain in tension and ε_t^{pl} is the equivalent plastic strain in tension and can be obtained from equation (3.27).

The post-failure behaviour in tension is described as a function of cracking strain ε_t^{ck}, which can be shown as

$$\varepsilon_t^{ck} = \varepsilon_t - \varepsilon_{0t}^{el} \tag{3.25}$$

$$\varepsilon_{0t}^{el} = \left({\sigma_t}/{E_0}\right) \tag{3.26}$$

$$\varepsilon_t^{pl} = \varepsilon_t^{ck} - \frac{d_t}{(1-d_t)}\frac{\sigma_t}{E_0} \tag{3.27}$$

Where ε_{0t}^{el} is the elastic tensile strain.

The loss of elastic stiffness in uniaxial stress can be calculated as

$$(1 - d) = (1 - s_t d_c)(1 - s_c d_t) \tag{3.28}$$

s_t and s_c are stress state functions and they are presented to simulate the stiffness recovery effects due to stress reversal. s_t and s_c can be found by

$$s_t = 1 - w_t H(\sigma) \tag{3.29}$$

$$s_c = 1 - w_c\left(1 - H(\sigma)\right) \tag{3.30}$$

w_t and $w_c$are the weight factors that regulate improvement of tensile and compressive stiffness against load reversal. The value can vary from 0 to 1, which means no stiffness recovery or total stiffness recovery respectively. $H(\sigma)$ is the Heaviside function that follows assumption below

$$\begin{cases} H(\sigma) = 1 & \sigma > 0 \\ H(\sigma) = 0 & \sigma < 0 \end{cases} \tag{3.31}$$

Figure (34) illustrates uniaxial tensile and compressive response that characterized by damage plasticity.

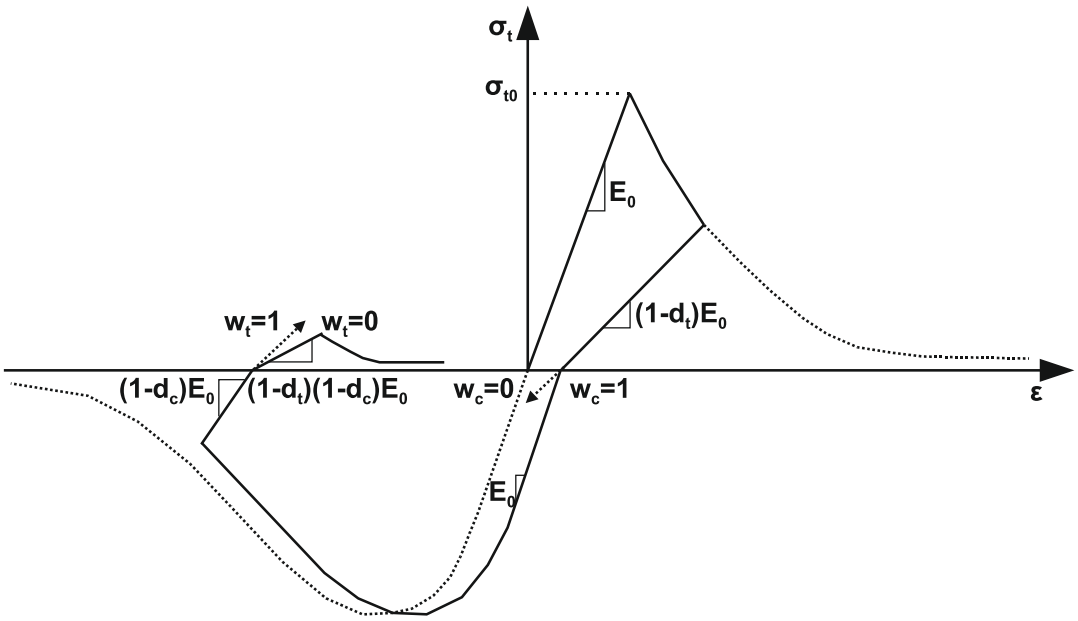

Figure 34: uniaxial load cycle with assumption of default values for stiffness recovery factors of $w_t = 0, w_c = 1$, [260]

3.2.1.2 FRP Modelling

The consideration of damage in fibre-reinforced materials plays a pivotal role in the modelling and analysis of such materials. Fiber-Reinforced Polymers (FRP), characterized by their elastic and brittle behaviour, are prone to damage without experiencing significant plastic deformation. Consequently, when modelling the behaviour of FRP bars, plasticity can be reasonably neglected.

In this study, the modelling of FRPs incorporates initiation criteria for fibre-reinforced composites, drawing upon the work of Hashin [261] [262] and the Lapezyk theory [263]. Hashin's theory defines a failure surface in the effective stress space, encompassing various mechanisms for damage initiation, including fibre tension, fibre compression, matrix tension, and matrix compression. While Hashin's theory has been widely adopted in the industry, it has been noted in previous studies that it may not precisely predict the onset of failure, particularly in cases involving matrix and fibre compression modes. To address this potential limitation, Lupczyk integrated the LaRC04 failure criteria proposed by Davilia and Camanho [264], offering a more comprehensive framework to overcome any shortcomings in the modelling of damage initiation in FRPs.

The initiation criteria are in the following general formulas

Fiber Tension ($\hat{\sigma}_{11} \geq 0$):

$$F_{ft} = \left(\frac{\hat{\sigma}_{11}}{X^T}\right)^2 + \alpha\left(\frac{\hat{\sigma}_{12}}{S^L}\right)^2 = 1 \tag{3.2.1}$$

Fiber compression ($\hat{\sigma}_{11} < 0$):

$$F_{fc} = \left(\frac{\hat{\sigma}_{11}}{X^C}\right)^2 = 1 \tag{3.2.2}$$

Matrix tension ($\hat{\sigma}_{22} \geq 0$):

$$F_{mt} = \left(\frac{\hat{\sigma}_{22}}{Y^T}\right)^2 + \alpha\left(\frac{\hat{\sigma}_{12}}{S^L}\right)^2 = 1 \tag{3.2.3}$$

Matrix compression ($\hat{\sigma}_{22} < 0$):

$$F_{mc} = \left(\frac{\hat{\sigma}_{22}}{2S^T}\right)^2 + \left[\left(\frac{Y^C}{2S^T}\right)^2 - 1\right]\frac{\hat{\sigma}_{22}}{Y^C} + \left(\frac{\hat{\sigma}_{12}}{S^L}\right)^2 = 1 \tag{3.2.4}$$

Where $\hat{\sigma}_{11,}\hat{\sigma}_{12}\, and\, \hat{\sigma}_{22}$ are the components of the effective stress tensor, X^T and X^C are tensile and compressive strength in the fibre direction, Y^T and Y^C are tensile and compressive strengths in the matrix direction, S^L and S^T are the longitudinal and transverse shear strengths.

α is the coefficient to define the contribution of the shear stress to the fibre tensile initiation criteria. The value for α can set to be 0 and $S^T = 0.5Y^C$, which refers to proposed model in Hashin and Rotem, [261], or by $\alpha = 1$ that refers to Hashin model, [262].

3.2.1.3 Steel modelling

In this study, it is assumed that the steel stirrups exhibit isotropic behaviour, meaning they behave similarly in both tension and compression, primarily demonstrating stiffness in the axial direction. To represent the behaviour of these steel stirrups, a Mises yield function has been selected. This function corresponds to a stress-strain relationship characterized by bilinear behaviour with strain hardening, as illustrated in Figure (35).

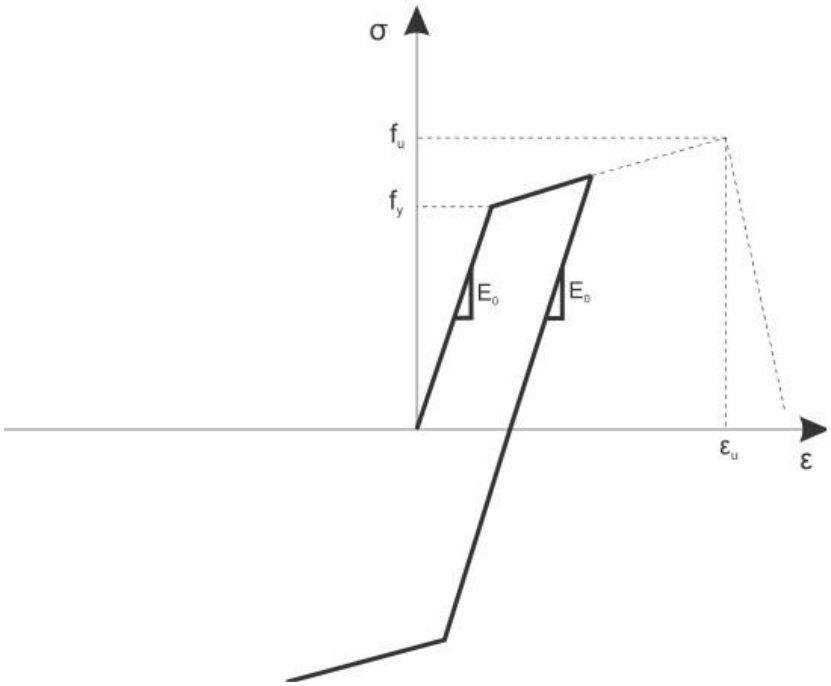

Figure 35: Steel yielding material model under uniaxial tension and compression, [265]

3.2.2 Bond-slip model

Various factors influence the intricate behaviour and mechanisms of different types of Fiber-Reinforced Polymer (FRP) bars. Consequently, a universally applicable bond-slip law has not yet been established. Among the numerous analytical bond-slip models available, the bond-slip model proposed by Baena [4] is widely acknowledged for its ability to accurately predict the interfacial bond-slip behaviour between FRP bars and the surrounding concrete.

Baena's study involved the calibration of the bond stress-slip and bond-slip relationships of the modified BPE model and the CMR model using a series of pull-out tests. The experimental results indicated the importance of incorporating the bar diameter into the bond stress-slip relationship, particularly when dealing with high-strength concrete.

Drawing upon the test data and insights from two theoretical approaches, namely the modified BPE model and the work by Cosenza [205] [232], the stress-strain curves for both pre-peak and post-peak bond behaviour are presented as follows:

$$\frac{\tau}{\tau_{max}} = \left(\frac{s}{s_m}\right)^{\alpha} \tag{3.3.1}$$

$$\frac{\tau}{\tau_{max}} = 1 - \frac{\rho \times (s - s_m)}{s_m} \tag{3.3.2}$$

Where α is a parameter for curve fitting that must be smaller than 1 to be actually meaningful, τ_{max} is the bond strength, s_m is the slip at peak bond stress, ρ is a parameter established on curve-fitting of tests data. The following equations are developed to account the effect of bar diameter for bond-slip behaviour

$$\tau_{max} = \tau_0 + \tau_1 d_b \tag{3.3.3}$$

$$s_m = m_0 e^{(m_1 d_b)} \tag{3.3.4}$$

$$\alpha = \alpha_0 \times d_b^{\alpha_1} \tag{3.3.5}$$

Where τ_0, τ_1, m_0, m_1 and α_0, α_1 are all curve fitting parameters. The values for mentioned parameters are fixed and contained from experimental data that presented in table (11).

Coefficients of tendency law τ_{max}		Coefficients of Sm tendency law		Coefficients of α tendency law		Coefficient of β tendency law		Coefficients of Sr tendency law	
τ_0	τ_1	m_0	m_1	α_0	α_1	β_0	β_1	r_0	r_1
27.681	-0.686	0.0118	0.317	0.4324	-0.3399	0.5316	-0.0291	0.0019	0.3021

Table 11: Fitted parameters of τ_{max}, s_m, α, β and s_r, [4].

The fitted values for equation (3.3.1) are presented in Table (11). From finding the values of τ with respect to each slip value, s, then converted to force with respect to

slip in order to apply in ABAQUS for simulating bond-slip. To find the force, calculated bond strengths were multiplied by the area of FRP bar in the beam model.

$$F = \tau \times 2\pi rh \tag{3.3.6}$$

3.2.3 Material Property

The nonlinear model under static loading calibrated based on experimental work by Nadjai, [3]. The three-dimensional model consists of three elements of: concrete, FRP bar and steel stirrups. The material properties of concrete and the bars are shown in Table (12) and (13) respectively.

Material	Concrete Strength, (MPa)	Mass Density, (Kg/m³)	Elastic modulus, (GPa)	Poisson's Raion
Concrete	43	2450	30.819	0.2

Table 12: Mechanical property of concrete.

Bar Material	Ultimate strength, (MPa)	Mass Density, (Kg/m³)	Elastic modulus, (GPa)	Poisson's Ratio
CFRP	1676	2500	135.9	0.15
Steel	421	7850	200	0.3

Table 13: Mechanical properties of reinforcing bars.

3.2.4 Geometry

Nadjai conducted an experimental test involving beams with dimensions of 2000 mm in length and a rectangular cross-section measuring 120 mm by 200 mm. These beams were subjected to a 4-point static load configuration. The beams were considered simply supported, with a span length of 1750 mm. The FRP (Fiber-Reinforced Polymer) bar used in the experiment had a diameter of 9.5 mm.

In the simulation, all three components were represented as isotropic elements. It is important to note that while FRP is inherently anisotropic in nature, in this particular simulation, it was modelled as a bar element rather than a sheet. Moreover, since

the FRP was tested under monotonic loading conditions, the decision to define it as an isotropic element would not significantly impact the accuracy of the simulation.

Within ABAQUS, the beam element was configured as a solid, homogeneous component, while the FRP bar and steel components were represented as truss elements to effectively capture their respective behaviours in the simulation.

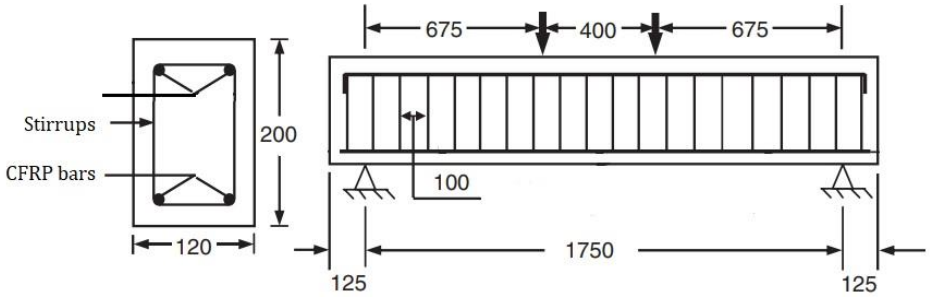

Figure 36: Detail of CFRP reinforced beam tested by Nadjai.

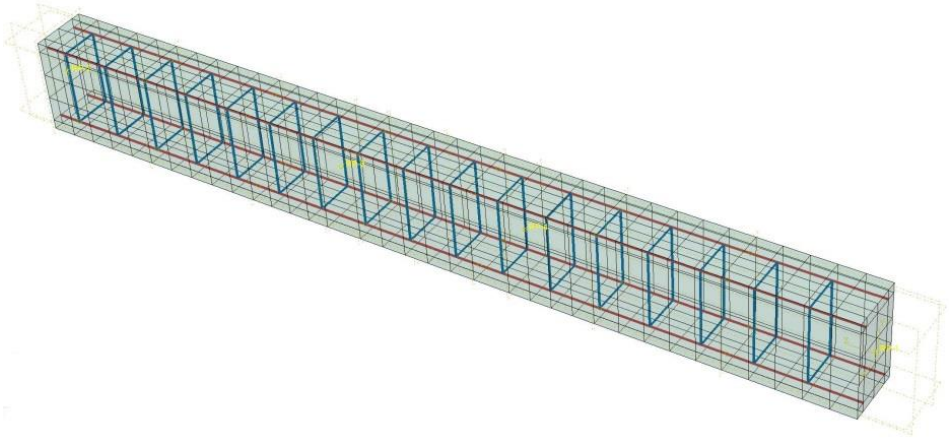

Figure 37: Calibrated CFRP reinforced beam in detail geometry.

3.2.5 Interactions

In composite models, it is a common practice to use cohesive elements to bond different components together. However, when deformation occurs, these cohesive elements can experience damage, either in shear or tension, or sometimes in both. Consequently, the originally bonded composite elements in the model may separate and come into contact with each other.

In the approach employed here, instead of introducing cohesive elements and friction coefficients between the interfaces of FRP bars and concrete, we have opted for a simplified model. We introduce nonlinear-elastic connectors between the FRP

and concrete surfaces to mimic the behaviour of epoxy and replicate the effects of pull-out debonding. To achieve this, we utilize the bond stress-slip model derived from Baena's experimental work [4] for these connectors, which connect the FRP nodes to the concrete nodes. These connectors are designed to emulate a uniaxial bond-slip effect.

These connectors are explained in a way that they create zero space between the concrete and FRP nodes using zero-x elements with partitioning and apply bond slip in the longitudinal direction of the FRP bars. As a result, we have connectors in place of traditional contact properties in the model.

3.2.6 Meshing and boundary conditions

In the process of modelling the bond interface between Fiber-Reinforced Polymer (FRP) and concrete, an 8-node solid element (C3D8R) is utilized to construct the geometric representation of the concrete, while a B31 truss element is employed to define the FRP bars. As previously discussed, the FRP element is directly connected to the concrete element by linking their nodes. It's essential in this study to create a comprehensive geometric model to accurately simulate the bond behaviour under various loading conditions at the FRP-concrete interface.

In order to maintain computational efficiency in these full-scale geometric models, it was imperative to minimize the number of nodes and utilize reduced integration techniques. In accordance with the test specimen BRC1 described in Nadjai, [3] the boundary conditions for modelling the FRP-reinforced concrete beam are illustrated in Figure (38). Specifically, the beam is supported with hinged supports at both ends and restrained in the middle, where two-point loads are applied, as per the configuration employed in Nadjai's experimental tests.

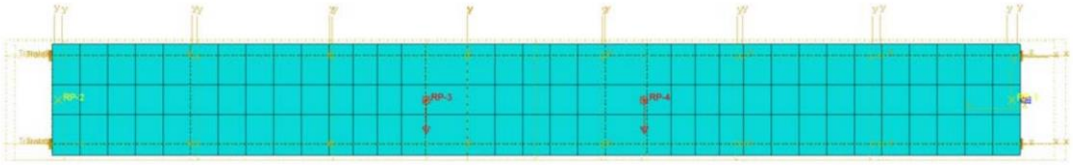

Figure 38: Boundary conditions and Finite Element Mesh in simulations of FRP RC beam with reference to beam specimen from Nadjai, [3].

3.2.7 Loading

As depicted in Figure (39), the two central points where loads were administered, corresponding to RP-3 and RP-4 in Figure (38) from Nadjai's test, are positioned 400 mm apart and are horizontally restrained. For this simulation, uniform displacements are imposed, and the process is controlled using displacement control within the ABAQUS software.

Figure 39: Applied Displacement in RP3 and RP4 nodes.

3.2.8 Analysis

In the analysis of this nonlinear static simulation, we employ the Newton-Raphson method as the chosen numerical technique for solving the problem. Additionally, the analysis incorporates the consideration of nonlinear large displacements to accurately capture the behaviour of the system.

3.2.9 Numerical validation

An experimental test involving a concrete beam reinforced with carbon fibre bars, as conducted by Nadjai, has been subjected to analysis using a simulated finite element model within the ABAQUS software. Specifically, the mid-deflection calculated

through the computational model is compared to the values observed in the experimental study. The numerical results obtained from the developed finite element model, accounting for bond slip effects, are meticulously compared and calibrated against the experimental data obtained by Nadjai, and these comparisons are illustrated in Figure (40).

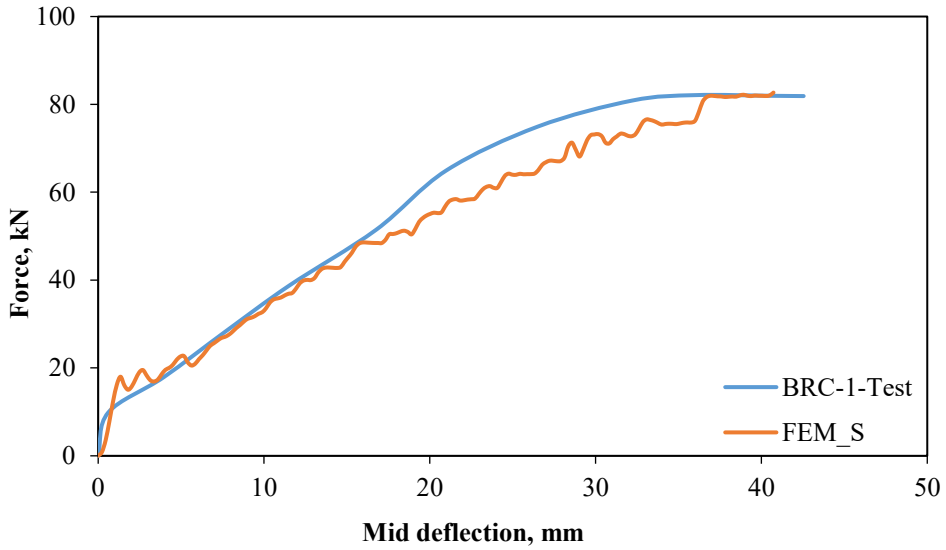

Figure 40: calibrated Load-deflection curves obtained from simulated FEM model and the experimental test by Nadjai.

3.3 Nonlinear Finite Element Modelling of FRP RC Beam Under Dynamic Load

In this chapter, a novel and efficient finite element model, denoted as FEM-D, has been developed within the ABAQUS software. This model is designed for conducting nonlinear finite element analyses of the bond behaviour exhibited by Fiber-Reinforced Polymer (FRP) reinforced concrete beams when subjected to impact loading.

The dynamic model is based on the experimental tests conducted by Zein Saleh [2], and Borosnyoi [1]. The FEM-D model shares the same material properties and geometry as the experimental study conducted by Saleh [2] but it incorporates different assumptions regarding the bond between the FRP and concrete interface. The bond-slip model employed in the dynamic model is akin to the static model discussed in Chapter 3.2, where the data for this model was extracted from Baena's experimental study [4]. In addition, rate dependency has been introduced to the connectors and material properties.

Furthermore, to account for rate dependency within this dynamic model, data from Borosnyoi's experimental study [1] has been incorporated

3.3.1 Constitutive models for simulations

Just as in the static model (FEM-S), the Concrete Damage Plasticity (CDP) model implemented in ABAQUS adopts a methodology that combines isotropic damage elasticity with isotropic tensile and compressive plasticity. This integrated approach is employed to accurately represent the inelastic behaviour of concrete.

3.3.1.1 Modelling of concrete

As previously discussed, the progression of the yield surface in the Concrete Damage Plasticity (CDP) model is governed by two hardening variables: the tensile plastic strain ε_t^{pl} and the compression plastic strain ε_c^{pl}. Both tensile and compression plastic strains are intricately linked to the failure mechanisms experienced under tension and compression loads, as elaborated upon in Chapter 3.2.1 and illustrated in Figures provided.

Similarly to the approach used in FEM-S, the Mander model is employed for modelling compression behaviour in confined concrete [266], while the Kent & Park model is applied to represent compression behaviour in unconfined concrete. A detailed description of the applied Mander and Kent & Park models can be found in sub-chapter 3.1.3.

3.3.1.2 Modelling of FRP

Incorporating the damage characteristics of Fiber-Reinforced Polymers (FRP) into the model involves the utilization of initiation criteria derived from Hashin, [261] [262] and the Lapczyk theory [263], as elaborated upon in detail in Chapter 3.2.1.2.

In finite element analysis, there are three distinct methods for modelling reinforcement. These approaches encompass discrete, smeared, and embedded models.

3.3.2 Bond-slip model and rate dependency

In the dynamic model, we employ the same bond-slip method as the static model, as derived from Baena [4], while incorporating an additional aspect related to rate dependency. The specific details of this methodology are expounded upon in Chapter 3.2.2.

Rate dependency is a crucial consideration in finite element modelling. To imbue this dynamic model with rate dependency, data from Borosnyoi's experimental study [1] is utilized. Consequently, a novel behaviour is introduced to the connectors linking the FRP reinforcement and the adjacent concrete element nodes. This is achieved by introducing sets of force-slip curves, each associated with a specific rate, to emulate rate-dependent behaviour. These rates are derived from Borosnyoi's experimental results, which establish the relationship between bond strength and the rate of loading at a temperature of 20 degrees Celsius.

To implement rate dependency, the ratio of bond strength between FRP and concrete under different loading rates, as depicted in Figure (41), is applied to the connectors defined in ABAQUS to make them rate dependent. These rates are then multiplied with forces in accordance with slip, as outlined in Equation (3.3.1).

Subsequently, loading rates ranging from 0 to 0.01 are applied between the FRP and concrete within the finite element model. Furthermore, an amplification factor is defined within the ABAQUS software. The specific rates applied to the connectors for a one model are presented in Table (42) as an example, and the rate dependency for the dynamic model can be found in Table (49) in Appendix (A).

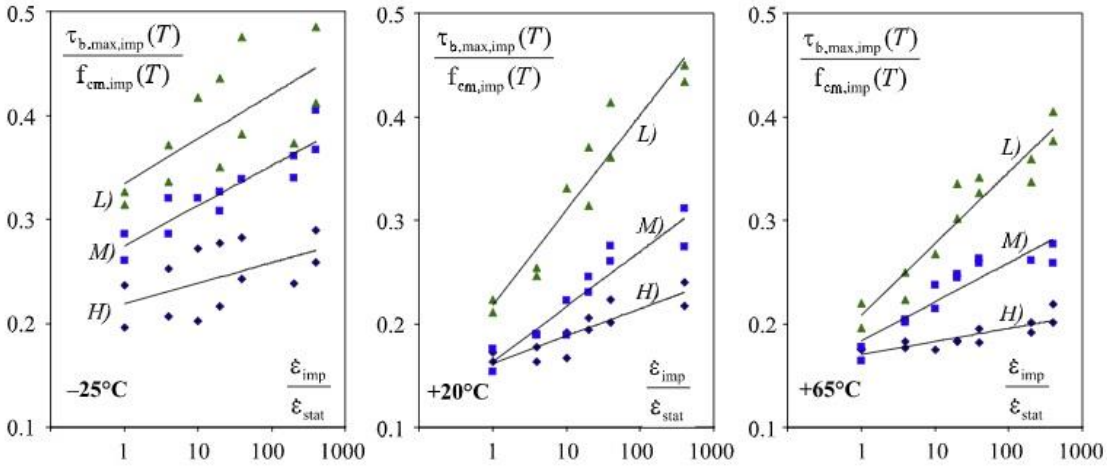

Figure 41: Relationship between bond strength and rate of loading for FRP bars conducted by Borosnyoi, [17].

S (mm)	τ (MPa)	F (N)
0	0	0
0.5	24.45417	27355.05
1	28.11321	31448.14
1.5	30.50241	34120.76
2	32.31974	36153.66
2.5	33.8036	37813.55
3	35.06643	39226.19
3.5	36.17088	40461.65
4	37.15568	41563.27
4.5	38.04656	42559.84
5	38.86157	43471.52
5.5	39.61386	44313.06
6	40.31336	45095.53
6.5	40.96774	45827.54
7	41.58307	46515.86
7.5	42.16423	47165.96
8	42.71522	47782.31

Figure 42: Calculated bond strength -slip for dynamic FE model.

3.3.3 Material property

The modelling of the nonlinear behaviour exhibited by a Fiber-Reinforced Polymer (FRP) reinforced concrete beam subjected to dynamic loading draws its basis from the experimental investigations carried out by Saleh [2]. The three-dimensional model comprises two elements representing concrete and FRP bars. Detailed material properties for both concrete and the bars are presented in Table (14) and Table (15), respectively. In this model, the Concrete Damage Plasticity (CDP) model is applied to capture the behaviour of concrete, and the rates associated with rate dependency are illustrated in Figure (118) within Appendix (A). Furthermore, Figure (43) provides a visualization of the stress-strain relationship

employed for FRP in the dynamic model developed within the ABAQUS software.

Material	Concrete Strength, (MPa)	Mass Density, (Kg/m³)	Elastic modulus, (GPa)	Poisson's Raion
Concrete	57.4	2450	35.608	0.2

Table 14: properties of concrete from experimental test by Saleh, (Saleh, 2019)

Bar Material	Ultimate strength, (MPa)	Mass Density, (Kg/m³)	Elastic modulus, (GPa)	Poisson's Ratio
GFRP	1764	2500	55.6	0.15

Table 15: properties of FRP bar in RC beam under impact load.

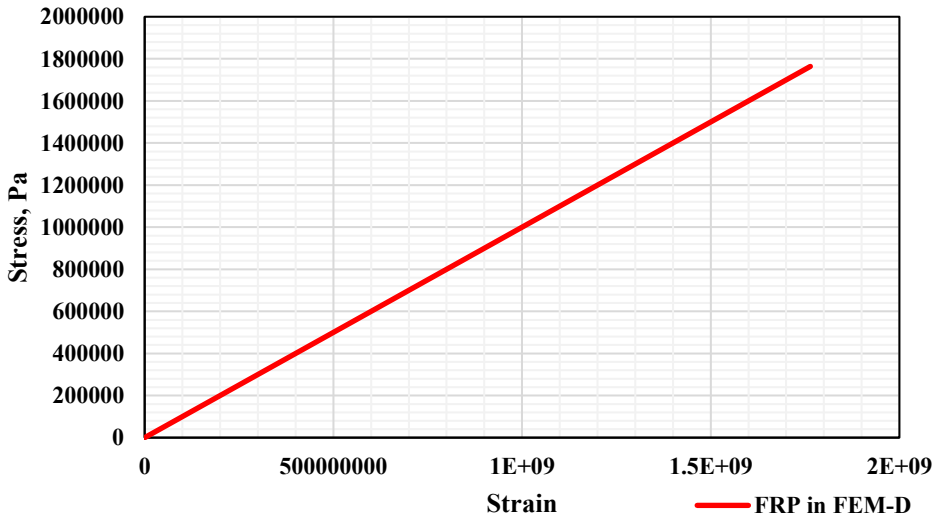

Figure 43: Stress-strain relationship for FEM-D used in ABAQUS, [2].

3.3.4 Geometry

The model is composed of two distinct parts separated by a 50 mm gap. Each part of the model possesses dimensions measuring 100×180×375 mm. To replicate the boundary conditions observed in the experimental test, the beam is modelled with pin and roller supports.

In the experimental test, the FRP bar was positioned to be bonded at the centre, with a bonding length of 75 mm, and left un-bonded on both sides. The FRP bar has a diameter of 9.5 mm. In this nonlinear model, both the FRP bar and concrete are simulated as isotropic materials. The concrete beam element is defined as a solid, homogeneous component, while the FRP bar and steel are represented as truss elements within the ABAQUS software.

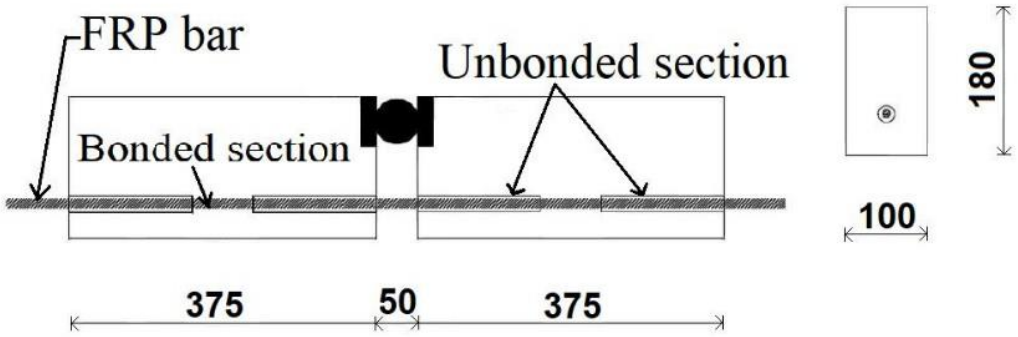

Figure 44: Detail of beam tested under impact load by Saleh, (Saleh, 2019). All measurements are in mm.

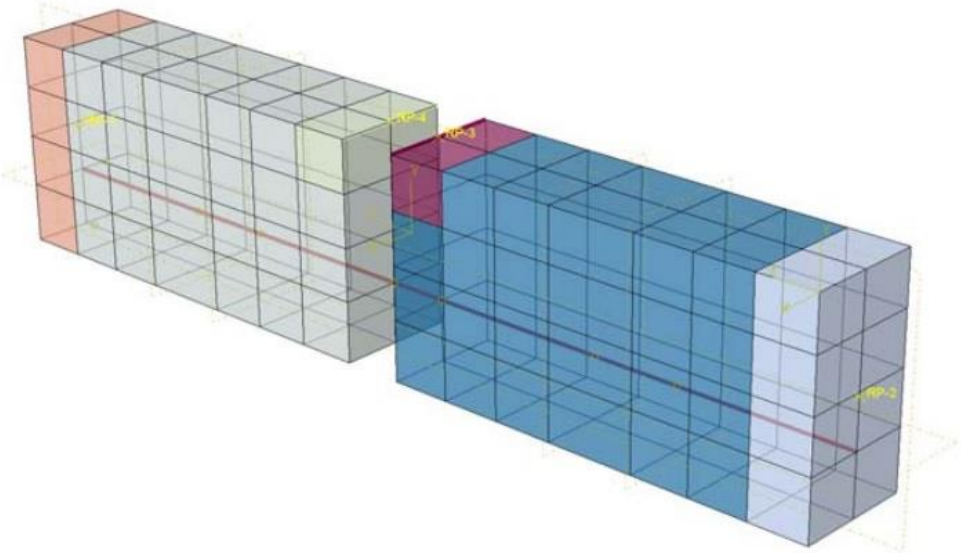

Figure 45: 3D model of the GFRP-RC beam under impact load.

3.3.5 Interactions

In a manner consistent with the calibrated static model, a set of nonlinear connectors has been introduced between the nodes representing FRP and concrete. These connectors incorporate the bond stress-slip model derived from Baena [4], along with additional considerations for rate dependency obtained from Borosnyoi's experimental study [1]. These enhancements are integrated into each individual connector linking the FRP and concrete nodes within the model. For a more comprehensive understanding, please refer to Chapter 3.2.5 and 3.3.2.

To model the concrete behaviour, an 8-node linear brick element (C3D8R) with reduced integration has been implemented, while a B31 truss element is employed to represent the FRP bars. The concrete model consists of eight nodes, with each node possessing three degrees of freedom in the x, y, and z directions. The use of reduced integration helps create fewer rigid elements, thereby leading to significant computational time savings. The C3D8R elements are capable of accurately predicting plastic deformation, crushing, and cracking phenomena in the concrete material.

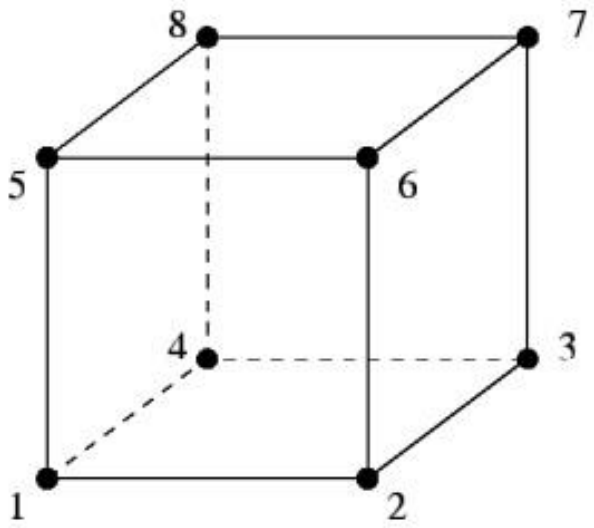

Figure 46: General model of eight nodes linear brick element.

3.3.6 Strain rate effect

Addressing the strain rate effect in concrete is one of the intricate challenges encountered in modelling. To accurately depict the material behaviour of substances like concrete under strain rate effects, the application of a mathematical model can

be highly beneficial. Strain rate effect refers to the phenomenon where an increase in strain rate results in a corresponding increase in concrete strength. This effect is particularly significant when modelling situations involving impact loads.

The impact of strain rate on the compressive and tensile strength of concrete is typically elucidated through the concept of the Dynamic Increase Factor (DIF). A precise formula for DIF is provided by the CEB model code, as presented in Chapter 2. More recent studies examining the behaviour of structural members under the influence of strain rate effects have suggested the inclusion of these effects in finite element modelling.

For instance, in a study conducted by Li and Meng [268], it was observed that an increase in concrete strength under high strain rates could be attributed to the lateral inertia of the specimens. This phenomenon is referred to as the pseudo-strain-rate effect and becomes particularly pronounced when the strain rate reaches approximately $10^2 s^{-1}$. Subsequent studies have been undertaken to further support this argument [269] [270]. These studies delve into the strain rate dependency of concrete, drawing from experimental work conducted by Saleh and incorporating stress-strain models proposed by Kent & Park and Mander.

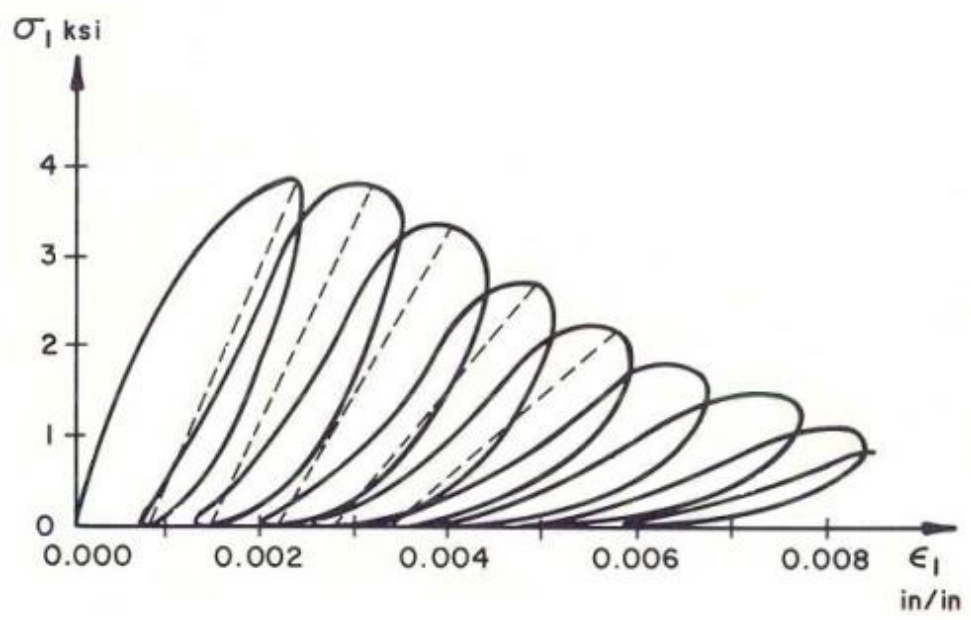

Figure 47: Cyclic uniaxial stress-strain in concrete compressive.

3.3.7 Meshing and boundary conditions

One of the initial steps in the modelling process involves meshing the model using finite element analysis. This process subdivides the model into smaller elements, and subsequently, when loads are applied, stress and strain values are calculated at integration points for each of these elements, [252]. A critical aspect of finite element modelling is the selection of an appropriate mesh size. It is crucial to determine the point at which an increase in the number of mesh elements has a negligible impact on the results.

Finite element analysis software such as ABAQUS is equipped to assist in selecting the optimal mesh size for models. Nevertheless, a mesh sensitivity study was conducted as part of the nonlinear analysis of the FRP reinforced concrete beam. The model exhibited satisfactory performance and accurately depicted the failure of the beam as well as the load-deflection curve.

For this study, element sizes of 1cm, 2.5cm, 3.5cm, and 5cm were considered, with the concrete member serving as the primary criterion for selecting the element size. The chosen size for the FRP elements matched the element size of the adjacent concrete. As depicted in Figure (48), the results obtained for all these different element sizes exhibit a strong agreement with the experimental data, particularly during the initial loading stage. However, as the cracking stage is reached, the experimental curve demonstrates greater stiffness compared to the numerical curves with various element sizes. Towards the final stage, the experimental curve exhibits a slight but noticeable difference, ultimately converging by the end of the loading process. An element size of 2.5 cm was deemed sufficient and was consequently employed in subsequent simulations.

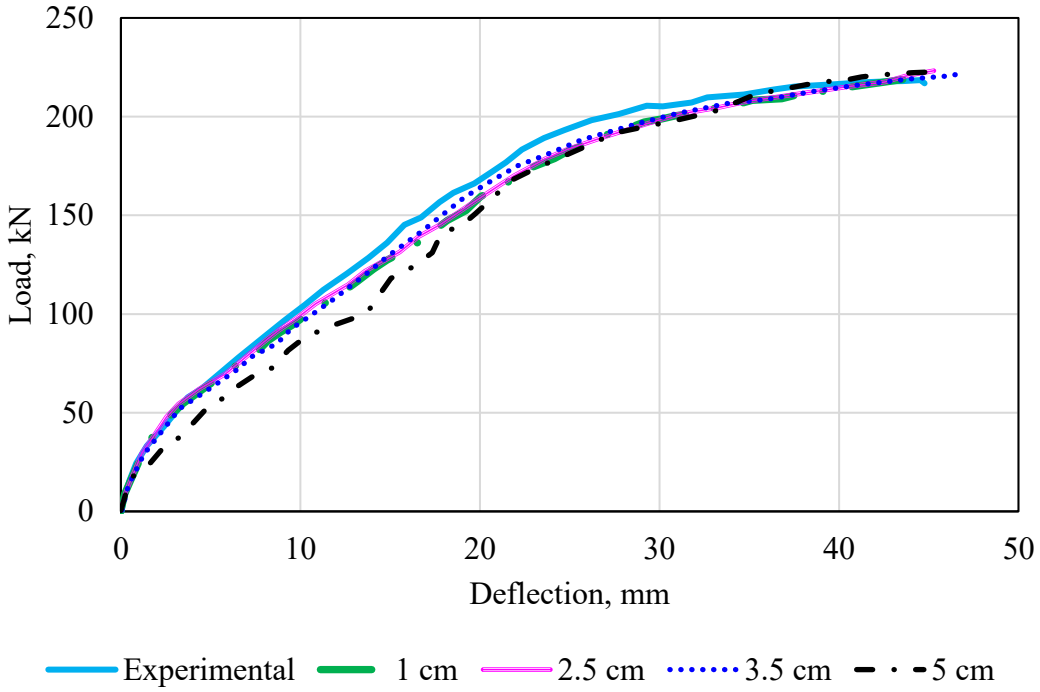

Figure 48: Comparison of mesh sensitivity results for FE models.

In order to replicate the boundary conditions observed in the real experiment conducted by Saleh, [2], The model was subjected to pin and roller supports. The pin support permits movement but restricts rotation around its major axis, whereas the roller support allows both translation and rotation. Additionally, to prevent any uplift of the beam following the application of the impact load, the nodes located above the supports at the top section of the beam were also restrained. Visual representations of these boundary conditions and the meshing applied can be observed in Figure (49) and (50).

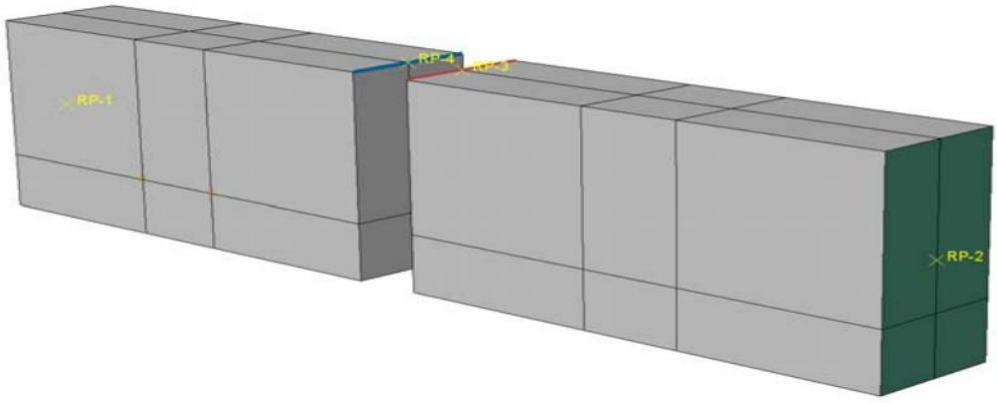

Figure 49: restrained area shows as colour green on both end sides, red and blue on the top surface of beam.

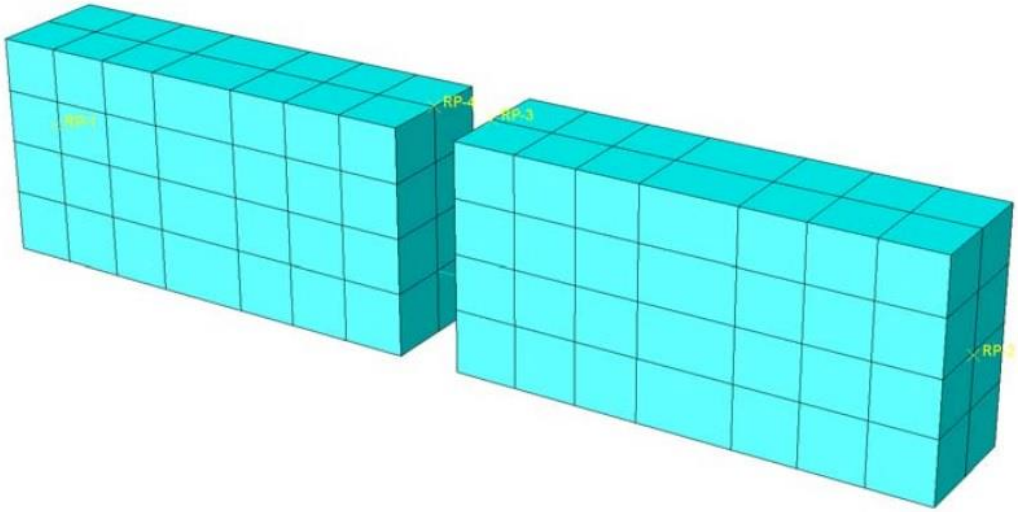

Figure 50: Meshed Dynamic model.

3.3.8 Loading

Saleh conducted an experimental study involving the application of an impact load using a dropped weight on an FRP reinforced concrete beam. In contrast, for the collaborative finite element model, load control was implemented instead of displacement control to achieve results that closely align with the experimental data. The finite element model was subjected to the same magnitude of load, at the same location, as observed in the experimental beam test. The applied impact load amounted to 70 kN, as per the Saleh experimental test.

Given the dynamic nature of this loading, it was applied using a dynamic/explicit approach, involving a series of load amplitudes over time. These applied amplitudes are delineated below and are further illustrated in Figure (119) within Appendix (A).

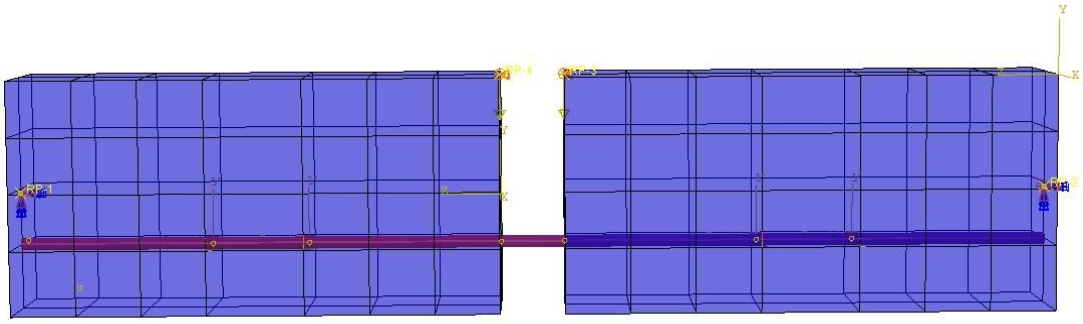

Figure 51: Side-view of concrete beam with applied loads shown as RP-3 and RP-4, ABAQUS.

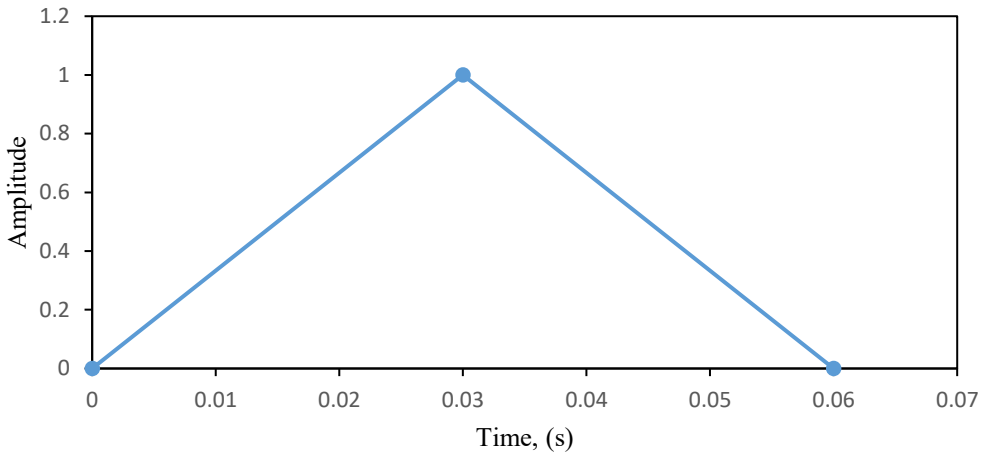

Figure 52: Applied amplitude in ABAQUS and graph of amplitude Vs. Time.

3.3.9 Increment size

The durability and accuracy of implicit time arrangements in dynamic explicit simulations are heavily influenced by the choice of time increment size. In this research, an increment size of $10^{-6}s$ and total step time of 0.1 s were employed, aligning with the recommended sizes suggested by prior studies [186] [2]. Previous research has shown that nonlinear explicit analysis yields reasonable results when the increment size is smaller than $T_1/20$. Consequently, the same recommendation was applied in the simulation of bond behaviour in FRP-reinforced concrete beams in this study. The specific increment size utilized in ABAQUS is depicted in Figure (120) within Appendix (A).

3.3.10 Rayleigh damping

To enhance and establish a consistent convergence pattern for the bond-slip model, Rayleigh damping was incorporated into the simulations conducted in this study. Stiffness-proportional Rayleigh damping was employed, with β set at 2×10^{-6} for the FRP bar and 2×10^{-5} for concrete material. The damping ratio corresponding to the vibration frequency was calculated by the simulation software, ABAQUS. The application of damping in ABAQUS is visually represented in Figure (119) within Appendix (A).

3.3.11 Analysis

A nonlinear dynamic analysis approach has been chosen to address the impact load problem, with a specific emphasis on incorporating nonlinear effects related to energy absorption within the analysis.

3.3.12 Numerical validation

An examination was conducted involving both experimental and numerical investigations of a concrete beam reinforced with GFRP bars subjected to impact loading, as conducted by Saleh. This analysis was carried out using the finite element software ABAQUS. The results obtained from the simulated model were subsequently compared to those obtained from Saleh's experimental study.

The analysis of the entire beam's internal energy, as derived from the model, demonstrated a substantial level of agreement with the results reported in Saleh's experimental study. Additionally, Figure (53) illustrates the strain-time curve generated by the FEM-D model, providing a comparative view alongside the experimental and numerical results from Saleh. Furthermore, Figure (54) displays the mid-deflection-time curve produced by the FEM-D model, which recorded a maximum deflection of 54.375 mm. This curve is compared to the experimental and numerical findings by Saleh.

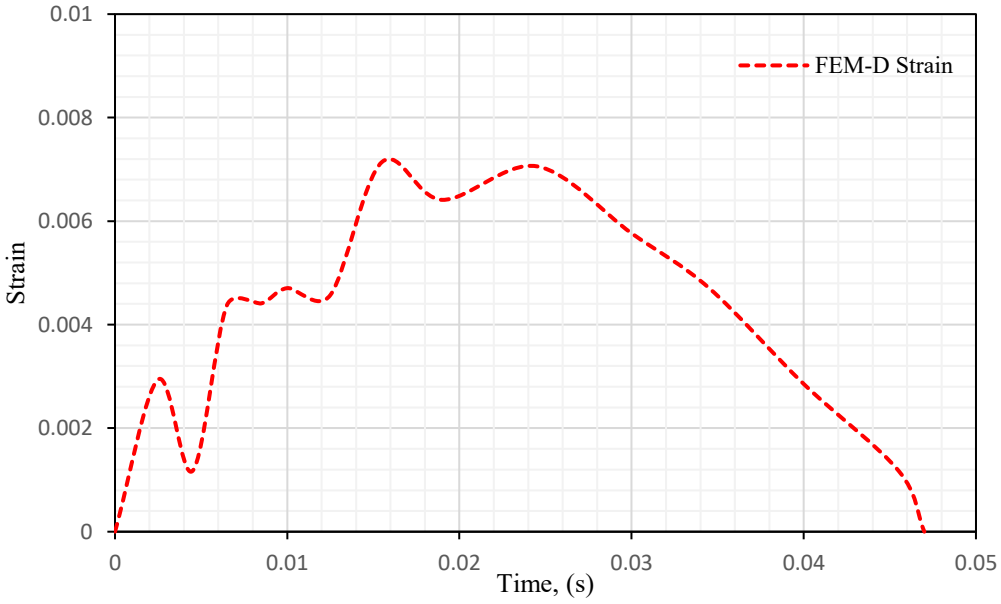

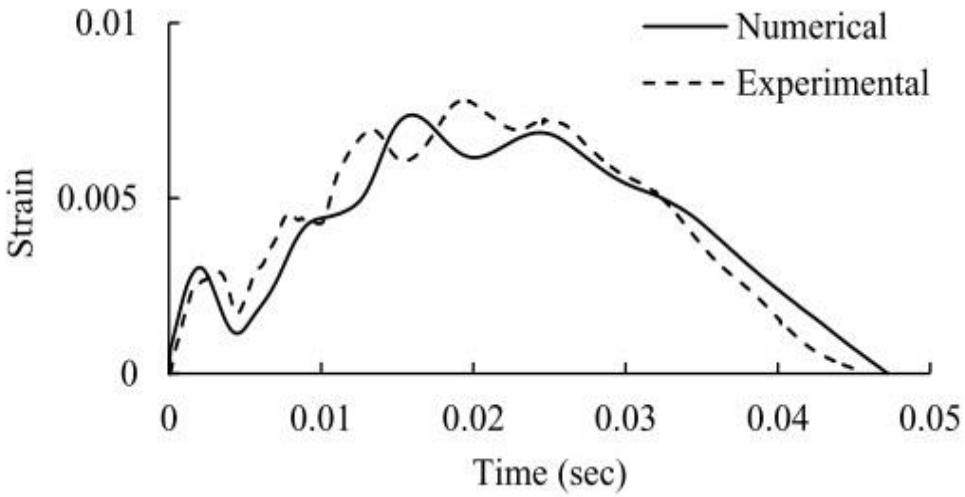

Figure 53: dynamic strain-time curve at the mid-span of GFRP bar reinforced concrete beam.

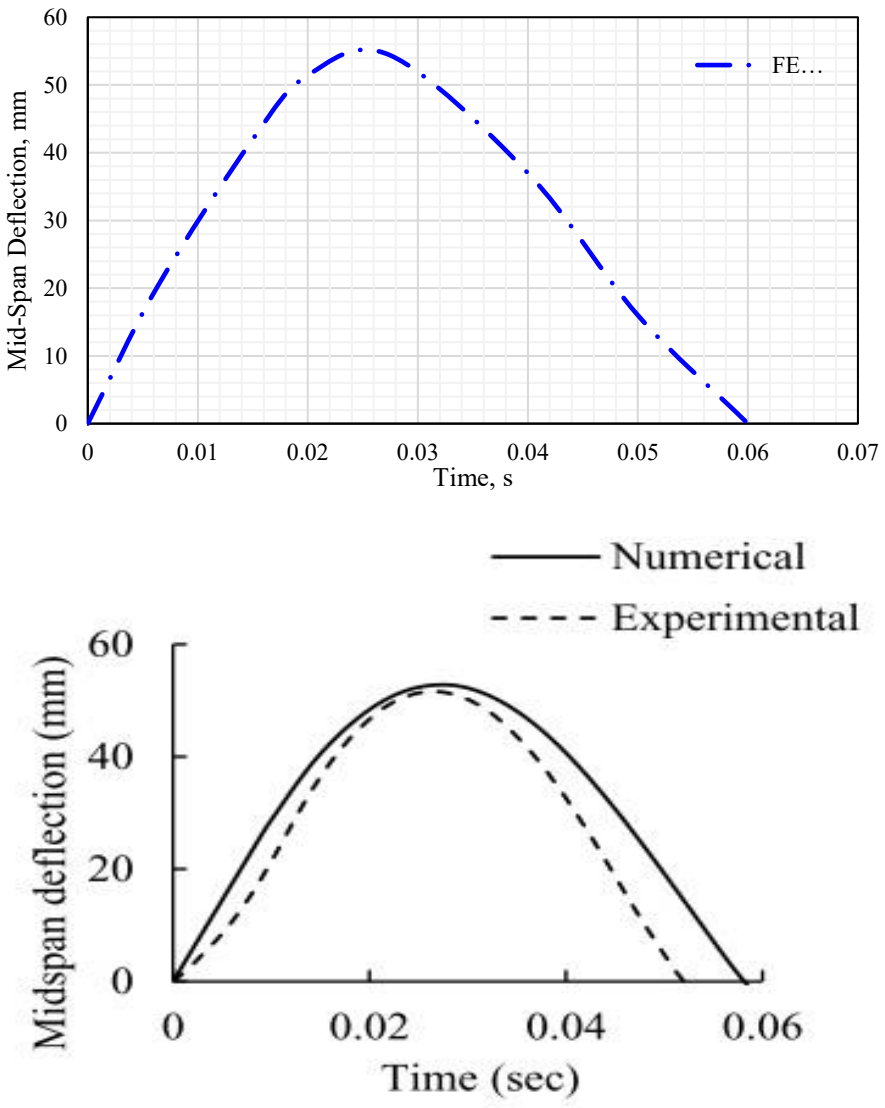

Figure 54: validation of deflection in mid-span for GFRP RC beam of FEM-D model in ABAQUS with numerical work by Saleh, [2]

3.4 Comparative Analysis of the Full Bond Model and Bond-Slip Model

In this section, a nonlinear finite element analysis was conducted to explore the interfacial behaviour of an FRP bar-reinforced concrete beam, assuming a complete bond between the materials. The obtained results were then compared with a finite element model of an FRP RC beam utilizing spring elements at the interface between the FRP bar and concrete. Figure (55) illustrates the impact of the full bond element in the finite element analysis.

The comparison between the two models reveals that the load-deflection behaviour of the bond-slip model is less rigid. The curves exhibit a similar shape but with larger deformations in the bond-slip model. This discrepancy can be attributed to the fact that the interface between the FRP bar and concrete in the bond-slip model allows for the possibility of slippage, which leads to increased deformation.

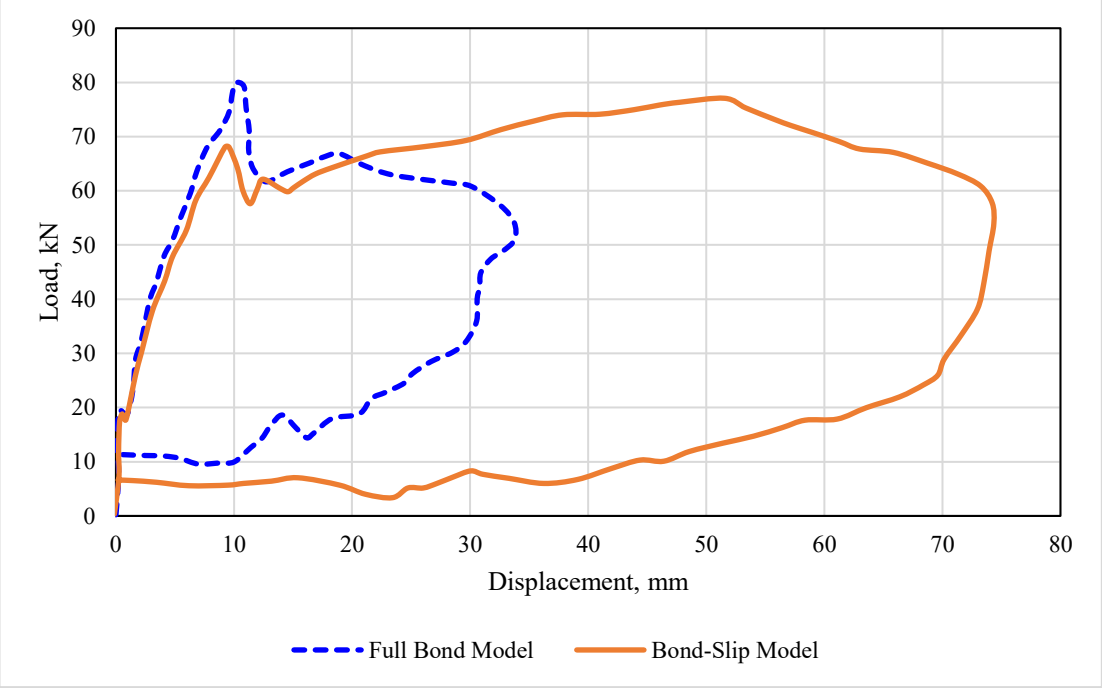

Figure 55: Comparison between effect of full-bond model and bond-slip model on load-displacement results.

Furthermore, the full bond model exhibited greater load-bearing capacity and reduced displacement, indicative of the effective confinement of FRP bars within the concrete, thereby minimizing available space for structural deformation.

In contrast, the bond-slip model demonstrates a lower load-carrying capacity but a more uniform displacement profile, suggesting the occurrence of slippage between the FRP bar and the adjacent concrete surface.

When subjected to an identical load magnitude, as presented in [2], the outcomes indicate a heightened correspondence between the experimental findings displayed in Figure (54) and the results obtained from the bond-slip model depicted in Figure 55. This serves as validation for the suitability of the bond-slip model within the context of this study.

One notable advantage of employing spring elements in the bond-slip finite element model is their capability to predict the debonding load and effectively describe the behaviour of elements right up to the point of failure.

3.5 Comparative Analysis of the Anchored Model and Bond-Slip Model

To achieve optimal strengthening results, it is crucial to ensure the desired performance of internal reinforcement and the overall strengthened structure. One effective method employed for both internal and external FRP-reinforced concrete beams is the use of anchorage systems. Enhancing the anchorage of FRP contributes to improved performance of the strengthened structure, particularly by increasing its ultimate capacity, delaying or preventing debonding, and altering the failure mode.

Consequently, a model of an anchored FRP RC beam was developed, where the ends of the FRP bars were inclined and securely fastened using tied contact to illustrate the impact of anchorage on the FRP RC beam. The tied contact method connects two surfaces within a contact pair throughout the analysis. In this case, it paired the nodes at the end of the 90-degree inclined FRP bars to the support surface. The contact between the internal FRP bar and the concrete was established using embedded element methods, by embedding nodes within the host nodes. In this context, the concrete is referred to as the host region, while the FRP bar is denoted as the embedded region.

Similar to the other models developed in ABAQUS, slippage was introduced for the anchored model using the same approach as outlined in Chapter (3.3.2). The results obtained from this model were then compared with those from the non-anchored FEM of the FRP RC beam and the experimentally tested beam conducted by Saleh.

The outcomes indicate that the displacement observed in the anchored model closely resembles that of the fully bonded FRP RC model, and the anchorage technique effectively prevents slippage. Conversely, the finite element model (FEM) of the FRP RC beam yields results that are more consistent with the experimental data. For the objectives of this study, which center on investigating the bond-slip behavior between the FRP bar and concrete, the selected finite element approach proves to be a viable and pertinent method.

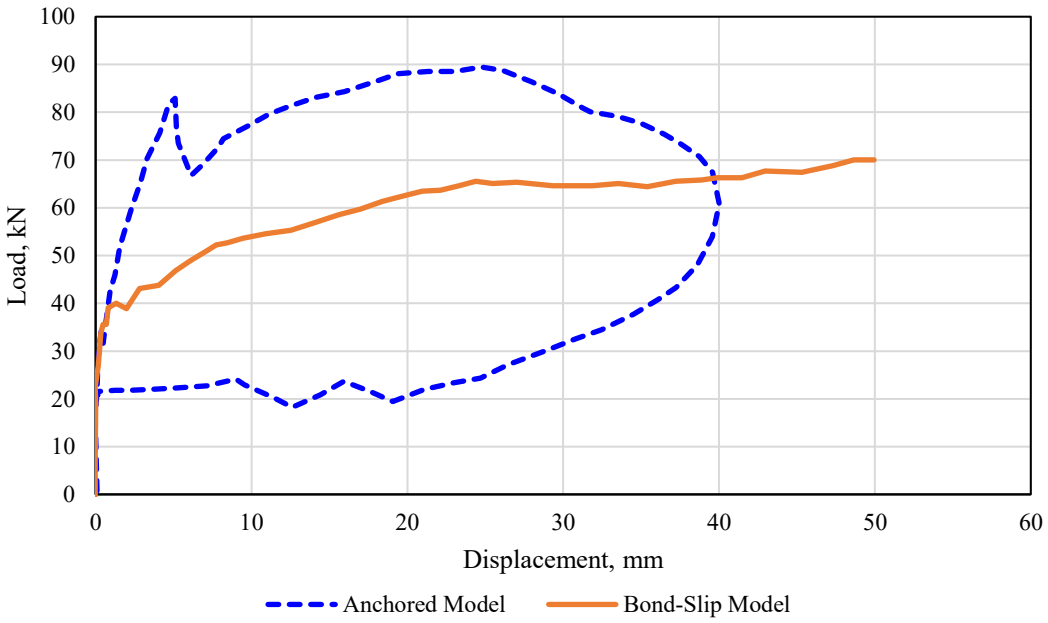

Figure 56: Comparison between effect of anchored model and bond-slip model on load-displacement results.

3.6 Conclusion

In this chapter, a comprehensive overview of the critical factors involved in modelling the bond-slip behaviour at the FRP-concrete interface is provided. Specifically, the FRP component is treated as an elastic isotropic material, while the concrete section is modelled using the Concrete Damage Plasticity (CDP) model, with detailed descriptions of the compression and tension stress-strain relationships. Additionally, the optimal finite element mesh size, taking into account computational efficiency and mesh sensitivity, is recommended for the models.

Detailed discussions are presented regarding various key parameters, including Rayleigh damping ratio, loading time, loading scheme, implicit dynamic loading approach, and increment size, based on insights from existing experimental research.

To validate the models, a static model was compared against experimental work conducted by Ali Nadjai [3]. Subsequently, a dynamic model was developed to depict the bond-slip behaviour at the FRP-concrete bonded interface and was validated against experimental data. The results from the ABAQUS model were then validated and compared to those obtained from a fully bonded beam model and an anchored zone FRP RC model. It was observed that in models with both full bonding and anchorage zones, the movement of the FRP bar within the concrete was restricted, preventing the occurrence of bond-slip phenomena.

Chapter 4: Finite Element Analysis of FRP bar RC beams

4.1 Introduction

In recent years, numerous researchers have extensively documented the impact behaviour of FRP-reinforced concrete beams. Several studies have specifically focused on experimental tests involving the effects of impact and blast loading, [271] [272] [273] [274]. While most of these studies have concentrated on experimentally observing the influence of FRP strengthening on the global structural response, they often overlooked the crucial aspect of thoroughly reporting the bond behaviour between the FRP and concrete. It has become apparent only recently that the debonding of FRP reinforcement from concrete can lead to the failure of strengthened concrete beams and frequently diminishes the effectiveness of strengthening applications [6] [275]. Furthermore, some studies have highlighted the relationship between strain rate and the strength of concrete, [276] [268].

Hence, this chapter is dedicated to the finite element modelling and analysis of FRP-reinforced concrete beams under impact loading. Finite element analysis was carried out on a series of FRP bar-reinforced concrete beams, based on experimental tests conducted by Saleh, [2]. The chapter provides a comprehensive description of the finite element models used, and ABAQUS software was employed for both pre-processing and post-processing of the FE models. Subsequent sections offer detailed insights into the description of the FE models and the selected parameters for the analysis.

4.2 FE modelling and detail of beams under impact load

A series of drop-weight tests, as detailed in Saleh's research [2], were conducted to investigate the behaviour of GFRP-reinforced concrete beams subjected to low-velocity impact loads. In order to validate the results obtained in this study, a benchmark model was developed based on these tests, aligning with the work conducted by Saleh, as discussed in Chapter 3.

This chapter focuses on the simulation of all models, utilizing parameters derived from Saleh's experiments. Three-dimensional finite element models were created

using ABAQUS simulation software. To expedite the simulation process and reduce solution times to manageable levels, a high-performance computer equipped with a Windows-based operating system was employed. Detailed information about the computer system utilized is provided in Table (16).

Computer type	HP EliteOne 800
Processor	Intel(R) Core(TM) i5-7500 @ 3.40GHz
Main memory	16 GB
Operating system	Windows 10 Enterprise
Finite element analysis software	ABAQUS version 2018
Post Processor software	ANOVA

Table 16: System specifications

The beams are composed of two segments, each measuring 100×180×375 mm and separated by a 50 mm gap, as illustrated in Figure (44). In the initial stage, the dimensions for both the FRP bar and concrete components are defined based on Figure (44) in three-dimensional representations. The concrete beams are represented within the ABAQUS software using eight-node linear brick elements (C3D8R), configured as solid, homogeneous elements. These concrete elements consist of eight nodes, each with three degrees of freedom in the x, y, and z directions.

For modelling the FRP bars, (B31) truss elements are employed. In the ABAQUS simulations, both the FRP bars and concrete are designated as isotropic materials, with the rationale for this choice explained in detail in Section (3.2.4).

The material properties for both the FRP and concrete components are then elaborated upon in ABAQUS. For the concrete's material behaviour, a damping value of 2×10^{-5} is defined.

Table (17) displays the default values suggested by the ABAQUS software for parameters such as eccentricity, dilation angle, and others that are input for the concrete in the ABAQUS simulation. The dilation angle influences the extent of plastic volume deformation. In finite element modelling utilizing the CDP model, the dilation angle value is typically assumed to be within the range of 20° to 42°. Opting for a

higher value enhances the concrete's stiffness. K_c represents the ratio of the second stress invariants on the tensile and compressive meridians, and it falls within the range of 0.5 to 1. This value can be calculated using the formulas mentioned in Chapter 3 of the constitutive concrete model, with the assumption that the plastic strain with stiffness degradation should be smaller than that without degradation. However, it's important to note that the total plastic strain may not decrease as deformation increases. Eccentricity relates to the plastic potential surface, and f_{b0}/f_{c0} is the ratio of biaxial strength to uniaxial strength in compression. It's worth mentioning that the values presented in Table (17) were obtained from the ABAQUS user's manual.

Table (18) provides material properties used for concrete, CFRP, GFRP, and AFRP bars.

Dilation Angle	**Eccentricity**	$\boldsymbol{fb0/fc0}$	**Kc**	**Viscosity Parameter**
32	0.1	1.16	0.67	0

Table 17: Concrete damage plasticity parameters for concrete members in ABAQUS.

Moreover, the Kent & Park concrete compressive model was employed for unconfined concrete, and the Mander model was incorporated for the confined concrete segment. For each model, where different concrete compressive strength serves as a parameter, the compressive and tensile behaviour of the concrete was characterized using strain rate-dependent data derived from experimental studies, specifically [1] [4]. Figure (123) in Appendix B provides a representative dataset illustrating the strain rate-dependent behaviour of concrete in terms of both compressive and tensile properties.

For all FRP, a value of 2×10^{-6} was defined for damping. Individual details for FRP material properties are shown in Table (20). Based on studies, CFRP and AFRP are not rate dependent, while glass fibres have shown strain rate dependency [277] [278]. Therefore, the plasticity behaviour of GFRP bars is defined with strain rate-dependent data. Table (50) shows an example of plasticity behaviour defined for GFRP, and

Figure (124) shows stress-strain for CFRP, AFRP and GFRP bars. Mentioned Table and figures are in Appendix B.

After a complete description of FRP and concrete parts, option" Assembly" is used to form the FRP RC beam. Figure (53) shows the FRP RC beam after the assembly of parts together.

Once the FRP RC beam assembly is complete, the "Step" module must be defined to specify crucial information related to the time duration, increment size, and mass scaling for the models. In all the beam models, a time period of 0.1 seconds is chosen, with an increment size of 10^{-6}. There are two damping coefficients associated with volumetric straining, which are utilized to enhance the simulation of explicit dynamic events. Initially, the linear and quadratic bulk viscosity parameters are set to their default values of 0.6 and 1.2, respectively. However, after conducting trial and error experiments within ABAQUS, these values are adjusted to 0.12 and 2.4 to achieve optimal results.

Furthermore, a symmetrical triangular-shaped pulse force is described, characterized by $t_d = 0.03\ s$ and $T_n = 0.06\ s$, ensuring a t_d/T_n ratio of $1/2$ as suggested by [279]. The data is entered in the amplitude section for all beam models. Another reason for explaining the time step and the values entered in amplitude was to have both forced and free vibration phases for beam models and plot the effects of these phases on corresponding maximum responses.

The interaction between the FRP bar and the concrete components must be explicitly defined to account for bond slip and rate dependency between the beam elements. The embedded method is employed in the FRP-reinforced concrete to separately evaluate the stiffness of concrete and FRP components, with FRP displacements corresponding to the displacements of the surrounding concrete. To facilitate this interaction within the beam model, a series of constraints and connectors were introduced. These connectors were established between the FRP bar and the surrounding concrete to function as springs, connecting the nodes of FRP and concrete to enable their interaction. Using the "Connector assignment manager"

function, these connectors were configured to allow for a 90° rotational angle about the Y-axis.

In all the models, the bond between the FRP bar and the concrete elements is established by implementing the Baena bond-slip model through the "CONNECTOR ASSIGNMENT" option. This allows for the incorporation of a force-slip graph for each node, taking into account the applied rates in the connectors as previously described.

As discussed in Chapter 3, the bond strength was computed using the B.P.E model with parameters tailored to fit the experimental data from Baena, which pertains to slip behaviour. To apply these calculated bond strengths to each connector, they were multiplied by the cross-sectional area of the FRP bar and the distance between connectors. ABAQUS automatically manages the spatial aspects to determine the force-slip relationship with respect to the strain rate, drawing from the findings of Borosnyoi's experimental work [1]. These strain rates are also applied to the compressive and tensile behaviour of concrete, as well as the plasticity behaviour of FRP.

Furthermore, rigid body restraints were applied to the nodes located at the top of the beam in the middle and at the support positions in ABAQUS to prevent vertical movement of the beam. All beams were modelled with pin and roller supports in accordance with the original experimental work conducted by [2].

At last, forces are exerted on designated nodes with initial velocities using the "pre-defined field manager" assignment. An illustration of the applied load and velocity is presented in Figure (61).

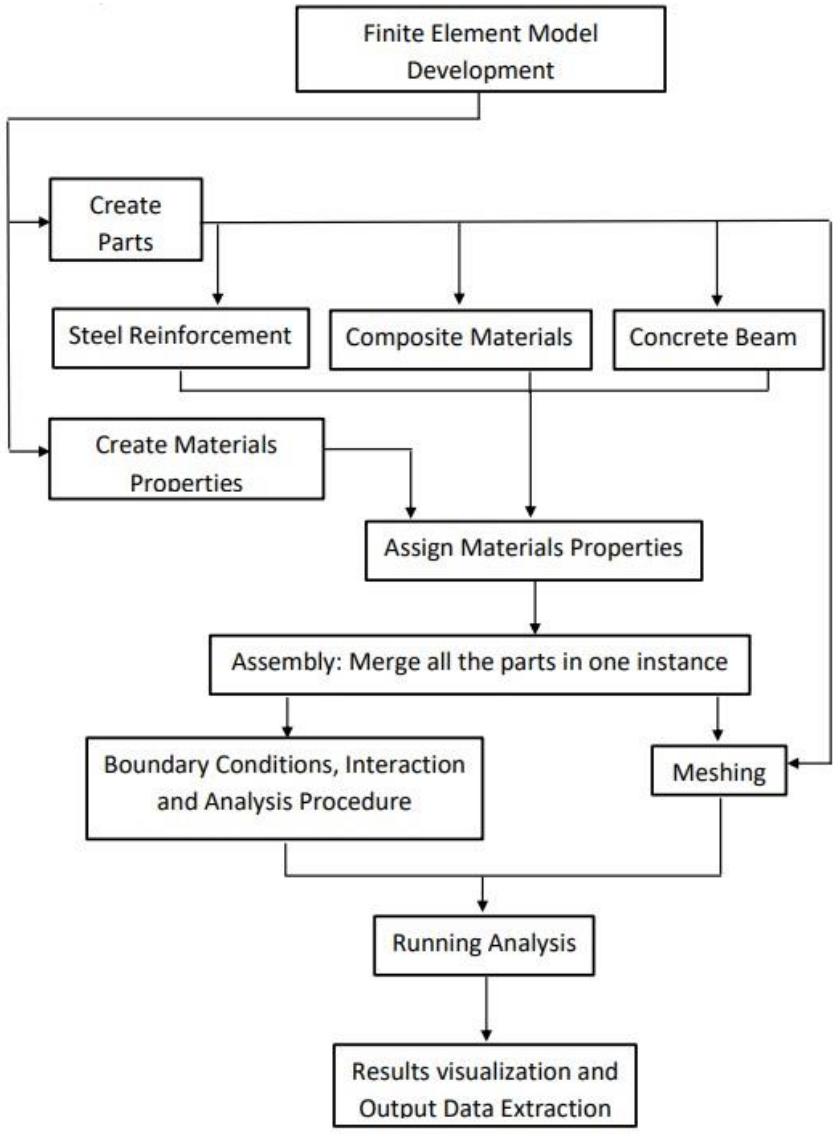

Figure 57: Flow chart of developing finite element model.

The primary aim of this review is to conduct a numerical investigation into the bond-slip behaviour of concrete beams reinforced with FRP bars subjected to impact loading. The numerical program employed for this analysis is depicted in Figure (49)

In total, three distinct sets of models were created, comprising 75 FRP RC beams, each with different study parameters. A total of 225 FRP RC beam models were simulated in ABAQUS under high-velocity impact loading conditions. You can find the complete list of beam models in Table (53) in Appendix B, and Figure (62) provides an explanation of the relevant symbols and characteristics.

Material	Ultimate strength, MPa	Mass Density, Kg/m^3	Elastic Modulus, GPa	Poisson's ratio	Plastic Strain
CFRP	1890	2500	136	0.15	0.014
GFRP	947	2500	45	0.15	0.03
AFRP	1400	2500	69	0.15	0.016
Concrete	57.4	2450	31.53	0.2	–

Table 18: Mechanical properties of materials used for models, [280] [281].

Figure 58: Models symbol description.

4.3 Study parameters

The choice of initial variables for this research was guided by existing experiments regarding the bond behaviour of FRP bars in concrete and identified gaps in the current body of research. Many parameters that affect bond behaviour have already been extensively studied by other researchers, providing the research community with a sufficient understanding of their impact. These parameters include embedment length, resin type, and the effects of confinement pressure.

However, this study seeks to investigate additional factors that require further examination to gain a deeper understanding of their ultimate influence on bond behaviour. The factors considered in this numerical program are as follows:

- Type of bar fibre (Carbon, Glass and Aramid)
- Concrete compressive strength
- FRP bar diameters
- FRP bar rupture strength

- High strain rate of applied load, which varies with different high velocity impact load.

A thorough evaluation of how these parameters affect bond behaviour is crucial for gaining a comprehensive understanding of FRP-reinforced concrete beams. Despite the fact that the impact of concrete compressive strength and bar diameter has been previously discussed, the author opted to include them in this study to enhance their own database for future research requirements, such as the refinement of bond-slip models.

FRP Rupture Strength, MPa	Kinetic energy, J	Concrete compressive Strength, MPa	Bar Diameter, mm
(A) 1400	800	25	8
(C) 1890	1600	30	10
(G) 947	3200	35	12
		40	14
		45	16

Table 19: Study parameters employed in the study that extracted from following references, [282] [281] [280].

4.4 Conclusion

In this chapter, a comprehensive explanation of the crucial procedures for modelling an FRP bar-reinforced concrete beam under impact loading is provided. Specifically, the FRP bar is treated as an elastic isotropic material, while the concrete section is represented using a concrete damaged plasticity model, which encompasses the definitions of compression stress-strain relationships, tension stress-strain behaviours, and damage factors. Additionally, the selection of finite element mesh size is proposed with consideration for computational accuracy and efficiency.

Furthermore, key parameters related to the dynamic loading approach, such as loading time and increment size, are introduced in detail, along with recommendations based on previous research findings [2] [186].

Chapter 5: Finite Element Analysis results and parametric study

5.1 Introduction

Following an extensive examination of bond-slip phenomena, this study undertook the modelling of Fiber-Reinforced Polymer (FRP) reinforced concrete beams employing the Baena model, which is founded on the Bond-Plasticity-Elasticity (B.P.E) bond-slip model. Mesh sensitivity was meticulously considered within the ABAQUS finite element analysis framework. The beams were categorized into three distinct sets, each subjected to impact loading scenarios of 40 kN, 80 kN, and 320 kN, centrally applied.

The analytical investigations encompassed various independent variables, notably high-velocity impact loads, concrete compression strength, types of FRP materials, and bar diameters. Subsequent to the simulations, the obtained results were meticulously post-processed for comparative analysis, not only amongst themselves but also concerning the broader context of pre-existing research findings. Remarkably, a typical simulation run for a beam with identical dimensions and mesh sensitivity parameters required approximately 110 minutes of computation time on the high-performance computing system detailed in Table 16.

In the forthcoming sections, an intricate and comprehensive comparison of finite element results, considering the diverse parameters explored in this study alongside existing research studies, will be presented. The ABAQUS analysis yielded a substantial volume of output data. For the purpose of comparing these results with experimental tests from the literature, key metrics such as energy histories, strain energy, and load history were employed as fundamental yardsticks. Additionally, data pertaining to slip, reaction force, and displacement histories were obtained. A rigorous series of regression analyses was subsequently conducted using these recorded data, culminating in the formulation of novel numerical equations, hitherto unprecedented, for predicting the behaviour of FRP-reinforced concrete beams.

5.2 Force-Time history response

The finite element analysis yielded impact force histories in the horizontal direction between Fiber-Reinforced Polymer (FRP) bars and concrete, achieved through the incorporation of connectors at the interfacial nodes connecting the two materials. The magnitudes of these forces and the corresponding slip between the nodes are contingent upon a multitude of factors, including the nature of the interfacial contact, stiffness properties, and the meshing configuration of the interface. These impact force-time histories for AFRP, CFRP, and GFRP are visually presented in Figures 136, 137, and 138, respectively, showcasing the responses under impact loads of 40 kN, 80 kN, and 320 kN. These graphical representations can be found in Appendix C.

To elucidate further, a comprehensive analysis was conducted involving a total of 225 models, all sharing identical geometric shapes and boundary conditions as expounded upon in Chapter 4. In Figure (59), a subset of 15 of these models is depicted, wherein various types of FRP bars (AFRP, CFRP, and GFRP) and differing bar diameters ranging from 8 mm to 16 mm were examined, all while maintaining consistent concrete compressive strength and subjecting them to a uniform loading condition of 320 kN. It is noteworthy that the peak impact forces observed in this context were 95.5646 kN, 90.6945 kN, and 90.6945 kN for AFRP, CFRP, and GFRP, respectively.

<u>Force-Time histories of 320 kN:</u>

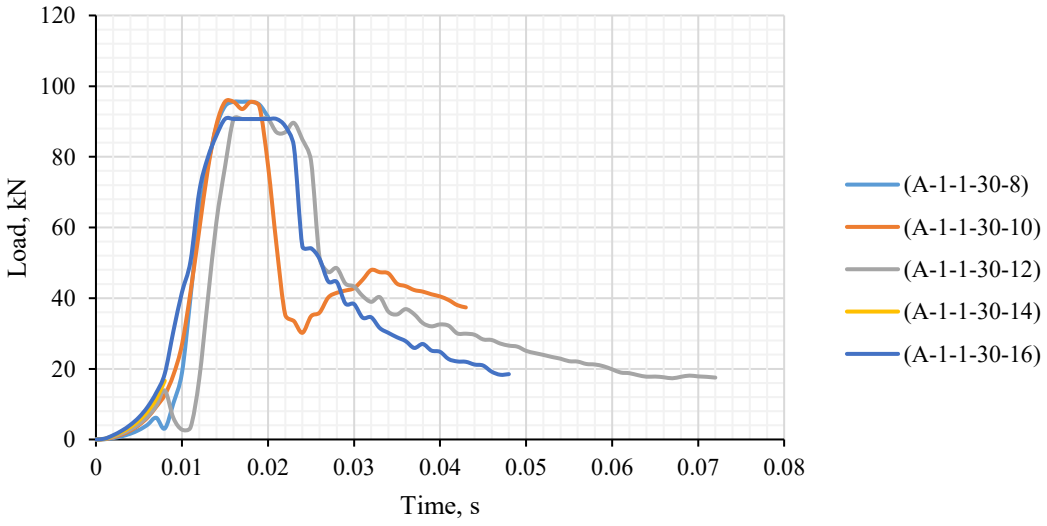

(A)

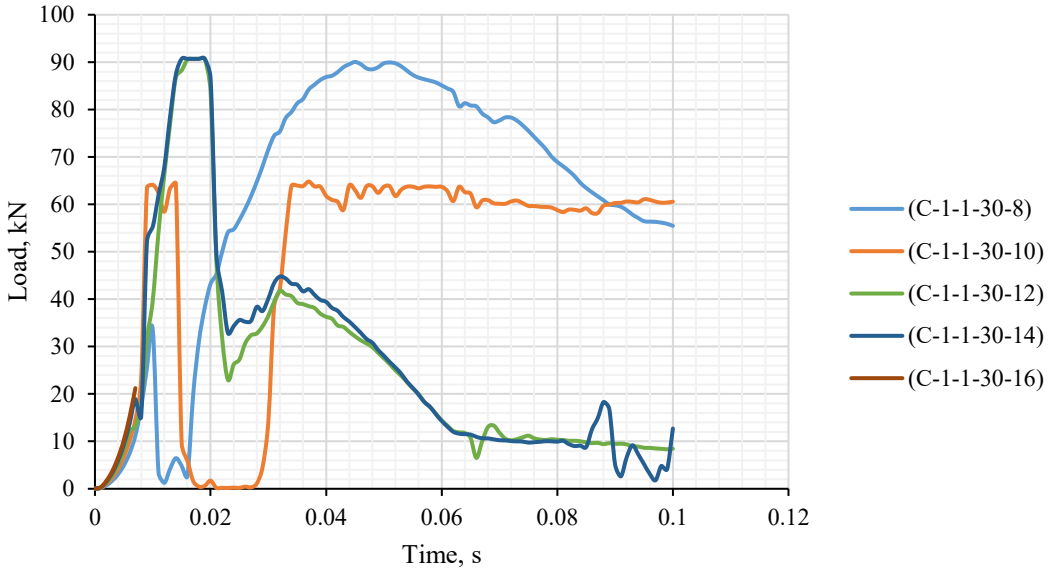

(B)

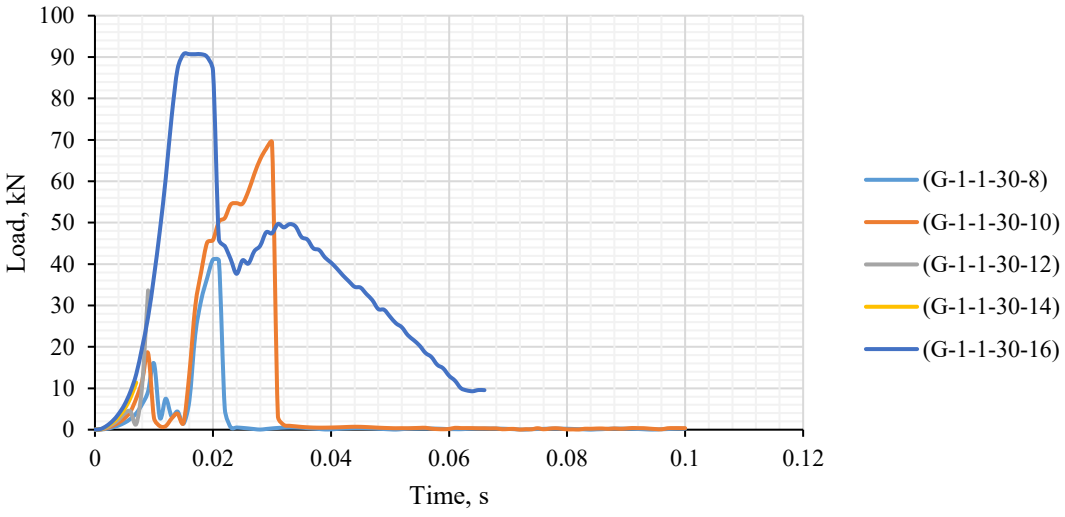

(C)

Figure 59: Impact Force-Time History response of (A) AFRP, (B) CFRP and (C) GFRP RC beams under 320 kN impact load.

Table (20) provides a summary of the maximum force values corresponding to each model depicted in Figure (59). These models were comprehensively characterized with respect to their response to impact forces over a time window of 100 milliseconds, ranging from 0 milliseconds to 100 milliseconds. For a comprehensive dataset detailing the behaviour of AFRP, CFRP, and GFRP reinforced concrete beams, as well as their respective maximum force values, please refer to Appendix (C).

MODEL	TIME,s	FORCE, kN	DURATION	MODEL	TIME,s	FORCE, kN	DURATION	MODEL	TIME,s	FORCE, kN	DURATION
A-1-1-30-8	0.016	95.5646	0.020001	C-1-1-30-8	0.045001	90.043	0.1	G-1-1-30-8	0.020001	41.1189	0.1
A-1-1-30-10	0.015001	95.5646	0.043	C-1-1-30-10	0.037	64.8126	0.1	G-1-1-30-10	0.030001	69.4095	0.1
A-1-1-30-12	0.016	90.6945	0.072001	C-1-1-30-12	0.017001	90.6945	0.1	G-1-1-30-12	0.009001	33.6458	0.009001
A-1-1-30-14	0.008	16.6418	0.008	C-1-1-30-14	0.015001	90.6945	0.1	G-1-1-30-14	0.007001	11.3771	0.007001
A-1-1-30-16	0.015001	90.6945	0.048	C-1-1-30-16	0.007001	21.2321	0.007001	G-1-1-30-16	0.015001	90.6945	0.066

Table 20: Peak force for AFRP, CFRP and GFRP models under 320 kN impact load.

The AFRP reinforced concrete (RC) beams subjected to an impact load of 320 kN were categorized into five distinct groups based on their concrete compressive strength. Figure (59-A) presents data pertaining to AFRP RC beams denoted as A-1-1-30-8 through A-1-1-30-16, while data for beams designated as (A-1-1-25-8, 16), (A-1-1-35-8, 16), (A-1-1-40-8, 16), and (A-1-1-45-8, 16) are detailed in Figure 136 within Appendix (C).

In a holistic perspective, the AFRP RC beams exhibited a distinct characteristic of a high-intensity, short-duration pulse, with peak force magnitudes ranging from 29.6176 kN to 95.5646 kN for beams (A-1-1-25-8, 16), 16.6418 kN to 95.5646 kN for beams (A-1-1-30-8, 16), 29.0055 kN to 95.5646 kN for beams (A-1-1-35-8, 16), 62.0178 kN to 95.5646 kN for beams (A-1-1-40-8, 16), and 54.7101 kN to 95.5646 kN for beams (A-1-1-45-8, 16) during the initial phase of impact. Subsequently, the impact forces were effectively counteracted by the flexural resistance offered by the AFRP RC beams, as visually represented in Figure (60) below.

The AFRP RC beams under impact loading of $320\ kN$ were broken up based on their concrete compressive strength into 5 groups. Figure (59-A) shows data for AFRP RC beams A-1-1-30-8 to A-1-1-30-16 and data for (A-1-1-25-8, 16), (A-1-1-35-8, 16), (A-1-1-40-8, 16) and (A-1-1-45-8, 16) are shown in Figure (136) in Appendix (C). In overall, AFRP RC beams shown a high magnitude short duration pulse between $29.6176\ kN$ to $95.5646\ kN$ for (A-1-1-25-8, 16), $16.6418\ kN$ to $95.5646\ kN$ for (A-1-1-30-8, 16), $29.0055\ kN$ to $95.5646\ kN$ for (A-1-1-35-8,16), $62.0178\ kN$ to $95.5646\ kN$ for (A-1-1-40-8, 16) and $54.7101\ kN$ to $95.5646\ kN$ for (A-1-1-45-8, 16) turned out at first and after this diminutive

period, the impact force was resisted by flexural resistance of AFRP RC beams as shown in Figure (60) below.

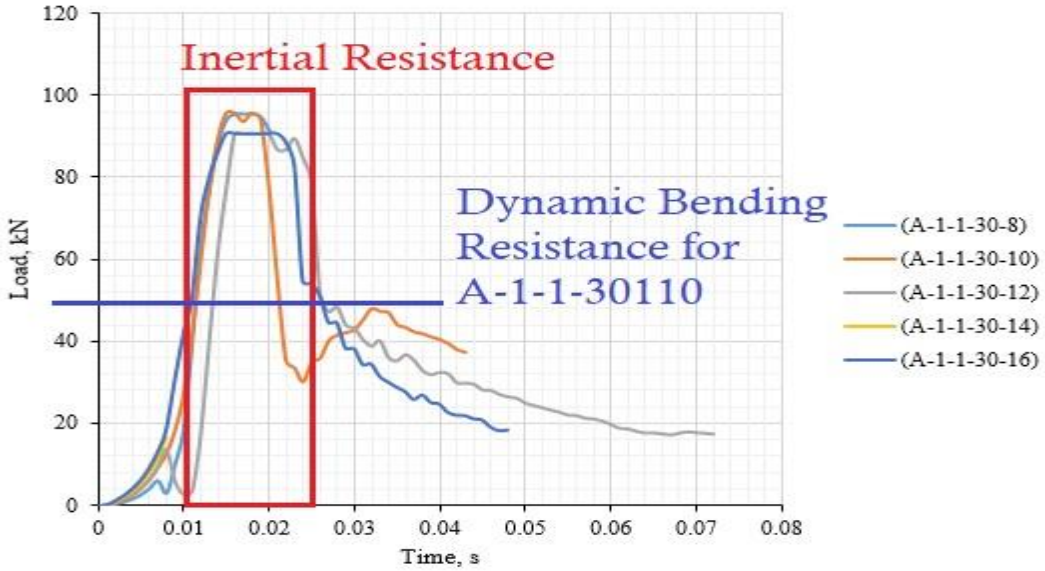

Figure 60: Impact Force-Time history for AFRP RC beams with 30 MPa concrete compressive strength and data for dynamic bending resistance.

The assessment of dynamic bending resistance across all models was derived from force-time history graphs. Within the subset denoted as (A-1-1-30-8, 16), it is noteworthy that only A-1-1-30-10 exhibited a dynamic bending resistance of 47.9644 kN at 32 milliseconds. The dynamic bending resistance was conspicuously evident for all AFRP RC beams except those in the (A-1-1-45-8, 16) category. In the case of these five models, the dynamic bending resistance could not be quantified. This outcome was attributed to the impact energy causing total pull-out failure in AFRP RC beams characterized by a concrete compressive strength of 45 MPa, spanning bar diameters from 8 mm to 16 mm. Consequently, the establishment of a well-defined dynamic bending resistance was precluded.

In contrast, CFRP RC beams exhibited a more favourable response compared to AFRP RC beams in the force-time history data. Figure 136 provides data for (C-1-1-25-8, 16), (C-1-1-35-8, 16), (C-1-1-40-8, 16), and (C-1-1-45-8, 16) within Appendix (C). Additionally, Figure (59-B) presents force-time histories for CFRP RC beams spanning from C-1-1-30-8 to C-1-1-30-16, showcasing an initial short-lived high-intensity pulse ranging from 21.2321 kN to 90.6945 kN, followed by the emergence of dynamic bending resistance in all models.

Notably, Model C-1-1-30-8 exhibited a brief pulse of 33.6142 kN at 10.001 ms, succeeded by dynamic bending resistance measuring 90.0430 kN at 45.001 ms, indicating an onset of failure upon the application of the 320 kN impact load. Meanwhile, Models C-1-1-30-12 and C-1-1-30-14 displayed dynamic bending resistance values of 41.7523 kN and 44.7765 kN, both occurring at 32 ms. In contrast, Model C-1-1-30-16 recorded the lowest peak force of 21.2321 kN at 7.001 ms. In a manner analogous to AFRP RC beams with a concrete compressive strength of 45 MPa, CFRP RC beams with the same compressive strength exhibited pull-out and de-bonding failures, leading to an absence of well-defined dynamic bending resistance.

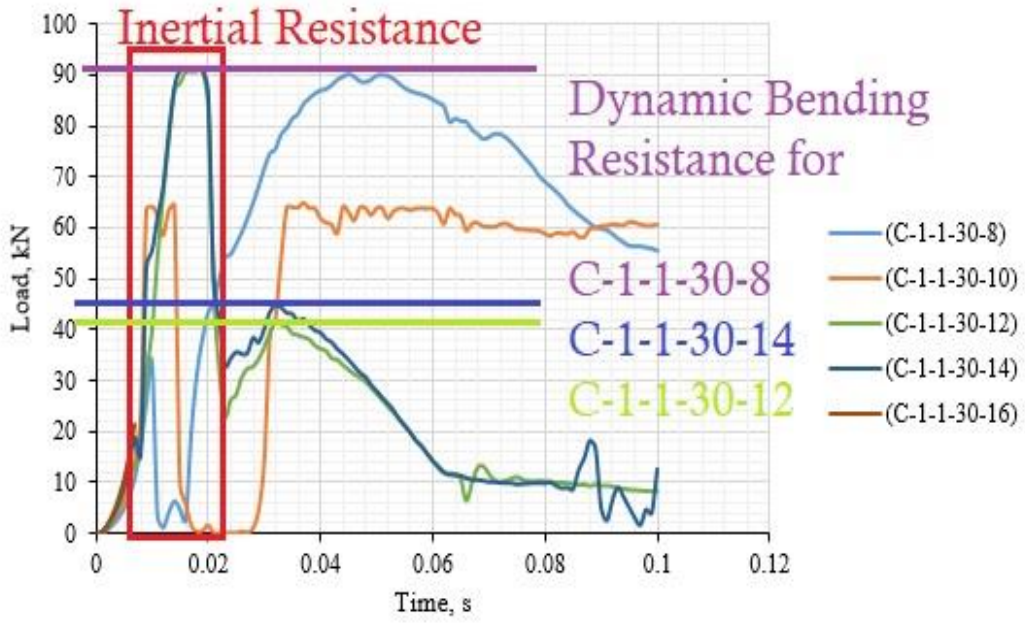

Figure 61: Dynamic Bending Resistance for CFRP RC beams with concrete compressive strength of 30 MPa.

Figure (136) shows force-time histories for GFRP RC beams of (G-1-1-25-8, 16), (G-1-1-35-8, 16), (G-1-1-40-8, 16) and (G-1-1-45-8, 16) in Appendix (C). Figure (59-C) shows force-time histories for GFRP RC beams with concrete compressive strength of $30\ MPa$ with FRP bar diameters of $8\ mm$ to $16\ mm$. Model G-1-1-30-10, G-1-1-30-12 and G-1-1-30-14 shown peak forces of $69.4095\ kN, 33.6458\ kN$ and $11.3771\ kN$, which performed with lower peak forces compare to other models of AFRP and CFRP RC beams with similar concrete compressive strength. Model G-1-1-30-16 showed highest peak force of $90.6945\ kN$ with dynamic bending resistance

of$49.6845\ kN$ at $31.001\ ms$. Similar to AFRP and CFRP RC beam with concrete compressive strength of $45\ MPa$, models G-1-1-45-8 to 16 shown more pull-out failures compare to other GFRP RC beams resulting in not well-defined dynamic bending resistance. Further details of dynamic peak forces are shown in Table (54) in Appendix (C).

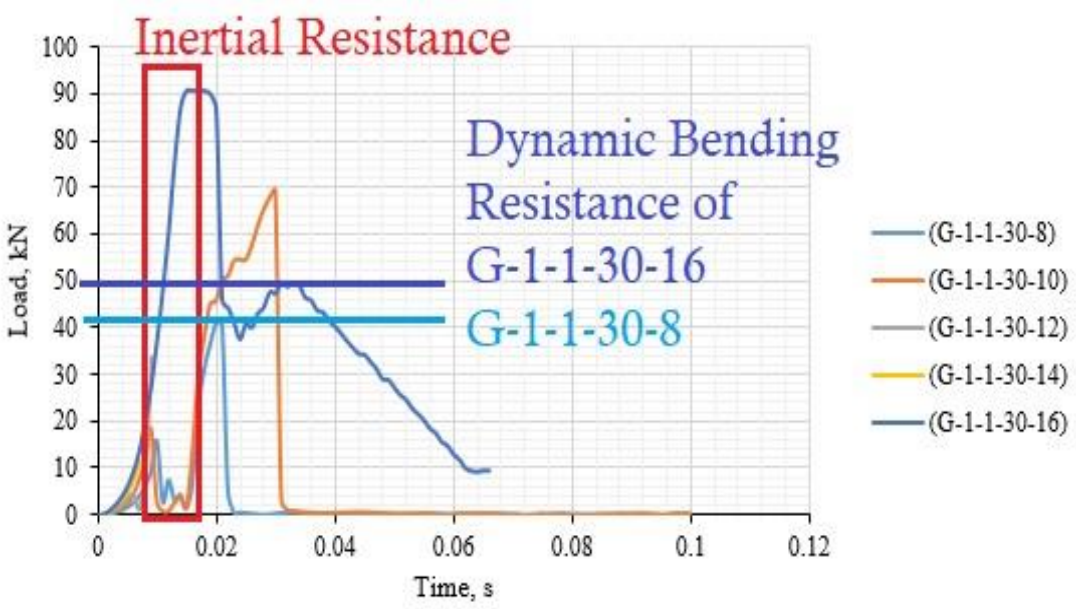

Figure 62: Dynamic Bending Resistance for GFRP RC beams with concrete compressive strength of 30 MPa.

Figure (63) depicts the response of models (A-2-1-30-8, 16), (C-2-1-30-8, 16), and (G-2-1-30-8, 16) subjected to an 80 kN impact load over a time interval of 100 milliseconds, commencing at 0 milliseconds and concluding at 100 milliseconds.

<u>Force-Time histories of 80 kN:</u>

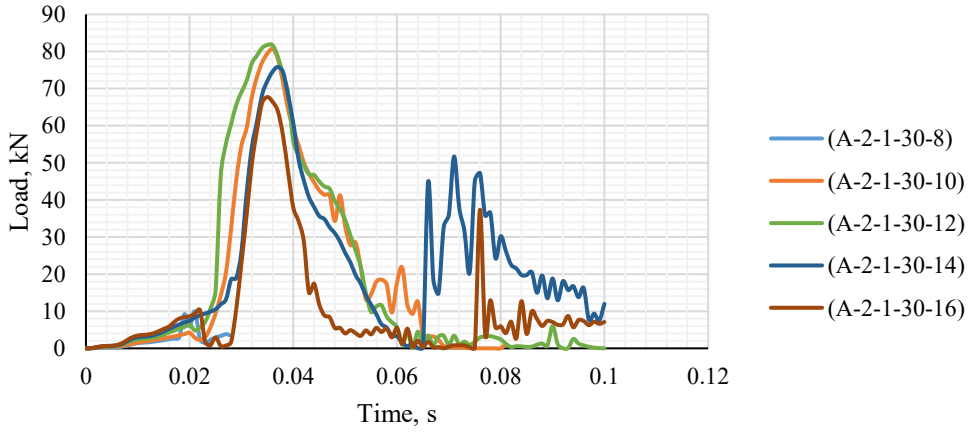

(A)

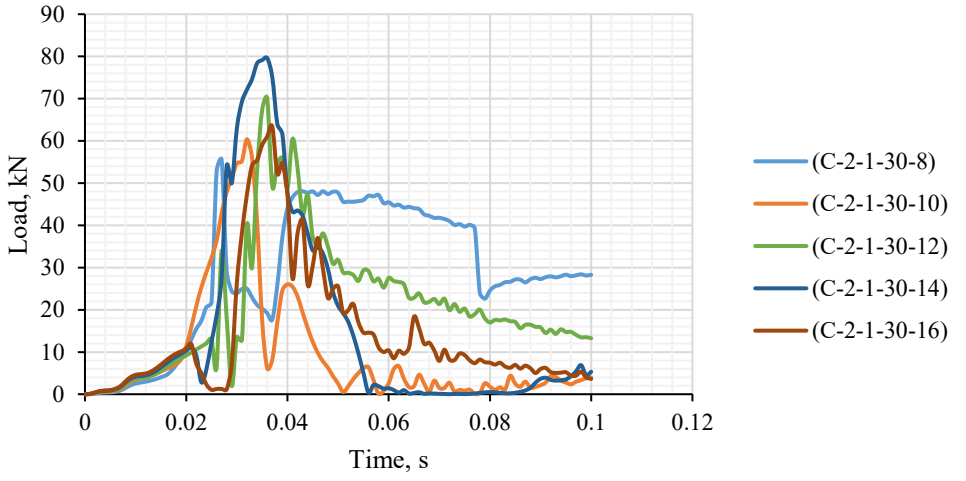

(B)

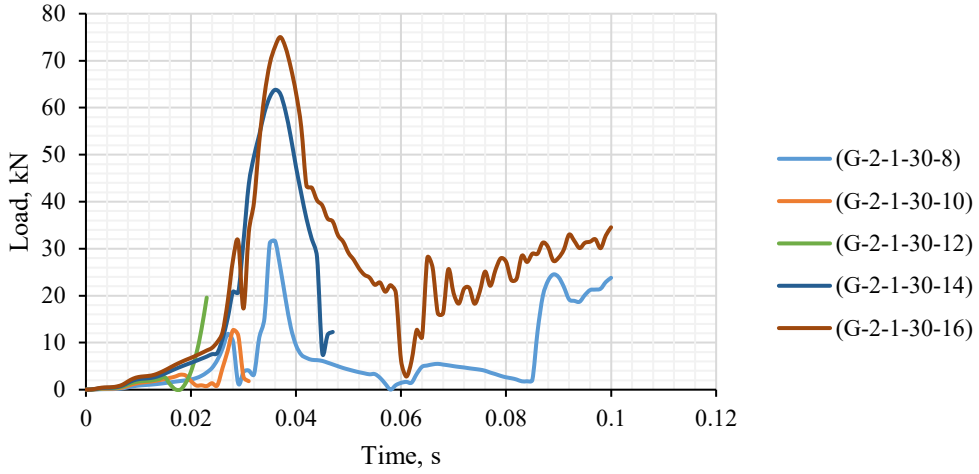

(C)

Figure 63: Impact Force-Time History response of (A) AFRP, (B) CFRP and (C) GFRP RC beams under 80 kN impact load.

In Figure (63), the AFRP, CFRP, and GFRP RC beams exhibit uniform concrete compressive strength of 30 MPa, coupled with bar diameters spanning 8, 10, 12, 14, and 16 mm. For a comprehensive display of force-time history data for all other models subjected to an 80 kN impact load, please refer to Figure 137 in Appendix (C).

Remarkably, all three types of FRP bars displayed analogous responses when exposed to an impact load characterized by a high velocity of 17.14 m/s. This response pattern was typified by an initial high-intensity pulse, succeeded by the emergence of dynamic bending resistance.

AFRP RC beams exhibited a consistent trend with an average peak impact force occurring at approximately 33.6 milliseconds, and most of them sustained this force for the entire duration of 100 milliseconds before experiencing failure, with the exception of model A-2-1-30-8 and A-2-1-30-10. Among these beams, model A-2-1-30-12 registered the highest peak force, measuring 81.7409 kN at the 35-millisecond mark. Notably, this model did not exhibit a discernible dynamic bending resistance following the initial high impulse. The subsequent peak force of 80.6932 kN was observed for model A-2-1-30-10 at 36.001 milliseconds, accompanied by a dynamic bending resistance of 21.7457 kN.

MODEL	TIME,s	FORCE, kN	DURATION	MODEL	TIME,s	FORCE, kN	DURATION	MODEL	TIME,s	FORCE, kN	DURATION
A-2-1-30-8	0.021001	99.7102	0.028001	C-2-1-30-8	0.027	55.5475	0.1	G-2-1-30-8	0.036001	31.6536	0.1
A-2-1-30-10	0.036001	80.6932	0.081	C-2-1-30-10	0.032	60.3984	0.1	G-2-1-30-10	0.028001	12.6544	0.031001
A-2-1-30-12	0.035	81.7409	0.1	C-2-1-30-12	0.036001	70.082	0.1	G-2-1-30-12	0.023001	19.5868	0.0230005
A-2-1-30-14	0.037	75.8324	0.1	C-2-1-30-14	0.036001	79.6264	0.1	G-2-1-30-14	0.036001	63.7906	0.0470005
A-2-1-30-16	0.035	67.7303	0.1	C-2-1-30-16	0.037	63.4205	0.1	G-2-1-30-16	0.037	75.0286	0.1

Table 21: Peak force for AFRP, CFRP and GFRP models under 80 kN impact load.

Conversely, both model A-2-1-30-8 and A-2-1-30-16 displayed lower strength results when compared to other AFRP RC beams sharing similar concrete compressive strength characteristics.

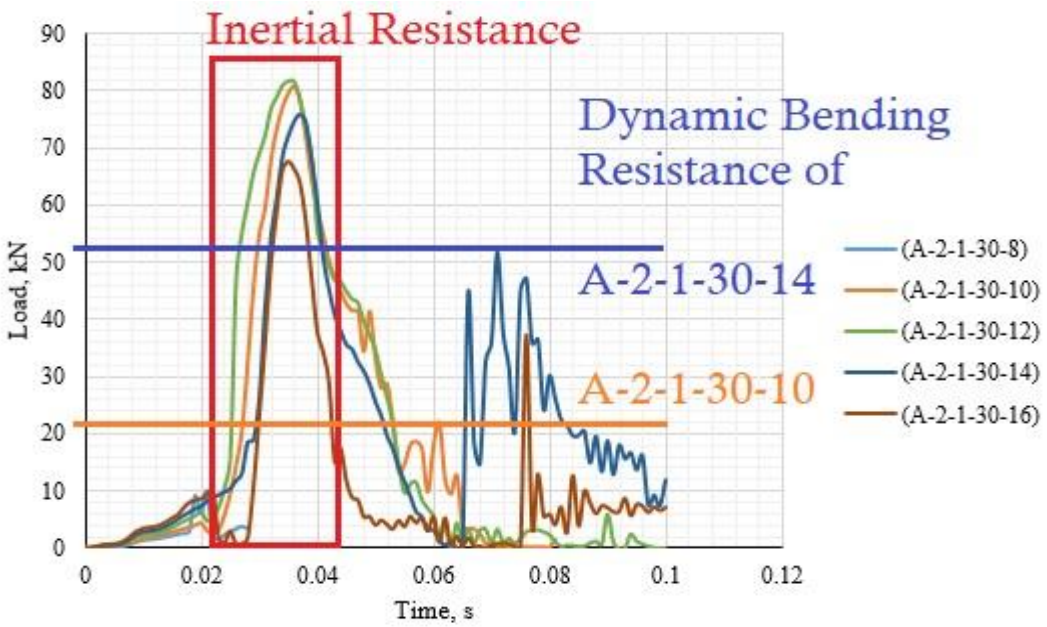

Figure 64: Dynamic Bending Resistance for AFRP RC beams with concrete compressive strength of 30 MPa under 80 kN impact load.

Similar to AFRP RC beams, CFRP RC beams exhibited comparable trends in Figure (63-B), especially those with bar diameters of 12 mm and 14 mm, displaying the highest peak forces of 70.0820 kN and 79.6264 kN, both occurring at the 36.001-millisecond mark. In contrast, models C-2-1-30-10 and C-2-1-30-16 demonstrated relatively lower strength compared to their CFRP RC beam counterparts in this specific group of models, registering peak forces of 60.3984 kN and 63.4205 kN at an average time of approximately 34 milliseconds.

An examination of the force-time histories among CFRP RC beams with varying concrete compression strengths reveals that models featuring smaller bar diameters tended to exhibit higher strength characteristics. This observation aligns well with findings from previous research studies cited as, [202] [108].

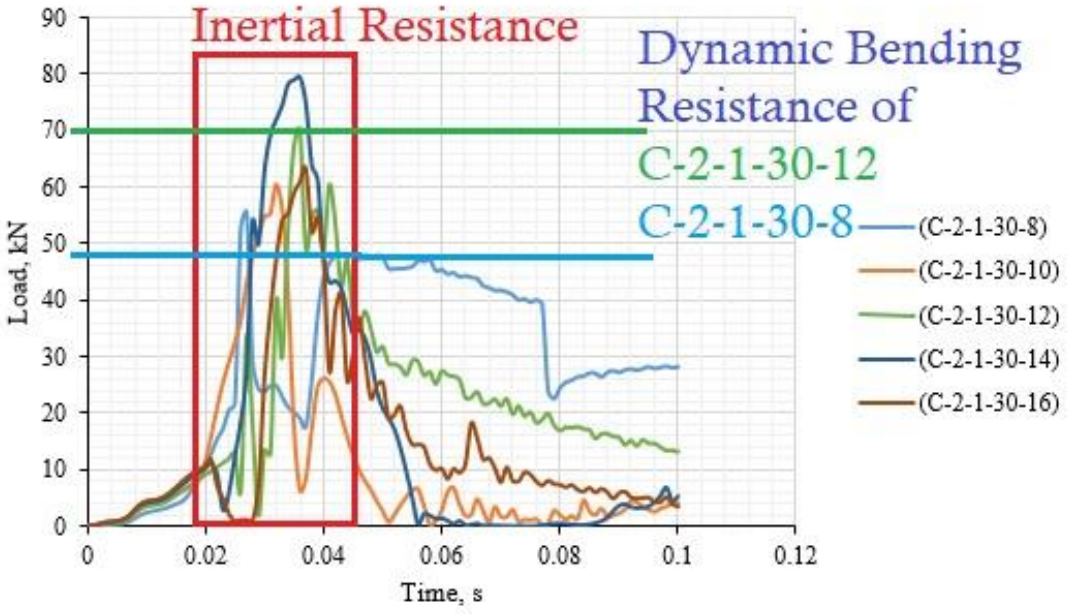

Figure 65: Dynamic Bending Resistance for CFRP RC beams with concrete compressive strength of 30 MPa under 80 kN impact load.

In contrast to AFRP and CFRP RC beams, GFRP RC beams exhibited diminished resistance when subjected to an 80 kN impact load. Notably, both G-2-1-30-14 and G-2-1-30-16 displayed higher initial resistance, with peak forces recorded at 63.79066

kN and 75.0286 kN at 37 milliseconds, respectively. Conversely, all models within the GFRP RC beam group, specifically G-2-1-30-8, G-2-1-30-10, and G-2-1-30-12, experienced failure before the 30-millisecond mark. In an overall assessment, GFRP RC beams featuring smaller bar diameters demonstrated superior resistance.

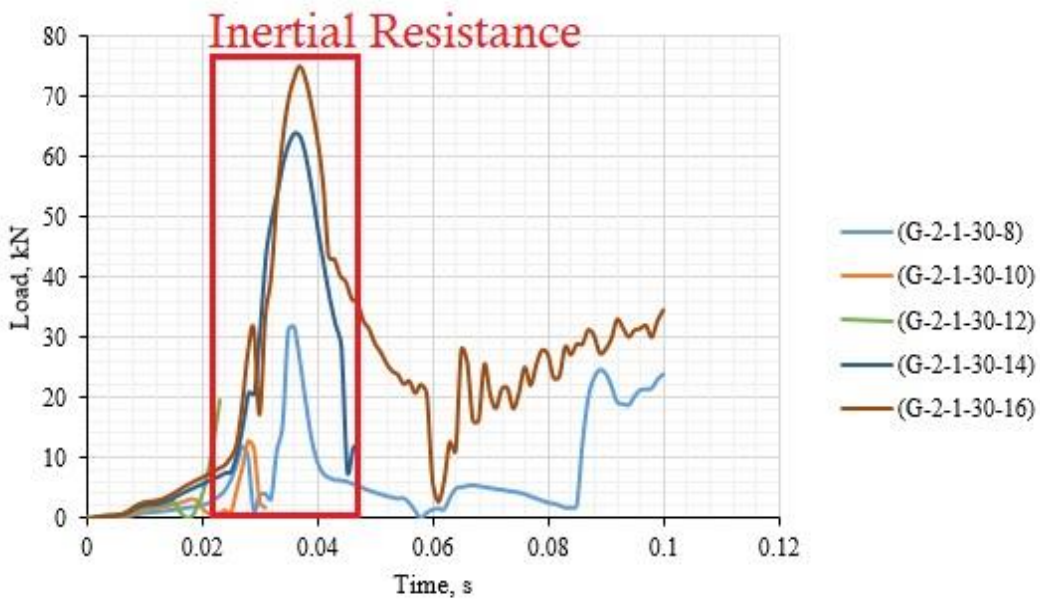

Figure 66: Dynamic Bending Resistance for GFRP RC beams with concrete compressive strength of 30 MPa under 80 kN impact load.

For an exhaustive account of force-time histories and peak forces associated with all GFRP RC beams, please refer to Figure (63-C). In a general sense, GFRP RC beams characterized by bar diameters of 12 mm and 14 mm exhibited enhanced resistance and higher peak forces when compared to their counterparts with varying bar diameters under the 80 kN impact load. It is noteworthy that, despite the smaller applied load compared to that of models in the first set, the analysis revealed considerably lower levels of dynamic bending resistance and a higher incidence of pull-out failure in this case.

Force-Time histories of 40 kN:

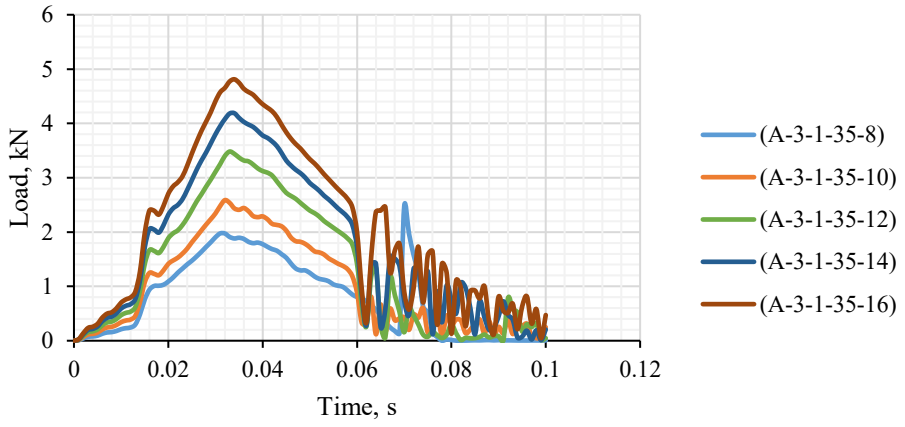

(A)

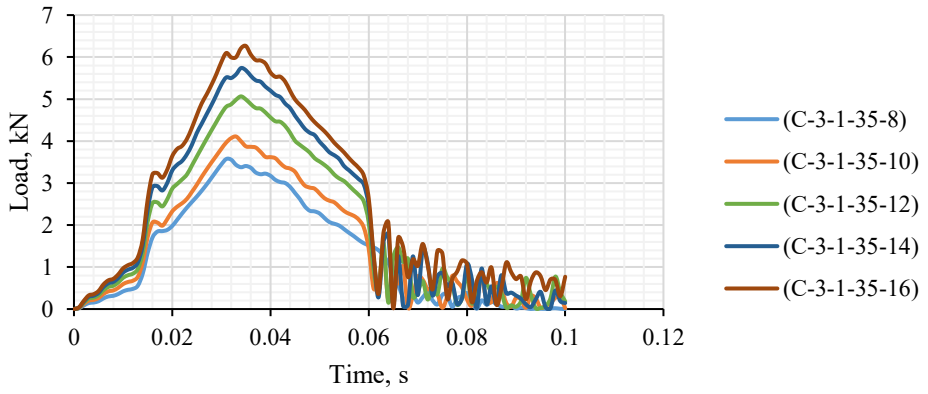

(B)

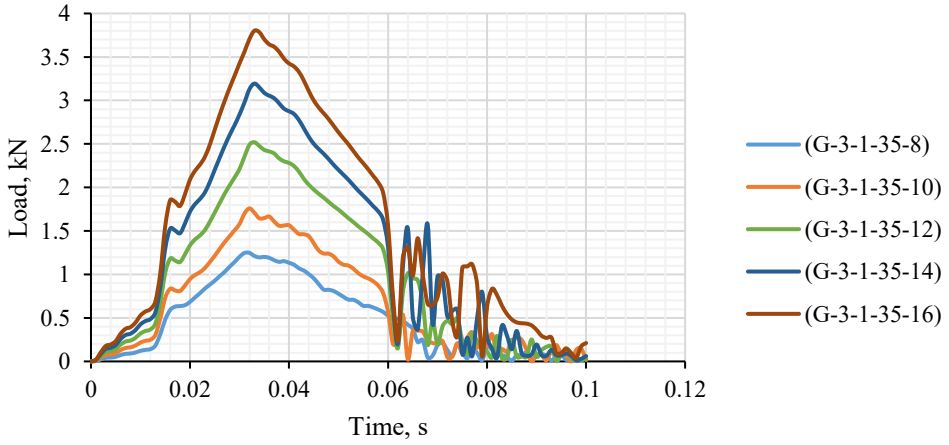

(C)

Figure 67: Force-Time histories of GFRP RC beams with concrete compressive strength of 35 MPa under 40 kN impact load.

Figure (67) provides an overview of the force-time histories of AFRP, CFRP, and GFRP RC beams, all characterized by a concrete compressive strength of 35 MPa, and subjected to the lowest applied impact load of 40 kN, with a velocity of 12.12 m/s. In the case of AFRP bars, there was a noticeable increase in strength with an increase in bar diameters, as evidenced by peak forces ranging from 2.47184 kN to 4.81176 kN, occurring at an average time of approximately 34 milliseconds. An interesting observation was made in model A-3-1-35-8, which exhibited a secondary dynamic bending resistance surpassing the initial resistance, measured at 1.97305 kN.

A similar trend was observed among CFRP RC beams, where an increase in peak force from 3.57283 kN to 6.26489 kN was noted at an average time of 34 milliseconds. Conversely, GFRP RC beams exhibited peak forces ranging from 1.24796 kN to 3.8013 kN, occurring at an average time of approximately 33 milliseconds. Based on the results presented in Figure (67), CFRP RC beams exhibited the highest resistance compared to other FRP bars, while GFRP RC beams demonstrated the lowest performance within the specified set.

For an extensive compilation of force-time histories detailing the performance of all AFRP, CFRP, and GFRP RC beams under the 40 kN impact load, please refer to Figure (138) in Appendix (B).

MODEL	TIME,s	FORCE, kN	DURATION	MODEL	TIME,s	FORCE, kN	DURATION	MODEL	TIME,s	FORCE, kN	DURATION
A-3-1-35-8	0.07	2.47184	0.1	C-3-1-35-8	0.031001	3.57283	0.1	G-3-1-35-8	0.032	1.24796	0.1
A-3-1-35-10	0.032	2.58761	0.1	C-3-1-35-10	0.033	4.10874	0.1	G-3-1-35-10	0.032	1.75913	0.1
A-3-1-35-12	0.033	3.48176	0.1	C-3-1-35-12	0.034001	5.06429	0.1	G-3-1-35-12	0.033	2.52005	0.1
A-3-1-35-14	0.034001	4.18722	0.1	C-3-1-35-14	0.034001	5.73818	0.1	G-3-1-35-14	0.033	3.19379	0.1
A-3-1-35-16	0.034001	4.81176	0.1	C-3-1-35-16	0.035	6.26489	0.1	G-3-1-35-16	0.033	3.8013	0.1

Table 22: Peak force for AFRP, CFRP and GFRP RC beams with concrete compressive strength of 35 MPa under impact load of 40 kN.

5.3 Mid-span deflection response

A substantial amount of data was generated through finite element analysis, yielding a significant volume of output information. Specifically, the displacement-time histories of the beams were recorded at the midpoint of the beams, near the area of interest, albeit not for all models due to instances of failure where some beams split into two separate parts. However, displacement histories were successfully recorded and graphically represented for all remaining models.

In the ensuing sections, the displacement histories of models utilizing AFRP, CFRP, and GFRP under various loading conditions will be systematically presented and discussed.

Mid-span deflection histories under 320 kN:

Figure (68) illustrates the vertical displacement histories of a total of 13 models comprising AFRP, CFRP, and GFRP RC beams. These beams were subjected to a uniform 320 kN impact load, simulated within the ABAQUS software environment. It's noteworthy that all beams in this section share consistent boundary conditions, featuring pin-ended supports, and each incorporates a single FRP bar as reinforcement spanning the entire length from one end to the other. Additionally, all the beams within this set possess a 50 mm gap situated at the midpoint of their length. For a comprehensive overview of the specific characteristics of these models used for the displacement-time history comparison in this section, please refer to Table 23.

Model	Type of FRP	Parameter (1) Bar Diameter, mm	Parameter (2) Concrete Comressive Strength, Mpa	Parameter (3) Impact load, kN	Parameter (4) Rupture Strength, Mpa
A-1-1-30-12	Aramid	12	30	160	1400
A-1-1-35-12	Aramid	12	35	160	1400
A-1-1-40-12	Aramid	12	40	160	1400
A-1-1-45-12	Aramid	12	45	160	1400
C-1-1-25-12	Carbon	12	25	160	1890
C-1-1-30-12	Carbon	12	30	160	1890
C-1-1-35-12	Carbon	12	35	160	1890
C-1-1-40-12	Carbon	12	40	160	1890
C-1-1-45-12	Carbon	12	45	160	1890
G-1-1-25-12	Glass	12	25	160	974
G-1-1-35-12	Glass	12	35	160	974
G-1-1-40-12	Glass	12	40	160	974
G-1-1-45-12	Glass	12	45	160	974

Table 23: Details of beams used for displacement history comparison.

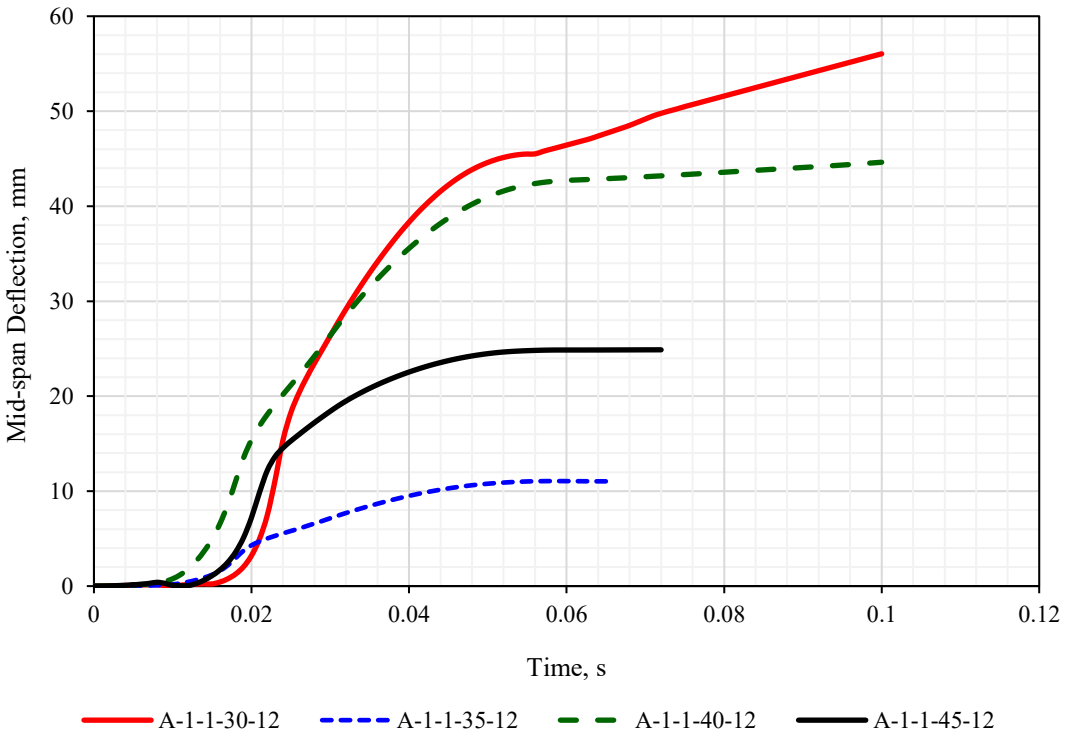
Mid-span Deflection, mm
60
50
40
30
20
10
0
0
0.02
0.04
0.06
0.08
0.1
0.12
Time, s
A-1-1-30-12
A-1-1-35-12
A-1-1-40-12
A-1-1-45-12

(A)

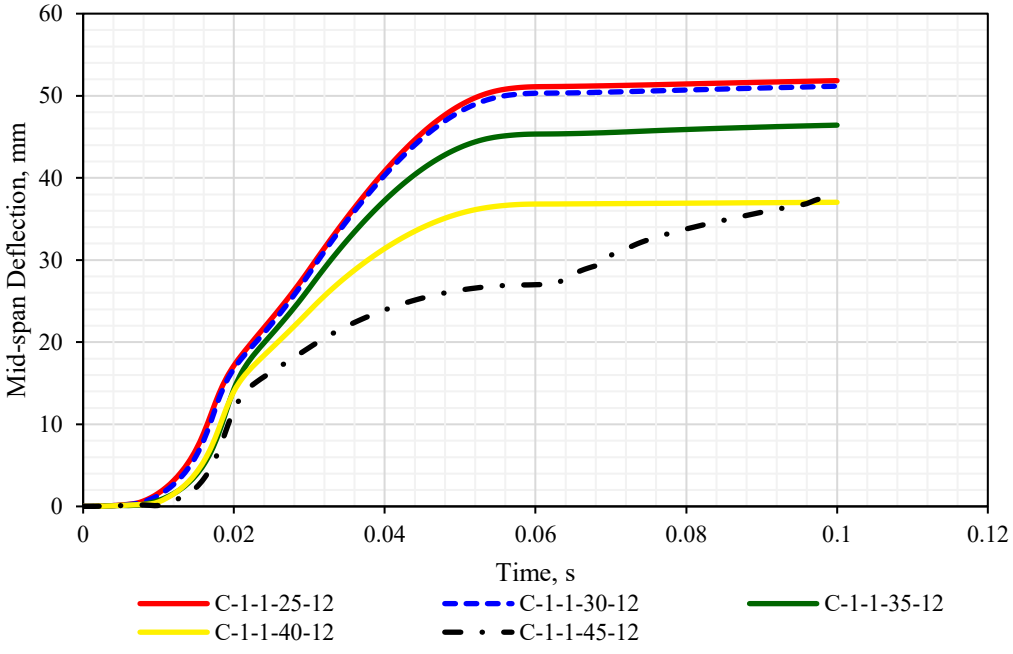
Mid-span Deflection, mm
60
50
40
30
20
10
0
0
0.02
0.04
0.06
0.08
0.1
0.12
Time, s
C-1-1-25-12
C-1-1-30-12
C-1-1-35-12
C-1-1-40-12
C-1-1-45-12

(B)

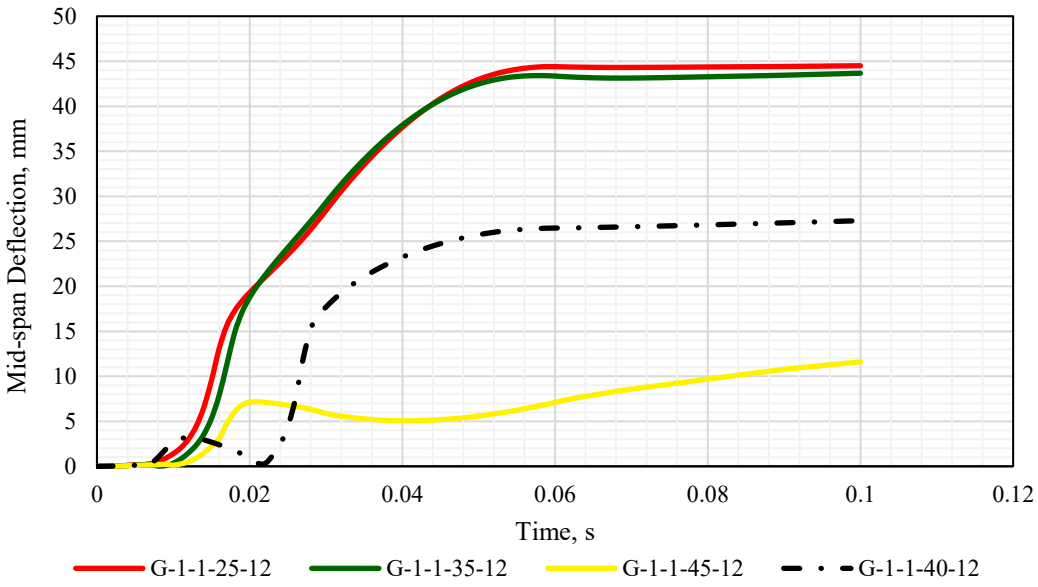

(C)

Figure 68: Mid-span Deflection-Time histories for AFRP, CFRP and GFRP with 12 mm bar diameter under 320kN impact load.

Figure (68) presents graphical representations of displacement histories for the specified models. It's worth noting that, for beams A-1-1-25-12 and G-1-1-30-12, displacement data could not be obtained due to the rupture of the FRP bar and subsequent splitting of the beams at the midpoint. The analysis reveals an increase in displacement for all AFRP RC beam models, with A-1-1-30-12 reaching a maximum displacement of 56.046 mm at 100 ms, A-1-1-35-12 attaining a peak displacement of 42.018 mm at 59 ms, A-1-1-40-12 exhibiting a maximum displacement of 44.626 mm at 100 ms, and A-1-1-45-12 reaching a maximum displacement of 24.881 mm at 72 ms. Notably, the graph demonstrates that as concrete compression strength increases, there is a corresponding decrease in maximum displacement.

Similarly, the displacement-time history graph for CFRP RC beams indicates a reduction in displacement with an increase in compressive strength for the models. Specifically, the C-1-1-25-12 model achieved a maximum displacement of 51.842 mm, model C-1-1-30-12 recorded a peak displacement of 51.167 mm, model C-1-1-35-12 exhibited a maximum displacement of 46.425 mm, model C-1-1-40-12 yielded

a maximum displacement of 37.032 mm, and model C-1-1-45-12 reached its maximum displacement of 56.046 mm at 100 ms.

A parallel trend is observed for GFRP RC beams, where model G-1-1-25-12 achieved a maximum displacement of 44.5 mm, model G-1-1-35-12 displayed a maximum displacement of 44.51 mm, model G-1-1-40-12 reached a maximum displacement of 27.291 mm, and model G-1-1-45-12 recorded a maximum displacement of 13.292 mm, all occurring at the 100 ms mark.

Mid-span deflection histories under 80 kN:

Figure (69), we observe displacement-time histories for Aramid, Carbon, and Glass Fiber-Reinforced Polymer (FRP) RC beams, all featuring an 8 mm bar diameter and subjected to an 80 kN impact load. These beams share identical boundary conditions, characterized by pin-ended supports. For a comprehensive overview of the specific characteristics of these beams used for the comparison of displacement histories in this section, please refer to Table 24. However, it is important to note that displacement data for models A-2-1-30-8 and A-2-1-40-8 could not be obtained from the software due to pull-out failure in these models.

Model	Type of FRP	Parameter (1) Bar Diameter, mm	Parameter (2) Concrete Comressive Strength, Mpa	Parameter (3) Impact load, kN	Parameter (4) Rupture Strength, Mpa
A-2-1-25-8	Aramid	8	25	80	1400
A-2-1-35-8	Aramid	8	35	80	1400
A-2-1-45-8	Aramid	8	45	80	1400
C-2-1-25-8	Carbon	8	25	80	1890
C-2-1-30-8	Carbon	8	30	80	1890
C-2-1-35-8	Carbon	8	35	80	1890
C-2-1-40-8	Carbon	8	40	80	1890
C-2-1-45-8	Carbon	8	45	80	1890
G-2-1-25-8	Glass	8	25	80	974
G-2-1-30-8	Glass	8	30	80	974
G-2-1-35-8	Glass	8	35	80	974
G-2-1-40-8	Glass	8	40	80	974
G-2-1-45-8	Glass	8	45	80	974

Table 24: Details of characteristics of beams used for comparison of mid-span deflection histories under 80 kN.

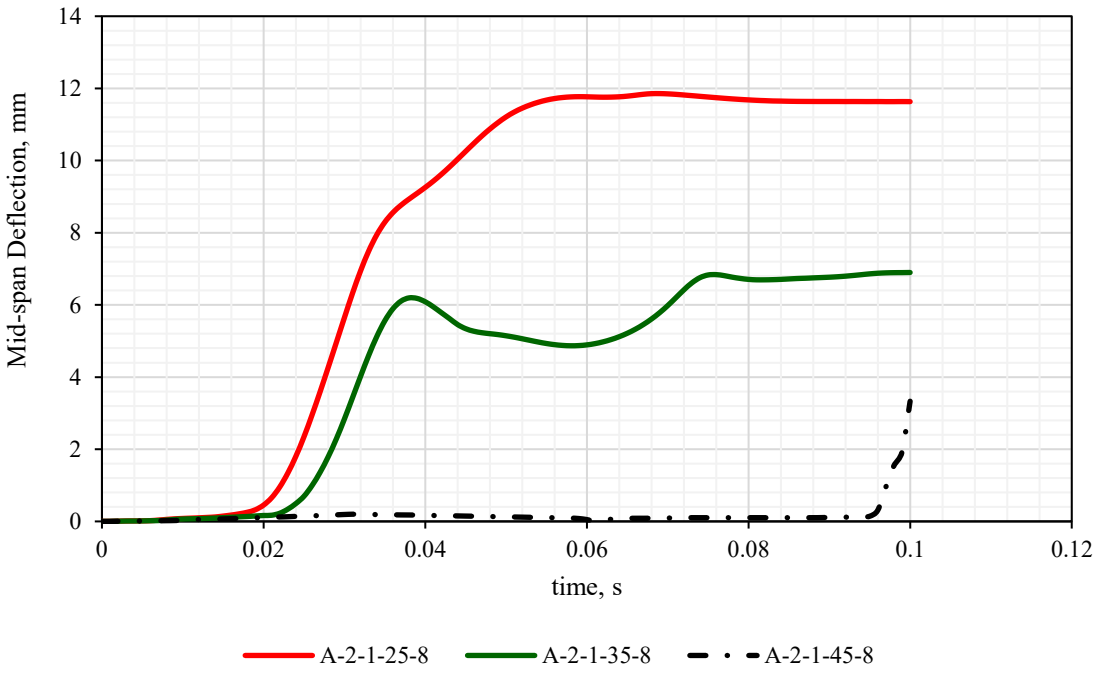
Mid-span Deflection, mm
14
12
10
8
6
4
2
0
0
0.02
0.04
0.06
0.08
0.1
0.12
time, s
A-2-1-25-8
A-2-1-35-8
A-2-1-45-8

(A)

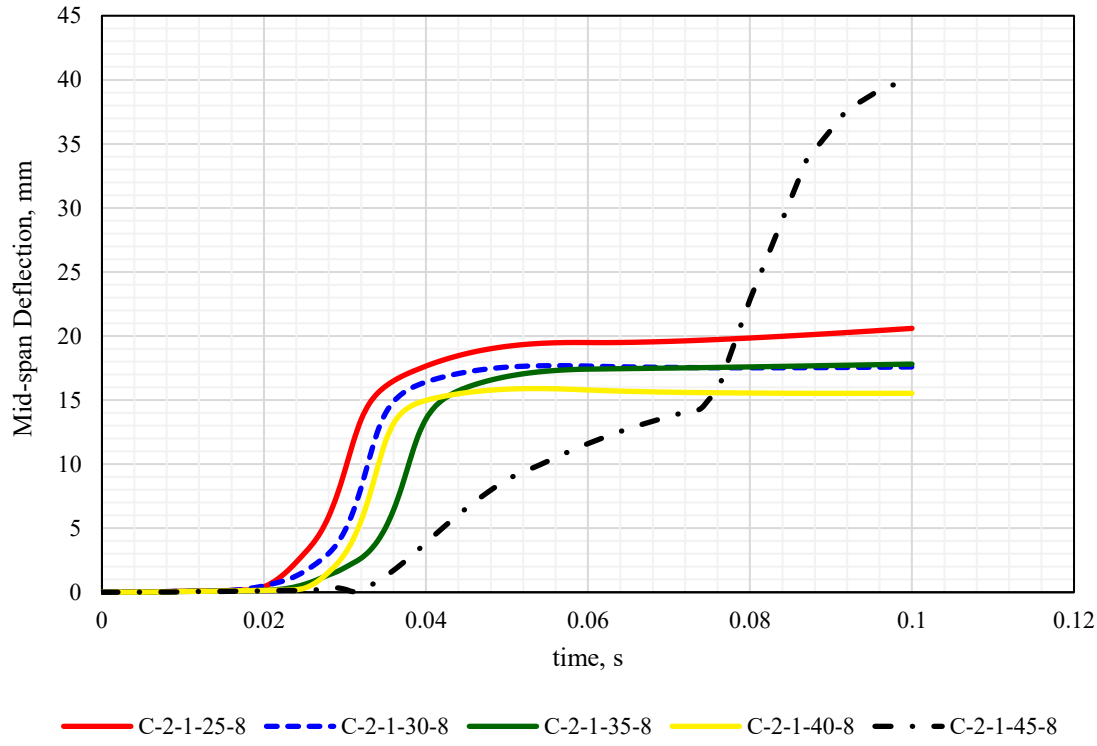
Mid-span Deflection, mm
45
40
35
30
25
20
15
10
5
0
0
0.02
0.04
0.06
0.08
0.1
0.12
time, s
C-2-1-25-8
C-2-1-30-8
C-2-1-35-8
C-2-1-40-8
C-2-1-45-8

(B)

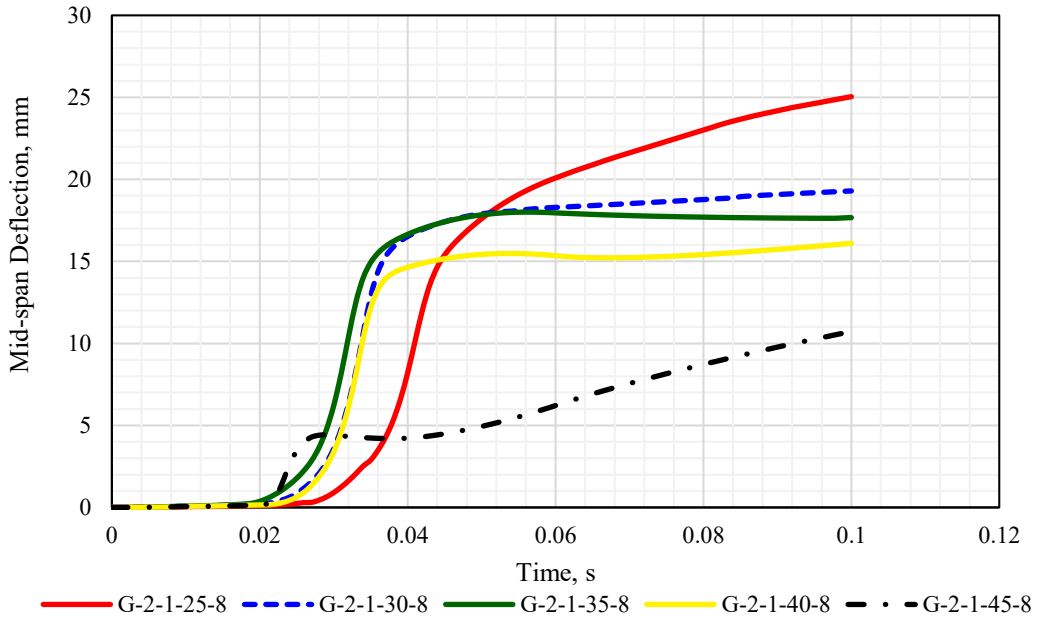

(C)

Figure 69: Mid-span Deflection-Time histories for (A) AFRP, (B) CFRP, (C) GFRP RC beams with bar diameter of 8 mm under 80kN impact load.

In Figure (69-A), we can observe the mid-span deflection profiles for AFRP RC beam models. Among these, A-2-1-25-8 exhibited the highest displacement, reaching 11.855 mm at 69 ms, whereas model A-2-1-35-8 achieved a maximum displacement of 6.898 mm at 100 ms, and model A-2-1-45-8 registered a peak displacement of 3.33 mm at 100 ms.

Moving on to the CFRP RC beams, their displacement profiles started at lower values and progressively increased, eventually reaching residual displacement. Specifically, model C-2-1-25-8 recorded a maximum displacement of 20.598 mm, model C-2-1-30-8 attained a peak displacement of 17.687 mm at 56 ms, model C-2-1-35-8 exhibited a maximum displacement of 17.809 mm at 100 ms, model C-2-1-40-8 yielded a peak displacement of 15.899 mm at 54 ms, and model C-2-1-45-8 reached a maximum displacement of 15.273 mm at 100 ms.

Displacement histories at the midpoint of the beams were derived from the analysis of beams subjected to an 80 kN impact load. Figure (69-C) provides insight into the displacement characteristics of five beams employing 8 mm GFRP bars. Overall, the shape of the displacement profiles for GFRP RC beams closely resembled that of CFRP RC beams in terms of both maximum displacement and residual displacement.

Notably, model G-2-1-25-8 exhibited a peak displacement of 536.682 mm, model G-2-1-30-8 reached a maximum displacement of 19.297 mm, model G-2-1-35-8 recorded a peak displacement of 18.005 mm at 56 ms, while model G-2-1-40-8 and G-2-1-45-8 displayed the lowest maximum displacements, measuring 16.102 mm and 13.995 mm, respectively, at 100 ms.

Mid-span Deflection histories under 40 kN:

Figure (70) illustrates the dynamic mid-span deflection responses of AFRP, CFRP, and GFRP RC beams, all featuring a 14 mm bar diameter. These response curves were generated through finite element analysis conducted in ABAQUS, simulating the effect of a 40 kN impact load with a high velocity of 12.125 m/s. The profiles of these curves exhibit a parabolic shape during the initial 0 to 60 ms interval, signifying the introduction of forced vibration in ABAQUS.

Subsequently, the displacement response transitions into a power curve, encapsulating the representation of residual displacement between 60 to 100 ms. For comprehensive details regarding the characteristics of the beams utilized in this section for the analysis of deflection-time histories, refer to Table (25).

All AFRP, CFRP, and GFRP RC beam models exhibited a consistent pattern in their displacement-time graphs. However, there were noteworthy variations in the peak displacements among individual beams, each reinforced with different FRP bars, despite the application of similar analysis conditions. As previously observed, an increase in concrete compression strength played a significant role in reducing mid-span deflection for FRP RC beams subjected to impact loading with high velocity. In all the models, beams with concrete compressive strengths of 40 MPa and 45 MPa were the only ones to reach their maximum displacements during the forced vibration phase, occurring at 31 ms. For all other beam models, the peak deflection was achieved during the subsequent free vibration phase when the applied load was removed.

Model	Type of FRP	Parameter (1) Bar Diameter, mm	Parameter (2) Concrete Comressive Strength, Mpa	Parameter (3) Impact load, kN	Parameter (4) Rupture Strength, Mpa
A-3-1-25-14	Aramid	14	25	40	1400
A-3-1-30-14	Aramid	14	30	40	1400
A-3-1-35-14	Aramid	14	35	40	1400
A-3-1-40-14	Aramid	14	40	40	1400
A-3-1-45-14	Aramid	14	45	40	1400
C-3-1-30-14	Carbon	14	30	40	1890
C-3-1-35-14	Carbon	14	35	40	1890
C-3-1-40-14	Carbon	14	40	40	1890
C-3-1-45-14	Carbon	14	45	40	1890
G-3-1-25-14	Glass	14	25	40	974
G-3-1-30-14	Glass	14	30	40	974
G-3-1-35-14	Glass	14	35	40	974
G-3-1-40-14	Glass	14	40	40	974
G-3-1-45-14	Glass	14	45	40	974

Table 25: Details of characteristics of AFRP, CFRP and GFRP RC beam models with 14mm bar diameter under 40 kN impact load for comparison of mid-span deflection.

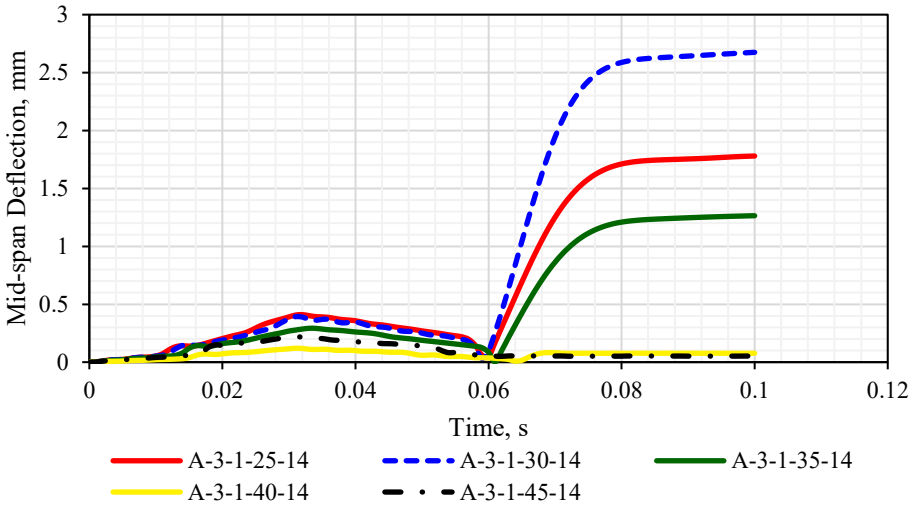

(A)

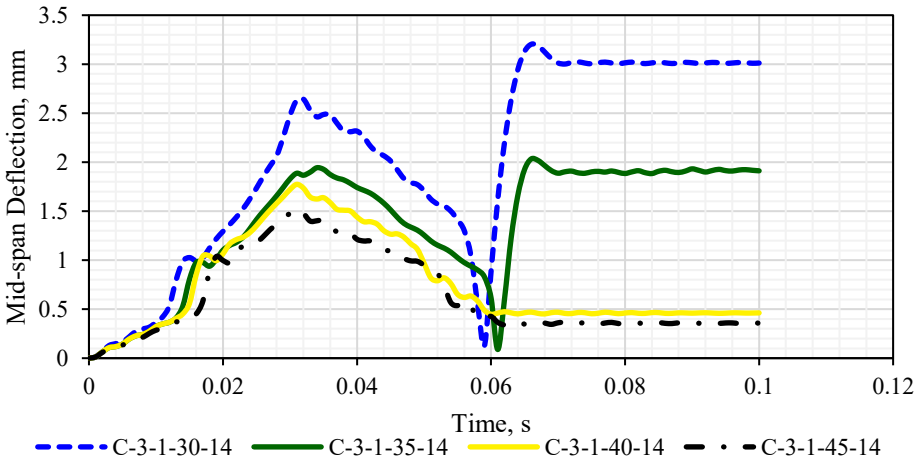

(B)

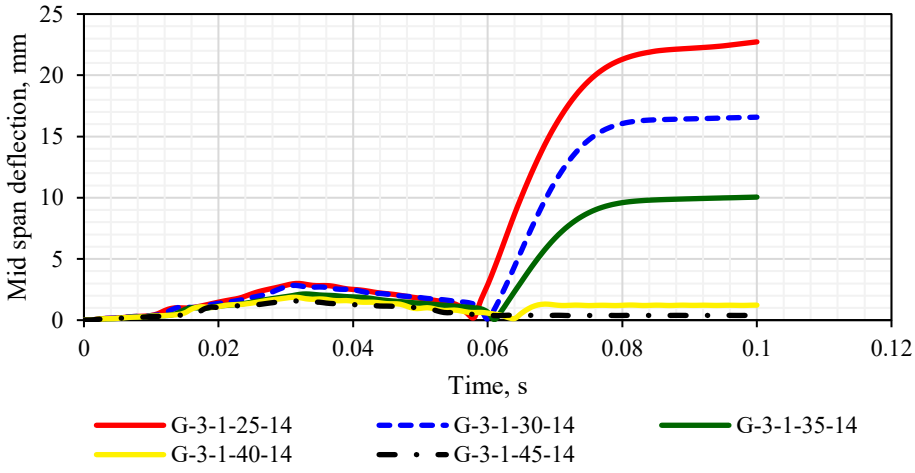

(C)

Figure 70:Mid-span Deflection-Time histories of (A) AFRP, (B) CFRP and (C) GFRP RC beams with 14 mm bar diameter under 40 kN impact load.

As Figure (70-A), all beams reached their maximum displacements after 60 ms, coinciding with the removal of the applied load. This phenomenon can be attributed to the persistence of waves generated within the beams from the initial impact load, which continue even after the load has been removed.

Model A-3-1-25-14, A-3-1-30-14, and A-3-1-35-14 exhibited maximum displacements of 1.779 mm, 2.674 mm, and 1.264 mm, respectively, at the 100 ms mark. However, only beam models A-3-1-40-14 and A-3-1-45-14 reached their maximum displacements of 0.261 mm and 1.556 mm at 31 ms when the maximum load was applied during forced vibration. Notably, both beam models A-3-1-40-14 and A-3-1-45-14 displayed higher maximum displacements compared to their respective residual displacements, measuring 0.167 mm and 0.058 mm, respectively. It is worth mentioning that the AFRP RC beam with a concrete compressive strength of 45 MPa exhibited a 16% reduction in maximum displacement compared to the AFRP RC beam with a concrete compressive strength of 40 MPa.

In a similar fashion, the displacement-time histories of CFRP RC beams, as shown in Figure (70-B), exhibited lower peak displacements in comparison to the AFRP RC beam models. Model C-3-1-30-14 and C-3-1-35-14 reached peak displacements of 0.455 mm and 0.289 mm at 66 ms. Conversely, beam models C-3-1-40-14 and C-3-1-45-14 achieved their maximum displacements of 0.252 mm and 0.216 mm at 31 ms. This indicates that the CFRP RC beam with a concrete compressive strength of 45 MPa experienced a 14% reduction in maximum displacement compared to the CFRP RC beam with a concrete compressive strength of 40 MPa.

Moving on to Figure (70-C), it showcases the maximum displacements for GFRP RC beams. Model G-3-1-25-14, G-3-1-30-14, and G-3-1-35-14 reached peak displacements of 3.231 mm, 2.356 mm, and 1.428 mm, respectively, at the 100 ms mark. Remarkably, both GFRP beams with concrete compressive strengths of 40 MPa

and 45 MPa attained their maximum displacements of 0.252 mm at 31 ms, resulting in a 15% reduction in peak displacement.

Detailed The extensive finite element modelling of FRP RC beams was conducted, and the outcomes of deflection-time histories were subject to comparison, leading to several noteworthy observations:

- The overall shape of the displacement-time curves for beams subjected to 320 kN and 80 kN impacts closely aligned with the findings of existing experimental studies [283], Additionally, the displacement histories of beams under a 40 kN impact load exhibited similarities to the experimental work conducted by Saleh, which involved high-mass, low-velocity impact loads, [2].
- The results unveiled discrepancies in the maximum displacement values among certain models, despite having identical conditions and applied loads as other models within the same set. Notably, some models with higher concrete compressive strength exhibited higher maximum displacements in comparison to identical beam models with lower concrete compressive strength. This phenomenon has also been observed in other experimental works and can be attributed to the increased brittleness of higher-strength concrete, [284] [285].
- An examination of the influence of the time step revealed that, for many models subjected to high-velocity impact loads (320 kN and 80 kN), the maximum displacement occurred during the free vibration phase. In contrast, for models with concrete compressive strengths of 40 MPa and 45 MPa under a 40 kN impact load with lower velocity, the maximum displacement was observed during the forced vibration time period.
- An overarching analysis of the results from 225 models of FRP RC beams subjected to a 320 kN impact load indicated that the use of CFRP improved the maximum displacement by 16% compared to AFRP RC beams. Furthermore, AFRP RC beams exhibited a 13% improvement in maximum displacement compared to FRP RC beams reinforced with glass fibres.

5.4 Impact and reaction forces response

The behaviour of FRP RC beams under impact load can be understood better, when impact force and reaction force are broken down. The impact forces and related reaction forces are shown in for a $100\ ms$ that includes forced vibration and free vibration for beams. In the following sections, results of AFRP, CFRP and GFRP beams under impact force of $320\ kN, 80\ kN$ and $40\ kN$ are explained and compared with each other. Overall, the relation between reaction forces and time were similar for all beams. Thus, only three graphs of impact force, reaction force and time history shown for comparison.

Beams under 320kN Impact load:

Figure (71) presents the time-histories of impact and reaction forces for AFRP, CFRP, and GFRP, with detailed beam characteristics outlined in Table (26). The impact behaviour of these beams comprises two distinct phases: the forced phase, occurring from 0 to 0.06 seconds, and the subsequent free vibration phase, spanning from 0.06 seconds to 0.1 seconds.

In the time history of the impact force, particularly for A-1-1-35-12 and C-1-1-3-12, a prominent peak is evident, followed by a gradual reduction, ultimately approaching zero within a matter of milliseconds. Notably, the peak of the impact force is observed during the forced phase, and this force progressively diminishes to zero during the free-vibration phase. Both CFRP and AFRP beams display a similar pattern, showcasing maximum reaction forces characterized by the occurrence of peak forces, followed by a decline to zero before the onset of the free-vibration phase.

In the case of G-1-1-35-12, the reaction force exhibits a distinct pattern with two peak-shaped triangular spikes, which are succeeded by a steady reduction leading to a zero value just prior to the initiation of the free vibration phase.

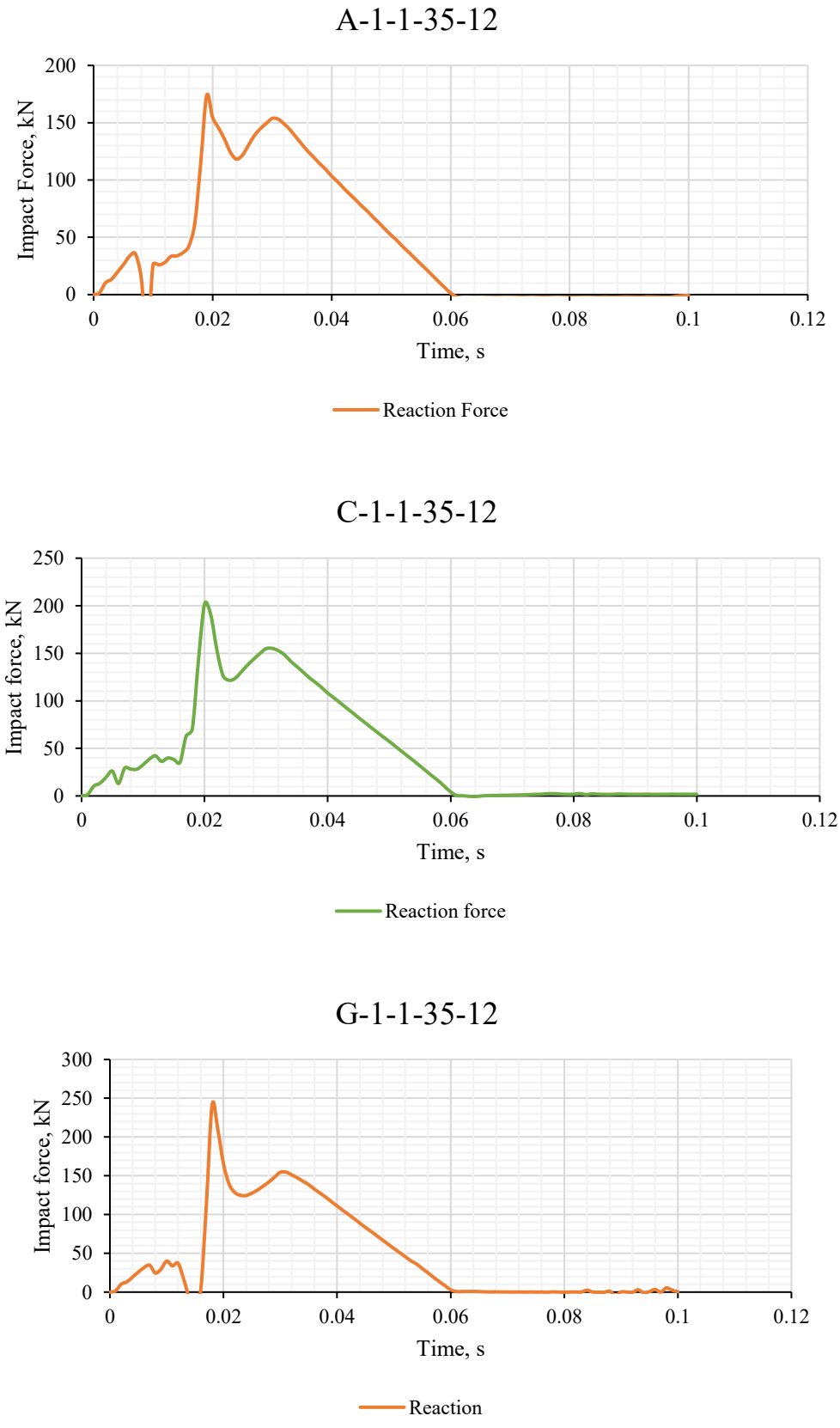

Figure 71: Time histories of reaction forces for AFRP, CFRP and GFRP RC beams with concrete compressive strength of 35 MPa and bar diameter of 12 mm under impact load of 320 kN.

Beam Name	Load, kN	Force, kN	Peak time, s	Reaction force, kN	Peak time, s
A-1-1-35-12	320	90.6945	0.018	173.661	0.019
C-1-1-35-12	320	90.6945	0.015	201.999	0.02
G-1-1-35-12	320	80.1648	0.046	241.428	0.018

Table 26: Maximum impact and reaction forces and peak times for beam models under 320 kN impact load.

Beams under 80 kN Impact load:

The resistance forces exhibited by FRP RC beams, encompassing both impact forces and reaction forces under an 80 kN impact load with a velocity of 17.145 m/s, are detailed in Appendix (C). This section focuses on presenting the impact forces and reaction forces for three types of FRP RC beams: AFRP, CFRP, and GFFRP, all of which possess a concrete compressive strength of 25 MPa and a bar diameter of 12 mm. These findings are visually represented in Figure 72.

For the three FRP RC beam models, namely A-2-1-25-12, C-2-1-25-12, and G-2-1-25-12, subjected to an 80 kN impact load, the impact load was applied from 0 to 30 ms and subsequently reduced to 0 kN from 30 ms to 60 ms. The figure also illustrates the free-vibration phase for these models, spanning from 60 ms to 100 ms.

The overall shape of the reaction forces is consistent across all AFRP, CFRP, and GFRP RC beams, characterized by a triangular-shaped peak reaction force featuring multiple triangular-shaped peaks that occur before the 100 ms mark. Both AFRP and CFRP RC beams maintain a constant force between the 60 ms and 100 ms time intervals. In contrast, GFRP RC beams display a reduction in force from the peak point to zero during the free vibration phase.

Comparing the performance of A-2-1-25-12, C-2-1-25-12, and G-2-1-25-12 reveals that both AFRP and CFRP beams closely align with each other in terms of maximum force between the FRP bar and concrete, as well as peak reaction force. AFRP RC

beam exhibits a slightly better performance, with a 9% advantage over CFRP RC beam. Conversely, model G-2-1-25-12 exhibits approximately 73% lower performance in terms of maximum force compared to AFRP and CFRP RC beams, as illustrated in Figure 72. Further details regarding peak forces, peak reaction forces, and peak times can be found in Table 27. This comparison underscores the disparity in load-bearing capabilities, with GFRP RC beams demonstrating a distinct behavior compared to CFRP and AFRP RC beams.

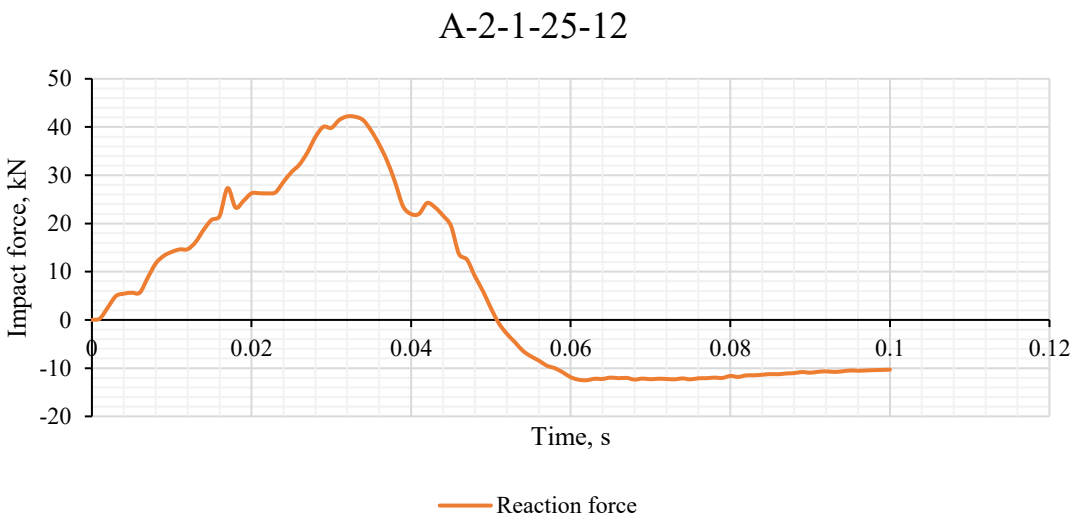

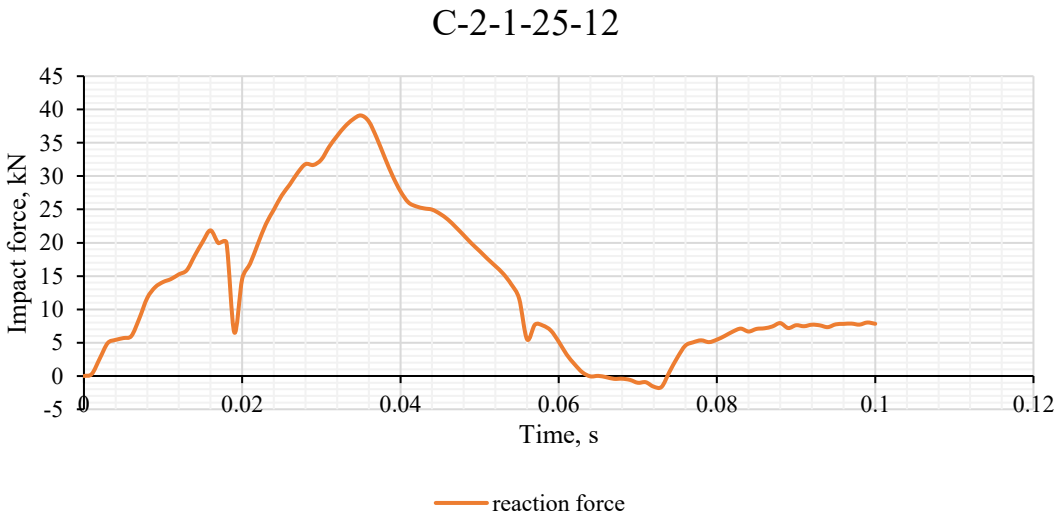

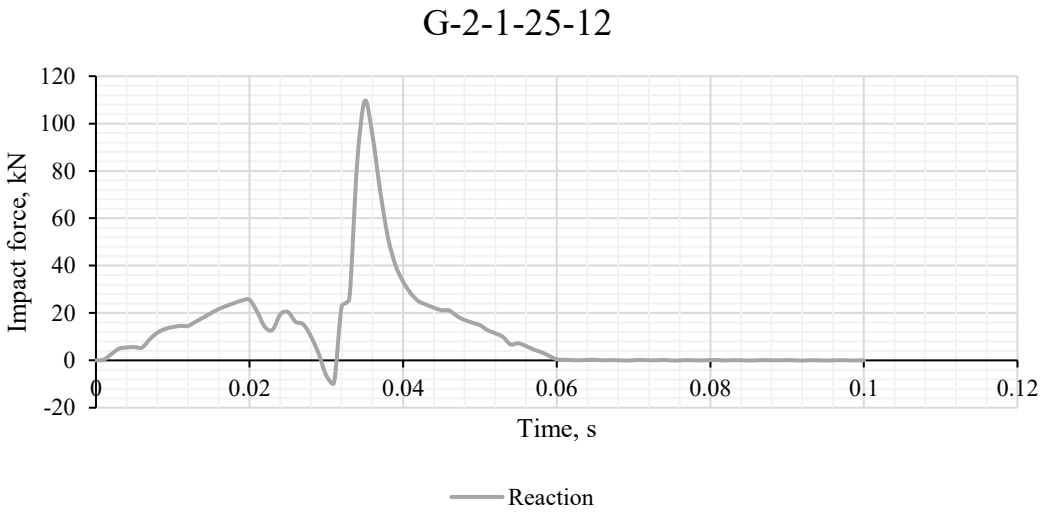

Figure 72: Time histories of the reaction forces for AFRP, CFRP and GFRP RC beams with concrete compressive strength of 25 MPa and bar diameter of 12 mm under impact load of 80 kN.

Beam Name	Load, kN	Force, kN	Peak time, s	Reaction force, kN	Peak time, s
A-2-1-25-12	80	79.4837	0.040001	42.2034	0.032
C-2-1-25-12	80	72.215	0.034001	39.1088	0.035
G-2-1-25-12	80	20.3215	0.032	109.509	0.035

Table 27: Maximum impact and reaction forces and peak times for beam models under 80 kN impact load.

Beams under 40 kN impact load:

The time histories of forces and reaction forces for AFRP, CFRP, and GFRP RC beams, all characterized by a concrete compression strength of 40 MPa and a bar diameter of 12 mm, are presented in Figure (73). These three beam models share identical load conditions, encompassing both the forced and free vibration phases, as well as the same boundary conditions.

Figure (73) depicts strikingly similar patterns in the time histories of forces and reaction forces for AFRP, CFRP, and GFRP RC beams. These patterns are characterized by triangular-shaped impact forces and reaction forces that gradually diminish to zero during the free vibration phase. This consistency in behaviour aligns with the observed patterns in models subjected to a 40 kN impact load with a velocity of

12.125 m/s. In this context, CFRP RC beams exhibit the most favourable performance, followed by AFRP and GFRP RC beams.

For a comprehensive understanding, Table (28) provides detailed information regarding maximum forces, peak reaction forces, and corresponding peak times for the beam models A-3-1-40-12, C-3-1-40-12, and G-3-1-40-12. These findings underscore the similarities in behaviour among these FRP RC beams and further emphasize the superior performance of CFRP RC beams, followed by AFRP and GFRP RC beams, under the specified conditions.

Beam Name	Load, kN	Force, kN	Peak time, s	Reaction force, kN	Peak time, s
A-3-1-40-12	40	3.05678	0.031001	20.368	0.031
C-3-1-40-12	40	4.5703	0.031	20.2986	0.031
G-3-1-40-12	40	2.1734	0.031	20.3424	0.031

Table 28: Maximum impact and reaction forces and peak times for beam models under 40 kN impact load.

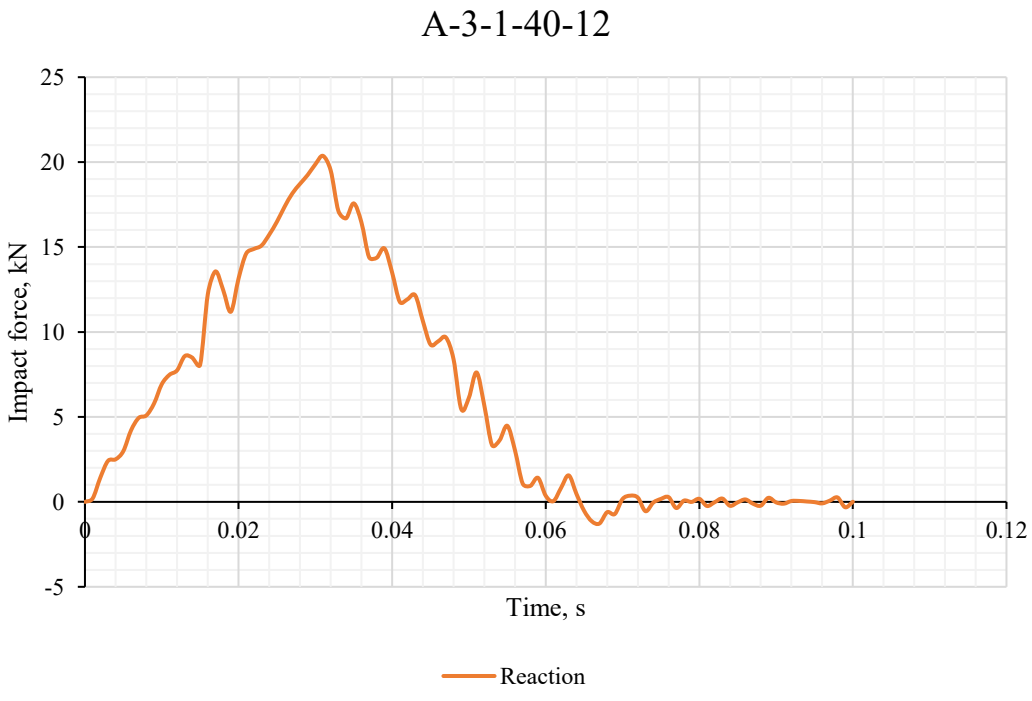

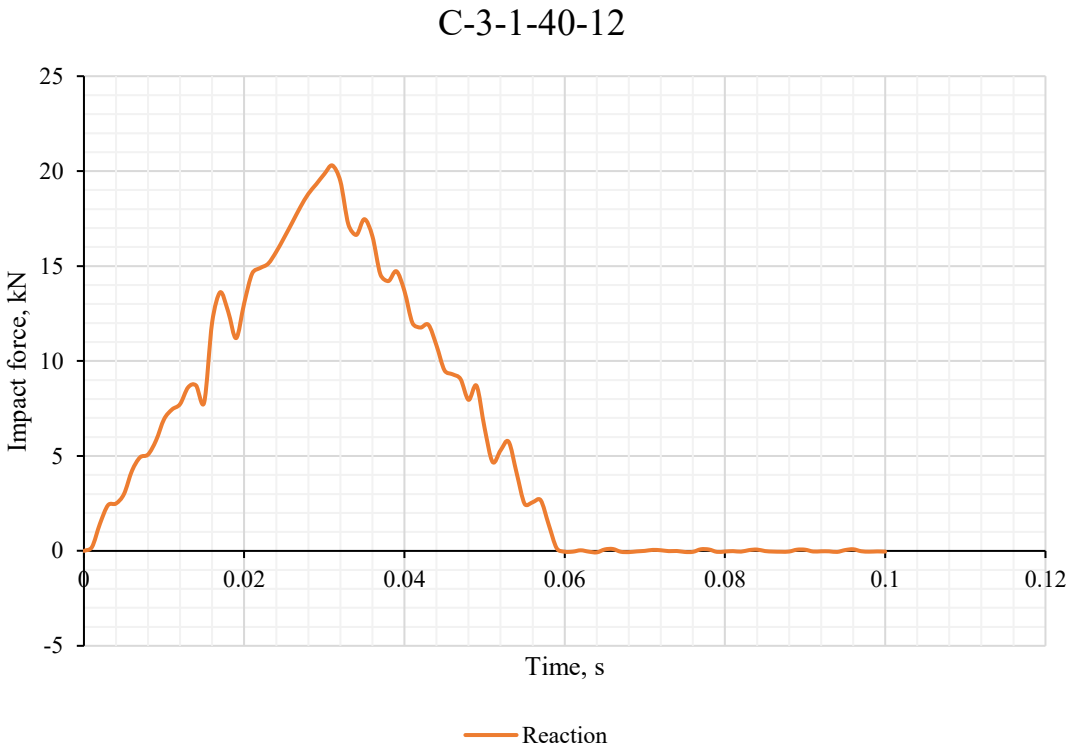

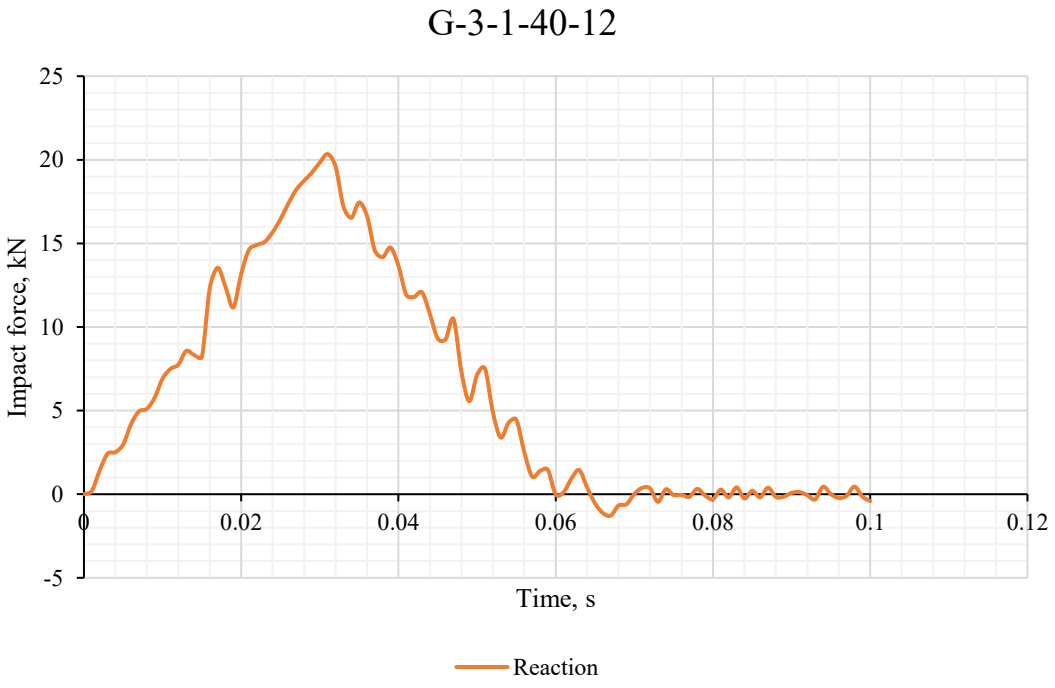

Figure 73: Time histories of the reaction forces for AFRP, CFRP and GFRP RC beams with concrete compressive strength of 40 MPa and bar diameter of 12 mm under impact load of 40 kN.

Figure (142), (143), and (144) in appendix (C) provide a comprehensive overview of the responses exhibited by AFRP, CFRP, and GFRP RC beams when subjected to three distinct loading conditions: 320 kN, 80 kN, and 40 kN impact loads, each with corresponding velocities of 24.245 m/s, 17.145 m/s, and 12.125 m/s, respectively. In these simulations, the impact loads are administered through high-magnitude, short-duration pulses during the force phase, spanning from 0 to 60 ms, and subsequently continue as free vibrations until the 100 ms mark.

At the initiation of the impact load, the force is transmitted to the beam supports, thereby activating the reaction forces starting at t=0 s. As the impact force escalates to its maximum magnitude, a corresponding increase in reaction forces is observed in the supports. This phenomenon signifies the resistance offered by the beams through flexural resistance.

5.5 Dynamic strain-Time histories response

The dynamic strain-time profiles for AFRP, CFRP, and GFRP RC beams under various loading rates are presented in Figures (145), (146), and (147) within Appendix (C). This section is dedicated to the examination and comparison of dynamic strain responses observed in AFRP, CFRP, and GFRP RC beams. These beams feature a concrete compression strength of 30 MPa and bar diameters ranging from 8 to 16 mm. The comparisons are conducted across three distinct loading scenarios, each characterized by different velocities.

Dynamic strain response under 320 kN impact load:

The dynamic strain-time profiles for a total of 15 models of AFRP, CFRP, and GFRP RC beams, all featuring a consistent concrete compressive strength of 30 MPa and bar diameters ranging from 8 to 16 mm, under an impact load of 320 kN with a velocity of 24.24 m/s, are illustrated in Figure (74) and detailed in Table (29).

In general, the behaviour exhibited by FRP RC beams indicates an initial linear increase in strain, as the models remain within the elastic range, followed by reaching a peak point before returning to their initial positions. Variations in the strain response observed in certain models may be attributed to the development of cracks in the beams or the initiation of rupture in the FRP bars. It's worth noting that some models experienced failure under the impact load before the completion of the specified time duration.

For instance, in the case of the AFRP RC beam model A-1-1-30-8, the strain rate exhibited a linear increase until the beam failed at 20 ms. The average maximum dynamic strain for this beam was 0.024, occurring at a peak time of 17 ms. This failure can be attributed to the brittleness of the composite material and the rupture of the AFRP bar under the high impact loading conditions.

Comparatively, the average maximum dynamic strains for AFRP, CFRP, and GFRP RC beams, all possessing a concrete compressive strength of 30 MPa, were found to be 1.23%, 0.64%, and 24.4%, respectively. Notably, GFRP RC beam models displayed a more ductile behaviour in contrast to AFRP and CFRP RC beams. Specifically, the GFRP RC beam model G-1-1-30-16 exhibited a return to its original form, whereas the other beams either experienced failure or a decrease in strain, albeit not a complete return to their original configurations.

Beam	Max strain	Peak time, s	Duration, s	Beam	Max strain	Peak time, s	Duration, s	Beam	Max strain	Peak time, s	Duration, s
A-1-1-30-8	0.02352	0.017	0.020	C-1-1-30-8	0.0131	0.045	0.1	G-1-1-30-8	0.6118	0.074	0.1
A-1-1-30-10	0.01799	0.016	0.043	C-1-1-30-10	0.0080	0.040	0.1	G-1-1-30-10	0.5873	0.1	0.1
A-1-1-30-12	0.01185	0.020	0.072	C-1-1-30-12	0.0059	0.016	0.1	G-1-1-30-12	0.0107	0.009	0.009001
A-1-1-30-14	0.00167	0.008	0.008	C-1-1-30-14	0.0044	0.018	0.1	G-1-1-30-14	0.0017	0.007	0.007001
A-1-1-30-16	0.00662	0.017	0.048	C-1-1-30-16	0.0008	0.007	0.007001	G-1-1-30-16	0.0102	0.018	0.066

Table 29: Maximum strain for AFRP, CFRP and GFRP RC beam models under 320 kN impact load.

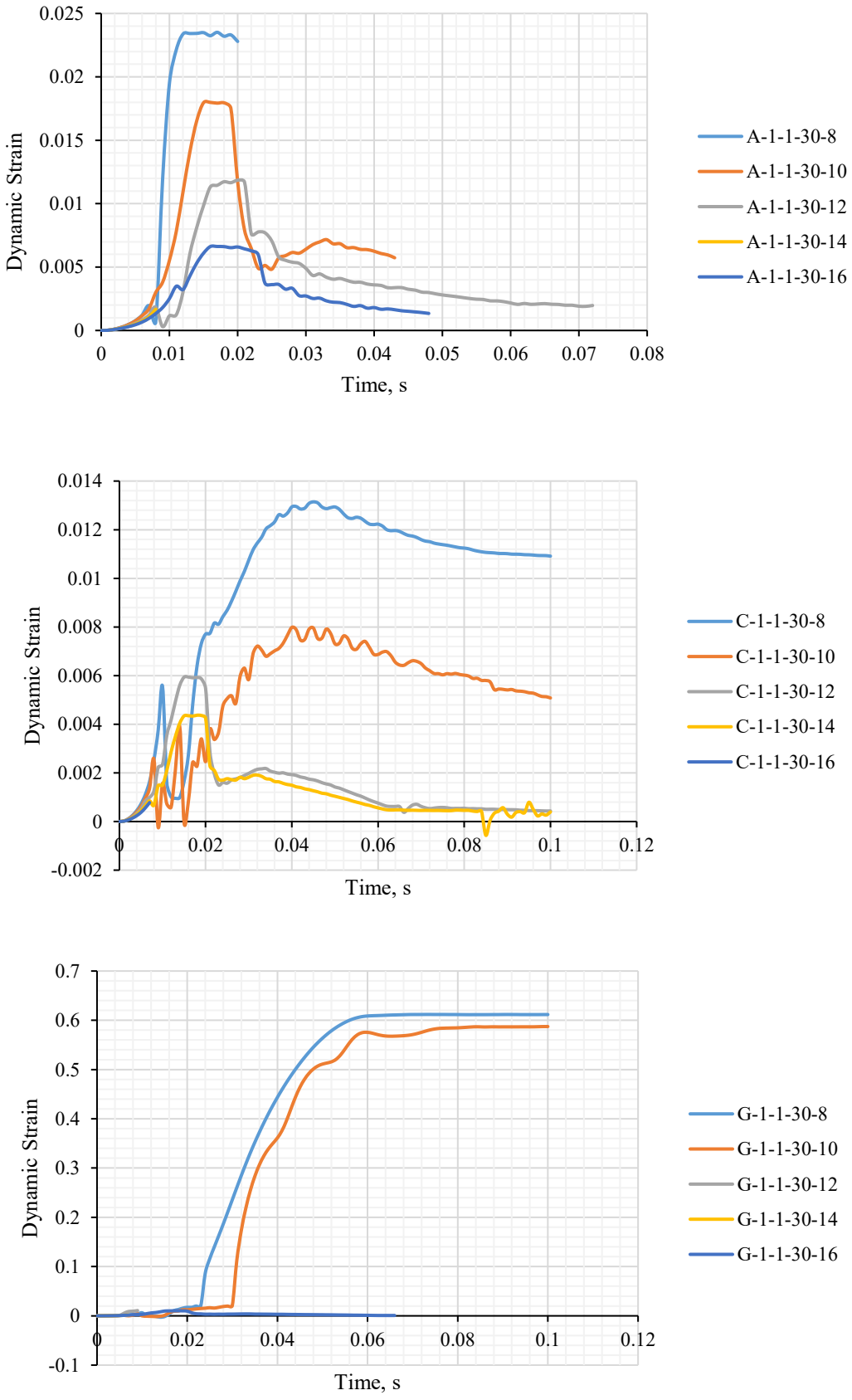

Figure 74: Dynamic strain time histories for AFRP, CFRP and GFRP RC beam models with concrete compressive strength of 30 MPa under 320 kN impact load.

Dynamic strain response under 80 kN impact load:

A comparable pattern of dynamic strain responses, as presented in Figure (75) for the models detailed in Table (30), was observed under an 80 kN impact load with a velocity of 17.14 m/s. The general trend indicated an initial linear rise in strain, culminating in the attainment of maximum strain at 32 ms, coinciding with the point at which the load reached its peak. For the majority of beam models, the strain decreased as the models transitioned into the free-vibration phase. Notably, certain models, including A-2-1-30-8, G-2-1-30-10, G-2-1-30-12, and G-2-1-30-14, experienced failure prior to the onset of the forced vibration phase at 60 ms.

For all three categories of AFRP, CFRP, and GFRP RC beam models featuring an 8 mm bar diameter, the strain rate exhibited linearity up to the point of maximum strain, followed by a slight decline leading up to the failure of the FRP RC beams. The average maximum strain values were determined to be 1.24% for AFRP RC beams, 0.41% for CFRP RC beams, and GFRP RC beams exhibited a maximum dynamic strain of 2.44%. These findings underscore the confirmation that CFRP RC beams demonstrate greater ductility in comparison to the other two categories of FRP RC beams.

Beam	Max strain	Peak time, s	Duration, s	Beam	Max strain	Peak time, s	Duration, s	Beam	Max strain	Peak time, s	Duration, s
A-2-1-30-8	0.02373	0.021	0.028	C-2-1-30-8	0.0061	0.038	0.1	G-2-1-30-8	0.0975	0.086	0.1
A-2-1-30-10	0.01467	0.034	0.081	C-2-1-30-10	0.0051	0.032	0.1	G-2-1-30-10	0.0029	0.028	0.031001
A-2-1-30-12	0.00982	0.035	0.1	C-2-1-30-12	0.0038	0.033	0.1	G-2-1-30-12	0.0032	0.023	0.0230005
A-2-1-30-14	0.00711	0.037	0.1	C-2-1-30-14	0.0033	0.035	0.1	G-2-1-30-14	0.0097	0.037	0.0470005
A-2-1-30-16	0.00668	0.036	0.1	C-2-1-30-16	0.0025	0.039	0.1	G-2-1-30-16	0.0086	0.037	0.1

Table 30: Maximum strain for AFRP, CFRP and GFRP RC beam models under 80 kN impact load.

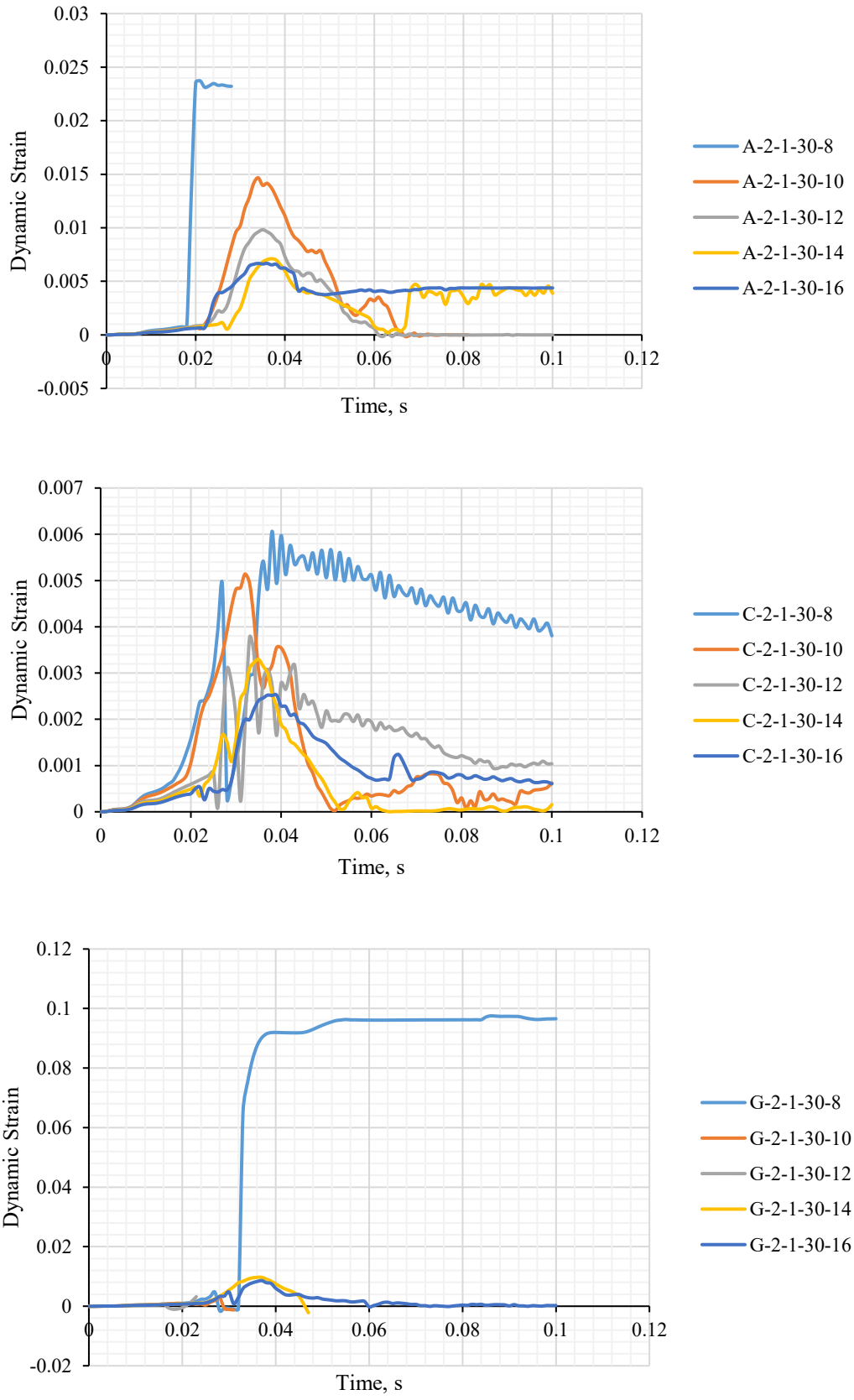

Figure 75: Dynamic strain time histories for AFRP, CFRP and GFRP RC beam models with concrete compressive strength of 30 MPa under 80 kN impact load.

Dynamic strain response under 40 kN impact load:

The dynamic strain time histories for AFRP, CFRP, and GFRP RC beam models characterized by a concrete compressive strength of 30 MPa under an impact load of 40 kN with a velocity of 12.12 m/s were extracted from ABAQUS software. In general, the dynamic strain observed in all the mentioned models commenced from zero and began to rise as the high strain rate and impact load increased, with the models remaining in the elastic phase. After reaching their peak load at 30 ms, the rate of dynamic strain gradually declined, exhibiting some fluctuations until the beams returned to their original positions.

Notably, dynamic strain in AFRP RC beam models featuring bar diameters of 10 and 12 mm, as well as GFRP RC beam models with a 12 mm bar diameter, exhibited an increase in dynamic strain during the free-vibration phase, which spanned from 60 ms to 100 ms. This phenomenon may be attributed to the heightened brittleness of the composite material as bar diameters increased, along with the occurrence of failures induced by the application of high-strain impact loads.

Beam	Max strain	Peak time, s	Duration, s	Beam	Max strain	Peak time, s	Duration, s	Beam	Max strain	Peak time, s	Duration, s
A-3-1-30-8	0.00071	0.032	0.1	C-3-1-30-8	0.00064	0.032	0.1	G-3-1-30-8	0.00069	0.032	0.1
A-3-1-30-10	0.00157	0.1	0.1	C-3-1-30-10	0.00055	0.031	0.1	G-3-1-30-10	0.00071	0.032	0.1
A-3-1-30-12	0.00183	0.097	0.1	C-3-1-30-12	0.00045	0.032	0.1	G-3-1-30-12	0.00369	0.1	0.1
A-3-1-30-14	0.00053	0.031	0.1	C-3-1-30-14	0.00037	0.032	0.1	G-3-1-30-14	0.00062	0.031	0.1
A-3-1-30-16	0.00123	0.056	0.1	C-3-1-30-16	0.00031	0.032	0.1	G-3-1-30-16	0.00058	0.032	0.1

Table 31: Maximum strain for AFRP, CFRP and GFRP RC beam models under 40 kN impact load.

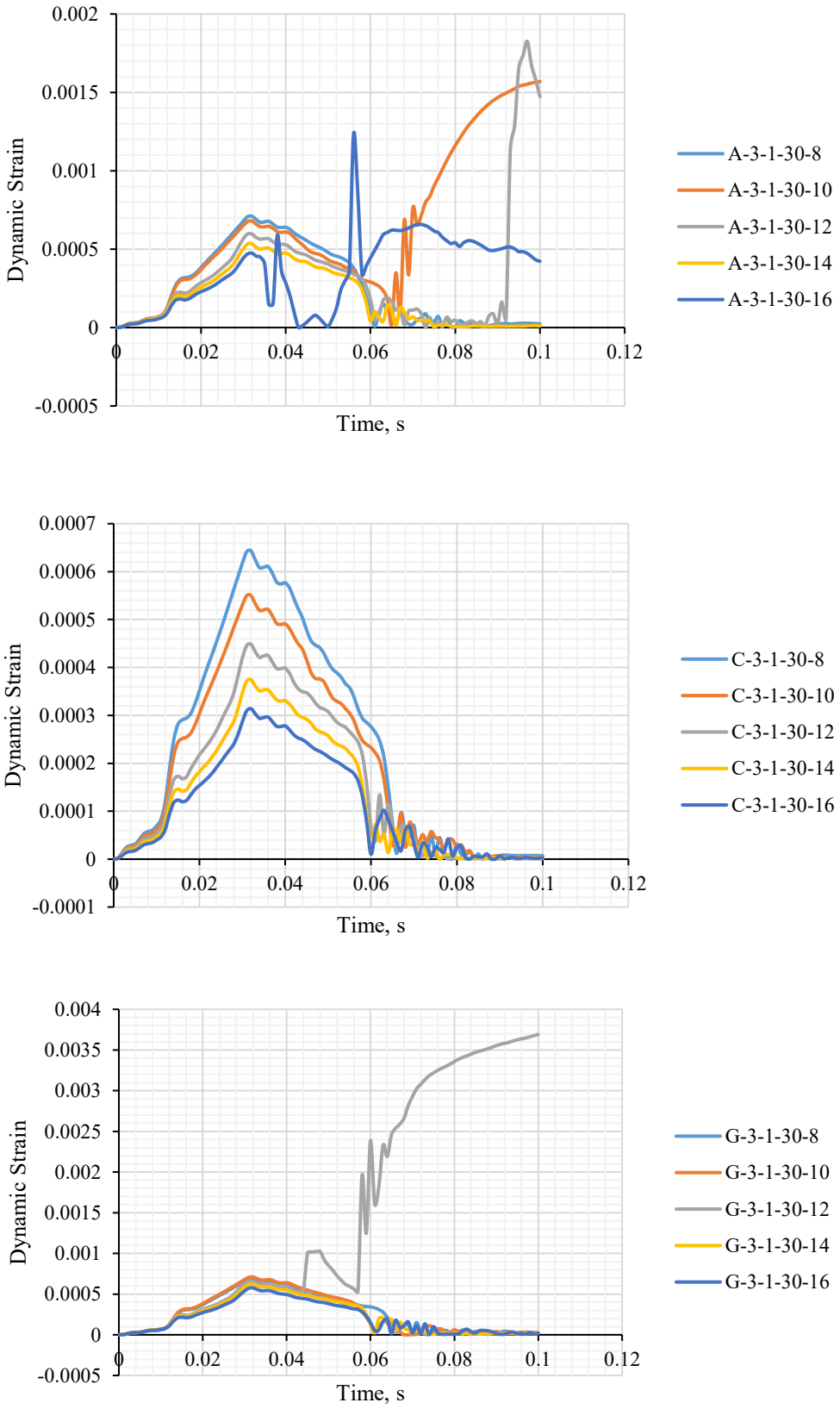

Figure 76: Dynamic strain time histories for AFRP, CFRP and GFRP RC beam models with concrete compressive strength of 30 MPa under 40 kN impact load.

Figure (74, 75, 76) displays the dynamic strain time histories for AFRP, CFRP, and GFRP RC beam models characterized by a concrete compressive strength of 30 MPa, subjected to various impact loading velocities. Tables (29, 30, 31) provide the maximum dynamic strain values and their corresponding peak times for these beam models. Based on the results mentioned, the following conclusions can be drawn:

- The ultimate dynamic strain increased with an escalation in both the impact load and velocity.
- Beams with smaller FRP bar diameters exhibited a more substantial increase in dynamic strain.
- When comparing models subjected to higher loading rates and velocities within shorter durations, sharper dynamic strain time history curves were observed compared to models under lower load velocities.
- A comparison between AFRP, CFRP, and GFRP RC beams indicated lower ductility in RC beams reinforced with glass fibres. Specifically, there was a 94.95% increase in the average maximum dynamic strain in GFRP RC beams compared to AFRP RC beams and a 97.37% increase compared to CFRP RC beams under a 320 kN impact load. Moreover, there was an increase in the average maximum strain rate of 49.16% and 82.94% for GFRP RC beams compared to AFRP and CFRP RC beams, respectively, under an 80 kN impact load. A similar pattern was observed in the average maximum dynamic strain for GFRP RC beams under a 40 kN impact load, with an increase of 7.14% and 62.69% compared to the average maximum dynamic strain of AFRP and CFRP RC beams, respectively.

5.6 Slip-Time histories response

Results of slip time histories for all beam models under three different loading with high velocity contained from ABAQUS that are presented in Figure (148), (149), and (150) in appendix (C). This section presents the result of slip time histories of AFRP, CFRP and GFRP RC beams with bar diameter of $10\ mm$ and concrete compressive strength of $25, 30, 35, 40$ and $45\ MPa$ under three different impact loads of $320\ kN, 80\ kN$ and $40\ kN$ with high velocity.

Slip time histories under 320 kN impact load:

Figure (77-A) illustrates the slip response of AFRP RC beam models featuring a 10 mm bar diameter when subjected to an applied impact load of 320 kN, covering the time range from 0 s to 0.06 s, followed by the free vibration zone extending from 0.06 s to 0.1 s. As depicted in Figure (77-A), all AFRP beam models initially exhibit a linear elastic response from 0 s to 0.017 s, characterized by high stiffness in the interfacial bond between the FRP bar and concrete, resulting in minimal slip. Between 0.017 s and 0.021 s, AFRP beams transition into a softening mode, likely due to the emergence of microcracks in the beams, which reduce bond stiffness and lead to increased shear slips. From 0.021 s to 0.1 s, the beam models experience complete debonding of the FRP bars, accompanied by a significant increase in slips. AFRP beams with a concrete compressive strength of 30 MPa ultimately undergo complete failure during the forced vibration phase.

Figure (77-B) presents the slip response of CFRP RC beam models, generally exhibiting smaller slips compared to AFRP RC beams. However, CFRP RC beams with a concrete compressive strength of 30 MPa initially demonstrate stiffness and minimal slip at the interfacial bond between the FRP and concrete, followed by an escalation towards total debonding and failure before the onset of the free vibration phase. Similarly, CFRP RC beams with a concrete compressive strength of 45 MPa display linear elastic responses initially and subsequently develop concrete cracks, leading to a substantial increase in slips within the CFRP bond.

Figure (77-C) illustrates the slip response of GFRP RC beam models, all of which initially exhibit linear elastic behaviour at the outset, characterized by minimal slip and high stiffness in the interfacial bond. Starting from 0.01 s, the beams undergo a decline in stiffness due to the development of cracks in the beam and an increase in slip within the interfacial bond between the FRP bar and concrete. Between 0.02 s and 0.1 s, the bond between the FRP and concrete continues to deteriorate, accompanied by increasing slips, ultimately culminating in complete debonding of the FRP bar.

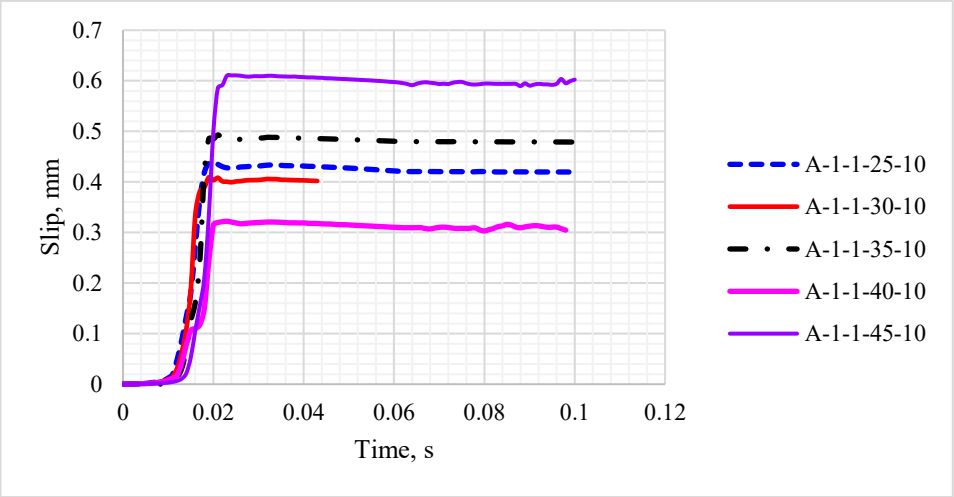

(A)

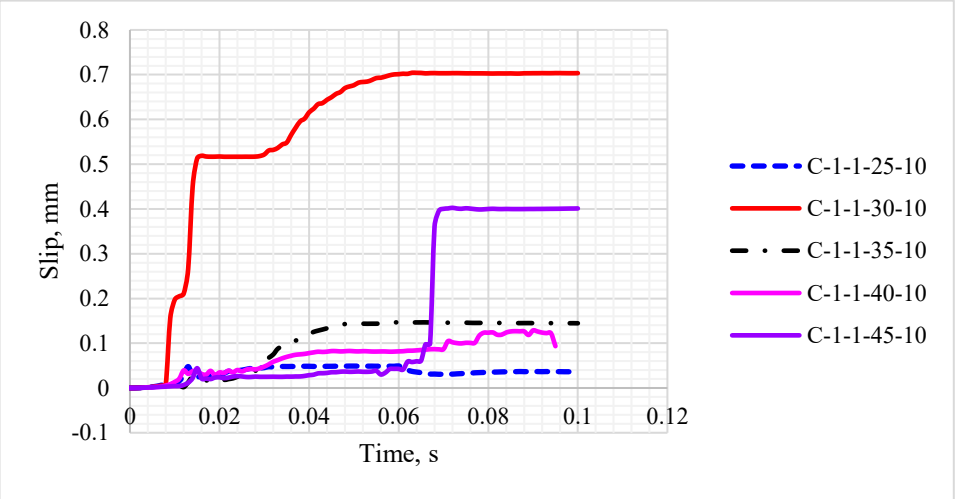

(B)

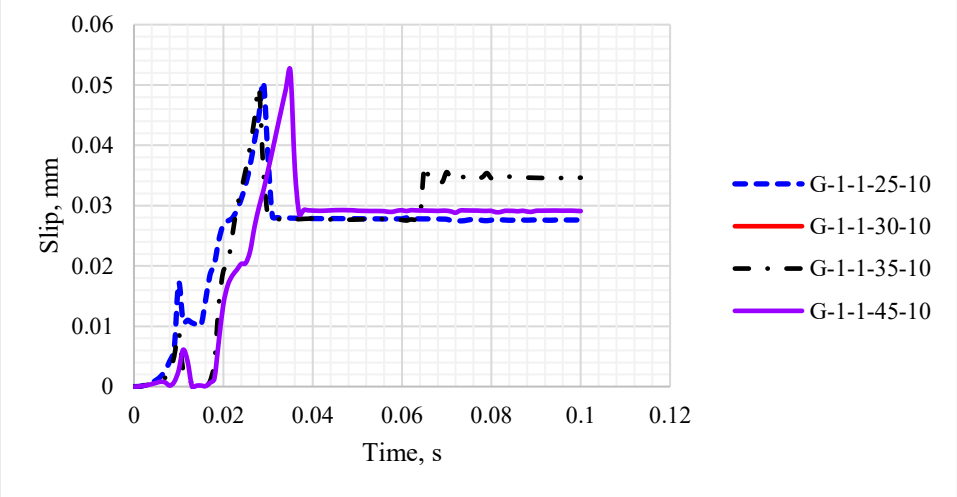

(C)

Figure 77: Slip-time histories of AFRP, CFRP and GFRP RC beams with bar diameter of 10 mm under 320 kN impact load.

Slip time histories under 80 kN impact load:

Figure (78-A) displays the slip-time history for AFRP RC beam models subjected to an 80 kN impact load. It is evident that all beams initially exhibited minor slips, indicating a high level of stiffness in the interfacial bond between the FRP and concrete. Gradually, as cracks developed and slips increased, the stiffness decreased, leading the beams toward debonding. As observed in other models, those with higher concrete compressive strength exhibited smaller slips.

In Figure (78-B), a similar slip pattern is observed for CFRP RC beams. However, the CFRP RC beam with a concrete compressive strength of 45 MPa initially underwent a linear elastic phase, characterized by high stiffness and minimal slip in the bond between the FRP bar and concrete. Subsequently, slip increased due to crack formation and a decrease in bond stiffness. After 0.045 s, the slip began to decrease and approached a value close to 0 mm.

Figure (78-C) depicts the slip response of GFRP RC beams under an 80 kN impact load. Overall, GFRP RC beams exhibited smaller slips compared to AFRP and CFRP RC beams under the same loading conditions, with only beams having concrete compressive strengths of 35 and 40 MPa showing significant debonding.

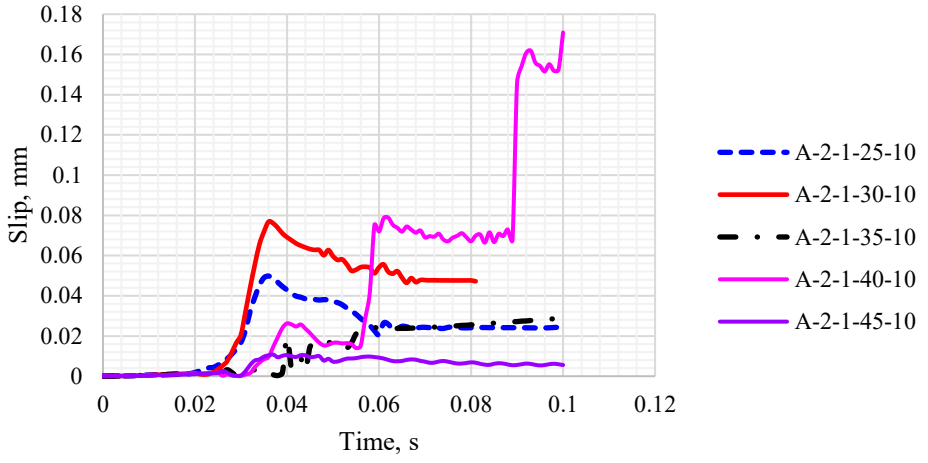

(A)

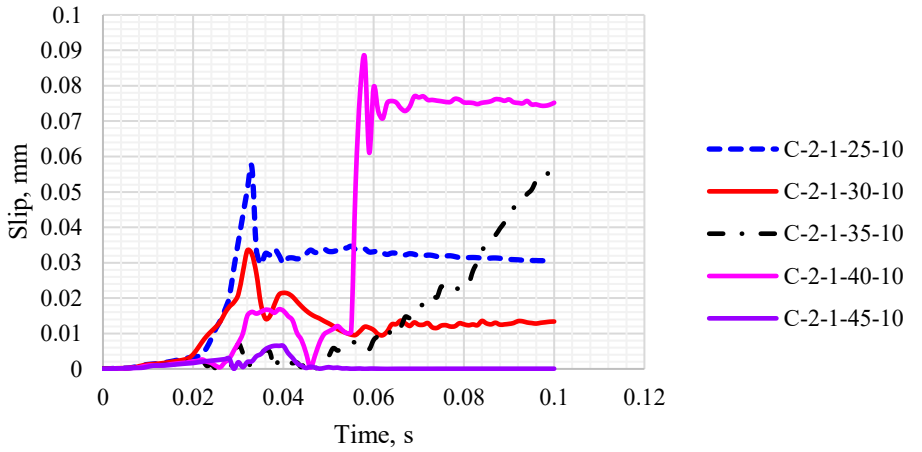

(B)

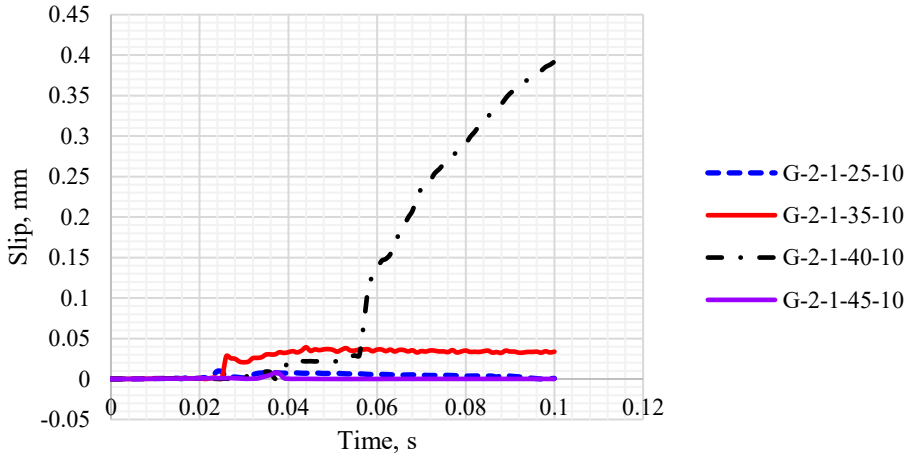

(C)

Figure 78: Slip-time histories of AFRP, CFRP and GFRP RC beams with bar diameter of 10 mm under 80 kN impact load.

Slip time histories under 40 kN impact load:

Figure (79) illustrates the slip-time history responses of AFRP, CFRP, and GFRP RC beams with a 10 mm bar diameter under a 40 kN impact load. The overall shapes of the graphs for the three FRP beam models were remarkably similar. The responses indicated that the beams initially exhibited an elastic mode characterized by high stiffness in the bond between the FRP bars and the concrete beam, resulting in minor slips from 0 s to 0.01 s.

Subsequently, the beam models entered the second stage, spanning from 0.01 s to 0.07 s, where softening in the bonding of the beams became apparent. During this stage, the beams experienced reduced bonding stiffness due to the development of microcracks and an increase in shear slips. Notably, in all FRP models, beam models with a concrete compressive strength of 45 MPa displayed more significant deterioration in the bonding between the FRP bars and the concrete interface. Conversely, other models exhibited minor fluctuations near 0 mm in slip.

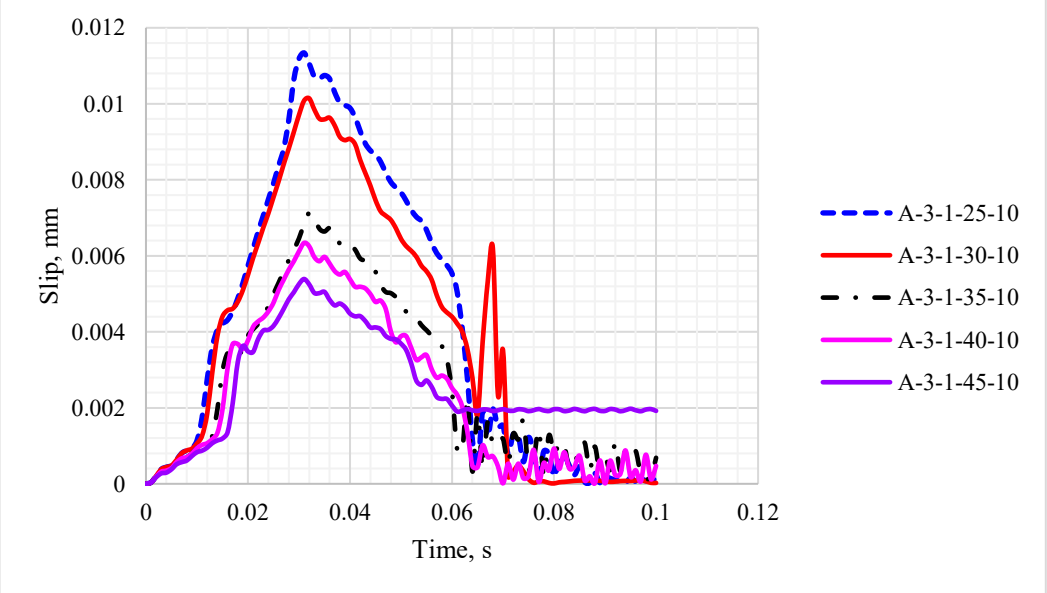

(A)

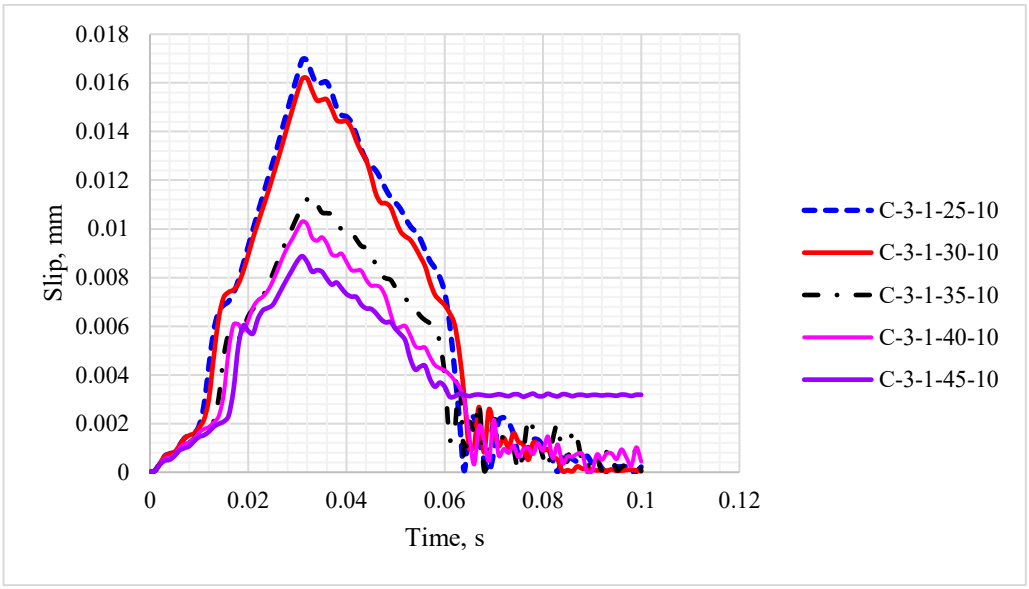

(B)

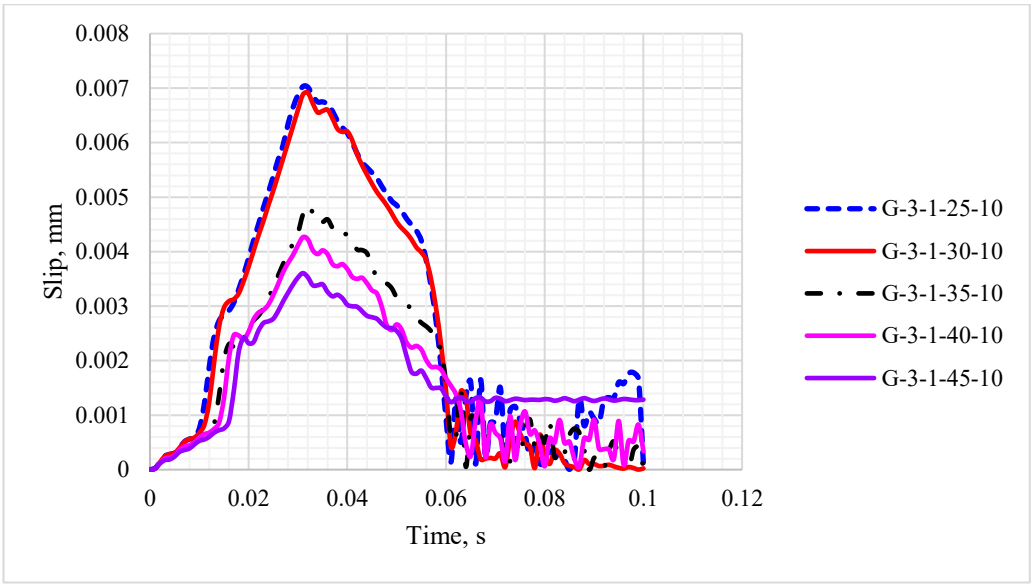

(C)

Figure 79: Slip-time histories of AFRP, CFRP and GFRP RC beams with bar diameter of 10 mm under 40 kN impact load.

Figure (148), (149), and (150) in appendix (C) depict the slip-time history responses of AFRP, CFRP, and GFRP RC beam models under impact loads of 320 kN, 80 kN, and 40 kN, respectively. Based on these results, several conclusions can be drawn:

- The overall shape of the slip response was quite similar for AFRP, CFRP, and GFRP beams under different loading conditions.
- All beam models subjected to 320 kN and 80 kN impact loads exhibited three stages of slip response. The first stage was characterized by linear elasticity, during which the beams experienced minor slips with high stiffness in the bond interface between the FRP bars and the concrete surroundings. The second stage involved softening, with increasing slip attributed to the development of minor cracks in the beams and a reduction in the stiffness of the interfacial bond in the FRP RC beams. The final stage, debonding, entailed the complete deterioration of the bond between the FRP bar and the concrete, resulting from the development of more cracks in the concrete and an increase in slips.
- Models with higher concrete compressive strength exhibited overall smaller slips over time compared to models with lower concrete compressive strength.
- Among FRP RC beams with a bar diameter of 10 mm subjected to a 320 kN impact load, GFRP RC beams demonstrated a 19% reduction in slip compared to CFRP RC beams and a 10.2% reduction in slip compared to AFRP RC beams.
- Under an 80 kN impact load, GFRP RC beams with a bar diameter of 10 mm exhibited a 48.1% reduction in slip compared to CFRP RC beams and a 26.3% decrease in slip compared to AFRP RC beams.
- For FRP RC beams with a bar diameter of 10 mm subjected to a 40 kN impact load, AFRP RC beams displayed a 72.46% reduction in slip compared to GFRP RC beams and a 54% decrease in slip compared to CFRP RC beams.

5.7 FE Parametric study

Since there is a scarcity of research focusing on the bond characteristics of FRP-reinforced concrete beams subjected to high-impact loads, the meticulously calibrated finite element beam models offer a unique opportunity to delve deeply into the dynamics of the interfacial bond between FRP bars and the encompassing concrete beams. Furthermore, it provides a platform for conducting an extensive parametric investigation into the impact of various factors that are anticipated to influence the beams' load-carrying capacity.

The subsequent sections of this work will present the results of a comprehensive parametric analysis, exploring the impact of variables such as bar diameter, concrete compressive strength, FRP material type, and impact loading conditions, including velocity. The objective is to gain a thorough understanding of how these factors collectively influence the performance and behaviour of FRP-reinforced concrete beams.

5.7.1 Effect of bar diameter, d_b

A parametric analysis was conducted to investigate the impact of bar diameter variations on 225 FRP RC beam models subjected to impact loading using ABAQUS software. The results yielded valuable insights into the influence of bar diameters on the bond behaviour of AFRP, CFRP, and CGFRP RC beams under various impact loading conditions, including their associated bond strength and failure modes. The calibrated beam test model specifically displayed two predominant failure modes: pull-out and debonding.

Figure (80) was generated to illustrate the relationship between failure modes and their correlation with bar diameters, embedment length, and concrete cover. As detailed in earlier chapters, five different bar diameters (8, 10, 12, 14, and 16 mm) were employed to model AFRP, CFRP, and GFRP RC beams. It is evident that pull-out failure is the significantly dominant mode, accounting for an average of 77% of all

failure occurrences, while debonding failure comprises an average of 23%. The data indicates that with an increase in bar diameter, pull-out failures decrease, while debonding failures rise. This phenomenon may be attributed to the stronger bond between smaller bar diameters and the surrounding concrete beams. Figure (80-B) presents data on concrete cover in relation to failure modes, where the number of failed FRP RC beams is plotted against the normalized concrete cover, $^{c}/_{d_b}$. It is observed that when the $^{c}/_{d_b}$ ratio exceeds 2, approximately 80 beam models experienced pull-out failure. This aligns with previous research findings that suggest mainly pull-out failures occur in beam tests when the concrete cover is twice the bar diameter, [286].

Similarly, embedment length, l_d, is another influential parameter affecting the bond behaviour of FRP RC beams. Figure (80-C) illustrates the occurrence of pull-out and debonding failures relative to the embedment length-to-bar diameter ratio,l_d/d_b. Pull-out failure prevails as the dominant mode when the l_d/d_b ratio exceeds 5. Among the 180 FRP RC beam models with l_d/d_b ratios greater than 5, 105 of these models experienced pull-out failure, constituting 58.33% of the total failures. In contrast, only 30% of FRP RC beam models with an embedment length-to-bar diameter ratio greater than 5 failed due to debonding.

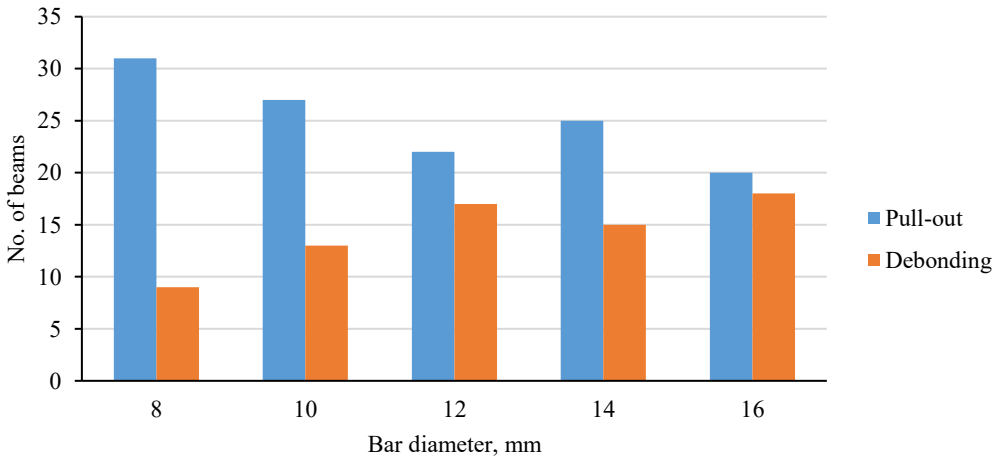

(a)

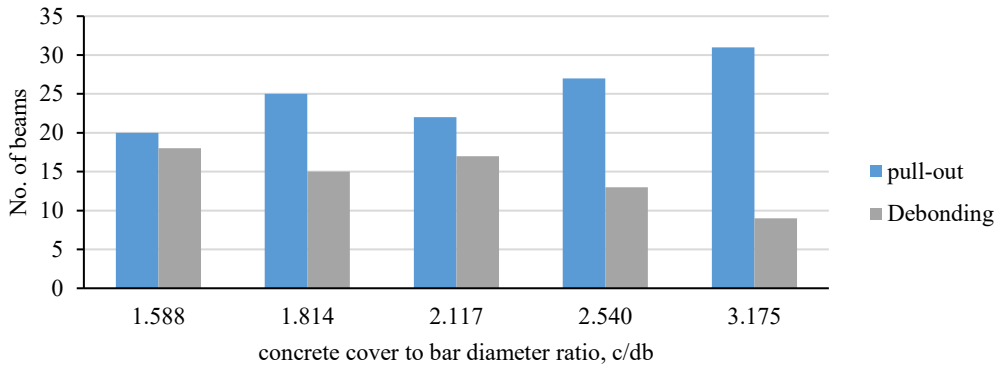

(b)

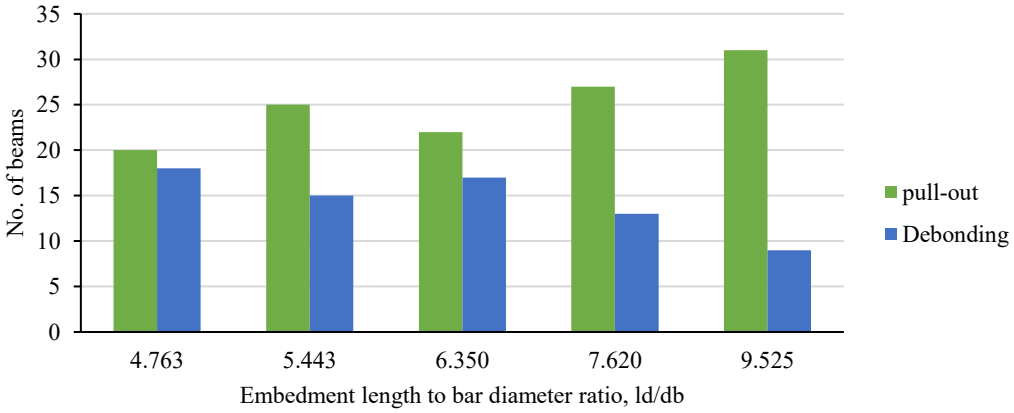

(c)

Figure 80: Failure modes associated with (a) bar diameters, (b) concrete cover, (c) embedment length.

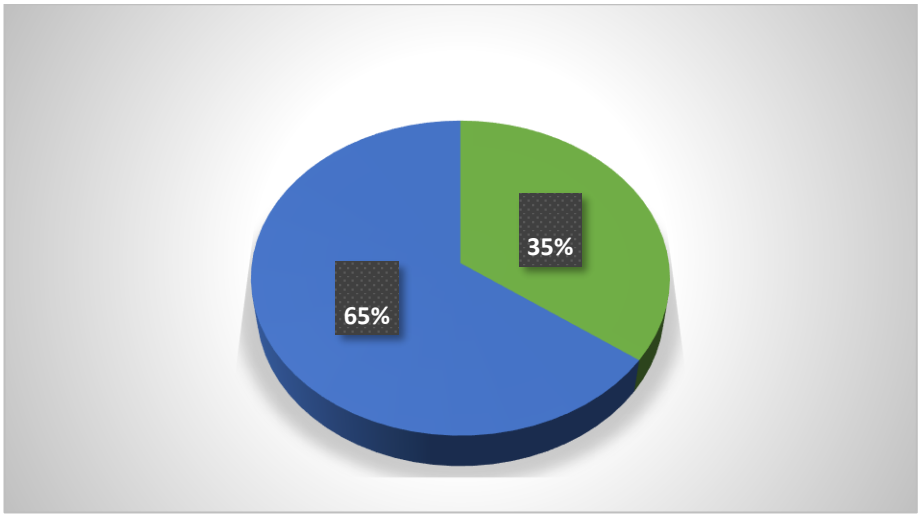

Figure 81: Two failure modes associated with varying bar diameters for 198 models that shown failure, 65% pull-out failure and 35% debonding failure.

Figure (82) presents the relationship between the maximum average bond strength,τ_{max} and bar diameter, d_b. It becomes evident that as the bar diameter increases, the bond strength decreases, resulting in a higher likelihood of failure. This phenomenon has been reported in previous studies and could be attributed to the increased contact area between the bar interface and concrete, thereby increasing the probability of weaker bonding between the FRP bar and concrete.

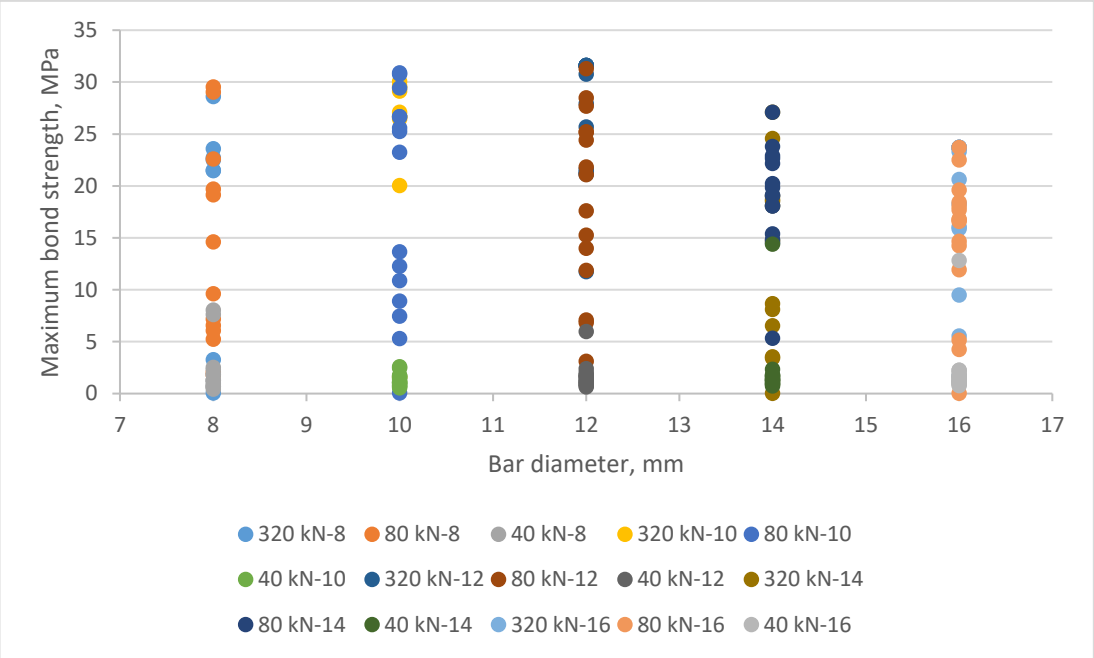

Figure 82: Maximum bond strength, τ_{max} versus bar diameter, d_b.

Figure (83) illustrates the correlation between the maximum bond strength and bar diameter for sets of models with identical concrete compressive strength subjected to the same impact loading conditions. It reveals that beam models with various bar diameters but similar concrete compressive strength experienced a decrease in bond strength as the bar diameters increased. Furthermore, RC beams reinforced with aramid and carbon fibre polymer bars exhibited superior bond strength performance compared to those reinforced with GFRP bars.

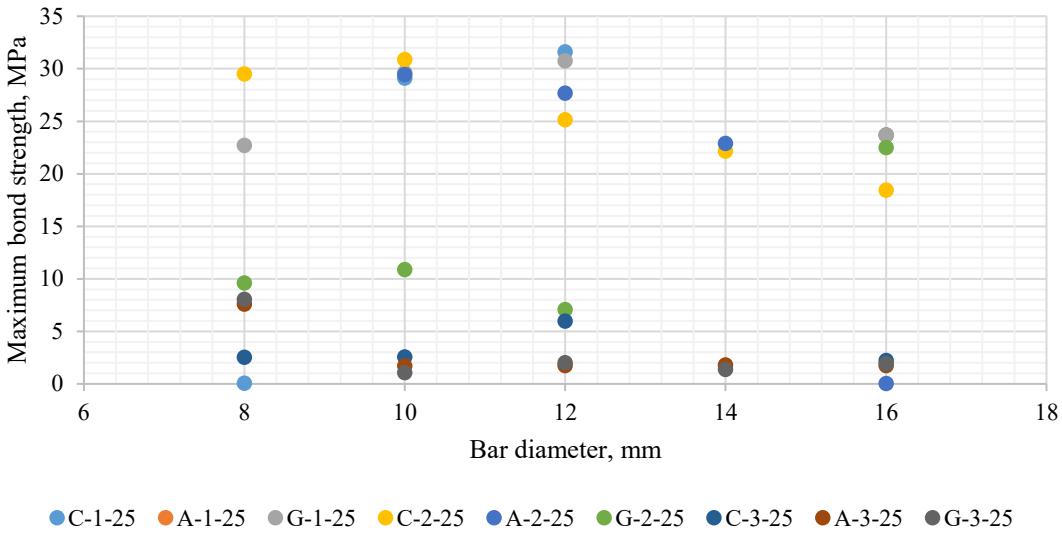
Maximum bond strength, MPa
35
30
25
20
15
10
5
0
6
8
10
12
14
16
18
Bar diameter, mm
C-1-25
A-1-25
G-1-25
C-2-25
A-2-25
G-2-25
C-3-25
A-3-25
G-3-25

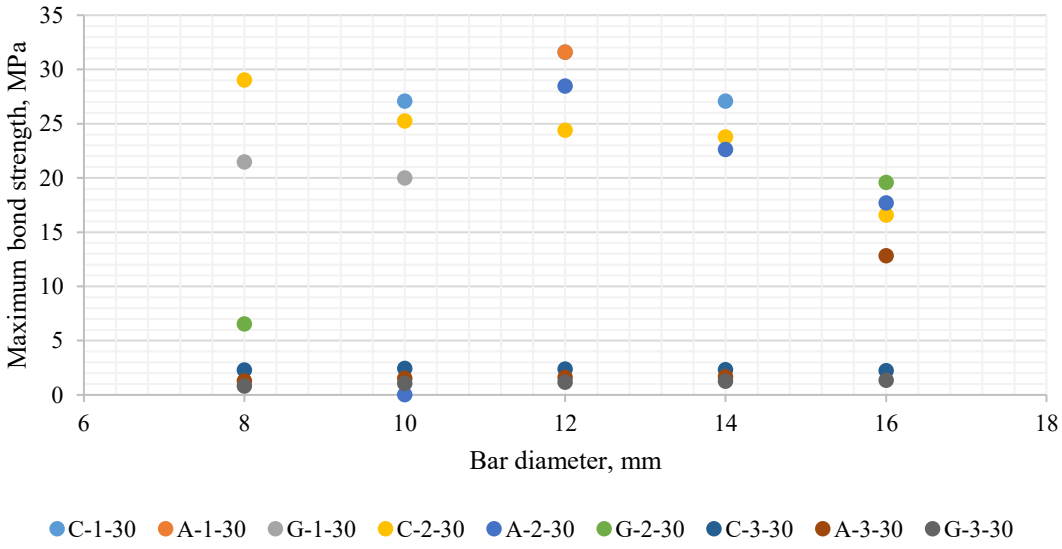
Maximum bond strength, MPa
35
30
25
20
15
10
5
0
6
8
10
12
14
16
18
Bar diameter, mm
C-1-30
A-1-30
G-1-30
C-2-30
A-2-30
G-2-30
C-3-30
A-3-30
G-3-30

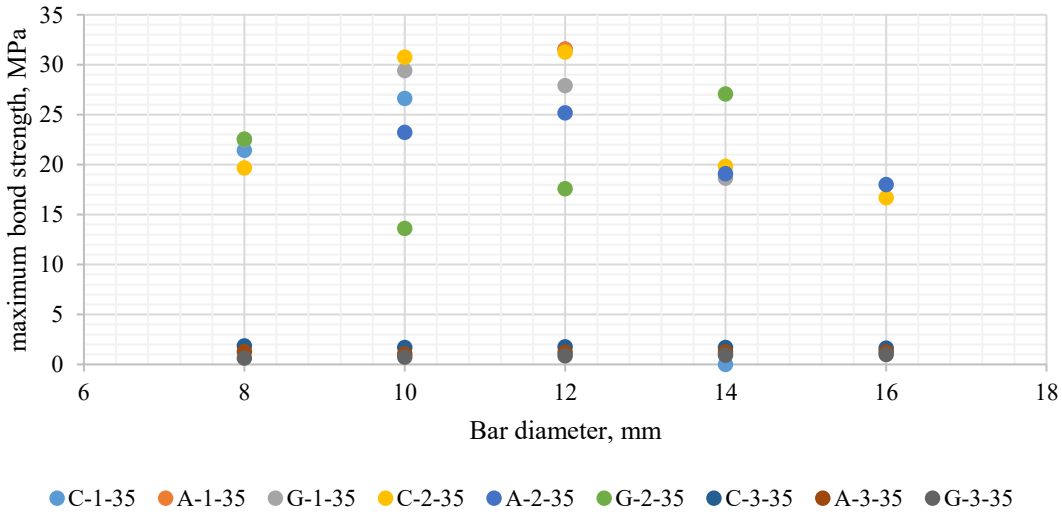
maximum bond strength, MPa
35
30
25
20
15
10
5
0
6
8
10
12
14
16
18
Bar diameter, mm
C-1-35
A-1-35
G-1-35
C-2-35
A-2-35
G-2-35
C-3-35
A-3-35
G-3-35

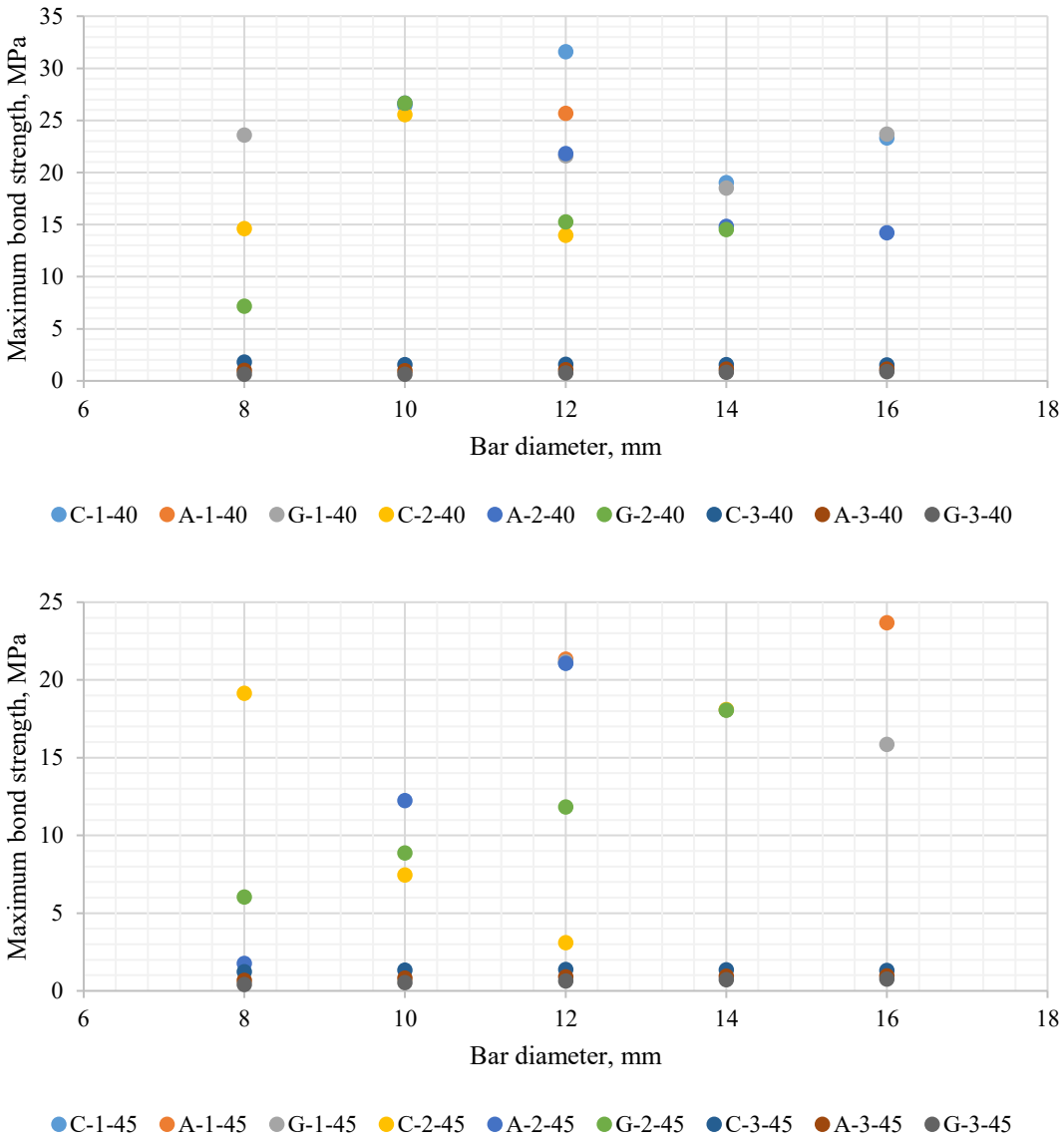

Figure 83: Maximum average bond strength versus bar diameters of models with similar concrete compressive strength.

Figure (84) depicts the relationships between bar diameter, d_b concrete cover, c/d_b and embedment length, l_d/d_b. It is evident that the normalised bond strength,τ^*_{max}, calculated by dividing the maximum bond strength by the concrete compressive strength, decreases as the bar diameter of the beam models increases.

In Figure (84-b), the correlation between normalized bond strength,$\tau_{max} / \sqrt{(fc')}$ with concrete cover, c/d_b is shown. It is observed that as the ratio of concrete cover to bar diameter increases, the normalized bond strength also increases, with the

main failure mode being pull-out. The results indicate that an increase in the concrete cover-to-bar diameter ratio from 1.58 to 3.17 results in an average increase of 20.45% in normalized bond strength.

Figure (84-c) illustrates the relationship between normalized bond strength, $\tau_{max} / \sqrt{(fc')}$ and embedment lengths, l_d/d_b. This figure also shows that as the ratio of embedment length to bar diameter increases, there is an increase in normalized bond strength.

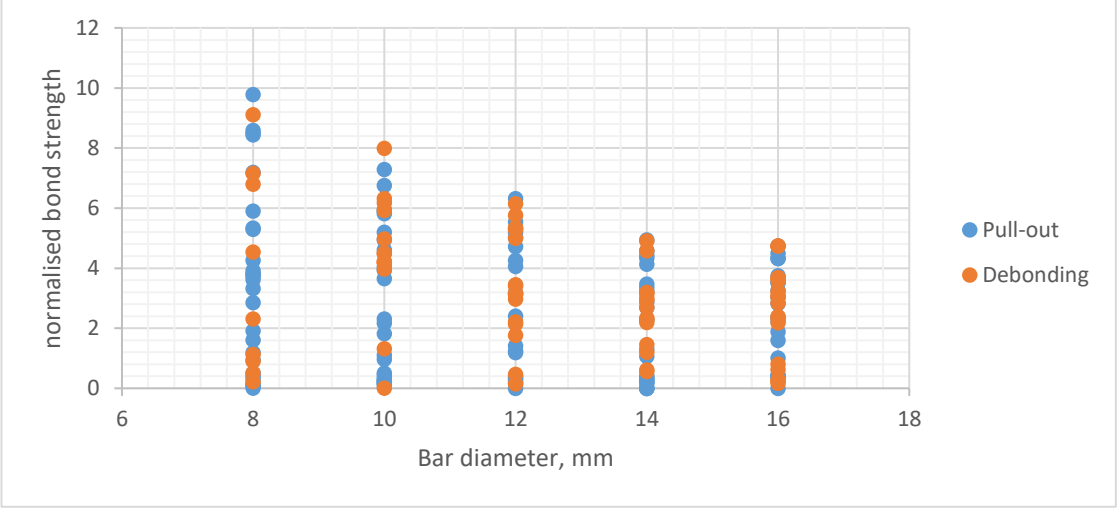

(a)

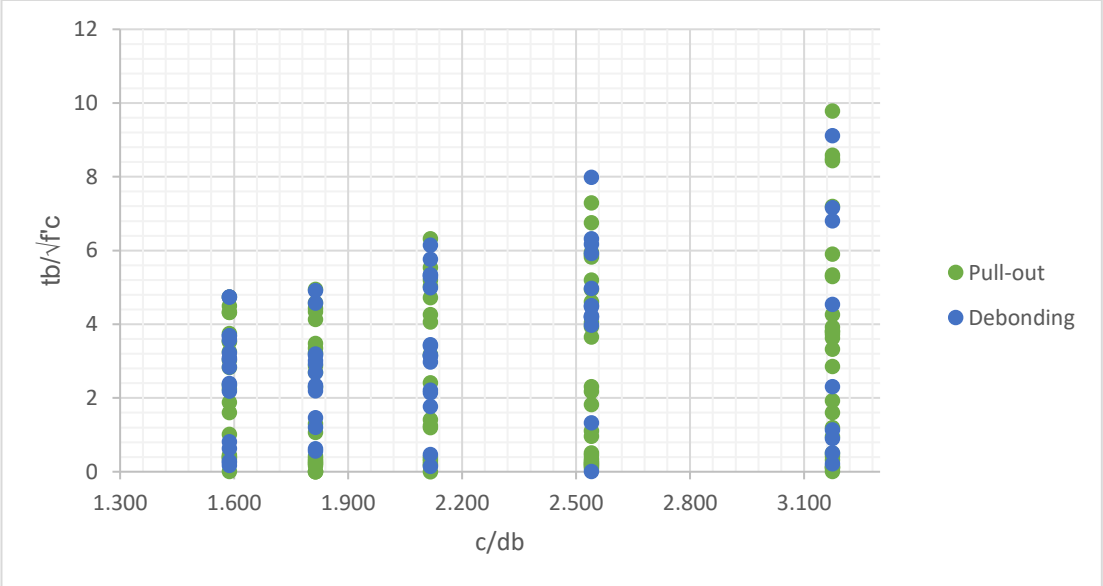

(b)

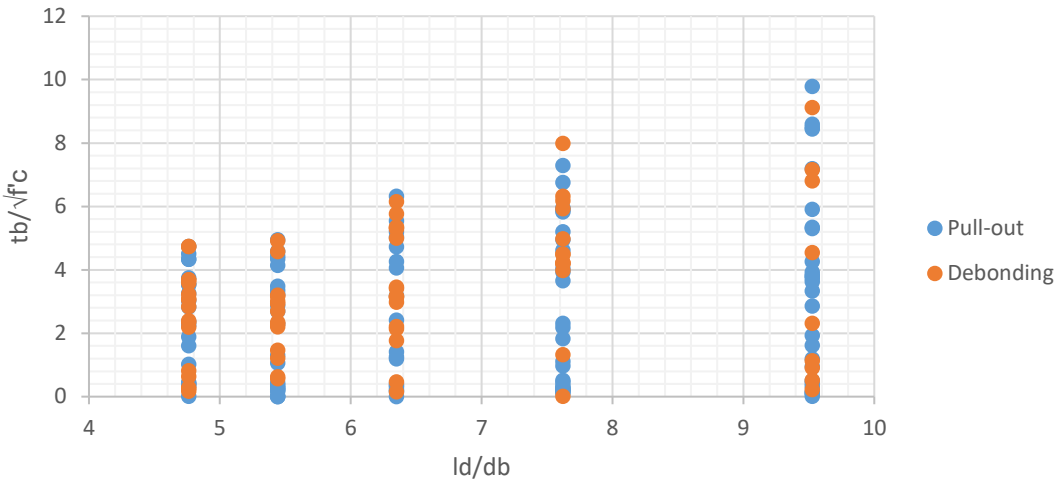

(c)

Figure 84: Normalised bond strength versus (a) bar diameter, (b) concrete cover and (c) embedment length.

Figure (85) represents the relationship between bond slip, s versus bar diameter, d_b. The plot indicates that as the bar diameter increases, there is a corresponding increase in bond slips in the beam models. This phenomenon occurs due to the higher bar diameter leading to a lower bond strength between the FRP bar and the concrete beam, ultimately resulting in increased bond slip. In these models, debonding becomes the dominant failure mode under impact loading conditions.

Figure (86) provides an overview of bond slip in AFRP, CFRP, and GFRP RC beam models that share similar concrete compressive strength values while highlighting the influence of different bar diameters.

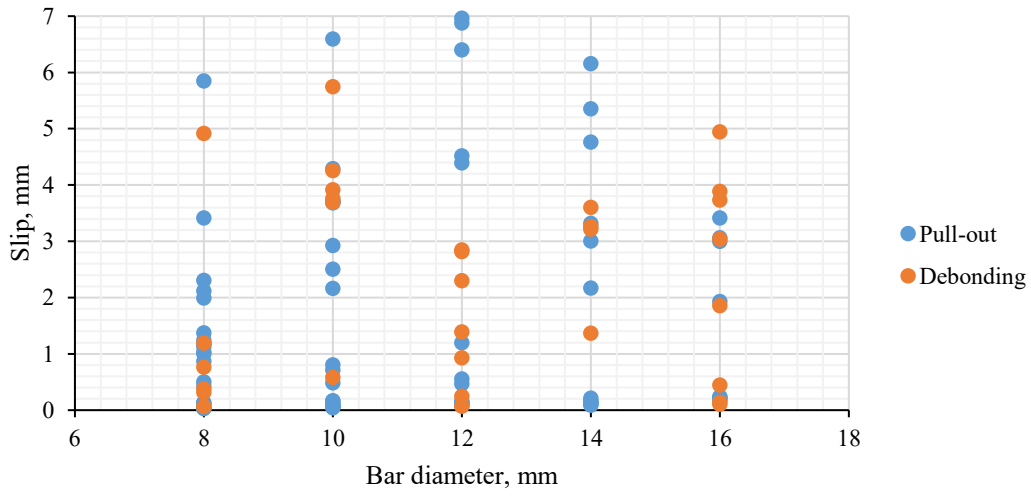

Figure 85: bond slip versus bar diameter.

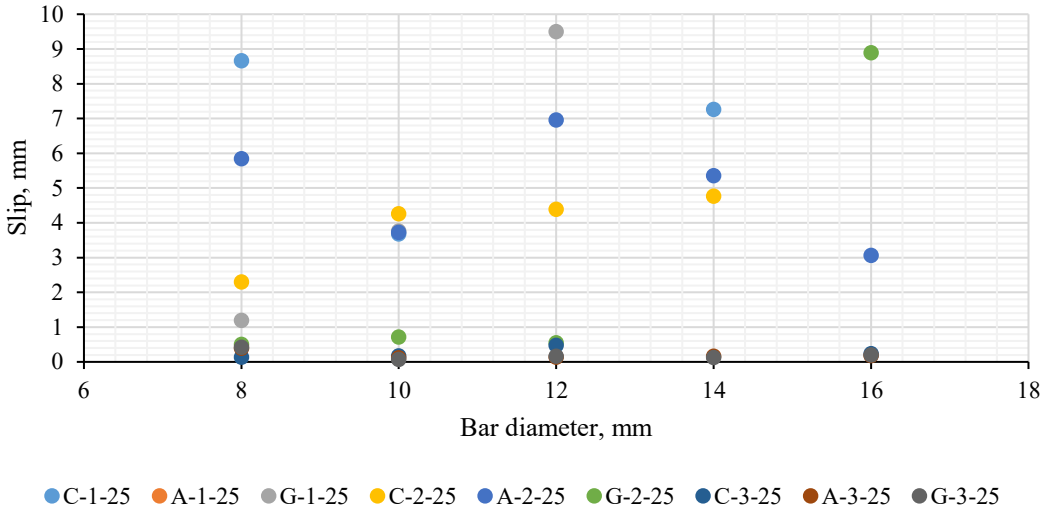
Slip, mm
Bar diameter, mm
C-1-25 A-1-25 G-1-25 C-2-25 A-2-25 G-2-25 C-3-25 A-3-25 G-3-25

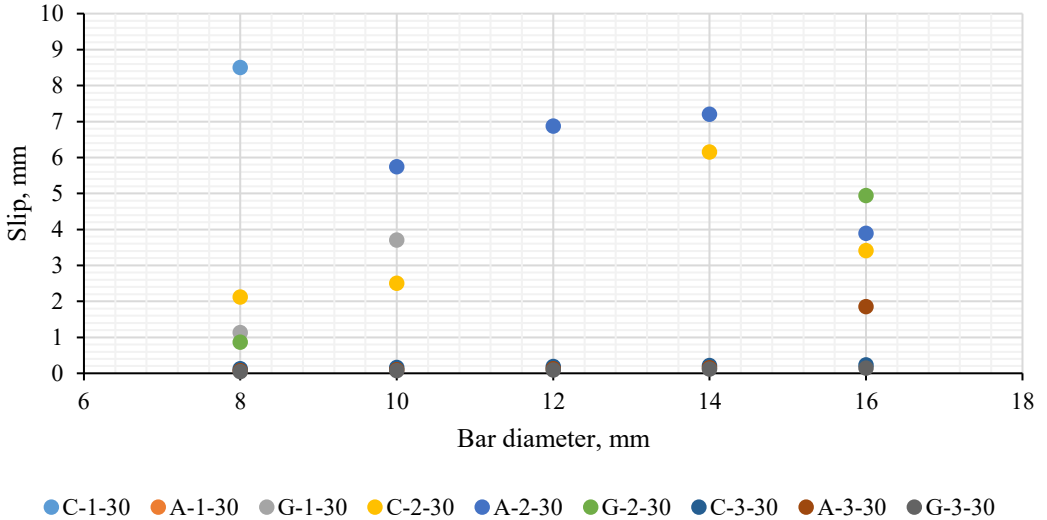
Slip, mm
Bar diameter, mm
C-1-30 A-1-30 G-1-30 C-2-30 A-2-30 G-2-30 C-3-30 A-3-30 G-3-30

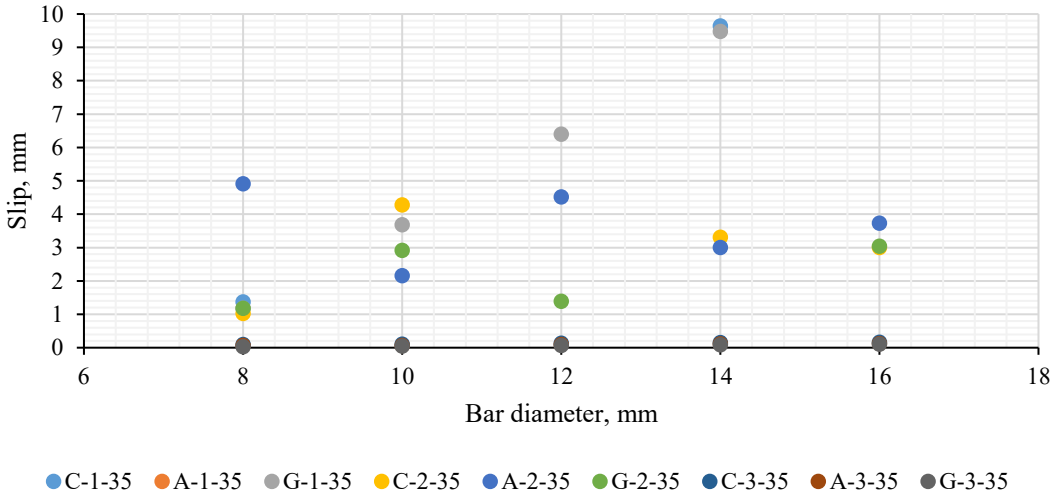
Slip, mm
Bar diameter, mm
C-1-35 A-1-35 G-1-35 C-2-35 A-2-35 G-2-35 C-3-35 A-3-35 G-3-35

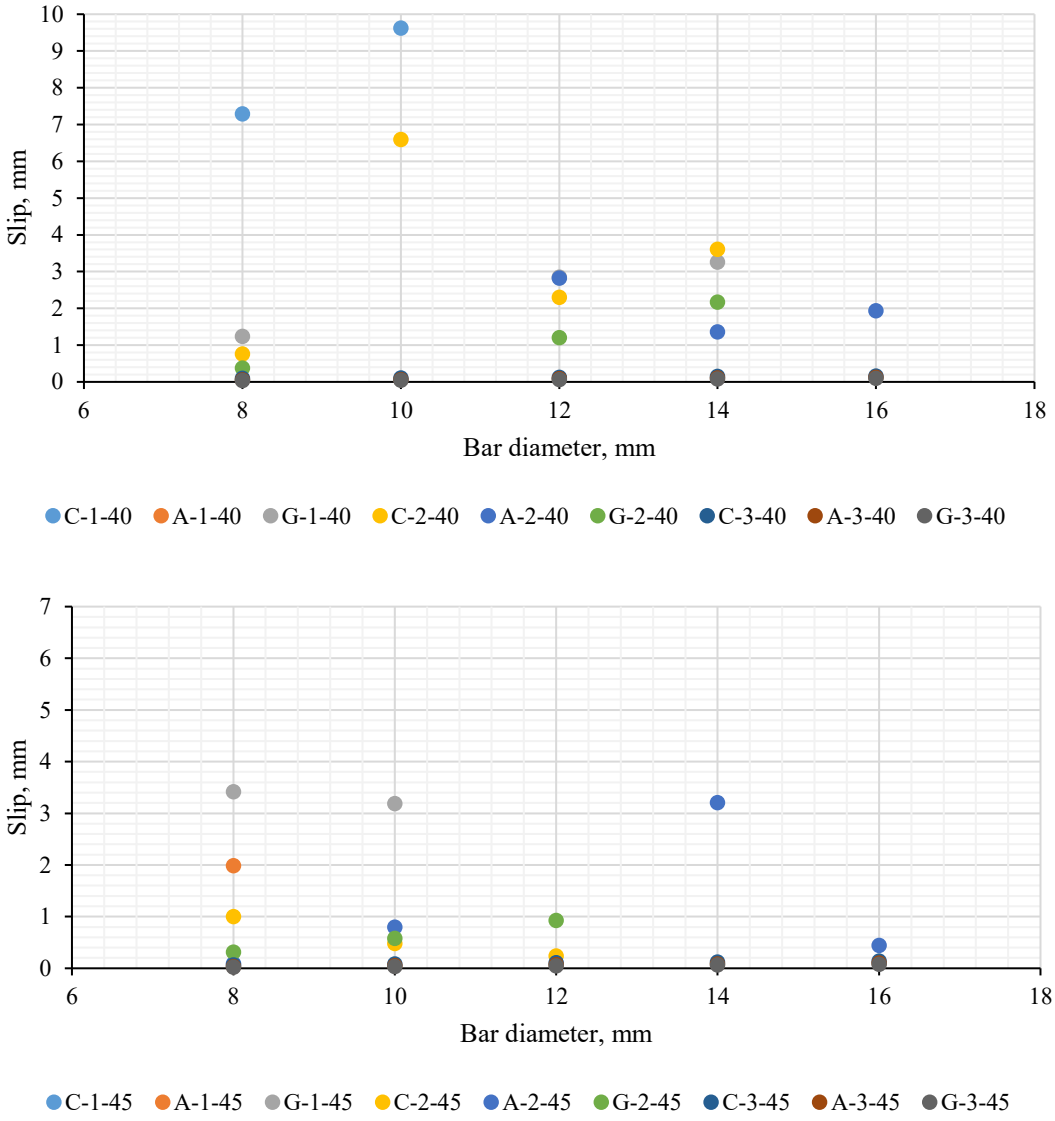

Figure 86: Effect of bar diameter as variable on slip for CFRP. GFRP and AFRP RC beams.

5.7.2 Effect of concrete compressive strength, f_c'

A comprehensive set of simulations was conducted to investigate the impact of concrete compressive strength, f_c', on various parameters such as maximum bond strength, maximum slip, mid-deflection, and dynamic strain. These simulations maintained consistent material properties, mechanical characteristics, and geometric dimensions across the models. The sole variable altered during the simulations was the concrete compressive strength, which ranged from 25 MPa to 45 MPa in increments of 5 MPa.

Due to the extensive dataset generated from a total of 225 models, this section presents the results from models with a bar diameter of 12 mm. To avoid redundancy, results from other models are included in Appendix (C). Figure (87) illustrates the relationship between maximum load and maximum mid-deflection concerning the concrete compressive strength's influence. There are nine distinct sets of FRP RC beam models, each consisting of five identical FRP RC beams with concrete strength as the varying parameter. These beam sets were subjected to different loading conditions, but only those with similar parameters and loading conditions were compared.

In general, an increase in concrete strength resulted in higher maximum loading capacity and reduced maximum mid-deflection. However, some models exhibited higher mid-deflection despite an increase in concrete strength. As previously discussed, this behaviour can be attributed to the increased brittleness of concrete.

Figure (88) provides insight into the relationship between maximum load and maximum mid-deflection for CFRP, AFRP, and GFRP RC beams. For both maximum loading and mid-deflection, CFRP RC beams with a 12 mm bar diameter outperformed AFRP and GFRP RC beams, demonstrating a 24.14% increase in maximum loading compared to AFRP and 23.26% compared to GFRP RC beams. In terms of maximum mid-deflection, CFRP RC beams with a 12 mm bar diameter exhibited a 36.69% decrease compared to AFRP and a 23.6% decrease compared to GFRP RC beams.

	FRP Type	db, mm	Load, kN		FRP Type	db, mm	Load, kN		FRP Type	db, mm	Load, kN
C-1-12	Carbon	12	320	C-2-12	Carbon	12	80	C-3-12	Carbon	12	40
A-1-12	Aramid	12	320	A-2-12	Aramid	12	80	A-3-12	Aramid	12	40
G-1-12	Glass	12	320	G-2-12	Glass	12	80	G-3-12	Glass	12	40

Table 32: Detail of Beam models shown in figure (91) and (92) for max load, Max mid-deflection, Max bond strength, Max slip associated with concrete compressive strength.

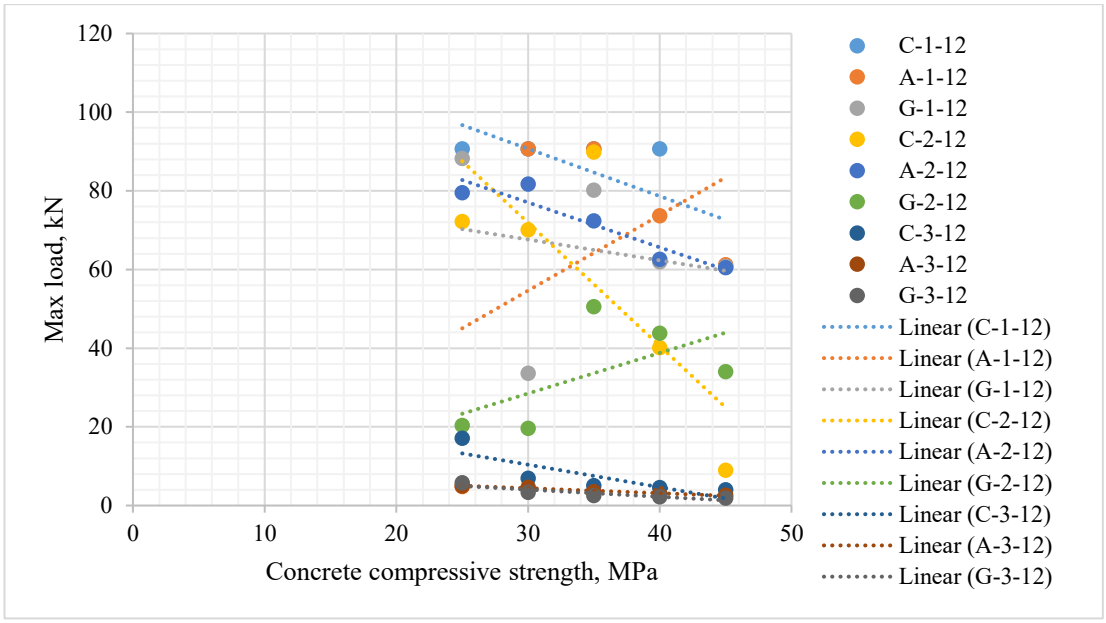

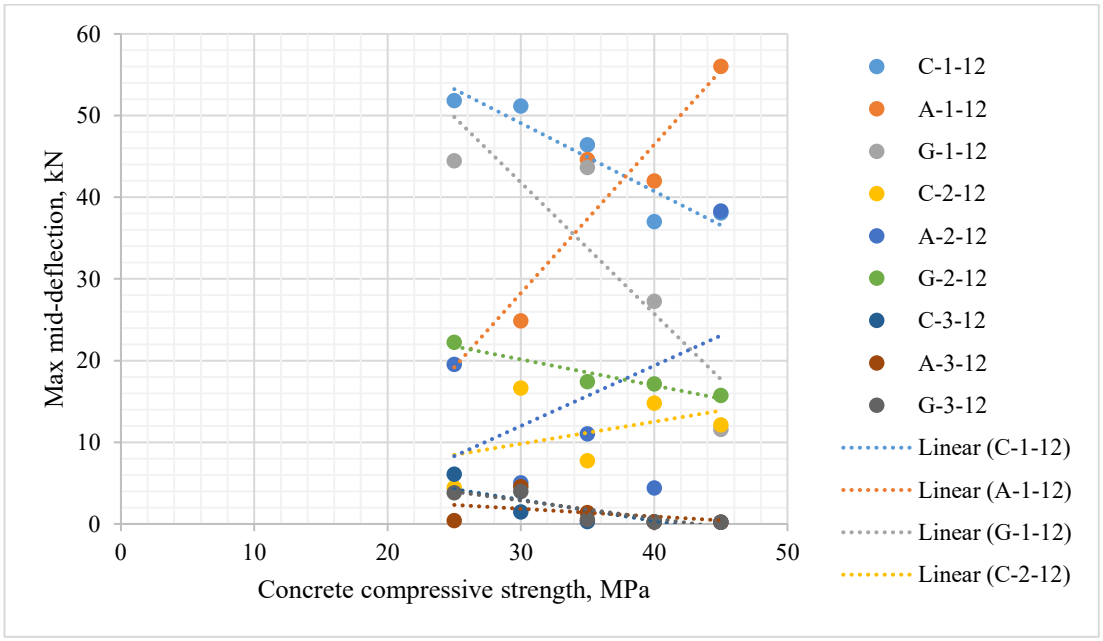

Figure 87: relationship of Maximum load and maximum mid-deflection of AFRP, CFRP and GFRP RC beams with concrete strength as variable.

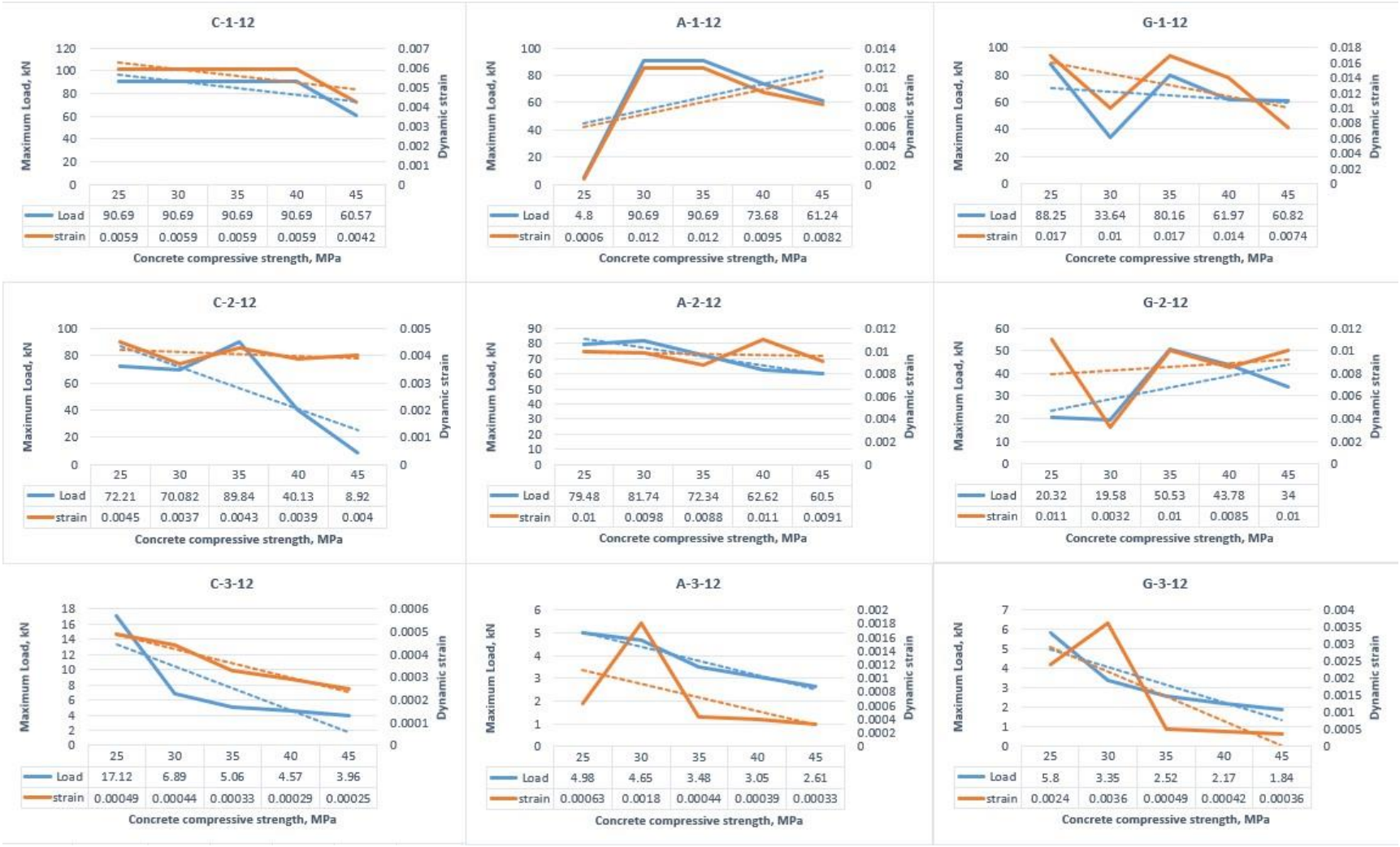

Figure 88: Effect of concrete strength on maximum load and maximum mid-deflection for AFRP, CFRP and GFRP RC beams with bar diameter of 12 mm.

Figure (92) illustrates the correlation between maximum bond strength,τ_{max} and slip, s, for CFRP, AFRP, and GFRP RC beams, all with a 12 mm bar diameter. The variable under investigation is the concrete compressive strength, f_c'. Additional data, including maximum bond strength and maximum slip for all models across various FRP bar types and concrete compressive strengths, can be found in Appendix (C). In general, Figure (92) indicates a rise in maximum bond strength as the concrete compressive strength increases. It is worth noting that FRP bars are commonly employed in conjunction with concrete compressive strengths ranging from 27 MPa to 55 MPa, as reported in prior studies, [124] [287]. However, it has also been observed that, in some instances, the ratio of maximum bond strength to concrete compressive strength diminishes as the concrete compressive strength increases. One explanation for this decrease in bond strength is the heightened brittleness of high-strength concrete, rendering it more prone to failure. Regarding maximum slip, Figure (92) demonstrates a reduction in maximum slip with an increase in concrete compressive strength. This implies that beam models concluded abruptly due to failures associated with increased concrete compressive strength.

Figure (89) delves into the relationship between failure modes and concrete compressive strength in FRP RC beam models. It reveals that pull-out failure predominates over debonding failure. Pull-out failures are evenly distributed across concrete compressive strength values ranging from 25 to 30 MPa, while debonding failures become more prevalent within the concrete compressive strength range of 30 to 45 MPa. Figure (91) provides the percentage distribution of failures within each concrete compressive strength range, spanning from 25 to 45 MPa.

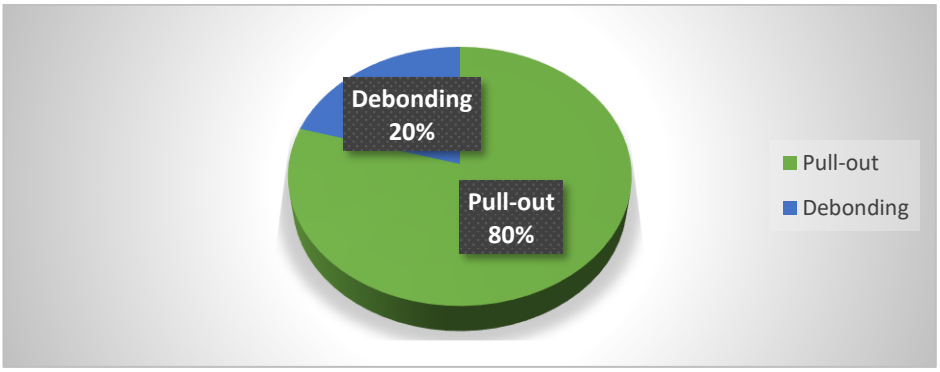

Figure 89: Two failure modes related to concrete compressive strength as variable out of 198 failed models.

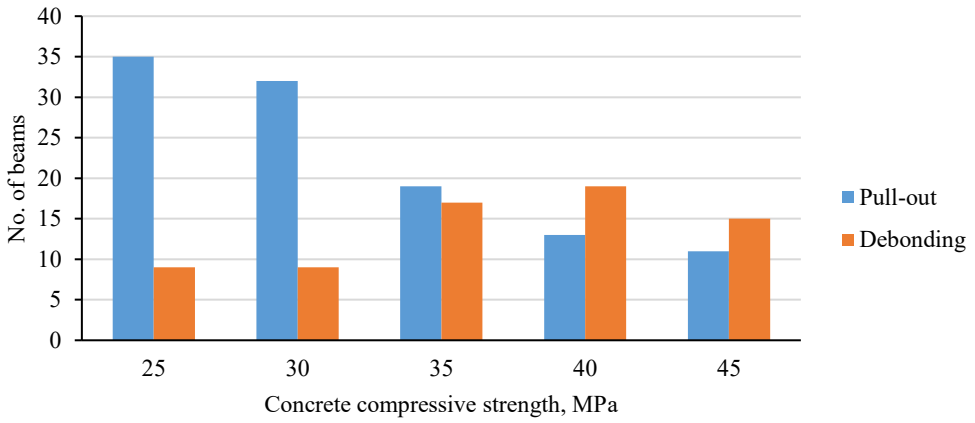

Figure 90: Failure modes associated with concrete compressive strength

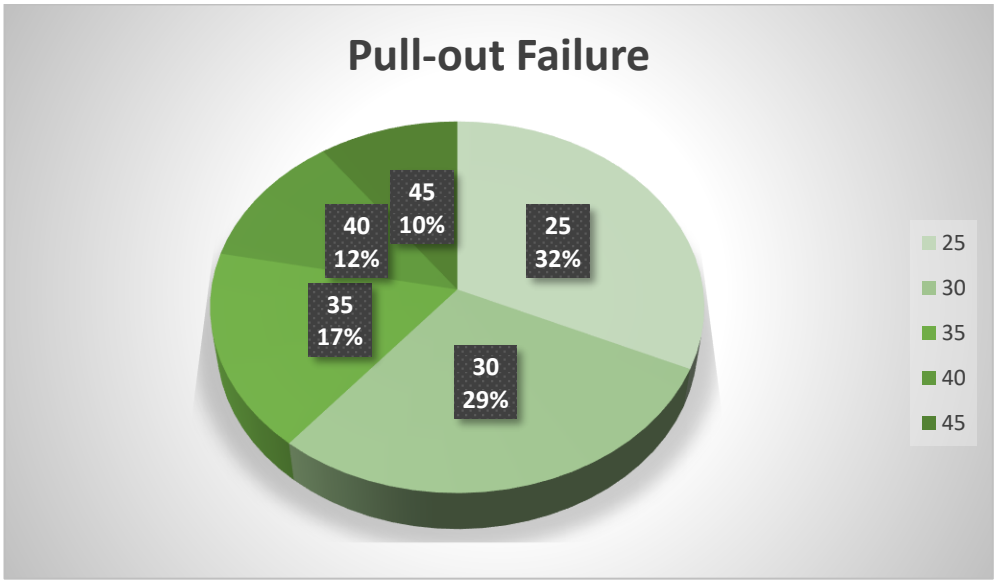

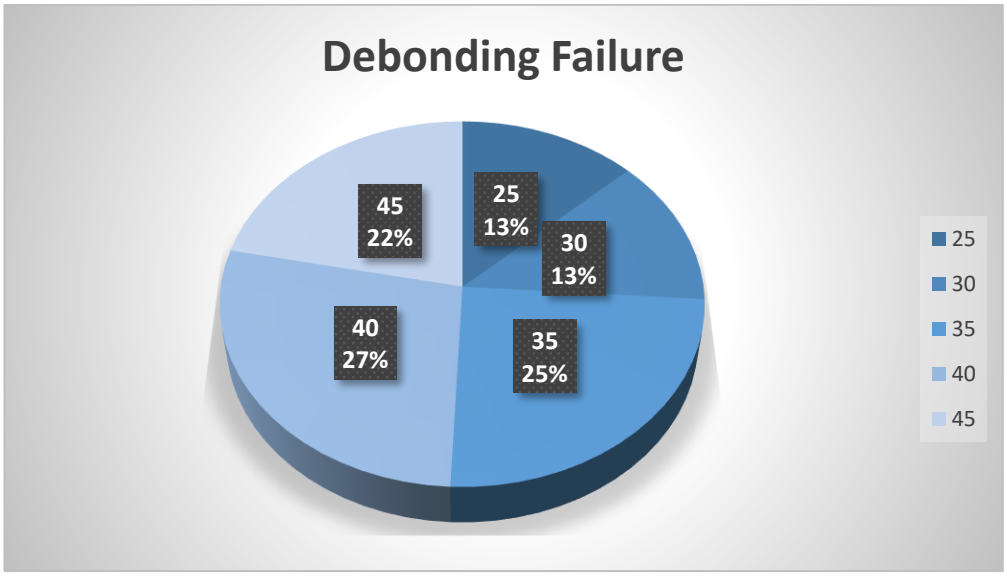

Figure 91: Two failure modes percentages associated with concrete compressive strength.

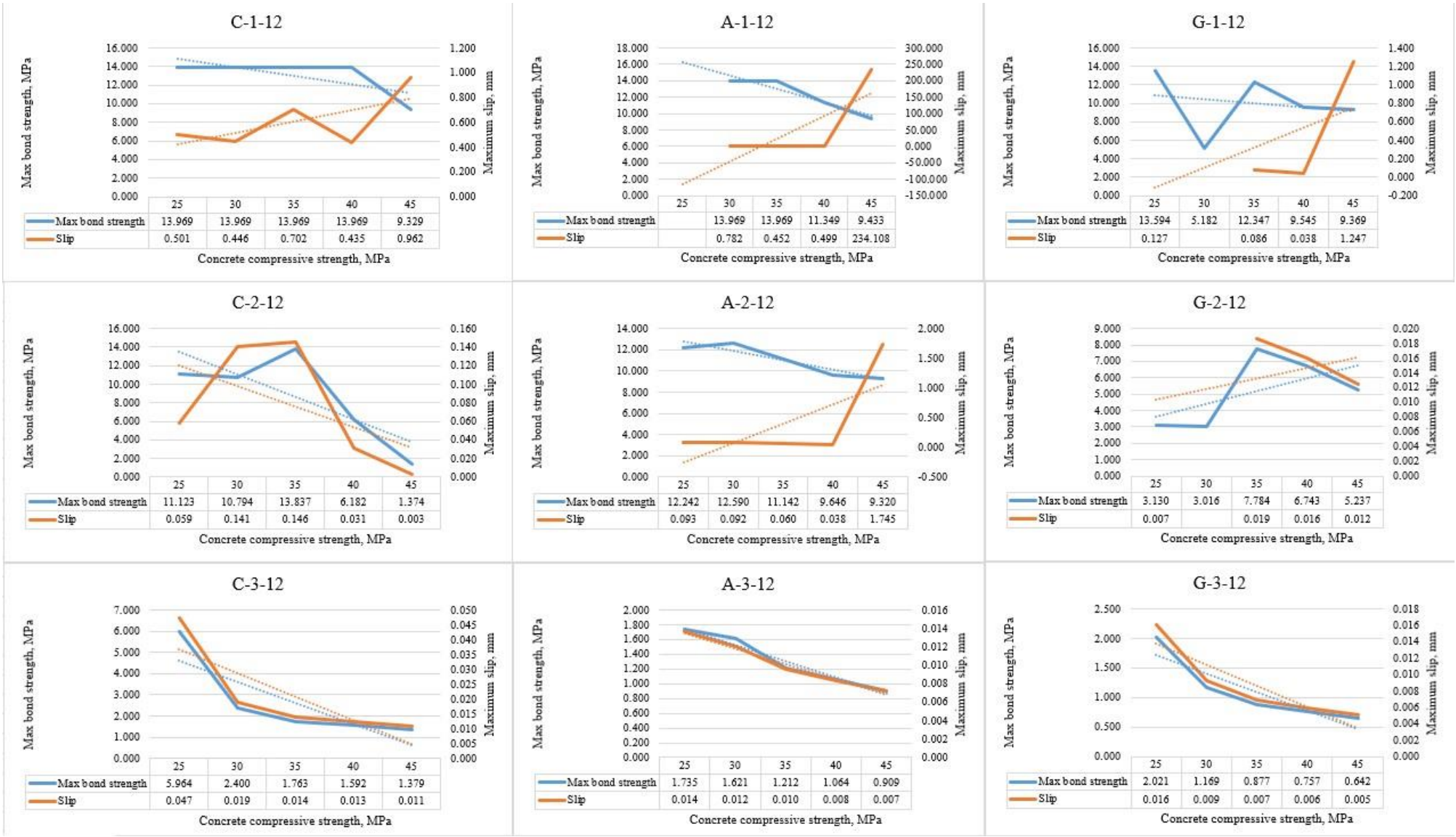

Figure 92: Maximum bond strength and maximum slip versus concrete compressive strength for models with bar diameter of 12mm under three different impact loading.

5.7.3 Effect of modulus of elasticity, E_f

In order to investigate and comprehend the impact of different types of FRP and their respective modulus of elasticity on RC beams, models incorporating CFRP, AFRP, and GFRP RC beams were simulated using ABAQUS. The average values of the Young's modulus for CFRP bars range from 37 to 784 GPa, while AFRP bars exhibit values between 41 and 175 GPa, and GFRP bars range from 35 to 51 GPa, as outlined in ACI guidelines, [44]. additionally, Kazemi, [281] conducted tests on CFRP and GFRP bars with Young's modulus values of 136 GPa and 45 GPa, respectively. Efe, [280], examined AFRP bars with a Young's modulus of 69 GPa. Therefore, the choice of modulus of elasticity for CFRP, AFRP, and GFRP bars in this study aligns with the previously mentioned experimental data and guidelines.

The analysis comprised three sets of 75 models, each set consisting of three distinct beam models utilizing CFRP, AFRP, and GFRP bars, all with identical concrete compressive strength, bar diameter, and applied impact load. The naming convention for these beam models consists of a series of numbers, with the first indicating the model group, the second representing the applied load, the third specifying the concrete compressive strength, and the last number indicating the bar diameter size. For example, the name "beam 1-1-25-8" denotes a beam subjected to an impact load of 320 kN, with a concrete compressive strength of 25 MPa and a bar diameter of 8 mm. The primary objective of this study was to investigate the influence of Young's modulus E_f on the bond behaviour between FRP and concrete, ultimate load capacity, maximum deflection, and energy absorption capacity of AFRP, CFRP, and GFRP RC beams.

Figure (93) displays the ultimate loads for CFRP, AFRP, and GFRP RC beams as a function of the Young's modulus E_f . In general, it was observed that the ultimate load increased with higher modulus of elasticity for the beams. For instance, as depicted in Figure (93-a), beam 1-1-40-12, featuring glass fibre and $E_f = 45\ GPa$,

exhibited an ultimate load of 61.97 kN. In comparison, beam 1-1-40-12 with aramid fibre and $E_f = 69\ GPa$ experienced an ultimate load of 73.68 kN, while beam 1-1-40-12 with carbon fibre and $E_f = 136\ GPa$ had an ultimate load of 90.69 kN. These results demonstrate a 15.8% increase in ultimate load for beam 1-1-40-12 as the E_f increased from 45 GPa to 69 GPa, and an 18.7% increase in ultimate load for the 1-1-40-12 beam model with a change in E_f from 69 GPa to 136 GPa, driven by the higher Young's modulus of the FRP bars. Additionally, it was noted that some models exhibited higher ultimate loads with AFRP bars compared to CFRP bars, even with a higher E_f value.

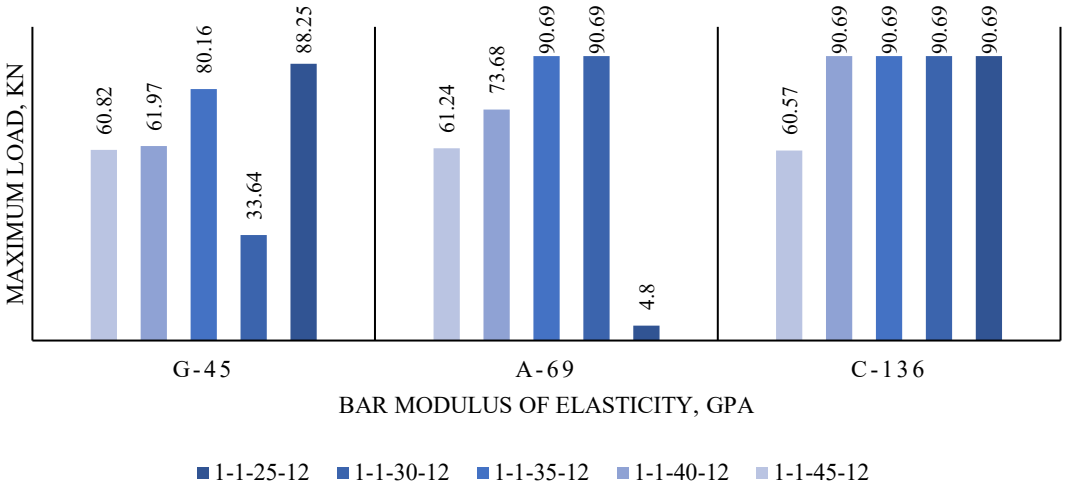

(A)

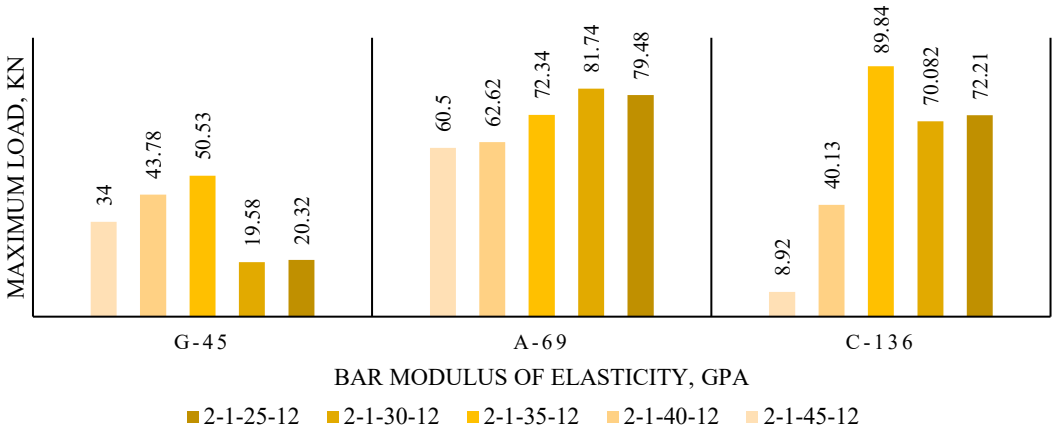

(B)

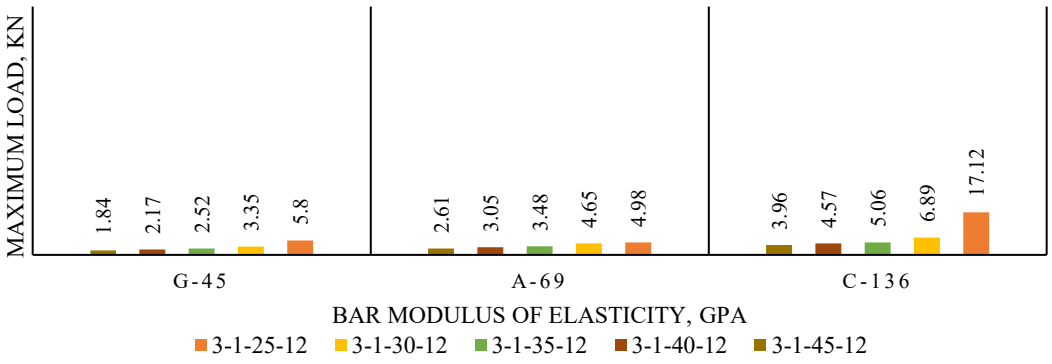

(C)

Figure 93:Effect of modulus of elasticity on maximum loads under a) 320 kN impact load, b) 80 kN impact load and c) 40 kN impact load for models with AFRP, CFRP and GFRP RC beams.

Figure (94) illustrates the maximum deflection of beams with the modulus of elasticity E_f as the varying parameter. In contrast to the corresponding ultimate load values, the maximum mid-span deflection exhibited opposite trends in response to changes in E_f. The results indicate that an increase in E_f led to a decrease in the maximum mid-span deflection for the beam models. For instance, beam 2-1-35-12 displayed maximum mid-deflection values of 373.635 kN, 237.081 kN, and 166.02 kN when equipped with glass fibre and E_f of 45 GPa, aramid fibre and E_f of 69 GPa, and carbon fibre and E_f of 136 GPa, respectively. The substantial decrease of 44.4% observed between the GFRP and CFRP RC beams for the 2-1-35-12 model was consistent with the increase in E_f of the FRP bars. Additionally, some models exhibited a lesser reduction in maximum mid-deflection with the increase in E_f.

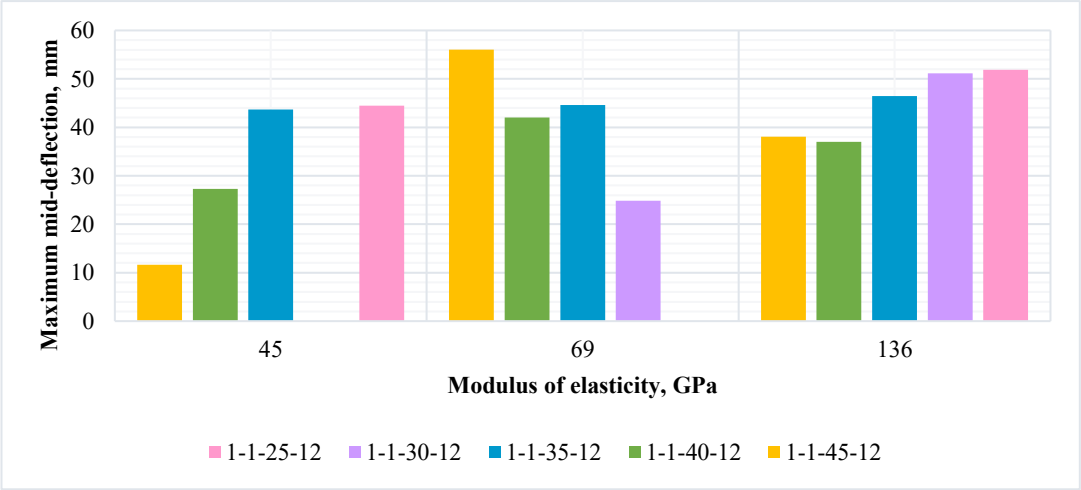

(A)

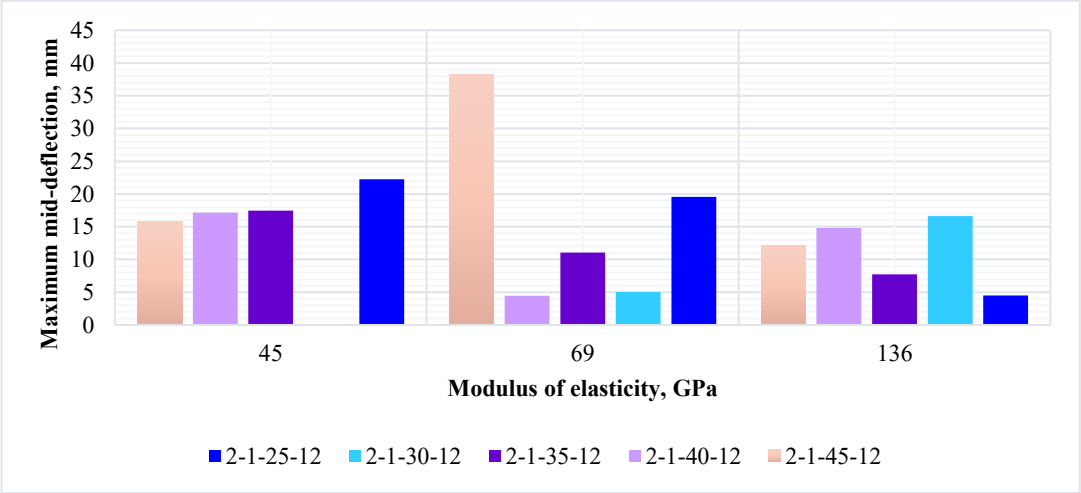

(B)

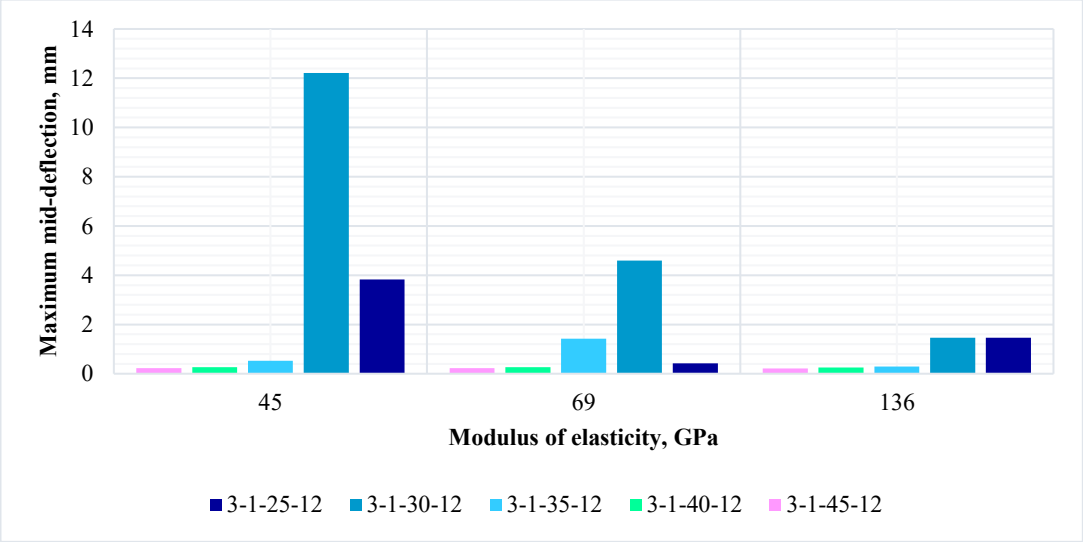

(c)

Figure 94: Effect of modulus of elasticity on maximum mid-deflection of beam models subjected to a) 320 kN impact load, b) 80 kN impact loading and c) 40 kN impact load.

Figure (95) and (96) depict the influence of the modulus of elasticity E_f on the maximum bond strength and ultimate slip for models equipped with a bar diameter of 12 mm and subjected to impact loads of 320 kN, 80 kN, and 40 kN. To avoid redundancy, figures illustrating the relationship between modulus of elasticity and maximum bond strength, as well as slip for all models, are presented in the appendix (C). It is evident that the bond performance of FRP bars varied significantly based on their modulus of elasticity and flexural behaviour. An increase in the modulus of elasticity of FRP bars led to an increase in both maximum bond strength and

maximum slip. The bond-slip relation curves for CFRP, GFRP, and AFRP RC beam models are presented in Figure (97) and (98).

Model	FRP	Load, kN	f'c	db	Model	FRP	Load, kN	f'c	db	Model	FRP	Load, kN	f'c	db
C-1-1-25-12	Carbon	320	25	12	C-2-1-25-12	Carbon	80	25	12	C-3-1-25-12	Carbon	40	25	12
A-1-1-25-12	Aramid	320	25	12	A-2-1-25-12	Aramid	80	25	12	A-3-1-25-12	Aramid	40	25	12
G-1-1-25-12	Glass	320	25	12	G-2-1-25-12	Glass	80	25	12	G-3-1-25-12	Glass	40	25	12
C-1-1-30-12	Carbon	320	30	12	C-2-1-30-12	Carbon	80	30	12	C-3-1-30-12	Carbon	40	30	12
A-1-1-30-12	Aramid	320	30	12	A-2-1-30-12	Aramid	80	30	12	A-3-1-30-12	Aramid	40	30	12
G-1-1-30-12	Glass	320	30	12	G-2-1-30-12	Glass	80	30	12	G-3-1-30-12	Glass	40	30	12
C-1-1-35-12	Carbon	320	35	12	C-2-1-35-12	Carbon	80	35	12	C-3-1-35-12	Carbon	40	35	12
A-1-1-35-12	Aramid	320	35	12	A-2-1-35-12	Aramid	80	35	12	A-3-1-35-12	Aramid	40	35	12
G-1-1-35-12	Glass	320	35	12	G-2-1-35-12	Glass	80	35	12	G-3-1-35-12	Glass	40	35	12
C-1-1-40-12	Carbon	320	40	12	C-2-1-40-12	Carbon	80	40	12	C-3-1-40-12	Carbon	40	40	12
A-1-1-40-12	Aramid	320	40	12	A-2-1-40-12	Aramid	80	40	12	A-3-1-40-12	Aramid	40	40	12
G-1-1-40-12	Glass	320	40	12	G-2-1-40-12	Glass	80	40	12	G-3-1-40-12	Glass	40	40	12
C-1-1-45-12	Carbon	320	45	12	C-2-1-45-12	Carbon	80	45	12	C-3-1-45-12	Carbon	40	45	12
A-1-1-45-12	Aramid	320	45	12	A-2-1-45-12	Aramid	80	45	12	A-3-1-45-12	Aramid	40	45	12
G-1-1-45-12	Glass	320	45	12	G-2-1-45-12	Glass	80	45	12	G-3-1-45-12	Glass	40	45	12

Table 33: List of models in Figure (97), (98), and (99).

Table (33) provides a list of the models used in the aforementioned figures. Figures (99), (100), and (101) examine the impact of the modulus of elasticity E_f on the energy absorption capacity (EAC) of beam models, with the modulus of elasticity as a variable, subjected to impact loads of 320 kN, 80 kN, and 40 kN. The figures collectively reveal that the energy absorption capacity (EAC) decreased in tension and increased in compression as the modulus of elasticity of FRP bars increased.

For instance, when comparing beam model 1-1-25-12 reinforced with CFRP, which has the highest E_f, to beam model 1-1-25-12 reinforced with GFRP, which has the lowest E_f, it is evident that under a 320 kN impact load, the EAC increased by 89% from the GFRP RC beam to the CFRP RC beam. Conversely, under the same load, the EAC reduced by 90.8% from the GFRP RC beam to the CFRP RC beam in tension. Similarly, for beam model 2-1-25-12, there was a 96% increase in EAC in compression from the GFRP RC beam to the CFRP RC beam and a reduction of 24.87% in EAC in tension when transitioning from E_f =45 GPa to E_f =136 GPa.

The decrease in EAC in the tension zone from the GFRP RC beam to the CFRP RC beam was relatively minor, at 6.29%, under a 40 kN impact load. However, EAC in compression increased by 87% when comparing GFRP bars to CFRP bars in model 3-1-25-12. Additional data on the effect of E_f on maximum load, ultimate mid-deflection, EAC, and bond behaviour can be found in Figures (153) to (165) in the appendix (C)

5.7.4 Effect of velocity

The research delved into examining the impact of high-velocity loads on the bond behaviour of FRP RC beams. This investigation involved subjecting the beams to three distinct velocities: 12.125 m/s, 17.145 m/s, and 24.245 m/s, with a consistent impact mass of 10.89 kg applied in all cases. The findings of this study align with previous reports, highlighting a notable influence of increased impact velocity on various critical parameters.

As demonstrated in previous chapters and consistent with the outcomes observed in this study, the alteration in impact velocity had a significant impact on several key factors. Notably, it had a pronounced effect on the maximum strain, ultimate mid-deflection, and ultimate force experienced by the FRP RC beams. These parameters play a vital role in assessing the structural performance and integrity of such beams under high-velocity impact loads.

The observed trends in the results underscore the importance of considering impact velocity as a critical factor in the design and assessment of FRP RC beams, as it can have a substantial impact on their overall behaviour and response to dynamic loading conditions. This research contributes to a better understanding of how velocity influences bond behaviour and offers valuable insights for optimizing the performance and safety of structures incorporating FRP RC beams subjected to high-velocity impact events.

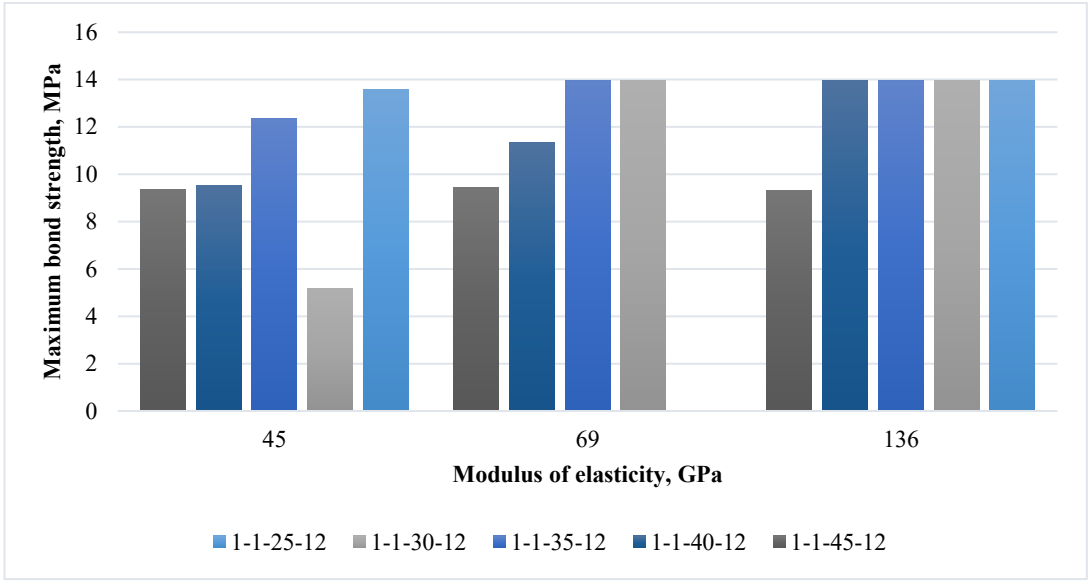

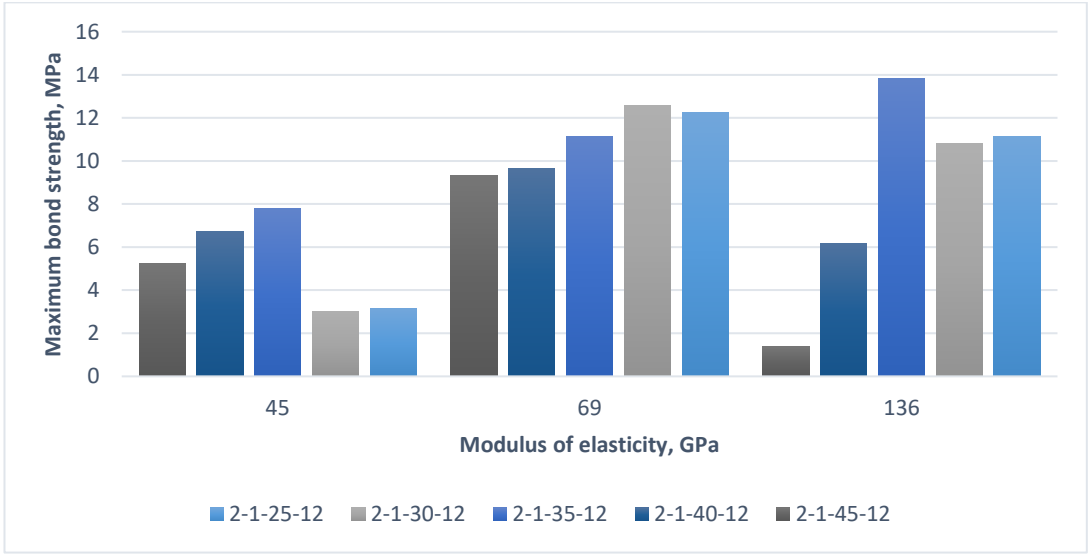

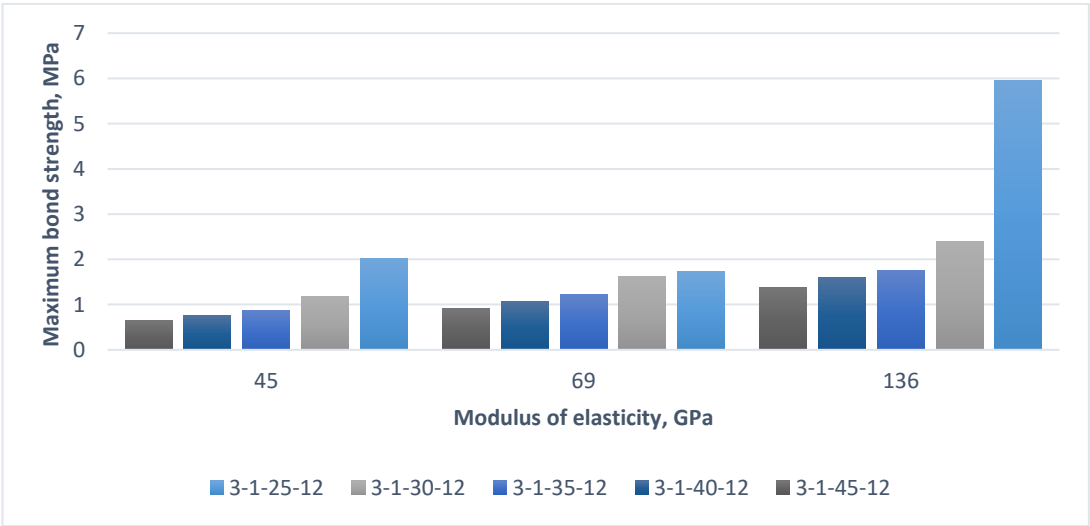

Figure 95: Effect of modulus of elasticity of FRP bars on maximum bond strength on beam models under impact loading.

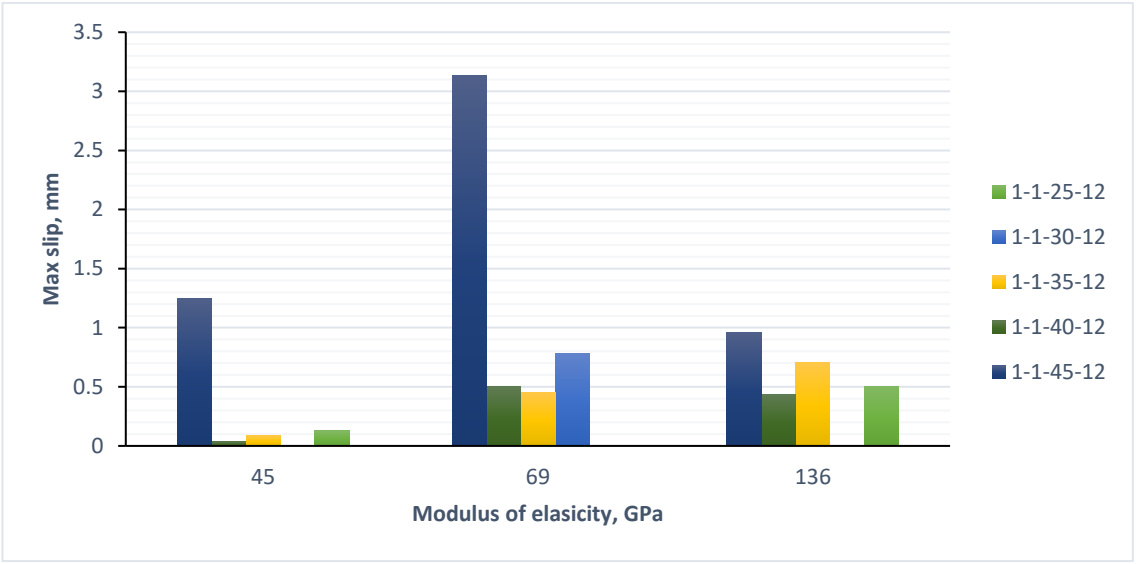

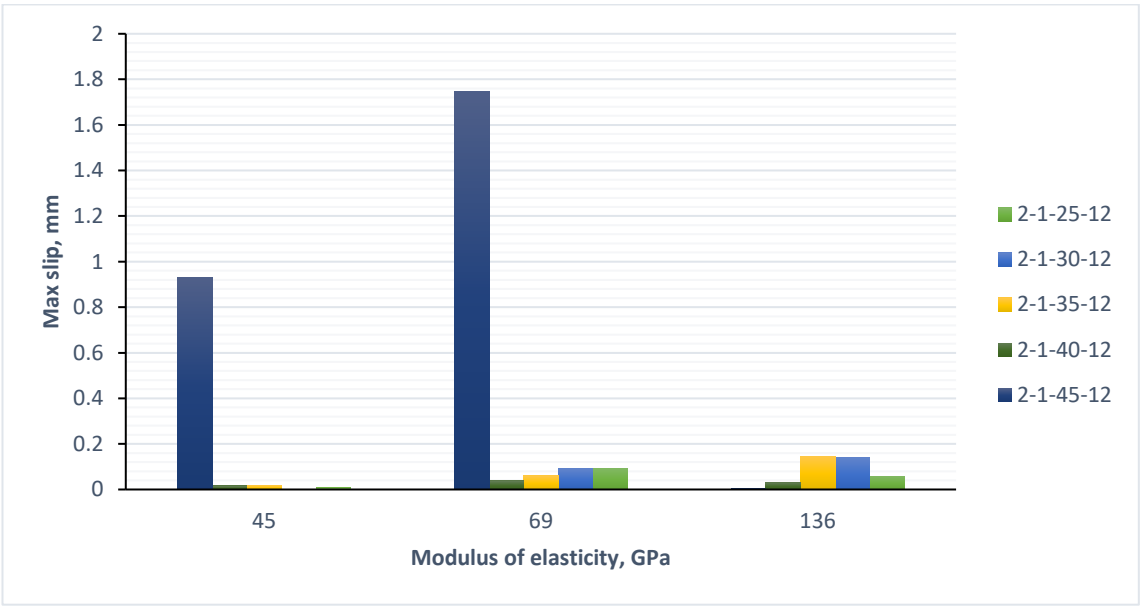

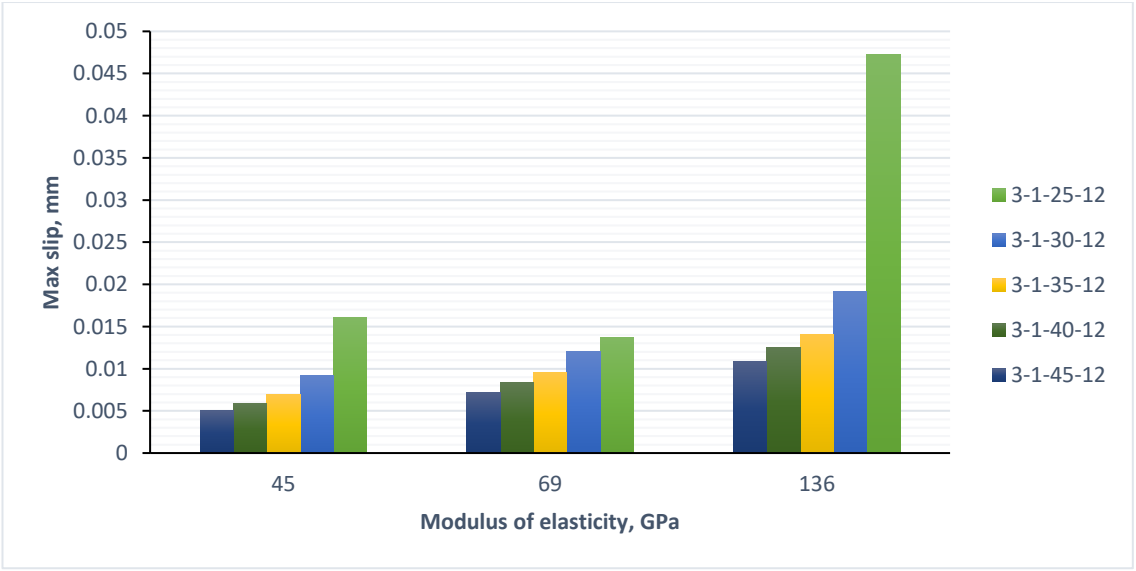

Figure 96: Effect of modulus of elasticity of FRP bars on maximum slip of beam models under impact load.

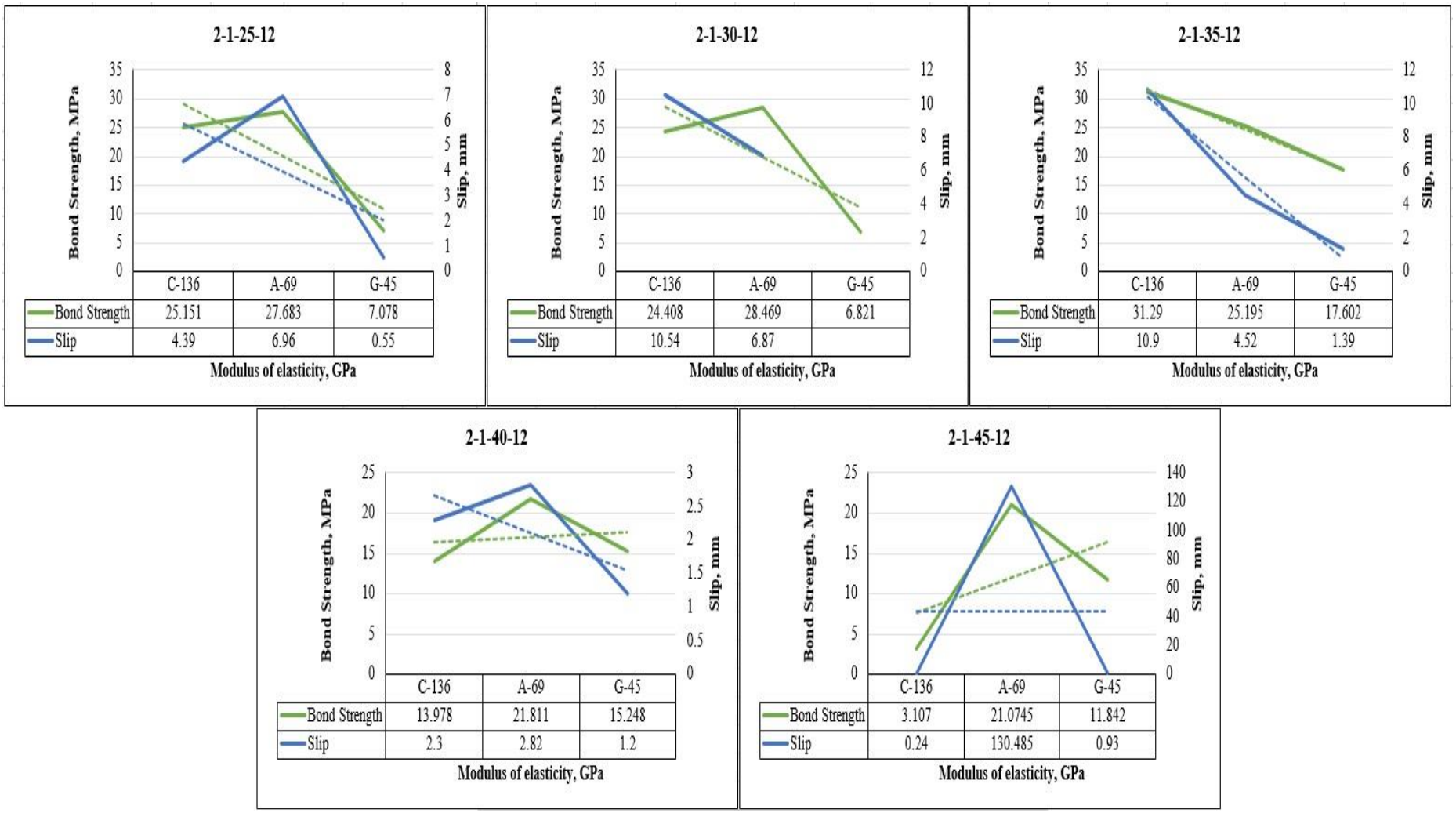

Figure 97: bond strength-slip relation curve with modulus of elasticity as variable under 80 kN impact load.

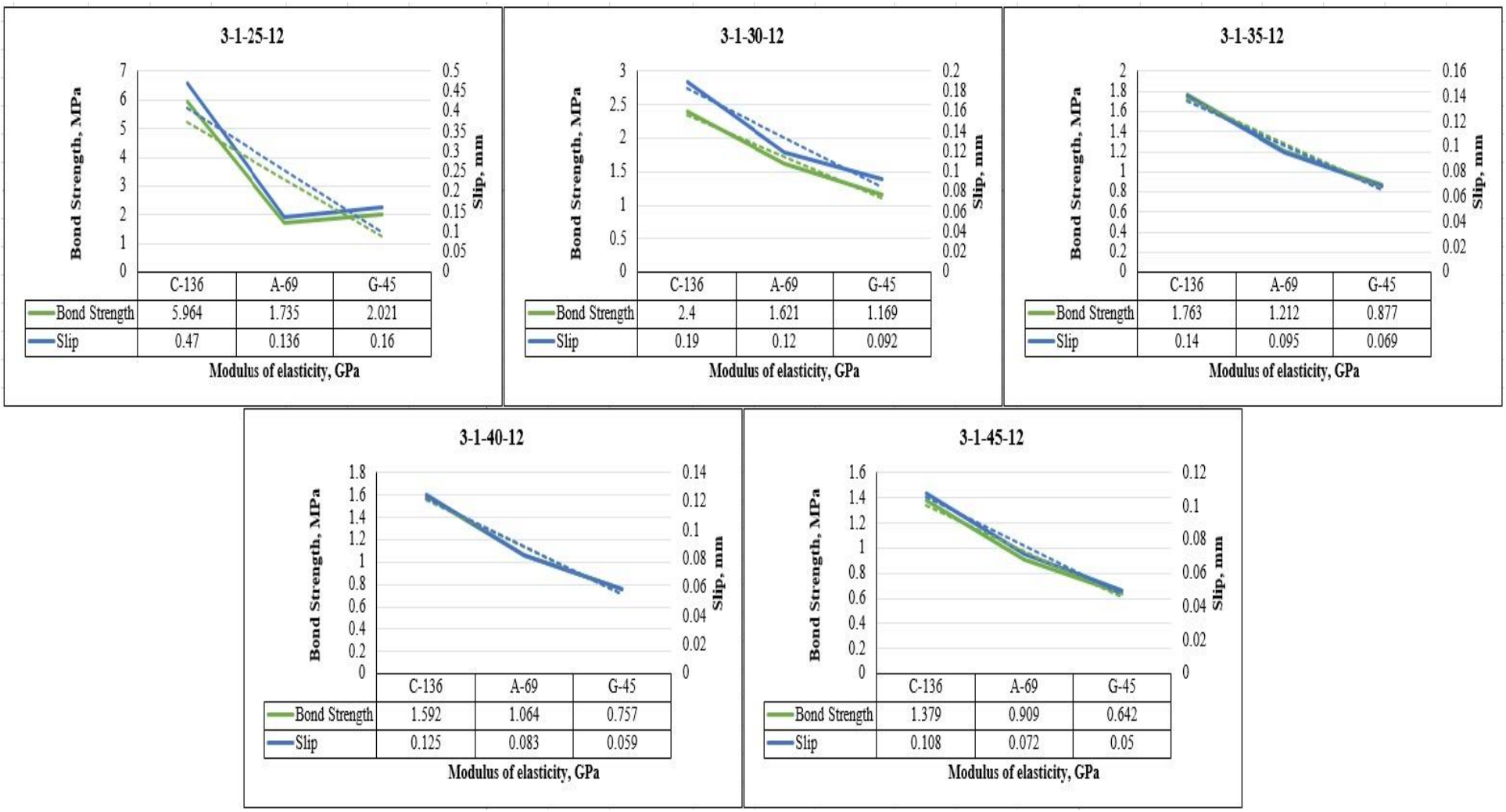

Figure 98: bond strength-slip relation curve with modulus of elasticity as variable under 40 kN impact load.

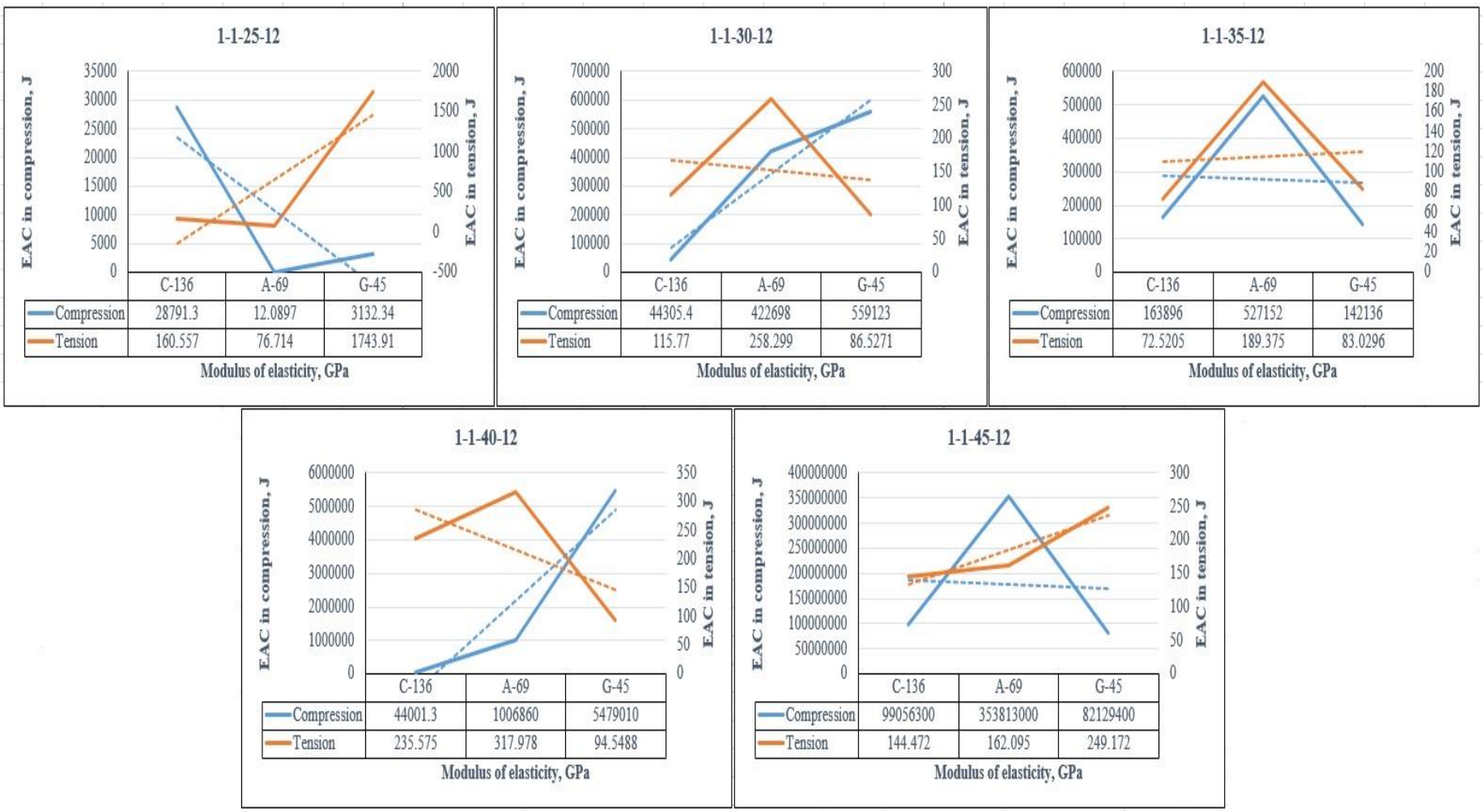

Figure 99: Effect of modulus of elasticity on energy absorption capacity of FRP RC beams under 320 kN impact load.

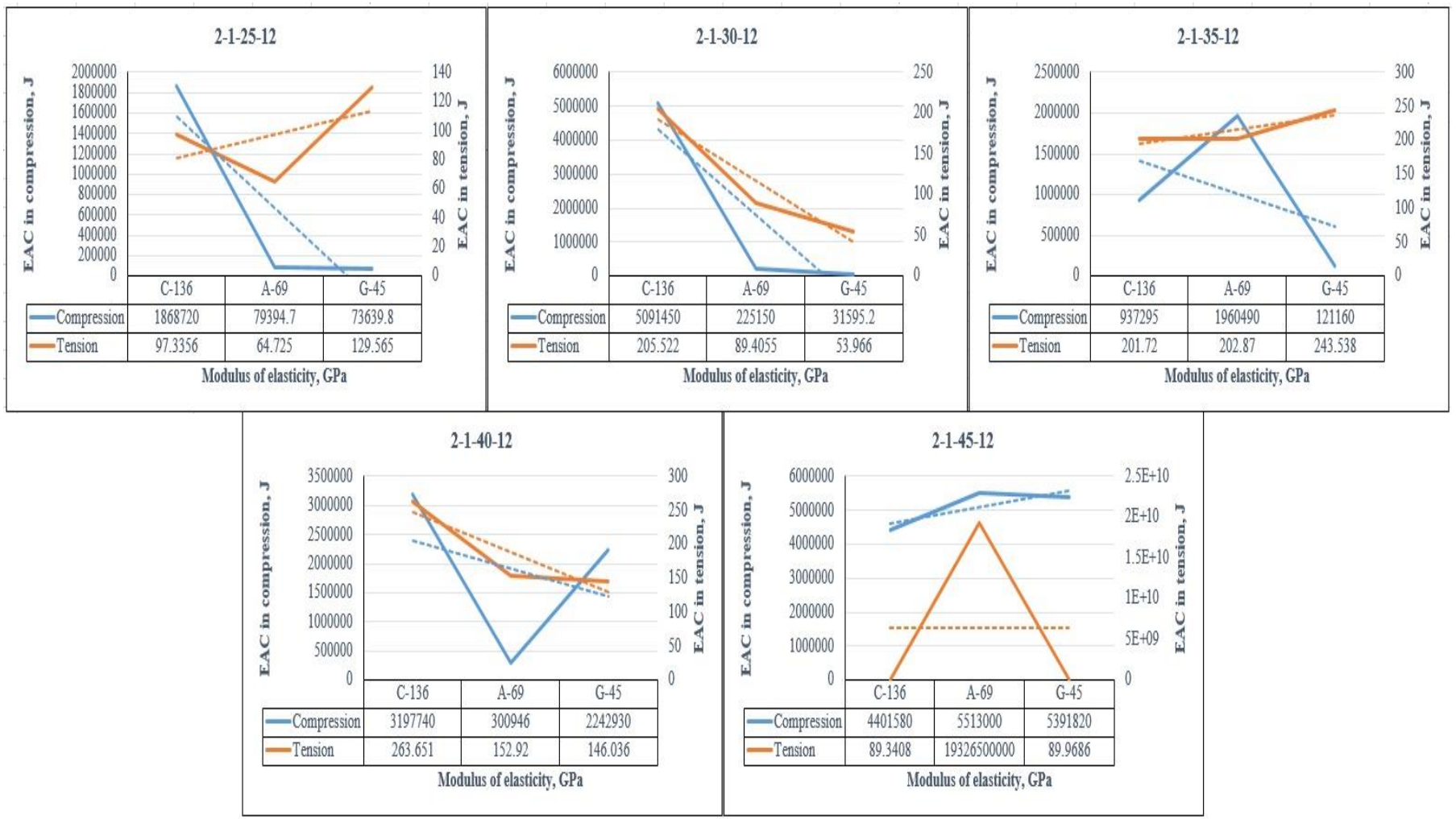

Figure 100: Effect of modulus of elasticity on energy absorption capacity of FRP RC beams under 80 kN impact load.

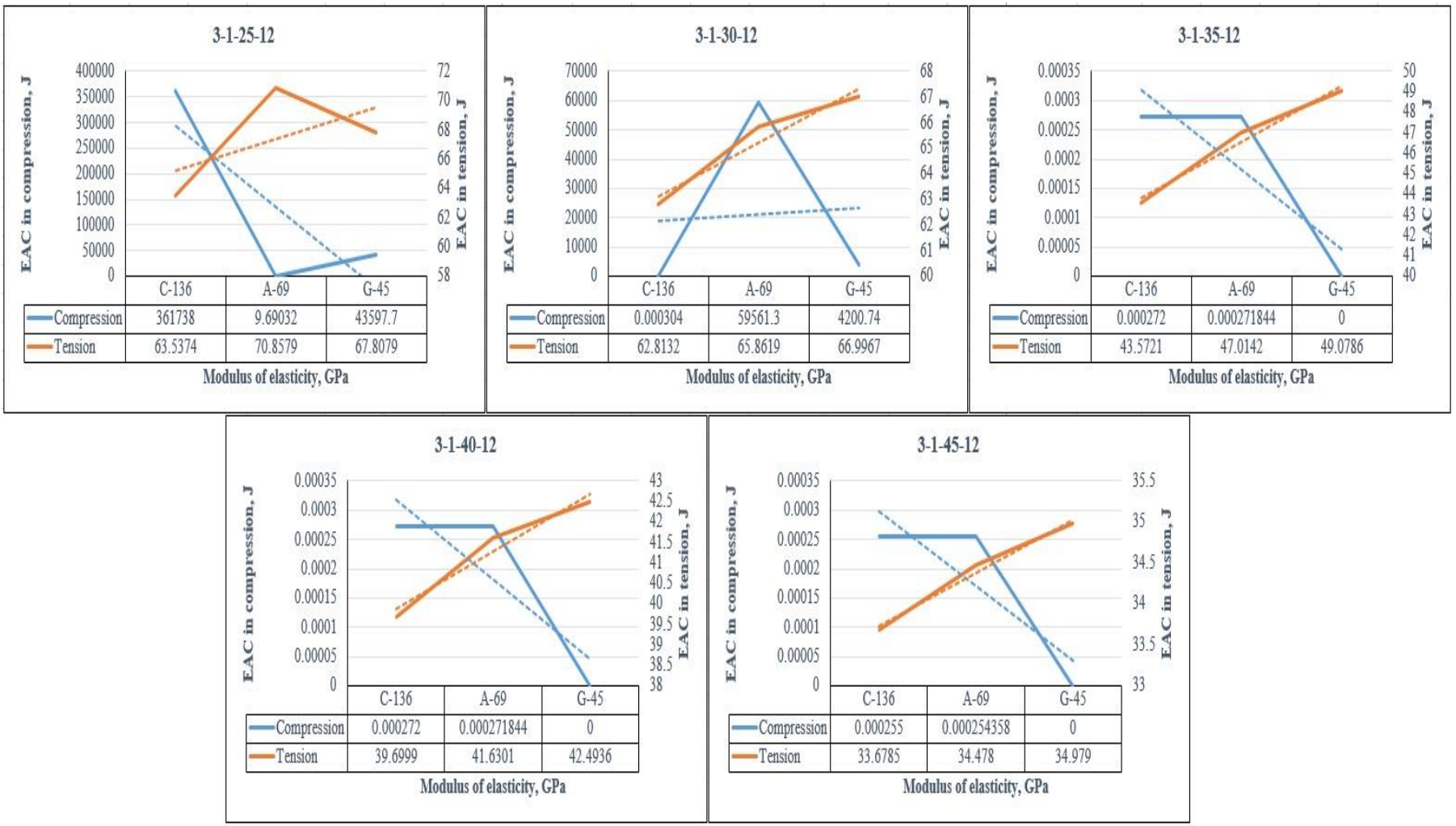

Figure 101: Effect of modulus of elasticity on energy absorption capacity of FRP RC beams under 40 kN impact load

The research encompassed a comprehensive parametric analysis involving a total of 225 models of GFRP, CFRP, and AFRP RC beam configurations, which were rigorously examined under high-velocity impact loads. This finite element-based parametric study was designed to systematically investigate the multifaceted interplay of various factors, including bar diameters, concrete compressive strength, elastic modulus of FRPs, and impact velocity, on the bond behaviour of FRP RC beam models and their overall response when subjected to dynamic impact loading conditions. The outcomes of this analysis yielded several noteworthy conclusions:

- Bar Diameter Influence: The findings revealed a substantial inverse relationship between bar diameter and average bond strength. Specifically, as the bar diameter increased, the bond strength exhibited a significant decrease. Furthermore, an increase in the ratio of concrete cover to bar diameter resulted in an average 20.45% increase in normalized bond strength. Notably, the predominant failure mode observed in FRP RC beams was pull-out failure, constituting approximately 77% of all failure modes, particularly in beams with smaller bar diameters. Debonding failure, on the other hand, accounted for approximately 23% of all failure modes.
- Concrete Compressive Strength: The study indicated that the maximum bond strength tended to increase with an escalation in concrete compressive strength. Nevertheless, in certain cases, a decrease in bond strength was observed, which could be attributed to an increase in the brittleness of the concrete matrix. Moreover, the maximum slip experienced by the beam models exhibited a significant reduction with an increase in concrete compressive strength. Pull-out failures were more commonly observed in beam models with concrete compressive strengths ranging from 25 MPa to 30 MPa, while debonding failures were prevalent in beam models with higher concrete compressive strengths, typically falling within the 35-45 MPa range.
- Modulus of Elasticity of FRP Bars: The ultimate load capacity of the beams was found to increase with a rise in the modulus of elasticity E_f of the FRP bars. Conversely, there was a discernible decrease in the ultimate mid-deflection of the beams with higher E_f values. Additionally, there was clear evidence of

an increase in maximum bond strength with an elevation in the E_f of the FRP bars.

- Impact Velocity: The increase in impact velocity had a substantial influence on various key parameters, including maximum mid-deflection, ultimate load, and the bond between FRP bars and the surrounding concrete. As the impact velocity increased, these parameters exhibited corresponding increases.

These findings collectively contribute valuable insights into the intricate dynamics governing the behaviour of FRP RC beams under high-velocity impact loads. Understanding the impact of factors such as bar diameter, concrete properties, FRP modulus of elasticity, and impact velocity is crucial for optimizing the design and performance of structures incorporating FRP RC beams subjected to dynamic loading conditions. This research enhances our knowledge of how these factors interact and influence the structural response, ultimately aiding in the development of more resilient and effective engineering solutions.

5.8 Advanced Regression Analysis and Formulation of Novel Equations for FRP RC Beam Responses to Impact Loads

In the previous section, a comprehensive database of 225 FRP RC beam models generated through finite element analysis was presented. The aim of this FEA was to examine the influence of various parameters, including concrete compressive strength, bar diameter, different types of FRPs, and impact loading, on the bond behaviour and peak mid-deflection of these beams. In this section, a generalized formula for FRP RC beams is proposed to estimate slip, maximum bond strength, and mid-deflection based on the data obtained from finite element analysis using ABAQUS software and ANOVA.

For the regression analysis, a three-way ANOVA statistical testing approach was selected, taking into account the numerous factors considered in the comprehensive ABAQUS models. Regression analysis is a widely used statistical method for analysing experimental or finite element data. ANOVA divides the observed variance into distinct groups, facilitating meaningful tests by comparing the means of these groups to determine whether there are statistically significant differences among them.

Regression analysis is a statistical technique commonly applied to explore the relationship between one or more independent variables and a dependent variable. By modelling this relationship using statistical methods, the goal is to predict the future state of the dependent variable. In cases involving multiple independent variables, it is referred to as multiple regression analysis. The mathematical formula that defines the relationship between dependent and independent variables is known as a regression model. A representation of a simple non-linear regression analysis can be found in Equation (5.1):

$$y = intercept + a_1 x_1 + a_2 x_2 + \cdots + a_n x_n + \varepsilon \quad (5.1)$$

In the context of regression analysis, the formula presented can be understood as follows: "y" represents the dependent variable being studied, "intercept" denotes

the point at which the regression line intersects the y-axis, "a" signifies the regression coefficient, "x" represents the value of the independent variable, and "ε" is the error term, accounting for the variability not explained by the regression model.

Figure (102) to (104) provides a visual representation of how various parameters, including concrete compressive strength, bar diameters, FRP rupture strength, and impact load, influence the slip between the FRP bar and the surrounding concrete beam in FRP RC beams. Each data point on the scatter plot corresponds to the maximum slip value observed for different types of FRP RC beams: (a) CFRP RC beams, (b) AFRP RC beams, and (c) GFRP RC beams.

Statistical significance is determined by comparing the observed results to a predefined threshold probability. If the calculated probability exceeds this threshold, the result is considered statistically significant, leading to the rejection of the null hypothesis. The null hypothesis, in this context, assumes that there are no effects of independent variables or study factors on the dependent variables, specifically the bond characteristics between the FRP bar and the concrete beam.

To differentiate between different levels of the assumed factors and reject the null hypothesis, a significance level of 0.05 was chosen for this analysis. Statistical analysis was performed using IBM SPSS Statistics (v27) to assess the significance of the observed effects.

In the realm of regression analysis, there are several key independent factors that are considered distinct variables. These factors encompass bar diameter, energy, concrete compressive strength, and FRP rupture strength. In order to facilitate a meaningful regression analysis, certain prerequisites must be met. Six specific assumptions have been delineated for this analysis.

The first assumption necessitates the presence of a single continuous dependent factor, and this condition is met as each analysis focuses solely on one dependent variable, such as slip, bond strength, or mid-span deflection. The second assumption calls for the inclusion of more than two independent variables, such as bar diameter. Additionally, impartiality of observations is required, which is assured by utilizing ABAQUS finite element results.

The treatment of outliers represents another assumption that must be satisfied. Furthermore, the dependent variables need to exhibit distribution characteristics for each set of independent variables. The final assumption entails an examination of the homogeneity of variances.

To address the issue of non-homogeneous variances, the Welch's version of ANOVA is employed in this analysis. This approach renders the analysis meaningful even in cases where the assumption of homogeneity of variances is not strictly met. This approach is deemed suitable for the dataset used in this study, particularly when dealing with large sample sizes.

Due to constraints such as limited variables provided by the finite element method (e.g., not all concrete compressive strength values are available) and time limitations, the analysis matrix may contain some empty cells, indicating that not every possible combination was tested. Additionally, the statistical analysis yields a moderate determination coefficient denoted as R^2 . This value represents the percentage of variation in the dependent factor (e.g., slip) that can be attributed to the involved parameters and their interactions.

The statistical regression analysis adheres to the following methodology: initially, all factorial statistical analyses, encompassing main factors and their interactions, are conducted. Subsequently, the analysis of significance levels commences with the examination of three-way interactions. Any interaction that does not exhibit statistical significance is excluded from the model. If a multi-way interaction is deemed significant, all interactions are incorporated into the model. Finally, the results are summarized and analysed.

Based on this explained methodology, the statistical analysis encompasses the results and equations pertaining to slip, bond strength, and mid-span deflection. Moreover, coefficients for each variable are provided, enabling the calculation of these aforementioned factors.

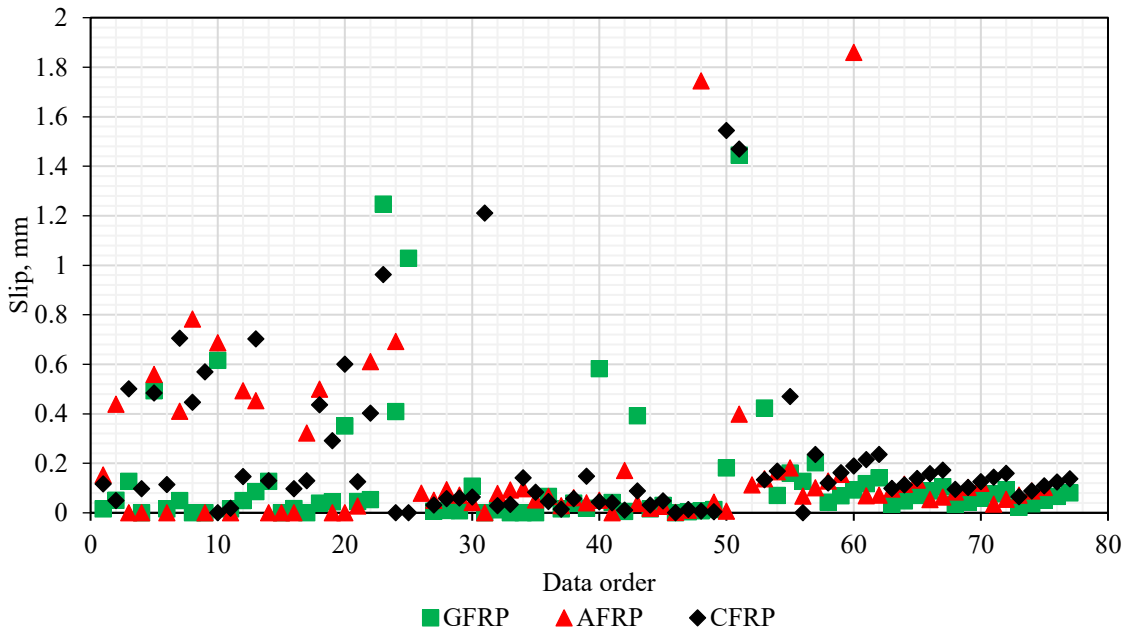

Figure 102: Effect of parameter studies on slip between (a) CFRP RC beams, (b) AFRP RC beams, and (c) GFRP RC beams.

Table (34) and (35) present the outcomes of the regression analysis based on transformed data related to the slip occurring between the FRP bars and concrete beams. These tables provide various statistical parameters that help in the interpretation of the regression results.

Regression df (Degrees of Freedom): This metric indicates the number of independent variables involved in the regression analysis.

Residual df (Degrees of Freedom): It denotes the total number of observations within the dataset minus the estimated variables.

SS (Sum of Squares): This value represents the sum of squares, which quantifies the difference between the actual observations and the predictions made by the regression model.

MS (Mean Square): Mean Square is a measure of the variability in the data. It's calculated by dividing the Sum of Squares, SS by the corresponding degrees of freedom f .

F (F-statistic): The F-value is a test statistic that assesses the overall significance of the regression model. It is computed by dividing the Regression Mean Square, MS by the Residual, MS.

Significance F (F-statistic p-value): This is the p-value associated with the F-statistic. It tests the hypothesis that the coefficients of the independent variables are all equal to zero. A p-value less than 0.05 indicates that there is a 95% confidence that the regression line has a non-zero slope, implying a linear relationship between the dependent and independent variables. On the other hand, a p-value greater than 0.05 suggests that there is insufficient evidence to establish a linear relationship.

t-Stat (t-Statistic): This statistic assesses the significance of individual coefficients (independent variables) within the regression model.

Standard Errors: These values indicate the probable standard deviation of the distribution of coefficients' deviations from their mean values.

In essence, these statistical metrics provide valuable insights into the significance and reliability of the regression model, helping researchers determine the strength and nature of the relationships between dependent and independent variables.

	df	SS	MS	F	Significance F
Regression	4	0.00217	0.00037	7.586	5.16402E-05
Residual	67	0.00455	6.119E-05		
Total	71	0.00628	—		

Table 34: ANOVA statistical test results of transformed data.

	Coefficients	Standard Errors	t Stat	P-value	Lower 95%	Upper 95%	Lower 95%	Upper 95%
Intercept	4.33E-02	1.86E-02	5.10E+00	4.99E-02	6.22E-03	8.03E-02	6.22E-03	8.03E-02
α	-5.56E-06	5.09E-06	-2.39E+00	6.10E-01	-1.57E-05	4.60E-06	-1.57E-05	4.60E-06
β	-1.07E-05	1.99E-06	-1.17E+01	2.43E-06	-1.47E-05	-6.71E-06	-1.47E-05	-6.71E-06
γ	-9.99E-05	2.45E-04	-8.93E-01	1.50	-5.89E-04	3.89E-04	-5.89E-04	3.89E-04
ω	-2.26E-03	1.24E-03	-4.00E+00	1.59E-01	-4.73E-03	2.12E-04	-4.73E-03	2.12E-04

Table 35: ANOVA test results of transformed data on Slip.

The "intercept" signifies the point at which the linear regression line intersects the Y-axis when the value of X is equal to zero. In Table (35), you can find the coefficients denoted as α for FRP rupture strength, β for energy, γ for concrete compressive strength, and ω for bar diameters. The coefficient of determination, represented as R^2 , is calculated to be 0.813, indicating that approximately 81.3% of the variation in slip can be attributed to the factors considered.

The equation (5.1) encapsulates the influence of these mentioned parameters, allowing for the calculation of slip. It provides a quantitative representation of how these factors collectively affect the slip behaviour in the given context.

$$s = Intercept + \alpha f_{r,frp} + \beta E_{frp} + \gamma f_c' + \omega d_b \quad (5.1)$$

Figure (103) illustrates the impact of various parameters such as concrete compressive strength, bar diameters, FRP rupture strength, and impact load on the bond strength of FRP RC beams. Each bar within the chart represents the maximum reaction force observed for (a) CFRP RC beams, (b) AFRP RC beams, and (C) GFRP RC

beams. This graphical representation provides insights into how these factors influence the bond strength of the different types of FRP RC beams.

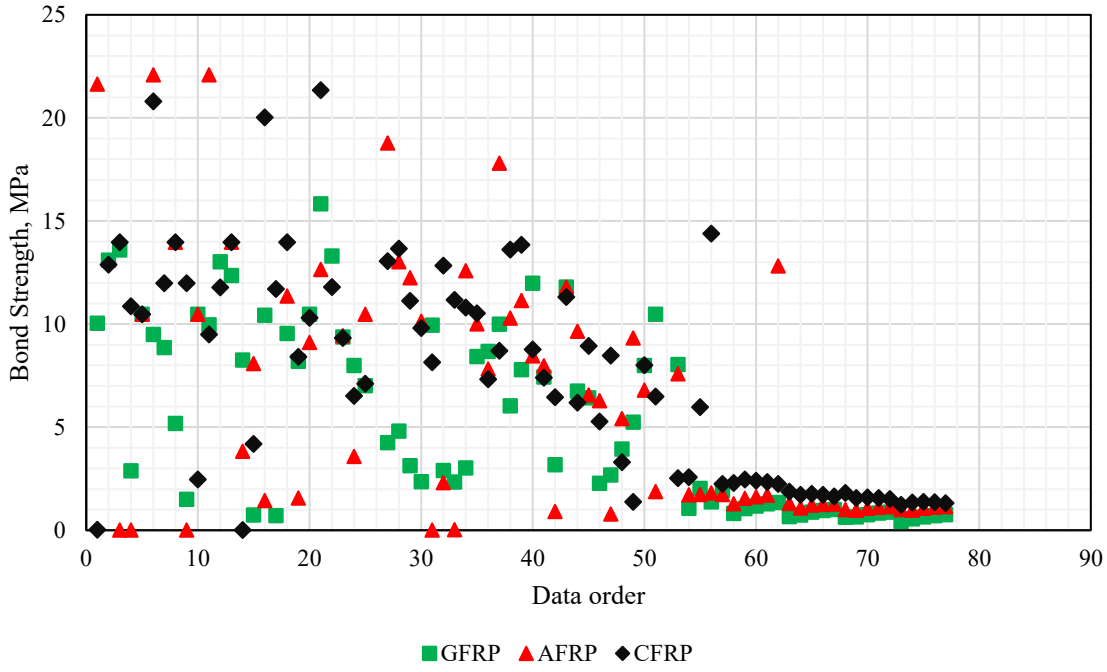

Figure 103: Effect of parameters on reaction force for (a) CFRP RC beams, (b) AFRP RC beams, and (c) GFRP RC beams.

Conducting regression on the transformed datasets allows us to assess the impact of specific parameters on the reaction force exhibited by FRP RC beams. The outcomes of these regression analysis are presented in Table (36) and (37), which provide valuable statistical insights into the relationship between the examined parameters and the reaction force of FRP RC beams. Equation (5.2) offers a means to calculate the reaction force for FRP RC beams based on the parameter variables and coefficients derived from Table (37).

	df	SS	MS	F	Significance F
Regression	4	1.200E+14	2.999E+13	0.6215	0.3465
Residual	60	2.083E+15	3.472E+13		
Total	64	2.203E+15	—		

Table 36: ANOVA statistical test results of transformed data.

	Coefficients	Standard Errors	t Stat	P-value	Lower 95%	Upper 95%
Intercept	-868185.071	609843.577	-0.830	0.093	-2088053.851	351683.708
a	1.793	188.817	0.006	0.579	-375.897	379.484
b	56.215	77.153	0.425	0.273	-98.114	210.545
c	11122.467	8440.436	0.768	0.112	-5760.918	28005.852
d	50227.616	40435.128	0.724	0.128	-30654.682	131109.914

Table 37: ANOVA test results of transformed data on bond strength

$$\tau = Intercept + af_{r,frp} + bE_{frp} + cf_c' + d.d_b \quad (5.2)$$

The coefficient of determination, denoted as R^2, is calculated to be 0.72, indicating that it accounts for approximately 72.4% of the variation in the reaction force. Figure (104) illustrates the impact of various parameters, including concrete compressive strength, bar diameters, FRP rupture strength, and impact load, on the mid-span deflection of FRP RC beams. Each column in the figure represents the maximum mid-span deflection for (a) CFRP RC beams, (b) AFRP RC beams, and (c) GFRP RC beams.

The application of ANOVA tests to the transformed datasets reveals the influence of the specified parameters on the mid-span deflection of FRP RC beams. Table (38) and (39) present the coefficients that correspond to the studied parameters based on the results of the ANOVA statistical test. Equation (5.3) provides a means to calculate the mid-span deflection for FRP RC beams, taking into account the parameter variables and coefficients derived from Table (39). The coefficient of determination for this analysis, denoted as R^2, has a value of 0.734, signifying that it explains approximately 73.4% of the variation in mid-deflection.

$$\delta_{mid} = Intercept + zf_{r,frp} + kE_{frp} + uf_c' + wd_b \quad (5.3)$$

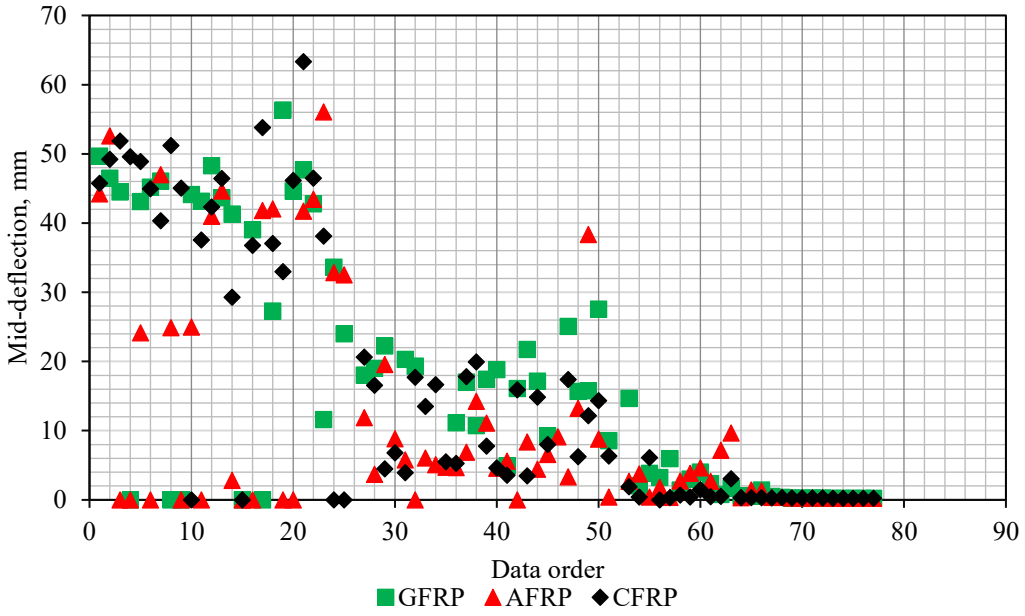

Figure 104: Effect of parameters on mid-deflection of (a) CFRP RC beams, (b) AFRP RC beams, and (c) GFRP RC beams.

	df	SS	MS	F	Significance F
Regression	4	0.2965	0.0741	3.05346	0.005912
Residual	51	0.9660	0.0189		
Total	55	1.2625	—		

Table 38: ANOVA statistical test results of transformed data.

	Coefficients	Standard Errors	t Stat	P-value	Lower 95%	Upper 95%
Intercept	-0.67279	0.3021	-3.6359	-3.6359	-1.2793	-0.06626
z	0.00016	8.9903E-05	2.8777	2.8777	-2.203E-05	0.00034
k	-0.00017	6.3103E-05	-4.4476	-4.4476	-0.00030	-4.522E-05
u	0.00759	0.0042	2.9512	2.9512	-0.00084	0.01602
w	0.02135	0.0206	1.6890	1.6890	-0.02009	0.06279

Table 39: ANOVA test results of transformed data on mid span deflection.

5.8.1 Accuracy of regression analysis for different parameters

The objective of this analysis was to evaluate the predictive capabilities of the regression models developed in this study. These models aimed to estimate various critical factors in the behaviour of FRP RC beams, including slip, bond strength, and mid-span deflection, under different conditions. To assess the accuracy of these models, a comprehensive comparison was conducted by applying them to six distinct beam models, each characterized by specific parameters detailed in Table (40).

Beam Name	*FRP Type*	d_b, mm	f_c', MPa	*Load, kN*
C-13-50	Carbon	13	50	70
C-13-60	Carbon	13	60	70
C-18-50	Carbon	18	50	70
C-18-60	Carbon	18	60	70
C-20-50	Carbon	20	50	70
C-20-60	Carbon	20	60	70

Table 40: Detail of finite element beam models.

Upon scrutinizing the data collected from this comparative analysis, a notable trend emerged. The results obtained from ABAQUS simulations exhibited a strong concordance with the predictions generated by the regression models. This suggests that the regression models were effective in capturing the underlying relationships between the input parameters and the desired output variables. In essence, the regression models provided estimations that closely mirrored the outcomes obtained through detailed finite element simulations.

In contrast, when the machine learning-based predictions were contrasted with the results derived from the ACI (American Concrete Institute) code, some differences became apparent. Specifically, the estimations based on the ACI code tended to yield lower values when compared to the corresponding machine learning predictions. This phenomenon indicates that the ACI code generally takes a more conservative approach when forecasting the behaviour of FRP RC beams under various conditions.

This conservatism can be advantageous in ensuring the safety and reliability of structural designs.

A more granular analysis of the data revealed valuable insights. The regression models demonstrated an approximate 73% level of agreement with the ABAQUS dataset. This percentage signifies a robust alignment between the predictions generated by the regression models and the outcomes obtained through rigorous finite element simulations, highlighting the models' capacity to accurately predict the behavior of FRP RC beams.

Additionally, there was a 66% correspondence observed between the regression model predictions and the ACI code. While this alignment is slightly lower than the agreement with the ABAQUS dataset, it still signifies a meaningful level of congruence. It's important to note that the ACI code, being a well-established industry standard, tends to prioritize safety by providing conservative estimates.

To visually represent these comparative findings, Figure (105) was created. This figure serves as a graphical depiction of the disparities and agreements across the results for slip, bond strength, and mid-span deflection, providing a clear overview of the performance of the regression models in relation to ABAQUS simulations and ACI code predictions.

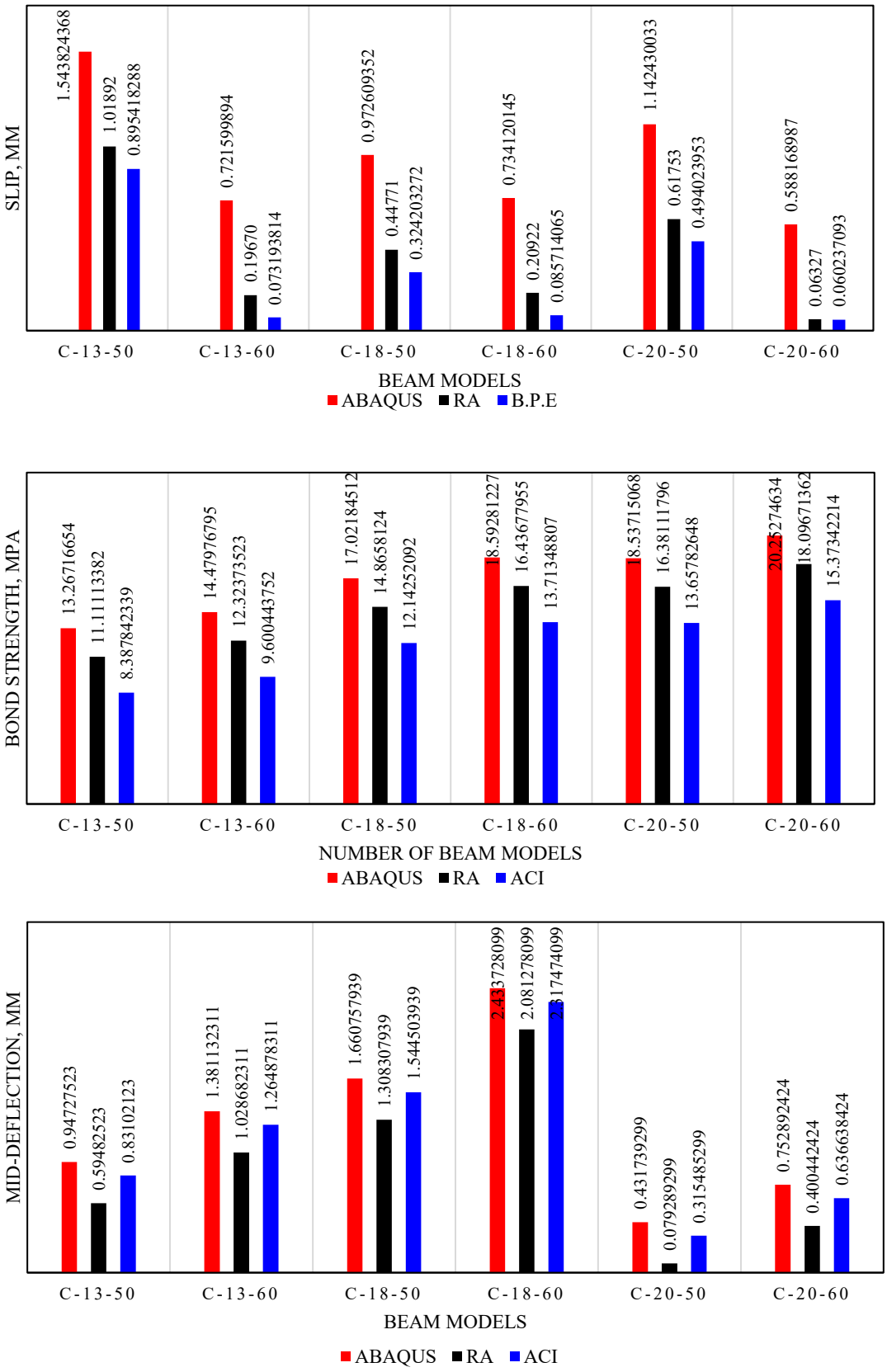

Figure 105: Comparison of estimated values from regression analysis modes, ABAQUS analysis, and existing codes.

5.9 Conclusion:

The primary focus of this study was to investigate the impact of high-velocity loading on the bond behaviour of Fiber Reinforced Polymer Reinforced Concrete (FRP RC) beams. To comprehensively explore this phenomenon, a set of diverse parameters were considered, including bar diameter (ranging from 10 mm to 16 mm), concrete compressive strength (ranging from 25 MPa to 45 MPa), FRP rupture strength (with values of 947 MPa, 1400 MPa, and 1890 MPa), and kinetic energy (ranging from 600 joules to 3200 joules). This extensive array of parameters resulted in the analysis of a total of 225 distinct beam models. The selection of these parameters was informed by previous experimental studies documented in the literature, ensuring that the study aligned with established research in the field.

The research methodology involved the development and calibration of both static and dynamic models in ABAQUS, a finite element analysis software. These models served as a computational framework to simulate the behaviour of FRP RC beams under high-velocity impact conditions. The calibration process involved fine-tuning the models to ensure they accurately represented real-world scenarios. Methodological aspects, including model construction and the interpretation of results, were discussed in depth to provide a comprehensive understanding of the study's approach.

The statistical analysis employed in this study involved the use of Analysis of Variance (ANOVA) to assess the statistical significance of various parameters on the factors of interest, namely slip, reaction force, and mid-deflection. Multi-way ANOVA was the chosen statistical tool for this purpose, allowing for the examination of interactions between different parameters and their collective impact on the observed outcomes.

The study yielded several key findings and conclusions:

- Despite some inherent variability in the results, the analysis demonstrated a high level of accuracy, as indicated by the coefficient of determinationR^2. This

metric, which quantifies the goodness of fit of the models, provided assurance of the reliability of the study's findings.

- The statistical analysis confirmed the significant influence of bar diameter, energy input, concrete compressive strength, and FRP rupture strength on the bond behaviour of FRP RC beams. Furthermore, it identified and validated the interactions among these parameters, emphasizing their combined impact on the observed outcomes.

- The research culminated in the proposal of specific values for parameters α, β, γ, and ω within the regression models. These parameter values serve as the basis for calculating slip, reaction force, and mid-deflection in FRP RC beams. These equations provide valuable tools for engineers and researchers to predict and analyse the behaviour of FRP RC beams under high-velocity impact conditions.

In summary, this study advanced our understanding of the bond behaviour of FRP RC beams subjected to high-velocity loading. Through rigorous computational modelling, statistical analysis, and the development of predictive equations, it provided valuable insights into the complex interplay of parameters affecting FRP RC beam behaviour under such extreme conditions.

Chapter 6: Dynamic Increase Factor (DIF) Development and Enhancement of Flexural Capacity Assessment

6.1 Introduction

Chapter 2 introduced the concept of the Dynamic Increase Factor (DIF). This chapter delves deeper into the topic by focusing on the practical application of a finite element framework. The aim is to assess how high strain rates impact the DIF values of CFRP, AFRP, and GFRP RC beams, and how these changes affect the flexural capacity of FRP RC beams.

After the introduction, the chapter provides a comprehensive overview of DIF and outlines the design flexure guidelines as specified by ACI. To investigate the impact of dynamic strain rate effects on DIF values for FRP RC beams, a finite element model implemented in ABAQUS is selected as the analytical tool. The discussion revolves around the intricacies of high strain rate loading conditions and the factors influencing the bond between the FRP reinforcement and the concrete interface.

6.2 DIF and flexural moment

In the context of structures constructed with concrete materials exposed to dynamic or blast loading conditions, there is often a need to understand their response under extreme strain rates, which can reach values as high as $10^4/s$. Notably, it has been observed that concrete exhibits a significant increase in strength when subjected to such extreme high strain rates. This phenomenon is quantified by the dynamic increase factor (DIF), which represents the ratio of the material's dynamic strength to its static strength.

Existing experimental research has elucidated that the DIF is dependent on the applied strain rate, as supported by various studies [289] [268] [290]. However, the mechanisms underlying the experimentally determined DIF values continue to be a subject of ongoing debate. The central question revolves around whether the DIF

should be regarded as an intrinsic material property. It is worth noting that the CEB-FIP code has categorized the DIF as a material property. Nevertheless, current consensus suggests that, especially under uniaxial compression conditions, the DIF should be considered not as an inherent material property but rather as a dynamic structural effect.

Recent research studies have provided substantial evidence that the phenomenon of inertia-induced radial confinement exerts a significant influence on the enhancement of dynamic compressive strength [268] [291] [292]. When subjected to a high compressive stress pulse, the concrete specimen expands in the radial direction, generating a radial inertia force equivalent to a confining stress. This radial inertia force subsequently contributes to an increase in the axial compressive strength of the concrete. Consequently, there is an ongoing debate regarding whether the dynamic increase factor (DIF) for concrete under compression should be incorporated into the material's constitutive model or simply set to unity for material models employing DIF in finite element analyses.

Conversely, the direction of the inertia-induced radial force changes when concrete is subjected to tension. Furthermore, the impact of inertia stress on axial tensile strength differs significantly from the effect of confining stress on axial compressive strength, with tensile failure in concrete being more localized compared to compressive failure. Additionally, experimental findings have indicated that the DIF for tension can be notably higher than that for compression at the same applied strain rate.

The study conducted by [293] has indicated that the DIF observed in dynamic tensile tests, affecting tensile strength, is a material-related effect closely tied to factors such as inertia effects, the Steff effect at the crack tip, and structural responses at the macroscopic level. Moreover, the numerical model developed by [276] supports the consideration of DIF as a material-related effect. Furthermore, certain empirical investigations involving tensile Split Hopkinson Pressure Bar (SHPB) tests have suggested that it is reasonable to incorporate DIF values for dynamic tensile strength

into the material properties when analysing scenarios where tension plays a predominant role, [294] [295].

Recently, finite element models incorporating local concrete models have become increasingly prevalent in the investigation of dynamic concrete behaviour, [296]. This research highlighted that the direct application of DIF-strain relationships from previous experiments to define dynamic properties of concrete is not feasible. Instead, a parametric regression approach relating DIF to strain rate is deemed necessary. Sallier [297] employed the Hillerborg regularization technique to simulate the softening behaviour of concrete subjected to dynamic tensile loading. Although this method proved effective in reducing mesh size dependency in quasi-static loading scenarios, it was observed that it could not mitigate the impact of mesh size on concrete structures under dynamic loading conditions.

This chapter is dedicated to finding an appropriate approach for incorporating both compression and tension DIF values within a general finite element framework employing a local concrete model. Following this introduction, a comprehensive overview of the general relationship between DIF and strain rate for both compression and tension is presented.

Figures (106) and (107) depict experimental data from concrete compression and tension Split Hopkinson Pressure Bar (SHPB) tests, illustrating the relationship between DIF and strain rate. It is crucial to note that DIF represents the ratio between dynamic concrete strength and static concrete strength. However, concrete strength is influenced by test methods and specimen scale effects, rendering the data presented in Figures (106) and (107) highly case-specific. Particularly at high strain rates, specimens may not reach a stress equilibrium state, potentially explaining the variability observed in the DIF-strain rate relationship. Nevertheless, it can be largely concluded that empirical formulas based on regression analysis provide a more reliable representation of the DIF.

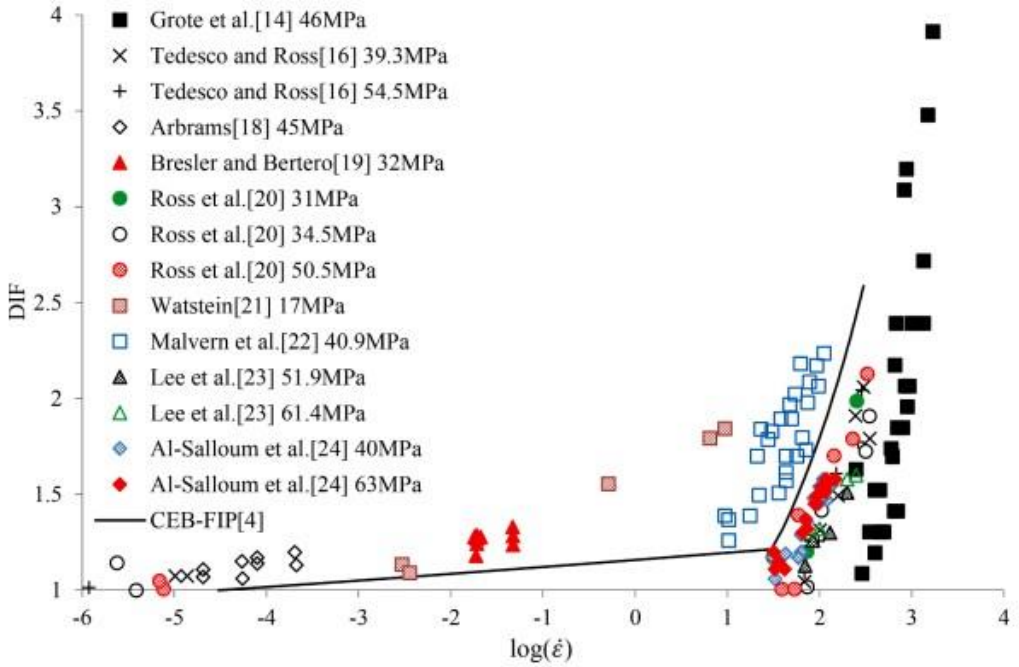

Figure 106: Compressive DIF vs. strain rate relationship based on SHPB compressive test data collections.

Table (41) and (42) compile a comprehensive set of existing curves representing the relationship between DIF and strain rate for concrete under both compression and tension. Among these relationships, the DIF strain rate curve defined by CEB-FIP stands out as the most commonly employed one for assessing the dynamic behaviour of concrete structures.

In this chapter, the DIF strain rate curve recommended by CEB-FIP is adopted as the appropriate basis for establishing compressive and tensile DIF and strain relationships. When employing finite element models with local concrete damage models, the primary focus should be on ensuring the congruence between the finite element outputs and the selected DIF empirical formulas derived from regression analysis, rather than being overly reliant on any specific set of analytical data.

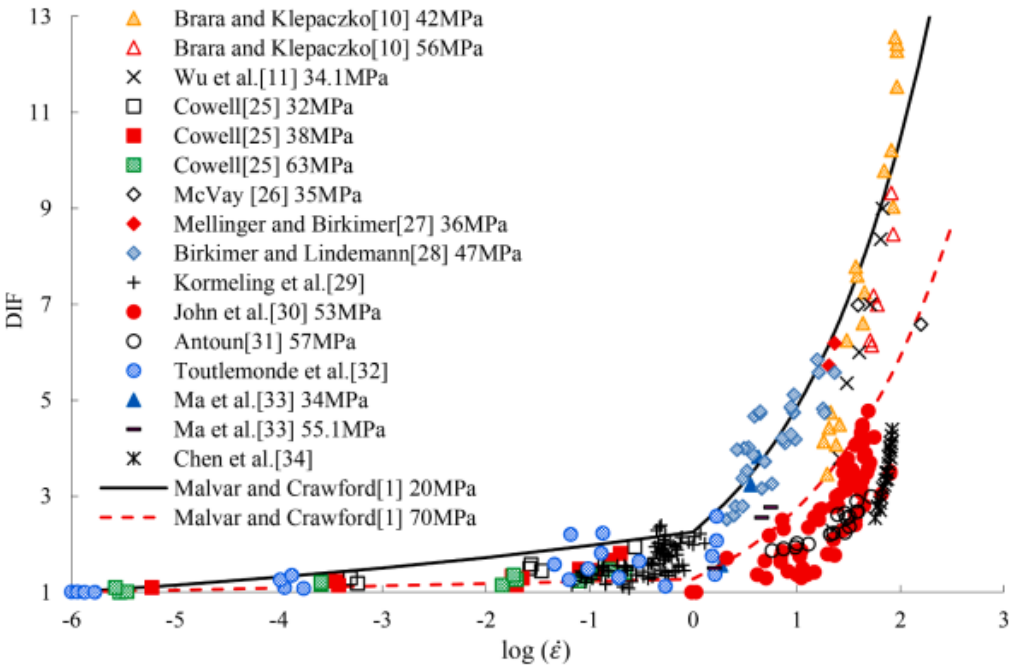

Figure 107: Tensile DIF vs. strain rate relationship based on SHPB tensile test data collections

References	Formulas	Remarks
Tedesco and Ross	$DIF = 1 + 0.1425(log\dot{\varepsilon} + 5.8456) \geq 1\ \dot{\varepsilon} \leq 2.32\ s^{-1}$ $DIF = 1 + 2.929(log\dot{\varepsilon} - 0.0635) \leq 6\ \dot{\varepsilon} > 2.32\ s^{-1}$	
Lu and Xu	$DIF = 1 + 1.505\dot{\varepsilon}^{0.295}$	
CEB-FIP	$DIF = \left(\frac{\dot{\varepsilon}}{\dot{\varepsilon}_s}\right)^{0.018} \quad \dot{\varepsilon}_s \leq \dot{\varepsilon} \leq 10\ s^{-1}$ $DIF = 0.0062\left(\frac{\dot{\varepsilon}}{\dot{\varepsilon}_s}\right)^{0.33} \quad \dot{\varepsilon} > 10\ s^{-1}$	$\dot{\varepsilon}_s = 1 \times 10^{-6} s^{-1}$
CEB Model Code	$DIF = \left(\frac{\dot{\varepsilon}}{\dot{\varepsilon}_s}\right)^{1.016\alpha_s} \quad \dot{\varepsilon}_s \leq \dot{\varepsilon} \leq 30\ s^{-1}$ $DIF = \gamma_s\left(\frac{\dot{\varepsilon}}{\dot{\varepsilon}_s}\right)^{0.33} \quad \dot{\varepsilon} > 30\ s^{-1}$	$\gamma_s = 10^{(7.11\alpha_s - 2.33)}$ $\alpha_s = 1/(10 + 6f_c'/f_{co})$ $\dot{\varepsilon}_s = 3 \times 10^{-6} s^{-1}$ $f_{co} = 10$ MPa
Malvar and Crawford	$DIF = \left(\frac{\dot{\varepsilon}}{\dot{\varepsilon}_s}\right)^{\alpha_s} \quad \dot{\varepsilon}_s \leq \dot{\varepsilon} \leq 1\ s^{-1}$ (2a) $DIF = \gamma_s\left(\frac{\dot{\varepsilon}}{\dot{\varepsilon}_s}\right)^{0.33} \quad \dot{\varepsilon} > 1\ s^{-1}$ (2b)	$\alpha_s = 1/(1 + 8f_c'/f_{co})$ $\gamma_s = 10^{6\alpha_s - 2}$ $\dot{\varepsilon}_s = 1 \times 10^{-6} s^{-1}$

Table 41: DIF- Strain rate formulas for concrete in tension.

References	Formulas	Remarks
Grote et al.	$DIF = 0.0235log\dot{\varepsilon} + 1.07\ \dot{\varepsilon} \leq 266s^{-1}$ $DIF = 0.882(log\dot{\varepsilon})^3 - 4.4(log\dot{\varepsilon})^2 + 7.22log\dot{\varepsilon} - 2.64\ \dot{\varepsilon} > 266s^{-1}$	
Tedesco and Ross	$DIF = 0.00965log\dot{\varepsilon} + 1.058 \geq 1.0\ \dot{\varepsilon} \leq 63.1\ s^{-1}$ $DIF = 0.758log\dot{\varepsilon} - 0.289 \leq 2.5\ \dot{\varepsilon} > 63.1\ s^{-1}$	
Li and Meng	$DIF = 0.03438(log\dot{\varepsilon} + 3) + 1\ \dot{\varepsilon} \leq 100s^{-1}$ $DIF = 1.729(log\dot{\varepsilon})^2 - 7.1372log\dot{\varepsilon} + 8.5303\ \dot{\varepsilon} > 100s^{-1}$	
Al-Salloum et al.	$DIF = (3.54\dot{\varepsilon} + 430.6)/(\dot{\varepsilon} + 447.3)$	
Lu and Xu	$DIF = 1 + 0.15\dot{\varepsilon}^{0.2} + 0.0013\dot{\varepsilon}^{0.2}$	
Ngo et al.	$DIF = \left(\frac{\dot{\varepsilon}}{\dot{\varepsilon}_s}\right)^{1.026\alpha}\ \dot{\varepsilon} \leq \dot{\varepsilon}_1$ $DIF = A_1 \ln\dot{\varepsilon} - A_2\dot{\varepsilon}\ > \dot{\varepsilon}_1$	$\dot{\varepsilon}_s = 3 \times 10^{-5}s^{-1}$ $\alpha = 1/(20 + f'_c/2)$ $\dot{\varepsilon}_1 = 0.0022f_c'^2 - 0.1989f'_c + 46.137$ $A_1 = -0.0044f'_c + 0.9866$ $A_2 = -0.0128f'_c + 2.1396$
CEB-FIP	$DIF = \left(\frac{\dot{\varepsilon}}{\dot{\varepsilon}_c}\right)^{0.014}\ \dot{\varepsilon} \leq 30s^{-1}$ (1a) $DIF = 0.012\left(\frac{\dot{\varepsilon}}{\dot{\varepsilon}_c}\right)^{\frac{1}{3}}\ \dot{\varepsilon} > 30s^{-1}$ (1b)	$\dot{\varepsilon}_c = 3 \times 10^{-5}s^{-1}$

Table 42: DIF- Strain rate formulas for concrete in compression.

As mentioned, both tensile and compressive strength of concrete are rate dependent, a relationship that provides the increase in concrete strength based on strain rate is provided, [298] [299] [300].

$$\frac{f_{c,d}}{f_{c,s}} = \begin{cases} \left(\frac{\dot{\varepsilon}}{30\times10^{-6}}\right)^{0.014}, & \dot{\varepsilon} \leq 30/s \\ 0.012\left(\frac{\dot{\varepsilon}}{30\times10^{-6}}\right)^{1/3}, & 30/s \leq \dot{\varepsilon} \leq 300/s \end{cases} \quad (6.1)$$

$$\frac{f_{t,d}}{f_{t,s}} = \begin{cases} \left(\frac{\dot{\varepsilon}}{1\times10^{-6}}\right)^{0.018}, & \dot{\varepsilon} \leq 10/s \\ 0.0062\left(\frac{\dot{\varepsilon}}{1\times10^{-6}}\right)^{1/3}, & 10/s \leq \dot{\varepsilon} \leq 300/s \end{cases} \quad (6.2)$$

As previously discussed in the literature review, the CEB, [299] proposed DIF (Dynamic Increase Factor) curves and equations for both compression and tension subjected to high strain rate loading conditions. In this research, we aim to determine the DIF values based on the outcomes of finite element analysis. To achieve this, we will employ the DIF formula advocated by Yandizo, [301], as outlined below:

$$DIF = \sigma_{dm}/\sigma_m \tag{6.3}$$

In the provided formula σ_{dm} represents the dynamic maximum stress experienced at a specific strain rate, while σ_m signifies the maximum stress observed under static conditions. Previous experimental investigations on DIF and its incorporation into the strain rate effect primarily focused on establishing the relationship between the standard global DIF and strain rate based on stress-wave time histories, with the aim of deriving local DIF values. Consequently, these findings are rooted in the collective behaviour of structural members.

Finite element modelling offers a distinct advantage in addressing the concept of localization, allowing for a more detailed exploration of structural behaviours. The rationale behind adopting the aforementioned formula lies in its capacity to determine DIF values based on stress-wave time histories obtained from finite element analyses conducted on FRP RC beam models exposed to high strain rate loading conditions. This approach facilitates a more explicit examination of the behaviour at the interface between the FRP bars and concrete.

According to the ACI reports, [44] the design approach for the flexural behaviour of FRP RC (Fiber-Reinforced Polymer Reinforced Concrete) members is akin to that applied for concrete members reinforced with steel. It is a common practice in structural engineering to under-reinforce steel-reinforced concrete members. This approach ensures that the steel reinforcement yields prior to the concrete crushing, thereby providing ductility to the member. In essence, it serves as an early warning system for potential failure. However, when it comes to FRP reinforcement, a more nuanced approach to flexural design is warranted.

FRP reinforcements exhibit brittleness, and therefore, the conventional under-reinforcement strategy needs re-evaluation. FRP RC members can undergo two primary modes of failure: FRP rupture and concrete crushing failure. In cases where FRP reinforcement ruptures, the failure is sudden and catastrophic. In contrast, for flexural members reinforced with FRP bars, concrete crushing failure is a more favourable outcome. This is because flexural members typically display a degree of plasticity behaviour just before failure.

The evaluation of the ultimate moment in an FRP RC beam is conducted through force equilibrium considerations and adheres to certain assumptions, [44]:

- The maximum compressive strain of concrete is assumed to be equal 0.003;
- There is a proportion between strain in the concrete and the FRP to the distance from the neutral axis;
- The concrete tensile strength is neglected;
- The perfect bond assumed between interface of FRP and concrete; and
- The FRP reinforcement tensile behaviour acts linearly elastic until failure.

The ultimate flexural strength of an FRP RC member can be calculated established on internal force and strain equilibrium, and specifying the failure mode.

Figure (108) shows stress-strain and internal forces for FRP RC beam in three different failures.

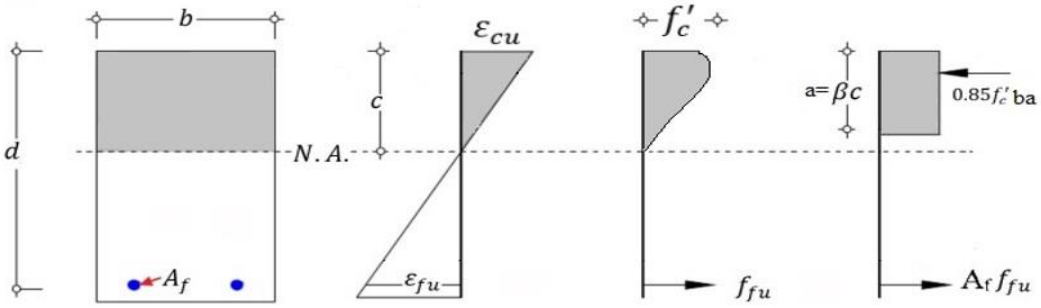

(a)

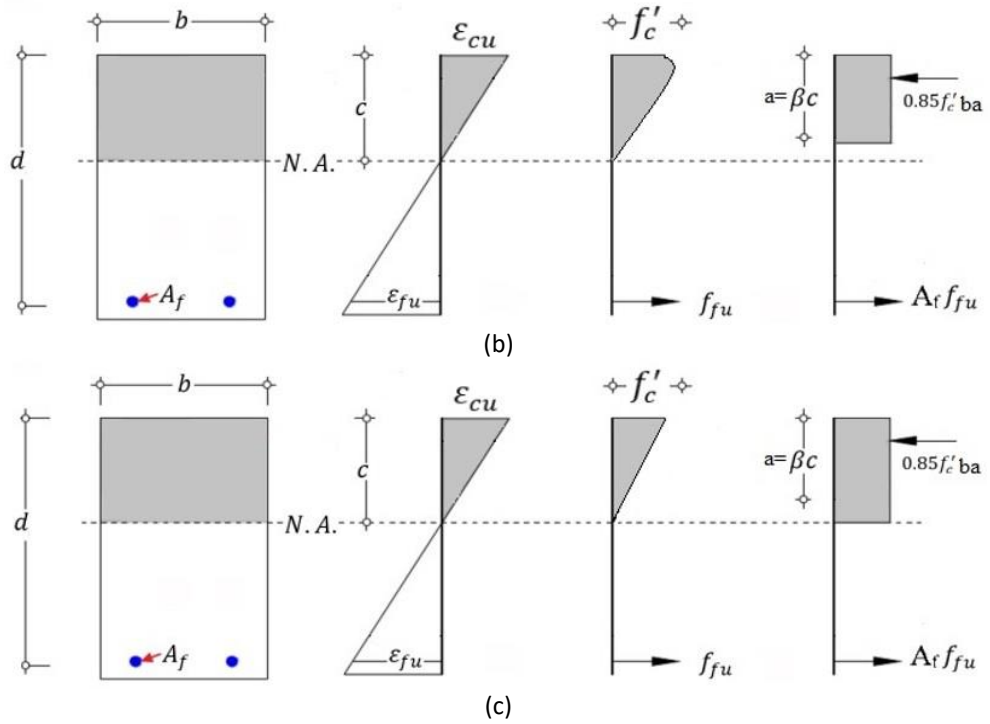

Figure 108: Strain and stress distribution of FRP RC beam with (a) balanced failure condition, (b) concrete crushing failure, and (c) FRP rupture failure at ultimate conditions.

To calculate the flexural capacity of a FRP reinforced concrete flexural member, first the failure mode needs to be recognized. There are either FRP reinforced rupture or concrete crushing that governing the failure. To determine the failure, FRP reinforcement ratio can be compared to the balanced reinforcement ratio using its design tensile strength. FRP reinforcement ratio and balanced FRP reinforcement ratio can be calculated from equation (6.4) and (6.5):

$$\rho_f = \frac{A_f}{bd} \tag{6.4}$$

$$\rho_{fb} = 0.85\beta \frac{f'_c}{f_{fu}} \frac{E_f \varepsilon_{cu}}{E_f \varepsilon_{cu} + f_{fu}} \tag{6.5}$$

Where ρ_f is FRP reinforcement ratio, A_f is area of FRP reinforcement, b is width of rectangular cross section, and d is distance from extreme compression fibre to centroid of tension reinforcement. β is ratio of distance from neutral axis to extreme tension fibre to distance from neutral axis to centre of tensile reinforcement, E_f is FRP modulus of elasticity, ε_{cu} is ultimate strain in concrete, and f_{fu} is design tensile strength of FRP. If FRP reinforcement ratio is less than the balanced FRP reinforcement ratio, the failure governed by FRP rupture failure mode. Otherwise,

the failure is governed by concrete crushing failure. Based on the force equilibrium and strain compatibility, the following flexural strength can be driven for concrete crushing failure:

$$M_u = A_f f_f (d - \frac{a}{2}) \tag{6.6}$$

$$f_f = E_f \varepsilon_{cu} \frac{\beta d - a}{a} \tag{6.7}$$

where f_f is stress in FRP reinforcement in tension and a is depth of equivalent rectangular stress block and can be calculated from equation (6.8):

$$a = \frac{A_f f_f}{0.85 f_c' b} \tag{6.8}$$

The stress in FRP reinforcement in tension can be estimated by substituting the equation (6.6) into equation (6.7):

$$f_f = \left(\sqrt{\frac{(E_f \varepsilon_{cu})^2}{4} + \frac{0.85 \beta f_c'}{\rho_f} E_f \varepsilon_{cu}} - 0.5 E_f \varepsilon_{cu} \right) \leq f_{fu} \tag{6.9}$$

Alternatively, flexural strength for concrete crushing failure can be calculated from following equation:

$$M_u = \rho_f f_f \left(1 - 0.59 \frac{\rho_f f_f}{f_c'}\right) b d^2 \tag{6.10}$$

When the dominant failure is FRP bar rupture failure, the ACI stress block is not appropriate, as the assumed maximum strain for concrete (0.003) might not be reached. Hence, a corresponding stress block needs to be used that estimates the stress distribution in the concrete at certain strain level. For this matter, analysis introduce two unknowns, the depth to the neutral axis, c and concrete compressive strain at failure, ε_c.

The neutral axis location in a beam section can be computed as follows:

$$k_1 c^2 + k_2 c + k_3 = 0 \tag{6.11}$$

$$k_1 = 0.85 f_c' b \beta \tag{6.12}$$

$$k_2 = -\left(A_s f_y - \varepsilon_{cu} A_f E_f\right) \tag{6.13}$$

$$k_3 = -\left(A_f E_f \varepsilon_{cu} d_f\right) \tag{6.14}$$

$$c = \frac{-k_2 \mp \sqrt{k_2^2 - 4k_1 k_3}}{2k_1} \tag{6.15}$$

Meanwhile strain of FRP bar can be calculated from equation (6.16):

$$\varepsilon_f = \frac{\varepsilon_{cu}}{c} d_f - \varepsilon_{cu} \tag{6.16}$$

Where $d_f$is effective depth of the FRP reinforcement. Hence, the ultimate moment can be expressed by following formula:

$$M_u = \varepsilon_f A_f E_f \left(d_f - \frac{\beta c}{2}\right) \tag{6.17}$$

In accordance with the guidelines provided by ACI guidelines, [44], the design flexural strength should surpass the factored moment. The design flexural strength is determined by multiplying the strength reduction factor by the flexural strength of the member. On the other hand, the factored moment is calculated by considering the moments derived from factored loads, [302].

$$\varphi M_u \geq M_f \tag{6.18}$$

Due to brittle nature of FRP members, a strength reduction factor introduced to deliver a higher replacement of strength in the member. The strength reduction factor for flexure can be calculated from equation (6.18), where $\rho_f \geq 1.4\rho_{fb}$ represent the strength reduction factor for compression controlled FRP reinforced concrete section, $\rho_f \leq \rho_{fb}$ represent a tension controlled FRP reinforced concrete section, and $\rho_{fb} < \rho_f < 1.4\rho_{fb}$ represents section that dominated by concrete crushing limit state and a reduced value for strength reduction factor needs to be used based on a compression controlled section. Figure (109) shows the strength reduction factor as function of reinforcement ratio.

$$\varphi = \begin{cases} 0.55 & \rho_f \leq \rho_{fb} \\ 0.3 + 0.25\frac{\rho_f}{\rho_{fb}} & \rho_{fb} < \rho_f < 1.4\rho_{fb} \\ 0.65 & \rho_f \geq 1.4\rho_{fb} \end{cases} \tag{6.19}$$

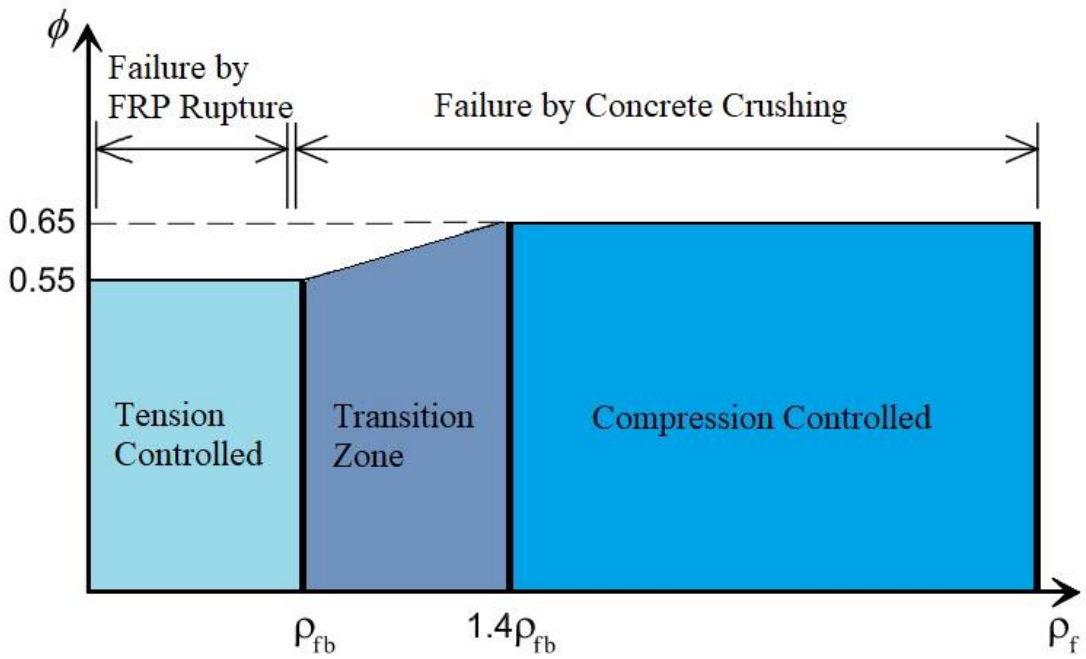

Figure 109: the flexural strength reduction factor as a function of reinforcement ratio.

6.3 FE modelling of DIF and results

Following Yan's recommendation as outlined in [202], a specific subset of beams was carefully selected for a more focused investigation into the Dynamic Increase Factor (DIF) phenomenon. These beams were meticulously chosen based on their distinct characteristics, including a uniform bar diameter of 12 mm and varying concrete compressive strengths, specifically 25, 35, and 45 MPa. The objective was to thoroughly examine how DIF manifests in response to three separate sets of high-strain impact loading scenarios.

Table (43) serves as a comprehensive reference, providing detailed information about each of the selected beams, along with the key factors employed during the finite element modelling process. It's important to note that all physical attributes and material properties of these beams align precisely with those discussed in previous chapters, particularly Chapters Four and Five. This ensures a consistent and coherent framework for analysis and comparison.

The investigation of DIF for these chosen beam models closely adhered to the established methodology detailed in Chapter Four. Leveraging the power of ABAQUS software, the finite element modelling process was executed with great precision. However, what sets this analysis apart is the need to attain dynamic design stress levels under varying loading rates. This requirement acknowledges the dynamic and time-dependent nature of the loading conditions, which is essential for capturing the true behaviour of these FRP RC beams under high-strain impact.

In essence, this section of the research endeavours to provide a more nuanced understanding of how DIF operates within the context of FRP RC beams, shedding light on its behaviour across different loading scenarios, concrete strengths, and bar diameters. Through rigorous finite element analysis and empirical data collection, this study aims to contribute valuable insights into the dynamic performance of such structural elements and, by extension, enhance the overall understanding of their behaviour under extreme conditions.

The concrete beams were simulated in ABAQUS, encompassing a spectrum of strain and loading rates, eliminating the need for equations (6.18) and (6.19) in this modelling approach. The primary objective was to accurately determine the dynamic design stress for each beam. To achieve this, each beam underwent four distinct simulations, each featuring different time durations and amplitudes.

For a comprehensive investigation into dynamic behaviour, each beam was subjected to four unique simulations, each characterized by a distinct loading time history. These simulations involved a sequence where the applied load transitioned from zero to its maximum value and then returned to zero. The loading times were set at 1, 10, 100, and 1000 milliseconds, representing various loading frequencies.

The amplitudes of the applied loads were adjusted in proportion to their respective time frequencies, adhering to a symmetrical triangular pulse force shape. To illustrate this approach and its impact on the analysis, Table (44) and Figure (110) provide an

example featuring Beam A-1-1-25-12, showcasing how it was modelled under different time histories. This approach allowed for a thorough exploration of the beam's dynamic response under diverse loading conditions, contributing to a more comprehensive understanding of its behaviour and performance.

Beam	**FRP type**	d_b, **mm**	f'_c, **MPa**	**L, kN**	f_{fr}, **MPa**
C-1-1-25-12	Carbon	12	25	320	1890
C-2-1-25-12	Carbon	12	25	80	1890
C-3-1-25-12	Carbon	12	25	40	1890
C-1-1-35-12	Carbon	12	35	320	1890
C-2-1-35-12	Carbon	12	35	80	1890
C-3-1-35-12	Carbon	12	35	40	1890
C-1-1-45-12	Carbon	12	45	320	1890
C-2-1-45-12	Carbon	12	45	80	1890
C-3-1-45-12	Carbon	12	45	40	1890
G-1-1-25-12	Glass	12	25	320	974
G-2-1-25-12	Glass	12	25	80	974
G-3-1-25-12	Glass	12	25	40	974
G-1-1-35-12	Glass	12	35	320	974
G-2-1-35-12	Glass	12	35	80	974
G-3-1-35-12	Glass	12	35	40	974
G-1-1-45-12	Glass	12	45	320	974
G-2-1-45-12	Glass	12	45	80	974
G-3-1-45-12	Glass	12	45	40	974
A-1-1-25-12	Aramid	12	25	320	1400
A-2-1-25-12	Aramid	12	25	80	1400
A-3-1-25-12	Aramid	12	25	40	1400
A-1-1-35-12	Aramid	12	35	320	1400
A-2-1-35-12	Aramid	12	35	80	1400
A-3-1-35-12	Aramid	12	35	40	1400
A-1-1-45-12	Aramid	12	45	320	1400
A-2-1-45-12	Aramid	12	45	80	1400
A-3-1-45-12	Aramid	12	45	40	1400

Table 43: beams and factors used in FE modelling to investigate their DIF under high strain impact loading.

Model	*Loading time, ms*	*Time frequency, s*	*Amplitude*
A-1-1-25-12-1	1	0, 0.001, 0.002	0, 1, 0
A-1-1-25-12-10	10	0, 0.01, 0.02	0, 1, 0
A-1-1-25-12-100	100	0, 0.1, 0.2	0, 1, 0
A-1-1-25-12-1000	1000	0, 1, 2	0, 1, 0

Table 44: Example of time-histories models for beam A-1-1-25-12.

All he subsequent procedures and processing steps closely mirror the modelling approach outlined in the preceding chapters, which were systematically elucidated in Chapter 4. Following the rigorous modelling and analysis procedures, the results of the ABAQUS simulations have been compiled and assessed.

Table (45) provides a comprehensive overview of 108 models representing CFRP, AFRP, and GFRP RC beams subjected to impact loads of 320, 80, and 40 kN.

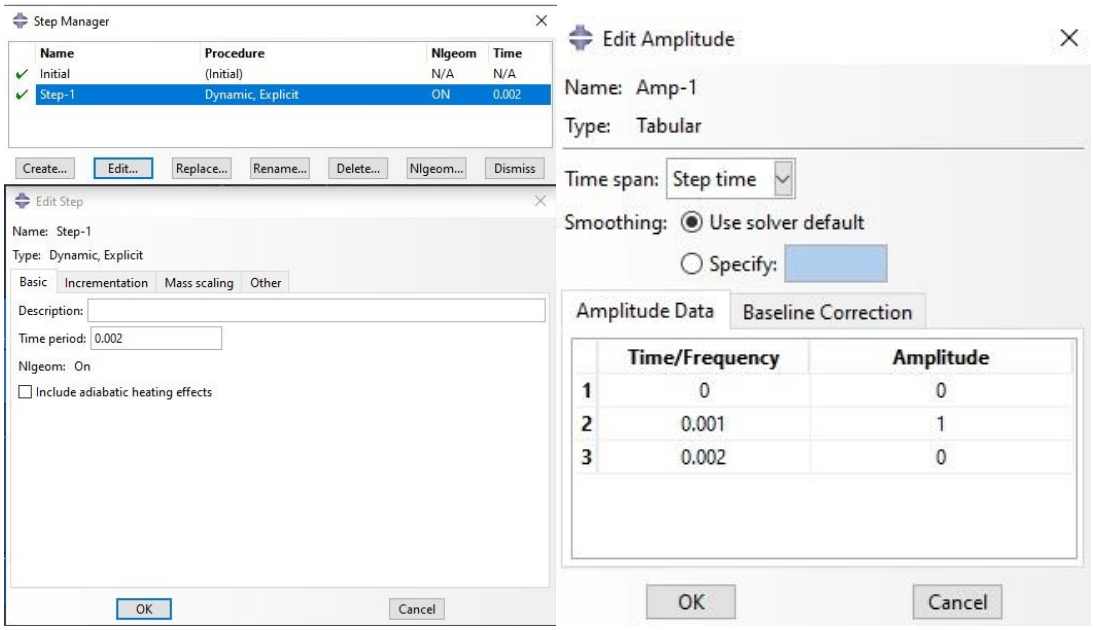

Figure 110: beam model A-1-1-25-12-1 with time step of 2 ms and amplitude respectively.

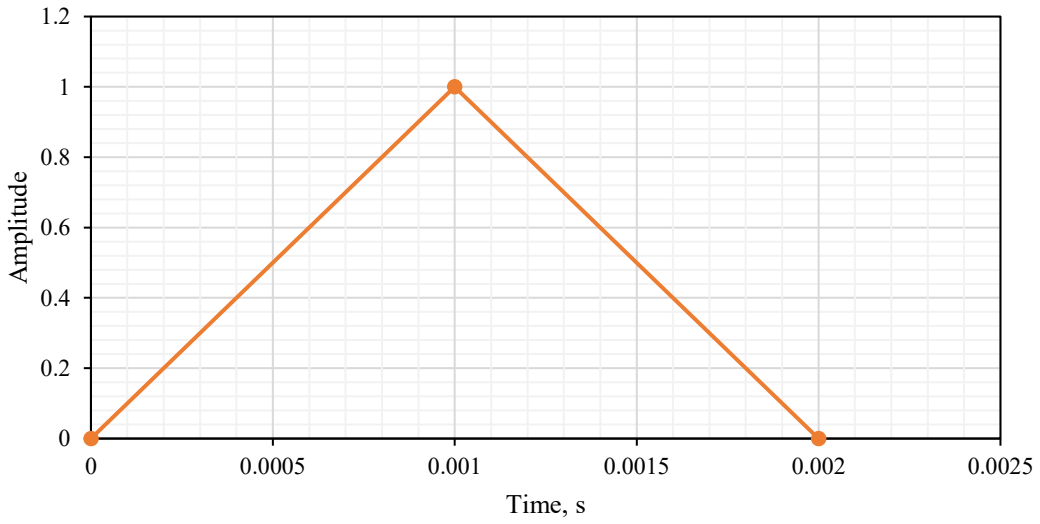

Figure 111: triangular pulse with respect to time frequency of 1 ms for model A-1-1-25-12-1.

The data presented in this table pertains to the maximum stress levels observed in these beams in relation to rate dependency and the bond between the FRP bars and the concrete matrix. The Dynamic Increase Factor (DIF) for each beam member was computed using Equation (6.3), where the maximum stress under a specific strain rate was divided by the maximum stress observed under static conditions.

Subsequently, the average DIF for each FRP RC beam, with respect to loading time, was calculated. This step culminated in the determination of the final values of DIF for each type of FRP bar (CFRP, AFRP, and GFRP) under specific loading durations. The results for DIF values for FRP bars are tabulated in Table (46), offering valuable insights into the dynamic response characteristics of these materials under varying loading conditions.

Beam models	Max Stress, Pa	DIF	Beam models	Max Stress, Pa	DIF	Beam models	Max Stress, Pa	DIF
A-1-1-25-12-1	8.74E+08	1.21E+00	A-2-1-25-12-1	4.39E+08	1.03E+00	A-3-1-25-12-1	5.49E+08	1.02E+01
A-1-1-25-12-10	8.74E+08	1.21E+00	A-2-1-25-12-10	4.39E+08	1.03E+00	A-3-1-25-12-10	5.49E+08	1.02E+01
A-1-1-25-12-100	8.40E+08	1.17E+00	A-2-1-25-12-100	4.29E+08	1.00E+00	A-3-1-25-12-100	5.48E+07	1.02E+00
A-1-1-25-12-1000	7.20E+08	1.00E+00	A-2-1-25-12-1000	4.28E+08	1.00E+00	A-3-1-25-12-1000	5.38E+07	1.00E+00
A-1-1-35-12-1	8.76E+08	1.23E+00	A-2-1-35-12-1	4.34E+08	1.01E+00	A-3-1-35-12-1	2.75E+07	1.02E+00
A-1-1-35-12-10	8.76E+08	1.23E+00	A-2-1-35-12-10	4.34E+08	1.01E+00	A-3-1-35-12-10	2.75E+07	1.02E+00
A-1-1-35-12-100	8.73E+08	1.22E+00	A-2-1-35-12-100	4.31E+08	1.00E+00	A-3-1-35-12-100	2.73E+07	1.01E+00
A-1-1-35-12-1000	7.15E+08	1.00E+00	A-2-1-35-12-1000	4.30E+08	1.00E+00	A-3-1-35-12-1000	2.69E+07	1.00E+00
A-1-1-45-12-1	8.75E+08	1.63E+00	A-2-1-45-12-1	4.39E+08	1.02E+00	A-3-1-45-12-1	2.74E+07	1.02E+00
A-1-1-45-12-10	8.75E+08	1.63E+00	A-2-1-45-12-10	4.39E+08	1.02E+00	A-3-1-45-12-10	2.74E+07	1.02E+00
A-1-1-45-12-100	8.74E+08	1.63E+00	A-2-1-45-12-100	4.30E+08	1.00E+00	A-3-1-45-12-100	2.68E+07	1.00E+00
A-1-1-45-12-1000	5.37E+08	1.00E+00	A-2-1-45-12-1000	4.29E+08	1.00E+00	A-3-1-45-12-1000	2.68E+07	1.00E+00

Beam models	Max Stress, Pa	DIF	Beam models	Max Stress, Pa	DIF	Beam models	Max Stress, Pa	DIF
C-1-1-25-12-1	8.49E+08	1.18E+00	C-2-1-25-12-1	4.38E+08	5.23E-01	C-3-1-25-12-1	2.20E+08	1.03E+00
C-1-1-25-12-10	8.49E+08	1.18E+00	C-2-1-25-12-10	4.38E+08	5.23E-01	C-3-1-25-12-10	2.20E+08	1.03E+00
C-1-1-25-12-100	8.38E+08	1.16E+00	C-2-1-25-12-100	4.30E+08	5.13E-01	C-3-1-25-12-100	2.18E+08	1.02E+00
C-1-1-25-12-1000	7.16E+08	9.94E-01	C-2-1-25-12-1000	4.28E+08	5.11E-01	C-3-1-25-12-1000	2.14E+08	1.00E+00
C-1-1-35-12-1	8.78E+08	1.23E+00	C-2-1-35-12-1	4.34E+08	4.95E-01	C-3-1-35-12-1	5.49E+07	1.02E+00
C-1-1-35-12-10	8.78E+08	1.23E+00	C-2-1-35-12-10	4.34E+08	4.95E-01	C-3-1-35-12-10	5.49E+07	1.02E+00
C-1-1-35-12-100	8.77E+08	1.23E+00	C-2-1-35-12-100	4.31E+08	4.91E-01	C-3-1-35-12-100	5.39E+07	1.01E+00
C-1-1-35-12-1000	8.72E+08	1.22E+00	C-2-1-35-12-1000	4.29E+08	4.89E-01	C-3-1-35-12-1000	5.36E+07	1.00E+00
C-1-1-45-12-1	6.67E+08	1.24E+00	C-2-1-45-12-1	4.30E+08	6.48E-01	C-3-1-45-12-1	3.51E+07	1.31E+00
C-1-1-45-12-10	6.67E+08	1.24E+00	C-2-1-45-12-10	4.30E+08	6.48E-01	C-3-1-45-12-10	3.51E+07	1.31E+00
C-1-1-45-12-100	6.64E+08	1.24E+00	C-2-1-45-12-100	4.30E+08	6.48E-01	C-3-1-45-12-100	2.69E+07	1.00E+00
C-1-1-45-12-1000	6.56E+08	1.22E+00	C-2-1-45-12-1000	4.28E+08	6.45E-01	C-3-1-45-12-1000	2.68E+07	1.00E+00

Beam models	Max Stress, Pa	DIF	Beam models	Max Stress, Pa	DIF	Beam models	Max Stress, Pa	DIF
G-1-1-25-12-1	5.98E+08	8.31E-01	G-2-1-25-12-1	4.39E+08	7.34E-01	G-3-1-25-12-1	2.74E+08	1.02E+00
G-1-1-25-12-10	5.98E+08	8.31E-01	G-2-1-25-12-10	4.39E+08	7.34E-01	G-3-1-25-12-10	2.74E+08	1.02E+00
G-1-1-25-12-100	5.98E+08	8.31E-01	G-2-1-25-12-100	4.37E+08	7.31E-01	G-3-1-25-12-100	2.69E+08	1.00E+00
G-1-1-25-12-1000	5.37E+08	7.46E-01	G-2-1-25-12-1000	4.30E+08	7.19E-01	G-3-1-25-12-1000	2.68E+08	1.00E+00
G-1-1-35-12-1	4.72E+08	6.60E-01	G-2-1-35-12-1	4.38E+08	1.00E+00	G-3-1-35-12-1	2.75E+08	1.03E+00
G-1-1-35-12-10	4.72E+08	6.60E-01	G-2-1-35-12-10	4.38E+08	1.00E+00	G-3-1-35-12-10	2.75E+08	1.03E+00
G-1-1-35-12-100	4.38E+08	6.13E-01	G-2-1-35-12-100	4.29E+08	9.79E-01	G-3-1-35-12-100	2.68E+08	1.00E+00
G-1-1-35-12-1000	4.38E+08	6.13E-01	G-2-1-35-12-1000	4.29E+08	9.79E-01	G-3-1-35-12-1000	2.68E+08	1.00E+00
G-1-1-45-12-1	4.41E+08	8.21E-01	G-2-1-45-12-1	4.39E+08	1.00E+00	G-3-1-45-12-1	1.76E+07	1.31E+00
G-1-1-45-12-10	4.41E+08	8.21E-01	G-2-1-45-12-10	4.39E+08	1.00E+00	G-3-1-45-12-10	1.76E+07	1.31E+00
G-1-1-45-12-100	4.38E+08	8.16E-01	G-2-1-45-12-100	4.37E+08	9.98E-01	G-3-1-45-12-100	1.34E+07	1.00E+00
G-1-1-45-12-1000	4.30E+08	8.01E-01	G-2-1-45-12-1000	4.29E+08	9.79E-01	G-3-1-45-12-1000	1.34E+07	1.00E+00

Table 45: Result of dynamic design stress and DIF for chosen 108 models of Aramid, Carbon and Glass FRP RC beams.

Loading time, ms	Bar material		
	AFRP	**CFRP**	**GFRP**
1	1.13	1.07	1.07
10	1.13	1.07	1.07
100	1.12	1.03	1.02
1000	1.00	1.00	1.00

Table 46:Dynamic increase factor for Aramid, Carbon, and Glass FRP bars

Based on equation (6.15) for ultimate moment, M_u, reduction strength factor,φ from equation (6.17) and DIF found from finite element analysis that provided in Table (47), the design flexural strength can be calculated from following equation:

$$M_{u,d} = (\varphi)(DIF)(M_u) \tag{6.20}$$

6.3.1 Stress-strain relationship

Figure (112) presents an illustrative depiction of the correlation between maximum stress and strain rate for various FRP RC beam models, specifically those incorporating carbon, aramid, and glass FRP, and subjected to impact loads of 40, 80, and 320 kN at four distinct loading rates. An examination of the maximum stress results reveals a discernible trend wherein most beams exhibit a notable increase in strength as the strain rates escalate. Notably, beam models characterized by lower concrete compressive strength levels tend to display higher peak stress values, whereas their counterparts with higher concrete compressive strength exhibit lower peak stress levels and experience higher strain rates when subjected to similar loading conditions.

The diminished strain rate observed in models with higher concrete compressive strength can be attributed to the propensity of concrete to dissipate energy owing to its inherent stiffness, thereby contributing to a reduction in strain rate. It is noteworthy that despite the disparities in material properties among AFRP, CFRP, and GFRP, beam models reinforced with AFRP consistently demonstrated superior performance in terms of strain rate and peak stress when compared to GFRP and CFRP beam models. This observation underscores the influence of the choice of FRP material on the dynamic response characteristics of these structures.

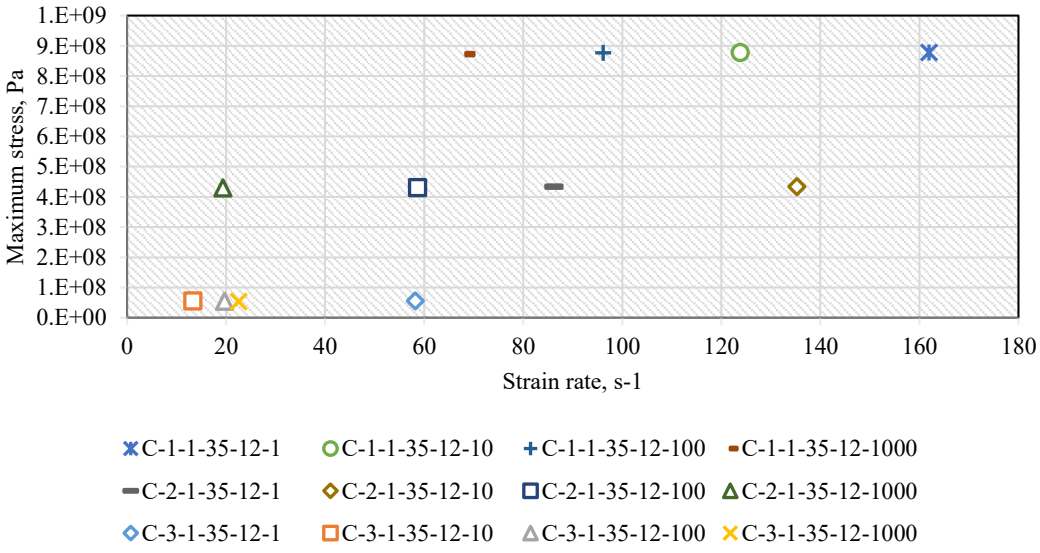

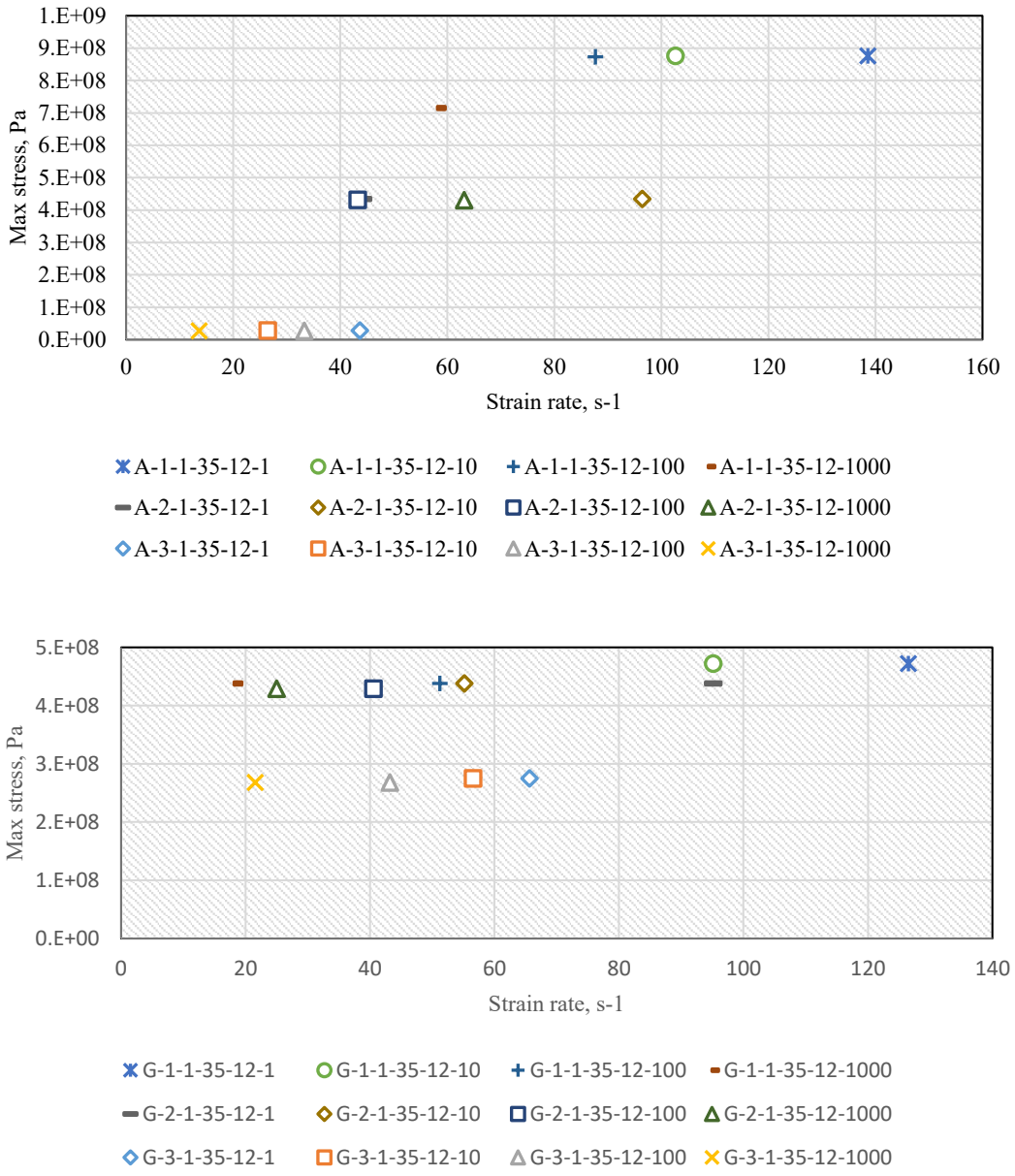

Figure 112: Peak stress as a function of strain rate for different beam model sets.

Furthermore, it's worth noting that there were variations observed in models featuring higher concrete compressive strength levels compared to beam models with a concrete compressive strength of 25 MPa. For a more comprehensive view of the peak stress and strain rate relationship in additional FRP RC beam models subjected to varying loading conditions, refer to Figure (167) presented in the supplementary materials, specifically in appendix (C).

Figure (114) illustrates the stress-strain curves for various impact loads corresponding to CFRP, GFRP, and AFRP RC models, all featuring a concrete compressive strength of 30 MPa. These models are subjected to an 80kN load, which equates to an impact velocity of 17.145 m/s.

Additionally, Figure (113) showcases CFRP RC models with bar diameters ranging from 8mm to 16mm. These models are constructed with concrete having compressive strengths of 25 MPa, 30 MPa, 35 MPa, 40 MPa, and 45 MPa, and they are subjected to an 80kN impact load.

Upon scrutinizing the results presented in Figure (114), a consistent pattern becomes evident. CFRP models consistently exhibit higher maximum stress values and greater stiffness, all while experiencing less deformation when compared to their AFRP and GFRP counterparts. Furthermore, as the diameter of FRP bars increases, there is a noticeable augmentation in both strength and ductility. Notably, it's crucial to emphasize that the initial stiffness of concretes with varying compressive strengths remains consistent.

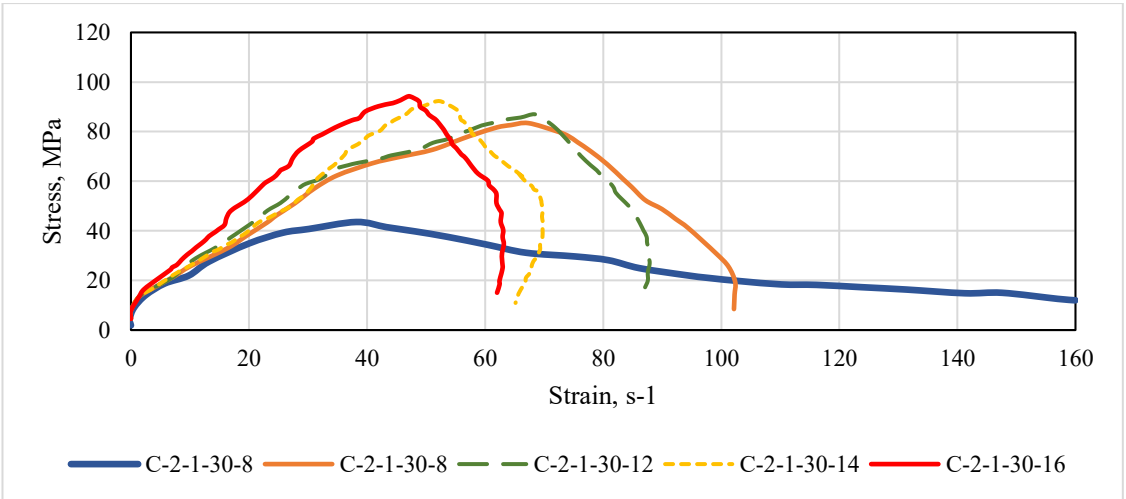

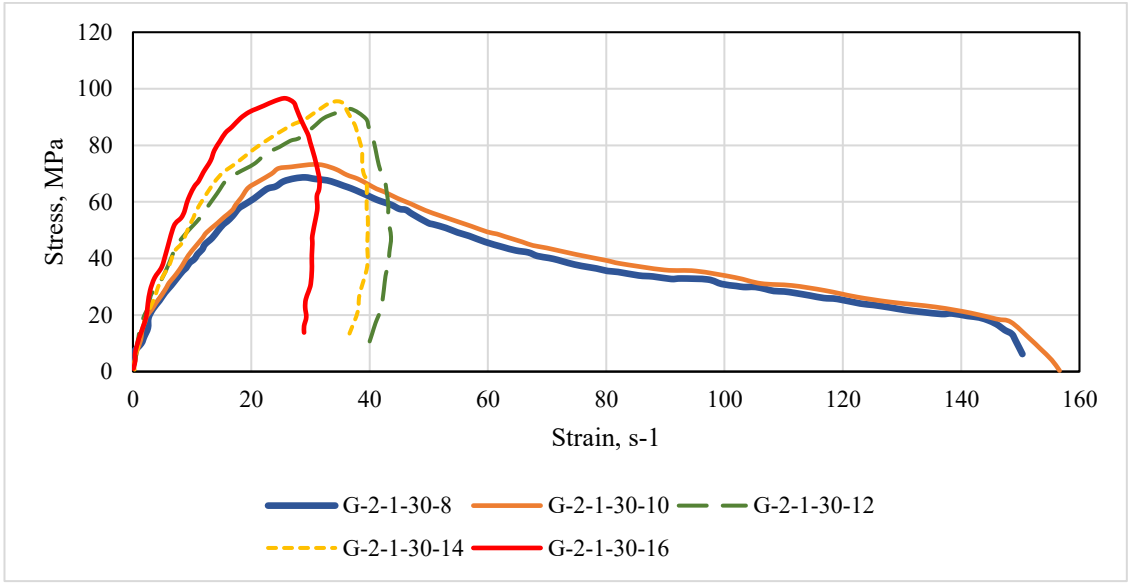

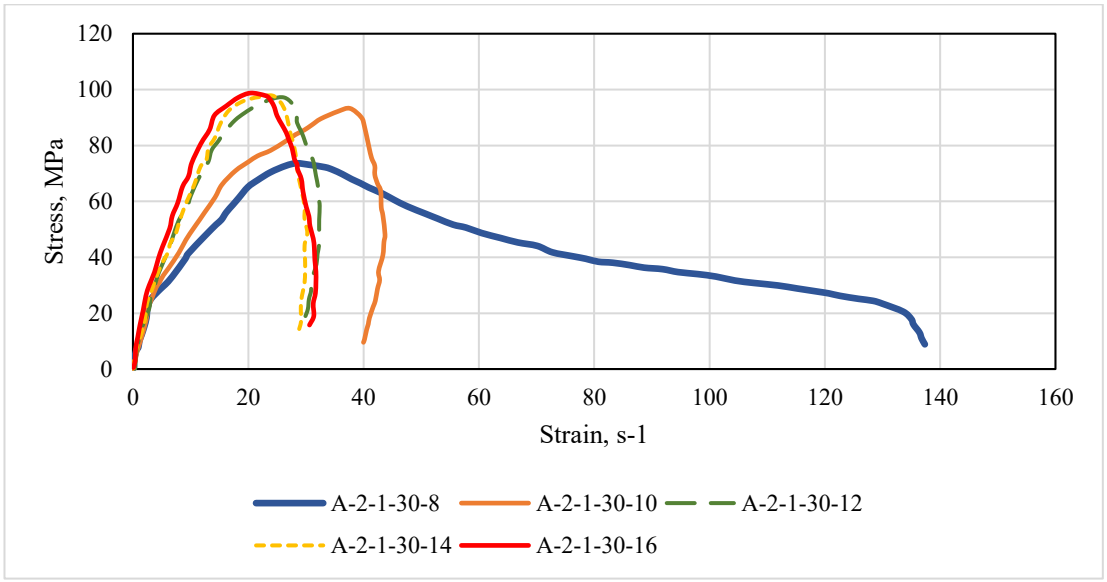

Figure 113: Stress-strain of FRP RC beams response under 80kN Impact load with respect to DIF factor.

Furthermore, at a relatively low velocity of 12.125 m/s, the concrete exhibited a maximum stress of approximately 1.0 MPa. This observed maximum stress value proved insufficient to significantly impact the compressive strength of concrete, even when varying within the range of 30 MPa to 45 MPa under the influence of impact loading. This observation is further supported by Figure (114), where the stress-strain graph demonstrates elastic recovery, indicating that failure criteria were not met. The ability of the material to nearly return to its original shape upon load removal substantiates this conclusion.

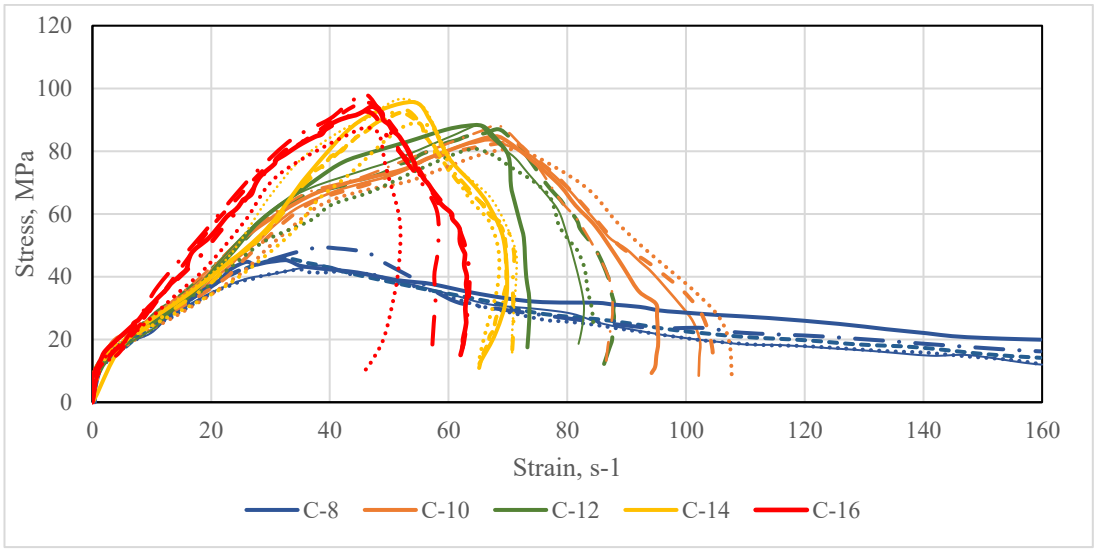

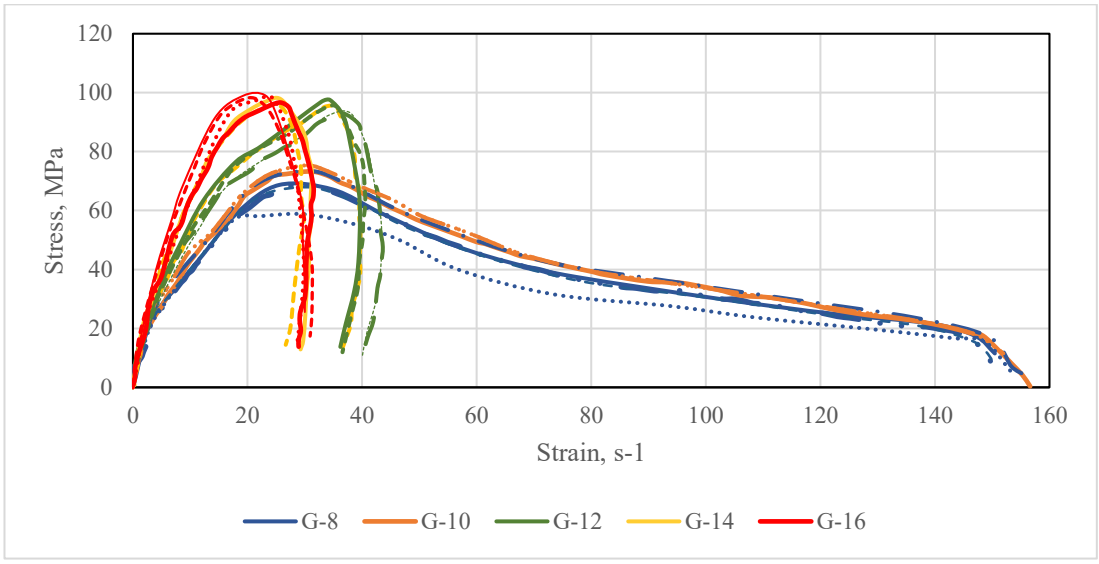

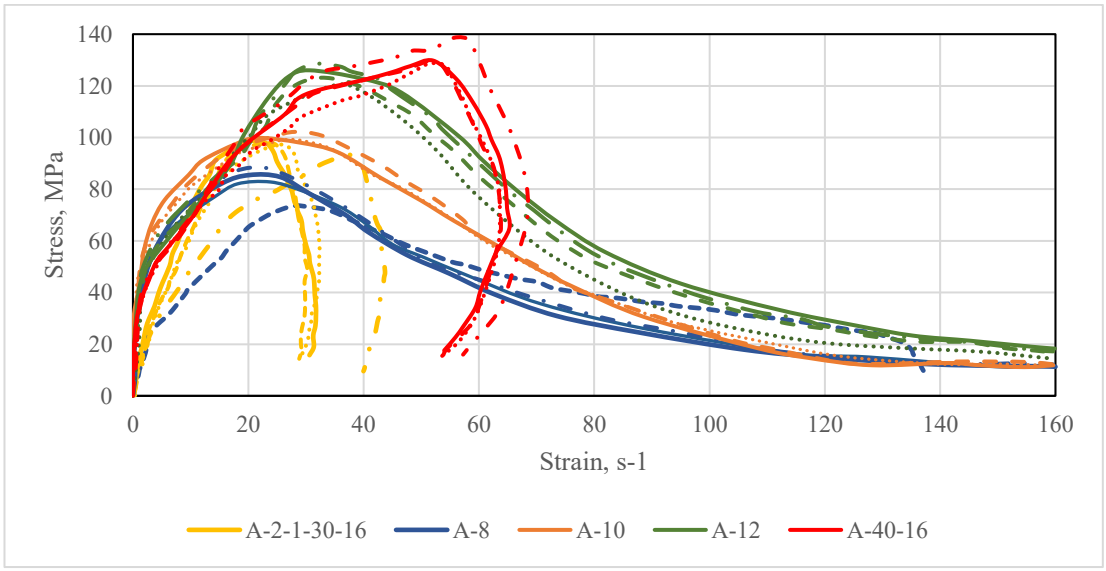

Figure 114: Stress-strain response of models under different loading with respect to DIF factor.

6.3.2 Strength

Figure (115) presents a comprehensive overview of the maximum stress values derived from Figure (114), showcasing their relationship with strain rate. In this analysis, it becomes evident that models which did not exhibit any signs of failure are associated with lower strain rates. This lower strain rate is a result of the gradual deformation observed at maximum stress levels, which is linked to the model's capacity to absorb the impact energy without undergoing any failure mode. In simpler terms, when the strain rate is low, it indicates that the material is deforming slowly and can withstand the applied load without failing.

However, when examining the models that did experience failure, a distinct trend emerges from Figure (115). Specifically, concrete specimens reinforced with larger bar diameters demonstrate a noticeable increase in strength as the strain rate rises. This signifies that the concrete becomes stronger and more resilient under high-speed loading conditions, particularly in models with larger bar diameters. Conversely, the increase in strength due to higher strain rates is less pronounced in models with smaller bar diameters. In essence, smaller bar diameters are associated with higher strain rates, and as the bar diameter increases, the strain rate decreases in these models.

It's worth noting that there is a wider range of variability in the results for concrete models reinforced with a 14 mm bar diameter, as evidenced by the larger dispersion observed. This suggests that the behaviour of these models is more variable and less predictable compared to those with different bar diameters. This variability could be attributed to various factors, such as material properties, geometry, and the specific conditions of each model.

In summary, Figure (115) provides valuable insights into how strain rate affects the maximum stress in concrete models. Lower strain rates are associated with models that don't fail, while higher strain rates lead to increased strength, particularly in

models with larger bar diameters. However, concrete models reinforced with a 14 mm bar diameter exhibit a wider range of variability in their responses to strain rate. These findings contribute to a deeper understanding of the behaviour of FRP RC beam models under varying loading conditions.

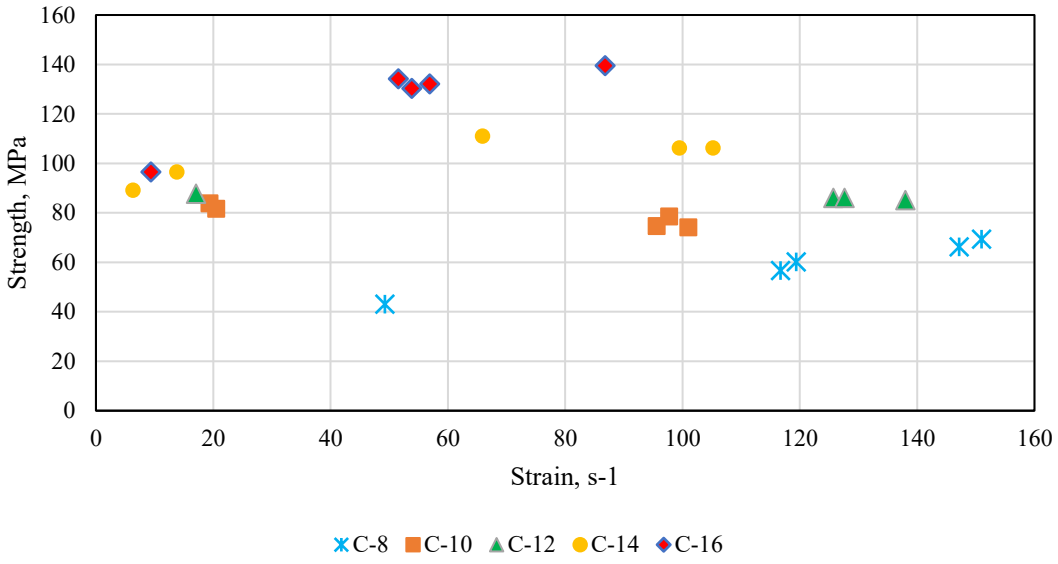

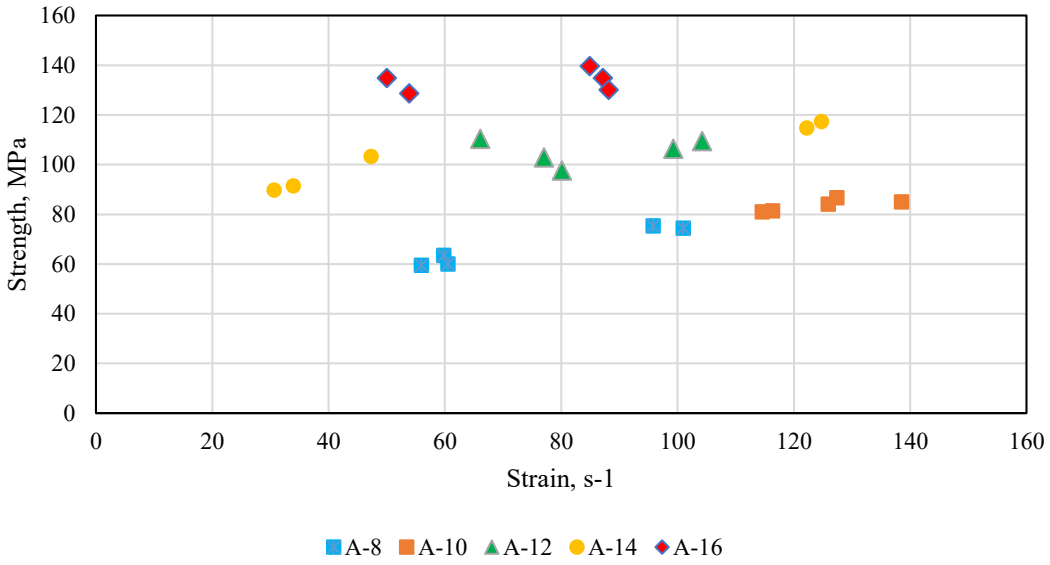

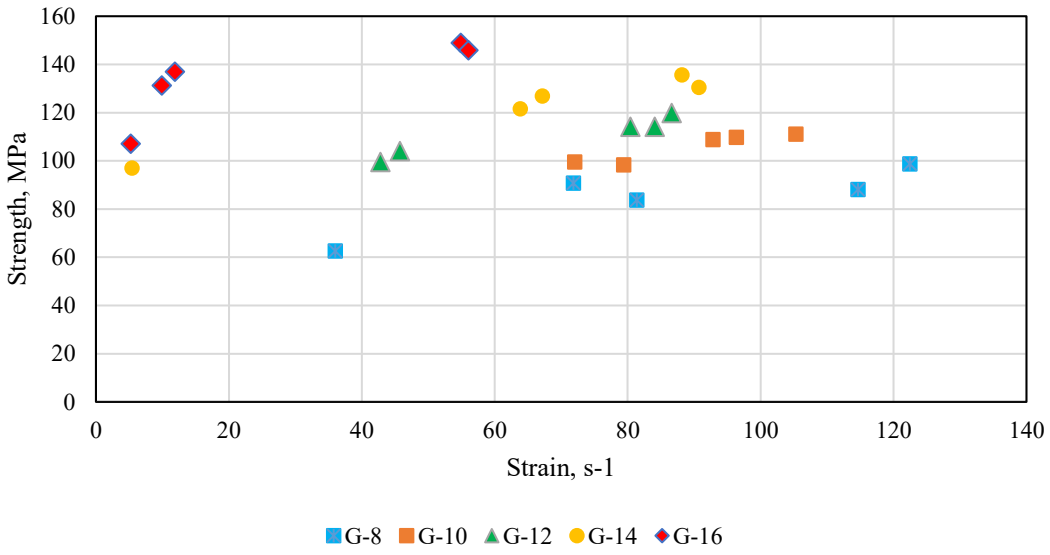

Figure 115: Strength-Strain Response of Models under Varied Loading Conditions Considering the (DIF).

6.3.3 Validation of Dynamic increase factor

Figure (116) illustrates the relationship between the Dynamic Increase Factor (DIF) and strain rate for beam models featuring concrete compressive strength of 25 MPa subjected to various loading conditions. The DIF values were determined through simulation of the beam models using static stress as the reference point.

The findings indicate a notable increase in the DIF for FRP RC beam models as the strain rate escalates. Notably, the DIF for AFRP RC beams with a concrete compressive strength of 45 MPa reaches 1.63 at a strain rate of 75.16 s^{-1}. When comparing these results to DIF values reported in other experimental studies, they fall within a similar range, although there is a slight overestimation observed for the concrete beams with 25 MPa, as noted in previous studies, [303] [304]. This observation underscores the consistency of the obtained DIF values in this research with those reported in the existing literature.

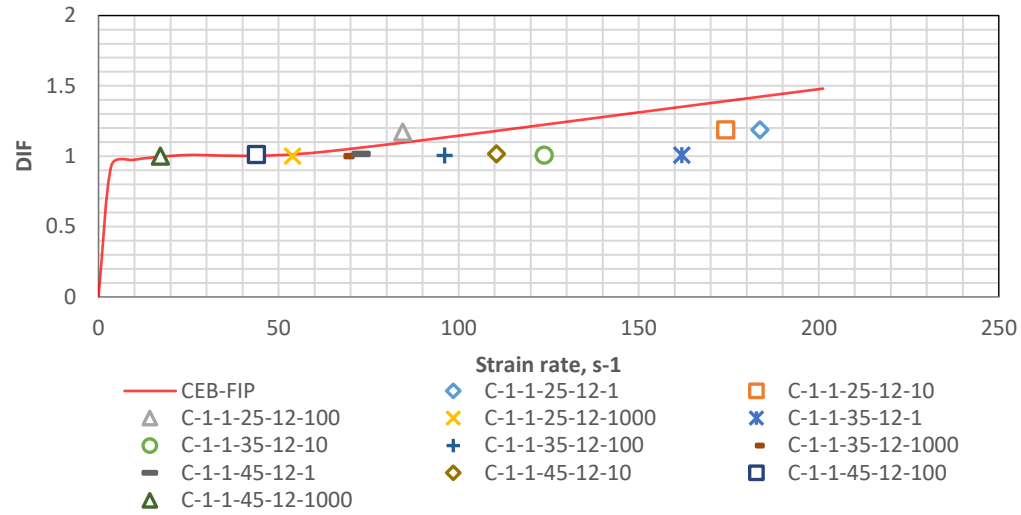

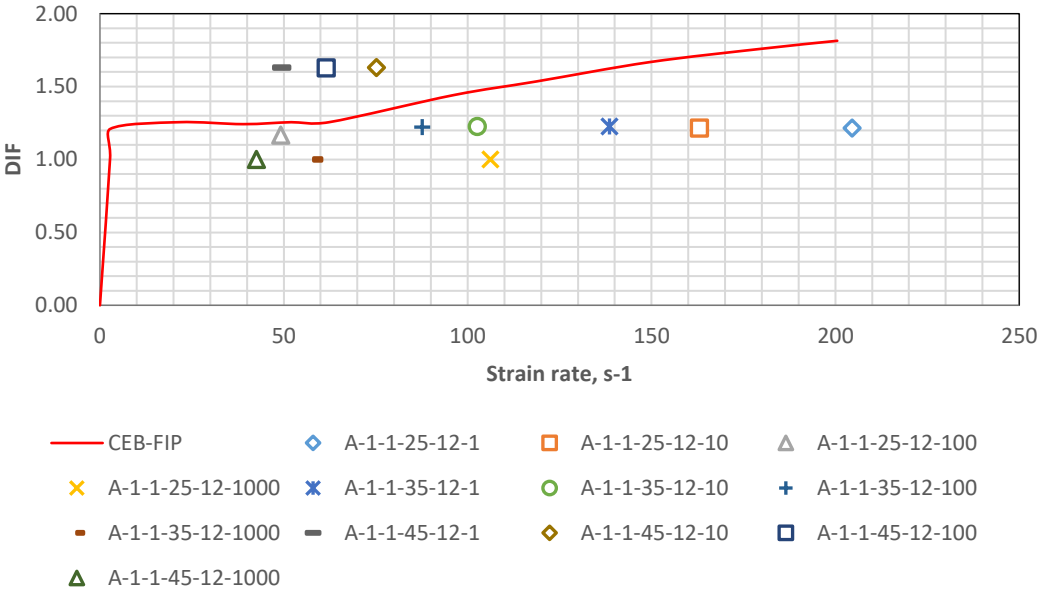

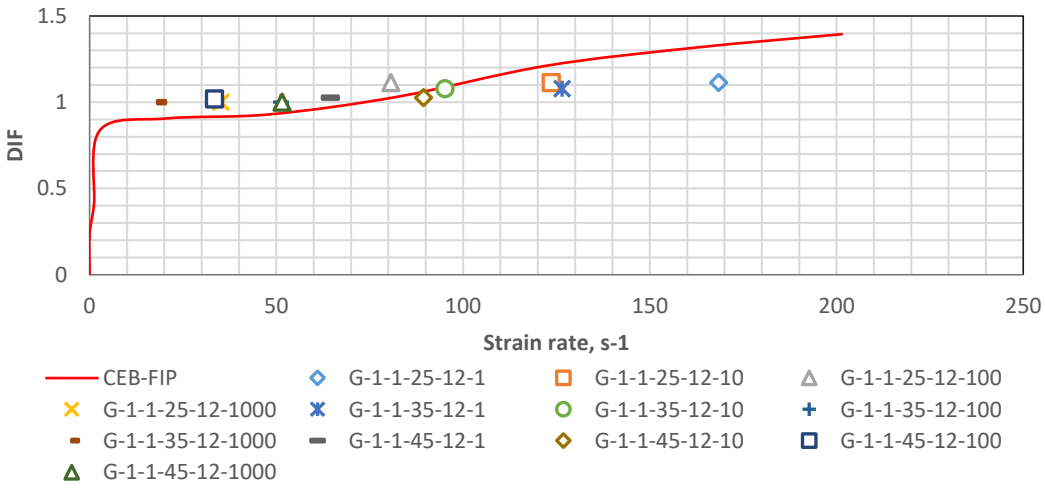

Figure 116: DIF Vs strain rate for CFRP, AFRP, and GFRP RC beams under different set of loading.

Furthermore, the results of this study indicate that AFRP RC beams exhibit a relatively high sensitivity to changes in strain rates. However, it's important to note that due to the limited availability of experimental data on the Dynamic Increase Factor (DIF) for Aramid fibre-reinforced concrete beams, a comprehensive comparison between the results of this study and existing experimental data is not feasible. For a more comprehensive view of the DIF results for other simulated FRP RC beams as a function of strain rate, please refer to the data presented in Appendix (C).

Moreover, the findings of this study are consistent with the provisions outlined in the CEB-FIP code. The DIF values predicted for the models using recommendations from CEB-FIP code are presented in Figure (116) and exhibit agreement with CFRP and GFRP models. However, it's worth noting a slight overestimation in the case of the AFRP model. For those models that experienced failure modes, the DIF appears to be independent of the strain rate effect. This observation is attributed to the fact that these models did not reach their maximum strength, resulting in a lower DIF value.

Figure (1) offers a comparison between the bending moments predicted by the American Concrete Institute (ACI) guidelines and those calculated using the equation (6.20) for a specific FRP RC beam. This graph presents the analytical model's results alongside the ACI's recommended values for predicting bending moments concerning deflection. Impressively, the bending moments derived from the analytical model exhibit a remarkably close alignment with the ACI's prescribed values, indicating a robust agreement between the two approaches. In the context of the beam depicted in figure (1), the ratio of ACI's calculated bending moment M_u to that obtained through the analytical model is approximately 1.12, emphasizing a strong correspondence. This level of agreement underscores the reliability and accuracy of the analytical model in predicting bending moments for FRP RC beams, reinforcing its utility as a valuable tool for structural design and analysis in engineering applications.

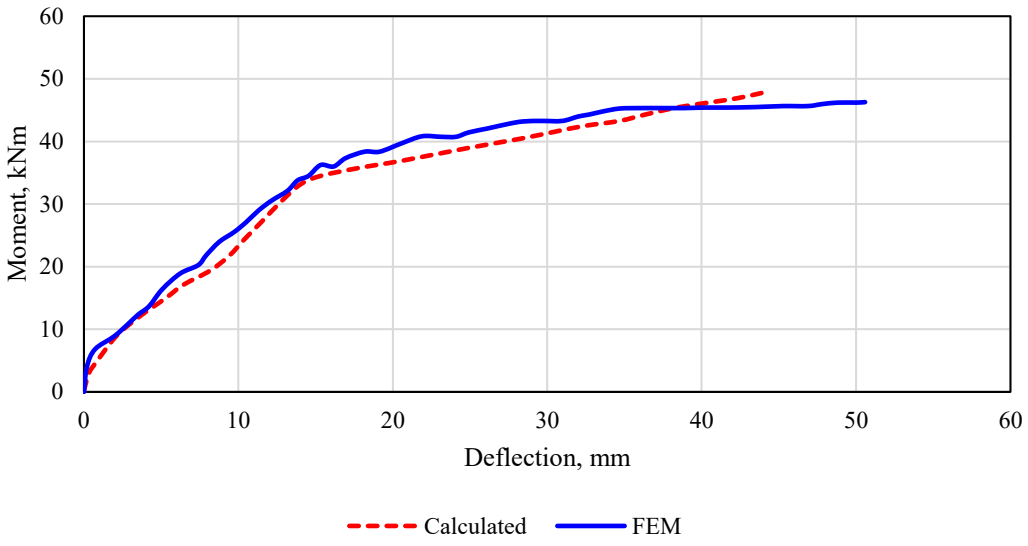

Figure 117:Analytical evaluation of moment-deflection relationship in comparison to ACI.

6.4 Conclusion

Existing Previous research has extensively explored the phenomenon of increased concrete strength under dynamic loading conditions and its correlation with strain rates. However, the existing body of work has overlooked the specific impact of high strain rates on various types of Fiber-Reinforced Polymer (FRP) materials and their distinctive effects on reinforced concrete structures, with the exception of some studies that have focused on concrete-filled steel tubes and Aramid Fiber-Reinforced Polymer (AFRP) materials in confined concrete structures [305] [306].

In this chapter, we conducted a comprehensive numerical investigation into the behaviour of Carbon Fiber-Reinforced Polymer (CFRP), Aramid Fiber-Reinforced Polymer (AFRP), and Glass Fiber-Reinforced Polymer (GFRP) reinforced concrete beams subjected to high strain rates. These models were characterized by different bar diameters, ranging from 8mm to 16mm, and varying concrete compressive strengths between 25 MPa and 45 MPa. The simulations involved subjecting these models to dynamic impact loads and high strain rates, ranging from 10 to $10^{-4}\ s^{-1}$. The results of our study revealed a consistent increase in the strength of these FRP RC beams as both the bar diameter and strain rate increased. Furthermore, our findings on the Dynamic Increase Factor (DIF) were in line with the existing literature

and conformed to the provisions outlined in the CEB-FIP code, which is based on the static concrete strength and assumes a length-to-diameter ratio of 2. Notably, lower DIF values were observed for models with lower length-to-diameter ratios.

Additionally, we observed a trend in deformability at the point of failure, with CFRP models exhibiting approximately 1.3% deformation, AFRP models showing 2.8% deformation, and GFRP models displaying 2.3% deformation. It's important to emphasize that all the FRP RC beam models in our study exhibited sensitivity to strain rate and displayed a degree of dependency on it.

A more extensive investigation involving a larger number of FRP RC beam models subjected to high strain rates would undoubtedly contribute to a deeper understanding of this phenomenon, ultimately facilitating its practical application in engineering and construction practices.

Chapter 7: Conclusions and recommendations for future work

7.1 Thesis Summery

The primary objective of this research was to investigate the influence of high strain rate on the bond behaviour of fibre-reinforced polymer bar-reinforced concrete beams (FRP RC beams) subjected to high-velocity impact loading. The study focused on subjecting carbon, glass, and aramid FRP RC beams to low-mass, high-velocity impact loads, with the intention of analysing their local and global response under dynamic loading conditions. To achieve this, numerical modelling was conducted employing the commercial ABAQUS software, drawing upon prior experimental studies that were referenced and validated in Chapter 3. The three-dimensional finite element modelling was based on the beam tests carried out by Saleh and Borosnyoi, [1] [2], which were extensively explained in Chapter 4.

Following the validation of static and dynamic numerical models, parametric studies were performed to investigate their effect on the behaviour of CFRP, GFRP, and AFRP RC beams under impact loading. Additionally, a regression analysis was conducted to predict the behaviour of FRP RC beams under impact loading, considering various parameters such as five different bar diameters, five compressive strengths, and three high-velocity impact loads. The application of three increasing impact loads to the FRP RC beams resulted in the generation of 225 beam models. Furthermore, an additional 108 models were constructed to determine the design stress and DIF (Design Impact Factor) for FRPs, thus facilitating the calculation of the design flexural strength for reinforced concrete beams with FRP bars.

7.2 Achievements and Contributions

The analysis yielded several noteworthy achievements and contributions, as outlined below:

- FRP reinforced concrete beams were effectively modelled in a beam test simulation that incorporated a rate-dependent bond-slip model. The results

obtained from both static and dynamic models were rigorously validated against existing experimental tests, demonstrating excellent agreement.

- Through a comprehensive examination involving 225 detailed finite element analyses of glass, carbon, and aramid FRP reinforced concrete beams, an equation was formulated. This equation enables the prediction of slip, maximum bond strength, and deflection in relation to four distinct parameters and their corresponding coefficients. These coefficients are presented in Chapter 5.8, derived from a multi-way ANOVA analysis for each scenario.

- The research introduced a strain rate-dependent model, designed to achieve DIF (Dynamic Increase Factor) objectivity within finite element modelling of FRP RC beams subjected to high-strain impact loads.

- An interesting observation was made regarding the dynamic increasing factor, which was found to be approximately 5.3-8% higher in AFRP bars compared to CFRP and GFRP bars under impact loading conditions.

- The study comprehensively compared all local and global responses of FRP RC beams with existing experimental works, revealing a robust coordination and agreement.

- Development of a strain-load dependent 3D model to simulate FRP bond-slip behaviour, pull-out and de-bonding failure for the first time under high impact load.

- A significant contribution was made through the development of a strain-load dependent 3D model. This model is capable of simulating FRP bond-slip

behaviour, pull-out, and de-bonding failure under high impact loads, marking the first instance of such simulation.

- A novel equation was derived for predicting slip, maximum bond strength, and deflection of FRP RC beams, with consideration given to the developed coefficients.

- A pioneering effort was made in determining the design stress for FRP RC beams under the influence of high strain rates and impact loads. This determination was based on a vast set of results obtained from simulating FRP RC beam models and providing DIF values for AFRP, CFRP, and GFRP bars under various loading durations.

7.3 Conclusions

As an effort to model the strain rate effect on FRP RC beams subjected to high velocity impact loading, the subsequent conclusions are drawn:

- Under impact loads, FRP RC beams with smaller bar diameters exhibited higher strength, with GFRP RC beams displaying lower slip compared to AFRP and CFRP RC beams prior to failure. However, CFRP and AFRP RC beams demonstrated an overall better performance.

- Models with higher concrete compressive strength showcased smaller slip over time compared to similar models with lower concrete compressive strength. This observation stemmed from the increased brittleness of higher strength concrete models.

- The influence of time step revealed that, for many models under impact loading, the maximum displacement occurred during the free vibration phase. In contrast, for the same models, the maximum displacement was reached in the forced vibration phase under lower velocity impact loads.

- The ultimate dynamic strain of models increased with an increase in impact load and velocity. Notably, GFRP RC beams exhibited a significant increase in average maximum dynamic strain compared to AFRP and CFRP RC beams under various impact loads.

- An increase in bar diameter of models led to a decrease in pull-out failure while de-bonding failure increased. Pull-out failure accounted for an average of 77% of all failure modes, while de-bonding failure constituted an average of 23%. This phenomenon could be attributed to the stronger bond between smaller bar diameters and the surrounding concrete beams.

- Under impact loads, an increase in the modulus of elasticity of FRP bars resulted in higher ultimate loads and maximum bond strengths. Conversely, slip and mid-span deflection decreased with an increase in modulus of elasticity.

- Models with a $^{c}/_{d_b}$ ratio greater than 2 experienced pull-out failure, particularly in cases where concrete cover was twice the bar diameter, aligning with findings from previous studies.

- Pull-out failure predominated when the embedment length to bar diameter ratio l_d/d_b exceeded 5, with 58.33% of overall failed modes being attributed to

pull-out. Only 30% of FRP RC beam models with an embedment length to bar diameter ratio greater than 5 failed due to de-bonding.

- An increase in the ratio of concrete cover to bar diameter resulted in an increase in normalized bond strength. Beam models displayed an average of 20.45% higher normalized bond strength as the ratio of concrete cover over bar diameter increased from 1.58 to 3.17.

- CFRP RC beams with a 12 mm bar diameter outperformed AFRP and GFRP RC beams, exhibiting a 24.14% and 23.26% increase in maximum loading, respectively. In terms of maximum mid-deflection, CFRP RC beams with a 12 mm bar diameter displayed a 36.69% and 23.6% decrease compared to AFRP and GFRP RC beams, respectively.

- Pull-out failure was associated with concrete compressive strength values between 25 and 30 MPa, while de-bonding failure was linked to concrete compressive strength ranging from 30 to 45 MPa.

- The results indicated a 15.8% increase in ultimate load for beams with concrete compression of 45 MPa and a 12 mm bar diameter, and an increase in ultimate load by 18.7% for the mentioned beam model with a change in the modulus of elasticity of FRP bars from 45 GPa to 69 GPa, and subsequently from 69 GPa to 136 GPa. This increase was attributed to the rise in the young's modulus of FRP bars.

- The results for DIF (Design Impact Factor) demonstrated increased strength with an increase in bar diameter and strain rate. Lower DIF values were observed for

models with lower length to diameter ratios, aligning with existing literature and CEB-FIP code, which considers static concrete strength with a length to diameter ratio of 2.

- A trend in deformability at failure was identified, with CFRP models exhibiting approximately 1.3% deformability, AFRP models displaying around 2.8%, and GFRP models exhibiting about 2.3%. All FRP RC beam models were influenced by strain rate and showed dependency. Further investigations into a greater number of FRP RC beam models subjected to high strain rates are needed for a more comprehensive understanding and practical applications.

7.4 Recommendation for future work

Based on the numerical investigations conducted in this study, several areas for further research can be identified to enhance our understanding of the bond behaviour of FRP RC beams. The following recommendations for future work are presented:

- **Exploration of Various Time Histories:** This study examined the impact of a single time history on FRP RC models. To gain a more comprehensive understanding of the bond behaviour of FRP RC beams under impact loading, it is essential to investigate the influence of different time histories on impact loads and the bond behaviour of these beams as it effects structure vibrates and response to impact wave form. Furthermore, it leads to amplified displacements and stresses. Other effects caused by importance of time histories is the result in structural damage and failures.

  Time history also influences on energy absorption of structure under the impact. Adequate energy dissipation mechanisms, such as damping, are critical for mitigating damage.

- **Effect of Pre-Stressing**: Many reinforced concrete structures incorporate pre-stressing. Therefore, it is valuable to explore the impact of pre-stressing on the bond behaviour of FRP-reinforced concrete under dynamic loading conditions, such as high-velocity impact and see the effect on type of failures develops.

- **Strain Rate Effects in High Mass Impact Loading:** Further research should be conducted to examine the influence of strain rate in the context of high-mass impact loading on FRP RC members. Understanding how strain rate affects bond behaviour under such conditions is crucial for structural engineering applications.

- **Cross-Sectional Variation:** This study primarily focused on rectangular cross-section beams. Future investigations should encompass a broader range of cross-sectional shapes, including I-shaped and T-shaped profiles, as well as other FRP RC structural members, subjected to high-velocity impact loads.

- **Exploration of Additional FRP Materials:** While this study examined Carbon, Aramid, and Glass FRP bars, it is advisable to explore the bond behaviour of FRP RC beams reinforced with other types of FRP materials, such as Basalt. This can provide valuable insights into the applicability of different FRP materials in high-velocity impact scenarios.

- **Cracking and Failure Mode Analysis:** Future studies should delve into the detailed analysis of cracking patterns and failure modes exhibited by FRP RC beams under high-velocity impact loading. Understanding how these beams respond to dynamic loads and identifying critical failure mechanisms can inform safer and more resilient structural designs.

Reference

[1] A. Borosnyoi, “Influence of sevice temperature and strain rate on the bond performance of CFRP reinforcement in concrete,” *Composite Structures,* no. 127, pp. 18-27, 2015.

[2] Z. Saleh, “Numerical analysis of behaviour of glass fiber-reinforced polymer bar-reinforced concrete beams under impact loads,” *ACI Structural Journal,* vol. 116, no. 5, pp. 151-160, 2019.

[3] A. Nadjai, “Experimental testing o concrete beams reinforced with carbon FRP bars,” *Journal of composite materials,* vol. 41, no. 22, pp. 2657-2673, 2007.

[4] M. Baena, “Experimental study on bond behaviour between concrete and FRP bars using pull-out test,” *Composites: Part B,* vol. 40, no. 8, pp. 784-797, 2009.

[5] W. Zhao, “Crack and deformation behaviour of FRP reinforced concrete structures,” University of Sheffield, Sheffield , 1999.

[6] P. Buchana, “Blast resistance of FRP composite and polymer strengthened concrete and masonary structures-A state-Of-Art-Review,” *Cmpos. Part-B Engineering,* vol. 38, no. 5-6, pp. 509-522, 2007.

[7] H. Zhang, “Bond failure performances between near-surface mounted FRP bars and concrete for flexural strengthening concrete structures,” *Engineering failure analysis,* vol. 56, pp. 39-50, 2015.

[8] I. F. Kara, “deflection of concrete structures reinforced with FRP bars,” *composites: Part B,* vol. 44, pp. 375-384, 2013.

[9] A. G. Razaqpour, “blast loading response of reinforced concrete panels reinforced with externally bonded GFRP laminates,” *Composites part B: Engineering,* vol. 38, pp. 535-546, 2006.

[10] A. c. 440R-6, “FRP composites: an overview of constituent materials,” in *state-of-art report on fiber reinforced plastic (FRP) reinforcement for concrete structures*, MI, Ed., Detroit, American concrete institution , 1996, pp. 18-20.

[11] J. Bai, “Polyester resins as a matrix material in advanced fibre-reinforced polymer (FRP) composites,” in *Advanced fibre-reinforced polymer (FRP) composites for structural applications*, Woodhead Publishing Limited, 2013, pp. 51-55.

[12] I. c. solutions, “intera link techno,” [Online]. Available: http://www.intralinktechno.com/pultrusion-process/. [Accessed 19 December 2016].

[13] M. Guadagnini, “To advance present Knowledge university of sheffield,” 2010. [Online]. Available: http://mguadagnini.staff.shef.ac.uk/frp/frp.php. [Accessed 19 December 2016].

[14] A. Farghali and B. Benmokrane, “Evaluation of Flexural behavior and serviceability performance of concrete beams reinforced with FRP bars,” *Composites for constructions,* vol. 15, no. 5, pp. 682-695, 2011.

[15] E. Cosenza, “Behavior and modeling of bond of FRP rebars to concrete,” *Journal of composites for construction,* vol. 1, no. 2, pp. 40-51, May 1997.

[16] Abrate. S, “Impact on composite structures,” Cambridge, 2005.

[17] M. J. Cantwell. W, “The impact resistance of composite materials- a review,” *Composites,* no. 22, pp. 347-62, 1991.

[18] M. B. Munoz, “study of bond behaviour between FRP reinforcement and concrete,” A thesis submitted for the degree of Doctor of Philosophy, University of Girona, 2010.

[19] V. Srikanth, “Models for the strain-rate-dependet behavior of polymer composites,” *Composites science snd Technology,* vol. 61, pp. 1-12, 2001.

[20] J. Dai, “"A critical steel yielding length model for predicting intermediate crack-induced debonding in FRP-strengthened RC members",” *Steel & composite structures,* vol. 8, no. 6, pp. 457-473, 2008.

[21] D. Shen, “Strain rate effect on effective bond length of basalt FRP sheet bonded to concrete,” *Construction and Building Materials,* no. 82, pp. 206-218, 2015.

[22] D. Shen, “Strain rate effect on bond stress-slip relationship between basalt fiber-reinforced polymer sheet and conscrete,” *Reinforced plastics & composites,* vol. 34, no. 7, pp. 547-563, 2015.

[23] M. Goldstone, “Experimental investigation of the behaviour of concrete beams reinforced with GFRP bars under static and impact loading,” *Engineering Structures,* vol. 113, pp. 220-232, 2016.

[24] ASSHTO, Guide specifications and commentary for vessel collision design of highway bridges, Washington, D.C. USA: American association of state highway and transportation, 1991.

[25] UKAEA. Barr. P, Guidelines for the design and assessmnet of concrete structures subjected to impact, Warrington, Chesire, UK: UK atomic energy authority safety and reliability directirate, 1990.

[26] G. MW, “Flexural behavioour of GFRP reinforced high strength and ultra high strength concrete beams,” *construction and building materials,* no. 131, pp. 606-17, 2017.

[27] G. MW, “Experimental investigation on the behaviour of GFRP bar reinforced HSC and UHSC beams under static and impact loading,” *Structures,* no. 22, pp. 109-23, 2019.

[28] Z. Saleh, “Numerical analysis of behaviour of glass fibre-reinforced polymer bar-reinforced concrete beams under impact loads,” *ACI structural journal,* no. 116, pp. 151-60, 2019.

[29] J. M. Plecnik, “Transfer of composite technology to design and construction of bridges,” Federal Highway Administration, NC USA, 1989.

[30] 4. ACI committee, “ACI 440R - 07, Report on fibre-reinforced polymer (FRP) reinforcement for concrete structures,” American Concrete Institute, Farmington Hills, MI, 2007.

[31] A. Nanni, “FRP reinforcement,” in *Reinforced concrete with FRP bars*, Taylor & Francis Group, 2014, pp. 4-5.

[32] A. K. Kaw, mechanics of composite materials, 2nd ed., Boca Raton: Taylor & Francies , 2005.

[33] L. c. Bank, “FRP reinforcements for new concrete structural members,” in *composites for construction: structural design with FRP materials*, Canada, John Wiley & sons, INC, 2007, pp. 1-39.

[34] C. Bakis, “Fibre-reinforced polymer composites for construction: State-of-the art review,” *ASCE Journal of Composites for Construction,* vol. 2, no. 6, pp. 73-87, 2002.

[35] H. Fukuyama, “FRP composites in Japan,” *Concrete International,* vol. 10, no. 21, pp. 29-32, 1999.

[36] L. C. Bank, “Properties of FRP reinforcement for concrete,” in *fiber-reinforced-plastic reinforcement for concrete structures: properties and applications*, A. Nanni, Ed., Amesterdam, Elsevier, 1993, pp. 59-86.

[37] ISIS-canada, “FRP reinforcing materials,” in *Reinforcing concrete structures with Fibre-reinforced polymers design manual*, Leslie Jaeger, ed., Canada, ISIS Canada REsearch network, 2007, pp. 22-34.

[38] E. ,. C. A. Frollini, “Phenolic resins and composites,” in *Wiley encyclopedia of composites*, New York, John Wiley & Sons, 2012, pp. 2059-2068.

[39] C. Au, “Moisture degradation in FRP bonded concrete systems: An interface fracture approch,” PhD Thesis, Massachusetts Institute of Technology, 2005.

[40] A. Mouritz, “fire properties of polymer composite materials,” Springer, Dordrecht, Netherlands, 2006.

[41] B. Benmokrane, “Glass fibre reinforced plastic (GFRP) rebars for concrete structures,” *Construction and Building Materials,* vol. 9, no. 6, pp. 353-364, 1995.

[42] M. Erki, “FRP reinforcement for concrete structures,” *Concrete International,* vol. 15, no. 6, pp. 48-53, 1993.

[43] A. Nanni, “Material properties,” in *Reinforced concrete with FRP bars*, U.S, CRC press-Taylor and Francis group, 2014, pp. 23-33.

[44] A. 440.1R-15, “Guide for the design and constructioon of structural concrete reinforced with fibre-reinforced polymer (FRP) bars,” American Concrete Institute, Farmington hills, Michigan, 2015.

[45] M. Choi, “The effect of coupling agent on electrical and mechanical properties of carbon fibre/phenolic resin composites,” *Polymer,* vol. 41, no. 9, pp. 3243-3252, 2000.

[46] H. Ogawa, “Architectual application of carbon fibres: Development of new carbon fibre reinforced glulam,” *Carbon,* vol. 38, no. 2, pp. 211-226, 2000.

[47] J. Sim, “characteristics of basalt fibre as a strengthening material for concrete structures,” *Composites Part B: Engineering,* vol. 36, no. 6-7, pp. 504-512, 2005.

[48] A. Gardziella, “Production of phenolic resins,” in *Phenolic Resins: chemistry, applications, standardization, safety and ecology*, Berlin, Germany, Springer, 2000, pp. 83-90.

[49] S. Peters, Handbook of composites, 2nd ed., California: Springer, 1998.

[50] G. Eckold, Design and manufacture of composite structures, Cambridge, England: Woodhead publishing limited, 1994.

[51] W. Wu, “Thermo mechanical properties of fiber reinforced plastic (FRP) bars, PhD Thesis,” West Virginia University, Morgantown, 1990.

[52] E. Gudonis, “FRP reinforcement for concrete structures: state-of-the-art review of application and design,” *engineering structures and Technology,* vol. 5, no. 4, pp. 147-158, 2013.

[53] G. Portnov, “FRP reinforcing bars- Designs and Methods of Manufacture,” *Mechanics of Composite Materials,* vol. 49, no. 4, pp. 569-596, 2013.

[54] D. Kopeliovich, “SubsTech- Substances & Technologies,” 2012. [Online]. Available: http://www.substech.com/dokuwiki/doku.php?id=pultrusion. [Accessed 08 February 2017].

[55] C. Burgoyne, “Why is FRP not a financial success,” Greece, 2007.

[56] A. C. M. Association, “Guidelines and Recommended Practices for Fiber-Reinforced Polymer (FRP) Architectural Products,” American Composites Manufacturers Association, Unites states, 2016.

[57] R. Davies, “The effect of strain rate upon the tensile deformation of materials,” *J. Eng. Mater. Technol,* vol. 97, no. 2, pp. 151-155, 1975.

[58] A. Rotem and J. Lifshitz, “Longitudinal strength of unidirectional fibrous composite under high rate of loading, "26th annual technical conference,” 1971.

[59] J. Lifshitz, “Impact strength of angle ply fiber reinforced materials,” *Journal of composite materials,* vol. 10, no. 1, pp. 92-101, 1976.

[60] O. Okoli, “Overcoming inertial problems in the high strain rate testing of a Glass/Epoxy composite. Proceedings of Society of Plastics Engineers Annual Technical Conference, Vol. 2, pp. 2998-3002,” 1995.

[61] O. Okoli, “Development of a semi-empirical method for obtaining the dynamic young's modulus in random continuous reinforced Glass/Epoxy composites,” *Journal of reinforced plastics and composites,* vol. 19, no. 4, pp. 292-300, 2000.

[62] O. Okoli, “Aspects of the tensile response of random continuous Glass/Epoxy composites,” *Journal of reinforced plastics and composites,* vol. 18, no. 7, pp. 606-613, 1999.

[63] A. Armenakas, “Experimental investigation of the failure mechanism of fiber-reinforced composites subjected to uniaxial tension,” *Experimental Mechanics,* vol. 13, no. 2, pp. 49-58, 1973.

[64] J. Harding, “A tensile testing technique for fibre-reinforced composites at impact rates of strain,” *Journal of Materials Science,* vol. 18, no. 6, pp. 1810-1826, 1983.

[65] L. Welsh, “Effect of strain-rate in the tensile failure of woven reinforced polyester resin composites,” *Journal De Physique,* vol. 46, pp. C5-405 - C5-414, 1985.

[66] V. Shim, “Dynamic tensile response of a carbon-fiber-reinforced LCP composite and its temperature sensivity, proceeding volume 4317,” 2001.

[67] S. Bai, “Tensile properties of rigid glass bead/HDPE composites,” *Polym polym Composites,* vol. 8, no. 6, pp. 413-418, 2000.

[68] I. Daniel, “Dynamic response of Carbon/Epoxy composites, in high strain rate effects on polymer, metal ceramic matrix composites and other advanced material,” *ASME,* vol. 48, pp. 167-177, 1995.

[69] S. Hayes, “Rate sensetive tensile impact properties of fully and partially loaded unidirectional composites,” *Journal of Testing and Evaluation,* vol. 10, no. 2, pp. 61-68, 1982.

[70] I. Daniel, “T. in proceedings of second international conference on composite materials,” Toronto, pp. 1003-1018, 1978.

[71] I. Daniel, “Strain rate effects on the mechanical properties of fiber composites,” Report NASA CR-135087, part 3, 1976.

[72] K. Kawata, “dynamic behaviour analysis of composite materials,” Tokyo-Japan, 1981.

[73] K. Kawata, “Mechanical behaviours in high velocity tension of composites,” Tokyo-Japan, 1982.

[74] B. Peterson, “static and high strain rate response of glass fiber reinforced thermoplastic,” *J. Compos. Mater,* vol. 25, pp. 887-906, 1991.

[75] J. Tzeng, “Dynamic compressive properties of laminated composites at high rates of loading,” 1996.

[76] J. Tzeng, “Dynamic compressive properties of composites at interior ballistic rate of loading, Experimental method,” *US, Army Research Laboratory,* vol. 5, no. 5, pp. 501-8, 1995.

[77] J. Tzeng, “An experimental method for compressive properties of laminated composites at high rates of loading,” *Journal of Thermoplastic Composite Materials,* vol. 11, pp. 133-143, 1998.

[78] C. Cazeneuve, “Etude du comportmenet de composites a fibre de graphite sous differentes vitesses de deformation,” *J. de Phys., Colloque C5,* vol. 46, pp. 551-556, 1985.

[79] FIB, Bond of Reinforcement in Concrete: State-of-the-art report, Lausanne, Switzerland: federation internationale du beton, January 2000.

[80] Tassios, Properties of bond between concrete and steel under load cycles idealising siesmic actions, 131 ed., Rome, Italy: CEB Bulletin, 1979.

[81] Z. Achillides, “Bond behaviour of FRP bars in concrete, PhD Thesis,” University of Sheffield, Sheffield, 1998.

[82] ACI.408_03, “Bond and development of straight reinforcing bars in tension,” American Concrete Institute, Farmington Hills, MI, 49pp, 2003.

[83] S. Quayyum, “Bond behaviour of fibre reinforced polymer (FRP) rebarsin concrete, MSc Thesis,” University of British Columbia, Research gate, Okanagan, 2010.

[84] B. Tighiouart, “Investigation of bond in concrete member with fibre reinforced polymer (FRP) bars,” *Construction and Building Materials,* vol. 12, pp. 453-462, 1998.

[85] T. Kanakubo, “Bond performance of concrete members reinforced with FRP bars,” *ACI international symposium on FR reinforcement for concrete structures,* vol. 138, pp. 767-788, 1993.

[86] J. Larralde, “bond and slip of FRP rebars in concrete,” *ASCE Journal of Materials in Civil Engineering,* vol. 5, no. 1, pp. 30-40, 1993.

[87] B. Benmokrane, “Bond strength and load distribution of composite GFRP reinfrocring bars in concrete,” *ACI Mater J,* vol. 93, no. 3, pp. 246-253, 1996.

[88] E. Makitani, “Investigation of bond in concrete member with fibre reinforced plastic bars,” *ACI International Symposium on FRP reinforcement for concrete structures,* vol. 138, pp. 315-332, 1993.

[89] EUROCRETE, “The development of non-ferrous reinforcement for concrete structures,” Euro-Projects (LTTC) Ltd, 1997.

[90] Z. Achillides, “bond behaviour of fibre reinforced polymer bars under direct pullout conditions,” *ASCE J Composer Construction,* p. 17, 2004.

[91] S. Daniali, “Bond strength of fibre reinforced plastic bars in concrete, Serviceability and Durability of Construction Materials,” Denvor, USA, 1990.

[92] S. S. Faza, “Bending and bond behaviour and design of concrete beams reinforced with fibre reinforced plastic rebars, PhD thesis,” west virginia university, west virginia , 1991.

[93] M. Ehsani, “Bond of GFRP Rebars to Ordinary-Strength Concrete,” *Special publication,* pp. 333-346, 1993.

[94] M. Ehsani, “Bond of hooked glass fibre reinforced plastic (GFRP) reinforcing bars to concrete,” *ACI Materials Journal,* vol. 92, no. 4, pp. 391-400, 1995.

[95] M. Ehsani, “Design recommendations for bond of GFRP rebars to concrete,” *Journal of Structural Engineering-ASCE,* vol. 122, no. 3, pp. 247-254, 1996.

[96] T. Kanakubo, “Bond performance of concrete members reinforced with FRP bars,” *ACI,* vol. 138, pp. 767-788, 1993.

[97] B. Benmokrane, “FRP C-bar as reinforcing rod for concrete structures,” Montreal, 1996.

[98] E. Cosenza, “Bond characteristics and anchorage length of FRP rebars,” 1996.

[99] E. Cosenza, “Bond between glass fibre reinforced plastic reinforcing bars and concrete-experimental analysis,” *ACI SP int. Symp on FRP in Reinforced Concrete,* pp. 347-358, 1999.

[100] R. Tepfers, “Pullout and tensile reinforcement splice tests with GFRP bars,” Arizona-USA, 1998.

[101] C. Shield, “Bond of glass fibre reinforced plastic reinforcing bar for consideration in bridge decks,” *ACI SP int. Symp on FRP in Reinforced Concrete,* pp. 393-406, 1999.

[102] C. Mosley, “Bond performance of fibre reinforced plastic (FRP) reinforced in concrete, MS thesis,” Purdue University, West Lafayette, 2000.

[103] M. Pecce, “Experimental and analytical evaluation of bond properties of GFRP bars,” *Journal of Materials in Civil Engineering,* vol. 13, no. 4, pp. 282-290, 2001.

[104] J. DeFreese, “Glass fibre reinforced polymer bars as top mat reinforcement for bridge decks,” Contract report for Virginia Transportation Research council, 2002.

[105] R. B. B. Aly, “Bond splitting strength of lap splicing of GFRP bars in concrete,” Toronto-Canada, 2005.

[106] R. Aly, “Stress along tensile lap-spliced fibre reinforced polymer reinforcing bars in concrete,” *Canadian Journal of Civil Engineering,* vol. 34, pp. 1149-1158, 2007.

[107] R. Okelo, “Realistic bond strength of FRP rebars in NSC from beam specimens,” *Journal of Aerospace Engineering,* vol. 20, no. 3, pp. 133-140, 2007.

[108] A. Nanni, “Bond of FRP reinforcement to concrete experimental results,” *2nd Int, RILEM Symp,* pp. 135-145, 1995.

[109] M. Al-Zahrani, “bond behaviour of fiber reinforced plastic (FRP) reinforcements with concrete, PhD Thesis,” Pennsylvania State University, USA, 1995.

[110] E. Makitani, “Investigation of bond in concrete member with fibre reinforced plastic bars,” *First International Symposium on Non-Metallic (FRP) Reinforcement for concreet Structures,* pp. 315-332, 1993.

[111] J. Lee, “Interfacial bond strength of glass fiber reinforced polymer bars in high strength concrete,” *Composites: Part B Engineering,* vol. 39, no. 2, pp. 258-270, 2008.

[112] CSA, CSA S806-02 Design and construction of Building Components with fiber-reinforced polymers, Canada: Canadian Standards Association, 2002.

[113] F. Al-Mahmoud, “Effect of surface pre-conditioning on bond of carbon fibre reinforced polymer rods to concrete,” *cement and Concrete Composites,* vol. 29, no. 9, pp. 677-689, 2007.

[114] L. Malvar, “Bond stress-slip characteristics of FRP rebars,” Office of Naval Research, Port Hueneme, 1994.

[115] A. Hattori, “A study on bond creep behaviour of FRP rebar embedded in concrete,” RILEM Symp, 1995.

[116] Q. Hao, “Bond strength of glass fiber reinforced polymer ribbed rebars in normal strength concrete,” *Construction and Building Materials,* vol. 23, no. 2, pp. 865-871, 2009.

[117] J. Larralde, “Bond and slip of FRP rebars in concrete,” *Journal of Materials in Civil Engineering,* vol. 5, no. 1, 1993.

[118] O. Chaallal, “Pullout and bond of glass-fibre rods embedded in concrete and cement grout,” *Materials and Structures,* vol. 26, no. 3, pp. 167-175, 1993.

[119] L. Pleimann, “Tension and bond pull-out tests of deformed fibreglass rods, Final report for Marshall-Vegas Corporation, Marshall, Arkansas, Civil Engineering Department,” University of Arkansas, Fayetteville, Ark, 5-11, 1987.

[120] S. Faza, “Bending and bond behvaiour of concrete beams reinforced with plastic rebars,” *Trasportation Research Record,* vol. 2, no. 1290, pp. 185-193, 1990.

[121] R. Okelo, “Bond strength of fibre reinforced polymer rebars in normal strength concrete,” *Journal of Composites for Construction,* vol. 9, no. 3, pp. 203-213, 2005.

[122] M. Karlsson, “Bond between C-bar FRP reinforcement and concrete, Graduation Thesis,” Chalmers University of Technology, Goteborg, Sweden, 1997.

[123] V. Rossetti, “Local bond stress-slip relationships of glass fibre reinforced plastic bars embedded in concrete,” *Material and Structures,* vol. 28, no. 6, pp. 340-344, 1995.

[124] R. Tepfers, “Atheory of bond applied to overlapped tensile reinforcement splices for deformed bars,” Publication 73:2, Division of concrete structures, Chalmers University of Technology, Goteborg, Sweden, 1973.

[125] C. O. Orangun, “Reevaluation of test data on development length and splices,” *ACI Journal,* vol. 74, no. 3, pp. 114-122, 1977.

[126] D. Darwin, “Effect of deformation height and spacing on bond strength of reinforcing bars,” *ACI Structural Journal,* vol. 90, no. 6, pp. 646-657, 1993a.

[127] D. Darwin, “Effect of deformation height and spacing on bond strength of reinforcing bars, SL Report 93-1,” University of Kansas Center for Research, Lawrence, Kans, 1993b.

[128] B. Wambeke, “Development length of glass fiber-reinforced polymer bars in cocrete,” *ACI Structural Journal,* vol. 103, no. 1, pp. 11-17, 2006.

[129] M. Guadagnini, “Tests for the evaluation of bond properties of FRP bars in concrete,” Adelaide, Australia, 2004.

[130] JSCE, “Test method for shear properties of continuous fiber reinforcing materials by double plane shear, JSCE-E 540,” Japan Society of Civil Engineers, Tokyo, Japan, 1995.

[131] JSCE, “Recommendation for design and construction of concrete structures using continuous fiber reinforcing materials, Concrete Engineering Series No.23,” Japan Society of Civil Engineers, Tokyo, Japan, 1997.

[132] ISIS, “Reinforcing concrete structures with fibre reinforced polymers,” The Canadian Network of Centres of Excellence on Intelligent Sensing for innovative Structures, Design Manual No.3, Winnipeg, Manitoba, Canada, 2001.

[133] CSA, “Design and construction of building structures with fibre-reinforced polymers,” Canadian Standards Association, S806-12, Ontario, Canada, 2012.

[134] ACI, “Guide for the design and construction of structural concrete reinforced with fiber-reinforced polymer (FRP) bars,” American Concrete Institute, ACI 440.1R-01, Farmington Hills, Michigan, USA, 2001.

[135] ACI, “Guide for the design and cinstruction of structural concrete reinforced with fiber-reinforced polymer (FRP) bars,” American Concrete Institute, ACI 440.1R-03, Farmington Hills, Michigan USA, 2003.

[136] ACI, “Guide for rhe design and construction of structural concrete reinforced with fiber-reinforced polymer (FRP) bars,” American Concrete Institute, ACI 440.1R-06, Farmington Hills, Michigan, USA, 2006.

[137] ACI, “Report on fiber-reinforced polymer (FRP) reinforcement for concrete,” American concrete Institute, ACI 440.XR-07, Farmington Hills, Michigan, USA, 2007.

[138] J. Clarke, “Design of concrete structures reinforced with fibre composite rods,” Proc., Non-Metallic (FRP) Reinforcement for Concrete Structures (FRPRCS-2),, London, 646-653, 1995.

[139] K. Pilakoutas, “Design philosophy issues of fibre reinforced polymer reinforced concrete structures,” *ASCE.J Compsite Construction,* vol. 6, no. 3, pp. 154-161, 2002.

[140] FIB, “FRP reinfocement in RC structures,” federattion International Du Beton, Lausanne, Switzerland, 2007.

[141] Eurocode2, “Design of Concrete Structures: Genral Rules and Rules for Buildings- EN 1992-1-1:2004,” CEN, Brussels, 2004.

[142] CNR, “Guide for the Design and Construction of Concrete Structures Reinforced with Fibre-Reinforced Polymer Bars,” Advisory Committee on Technical Recommendations for Construction, Italy, 2007.

[143] C. Mias, “Effect of Material Properties on Long-term Deflection of GFRP Reinforced Concrete Beams,” *Construction and Building Materials,* vol. 41, pp. 99-108, 2013.

[144] V. Gribniak, “Comparative analysis of deformations and tension-stiffening in concreet beams reinforced with GFRP or Stell bars and fibres,” *Composites Part B: Engineering,* vol. 50, pp. 158-170, 2013.

[145] R. Balendran, “Application of FRP bars as reinforcement in civil engineering structures,” *Structural Survey,* vol. 20, no. 2, pp. 62-72, 2002.

[146] A. McNaughton, “The maintanance and renewal of bridges,” *Network Rail sponsored supplier conference, Bristol,* pp. 22-23, 2006.

[147] P. I. J. Domone, “Application of FRP composites in Civil Engineering,” in *Construction Materials: Their Nature and Behaviour, Fourth Edition*, J. I. P. Domone, Ed., Boca raton, CRC Press, 2010, pp. 348-364.

[148] R. W. Clough, Dynamics of structures, 3rd ed., New York: Computers and Strucutres Incorprated, 2003.

[149] A. Ruiters, “analytical behaviour of FRP strengthened reinforced concrete beams under low velocity impact loads incorporating rate dependent material constitutive models, MSc Desertation,” University of Cape town, south Africa, 2014.

[150] A. Kappos, Dynamic loading and design of structures, London: spon press, 2001.

[151] M. Macaulay, Introducing to impact engineering, London: Springer Netherlands, 1987.

[152] Y. Hou, “Strain rate effects of tensile behaviors of 3-D orthogonal woven fabric: Experimental and finite element analysis,” *Textile Research Journal,* vol. 83, no. 4, pp. 337-354, 2013.

[153] S. Chocron, “Dynamic tensile testing of aramid and polyethylene fiber composites,” *International Journal of Impact Engineering,* vol. 19, no. 2, pp. 135-146, 1997.

[154] Y. Hao, “Numerical analysis of lateral intertial confinement effects on impact test of concrete compressive material properties,” *International Journal of Protective Structures,* vol. 1, no. 1, pp. 145-168, 2010.

[155] D. Adams, “A tensile impact test apparatus for composite materials,” *Experimental Mechanics,* vol. 29, no. 4, pp. 466-473, 1989.

[156] B. Harris, “Strength and fracture toughness of carbon fibre polyester composites,” *Journal of Materials Science,* vol. 6, no. 3, pp. 238-251, 1971.

[157] N. Hancox, “Izod impact testing of carbon-fibre-reinforced plastics,” *Composites,* vol. 2, no. 1, pp. 41-45, 1971.

[158] M. Shokrieh, “Tension behavior of unidirectional glass/epoxy composites under different strain rates,” *Composite Structures,* vol. 88, no. 4, pp. 595-601, 2009.

[159] A. Armenakas, “Response of glass-fiber-reinforced epoxy specimens to high rates of tensile loading,” *Experimental Mechanics,* vol. 13, no. 10, pp. 433-440, 1973.

[160] A. Bilotta, “FRP to concrete interface debonding,” *Composites Part B: Engineering,* vol. 42, no. 6, pp. 1539-1553, 2011.

[161] U. Neubauer, “Design aspects of concrete structures strengthened with externally bonded cfrp plates,” *Concrete and Composites,* vol. 2, pp. 109-118, 1997.

[162] JCI, “Technical report of technical committee on retrofit technology,” Japan Concrete Institute, 4-42, Tokyo, 2003.

[163] M. Savoia, “Non linear bond-slip law for FRP concrete interface. In: Proceedings of the sixth international symposium on FRP reinforcement for concrete structures, pp.163-172,” Singapore, 2003.

[164] H. Kim, “Debonding failure analysis of FRP-retrofitted concrete panel under blast loading,” *Structural Engineering and Mechanics,* vol. 38, no. 4, pp. 479-501, 2011.

[165] S. Al-Hassini, “Strain rate effect on GRP, KRP and CFRP composite laminates,” *Key Engineering Material,* Vols. 141-143, pp. 427-452, 1998.

[166] K. Kim, “Blast response of glass-fiber composite plates with progressive material damage model,” Newport Rhode Island, 2002.

[167] J. Nam, “Numerical evaluation of the retrofit effectiveness for GFRP retrofitted concrete slab subjected to blast pressure,” *Composite Structures,* vol. 92, no. 5, pp. 1212-1222, 2010.

[168] A. Pandey, “Damage prediction of RC containment shell under impact and blat loading,” *Structural Engineering and Mechanics,* vol. 36, no. 6, pp. 729-744, 2010.

[169] G. Yun, “A total strain-based hysteretic material model for reinforced concrete structures: Theory and Verifications,” *Computers and Concrete,* vol. 5, no. 3, pp. 217-241, 2008.

[170] UFC-3-340-02, “Uniform Facilities Criteria (UFC): Structures to resist the effects of Accidental Explosions,” U.S. Department of Defence, Washington DC, USA, 2008.

[171] S. Orton, “Strain rate effects in CFRP used for blast mitigation,” *Polymers,* vol. 6, pp. 1026-1039, 2014.

[172] B. Nejdar, “Modeling of unidirectional fibre-reinforced composites under fibre damage,” *Mechanics Research Communications,* vol. 56, pp. 115-122, 2014.

[173] L. Ascione, “Creep phenomena in FRP materials,” *Mechanics Research Communications,* vol. 43, pp. 15-21, 2012.

[174] R. Sierakowski, “Strain rate effects in composites,” *applied Mechanics Review,* vol. 50, no. 12, pp. 741-761, 1997.

[175] G. Jacob, “strain rate effects on the mechanical properties of polymer composite materials,” *Journal of Applied Polymer Science,* vol. 94, no. 1, pp. 296-301, 2004.

[176] F. Al-Salehi, “Experimental investigation into the strength of angle ply GRP tubes under high rate of loading,” *Journal of Composites Materials,* vol. 23, no. 3, pp. 288-305, 1989.

[177] M. Shokrieh, “Tension behaviour of unidirectional glass/epoxy composites under different strain rates,” *Composite Structures,* vol. 88, no. 4, pp. 595-601, 2009.

[178] D. Asprone, “Strain rate sensitivity of a pultruded E-glass/polyester composites,” *Journal of Composites for construction,* vol. 13, no. 6, pp. 558-564, 2009.

[179] M. Saiidi, “Strain rate effects on strength of unidirectional FRP fabrics and bond to concrete. In: Proceeding of the third international conference on FRP composites in civil engineering,” Miami, 2006.

[180] J. Shi, “Experimental study of the strain rate effect of FRP sheet-concrete interface,” *Chins Civil Engineering Journal,* vol. 45, pp. 99-107, 2012.

[181] M. Captain, “FRP rehabilitation of blast and impact damaged reinforced concrete,” Published Heritage Branch, Canada, 2009.

[182] N. Banthia, “Impact resistance of concrete, PhD thesis,” University of British Columbia, Vancouver, 1987.

[183] L. Simms, “Actual estimated impact resistance of some reinforced concrete units failing in bending,” *Journal of the instutive of civil engineering,* vol. 4, pp. 163-179, 1945.

[184] T. Pham, “Review of concrete structures strengthened with FRP against impact loading,” *Structures,* vol. 7, pp. 59-70, 2016.

[185] K. Fujikake, “Impact response of reinforced concrete beam and its analytical evaluation,” *J. Struct. Eng,* vol. 135, no. 8, pp. 938-950, 2009.

[186] Y. Chen, “Reinforced concrete members under drop-weight impacts,” *Proceeding of the institution of Civil Engineers,* vol. 162, no. 1, pp. 45-56, 2009.

[187] H. Ohnuma, “Dynamic response of local rupture of reinforced concrete beam and slab under impact loading,” Brussels, Belgium, 1985.

[188] S. Rostron, “The effect of reinforcement on flexural failure mechanisms in reinforced concrete beams subjected to impact loading, Bachelor of Civil Engineering Thesis,” University of Wollongong, Wollongong, Australia, 2012.

[189] N. Kishi, “Impact behaviour of Shear-Failure-Type RC beams without shear rebar,” *International journal of Impact Engineering,* vol. 27, no. 9, pp. 955-968, 2002.

[190] A. Thabet, “Three-dimensional finite element model for structural concrete subjected to impact loading, PhD Thesis,” Department of Civil and Offshore engineering, Heriot-Watt University, Edinburgh, UK, 1994.

[191] D. Haldane, “Three-dimensional simulation of nonlinear response of reinforced concrete members subjected to impact loading,” *ACI Structural Journal,* vol. 97, pp. 689-702, 2000.

[192] A. Sangi, “Reinforced concret structures under impact loads, PhD thesis,” School of the Built Environment, Heriot-Watt University, Edinburgh, Scotland, 2011.

[193] T. Ngo, “Blast loading and blast effects on structures- An overview,” *EJSE International Special Issue: Loading on Structures,* pp. 76-91, 2007.

[194] T. Ngo, “high strain rate behavior of concretecylinders subjected to uniaxial compressive impact loading,” Perth, Australia, 2004.

[195] D. Grote, “Dynamic behaviour of concrete at high strain rates and pressures,” *Journal of Impact Engineering,* vol. 25, pp. 869-886, 2001.

[196] Be'ton, “CEB-FIP model code,” redwood books, Wiltshire, UK, 1990.

[197] T. Lok, “Impact response of steel fiber-reinforced concrete using a split hopkinson pressure bar,” *Journal of Materials in Civil Engineering,* vol. 16, no. 1, pp. 54-59, 2004.

[198] CAN/CSA, “Canadian highway bridge designe code,” Canadian Standards Association, S6-06, Ontario, Canada, 2006.

[199] N. Newman, “Development length of straight FRP composite bars embedded in concrete,” *J Reinf Plas Compos,* no. 29, pp. 571-89, 2010.

[200] K. Hossein, “Bond strength of standard and high modulus GFRP bars in high strength concrete,” *J Mater Civ Eng,* no. 26, pp. 449-56, 2014.

[201] D. Ametrano, bond characteristics of glass fibre reinforced polymer bars embeded in high performance and ultra-high performance concrete, Ryerson University, 2011.

[202] F. Yan, “Bond mechanism and bond strength of GFRP bars to concrete: a review,” *Composites Part B: Engineering,* vol. 98, pp. 56-69, 2016.

[203] S. M. Pour, Investigation of compressive bond behaviour of steel and fiber reinforced polymer bars embedded in recycled aggregate concrete, University of British Columbia, 2016.

[204] E. Makhmalbaf, GFRP bar bond stress and strength: Comparison of beam-bond and pull-out tests results, McMaster University, 2015.

[205] E. Cosenza, “Analytical modelling of bond between FRP reinforcing bars and concrete,” *Non-Metallic (FRP) reinforcement for concrete structures. London: E & FN Spon,* pp. 164-171, 1995.

[206] R. Eligehausen, “Local bond stress-slip relationships of deformed bars under generalized excitations,” Earthquake Engineering Research Center, report to the National Science Foundation, California, 1983.

[207] M. Faoro, “Bearing and deformation behaviour of structural components with reinforcments comprising,” 1992.

[208] K. Nakaba, “Bond behaviour between fiber-reinforced polymer laminates and concrete,” *ACI Structural Journal,* vol. 3, no. 98, pp. 359-67, 2001.

[209] U. Neubauer, “Bond failure of concrete fiber reinforced polymer plates at inclined cracks-experiments and fracture mechanics model,” in *In: Proc. of 4th international symposium on fiber reinforced polymer reinforcement for reinforced concrete structures*, SP-188.

[210] M. Monti, “FRP adhesion in uncracked and cracked concrete zones,” in *World Scientific Publications*, Singapore, 2003.

[211] R. Murugan, “Experiment on rc beams reinforced with glass fibre reinforced pollymer reinforcements,” *Int. J. Innovative Technol Explor Eng,* vol. 8, no. 4, pp. 35-41, 2019.

[212] A.-A. M, “An experimental investigation into the bond-slip behaviour between CFRp composite and lightweight concrete,” *Construction and building materials,* no. 113, pp. 15-27, 2016.

[213] Z. Y.X, “Bond-slip behaviour of FRP-reinforced concrete beams,” *Construction and building materials,* no. 44, pp. 110-117, 2013.

[214] J. Pan, “Analytical modeling of bond behaviour between FRP plate and concrete,” *Composites: Part B,* no. 61, pp. 17-25, 214.

[215] X. Lu, “Bond-slip models for FRP sheets/plates bonded to concrete,” *Engineering Structures,* no. 27, pp. 920-937, 2005.

[216] J. Chen, “Anchorage strength models for FRP and steel plates bonded to concrete,” *Journal of Structural Engineering,* vol. 7, no. 27, pp. 784-791, 2001.

[217] H. N. J. Eskandari, “Dynamic testing of composite laminates with tensile split Hopkinson bar,” *J. Compos. Mater,* vol. 34, no. 4, pp. 260-73, 2003.

[218] I. Benloulo, “Dynamic tensile testing of aramid and polyethylene fiber composites,” *int. J. Impact energy,* vol. 19, no. 2, pp. 135-46, 1997.

[219] J. Rodriguez, “High strain rate properties of aramid and polyethylene woven fabric composites,” *Composites Part B,* vol. 27, no. 2, pp. 147-54, 1996.

[220] H. Kimura, “Mechanical characterization of unidirectional CFRP thin strip and CFRP cables under quasi-static and dynamic tension,” *Adv Comps Mater,* vol. 10, no. 2/3, pp. 177-87, 2001.

[221] A. Jadhav, “High strain rate properties of balance angle-ply graphite/epoxy composites,” *Composite Part B,* vol. 34, no. 4, pp. 339-46, 2003.

[222] A. Gilat, “Experimental study of strain-rate-dependent behaviour of carbon/epoxy composite,” *Composite Science and Technology,* vol. 62, no. 2, pp. 1469-76, 2002.

[223] M. Daniel, “New method for testing composites at very high strain rates,” *Experimental Mechanics,* vol. 21, no. 2, pp. 71-7, 1981.

[224] J. Lifshitz, “Response of fibre-reinforced polymers to high strain-rate loading in interlaminar tension and combined tension/shear,” *Composite Science and Technology,* vol. 58, no. 6, pp. 987-96, 1998.

[225] S. Barre, “Comparative study of strain rate effects on mechanical properties of glass fibre-reinforced thermoset matrix composite,” *Compos Par AAppl S,* vol. 27, no. 12, pp. 1169-81, 1996.

[226] N. Niak, “High strain rate tensile behaviour of woven fabric E-glass/epoxy composite,” *Polymer Testing,* vol. 29, no. 1, pp. 14-22, 2010.

[227] H. N. J. Eskandari, “Dynamic testing of composite laminates with a tensile split hopkinson bar,” *J. Compos Mater,* vol. 34, no. 4, pp. 260-73, 2003.

[228] R. Foroutan, “Experimental investigation of high strain-rate behaviour of fabric composites,” *Compos Struct,* vol. 106, pp. 264-9, 2013.

[229] F. Elgabbas, “Experimental testing of basalt-fiber-reinforced polymer bars in concrete beams,” *Composite Part B,* vol. 91, pp. 205-218, 2016.

[230] X. Lin and Y. Zhang, “Bond-slip behaviour of FRP-reinforced concrete beams,” *Construction and Building Materials,* vol. 44, pp. 110-117, 2013.

[231] J. Park, “Bond performance of fiber-reinforced polymer rebars in different casting position,” *Polymer Composites,* pp. 2098-2108, 2016.

[232] E. Cosenza, “Development length of FRP straight rebars,” *Composites Part B-Engineering,* vol. 33, no. 7, pp. 493-504, 2002.

[233] L. J. Malvar, “Tensile and bond properties of GFRP reinforcing bars,” *ACI Materials Journal,* vol. 92, no. 3, pp. 276-285, 1995.

[234] L. J. Malvar, “Bond between carbon fiber reinforced polymer bars and concrete, I: Experimental Study,” *Journal of Composites for Construction,* vol. 7, no. 2, pp. 154-163, 2003.

[235] M. Aiello, “Bond performances of FRP rebars-reinforced concrete,” *Journal of Materials in Civil Engineering,* vol. 19, no. 3, pp. 205-213, 2007.

[236] F. Focacci, “Local bond-slip relationships for FRP reinforcement in concrete,” *Journal of Composites for Construction,* vol. 4, no. 1, pp. 24-31, 2000.

[237] Z. Achillides, “FE modelling of bond interaction of FRP bars to concrete,” *Structural Concrete,* vol. 7, no. 1, pp. 7-16, 2006.

[238] L. Jendele, “Finite element modelling of reinforcement with bond,” *Computers and Structures,* vol. 84, no. 28, pp. 1780-1791, 2006.

[239] V. Tvergaard, “Effect of fibre debonding in a whisker-reinforced metal,” *Materials Science and Enginnering,* vol. 125, no. 2, pp. 203-213, 1990.

[240] J. L. Chaboche, “Numerical analysis of composite systems by using interphase/interface models,” *Computational Mechanics,* vol. 20, no. 1-2, pp. 3-11, 1997.

[241] M. Baena, “Experimental study of bond behaviour between concrete and FRP bars using a pull-out test,” *Elsevier, Composites: Part B,* vol. 40, pp. 784-797, 2009.

[242] C. Coulomb, “ESSAY ON MAXIMUMS AND MINIMUMS OF RULES TO SOME STATIC PROBLEMS RELATING TO ARCHITECTURE,” *the National academies of Sciences. Engineering. Medicine,* vol. 7, pp. 343-382, 1973.

[243] D. D.C, “Soil mechanics and plastic analysis for limit design,” *Quarterly of Applied Mathematics,* vol. 10, no. 2, pp. 157-165, 1952.

[244] “Uberdie scherfestigkeit des betons,” *Beton und Eisen,* vol. 34, no. 8, pp. 130-135, 1935.

[245] E. T. B. Evert Hoek, “Emperical Strength Criterion for Rock Masses,” *Journal of Geotechnical Engineerning Division,* vol. 106, no. 9, pp. 1013-1035, 1980.

[246] R. Von Mises, “Mechanic der festen Korper im plastisch deformablen Zustand,” *Gottin. Nachr. Math. Phys.,* vol. 1, pp. 582-592, 1913.

[247] P. Menetrey, “Triaxial Failure Criterion for concrete and its Generalization,” *ACI Structural Journal,* vol. 93, no. 3, pp. 311-318, 1995.

[248] O. Mohr, “Welche Umstande bedingen die Elastizitatsgrenze und den bruch eines Materials,” *Zeitschrift des Vereins Deutscher Ingenieure,* vol. 44, no. 45, pp. 1524-1530, 1900.

[249] N. S. Ottosen, “A Failure Criterion for Concrete,” *Journal of the Engineering Mechanics Division,* vol. 4, no. 103, pp. 527-535, 1997.

[250] J. Lubliner, “A plastic-damage model for concrete,” *International Journal of Solids and Structures,* vol. 25, no. 3, pp. 299-326, 1989.

[251] J. Lee, “Plastic-Damage Model for Cycling Loading of Concrete Structures,” *Journal of Engineering Mechanics, American society of Civil Engineering,* vol. 8, no. 127, pp. 892-900, 1998.

[252] ABAQUS, “ABAQUS 6.14 Analysis User's Manual,” Dassault Systemes, Providence, RI, USA, 2014.

[253] D. Kent, “Flexural members with confined concrete,” *Journal of the structural Division, ASCE,* vol. 97, pp. 1969-1990, 1971.

[254] E. Hognestad, “Concrete Stress Distributon in Ultimate Strength Design,” *ACI Journal,* vol. 52, no. 12, pp. 455-579, 1955.

[255] Z. Mei, Structural hybrid simulation with model updating of material constitutive model, Trento: Doctoral Dissertation, University of Trento, 2018.

[256] K. William, “Constitutive model for the triaxial behaviour of concrete,” *Proc., International Association fo rBridge and Structural Engineering,* vol. 19, pp. 1-30, 1975.

[257] G. Schickert, “Results from tests concerning strength and strain of concrete subjected to multiaxial compressive stresses,” Berlin, West Germany, 1977.

[258] S. Popovics, “A numerical approach to the complete stress-strain curves of concrete,” *Cement and Concrete Research,* vol. 3, no. 5, pp. 583-599, 1973.

[259] M. Reddier, “Stress-strain model of unconfined and confined concrete and stress-block parameters,” Doctoral Dissertation, A&M University, Texas, 2010.

[260] M. Valente, “Chapter 5 - Seismic assessment of historical masonry structures through advanced nonlinear dynamic simulations: applications to castles, churches, and palaces,” in *Numerical Modeling of Masonary and Historical Structures*, G. M. Bahman Ghiassi, Ed., In Woodhead Publishing Series in Civil and Structural Engineering, 2019, pp. 163-200.

[261] Z. Hashin, “AAtigue Failure Criterion for Fiber Reinforced Materials,” *Journal of Composite Materials,* vol. 7, pp. 448-464, 1973.

[262] Z. Hashin, “Failure Criteria for Unidirectional Fiber Composites,” *Journal of Applied Mechanics,* vol. 47, pp. 329-334, 1980.

[263] I. Lapczyk, “Progressive Damage Modeling in Fiber-Reinforced Materials,” *Composites Part A: Applied Science and Manufacturing,* vol. 38, no. 11, pp. 2333-2341, 2007.

[264] C. Davila, “Failure Criteria for FRP Laminates in Plane Stress,” *NASA\TM-2003-212663,* pp. 1-24, 2003.

[265] M. Yekrangnia, “Application of Endurance Time method in Ecaluation of Seismic Performance of a Typical Sandwich panel Building,” *Numerical Methods in Civil Engineering,* vol. 5, no. 2, pp. 45-51, 2020.

[266] J. Mander, “Theoretical stress-strain model for confined concrete,” *J. Struct. Eng,* vol. 114, no. 8, pp. 1804-1826, 1988.

[267] F. Tavarez, Simulation of behaviour of composite grid reinforced concrete beams using explicit finite element methods, Master's Thesis ed., Madison, Wisconsin: University of Wisconsin-Madison, 2001.

[268] Q. Li, “About the dynamic strength enhancement of concrete-like material sin a split Hopkinson pressure bar test,” *International Journal of Solids and Structures,* vol. 40, no. 2, pp. 343-360, 2003.

[269] Z. M, “Further investigation on the dynamic compressive strength enhancement of concrete-like materials based on split hopkinson pressure bar tests. Part i: Experiments,” *International journal of impact engineering,* no. 36, pp. 1327-1334, 2009.

[270] L. QM, “Local impact effects of hard missiles on concrete targets,” *internationla journal of impact engineering,* no. 32, pp. 224-284, 2005.

[271] M. Kabir, “Analytical and numerical study of FRP retrofitted RC beams under low velocity impact,” *Transaction A: Civil Engineering,* vol. 5, no. 16, pp. 415-428, 2009.

[272] C. Wu, “Blast testing of ultra-high performance fibre and FRP-retrofitted concrete slabs,” *Engineering Structures,* vol. 9, no. 31, pp. 2060-2069, 2009.

[273] T. Tang, “Behaviour of concrete beams strengthened with fiber-reinforced polymer laminates under impact loading,” *Journal of Composites for Construction,* vol. 3, no. 7, pp. 209-219, 2003.

[274] T. White, “Response of RC beams strengthened with CFRP laminates and subjected to a high rate of loading,” *Journal of Composites for Construction,* vol. 3, no. 5, pp. 153-162, 2001.

[275] K. Subramaniama, “Freeze-thaw degradation of FRP-concrete interface: impact on cohesive fracture response,” *Engineering Fracture Mechanics,* vol. 13, no. 75, pp. 3924-3940, 2008.

[276] Y. L. Q. Lu, “About the dynamic uniaxial tensile strength of concrete-like material,” *International Journal of Impact Engineering,* no. 38, pp. 171-180, 2011.

[277] E. S, “Analyzing the failure and damage of FRP composite laminates under high strain rates considering visco-plsticity,” *Engineering Failure Analysis,* no. 101, pp. 257-273, 2019.

[278] L. M, “Review of strain rate effects of fibre-reinforced polymer composites,” *Polymers,* vol. 13, pp. 1-31, 2021.

[279] Chopra. AK, “Response to arbitrary, step, and pulse excitations,” in *Dynamic of structures: theory and applications of earthquake engineering*, 5th, Ed., Pearson, 2019, pp. 119-148.

[280] S. Efe, “numerical analysis of AFRP reinforced concrete columns with replaceable structural fuses as energy dissipaters under cycic loading,” In Structures Congress 2018: Bridges, Transportation Structures, and Nonbuilding Structures, 2018.

[281] M. Kazemi, “Non-linear behaviour of concrete beams reinforced with GFRP and CFRP bars grouted in sleeves,” *Structures,* vol. 23, pp. 87-102, 2020.

[282] Y. J. Yu, “Investigation of behaviour of RC beams subjected to impact loading considering combination of mass and impact velocity,” *Procedia Engineering,* no. 210, pp. 353-359, 2017.

[283] M. Kadhim, “Finite element modelling and parametric analysis of FRPstrengthed RC beams under impact load,” *Journal of Building Engineering,* no. 32, pp. 1-14, 2020.

[284] A. Dancygier, “Effect of reinforced concrete properties on resistance to hard projectile impact,” *ACI Structure Journal,* vol. 2, no. 96, pp. 259-67, 1996.

[285] A. Dancygier, “Responce of high performance concrete plates to impact of non-deforming projectiles,” *Journal of Impact Engineering,* vol. 11, no. 34, pp. 1768-79, 2007.

[286] A. J., “Durability of GFRP bars under freeeze-thaw cycles and different loading rates,” *J Compos Mater,* vol. 1, no. 41, pp. 5-25, 2007.

[287] R. B. Esfahani. MR., “Local bond strength of reinforcing bars in normal strength and high-strength concrete (HSC),” *ACI structure Journal,* vol. 2, no. 95, 1998.

[288] B. MJ, “Non-normal data: is ANOVA still a valid point?,” https://doi.org/10.7334/psicothema2016.383., 2017.

[289] L. Malvar, “Dynamic increase factors for concrete.,” in *Naval facilities engineering service centre*, CA: Port Hueneme, 1998.

[290] Y. Guo, “Quasi-static and dynamic splitting of high strength concrete- tensile stress-strain responce and effects of strain rate,” *Int J Impact Eng,* vol. 125, pp. 188-211, 2019.

[291] M. Zhang, “Further investigation on the dynamic compressive strength enhancement of concrete -like materials based on split Hopkinson pressure bar test. Part I: experiments.,” *Int J Impact Eng,* vol. 36, no. 12, pp. 1327-34, 2009.

[292] L. Q.M, “Structural effects on compressive strength enhancement of concrete-like materials in a split hopkinson pressure bar test,” *Int J Impact Eng,* no. 109, pp. 408-18, 2017.

[293] X. Kong, “Numerical prediction of dynamic tensile failure in concrete by a corrected strain-rate dependent nonlocal material model.,” *Int J Impact Eng,* vol. 137, no. 3, pp. 103445.1-103445.18, 2020.

[294] A. Brara, “Experimental characterization of concrete in dynamic tension,” *Mech Mater,* vol. 3, no. 38, pp. 253-67, 2006.

[295] H. Wu, “Experimental and numerical investigation on the dynamic tensile strength of concrete,” *Int J Impact Eng,* Vols. 1-4, no. 32, pp. 605-17, 2005.

[296] T. Lv, “The 3D meso-scale model and numerical tests of split Hopkinson pressure bar of concrete specimen,” *Constr Build Mater,* no. 160, pp. 744-64, 2018.

[297] I. Sallier, “On the use of Hillerborg regulariziation method to model the softening behaviour of concrete subjected to dynamic tesnile loading,” *Eur Phys J Special Topics,* vol. 1, no. 206, pp. 97-105, 2012.

[298] CEB-FIB, Bulletin 65: model code 2010, 1 ed., CEB, 2010.

[299] CEB-FIP, “CEB-FIP model code 1990 design code,” Thomas Telford, Lausanne, 1993.

[300] CEB-FIB, “Bulletin 66: Model code 2010 (volume 2),” *CEB,* vol. 2, 2010.

[301] E. Yandizo, Protection of buildings against explosions, 244 ed., Steel Construction Institute, 1999.

[302] ACI318-05, Building code requirements for structural concrete and commentray, 2nd ed., Farmington Hills: American concrete institute, 2005.

[303] Y. H, "Experimental investigation of the behaviour of aramid fiber reinforced polymer confied concrete subjected to high strain ratecompression," *Constr. Build. Mater,* vol. 95, pp. 143-151, 2015.

[304] B. P.H, "Compressive behaviour of concrete at high strain rates," *Mater. Struct.,* vol. 6, no. 24, pp. 425-450, 1991.

[305] Y. Xiao, "Experimental studies on concrete filled steel tubes under high strain rate lading," *J. Mater Civ Eng,* vol. 10, no. 21, pp. 569-577, 2009.

[306] H. Yang, "Experimental investigation of the behaviour of aramid fiber reinforced polymer confined concrete subjected to high strain rate compression," *Constr Build. Mater.,* no. 95, pp. 143-151, 2015.

[307] H. Park, "A nonlinear solid shell element formulation, Thesis of Doctor of Philosophy," University of Maryland, Maryland, USA, 2003.

[308] G. Rehm, "The fundamentals of bond between steel reinforcement and concrete, Deutscher Ausschub fur Stahlbeton," Verlag W. Ernst & Sohn, Berlin, 1961.

[309] B. Taljsten, "Strengthening of concrete prisms using the plate-bonding technique," *International Journal of Fracture,* vol. 82, no. 3, pp. 253-266, 1996.

[310] F. An, "Modelling of FRP-concrete interfacial bond behaviour," Doctoral dissertation, University of Edinburgh, Edinburgh, 2015.

[311] Z. Wu, "Stress transfer and fracture propagation in different kinds of adhesive joints," *Journal of Engineering Mechanics, ASCE,* vol. 128, no. 5, pp. 562-573, 2002.

[312] H. Yuan, "Full-range behaviour of FRP-to-concrete bonded joints," *Engineering Structures,* vol. 26, no. 5, pp. 553-565, 2004.

[313] J. G. Dai, "Unified analytical approaches for determining shear bond characteristics of FRP-concrete interfaces through pull-out tests," *Journal of Advanced Concrete Technology,* vol. 4, no. 1, pp. 133-145, 2006.

Appendix A

Authors	Fibre composites	Strain rate investigated	Results
Davies & Magee	Glass/polyester	$10^{-3} - 10^{3}s$	Increase in ultimate tensile strength
Rotem & Lifshitz	Glass/epoxy	$10^{-6} - 30s$	Increase in tensile strength and modulus
Lifshitz	Graphite/epoxy	$Static - 4.2m/s$	Independent tensile modulus and failure stress
Melin & Asp	Carbon/epoxy	$10^{-3} - 10^{3}s$	Weak dependence of tensile property
Okoli & Smith	Glass/epoxy	0.008,mm/s-4m/s	Increase in tensile strength, tensile modulus, shear strength, shear modulus, flexural energy, shear and tensile
Armenakas & Sciamarella	Glass/epoxy	$0.0265min^{-1} - 30000min^{-1}$	Decrease in ultimate tensile strain and stress, increase in tensile modulus
Vashchenko	Glass/polyester	$3.3 \times 10^{-5} - 12m/sec$	Increase in tensile strength
Staab & Gilat	Glass/epoxy	$10^{-5} - 10^{3}s$	Increase in maximum tensile stress and strain
Harding & Welsh	Graphite/epoxy; glass/epoxy; glass/polyester; graphite/polyester; kelvar/polyester	$10^{-4} - 10^{3}s^{-1}$	Insensitive tensile modulus and failure stress for graphite/epoxy, increase in tensile modulus of glass/epoxy; glass/polyester; graphite/polyester; kelvar/polyester
Roberts & Harding	Glass/phenolic resin	1-20000mm/sec	Increase in tensile strength, stiffness and displacement
Bai	Glass bead/HDPE	$3 \times 10^{-5} - 8 \times 10^{-3}s^{-1}$	Increase in tensile strength and modulus

Daniel	Carbon/epoxy	$1 \times 10^{-4} - 500s^{-1}$	Increase in longitudinal tensile modulus and compression modulus; insensitive tensile and compression strength and strain; increase in transverse tensile and compression modulus and strength
Hayes & Adams	Glass/epoxy; graphite/epoxy	1.7-4.9 m/s	Decreas of tensile modulus and strength of graphite/epoxy; insensitive tensile modulus and strength of glass/epoxy
Daniel & Liber	Boron/epoxy; glass/epoxy; kelvar/epoxy; graphite/epoxy	$1.4 \times 10^{-4} - 27s^{-1}$	Increase in tensile modulus and failure strength of kelvar/epoxy; insensitive tensile modulus and failure strength for Boron/epoxy; glass/epoxy and graphite/epoxy
Chamis & Smith	Graphite/epoxy	$Static - 381s^{-1}$	Increase in transverse tensile and shear properties; insensitive longitudinal tensile strength
Daniel	Graphite/epoxy	$100s - 500s^{-1}$	Increase in transverse tensile and shear properties; insensitive longitudinal tensile strength
Kawata	Glass/polyester; glass/epoxy; short graphite fibre/nylon6,6	$0.001 - 2000s^{-1}$	Increase in tensile strength of graphite/epoxy and short graphite fibre/nylon;

			decrease in tensile strength of glass/epoxy and glass/polyester
Barre	Glass/phenolic resin; glass/polyester	$0.1 - 10s^{-1}$	Increase in tensile modulus and strength
Paterson	Chopped glass fiber in styrene/maleic anhydride resin	$1.67 \times 10^{-3} - 6s^{-1}$	Increase in tensile modulus and strength
Groves	Carbon/epoxy	$0 - 3000s^{-1}$	Increase in compressive and tensile properties
Powers	Graphite/epoxy; Graphite/polyimide	$49 - 1430s^{-1}$	Increase in compression yield stress and elastic strain of graphite/epoxy; insensitive ultimate strength and modulus of elasticity of both composites
Li	Short glass fibre/liquid crystalline polymer	$10^{-4} - 350s^{-1}$	Increase in compression modulus and strength
Takeda & Wan	Glass/polyester	$10^{-3} - 750s^{-1}$	Increase in compression strength
Tzeng & Abrahamian	Graphite/epoxy	10-100 in/s	Increase in strain and compression strength
Amijima & Fuji	Glass/polyester	$10^{-3} - 10^{3}s^{-1}$	Increase in compression strength
Cazeneuve & Maile	Graphite/epoxy	$10^{-3} - 600s^{-1}$	Increase in longitudinal and transverse compression strength
Sims	Glass mat/Polyester	$10^{-6} - 10^{-1}m/s$	Increase in flexural strength

Table 47: Experimental work on effect of strain rate on mechanical properties of FRP.

Bond-Slip model	Ascending branch $s \leq s_0$	Descending branch $s > s_0$	τ_{max}	s_0	s_f	β_w
Neubauer, [209]	$\tau_{max}\left(\frac{s}{s_0}\right)$	0	$1.8\beta_w f_t$	$\beta_w \times 0.202$	–	$\sqrt{1.125\frac{2-b_f/b_c}{1+b_f/400}}$
Nakaba, [208]	–	$\tau_{max}\left(\frac{s}{s_0}\right)\left[3/\left(2+\left(\frac{s}{s_0}\right)^3\right)\right]$	$3.5{f_c'}^{0.19}$	0.065	–	
Monti, [210]	$\tau_{max}\left(\frac{s}{s_0}\right)$	$\tau_{max}\frac{s_f-s}{s_f-s_0}$	$1.8\beta_w f_t$	$2.5\tau_{max}\left(\frac{t_a}{E_a}+\frac{50}{E_c}\right)$	$0.33\beta_w$	$\sqrt{1.5\frac{2-b_f/b_c}{1+b_f/100}}$
Savioa, [163]	–	$\tau\_max\ (s/s\_0\ )[2.86/(1.86 + (s/s\_0\ )\text{^}2.86\ )]$	$3.5{f_c'}^{0.19}$	0.051	$\alpha = 0.028\left(E_f t_f/1000\right)^{0.254}$	–

Table 48: Existing bond-slip models.

No.	Yield Force/ Moment	Plastic motion	Rate	No.	Yield Force/ Moment	Plastic motion	Rate
1	27355.05091	0.0005	0	33	45591.75152	0.0005	0.001
2	31448.13717	0.001	0	34	52413.56195	0.001	0.001
3	34120.76282	0.0015	0	35	56867.93803	0.0015	0.001
4	36153.66444	0.002	0	36	60256.1074	0.002	0.001
5	37813.5499	0.0025	0	37	63022.58317	0.0025	0.001
6	39226.19018	0.003	0	38	65376.98363	0.003	0.001
7	40461.65436	0.0035	0	39	67436.0906	0.0035	0.001
8	41563.27115	0.004	0	40	69272.11858	0.004	0.001
9	42559.83508	0.0045	0	41	70933.05847	0.0045	0.001
10	43471.52224	0.005	0	42	72452.53707	0.005	0.001
11	44313.0562	0.0055	0	43	73855.09367	0.0055	0.001
12	45095.5333	0.006	0	44	75159.22217	0.006	0.001
13	45827.53809	0.0065	0	45	76379.23015	0.0065	0.001
14	46515.85773	0.007	0	46	77526.42955	0.007	0.001
15	47165.95746	0.0075	0	47	78609.9291	0.0075	0.001
16	47782.30742	0.008	0	48	79637.17903	0.008	0.001
17	36473.40121	0.0005	0.0001	49	54710.10182	0.0005	0.01
18	41930.84956	0.001	0.0001	50	62896.27434	0.001	0.01
19	45494.35043	0.0015	0.0001	51	68241.52564	0.0015	0.01
20	48204.88592	0.002	0.0001	52	72307.32888	0.002	0.01
21	50418.06653	0.0025	0.0001	53	75627.0998	0.0025	0.01
22	52301.58691	0.003	0.0001	54	78452.38036	0.003	0.01
23	53948.87248	0.0035	0.0001	55	80923.30872	0.0035	0.01
24	55417.69487	0.004	0.0001	56	83126.5423	0.004	0.01
25	56746.44677	0.0045	0.0001	57	85119.67016	0.0045	0.01
26	57962.02965	0.005	0.0001	58	86943.04448	0.005	0.01
27	59084.07493	0.0055	0.0001	59	88626.1124	0.0055	0.01
28	60127.37773	0.006	0.0001	60	90191.0666	0.006	0.01
29	61103.38412	0.0065	0.0001	61	91655.07618	0.0065	0.01
30	62021.14364	0.007	0.0001	62	93031.71546	0.007	0.01
31	62887.94328	0.0075	0.0001	63	94331.91492	0.0075	0.01
32	63709.74323	0.008	0.0001	64	95564.61484	0.008	0.01

Table 49: Applied force-slip with rates on connectors between each nodes of FRP bars and concrete for Dynamic model in ABAQUS.

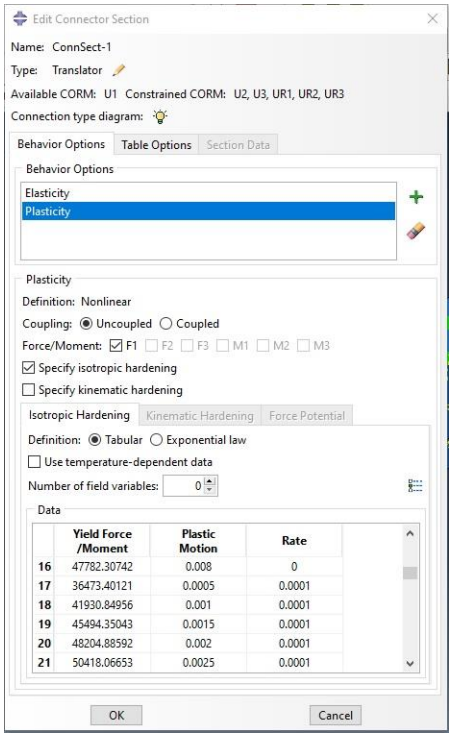

Figure 118: Applied rates for each connector for Dynamic model in ABAQUS.

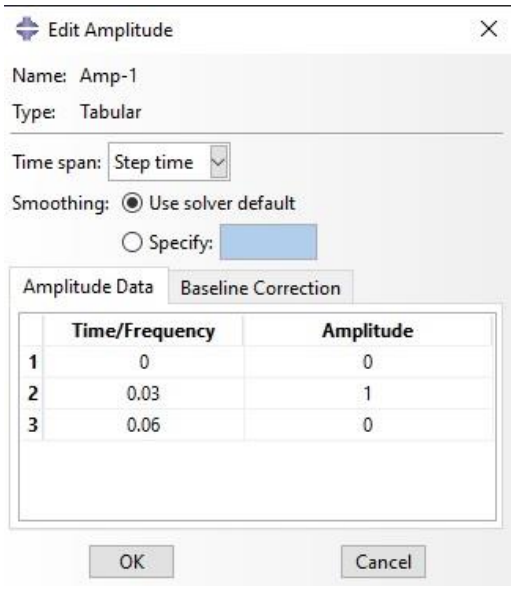

Figure 119: Applied amplitude for dynamic FE model in ABAQUS.

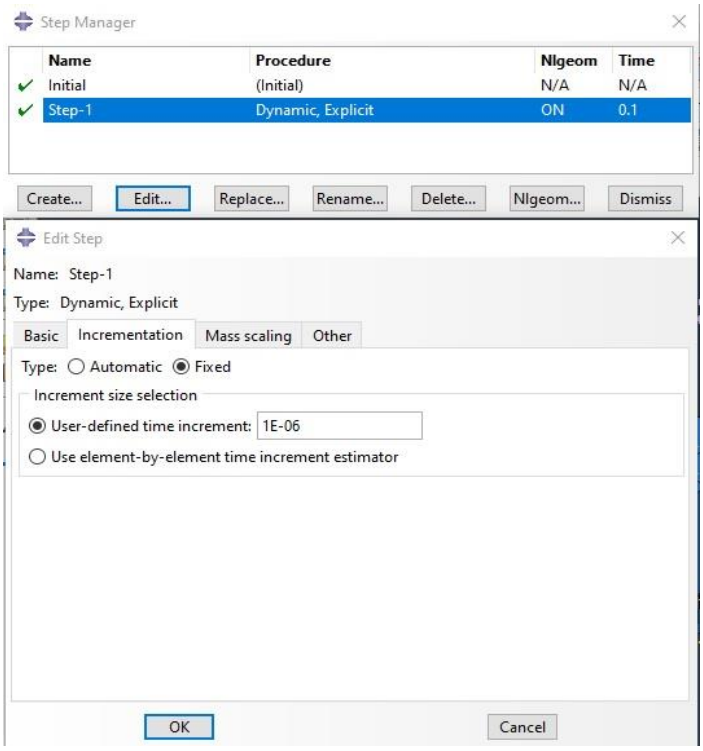

Figure 120: Applied increment size for time for Dynamic/Explicit model in ABAQUS.

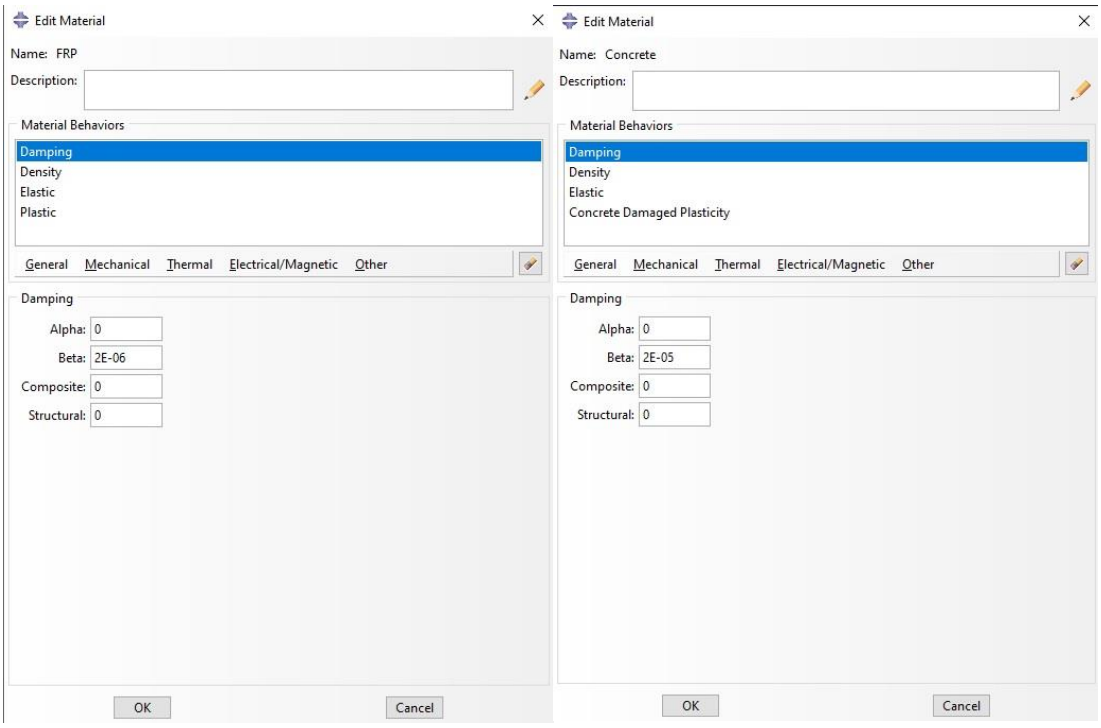

Figure 121: Applied Damping for FRP and concrete parts, ABAQUS.

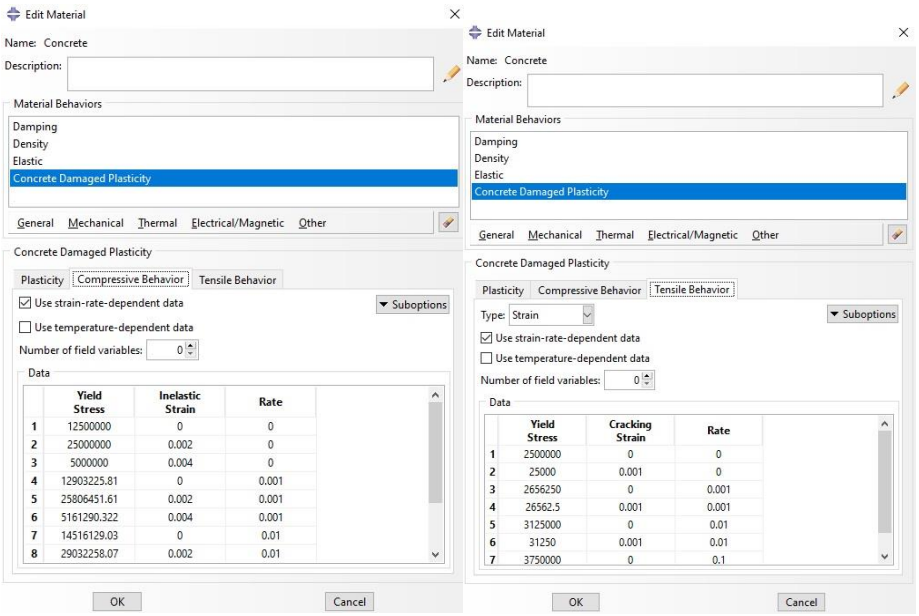

Figure 122: Applied rate in CDP of concrete for rate dependency.

Compressive behaviour			**Tensile Behaviour**		
Yield Stress	Inelastic Strain	Rate	Yield Stress	Cracking Strain	Rate
28700000	0	0	5740000	0	0
57400000	0.002	0	57400	0.001	0
11480000	0.004	0	6098750	0	0.001
29625806.5	0	0.001	60987.5	0.001	0.001
59251612.9	0.002	0.001	7175000	0	0.01
11850322.6	0.004	0.001	71750	0.001	0.01
33329032.3	0	0.01	8610000	0	0.1
66658064.5	0.002	0.01	86100	0.001	0.1
13331612.9	0.004	0.01			
35180645.2	0	0.1			
70361290.3	0.002	0.1			
14072258.1	0.004	0.1			

Table 50: Details for rate dependency of concrete material.

Appendix B

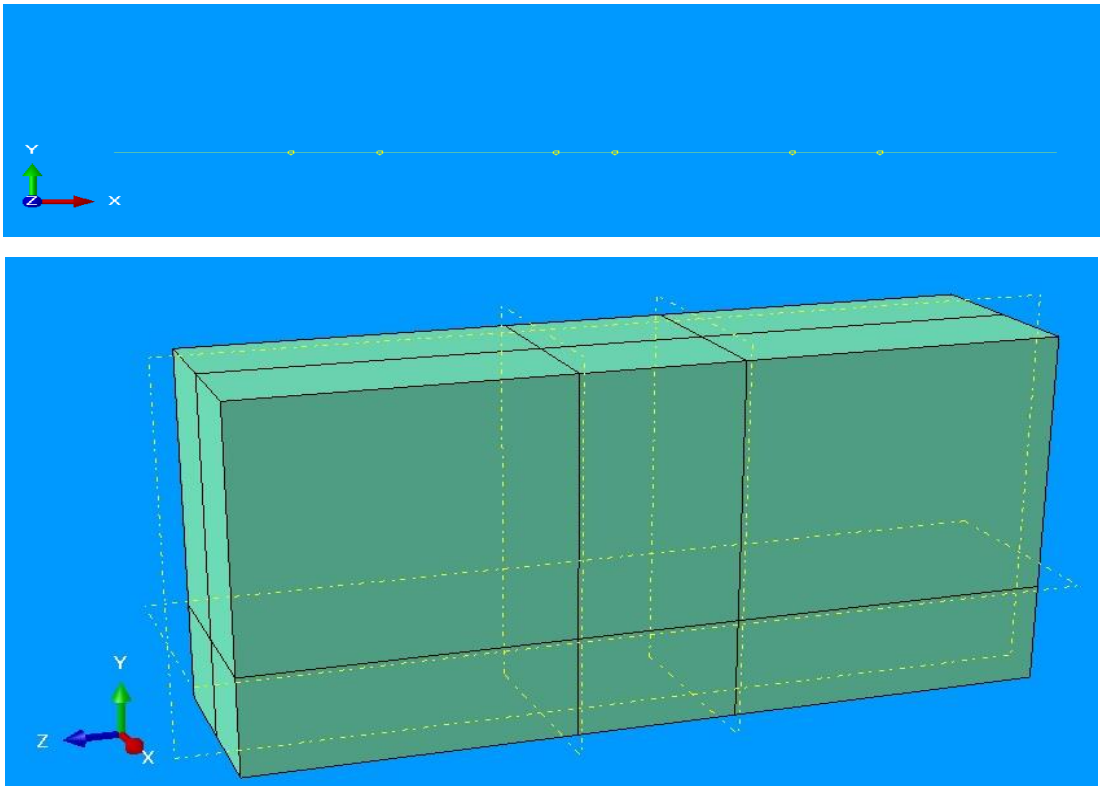

Figure 123: Modelling of FRP bar part and concrete part in ABAQUS.

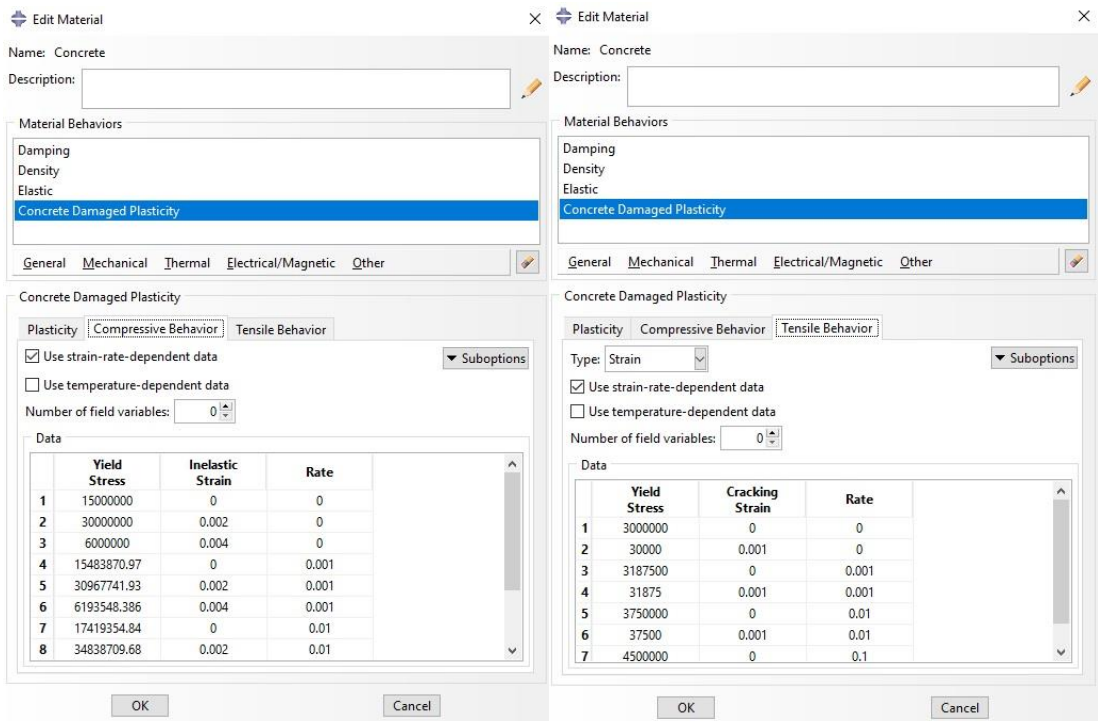

Figure 124: Example of defined CDP compressive and tensile behaviour for concrete in model G-1-1-30-14.

Yield Stress	Plastic Strain	Rate
947000000	0	0
9470000	0.03	0
1042000000	0	0.08
10420000	0.03	0.08
1136000000	0	0.9
11360000	0.03	0.9
1336000000	0	8.7
13360000	0.03	8.7
142000000	0	17.4
14200000	0.03	17.4
1515000000	0	43
15150000	0.03	43
1610000000	0	87
16100000	0.03	87
1800000000	0	174
18000000	0.03	174

Table 51: Example of plasticity behaviour defined for GFRP bar in G-1-1-30-14 model in ABAQUS.

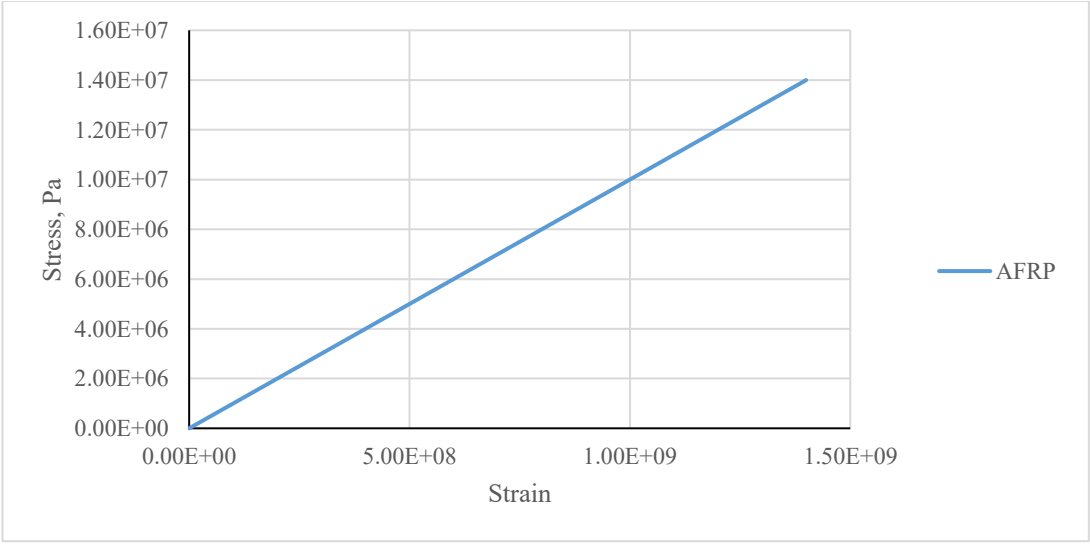

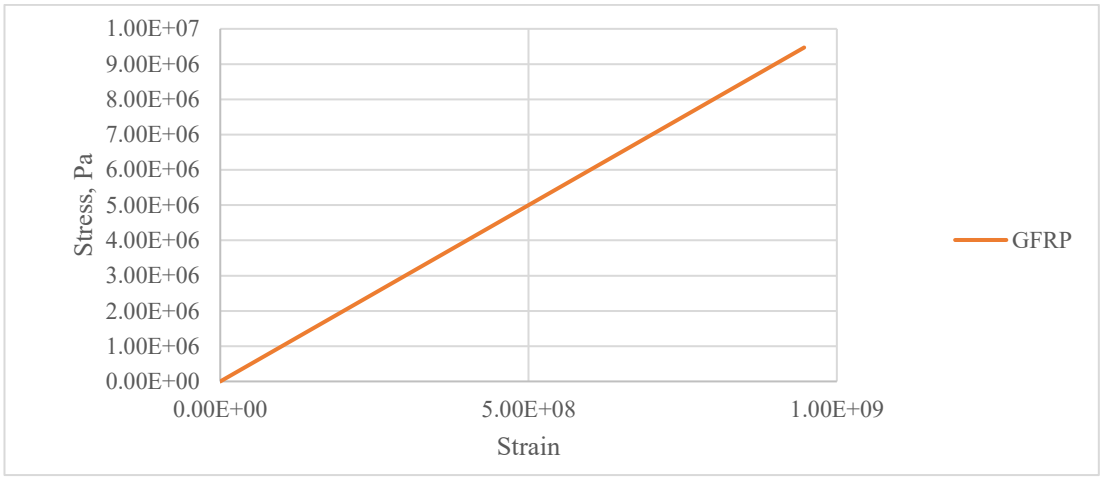

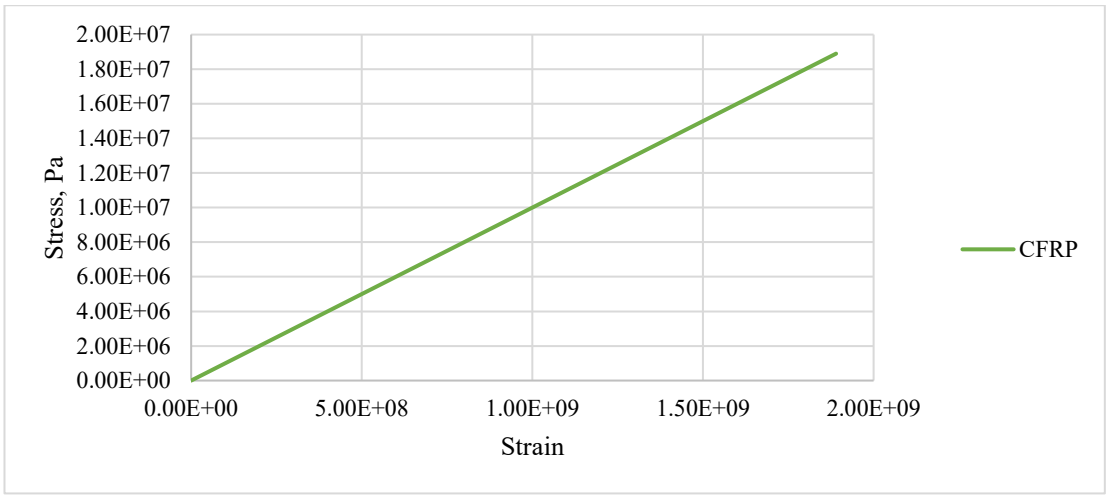

Figure 125: Stress-Strain for AFRP, GFRP, and CFRP bars.

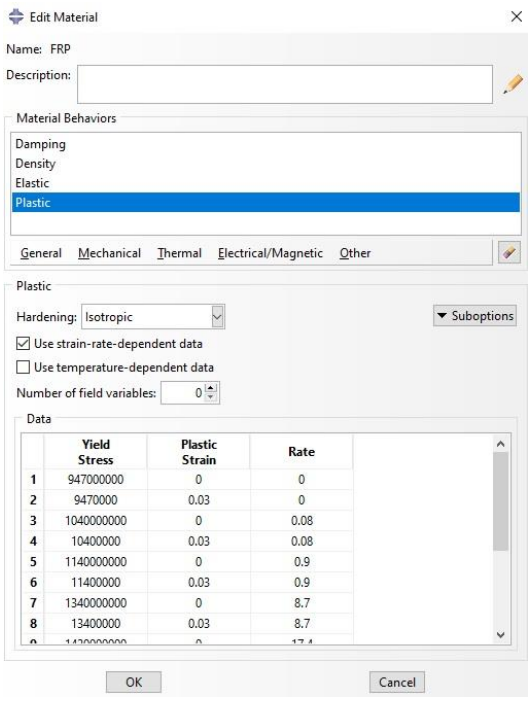

Figure 126: Example of defined plasticity behaviour for GFRP bar applied in ABAQUS

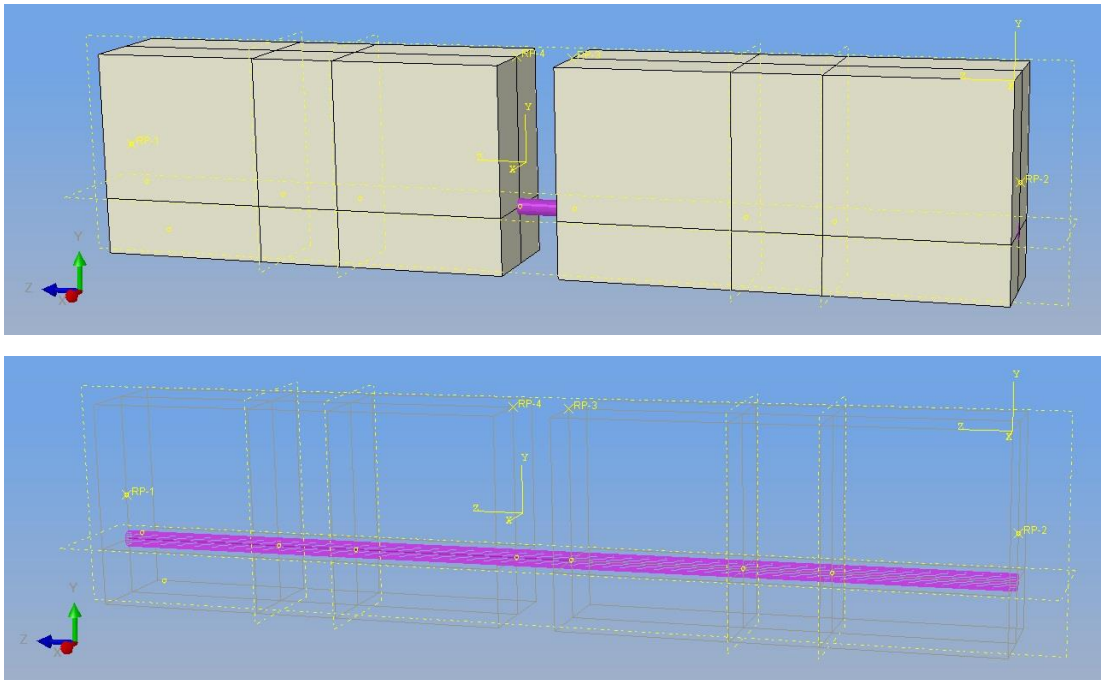

Figure 127: Example of FRP RC beam after defined FRP and concrete parts are assembled in ABAQUS.

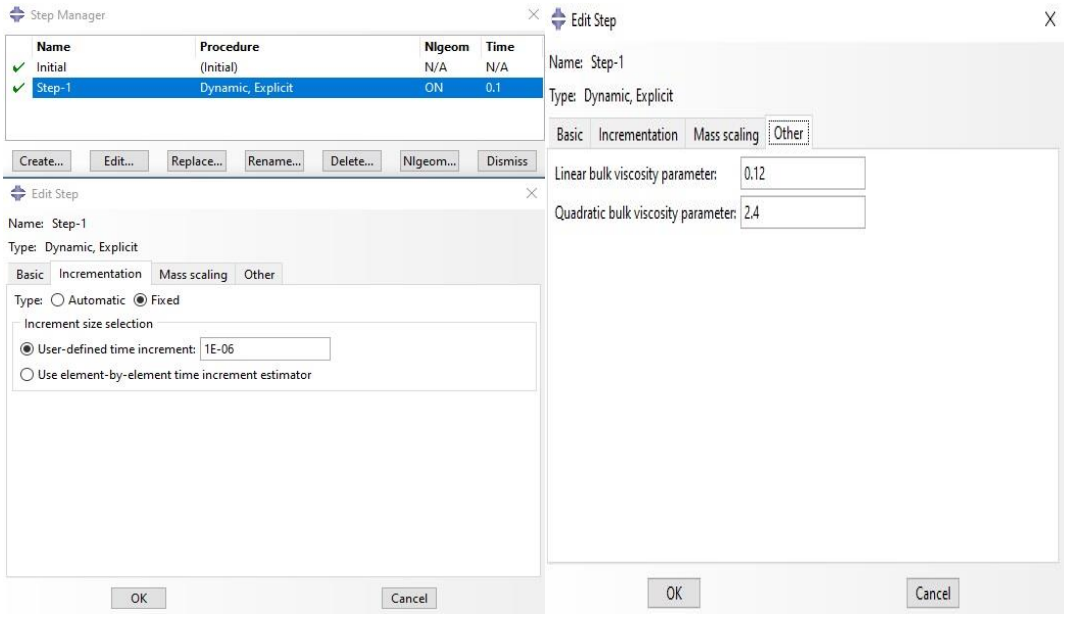

Figure 128: Example of defined time period and increment size for bema models in ABAQUS.

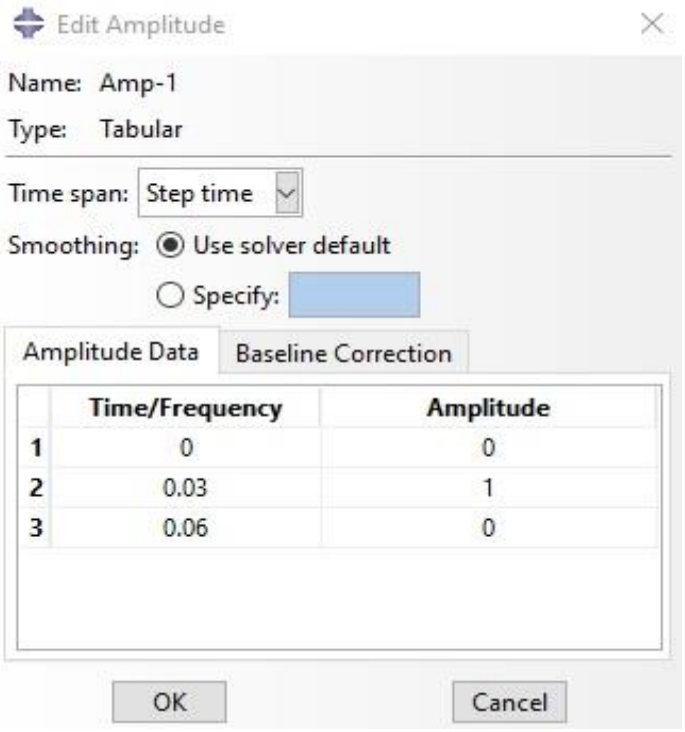

Figure 129: symmetrical triangular force time history for all FRP RC beam models in ABAQUS.

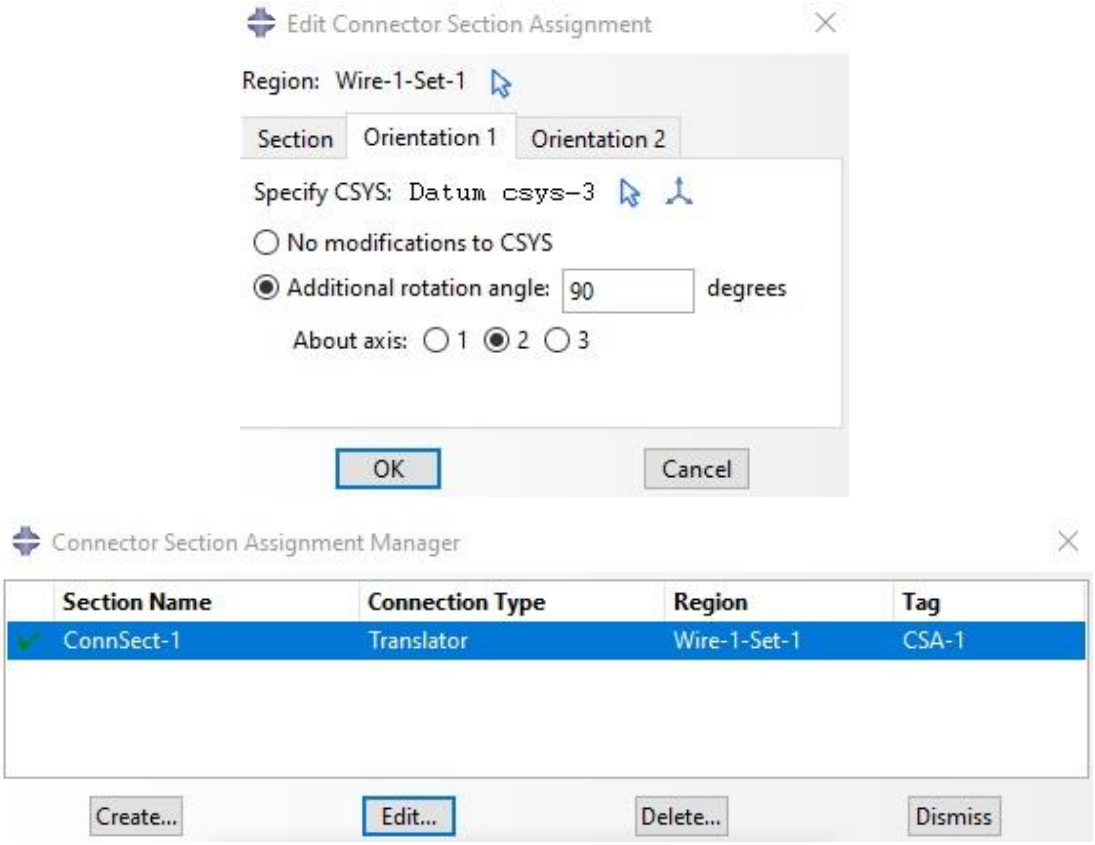

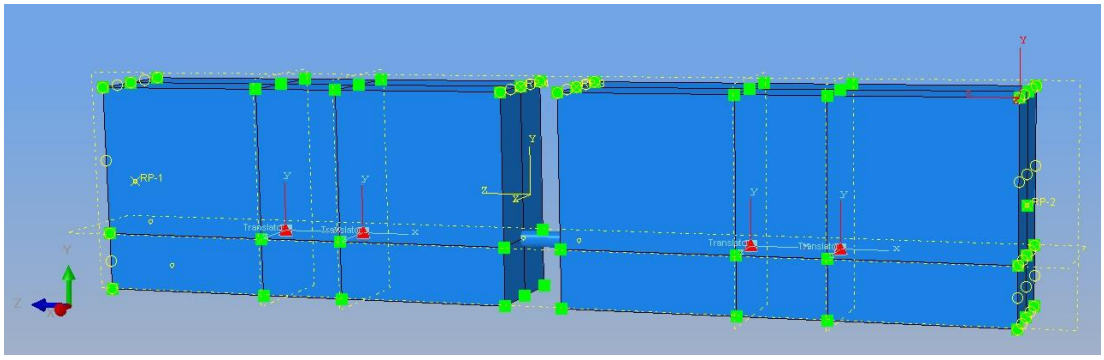

Figure 130: Example of assigning connectors between FRP bar and concrete beam in ABAQUS.

Yield Force/ Moment	Plastic Motion	Rate	Yield Force/ Moment	Plastic Motion	Rate	Yield Force/ Moment	Plastic Motion	Rate
36120.22738	0.0005	0.0001	45150.2842	0.0005	0.001	54180.3411	0.0005	0.01
41085.1836	0.001	0.0001	51356.4795	0.001	0.001	61627.7754	0.001	0.01
44300.12658	0.0015	0.0001	55375.1582	0.0015	0.001	66450.1899	0.0015	0.01
46732.60481	0.002	0.0001	58415.756	0.002	0.001	70098.9072	0.002	0.01
48710.99023	0.0025	0.0001	60888.7378	0.0025	0.001	73066.4853	0.0025	0.01
50389.46226	0.003	0.0001	62986.8278	0.003	0.001	75584.1934	0.003	0.01
51853.63301	0.0035	0.0001	64817.0413	0.0035	0.001	77780.4495	0.0035	0.01
53156.30017	0.004	0.0001	66445.3752	0.004	0.001	79734.4503	0.004	0.01
54332.47124	0.0045	0.0001	67915.5891	0.0045	0.001	81498.7069	0.0045	0.01
55406.62732	0.005	0.0001	69258.2841	0.005	0.001	83109.941	0.005	0.01
56396.60242	0.0055	0.0001	70495.753	0.0055	0.001	84594.9036	0.0055	0.01
57315.81606	0.006	0.0001	71644.7701	0.006	0.001	85973.7241	0.006	0.01
58174.63543	0.0065	0.0001	72718.2943	0.0065	0.001	87261.9531	0.0065	0.01
58981.24644	0.007	0.0001	73726.5581	0.007	0.001	88471.8697	0.007	0.01
59742.2328	0.0075	0.0001	74677.791	0.0075	0.001	89613.3492	0.0075	0.01
60462.97354	0.008	0.0001	75578.7169	0.008	0.001	90694.4603	0.008	0.01

Table 52: Example of calculated force-slip model applied to connectors with rate dependency.

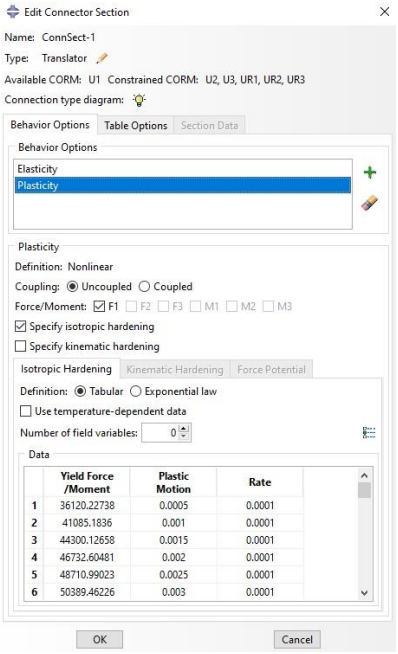

Figure 131: Example of calculated force-slip model applied to connectors with rate dependency in ABAQUS.

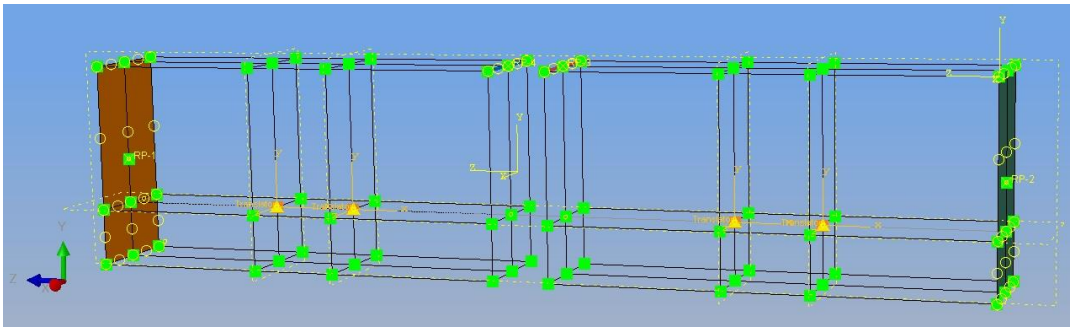

Figure 132: example of four constraints applied on FRP RC beams on both left and right sides, top middle side of the beam in ABAQUS.

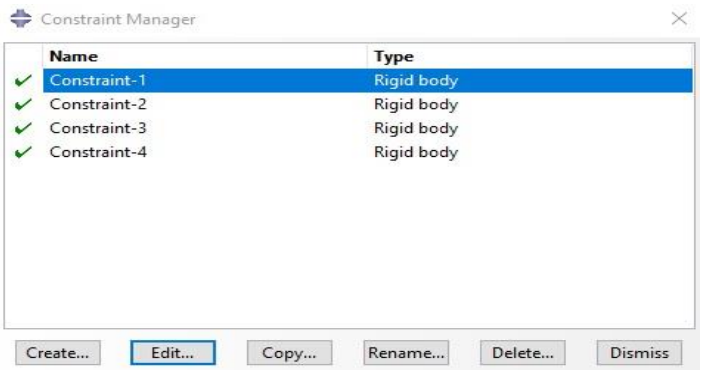

Figure 133: Constraints applied to FRP RC beam models in ABAQUS from constraints manager function.

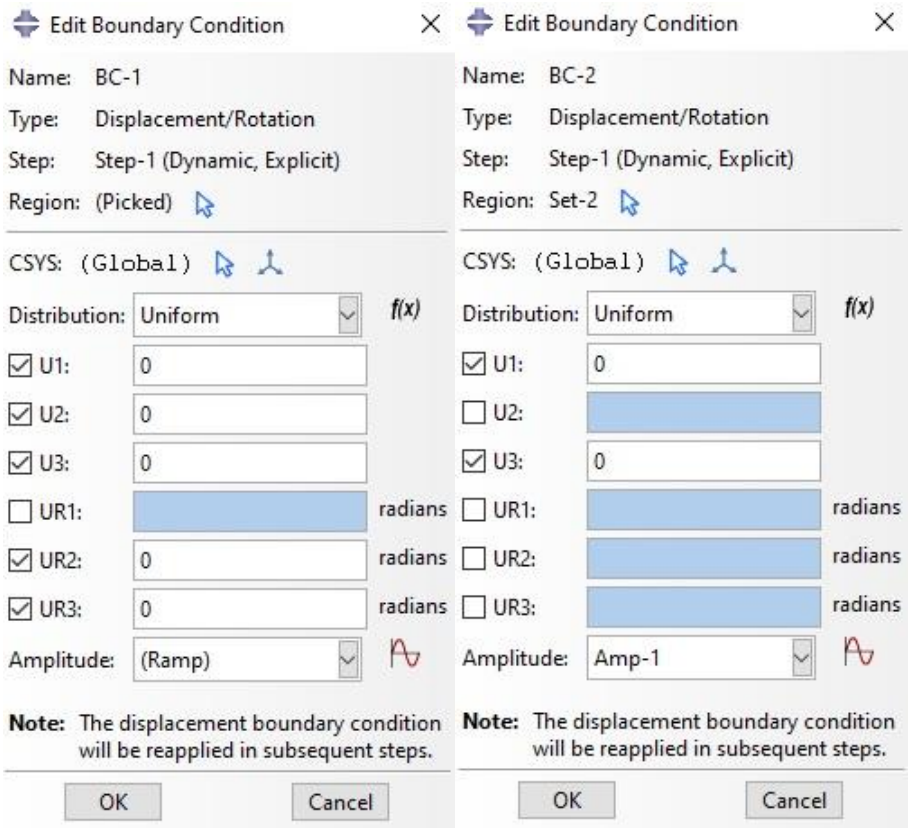

Figure 134: Applied boundary conditions for pin and roller supports.

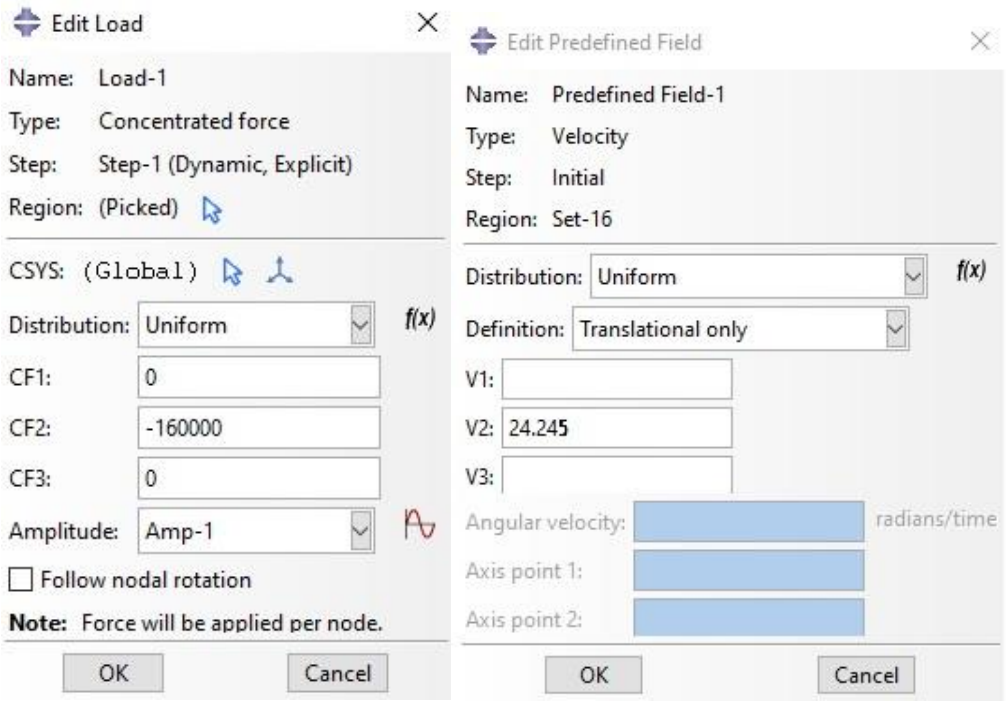

Figure 135: Example of applied initial velocity and impact load in ABAQUS.

Appendix C

	Parameter (1) Bar Diameter, mm	Parameter (2) Concrete Comressive Strength, Mpa	Parameter (3) Impact load, kN	Parameter (4) Rupture Strength, Mpa		Parameter (1) Bar Diameter, mm	Parameter (2) Concrete Comressive Strength, Mpa	Parameter (3) Impact load, kN	Parameter (4) Rupture Strength, Mpa		Parameter (1) Bar Diameter, mm	Parameter (2) Concrete Comressive Strength, Mpa	Parameter (3) Impact load, kN	Parameter (4) Rupture Strength, Mpa
C-1-1-25-8	8	25	160	1890	C-2-1-25-8	8	25	80	1890	C-3-1-25-8	8	25	40	1890
C-1-1-25-10	10	25	160	1890	C-2-1-25-10	10	25	80	1890	C-3-1-25-10	10	25	40	1890
C-1-1-25-12	12	25	160	1890	C-2-1-25-12	12	25	80	1890	C-3-1-25-12	12	25	40	1890
C-1-1-25-14	14	25	160	1890	C-2-1-25-14	14	25	80	1890	C3-1-25-14	14	25	40	1890
C-1-1-25-16	16	25	160	1890	C-2-1-25-16	16	25	80	1890	C-3-1-25-16	16	25	40	1890
C-1-1-30-8	8	30	160	1890	C-2-1-30-8	8	30	80	1890	C-3-1-30-8	8	30	40	1890
C-1-1-30-10	10	30	160	1890	C-2-1-30-10	10	30	80	1890	C-3-1-30-10	10	30	40	1890
C-1-1-30-12	12	30	160	1890	C-2-1-30-12	12	30	80	1890	C-3-1-30-12	12	30	40	1890
C-1-1-30-14	14	30	160	1890	C-2-1-30-14	14	30	80	1890	C-3-1-30-14	14	30	40	1890
C-1-1-30-16	16	30	160	1890	C-2-1-30-16	16	30	80	1890	C-3-1-30-16	16	30	40	1890
C-1-1-35-8	8	35	160	1890	C-2-1-35-8	8	35	80	1890	C-3-1-35-8	8	35	40	1890
C-1-1-35-10	10	35	160	1890	C-2-1-35-10	10	35	80	1890	C-3-1-35-10	10	35	40	1890
C-1-1-35-12	12	35	160	1890	C-2-1-35-12	12	35	80	1890	C-3-1-35-12	12	35	40	1890
C-1-1-35-14	14	35	160	1890	C-2-1-35-14	14	35	80	1890	C-3-1-35-14	14	35	40	1890
C-1-1-35-16	16	35	160	1890	C-2-1-35-16	16	35	80	1890	C-3-1-35-16	16	35	40	1890
C-1-1-40-8	8	40	160	1890	C-2-1-40-8	8	40	80	1890	C-3-1-40-8	8	40	40	1890
C-1-1-40-10	10	40	160	1890	C-2-1-40-10	10	40	80	1890	C-3-1-40-10	10	40	40	1890
C-1-1-40-12	12	40	160	1890	C-2-1-40-12	12	40	80	1890	C-3-1-40-12	12	40	40	1890
C-1-1-40-14	14	40	160	1890	C-2-1-40-14	14	40	80	1890	C-3-1-40-14	14	40	40	1890
C-1-1-40-16	16	40	160	1890	C-2-1-40-16	16	40	80	1890	C-3-1-40-16	16	40	40	1890
C-1-1-45-8	8	45	160	1890	C-2-1-45-8	8	45	80	1890	C-3-1-45-8	8	45	40	1890
C-1-1-45-10	10	45	160	1890	C-2-1-45-10	10	45	80	1890	C-3-1-45-10	10	45	40	1890
C-1-1-45-12	12	45	160	1890	C-2-1-45-12	12	45	80	1890	C-3-1-45-12	12	45	40	1890
C-1-1-45-14	14	45	160	1890	C-2-1-45-14	14	45	80	1890	C-3-1-45-14	14	45	40	1890
C-1-1-45-16	16	45	160	1890	C-2-1-45-16	16	45	80	1890	C-3-1-45-16	16	45	40	1890

	Parameter (1) Bar Diameter, mm	Parameter (2) Concrete Comressive Strength, Mpa	Parameter (3) Impact load, kN	Parameter (4) Rupture Strength, Mpa		Parameter (1) Bar Diameter, mm	Parameter (2) Concrete Comressive Strength, Mpa	Parameter (3) Impact load, kN	Parameter (4) Rupture Strength, Mpa		Parameter (1) Bar Diameter, mm	Parameter (2) Concrete Comressive Strength, Mpa	Parameter (3) Impact load, kN	Parameter (4) Rupture Strength, Mpa
A-1-1-25-8	8	25	160	1400	A-2-1-25-8	8	25	80	1400	A-3-1-25-8	8	25	40	1400
A-1-1-25-10	10	25	160	1400	A-2-1-25-10	10	25	80	1400	A-3-1-25-10	10	25	40	1400
A-1-1-25-12	12	25	160	1400	A-2-1-25-12	12	25	80	1400	A-3-1-25-12	12	25	40	1400
A-1-1-25-14	14	25	160	1400	A-2-1-25-14	14	25	80	1400	A-3-1-25-14	14	25	40	1400
A-1-1-25-16	16	25	160	1400	A-2-1-25-16	16	25	80	1400	A-3-1-25-16	16	25	40	1400
A-1-1-30-8	8	30	160	1400	A-2-1-30-8	8	30	80	1400	A-3-1-30-8	8	30	40	1400
A-1-1-30-10	10	30	160	1400	A-2-1-30-10	10	30	80	1400	A-3-1-30-10	10	30	40	1400
A-1-1-30-12	12	30	160	1400	A-2-1-30-12	12	30	80	1400	A-3-1-30-12	12	30	40	1400
A-1-1-30-14	14	30	160	1400	A-2-1-30-14	14	30	80	1400	A-3-1-30-14	14	30	40	1400
A-1-1-30-16	16	30	160	1400	A-2-1-30-16	16	30	80	1400	A-3-1-30-16	16	30	40	1400
A-1-1-35-8	8	35	160	1400	A-2-1-35-8	8	35	80	1400	A-3-1-35-8	8	35	40	1400
A-1-1-35-10	10	35	160	1400	A-2-1-35-10	10	35	80	1400	A-3-1-35-10	10	35	40	1400
A-1-1-35-12	12	35	160	1400	A-2-1-35-12	12	35	80	1400	A-3-1-35-12	12	35	40	1400
A-1-1-35-14	14	35	160	1400	A-2-1-35-14	14	35	80	1400	A-3-1-35-14	14	35	40	1400
A-1-1-35-16	16	35	160	1400	A-2-1-35-16	16	35	80	1400	A-3-1-35-16	16	35	40	1400
A-1-1-40-8	8	40	160	1400	A-2-1-40-8	8	40	80	1400	A-3-1-40-8	8	40	40	1400
A-1-1-40-10	10	40	160	1400	A-2-1-40-10	10	40	80	1400	A-3-1-40-10	10	40	40	1400
A-1-1-40-12	12	40	160	1400	A-2-1-40-12	12	40	80	1400	A-3-1-40-12	12	40	40	1400
A-1-1-40-14	14	40	160	1400	A-2-1-40-14	14	40	80	1400	A-3-1-40-14	14	40	40	1400
A-1-1-40-16	16	40	160	1400	A-2-1-40-16	16	40	80	1400	A-3-1-40-16	16	40	40	1400
A-1-1-45-8	8	45	160	1400	A-2-1-45-8	8	45	80	1400	A-3-1-45-8	8	45	40	1400
A-1-1-45-10	10	45	160	1400	A-2-1-45-10	10	45	80	1400	A-3-1-45-10	10	45	40	1400
A-1-1-45-12	12	45	160	1400	A-2-1-45-12	12	45	80	1400	A-3-1-45-12	12	45	40	1400
A-1-1-45-14	14	45	160	1400	A-2-1-45-14	14	45	80	1400	A-3-1-45-14	14	45	40	1400
A-1-1-45-16	16	45	160	1400	A-2-1-45-16	16	45	80	1400	A-3-1-45-16	16	45	40	1400

	Parameter (1) Bar Diameter, mm	Parameter (2) Concrete Comressive Strength, Mpa	Parameter (3) Impact load, kN	Parameter (4) Rupture Strength, Mpa		Parameter (1) Bar Diameter, mm	Parameter (2) Concrete Comressive Strength, Mpa	Parameter (3) Impact load, kN	Parameter (4) Rupture Strength, Mpa		Parameter (1) Bar Diameter, mm	Parameter (2) Concrete Comressive Strength, Mpa	Parameter (3) Impact load, kN	Parameter (4) Rupture Strength, Mpa
G-1-1-25-8	8	25	160	974	G-2-1-25-8	8	25	80	974	G-3-1-25-8	8	25	40	974
G-1-1-25-10	10	25	160	974	G-2-1-25-10	10	25	80	974	G-3-1-25-10	10	25	40	974
G-1-1-25-12	12	25	160	974	G-2-1-25-12	12	25	80	974	G-3-1-25-12	12	25	40	974
G-1-1-25-14	14	25	160	974	G-2-1-25-14	14	25	80	974	G-3-1-25-14	14	25	40	974
G-1-1-25-16	16	25	160	974	G-2-1-25-16	16	25	80	974	G-3-1-25-16	16	25	40	974
G-1-1-30-8	8	30	160	974	G-2-1-30-8	8	30	80	974	G-3-1-30-8	8	30	40	974
G-1-1-30-10	10	30	160	974	G-2-1-30-10	10	30	80	974	G-3-1-30-10	10	30	40	974
G-1-1-30-12	12	30	160	974	G-2-1-30-12	12	30	80	974	G-3-1-30-12	12	30	40	974
G-1-1-30-14	14	30	160	974	G-2-1-30-14	14	30	80	974	G-3-1-30-14	14	30	40	974
G-1-1-30-16	16	30	160	974	G-2-1-30-16	16	30	80	974	G-3-1-30-16	16	30	40	974
G-1-1-35-8	8	35	160	974	G-2-1-35-8	8	35	80	974	G-3-1-35-8	8	35	40	974
G-1-1-35-10	10	35	160	974	G-2-1-35-10	10	35	80	974	G-3-1-35-10	10	35	40	974
G-1-1-35-12	12	35	160	974	G-2-1-35-12	12	35	80	974	G-3-1-35-12	12	35	40	974
G-1-1-35-14	14	35	160	974	G-2-1-35-14	14	35	80	974	G-3-1-35-14	14	35	40	974
G-1-1-35-16	16	35	160	974	G-2-1-35-16	16	35	80	974	G-3-1-35-16	16	35	40	974
G-1-1-40-8	8	40	160	974	G-2-1-40-8	8	40	80	974	G-3-1-40-8	8	40	40	974
G-1-1-40-10	10	40	160	974	G-2-1-40-10	10	40	80	974	G-3-1-40-10	10	40	40	974
G-1-1-40-12	12	40	160	974	G-2-1-40-12	12	40	80	974	G-3-1-40-12	12	40	40	974
G-1-1-40-14	14	40	160	974	G-2-1-40-14	14	40	80	974	G-3-1-40-14	14	40	40	974
G-1-1-40-16	16	40	160	974	G-2-1-40-16	16	40	80	974	G-3-1-40-16	16	40	40	974
G-1-1-45-8	8	45	160	974	G-2-1-45-8	8	45	80	974	G-3-1-45-8	8	45	40	974
G-1-1-45-10	10	45	160	974	G-2-1-45-10	10	45	80	974	G-3-1-45-10	10	45	40	974
G-1-1-45-12	12	45	160	974	G-2-1-45-12	12	45	80	974	G-3-1-45-12	12	45	40	974
G-1-1-45-14	14	45	160	974	G-2-1-45-14	14	45	80	974	G-3-1-45-14	14	45	40	974
G-1-1-45-16	16	45	160	974	G-2-1-45-16	16	45	80	974	G-3-1-45-16	16	45	40	974

Table 53: Details of beam models used under impact loading in ABAQUS simulation.

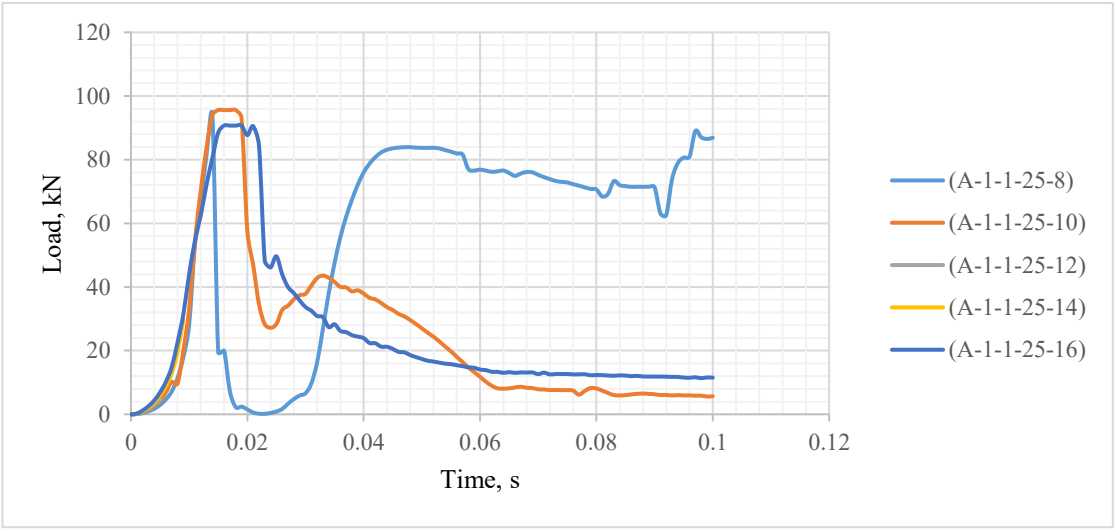

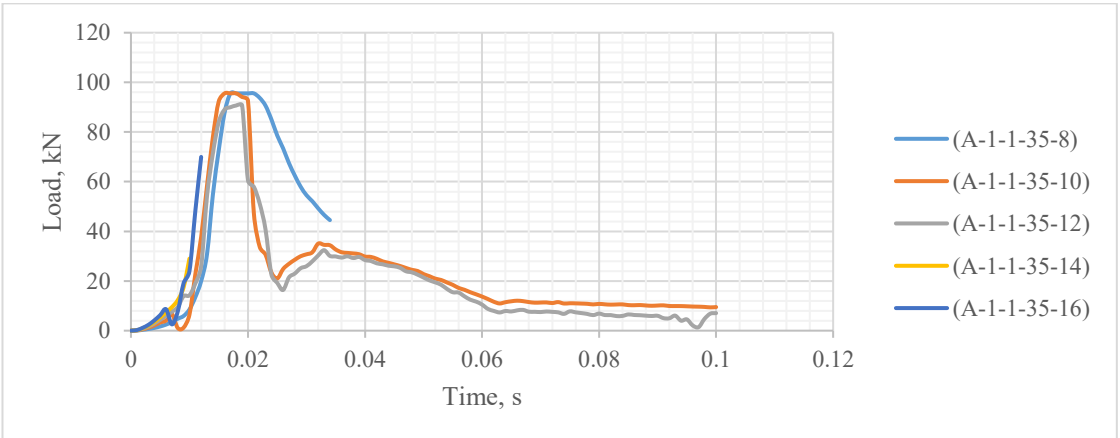

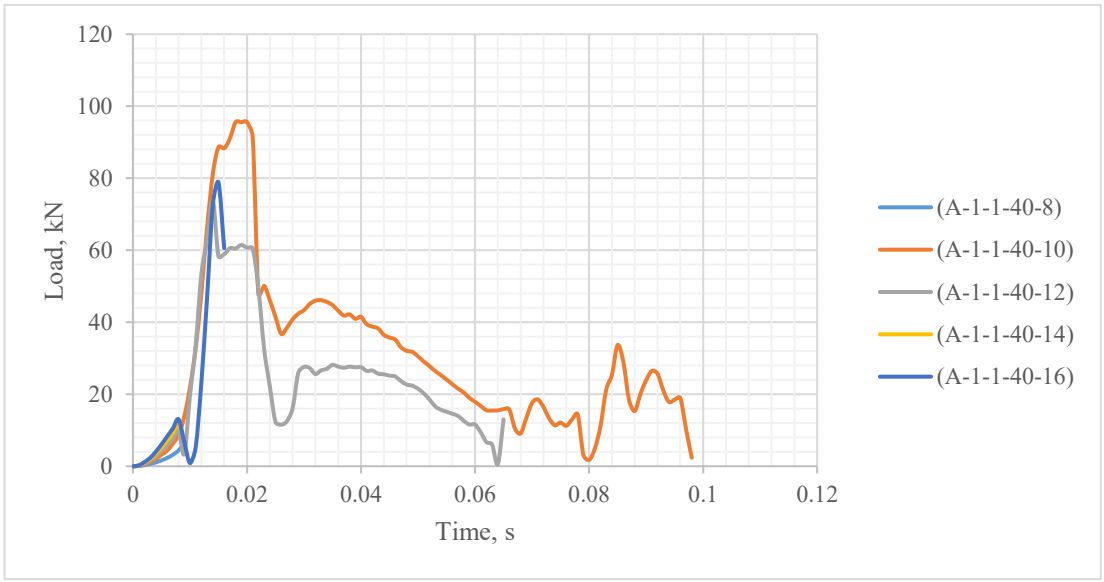
120
100
80
60
40
20
0
Load, kN
0
0.02
0.04
0.06
0.08
0.1
0.12
Time, s
(A-1-1-40-8)
(A-1-1-40-10)
(A-1-1-40-12)
(A-1-1-40-14)
(A-1-1-40-16)

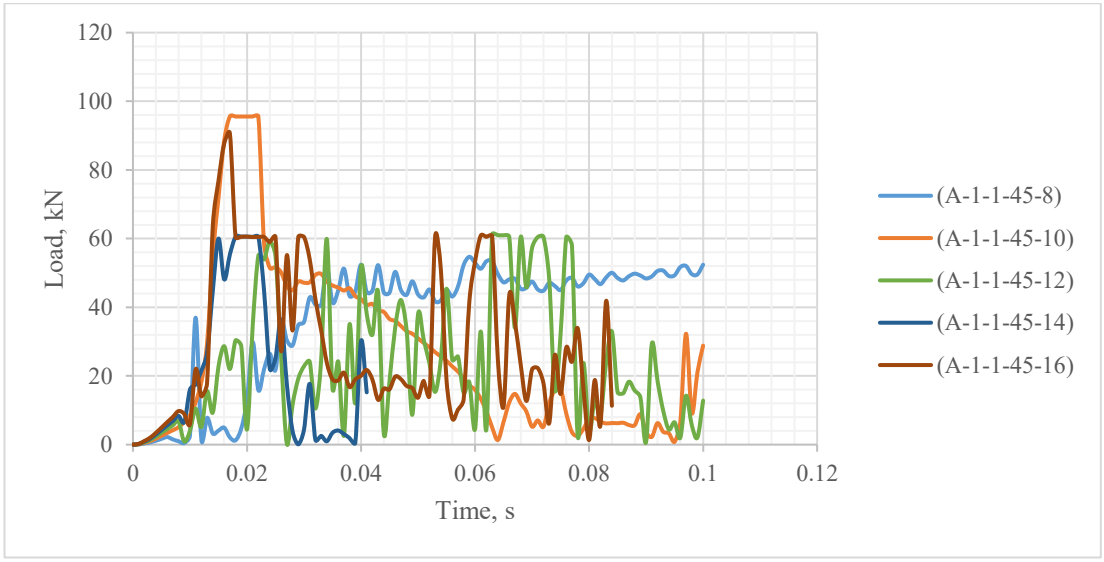
120
100
80
60
40
20
0
Load, kN
0
0.02
0.04
0.06
0.08
0.1
0.12
Time, s
(A-1-1-45-8)
(A-1-1-45-10)
(A-1-1-45-12)
(A-1-1-45-14)
(A-1-1-45-16)

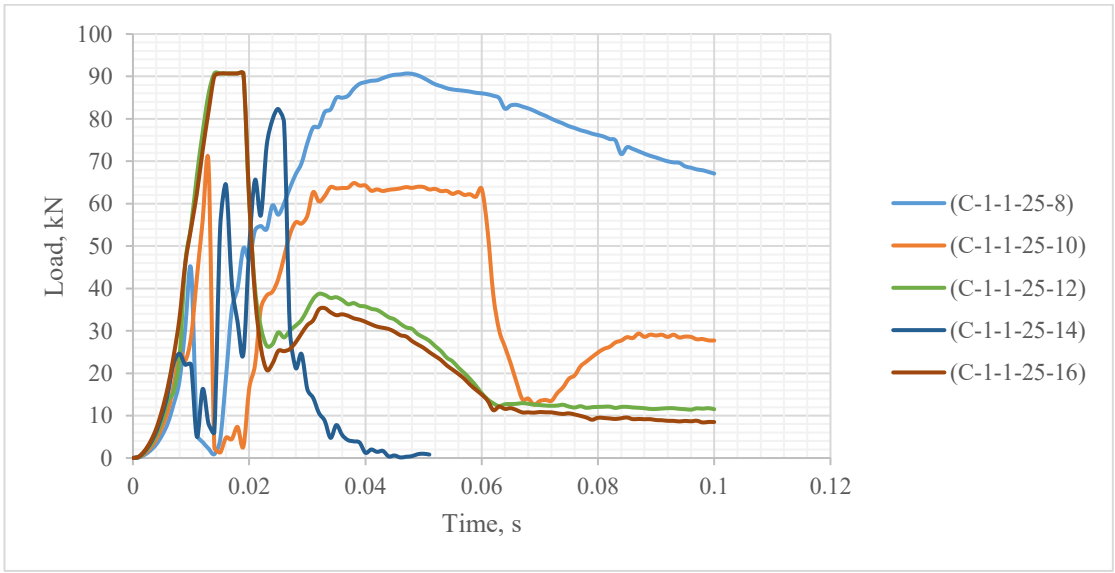
100
90
80
70
60
50
40
30
20
10
0
Load, kN
0
0.02
0.04
0.06
0.08
0.1
0.12
Time, s
(C-1-1-25-8)
(C-1-1-25-10)
(C-1-1-25-12)
(C-1-1-25-14)
(C-1-1-25-16)

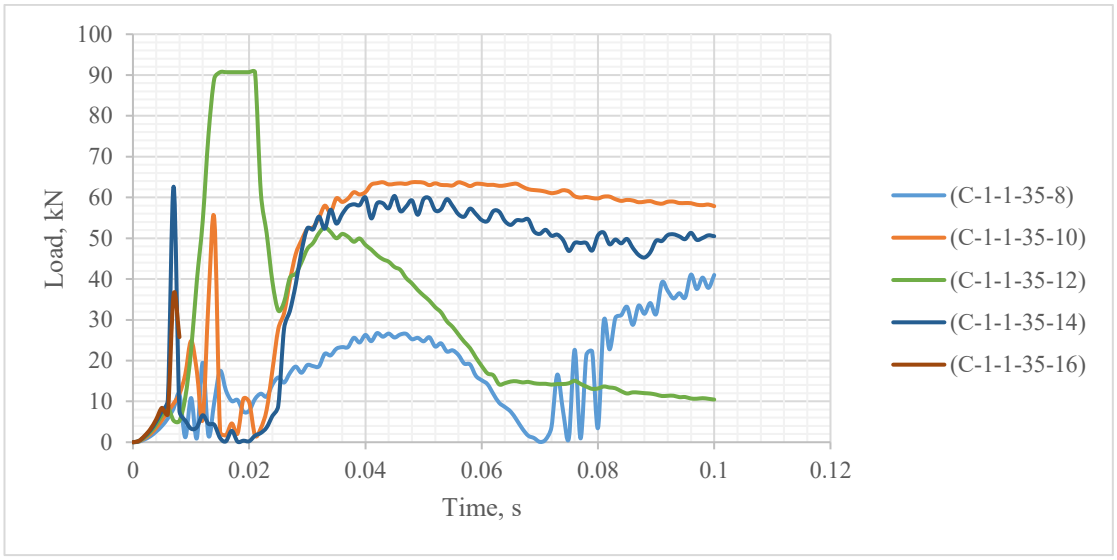
Load, kN
Time, s
(C-1-1-35-8)
(C-1-1-35-10)
(C-1-1-35-12)
(C-1-1-35-14)
(C-1-1-35-16)

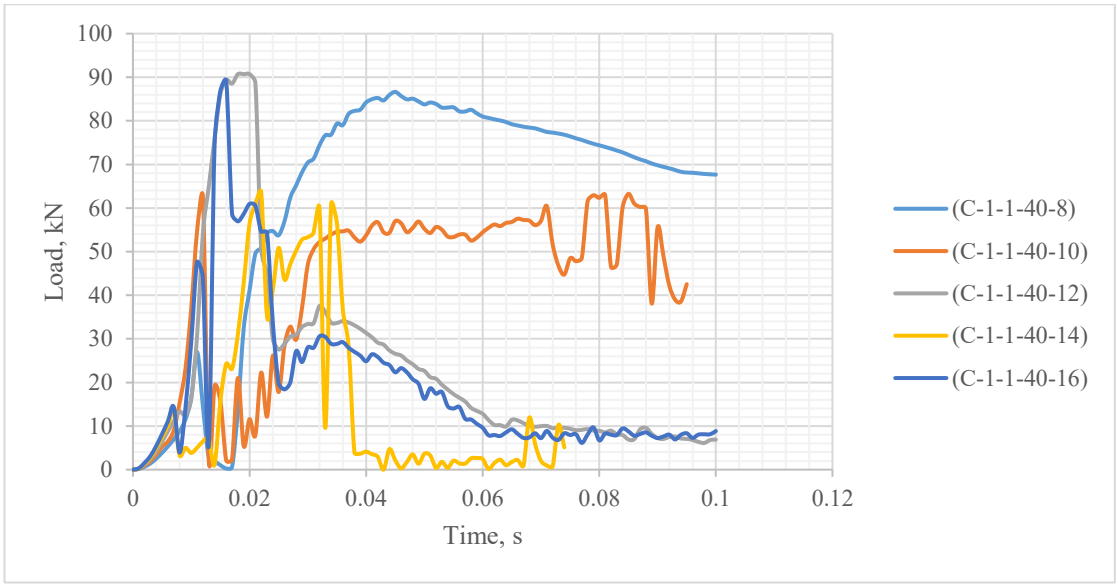
Load, kN
Time, s
(C-1-1-40-8)
(C-1-1-40-10)
(C-1-1-40-12)
(C-1-1-40-14)
(C-1-1-40-16)

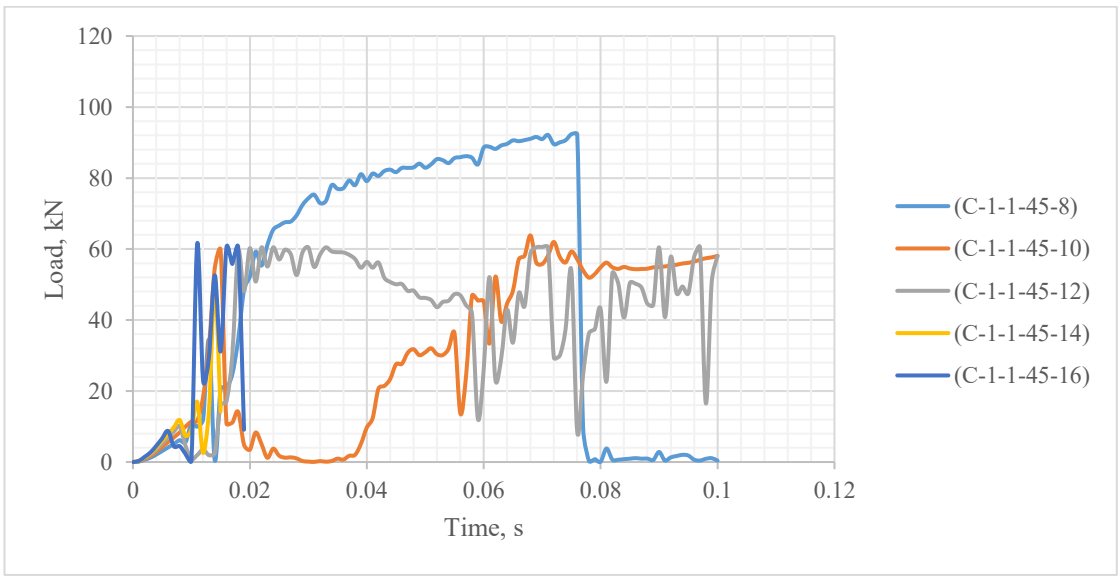
Load, kN
Time, s
(C-1-1-45-8)
(C-1-1-45-10)
(C-1-1-45-12)
(C-1-1-45-14)
(C-1-1-45-16)

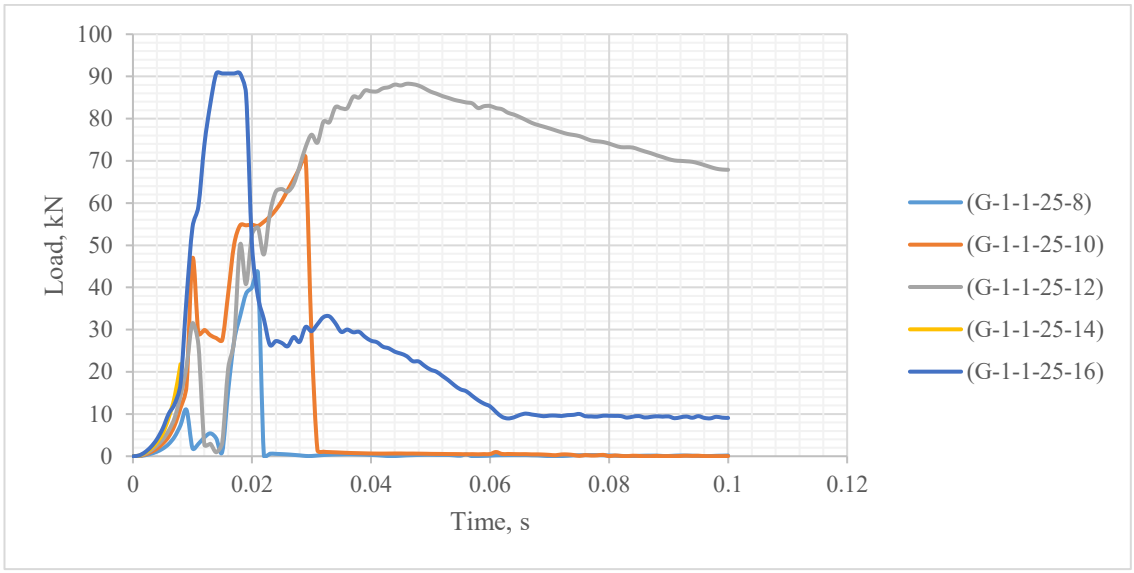
Load, kN
Time, s
(G-1-1-25-8)
(G-1-1-25-10)
(G-1-1-25-12)
(G-1-1-25-14)
(G-1-1-25-16)

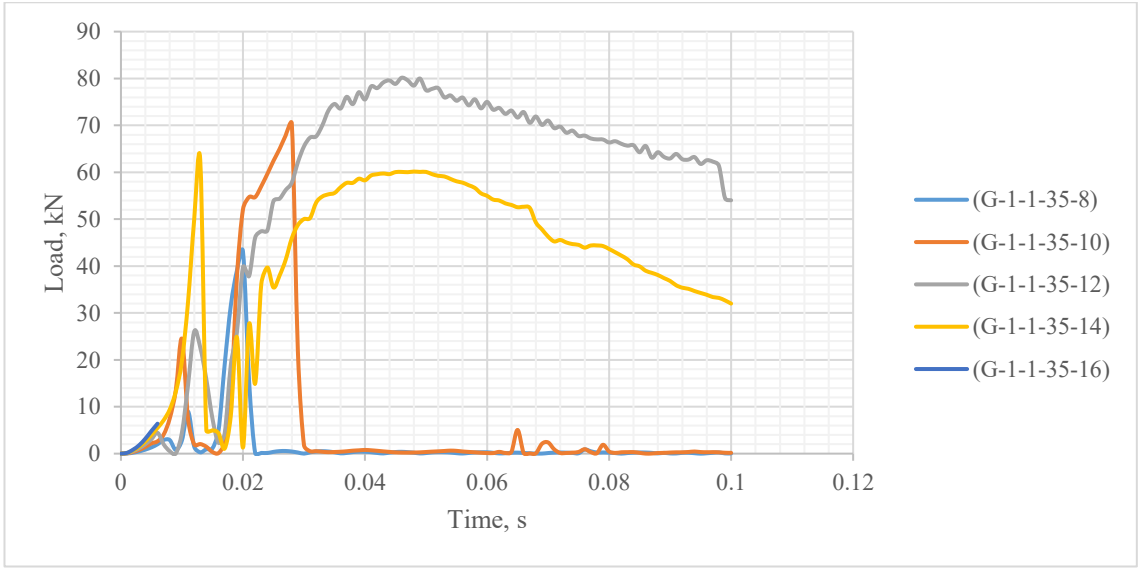
Load, kN
Time, s
(G-1-1-35-8)
(G-1-1-35-10)
(G-1-1-35-12)
(G-1-1-35-14)
(G-1-1-35-16)

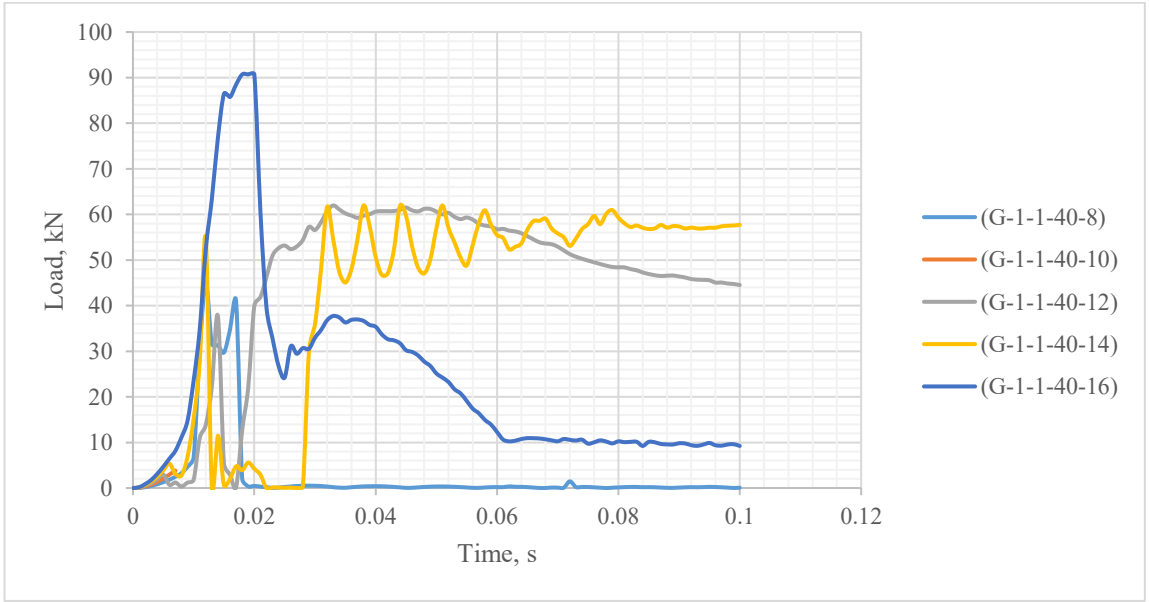
Load, kN
Time, s
(G-1-1-40-8)
(G-1-1-40-10)
(G-1-1-40-12)
(G-1-1-40-14)
(G-1-1-40-16)

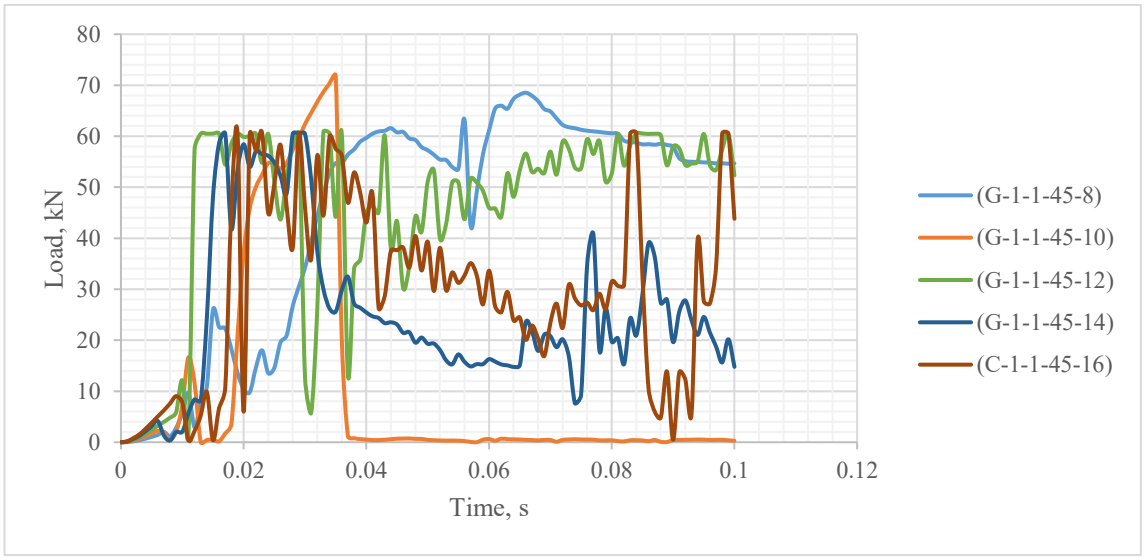

Figure 136: Impact Force-Time History response of (A) AFRP, (B) CFRP and (C) GFRP RC beams under 320 kN impact load.

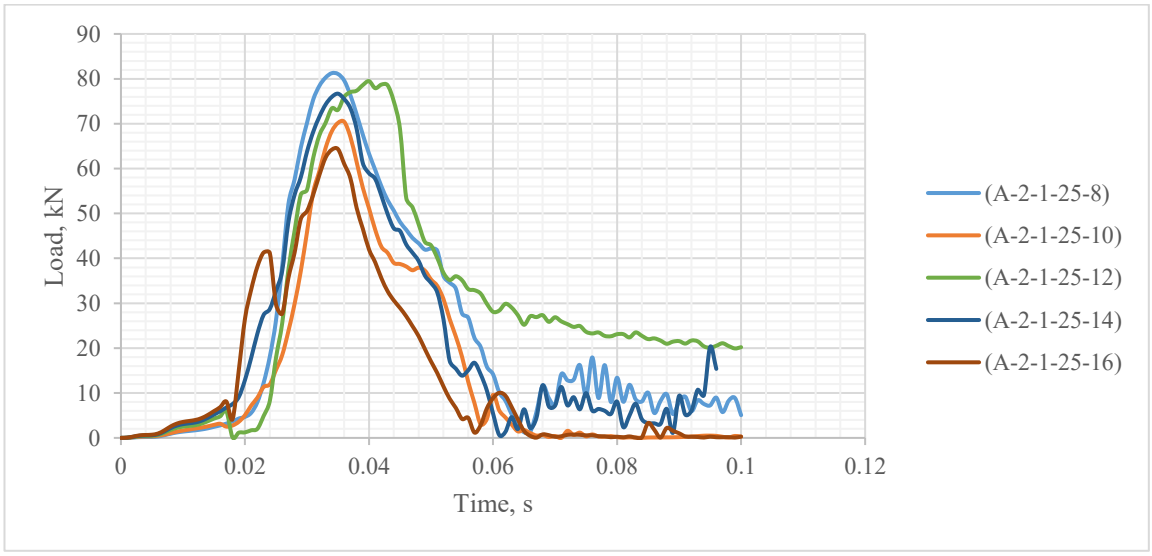

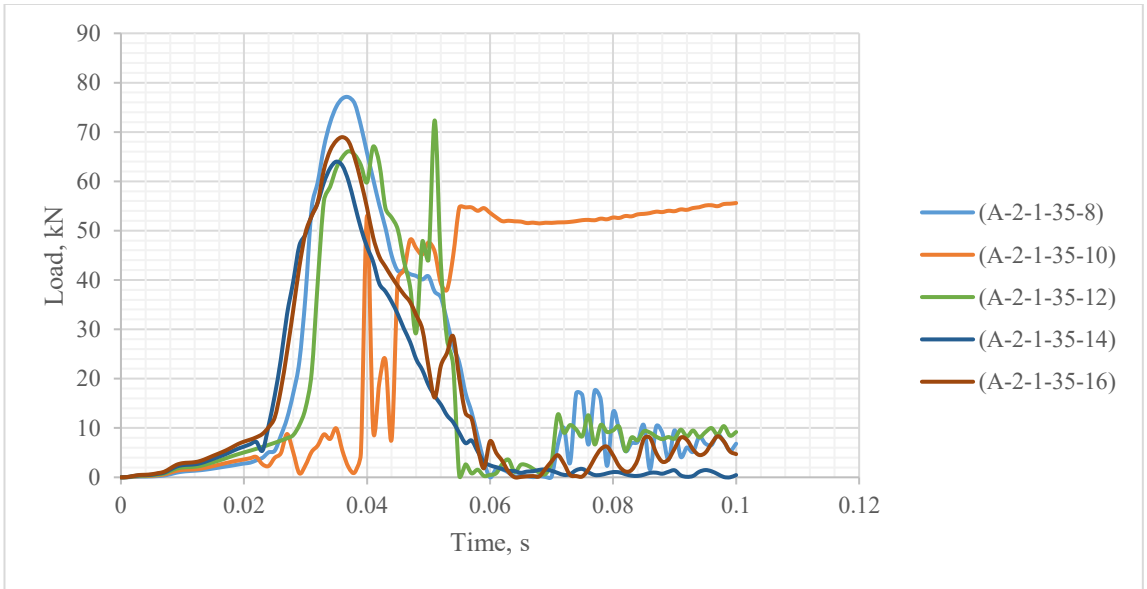

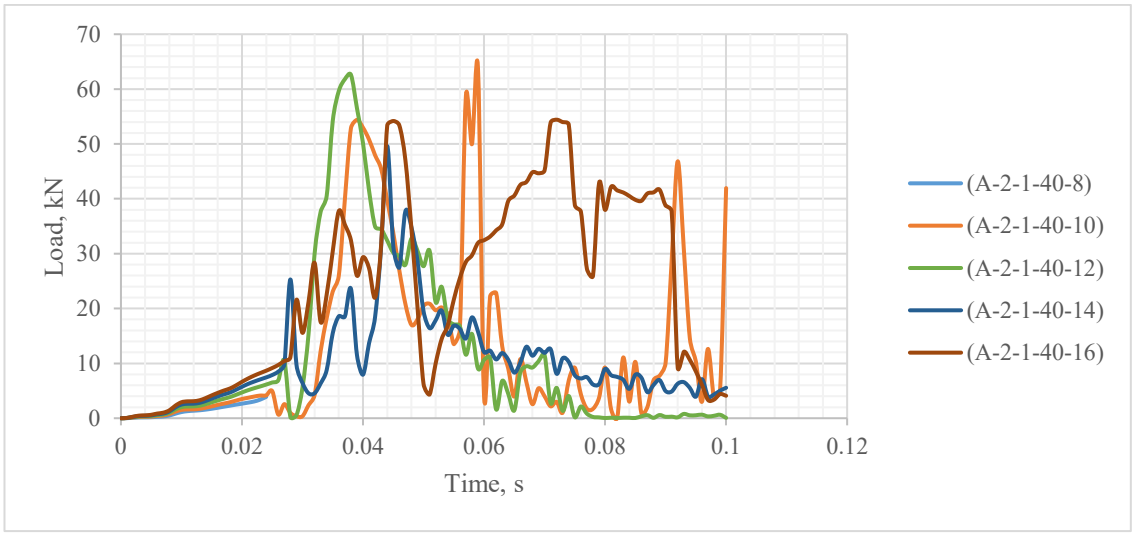
70
60
50
40
30
20
10
0
Load, kN
0
0.02
0.04
0.06
0.08
0.1
0.12
Time, s
(A-2-1-40-8)
(A-2-1-40-10)
(A-2-1-40-12)
(A-2-1-40-14)
(A-2-1-40-16)

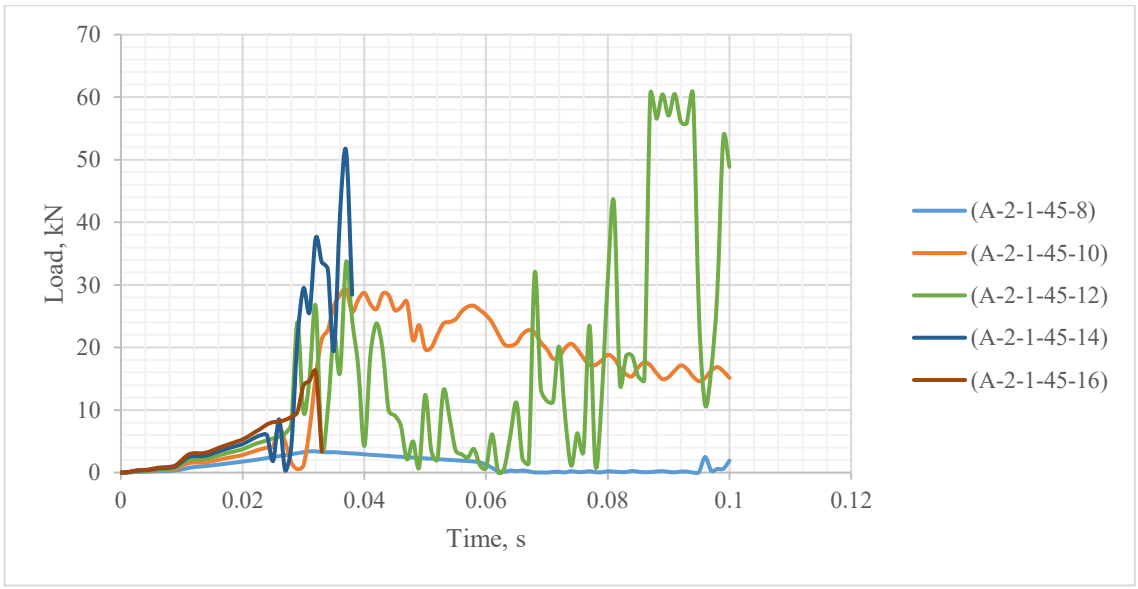
70
60
50
40
30
20
10
0
Load, kN
0
0.02
0.04
0.06
0.08
0.1
0.12
Time, s
(A-2-1-45-8)
(A-2-1-45-10)
(A-2-1-45-12)
(A-2-1-45-14)
(A-2-1-45-16)

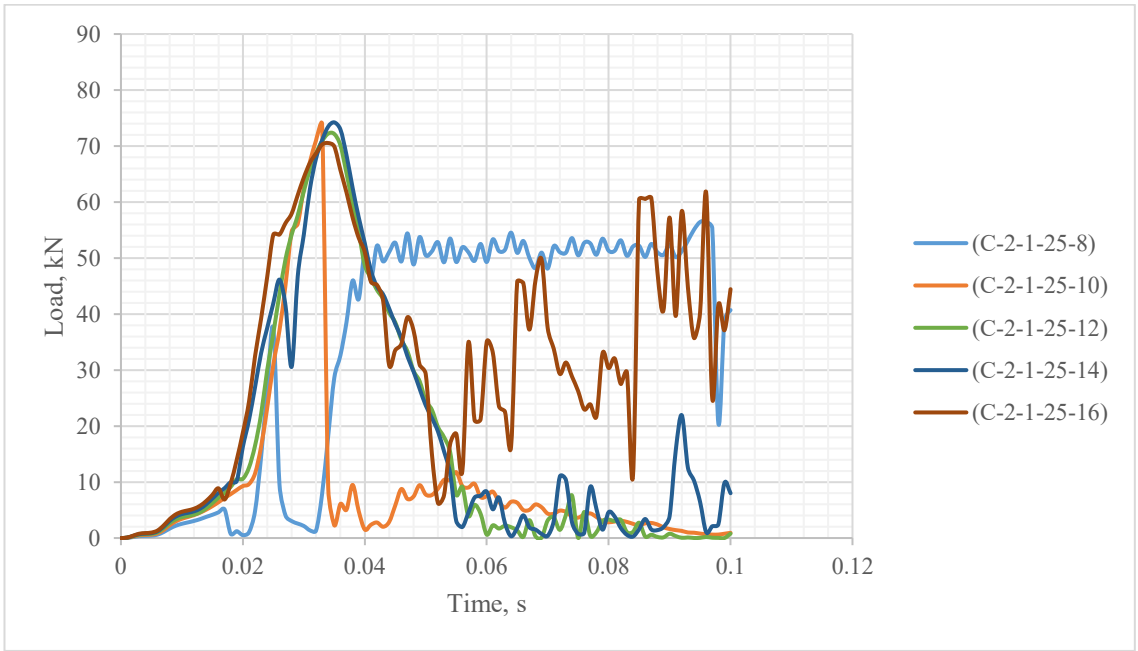
90
80
70
60
50
40
30
20
10
0
Load, kN
0
0.02
0.04
0.06
0.08
0.1
0.12
Time, s
(C-2-1-25-8)
(C-2-1-25-10)
(C-2-1-25-12)
(C-2-1-25-14)
(C-2-1-25-16)

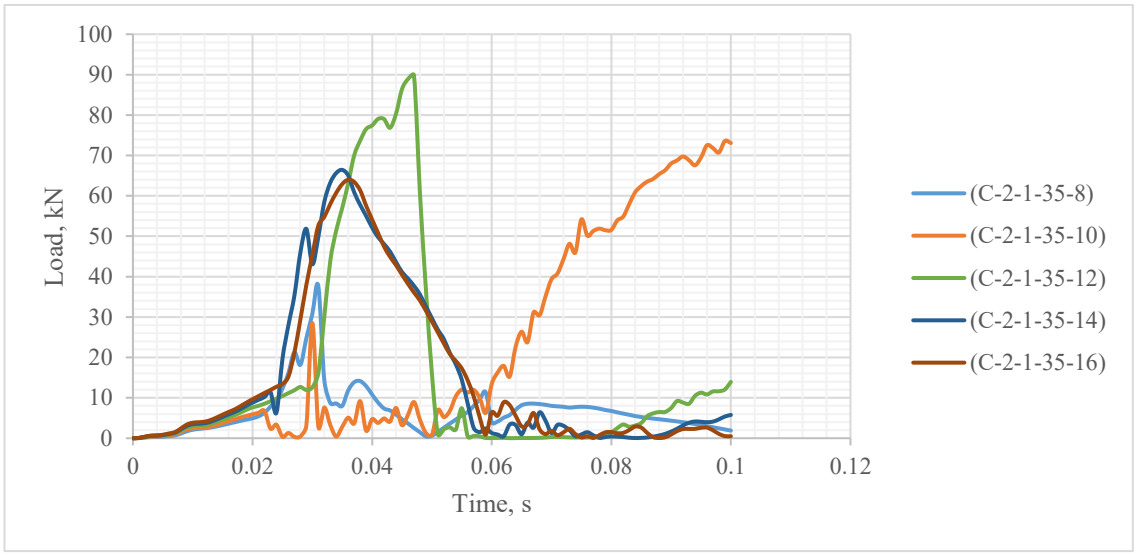
Load, kN
Time, s
(C-2-1-35-8)
(C-2-1-35-10)
(C-2-1-35-12)
(C-2-1-35-14)
(C-2-1-35-16)

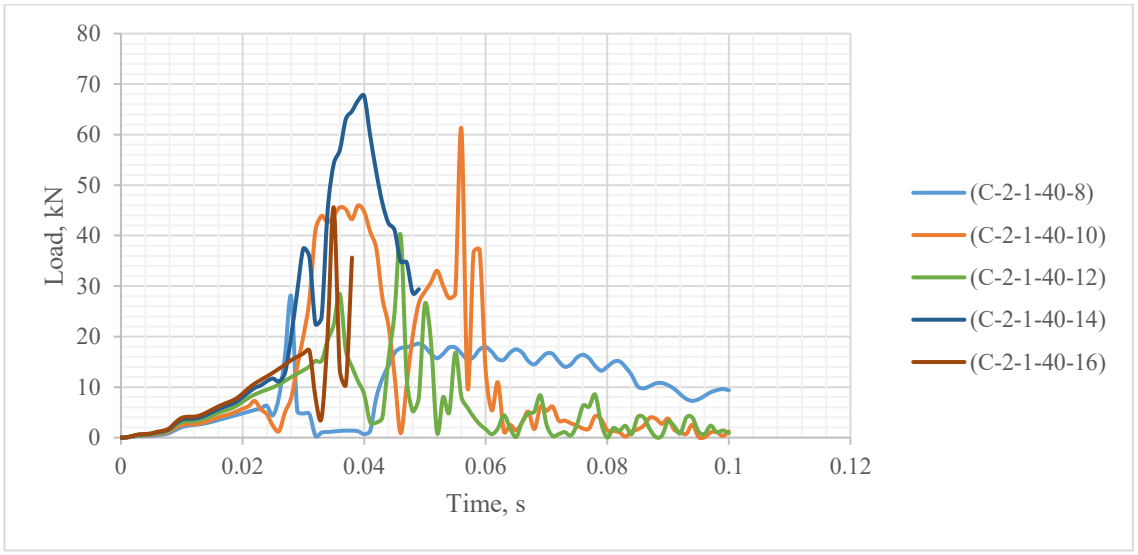
Load, kN
Time, s
(C-2-1-40-8)
(C-2-1-40-10)
(C-2-1-40-12)
(C-2-1-40-14)
(C-2-1-40-16)

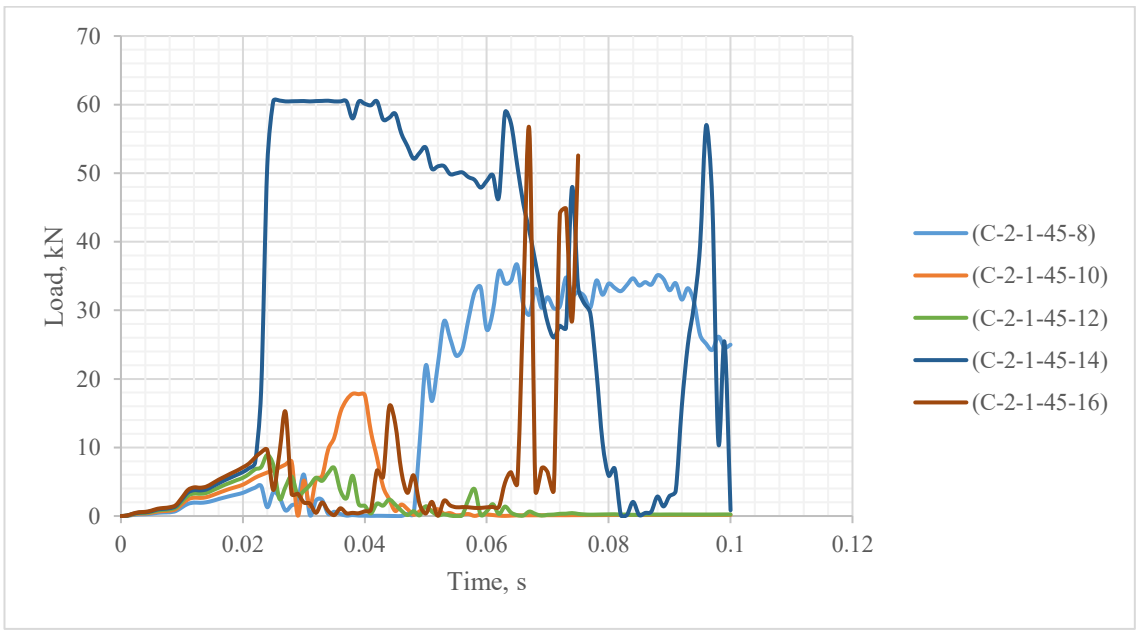
Load, kN
Time, s
(C-2-1-45-8)
(C-2-1-45-10)
(C-2-1-45-12)
(C-2-1-45-14)
(C-2-1-45-16)

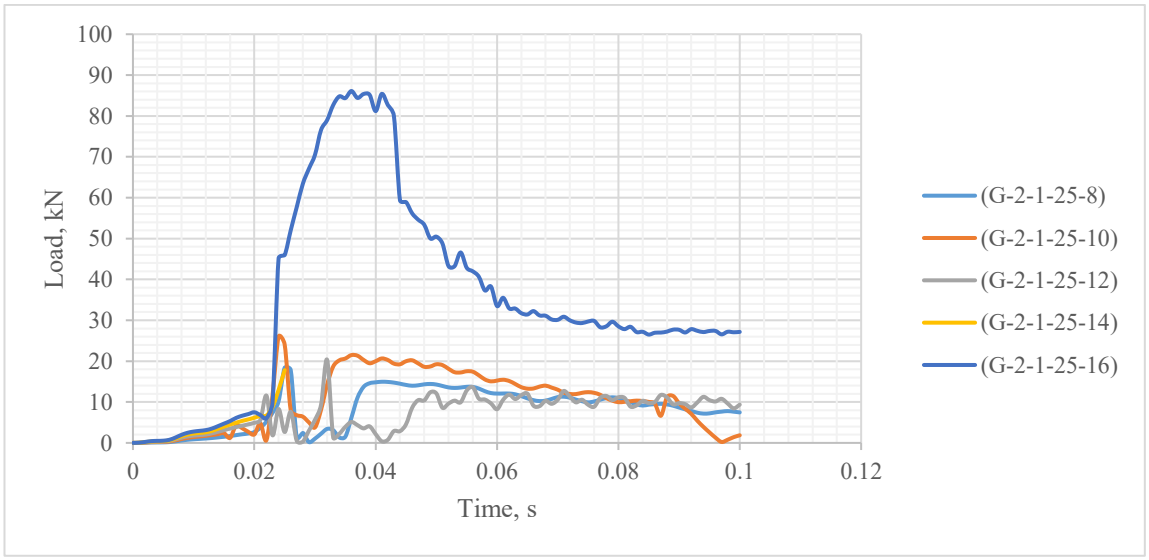
Load, kN
Time, s
(G-2-1-25-8)
(G-2-1-25-10)
(G-2-1-25-12)
(G-2-1-25-14)
(G-2-1-25-16)

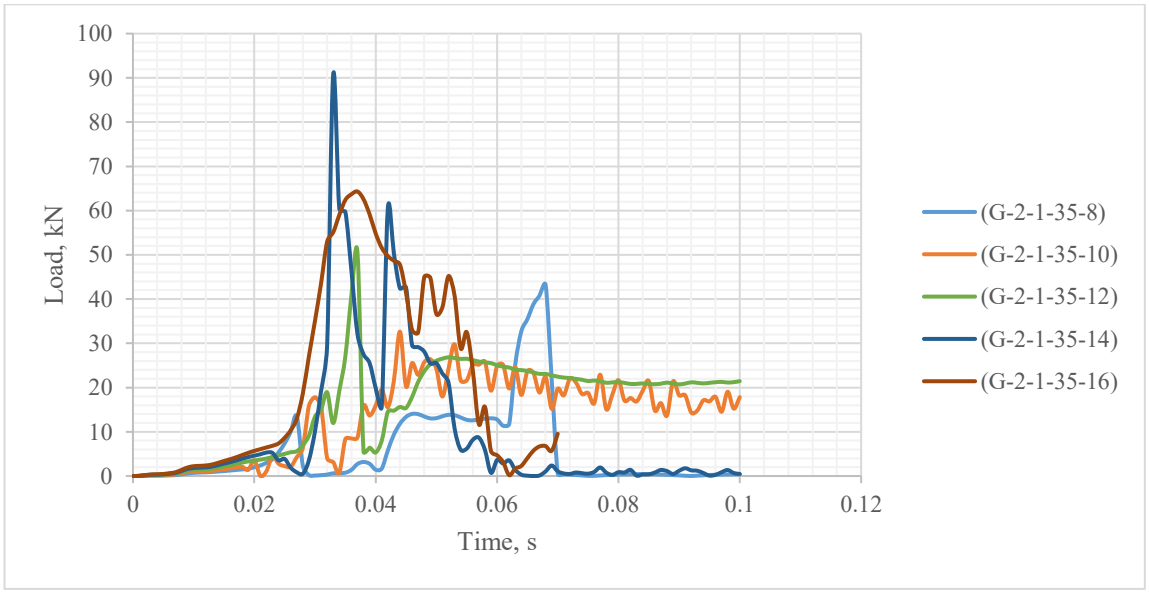
Load, kN
Time, s
(G-2-1-35-8)
(G-2-1-35-10)
(G-2-1-35-12)
(G-2-1-35-14)
(G-2-1-35-16)

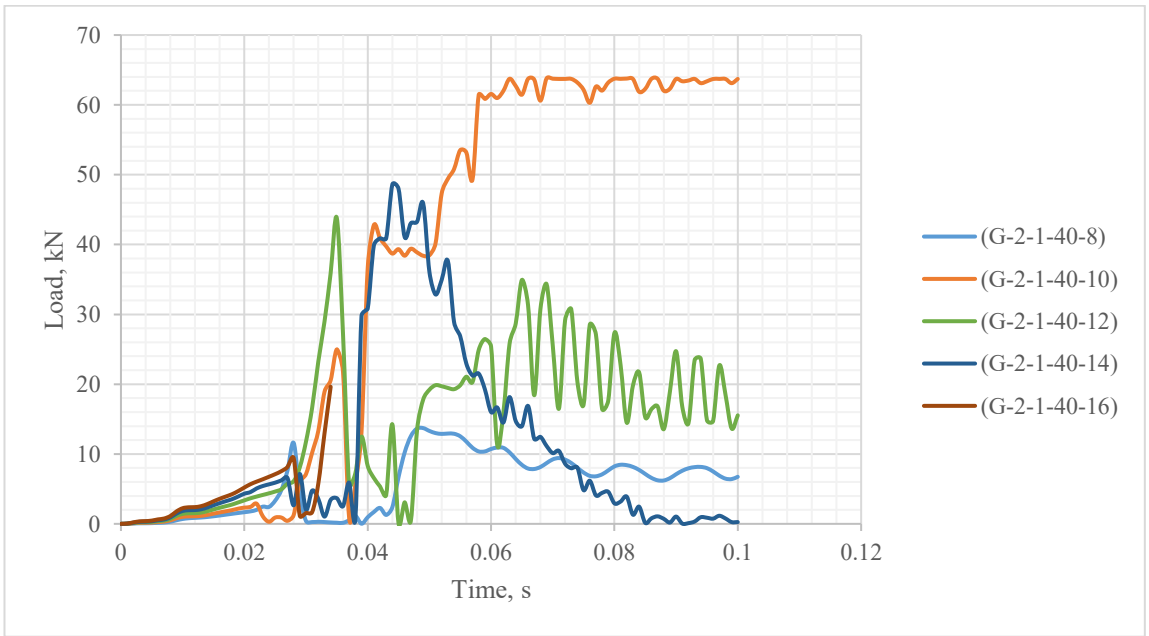
Load, kN
Time, s
(G-2-1-40-8)
(G-2-1-40-10)
(G-2-1-40-12)
(G-2-1-40-14)
(G-2-1-40-16)

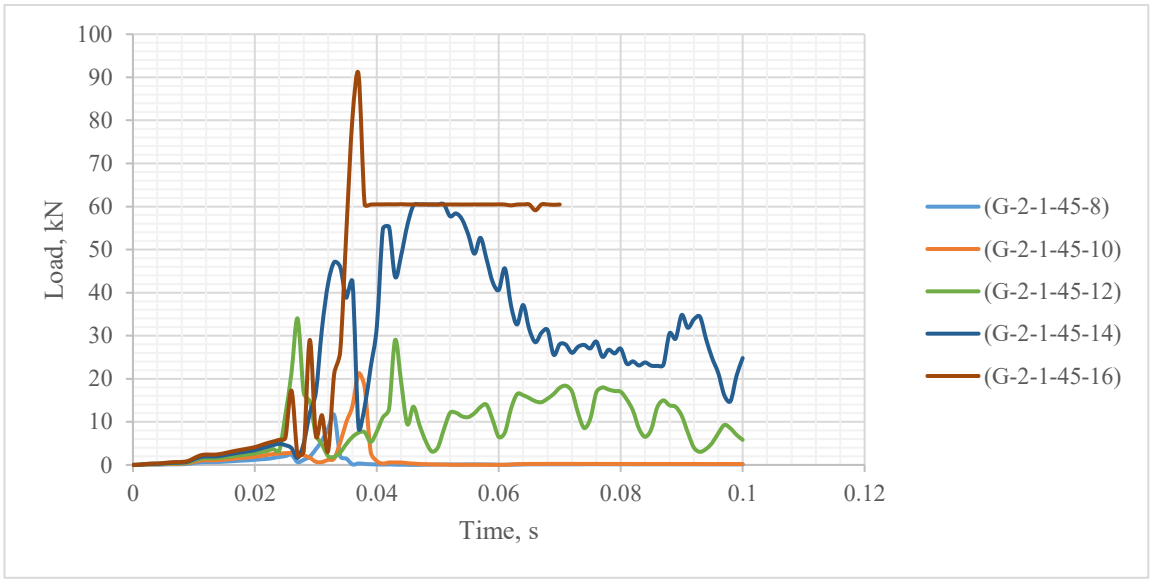

Figure 137: Impact Force-Time History response of (A) AFRP, (B) CFRP and (C) GFRP RC beams under 80 kN impact load.

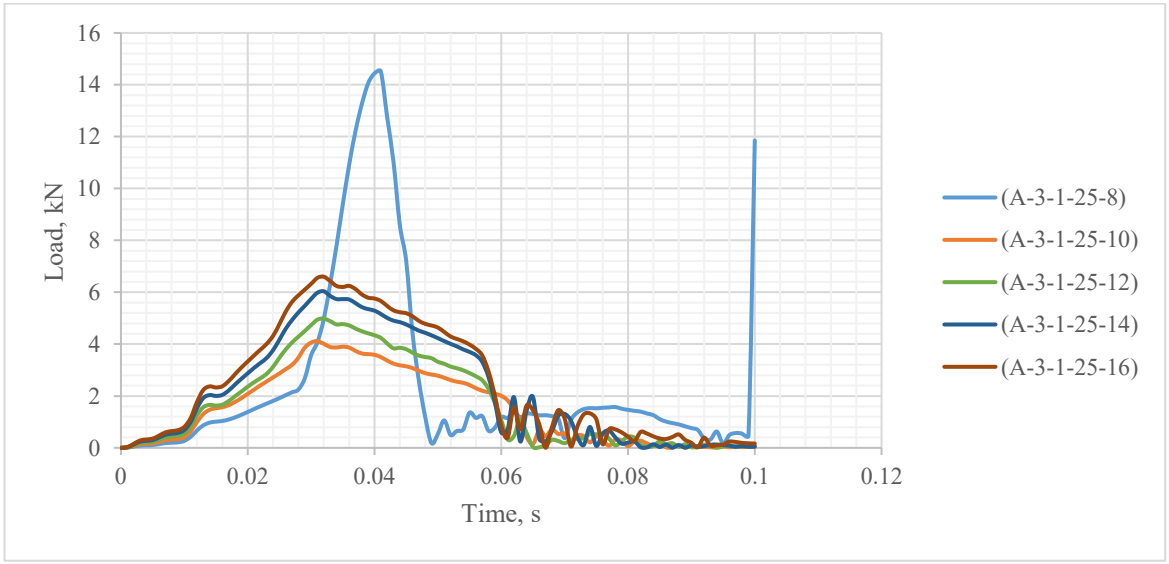

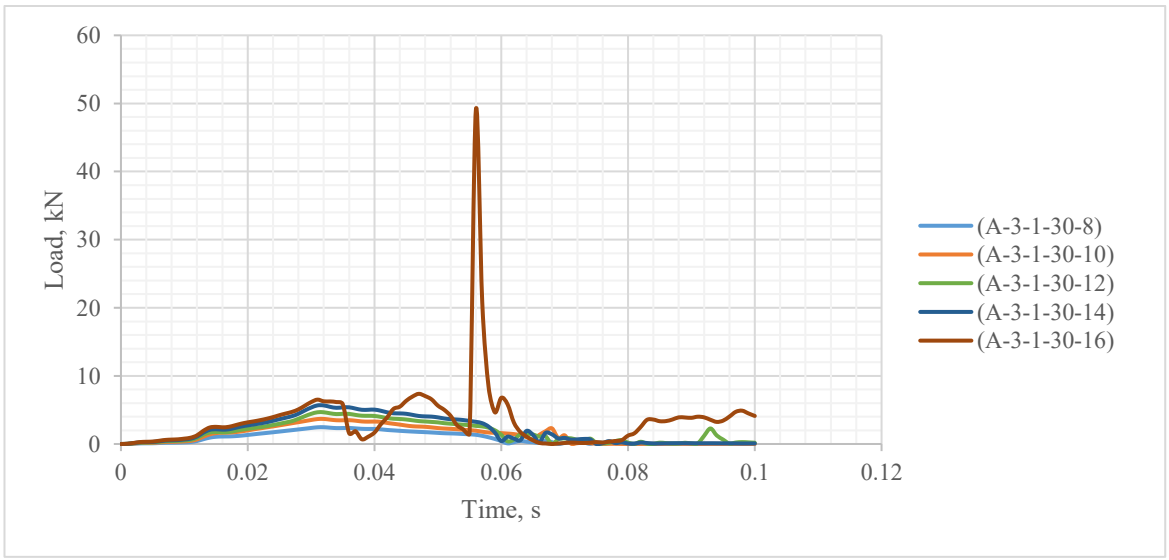

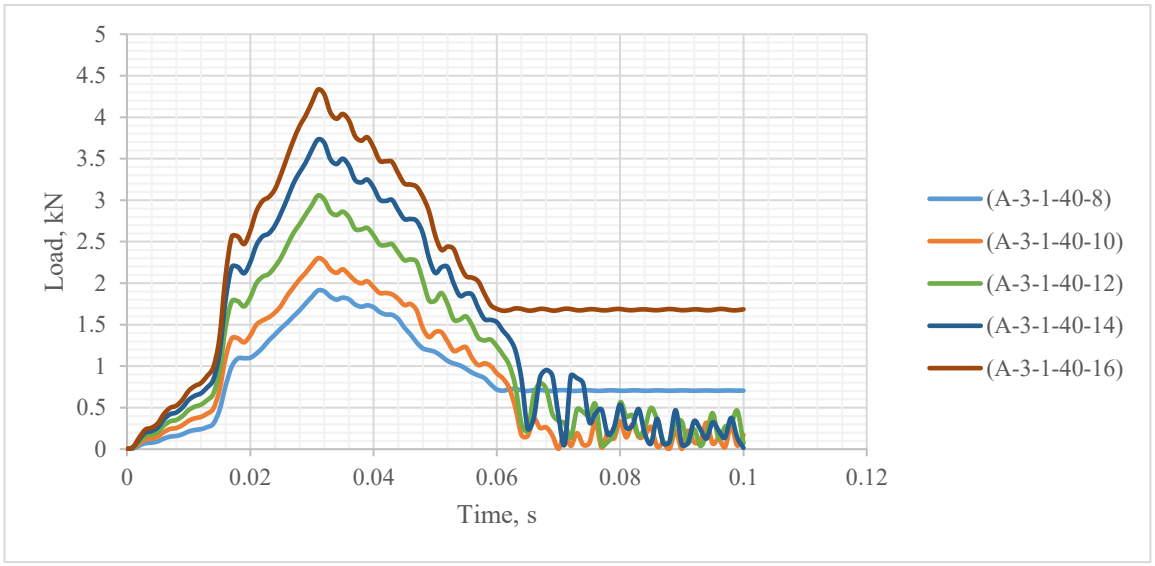
Load, kN
Time, s
0
0.5
1
1.5
2
2.5
3
3.5
4
4.5
5
0
0.02
0.04
0.06
0.08
0.1
0.12
(A-3-1-40-8)
(A-3-1-40-10)
(A-3-1-40-12)
(A-3-1-40-14)
(A-3-1-40-16)

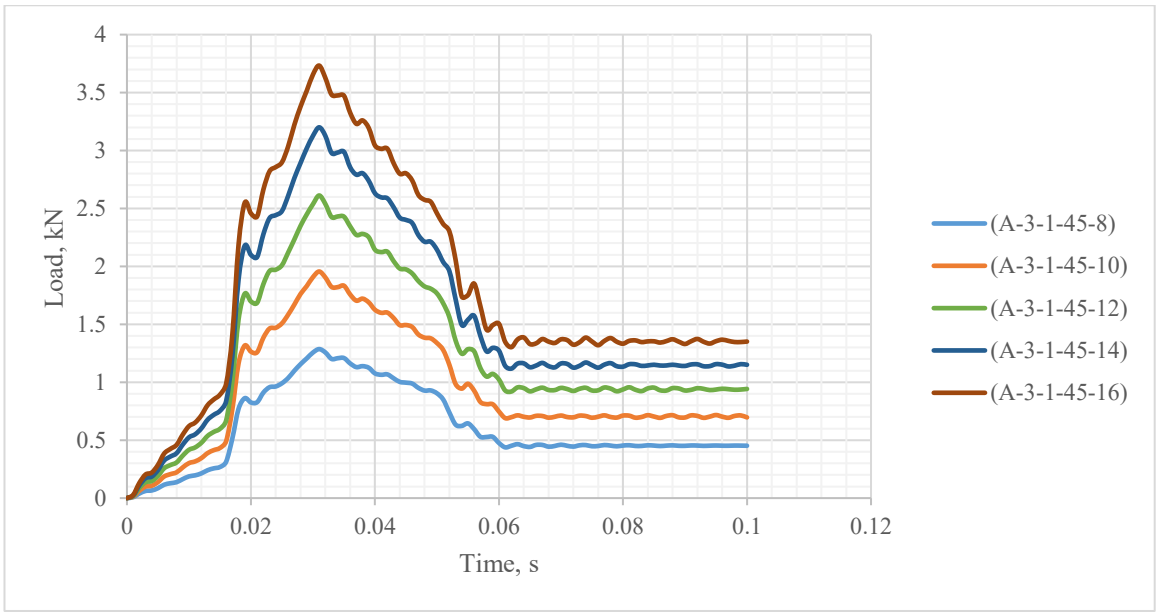
Load, kN
Time, s
0
0.5
1
1.5
2
2.5
3
3.5
4
0
0.02
0.04
0.06
0.08
0.1
0.12
(A-3-1-45-8)
(A-3-1-45-10)
(A-3-1-45-12)
(A-3-1-45-14)
(A-3-1-45-16)

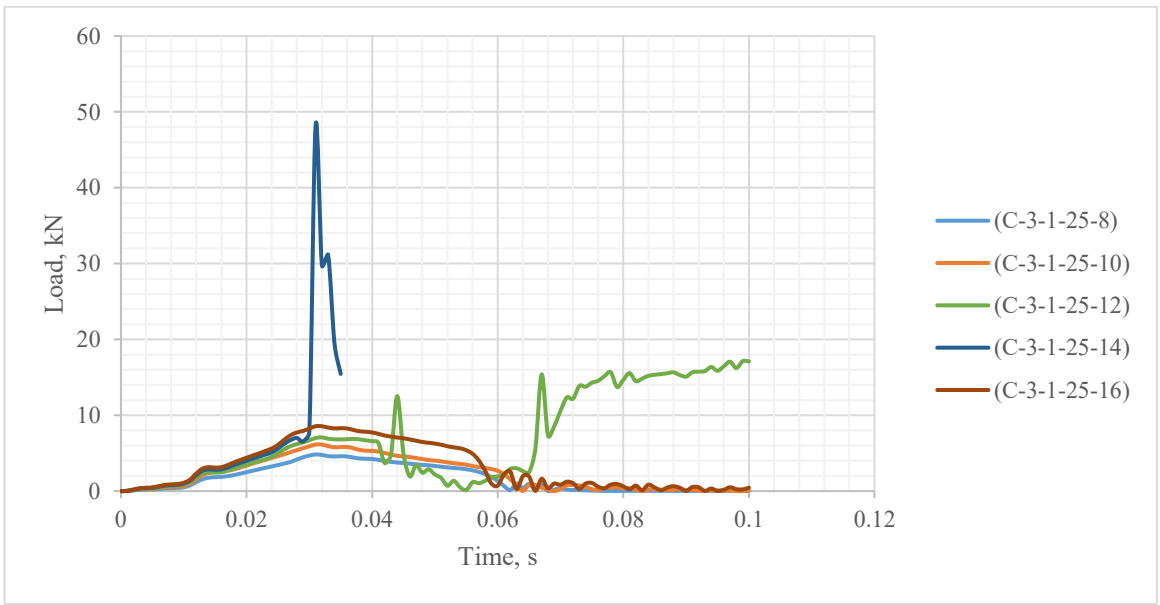
Load, kN
Time, s
0
10
20
30
40
50
60
0
0.02
0.04
0.06
0.08
0.1
0.12
(C-3-1-25-8)
(C-3-1-25-10)
(C-3-1-25-12)
(C-3-1-25-14)
(C-3-1-25-16)

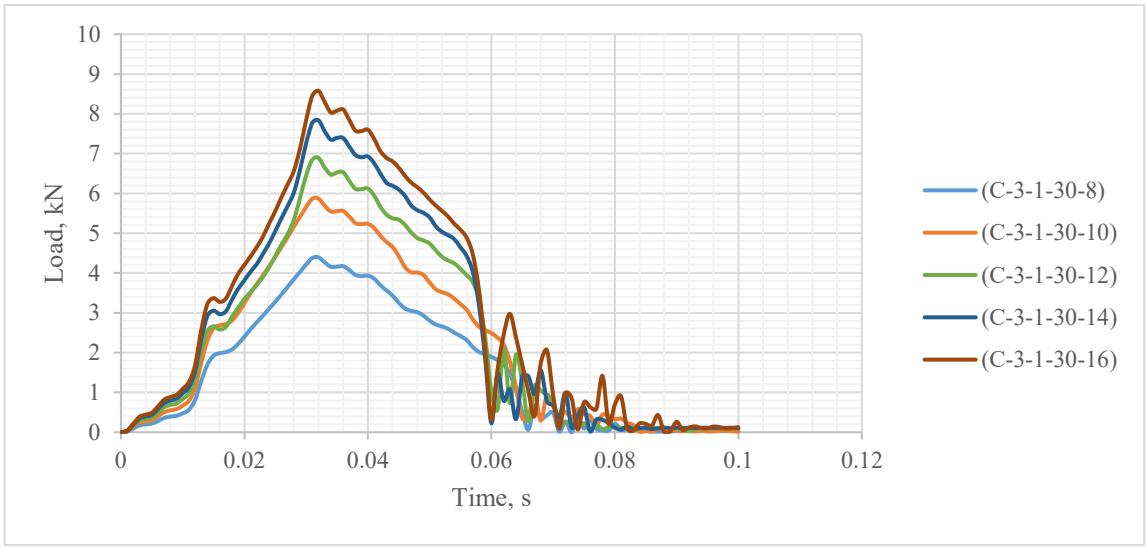
Load, kN
Time, s
0
1
2
3
4
5
6
7
8
9
10
0
0.02
0.04
0.06
0.08
0.1
0.12
(C-3-1-30-8)
(C-3-1-30-10)
(C-3-1-30-12)
(C-3-1-30-14)
(C-3-1-30-16)

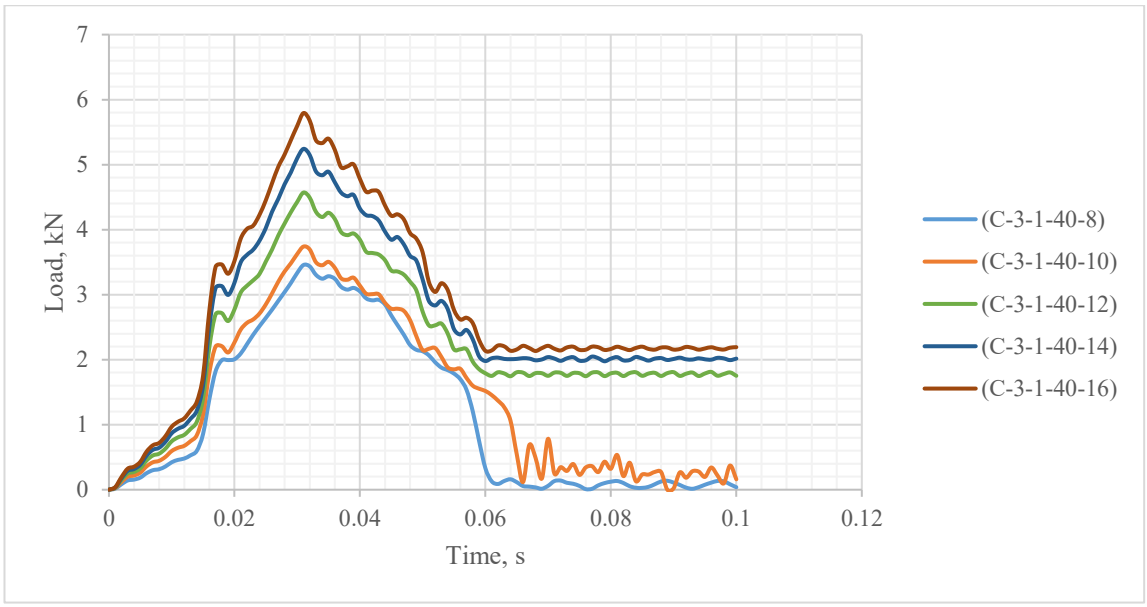
Load, kN
Time, s
0
1
2
3
4
5
6
7
0
0.02
0.04
0.06
0.08
0.1
0.12
(C-3-1-40-8)
(C-3-1-40-10)
(C-3-1-40-12)
(C-3-1-40-14)
(C-3-1-40-16)

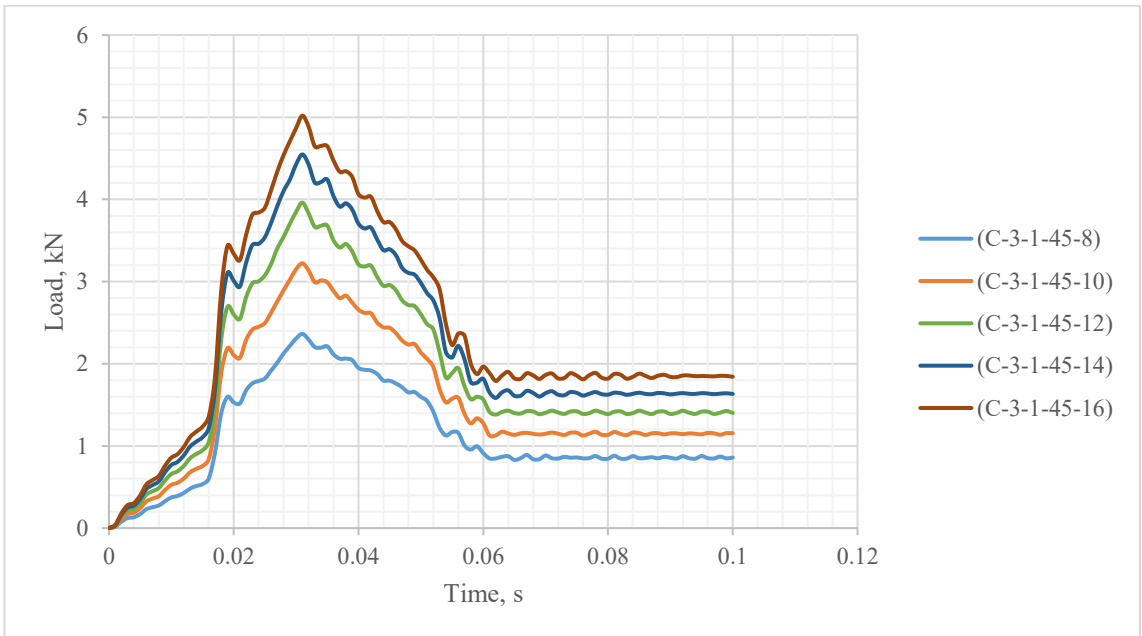
Load, kN
Time, s
0
1
2
3
4
5
6
0
0.02
0.04
0.06
0.08
0.1
0.12
(C-3-1-45-8)
(C-3-1-45-10)
(C-3-1-45-12)
(C-3-1-45-14)
(C-3-1-45-16)

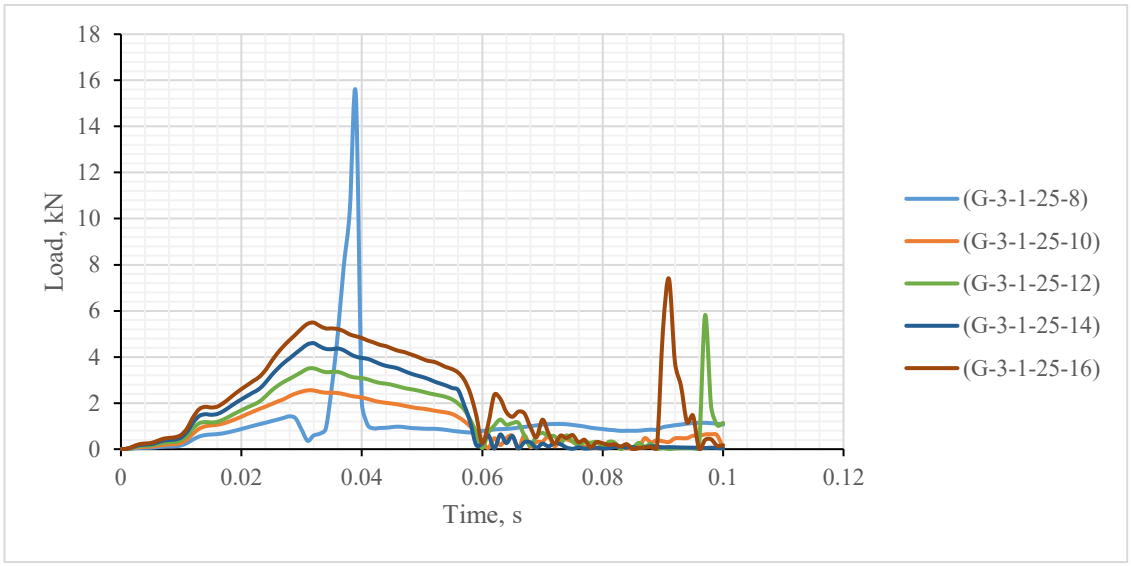
Load, kN
Time, s
(G-3-1-25-8)
(G-3-1-25-10)
(G-3-1-25-12)
(G-3-1-25-14)
(G-3-1-25-16)

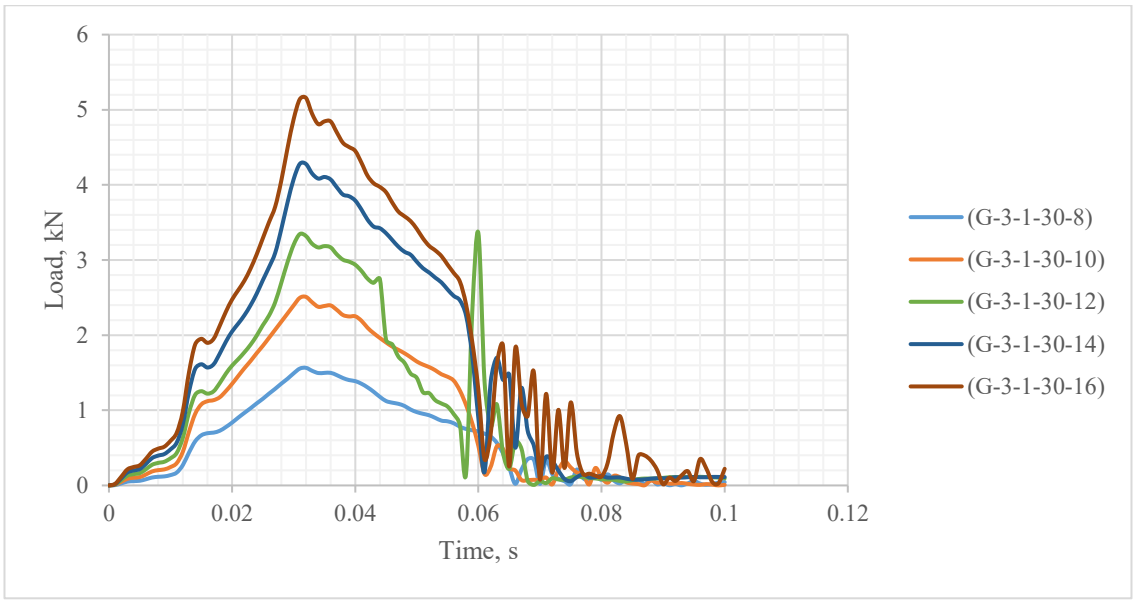
Load, kN
Time, s
(G-3-1-30-8)
(G-3-1-30-10)
(G-3-1-30-12)
(G-3-1-30-14)
(G-3-1-30-16)

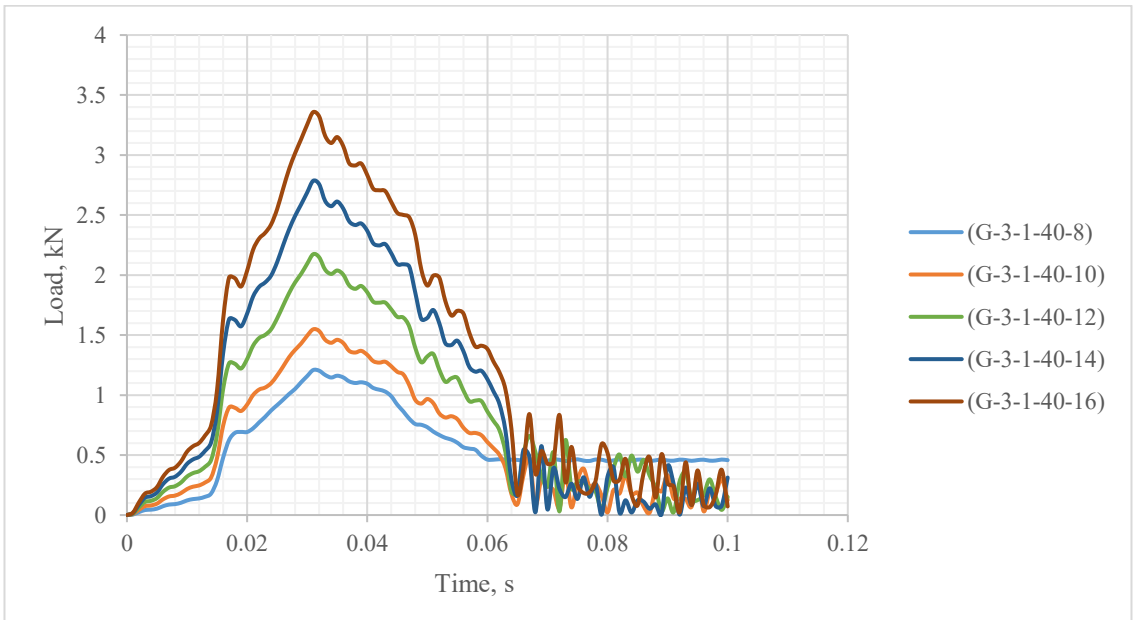
Load, kN
Time, s
(G-3-1-40-8)
(G-3-1-40-10)
(G-3-1-40-12)
(G-3-1-40-14)
(G-3-1-40-16)

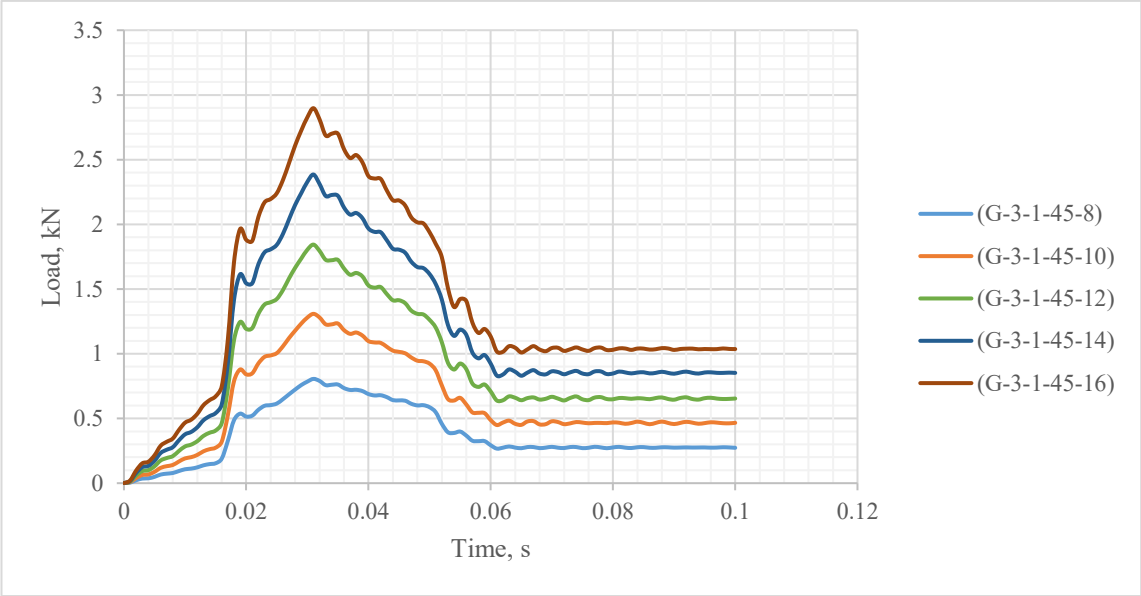

Figure 138: Force-Time histories of GFRP RC beams with concrete compressive strength of 35 MPa under 40 kN impact load.

MODEL	TIME,s	FORCE, kN	DURATION
A-1-1-25-8	0.014001	93.6427	0.1
A-1-1-25-12	0.005001	48.0881	0.005001
A-1-1-25-14	0.009001	29.6176	0.009001
A-1-1-25-16	0.017001	90.6945	0.1

MODEL	TIME,s	FORCE, kN	DURATION
A-1-1-35-8	0.017001	95.5646	0.034001
A-1-1-35-10	0.016	95.5646	0.1
A-1-1-35-12	0.018001	90.6945	0.1
A-1-1-35-14	0.010001	29.0055	0.0100005
A-1-1-35-16	0.012	69.9673	0.012

MODEL	TIME,s	FORCE, kN	DURATION
A-1-1-40-8	0.009001	6.20178	0.009001
A-1-1-40-10	0.018001	95.5646	0.098001
A-1-1-40-12	0.014001	73.685	0.065001
A-1-1-40-14	0.008	11.8619	0.008
A-1-1-40-16	0.015001	78.8549	0.016

MODEL	TIME,s	FORCE, kN	DURATION
A-1-1-45-8	0.059	54.7101	0.1
A-1-1-45-10	0.017	95.5646	0.1
A-1-1-45-12	0.063	61.2466	0.1
A-1-1-45-14	0.02	60.5936	0.041
A-1-1-45-16	0.017	90.6945	0.084

MODEL	TIME,s	FORCE, kN	DURATION
C-1-1-25-8	0.047001	90.694	0.1
C-1-1-25-10	0.013	69.6612	0.1
C-1-1-25-12	0.014001	90.6945	0.1
C-1-1-25-14	0.025	82.3172	0.051001
C-1-1-25-16	0.015001	90.6945	0.1

MODEL	TIME,s	FORCE, kN	DURATION
C-1-1-35-8	0.096	41.0757	0.1
C-1-1-35-10	0.049001	63.7417	0.1
C-1-1-35-12	0.015001	90.6945	0.1
C-1-1-35-14	0.007001	62.6392	0.1
C-1-1-35-16	0.007001	36.2533	0.008

MODEL	TIME,s	FORCE, kN	DURATION
C-1-1-40-8	0.045001	86.6397	0.095001
C-1-1-40-10	0.085	63.2549	0.095001
C-1-1-40-12	0.018001	90.6945	0.1
C-1-1-40-14	0.022001	63.6892	0.074
C-1-1-40-16	0.016	89.1914	0.1

MODEL	TIME,s	FORCE, kN	DURATION
C-1-1-45-8	0.075	92.3463	0.1
C-1-1-45-10	0.068	63.8219	0.1
C-1-1-45-12	0.07	60.5724	0.1
C-1-1-45-14	0.014	49.2956	0.015
C-1-1-45-16	0.011	61.4732	0.019

MODEL	TIME,s	FORCE, kN	DURATION
G-1-1-25-8	0.021001	43.4645	0.1
G-1-1-25-10	0.029001	70.8528	0.1
G-1-1-25-12	0.046001	88.2591	0.1
G-1-1-25-14	0.008	21.8304	0.008
G-1-1-25-16	0.014001	90.6945	0.1

MODEL	TIME,s	FORCE, kN	DURATION
G-1-1-35-8	0.020001	43.0743	0.1
G-1-1-35-10	0.028001	70.406	0.1
G-1-1-35-12	0.046001	80.1648	0.1
G-1-1-35-14	0.013	62.5448	0.1
G-1-1-35-16	0.006	63.8772	0.006

MODEL	TIME,s	FORCE, kN	DURATION
G-1-1-40-8	0.012	45.1219	0.1
G-1-1-40-10	0.007001	38.2549	0.0070005
G-1-1-40-12	0.033	61.9718	0.1
G-1-1-40-14	0.051001	61.9796	0.1
G-1-1-40-16	0.018001	90.6945	0.1

MODEL	TIME,s	FORCE, kN	DURATION
G-1-1-45-8	0.066	68.5338	0.1
G-1-1-45-10	0.035	71.9095	0.1
G-1-1-45-12	0.033	60.827	0.1
G-1-1-45-14	0.029	60.5377	0.1
G-1-1-45-16	0.023	60.6811	0.1

Table 54: Peak force for AFRP, CFRP and GFRP models under 320 kN impact load.

MODEL	TIME,s	FORCE, kN	DURATION
A-2-1-25-8	0.034001	81.258	0.1
A-2-1-25-10	0.036001	70.4134	0.1
A-2-1-25-12	0.040001	79.4837	0.1
A-2-1-25-14	0.035	76.6864	0.096
A-2-1-25-16	0.035	64.3295	0.1

MODEL	TIME,s	FORCE, kN	DURATION
A-2-1-35-8	0.037	77.0438	0.1
A-2-1-35-10	0.1	55.6031	0.1
A-2-1-35-12	0.051001	72.3414	0.1
A-2-1-35-14	0.035	63.9816	0.1
A-2-1-35-16	0.036001	68.9518	0.1

MODEL	TIME,s	FORCE, kN	DURATION
A-2-1-40-8	0.024	3.89604	0.024
A-2-1-40-10	0.059	63.7778	0.1
A-2-1-40-12	0.038001	62.6238	0.1
A-2-1-40-14	0.044001	49.6319	0.1
A-2-1-40-16	0.072001	54.4121	0.1

MODEL	TIME,s	FORCE, kN	DURATION
A-2-1-45-8	0.031	3.39617	0.1
A-2-1-45-10	0.037	29.2879	0.1
A-2-1-45-12	0.091	60.5096	0.1
A-2-1-45-14	0.037	51.4314	0.038
A-2-1-45-16	0.032	16.1897	0.033

MODEL	TIME,s	FORCE, kN	DURATION
C-2-1-25-8	0.096	56.4836	0.1
C-2-1-25-10	0.033	73.8769	0.1
C-2-1-25-12	0.034001	72.215	0.1
C-2-1-25-14	0.035	74.2195	0.1
C-2-1-25-16	0.034001	70.5342	0.1

MODEL	TIME,s	FORCE, kN	DURATION
C-2-1-35-8	0.031001	37.6611	0.1
C-2-1-35-10	0.099	73.5873	0.1
C-2-1-35-12	0.047001	89.8409	0.1
C-2-1-35-14	0.035	66.4216	0.1
C-2-1-35-16	0.036001	63.997	0.1

MODEL	TIME,s	FORCE, kN	DURATION
C-2-1-40-8	0.028001	27.9469	0.1
C-2-1-40-10	0.056	61.1544	0.1
C-2-1-40-12	0.046001	40.1357	0.1
C-2-1-40-14	0.040001	67.6648	0.049001
C-2-1-40-16	0.035	45.5729	0.38001

MODEL	TIME,s	FORCE, kN	DURATION
C-2-1-45-8	0.065	36.6442	0.1
C-2-1-45-10	0.038	17.8211	0.1
C-2-1-45-12	0.024	89.213	0.1
C-2-1-45-1	0.026	60.5864	0.1
C-2-1-45-16	0.067	56.1585	0.075

MODEL	TIME,s	FORCE, kN	DURATION
G-2-1-25-8	0.025	18.3895	0.1
G-2-1-25-10	0.024	26.0219	0.1
G-2-1-25-12	0.032	20.3215	0.1
G-2-1-25-14	0.025	17.7914	0.025
G-2-1-25-16	0.036001	86.1004	0.1

MODEL	TIME,s	FORCE, kN	DURATION
G-2-1-35-8	0.068001	43.2078	0.1
G-2-1-35-10	0.044	32.6388	0.1
G-2-1-35-12	0.037	50.5382	0.1
G-2-1-35-14	0.033	90.6945	0.1
G-2-1-35-16	0.037	64.3102	0.07

MODEL	TIME,s	FORCE, kN	DURATION
G-2-1-40-8	0.049001	13.712	0.1
G-2-1-40-10	0.069	63.7851	0.1
G-2-1-40-12	0.035	43.7802	0.1
G-2-1-40-14	0.044001	48.6049	0.1
G-2-1-40-16	0.034001	19.637	0.0340005

MODEL	TIME,s	FORCE, kN	DURATION
G-2-1-45-8	0.033	11.5786	0.1
G-2-1-45-10	0.037	21.2567	0.1
G-2-1-45-12	0.027	34.0018	0.1
G-2-1-45-14	0.048	60.4896	0.1
G-2-1-45-16	0.037	90.6945	0.07

Table 55: Peak force for AFRP, CFRP and GFRP models under 80 kN impact load.

MODEL	TIME,s	FORCE, kN	DURATION
A-3-1-25-8	0.041	14.5155	0.1
A-3-1-25-10	0.031001	4.11525	0.1
A-3-1-25-12	0.032	4.98233	0.1
A-3-1-25-14	0.032	6.03673	0.1
A-3-1-25-16	0.032	6.59869	0.1

MODEL	TIME,s	FORCE, kN	DURATION
A-3-1-30-8	0.032	2.46148	0.1
A-3-1-30-10	0.032	3.68092	0.1
A-3-1-30-12	0.031001	4.6548	0.1
A-3-1-30-14	0.032	5.66573	0.1
A-3-1-30-16	0.056001	4.9074	0.1

MODEL	TIME,s	FORCE, kN	DURATION
A-3-1-40-8	0.031001	1.91221	0.1
A-3-1-40-10	0.031001	2.30066	0.1
A-3-1-40-12	0.031001	3.05678	0.1
A-3-1-40-14	0.031001	3.73235	0.1
A-3-1-40-16	0.031001	4.33301	0.1

MODEL	TIME,s	FORCE, kN	DURATION
A-3-1-45-8	0.031	1.28589	0.1
A-3-1-45-10	0.031	1.95554	0.1
A-3-1-45-12	0.031	2.61181	0.1
A-3-1-45-14	0.031	3.20008	0.1
A-3-1-45-16	0.031	3.73287	0.1

MODEL	TIME,s	FORCE, kN	DURATION
C-3-1-25-8	0.031001	4.83027	0.1
C-3-1-25-10	0.031001	6.15035	0.1
C-3-1-25-12	0.099001	17.1247	0.1
C-3-1-25-14	0.031001	48.1554	0.035
C-3-1-25-16	0.031001	8.55701	0.1

MODEL	TIME,s	FORCE, kN	DURATION
C-3-1-30-8	0.032	4.39401	0.1
C-3-1-30-10	0.032	5.87051	0.1
C-3-1-30-12	0.032	6.89157	0.1
C-3-1-30-14	0.032	7.87305	0.1
C-3-1-30-16	0.032	8.57843	0.1

MODEL	TIME,s	FORCE, kN	DURATION
C-3-1-40-8	0.031001	3.45553	0.1
C-3-1-40-10	0.031001	3.73959	0.1
C-3-1-40-12	0.031001	4.5703	0.1
C-3-1-40-14	0.031001	5.2424	0.1
C-3-1-40-16	0.031001	5.79294	0.1

MODEL	TIME,s	FORCE, kN	DURATION
C-3-1-45-8	0.031	2.36406	0.1
C-3-1-45-10	0.031	3.22211	0.1
C-3-1-45-12	0.031	3.96089	0.1
C-3-1-45-1	0.031	4.54708	0.1
C-3-1-45-16	0.031	5.01854	0.1

MODEL	TIME,s	FORCE, kN	DURATION
G-3-1-25-8	0.039	15.3911	0.1
G-3-1-25-10	0.031001	2.55077	0.1
G-3-1-25-12	0.097	5.80486	0.1
G-3-1-25-14	0.032	4.59835	0.1
G-3-1-25-16	0.091001	7.39353	0.1

MODEL	TIME,s	FORCE, kN	DURATION
G-3-1-30-8	0.032	1.56564	0.1
G-3-1-30-10	0.032	2.50952	0.1
G-3-1-30-12	0.060001	3.35772	0.1
G-3-1-30-14	0.031001	4.27942	0.1
G-3-1-30-16	0.032	5.15781	0.1

MODEL	TIME,s	FORCE, kN	DURATION
G-3-1-40-8	0.031001	1.2084	0.1
G-3-1-40-10	0.031001	1.54776	0.1
G-3-1-40-12	0.031001	2.17341	0.1
G-3-1-40-14	0.031001	2.78537	0.1
G-3-1-40-16	0.031001	3.35783	0.1

MODEL	TIME,s	FORCE, kN	DURATION
G-3-1-45-8	0.031001	0.805807	0.1
G-3-1-45-10	0.031001	1.3084	0.1
G-3-1-45-12	0.031001	1.84339	0.1
G-3-1-45-14	0.031001	2.38494	0.1
G-3-1-45-16	0.031001	2.89754	0.1

Table 56: Peak force for AFRP, CFRP and GFRP models under 40 kN impact load.

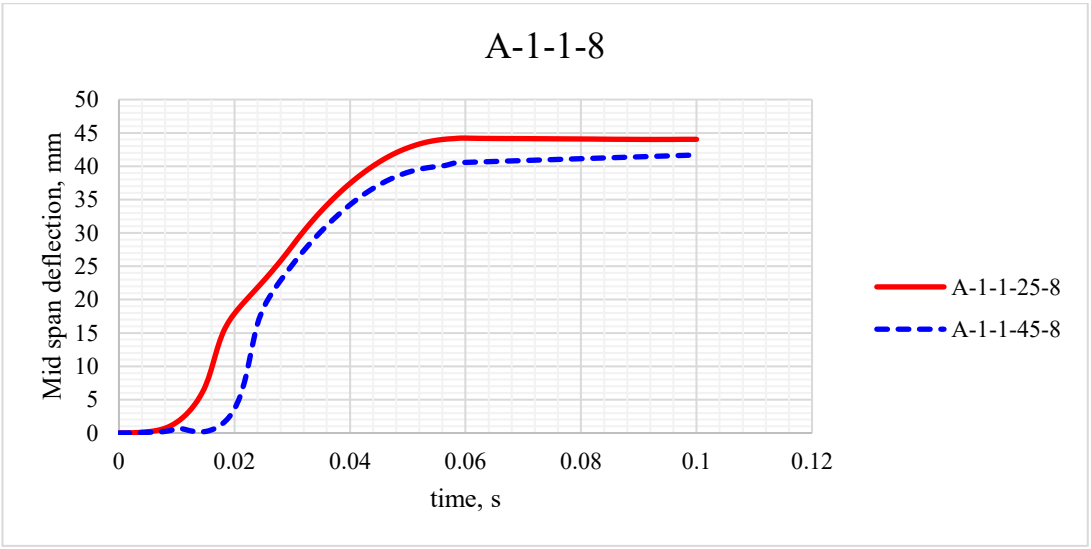

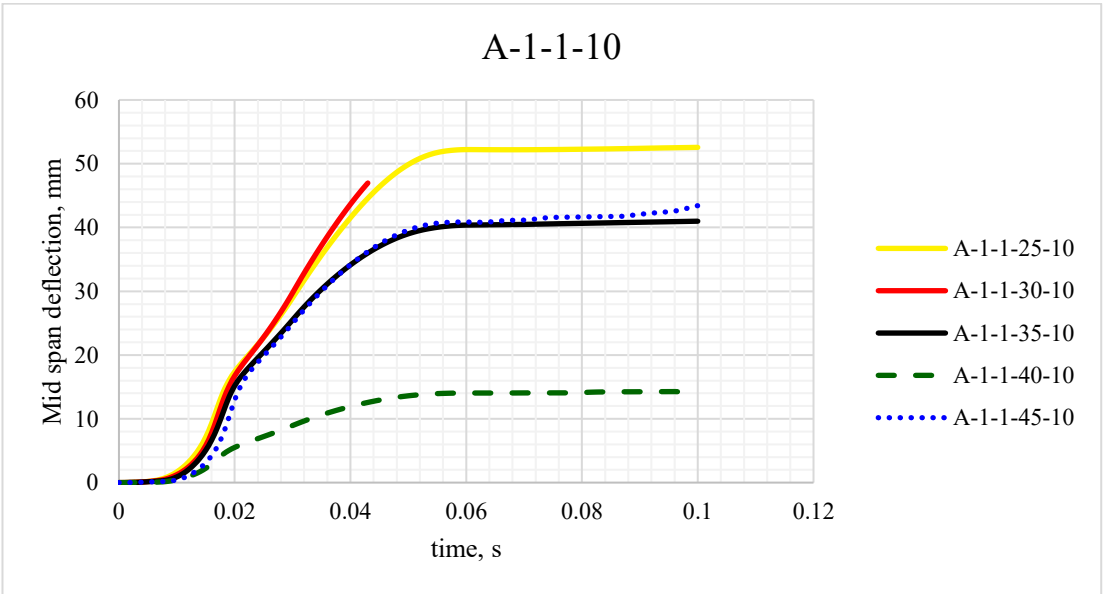

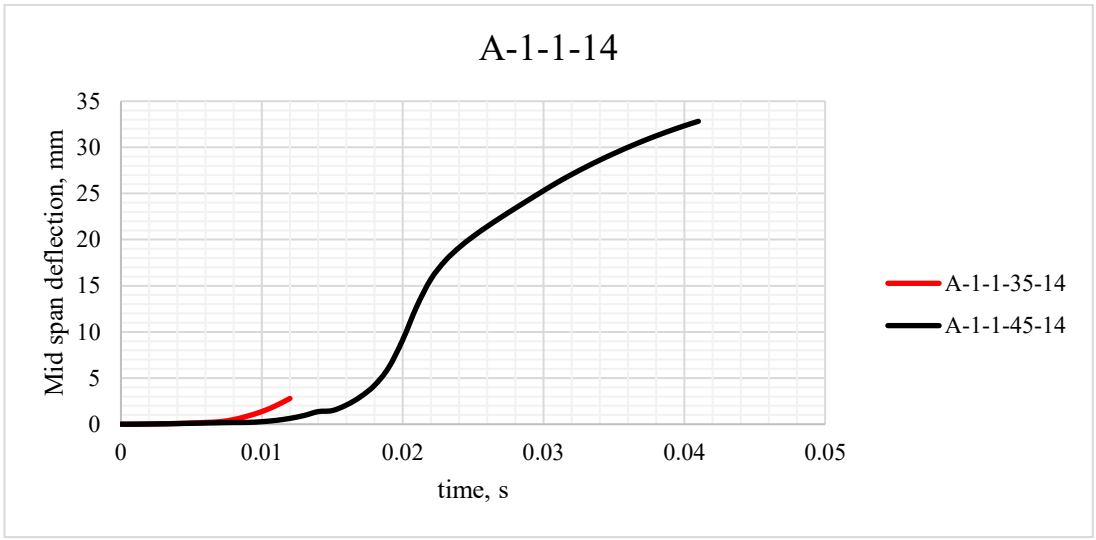
A-1-1-14
Mid span deflection, mm
35
30
25
20
15
10
5
0
0
0.01
0.02
0.03
0.04
0.05
time, s
A-1-1-35-14
A-1-1-45-14

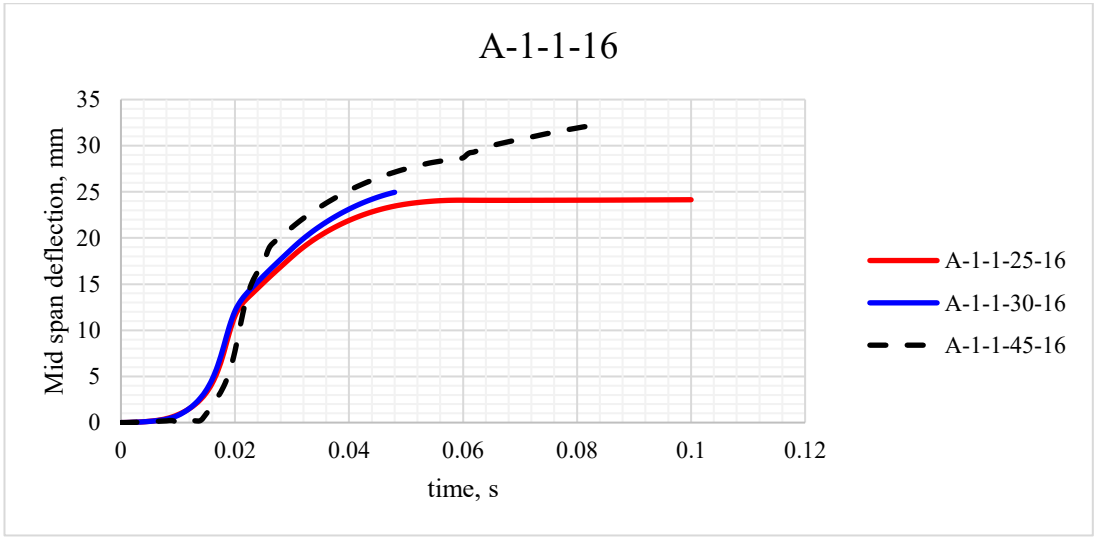
A-1-1-16
Mid span deflection, mm
35
30
25
20
15
10
5
0
0
0.02
0.04
0.06
0.08
0.1
0.12
time, s
A-1-1-25-16
A-1-1-30-16
A-1-1-45-16

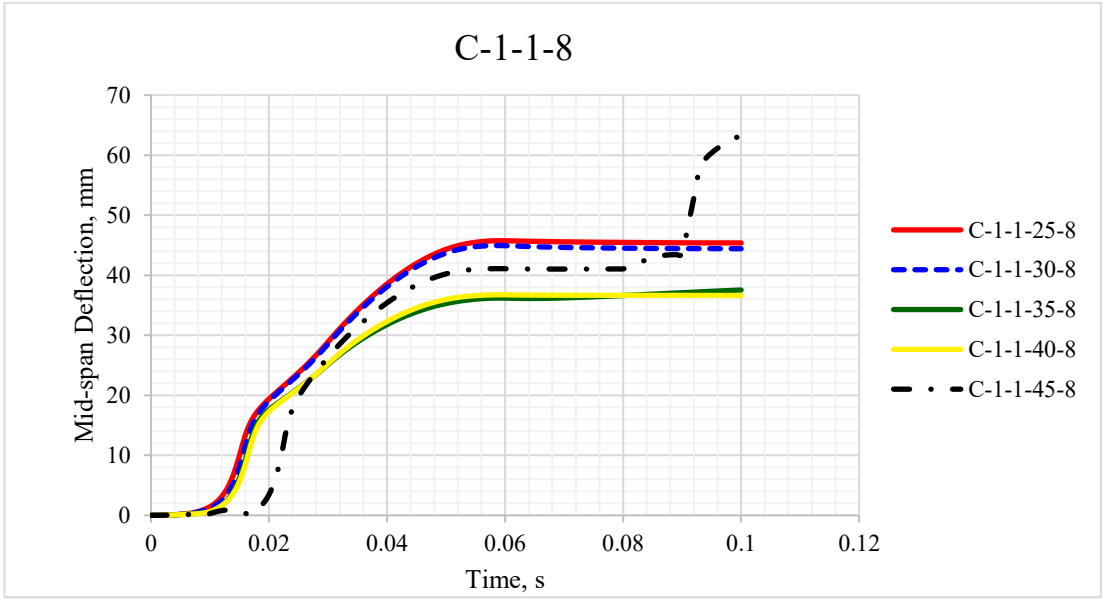
C-1-1-8
Mid-span Deflection, mm
70
60
50
40
30
20
10
0
0
0.02
0.04
0.06
0.08
0.1
0.12
Time, s
C-1-1-25-8
C-1-1-30-8
C-1-1-35-8
C-1-1-40-8
C-1-1-45-8

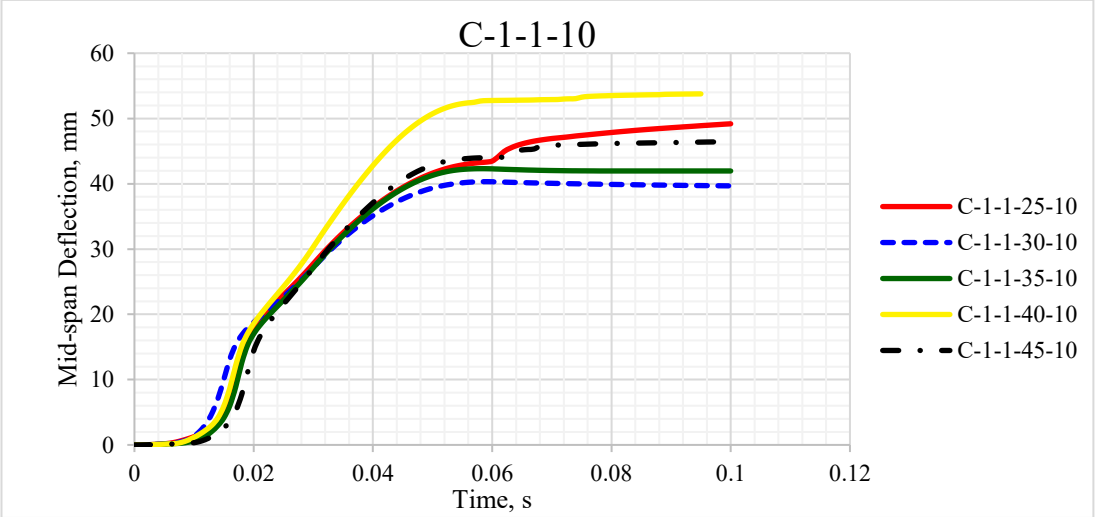
C-1-1-10
Mid-span Deflection, mm
Time, s
0
10
20
30
40
50
60
0
0.02
0.04
0.06
0.08
0.1
0.12
C-1-1-25-10
C-1-1-30-10
C-1-1-35-10
C-1-1-40-10
C-1-1-45-10

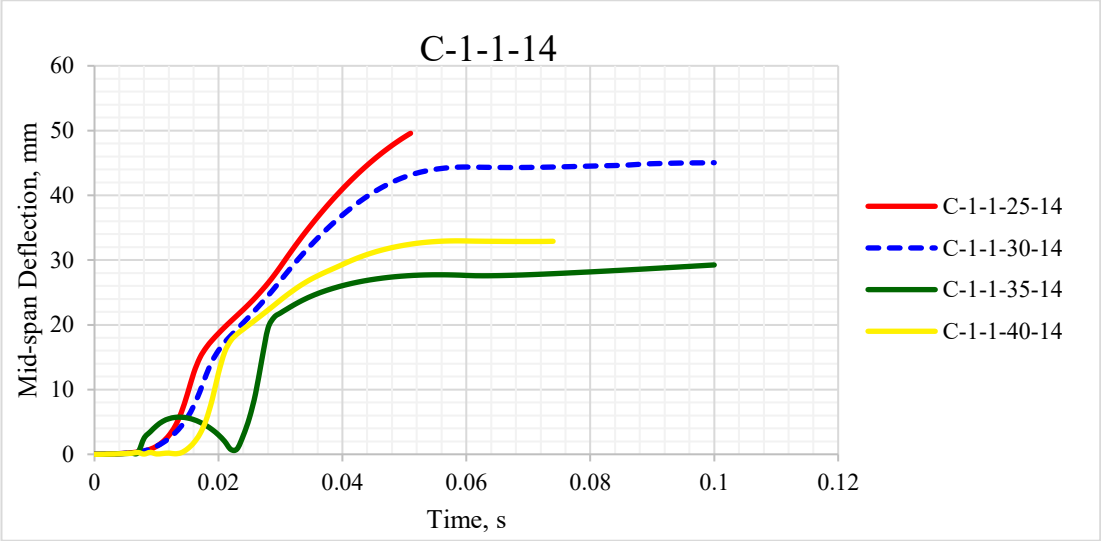
C-1-1-14
Mid-span Deflection, mm
Time, s
0
10
20
30
40
50
60
0
0.02
0.04
0.06
0.08
0.1
0.12
C-1-1-25-14
C-1-1-30-14
C-1-1-35-14
C-1-1-40-14

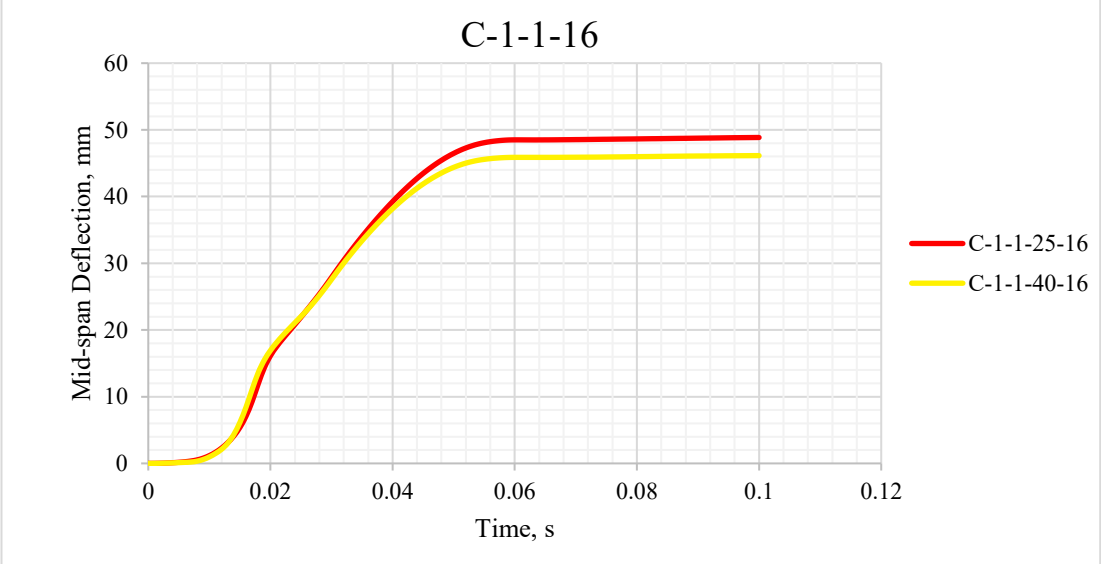
C-1-1-16
Mid-span Deflection, mm
Time, s
0
10
20
30
40
50
60
0
0.02
0.04
0.06
0.08
0.1
0.12
C-1-1-25-16
C-1-1-40-16

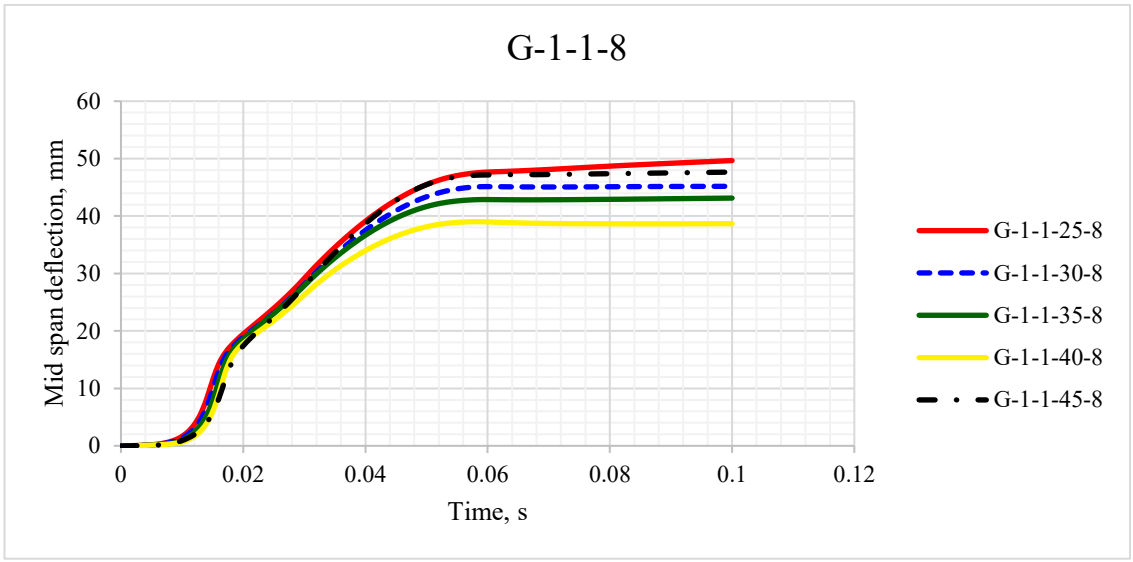
G-1-1-8
Mid span deflection, mm
Time, s
0
10
20
30
40
50
60
0
0.02
0.04
0.06
0.08
0.1
0.12
G-1-1-25-8
G-1-1-30-8
G-1-1-35-8
G-1-1-40-8
G-1-1-45-8

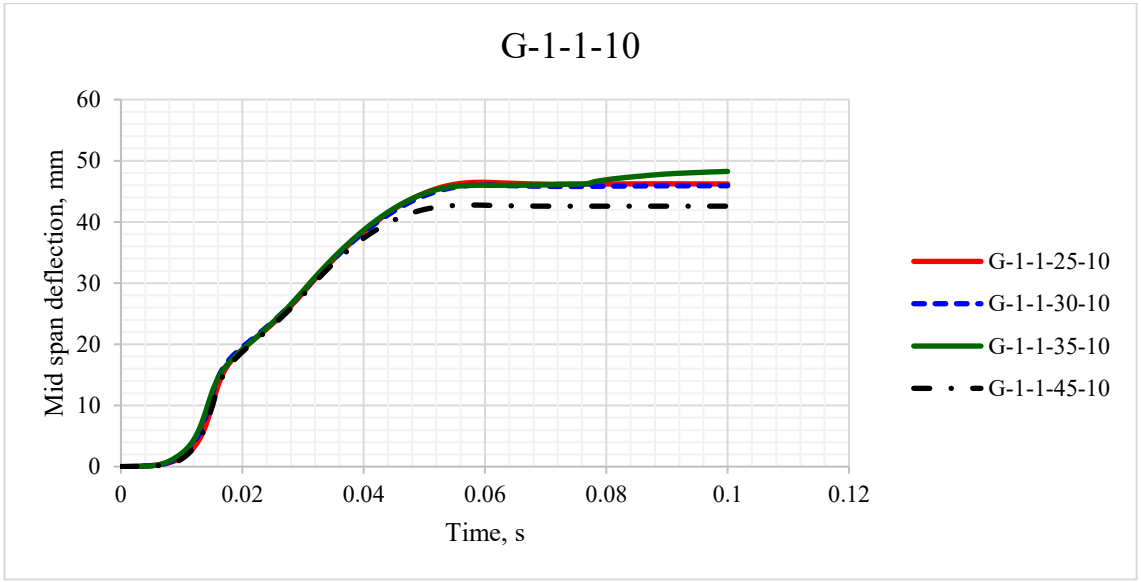
G-1-1-10
Mid span deflection, mm
Time, s
0
10
20
30
40
50
60
0
0.02
0.04
0.06
0.08
0.1
0.12
G-1-1-25-10
G-1-1-30-10
G-1-1-35-10
G-1-1-45-10

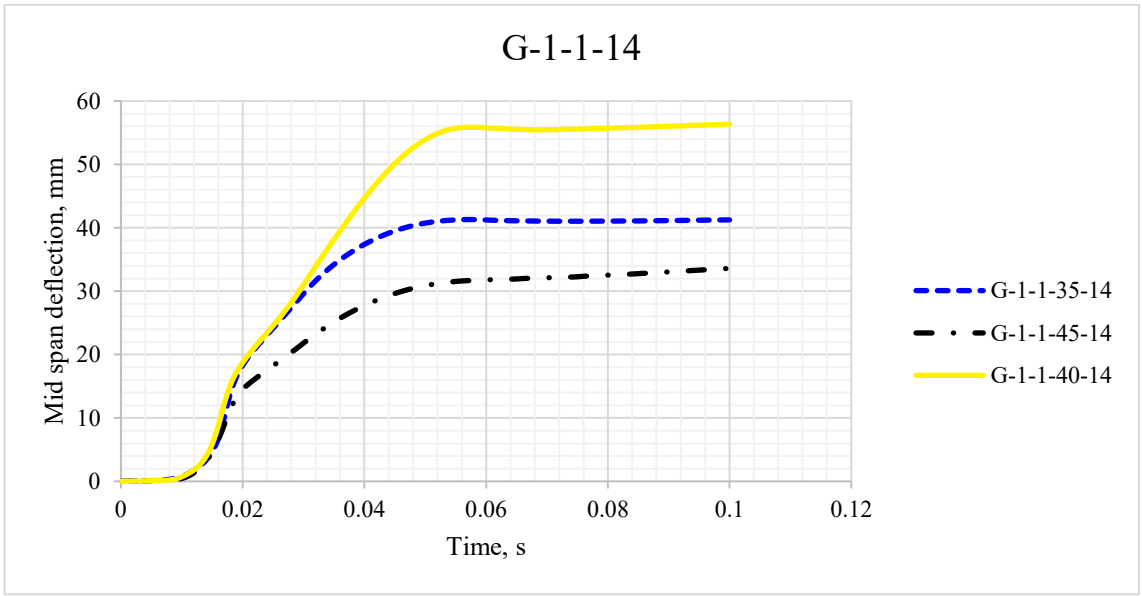
G-1-1-14
Mid span deflection, mm
Time, s
0
10
20
30
40
50
60
0
0.02
0.04
0.06
0.08
0.1
0.12
G-1-1-35-14
G-1-1-45-14
G-1-1-40-14

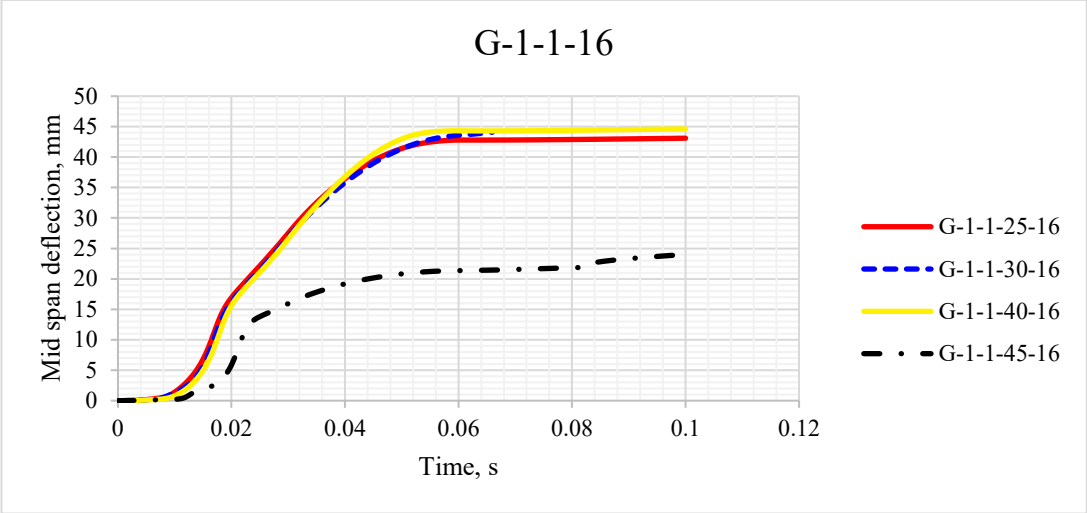

Figure 139:Mid-span Deflection-Time histories for AFRP, CFRP and GFRP RC beams under 320kN impact load.

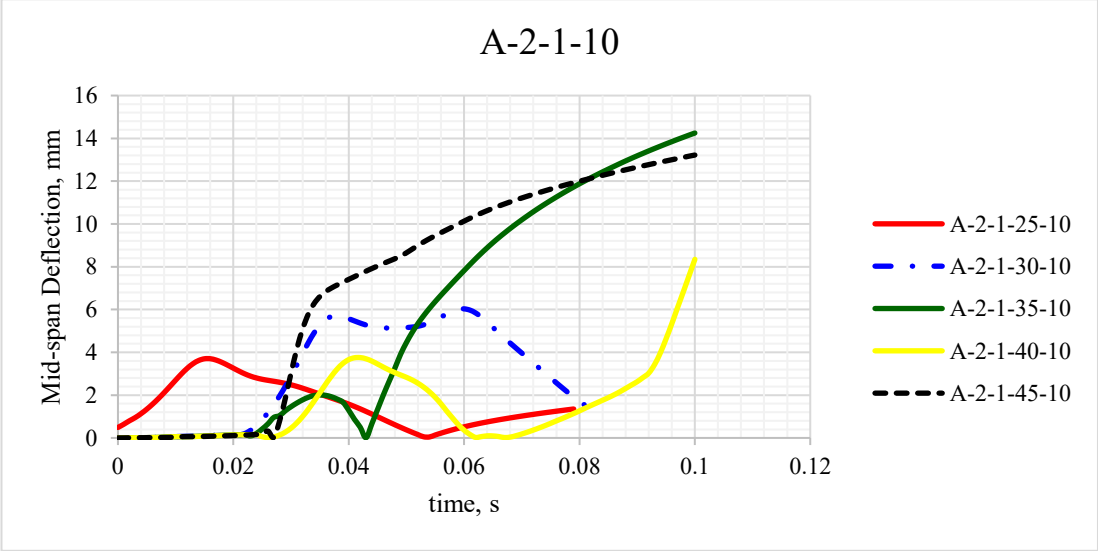

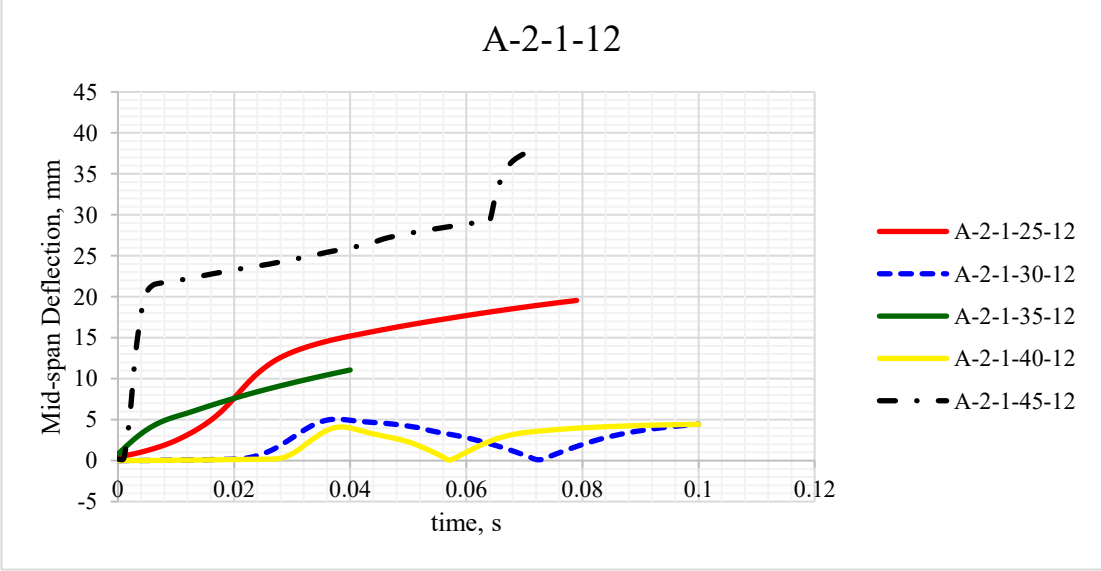

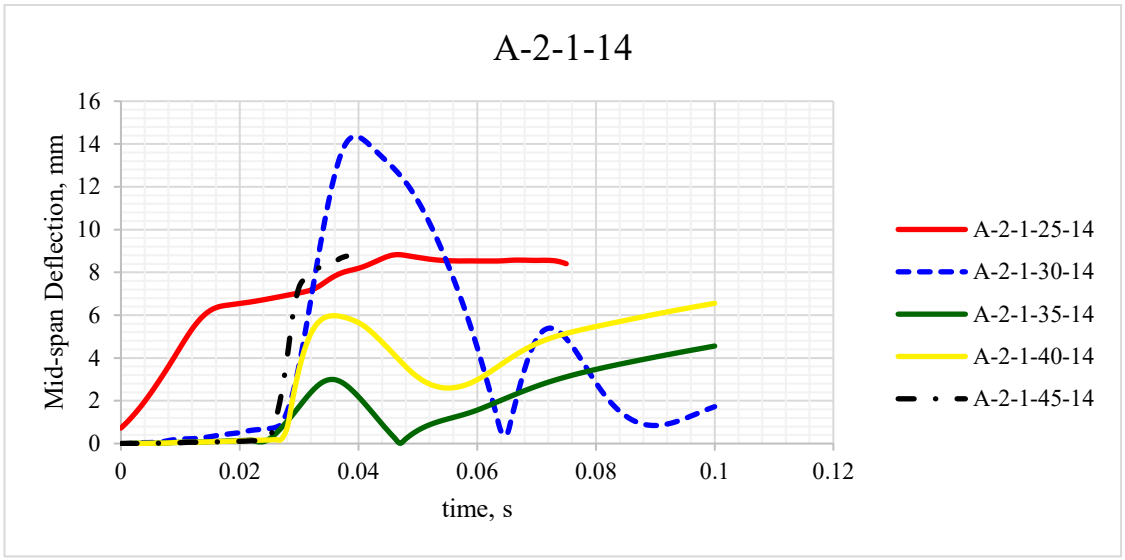
A-2-1-14
Mid-span Deflection, mm
time, s
A-2-1-25-14
A-2-1-30-14
A-2-1-35-14
A-2-1-40-14
A-2-1-45-14

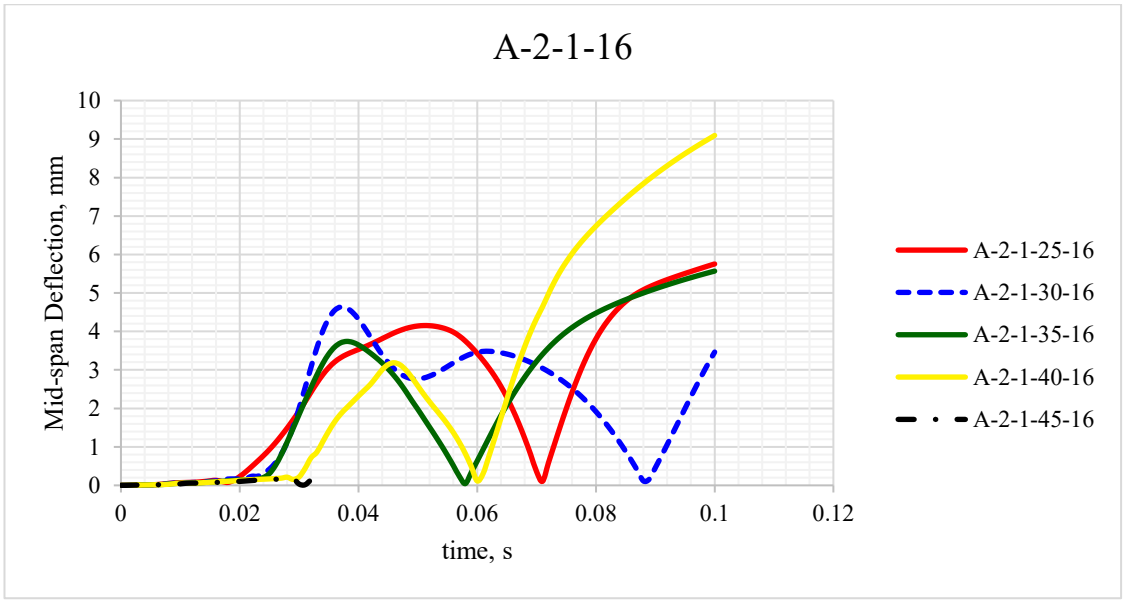
A-2-1-16
Mid-span Deflection, mm
time, s
A-2-1-25-16
A-2-1-30-16
A-2-1-35-16
A-2-1-40-16
A-2-1-45-16

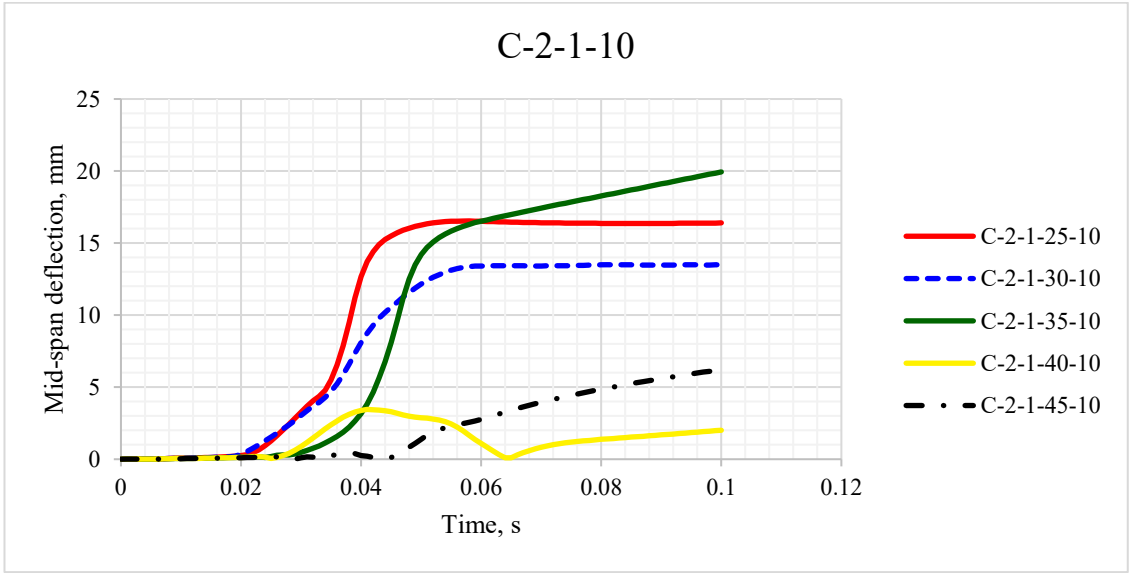
C-2-1-10
Mid-span deflection, mm
Time, s
C-2-1-25-10
C-2-1-30-10
C-2-1-35-10
C-2-1-40-10
C-2-1-45-10

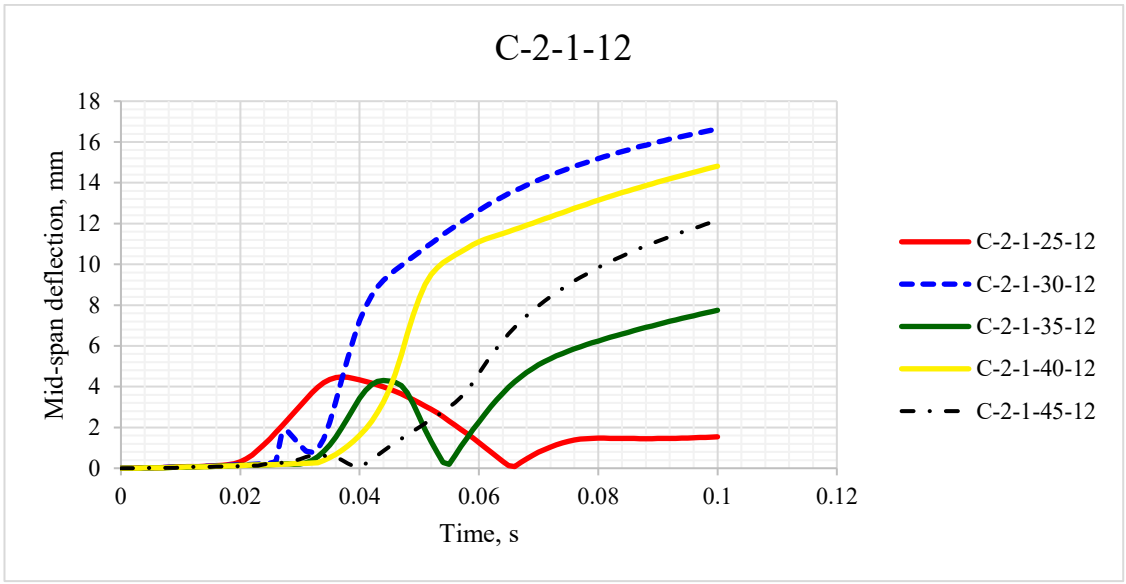
C-2-1-12
Mid-span deflection, mm
Time, s
C-2-1-25-12
C-2-1-30-12
C-2-1-35-12
C-2-1-40-12
C-2-1-45-12

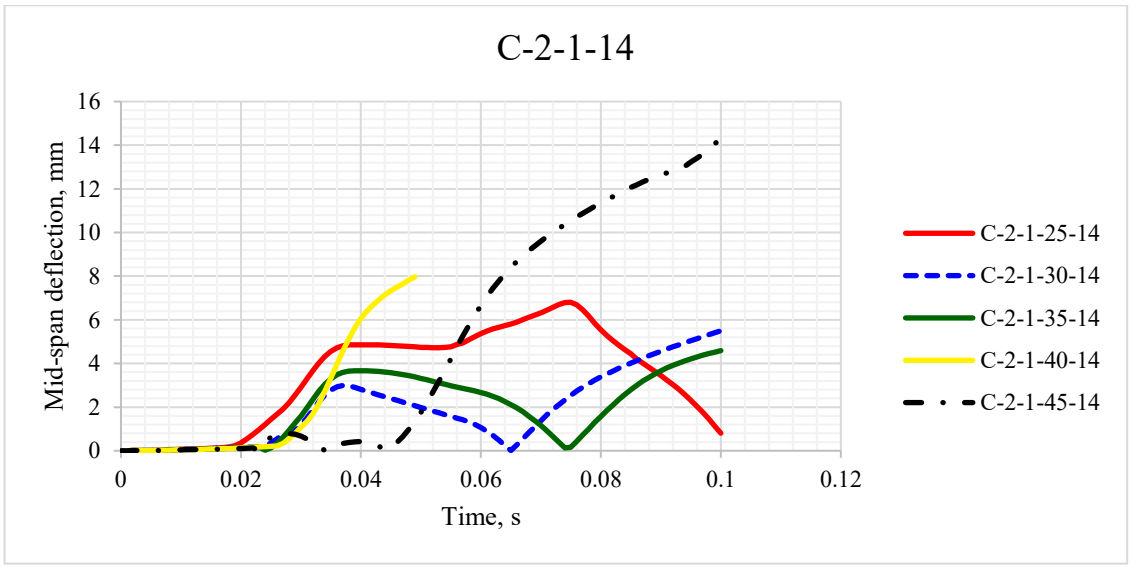
C-2-1-14
Mid-span deflection, mm
Time, s
C-2-1-25-14
C-2-1-30-14
C-2-1-35-14
C-2-1-40-14
C-2-1-45-14

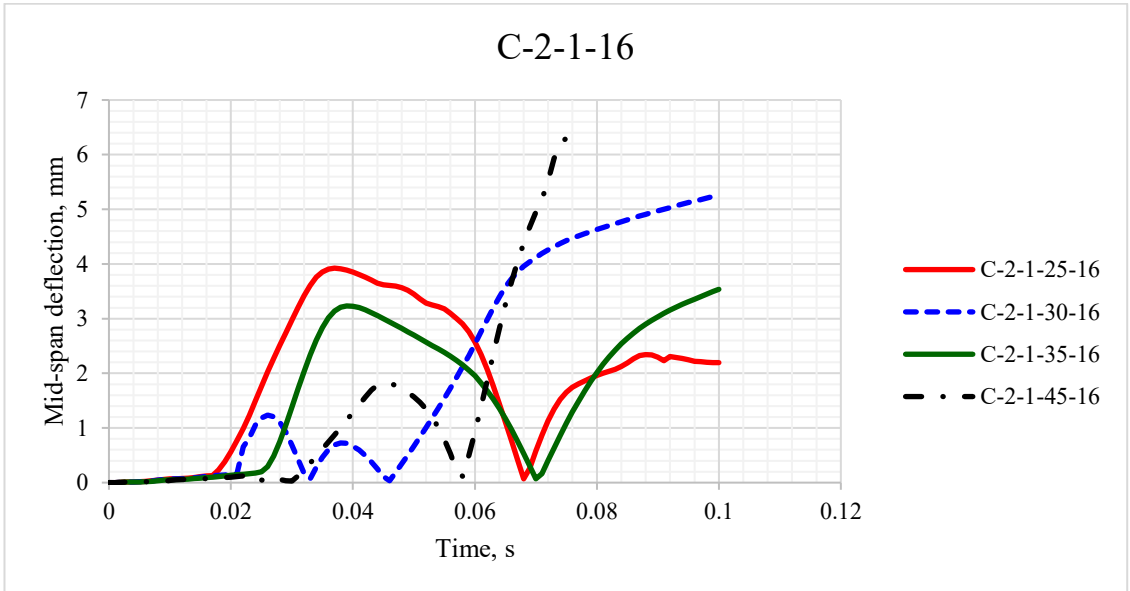
C-2-1-16
Mid-span deflection, mm
Time, s
C-2-1-25-16
C-2-1-30-16
C-2-1-35-16
C-2-1-45-16

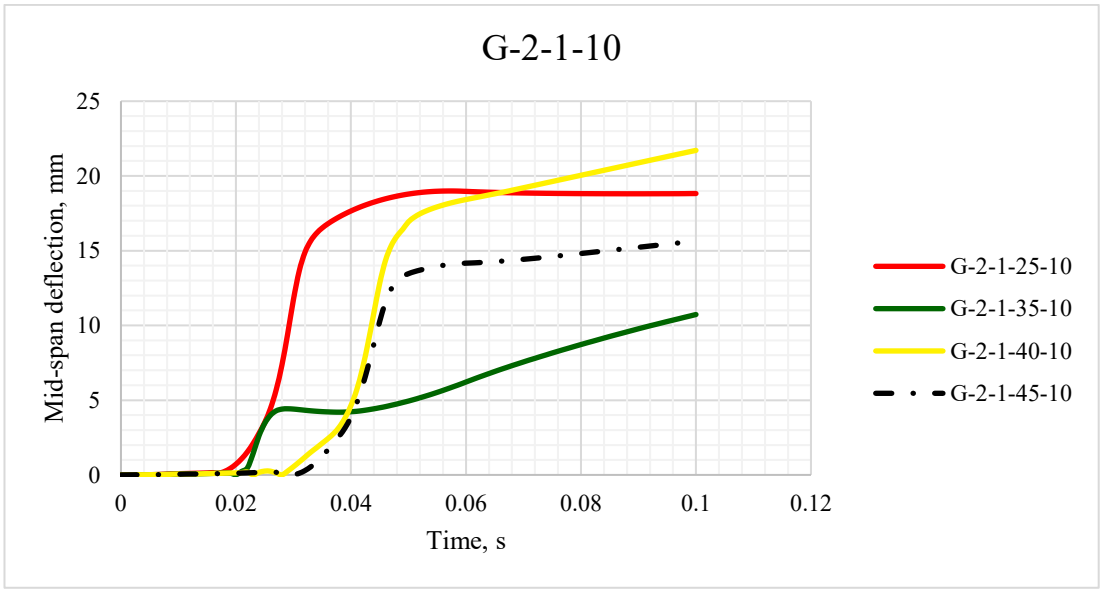
G-2-1-10
Mid-span deflection, mm
25
20
15
10
5
0
0
0.02
0.04
0.06
0.08
0.1
0.12
Time, s
G-2-1-25-10
G-2-1-35-10
G-2-1-40-10
G-2-1-45-10

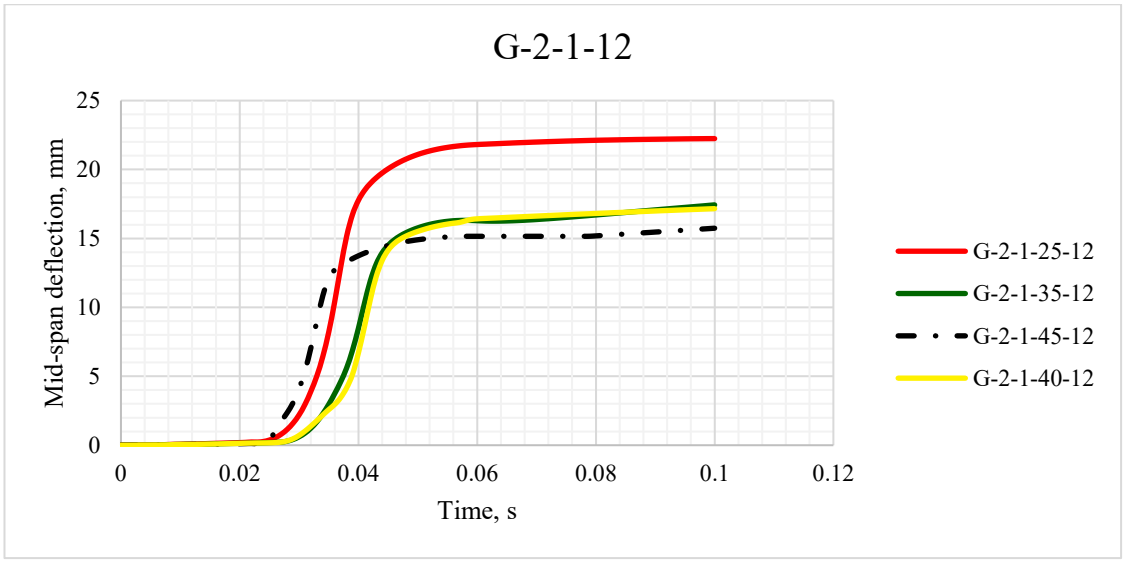
G-2-1-12
Mid-span deflection, mm
25
20
15
10
5
0
0
0.02
0.04
0.06
0.08
0.1
0.12
Time, s
G-2-1-25-12
G-2-1-35-12
G-2-1-45-12
G-2-1-40-12

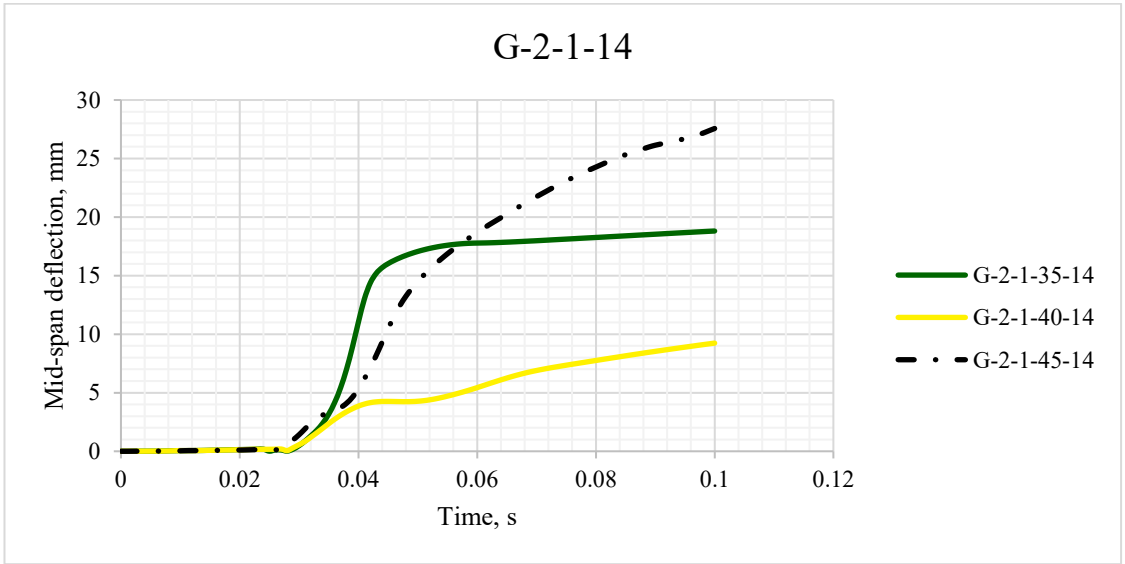
G-2-1-14
Mid-span deflection, mm
30
25
20
15
10
5
0
0
0.02
0.04
0.06
0.08
0.1
0.12
Time, s
G-2-1-35-14
G-2-1-40-14
G-2-1-45-14

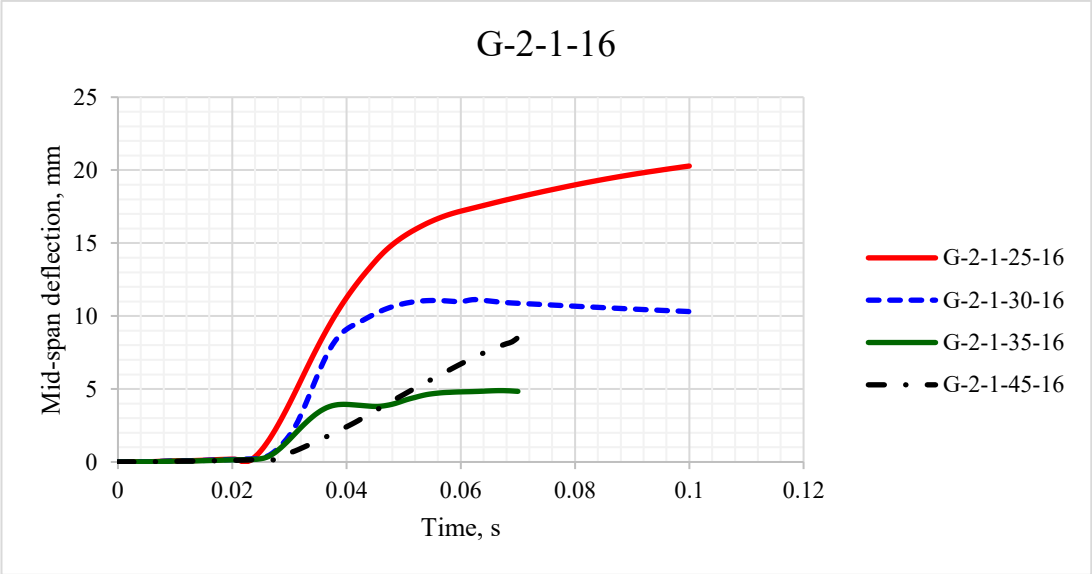

Figure 140: Mid-span Deflection-Time histories for AFRP, CFRP and GFRP RC beams under 80kN impact load.

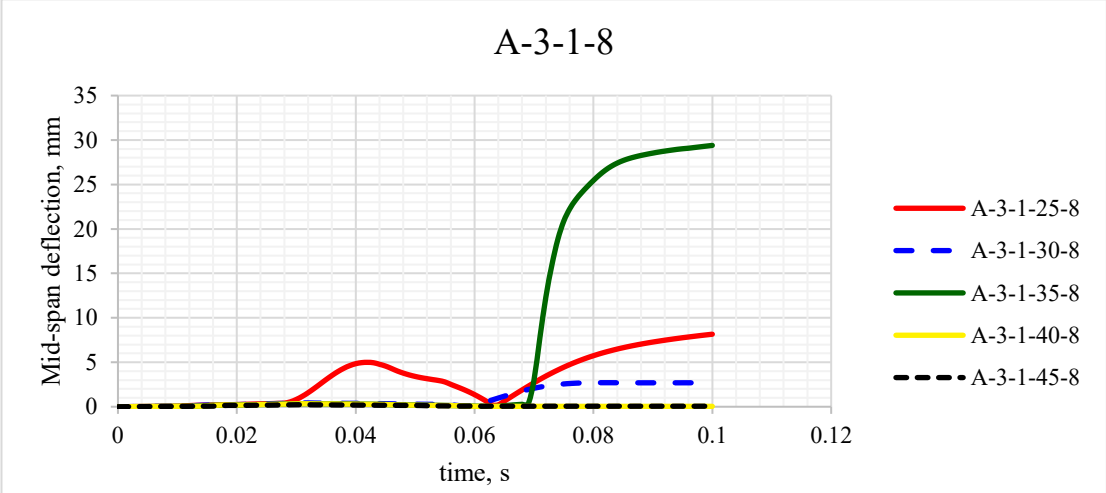

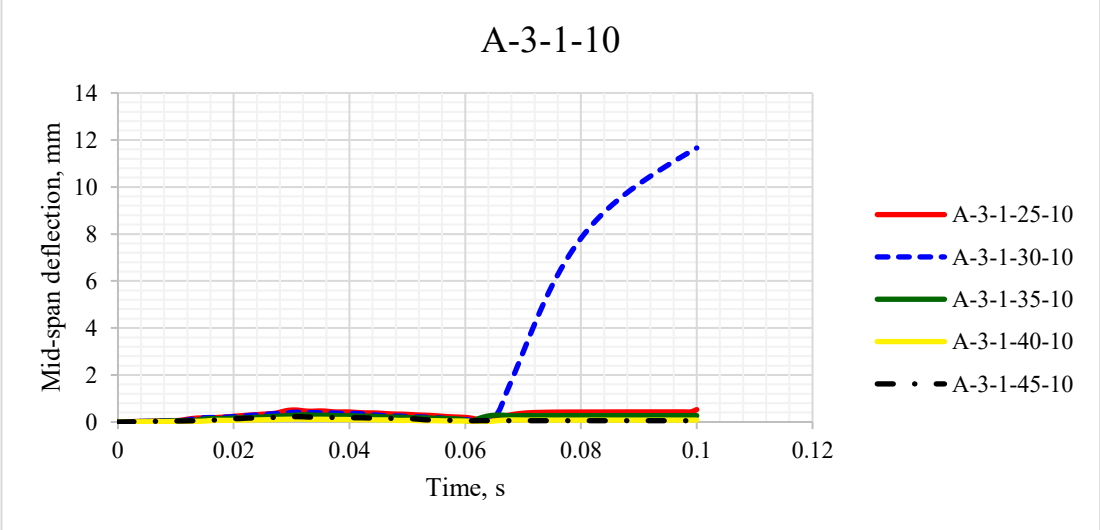

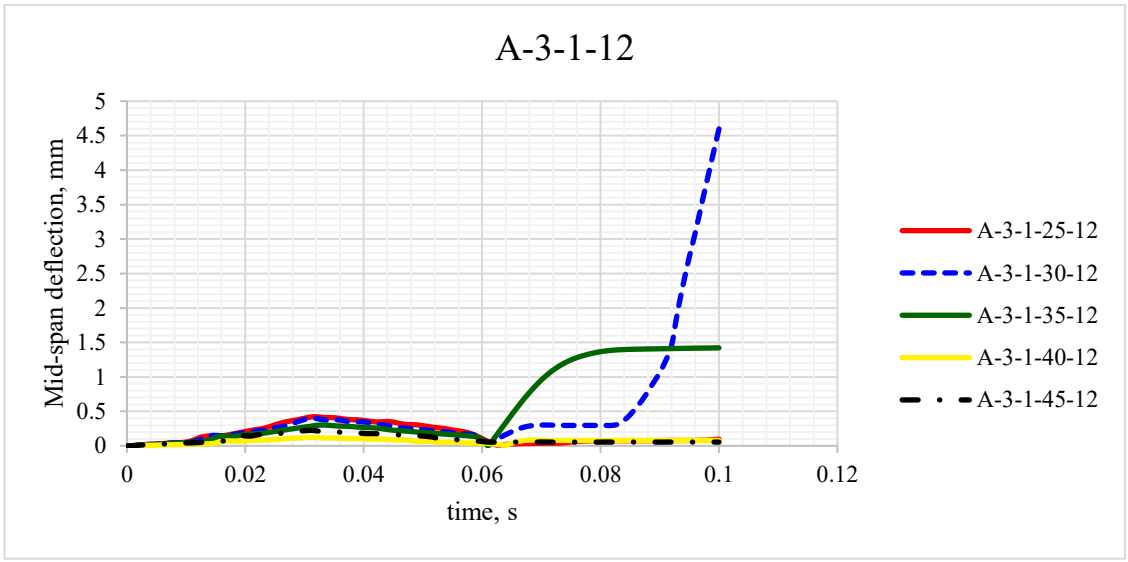
A-3-1-12
Mid-span deflection, mm
time, s
A-3-1-25-12
A-3-1-30-12
A-3-1-35-12
A-3-1-40-12
A-3-1-45-12

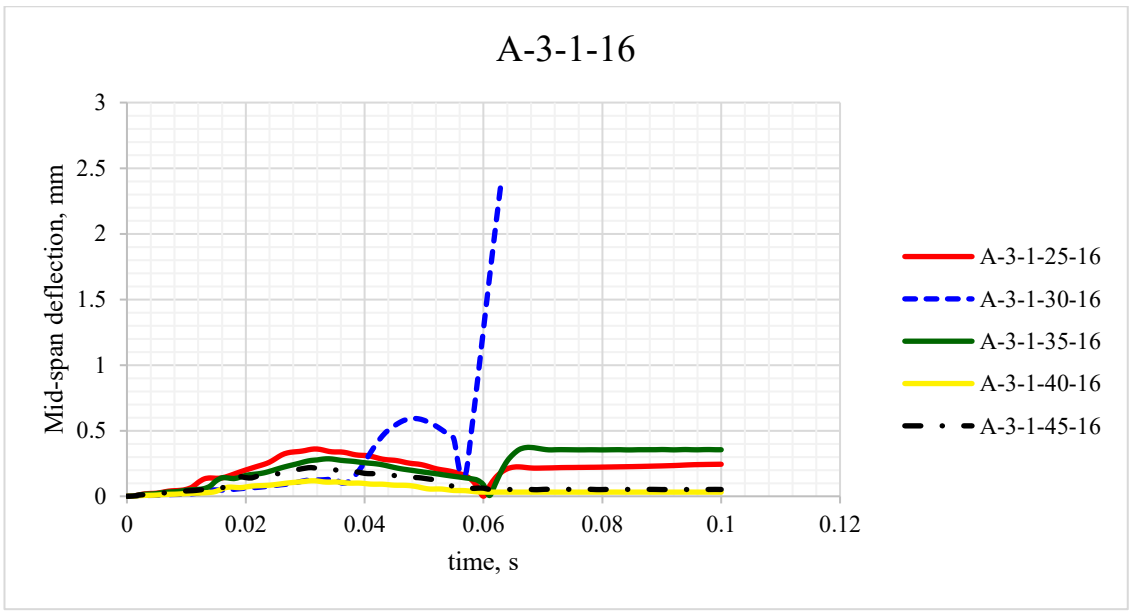
A-3-1-16
Mid-span deflection, mm
time, s
A-3-1-25-16
A-3-1-30-16
A-3-1-35-16
A-3-1-40-16
A-3-1-45-16

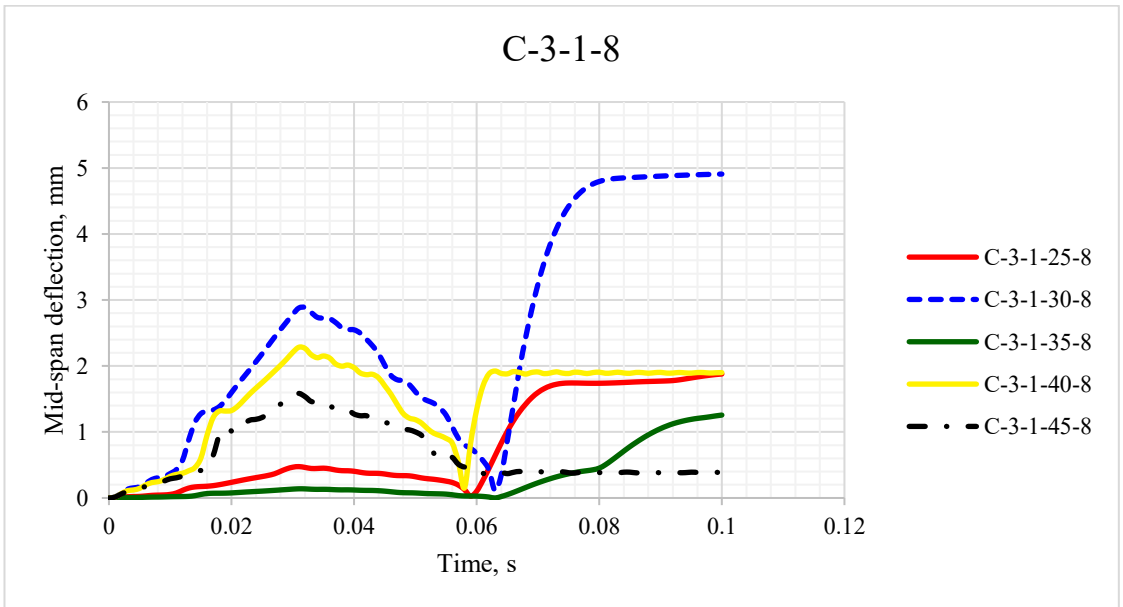
C-3-1-8
Mid-span deflection, mm
Time, s
C-3-1-25-8
C-3-1-30-8
C-3-1-35-8
C-3-1-40-8
C-3-1-45-8

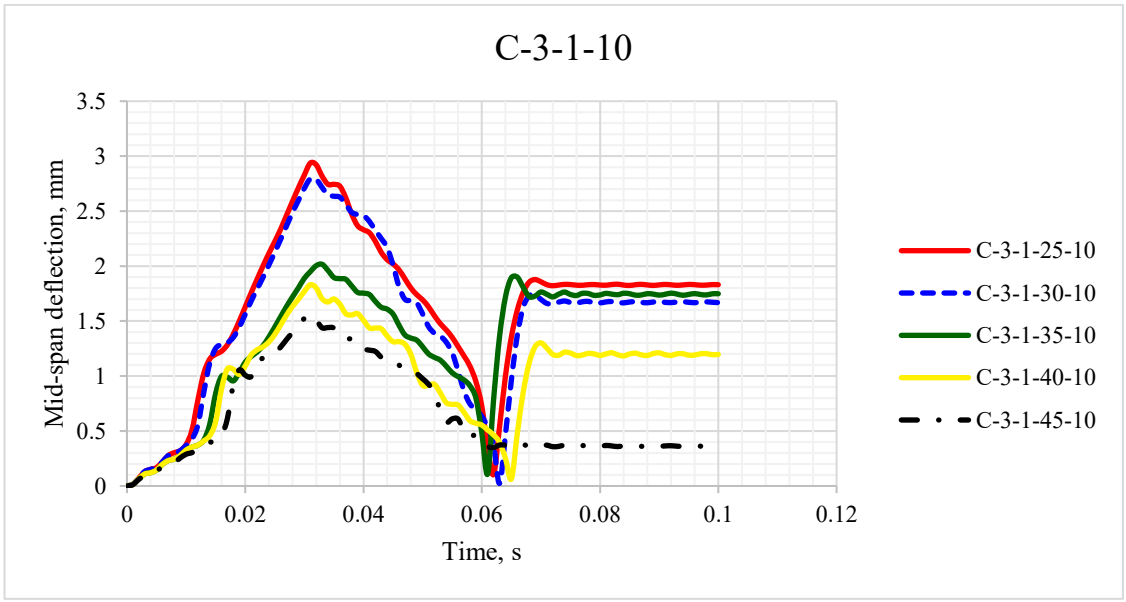
C-3-1-10
Mid-span deflection, mm
Time, s
C-3-1-25-10
C-3-1-30-10
C-3-1-35-10
C-3-1-40-10
C-3-1-45-10

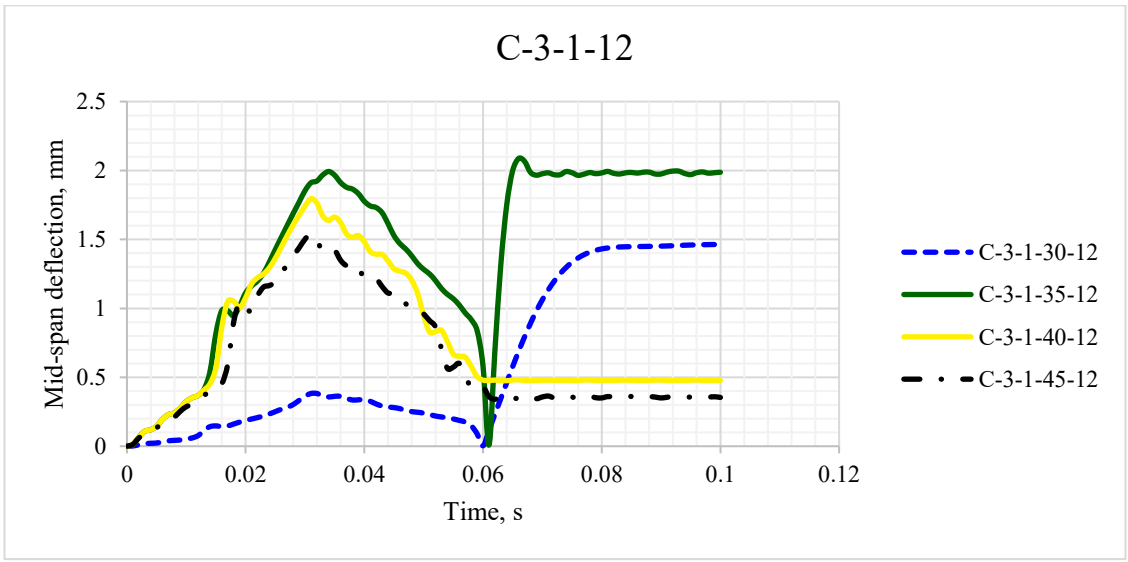
C-3-1-12
Mid-span deflection, mm
Time, s
C-3-1-30-12
C-3-1-35-12
C-3-1-40-12
C-3-1-45-12

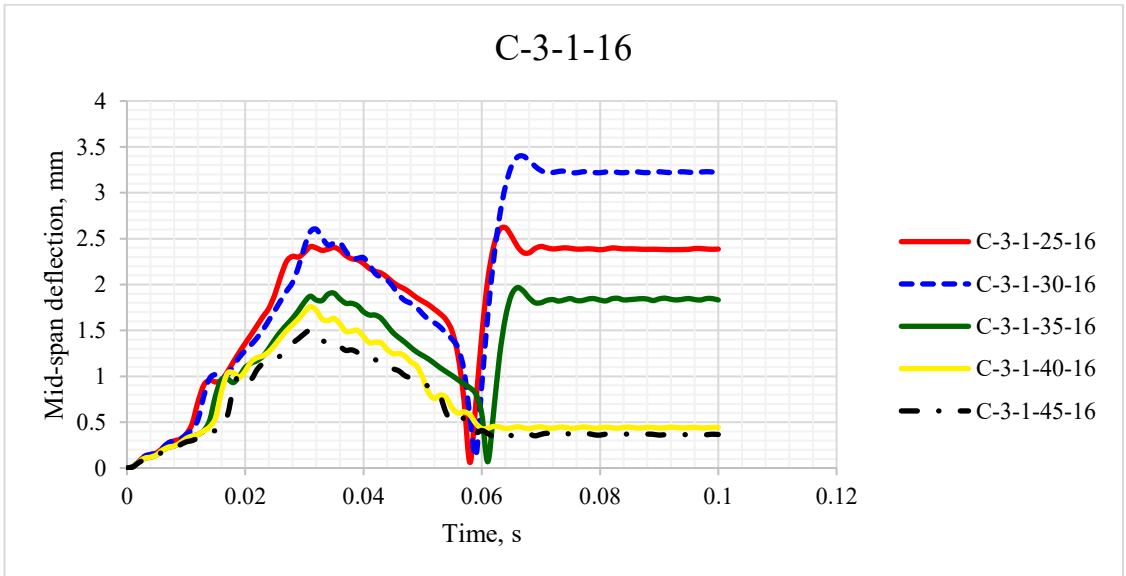
C-3-1-16
Mid-span deflection, mm
Time, s
C-3-1-25-16
C-3-1-30-16
C-3-1-35-16
C-3-1-40-16
C-3-1-45-16

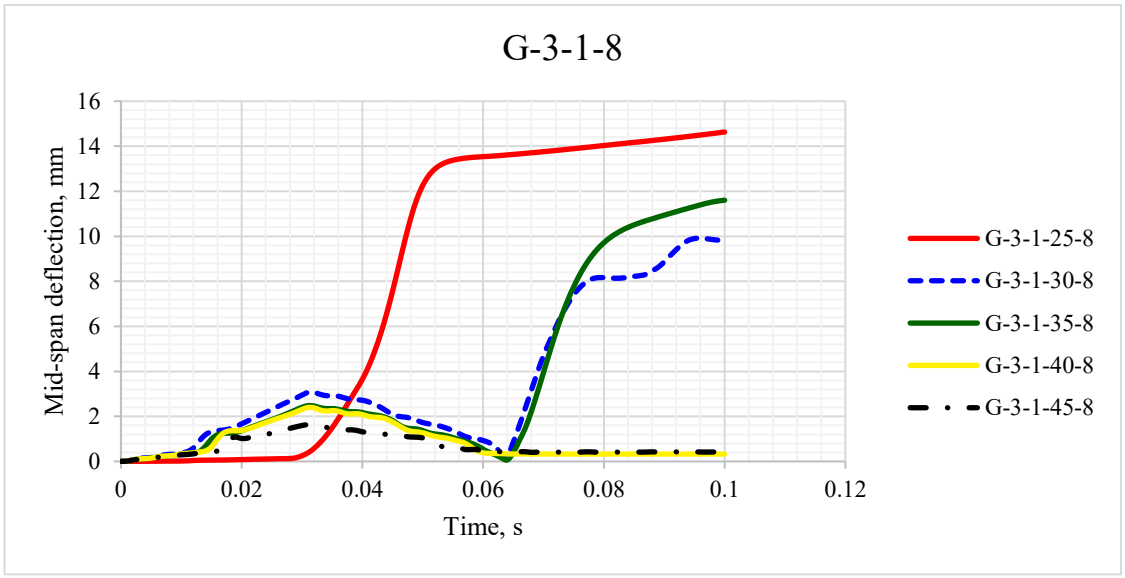
G-3-1-8
Mid-span deflection, mm
Time, s
G-3-1-25-8
G-3-1-30-8
G-3-1-35-8
G-3-1-40-8
G-3-1-45-8

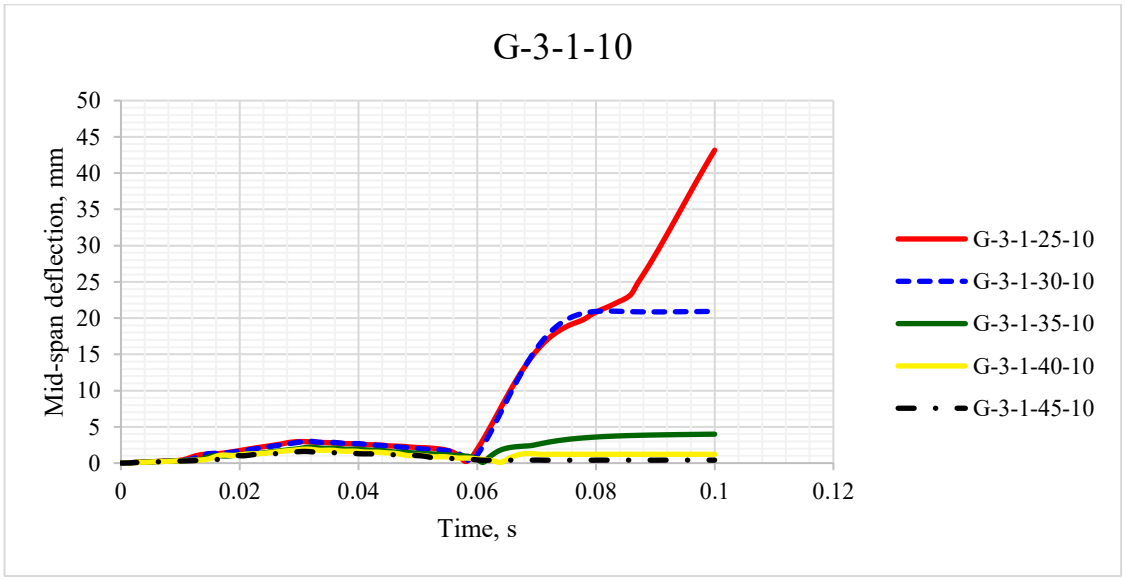
G-3-1-10
Mid-span deflection, mm
Time, s
G-3-1-25-10
G-3-1-30-10
G-3-1-35-10
G-3-1-40-10
G-3-1-45-10

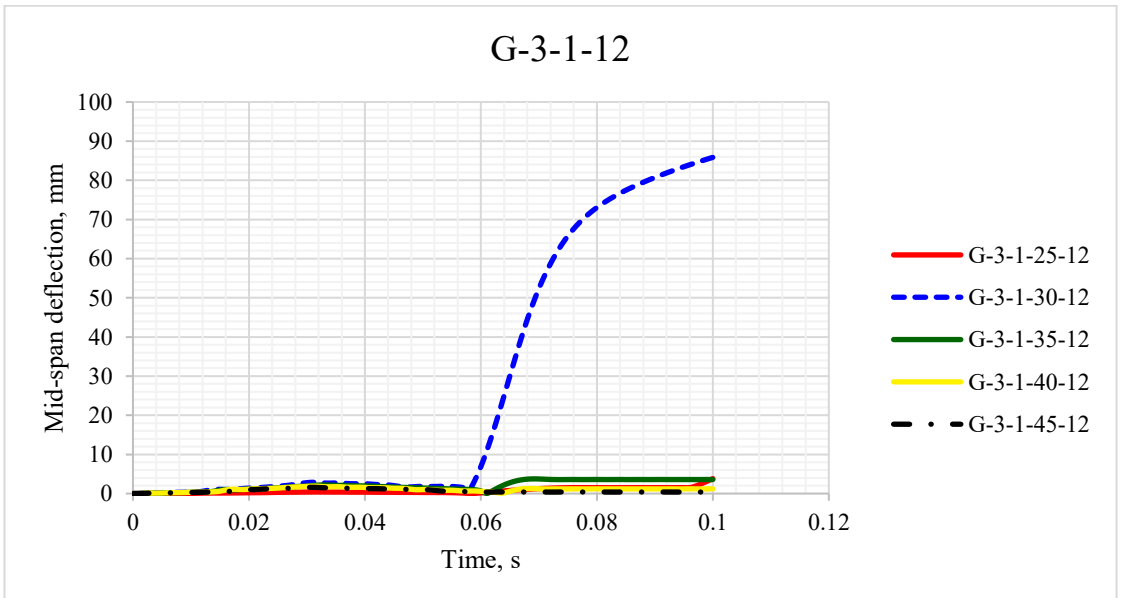
G-3-1-12
Mid-span deflection, mm
Time, s
G-3-1-25-12
G-3-1-30-12
G-3-1-35-12
G-3-1-40-12
G-3-1-45-12

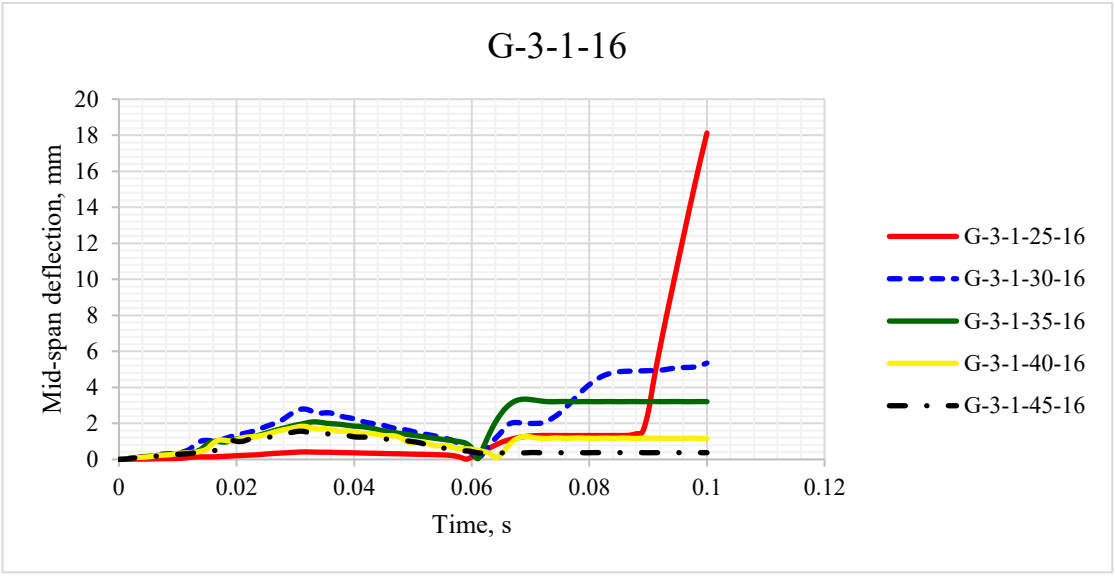

Figure 141: Mid-span Deflection-Time histories for AFRP, CFRP and GFRP RC beams under 40kN impact load.

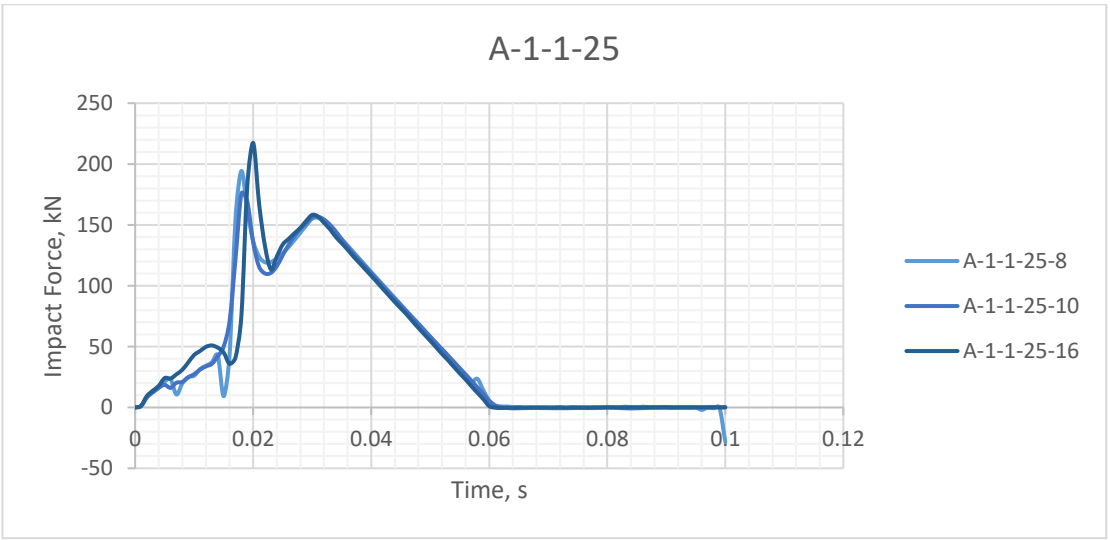

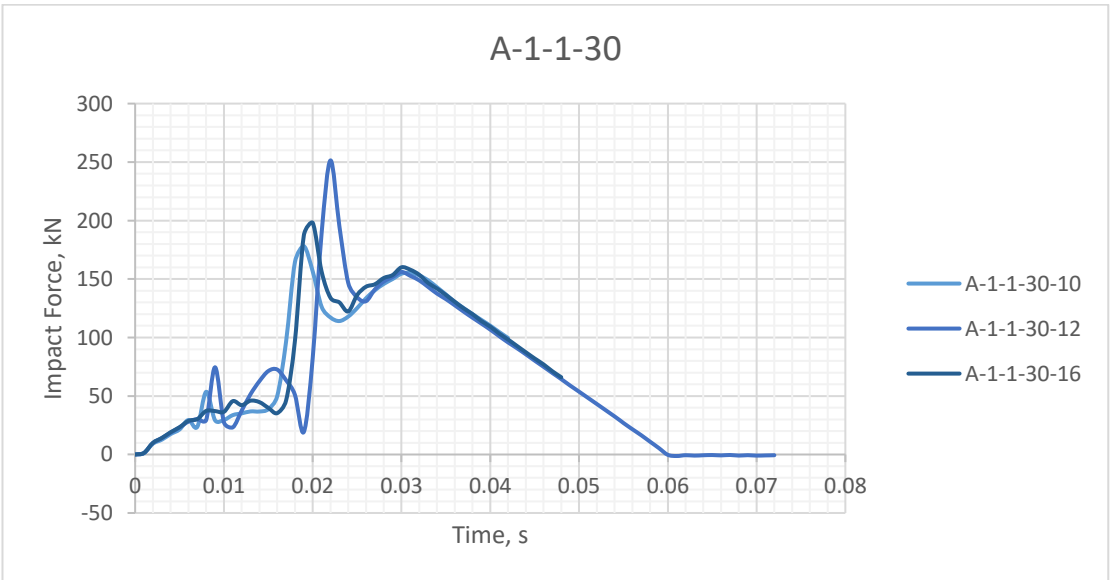

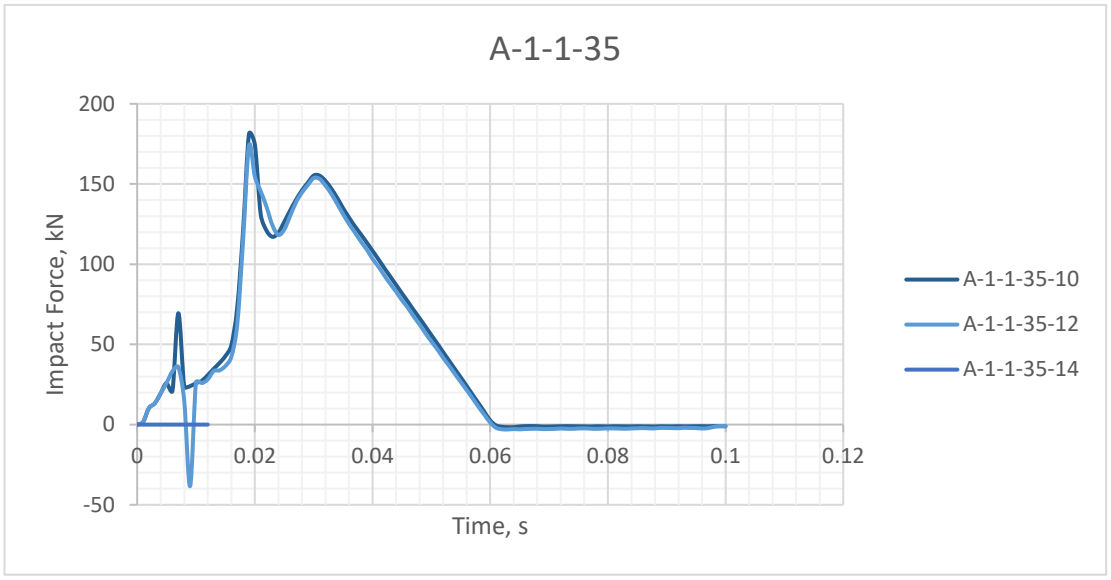
A-1-1-35
Impact Force, kN
200
150
100
50
0
-50
0
0.02
0.04
0.06
0.08
0.1
0.12
Time, s
A-1-1-35-10
A-1-1-35-12
A-1-1-35-14

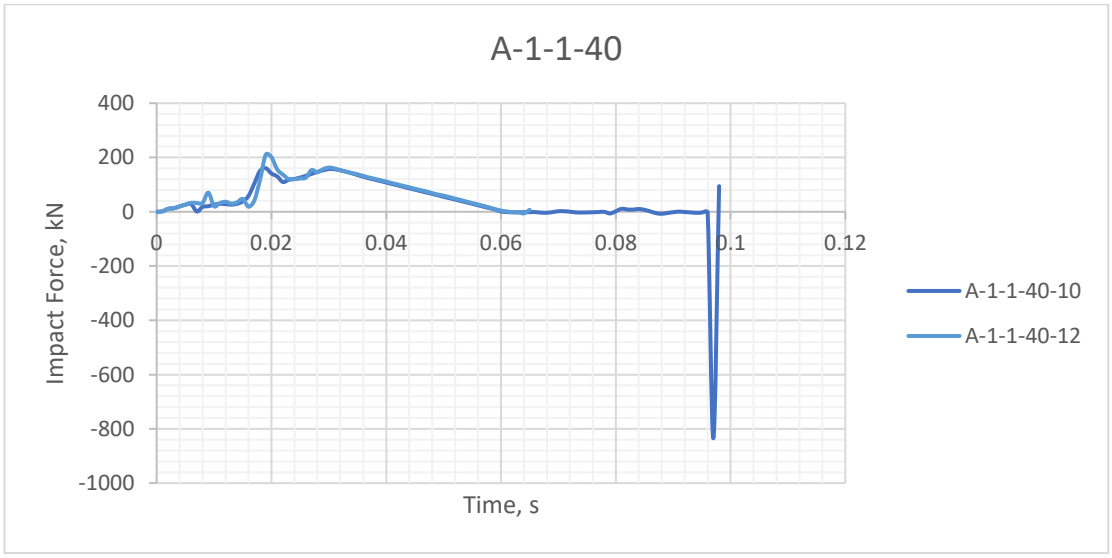
A-1-1-40
Impact Force, kN
400
200
0
-200
-400
-600
-800
-1000
0
0.02
0.04
0.06
0.08
0.1
0.12
Time, s
A-1-1-40-10
A-1-1-40-12

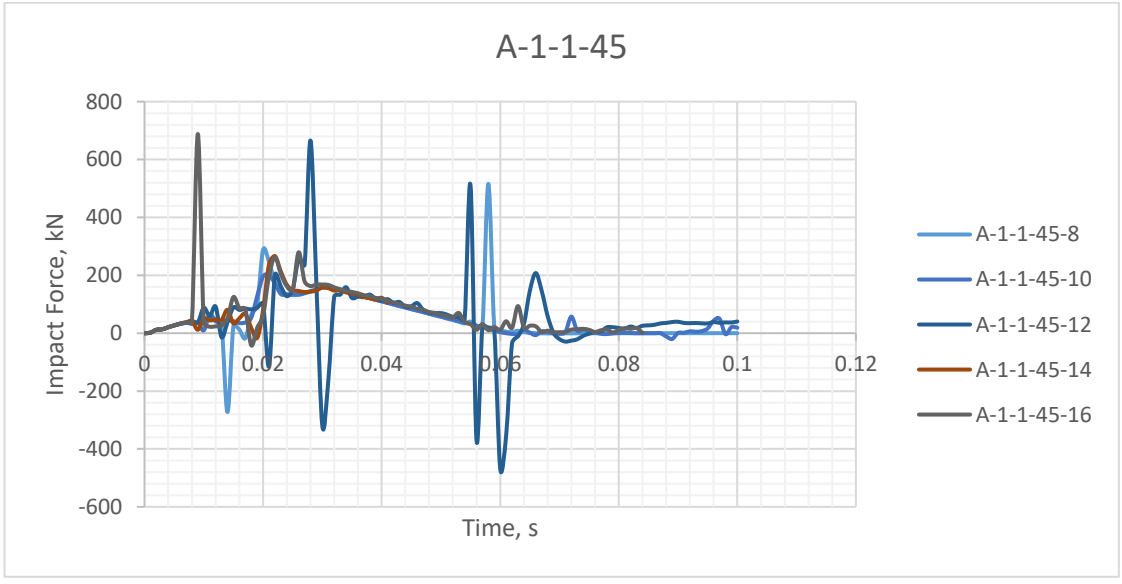
A-1-1-45
Impact Force, kN
800
600
400
200
0
-200
-400
-600
0
0.02
0.04
0.06
0.08
0.1
0.12
Time, s
A-1-1-45-8
A-1-1-45-10
A-1-1-45-12
A-1-1-45-14
A-1-1-45-16

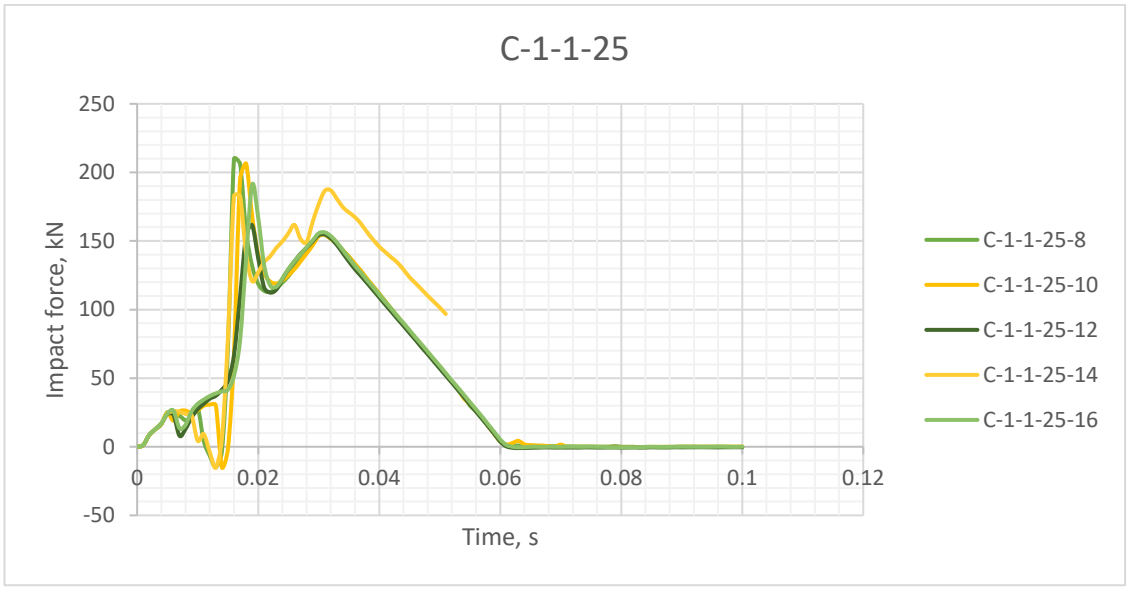
C-1-1-25
Impact force, kN
250
200
150
100
50
0
-50
0
0.02
0.04
0.06
0.08
0.1
0.12
Time, s
C-1-1-25-8
C-1-1-25-10
C-1-1-25-12
C-1-1-25-14
C-1-1-25-16

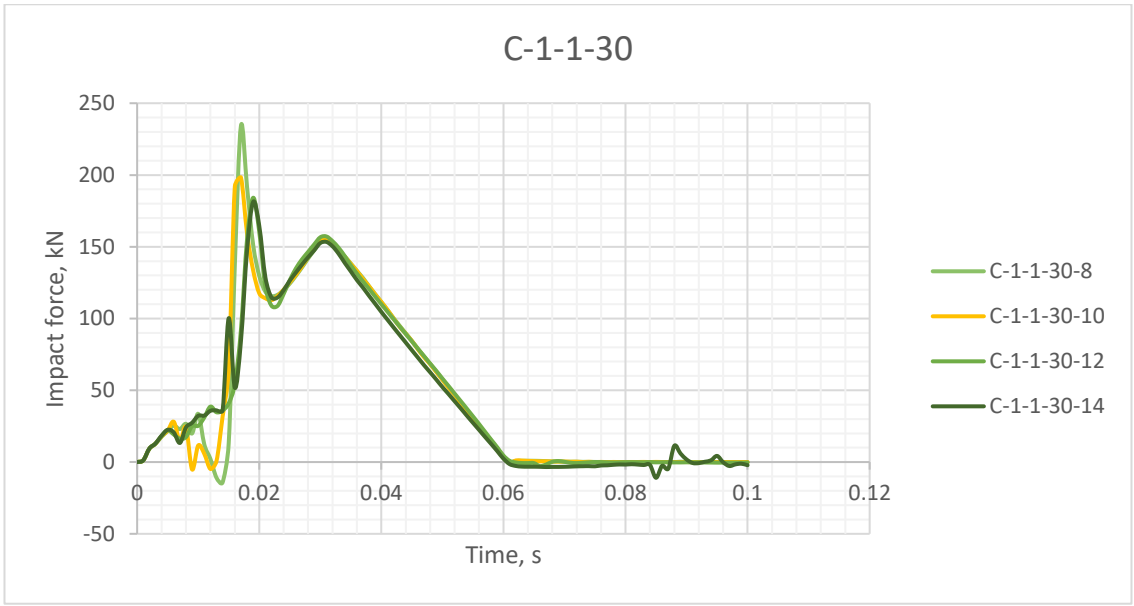
C-1-1-30
Impact force, kN
250
200
150
100
50
0
-50
0
0.02
0.04
0.06
0.08
0.1
0.12
Time, s
C-1-1-30-8
C-1-1-30-10
C-1-1-30-12
C-1-1-30-14

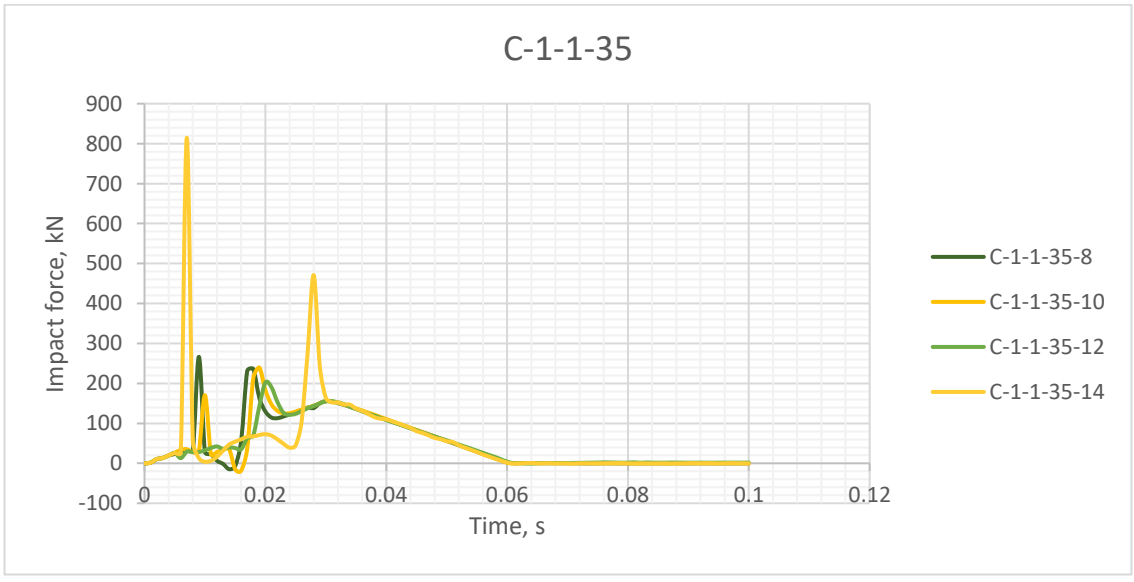
C-1-1-35
Impact force, kN
900
800
700
600
500
400
300
200
100
0
-100
0
0.02
0.04
0.06
0.08
0.1
0.12
Time, s
C-1-1-35-8
C-1-1-35-10
C-1-1-35-12
C-1-1-35-14

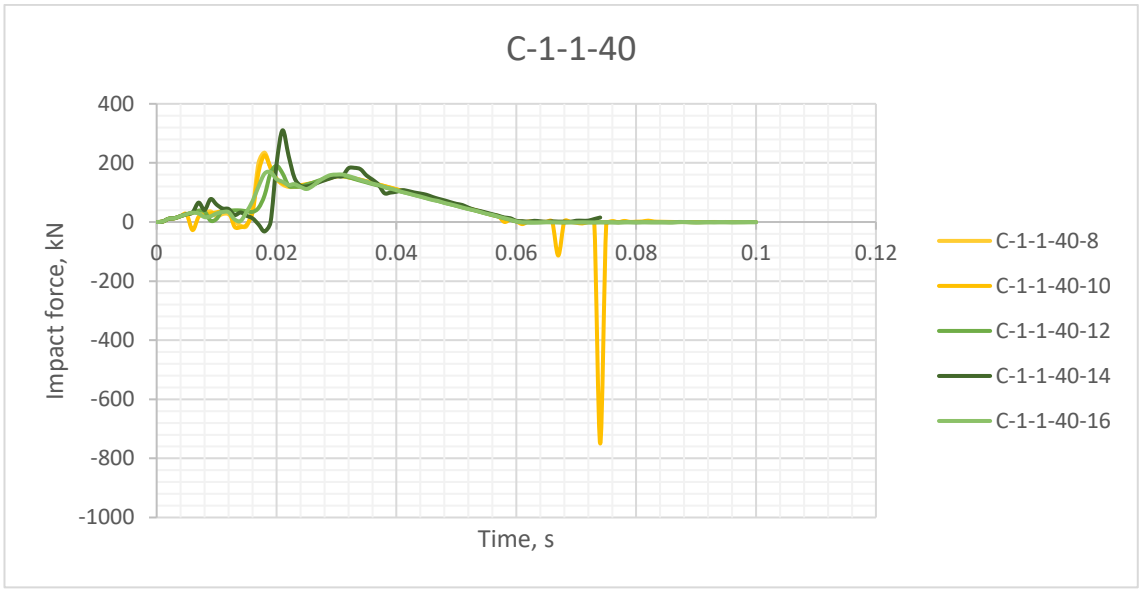
C-1-1-40
400
200
0
-200
-400
-600
-800
-1000
Impact force, kN
0
0.02
0.04
0.06
0.08
0.1
0.12
Time, s
C-1-1-40-8
C-1-1-40-10
C-1-1-40-12
C-1-1-40-14
C-1-1-40-16

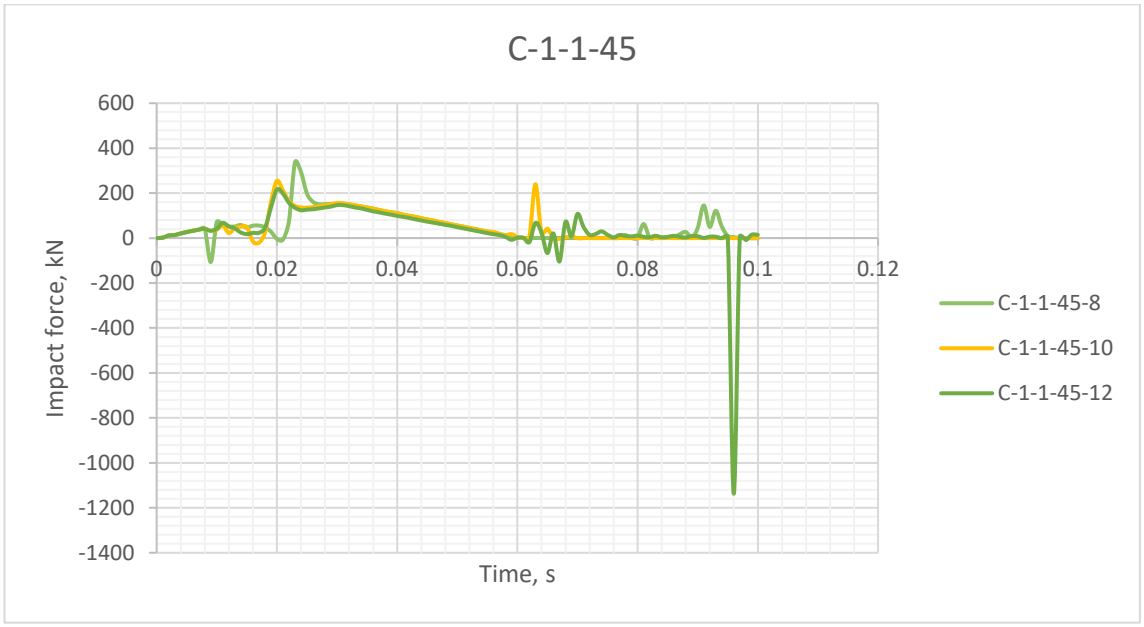
C-1-1-45
600
400
200
0
-200
-400
-600
-800
-1000
-1200
-1400
Impact force, kN
0
0.02
0.04
0.06
0.08
0.1
0.12
Time, s
C-1-1-45-8
C-1-1-45-10
C-1-1-45-12

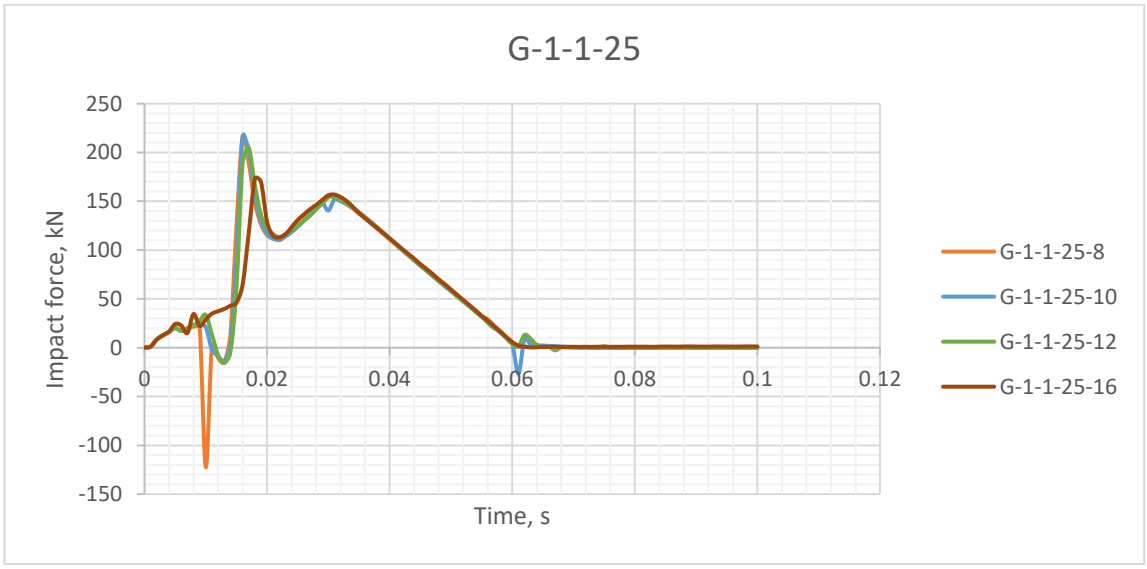
G-1-1-25
250
200
150
100
50
0
-50
-100
-150
Impact force, kN
0
0.02
0.04
0.06
0.08
0.1
0.12
Time, s
G-1-1-25-8
G-1-1-25-10
G-1-1-25-12
G-1-1-25-16

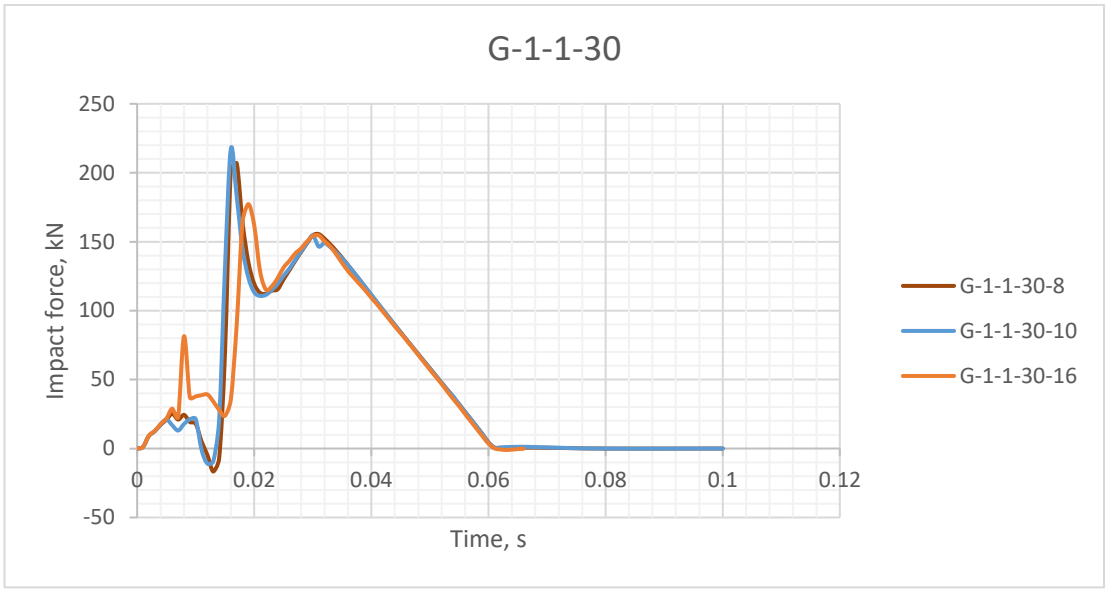
G-1-1-30
250
200
150
100
50
0
-50
Impact force, kN
0
0.02
0.04
0.06
0.08
0.1
0.12
Time, s
G-1-1-30-8
G-1-1-30-10
G-1-1-30-16

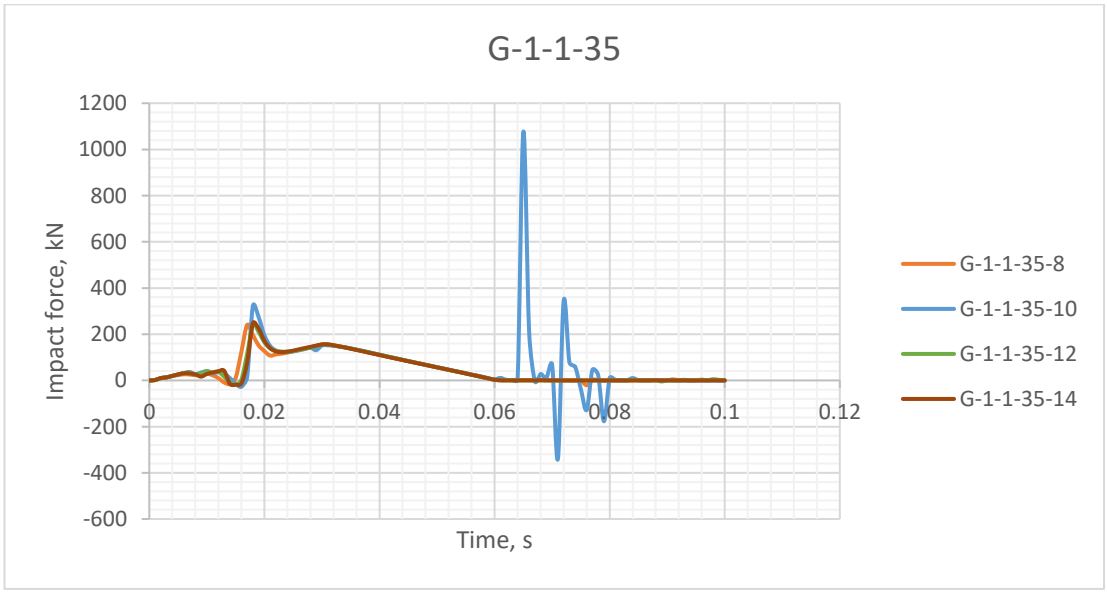
G-1-1-35
1200
1000
800
600
400
200
0
-200
-400
-600
Impact force, kN
0
0.02
0.04
0.06
0.08
0.1
0.12
Time, s
G-1-1-35-8
G-1-1-35-10
G-1-1-35-12
G-1-1-35-14

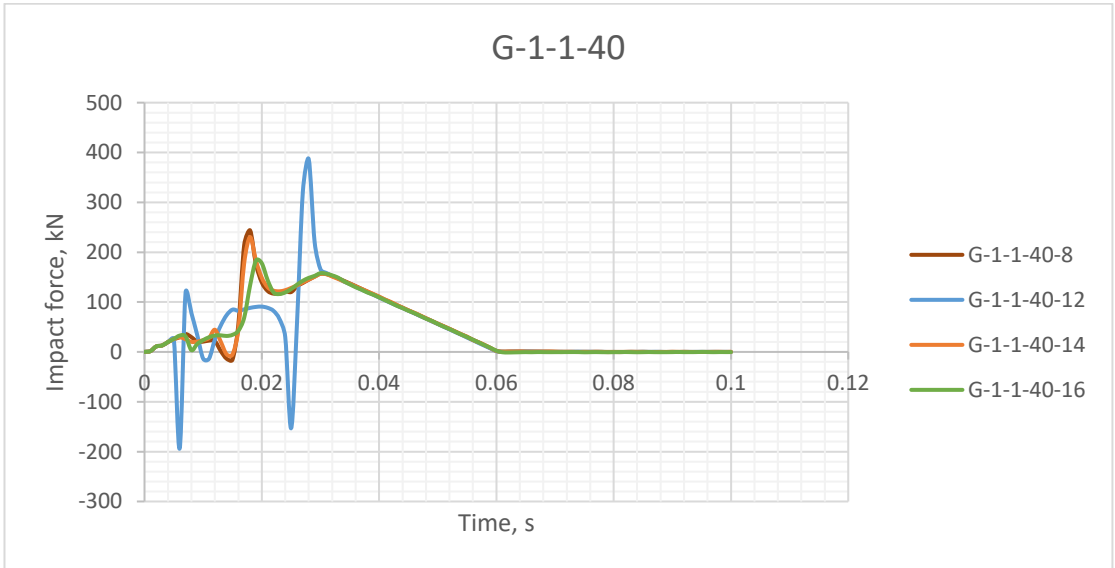
G-1-1-40
500
400
300
200
100
0
-100
-200
-300
Impact force, kN
0
0.02
0.04
0.06
0.08
0.1
0.12
Time, s
G-1-1-40-8
G-1-1-40-12
G-1-1-40-14
G-1-1-40-16

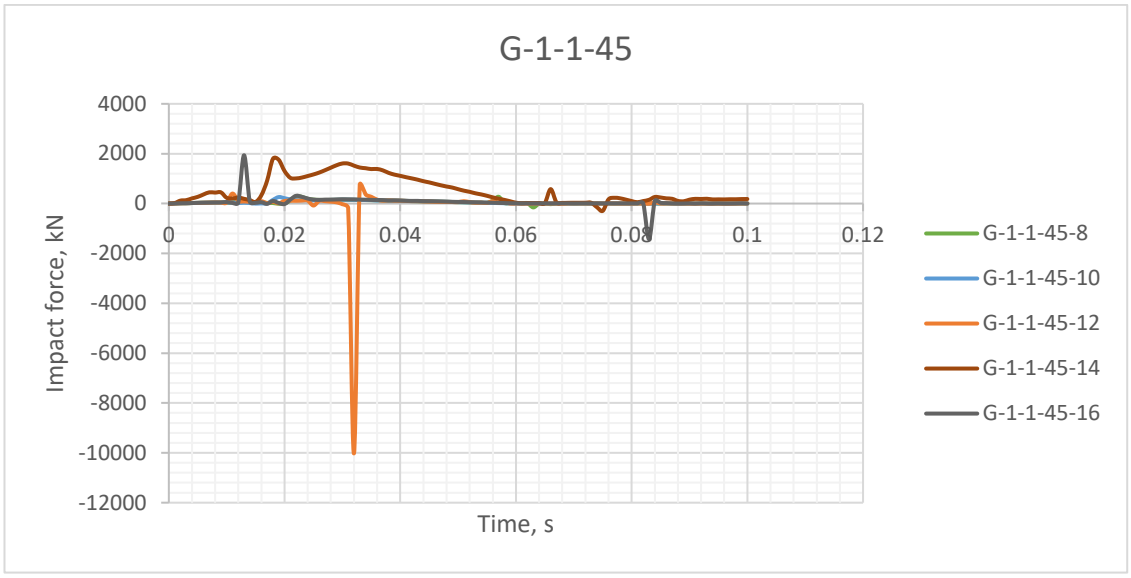

Figure 142: Reaction force time histories for AFRP, CFRP, GFRP RC beam models under 320 kN impact loading, ABAQUS.

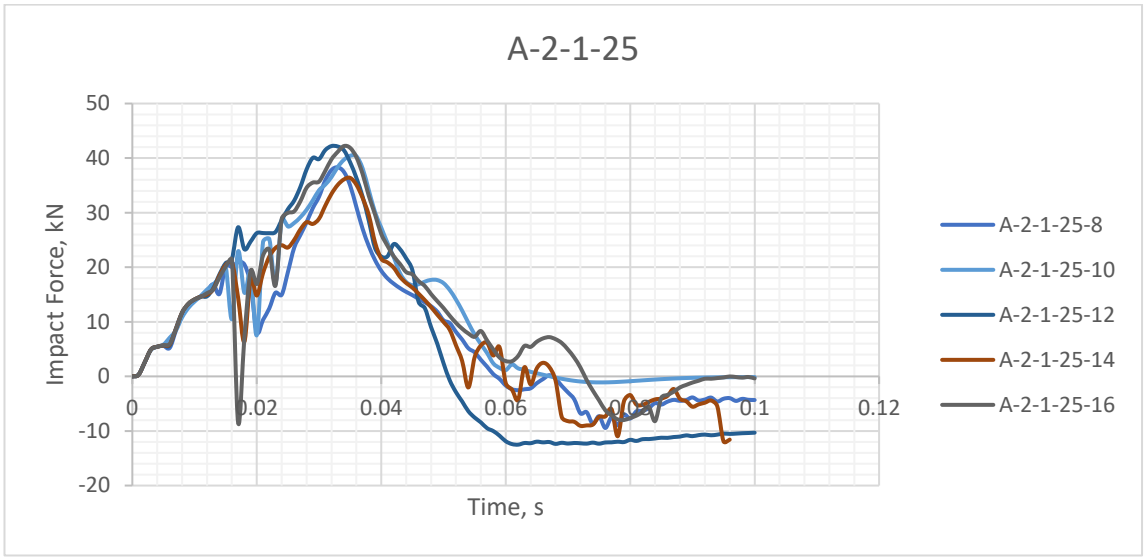

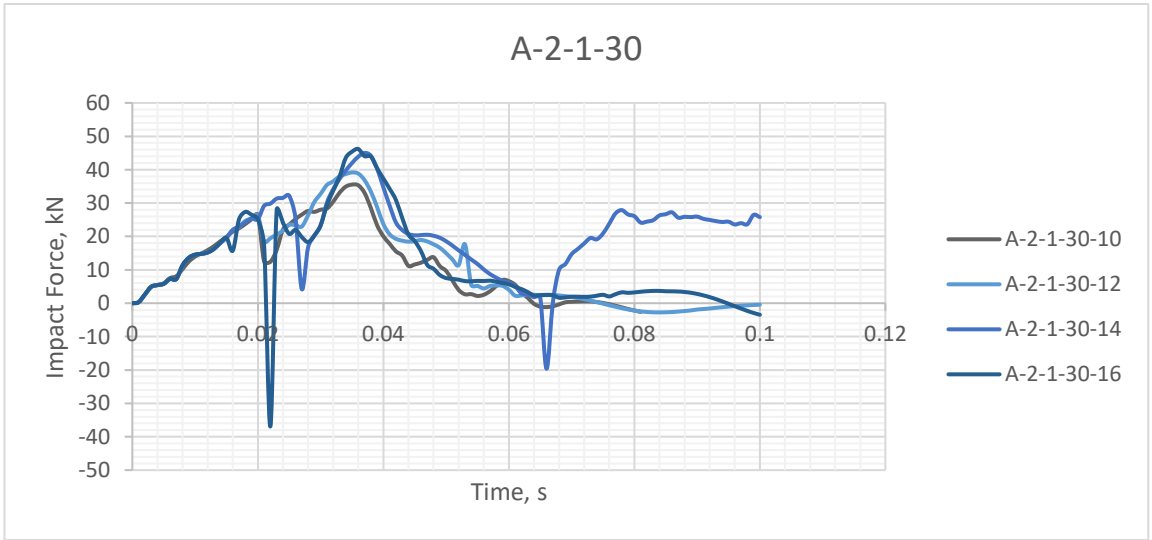

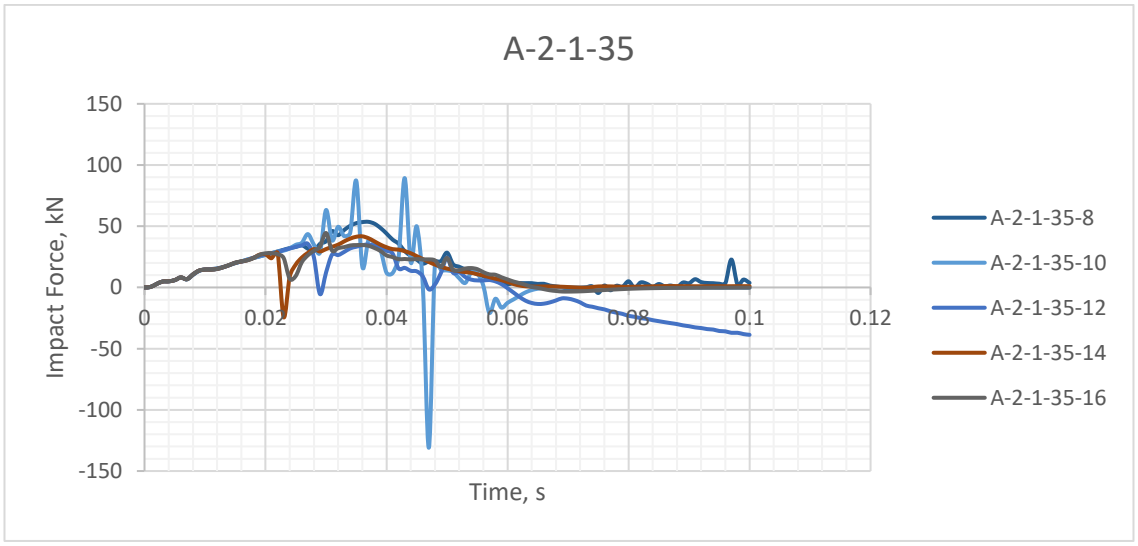
A-2-1-35
Impact Force, kN
Time, s
150
100
50
0
-50
-100
-150
0
0.02
0.04
0.06
0.08
0.1
0.12
A-2-1-35-8
A-2-1-35-10
A-2-1-35-12
A-2-1-35-14
A-2-1-35-16

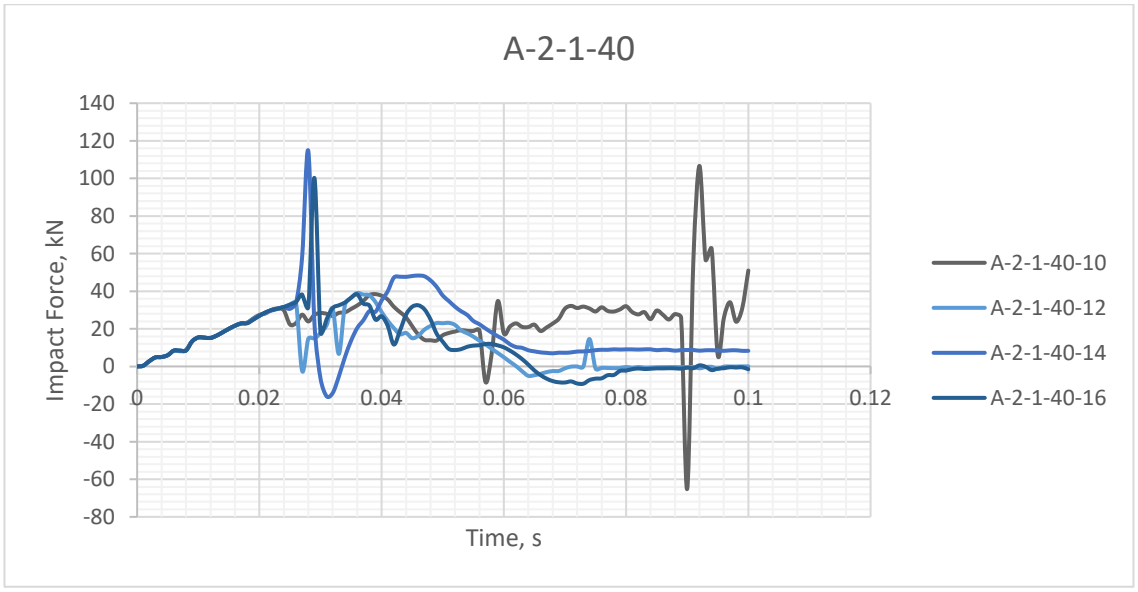
A-2-1-40
Impact Force, kN
Time, s
140
120
100
80
60
40
20
0
-20
-40
-60
-80
0
0.02
0.04
0.06
0.08
0.1
0.12
A-2-1-40-10
A-2-1-40-12
A-2-1-40-14
A-2-1-40-16

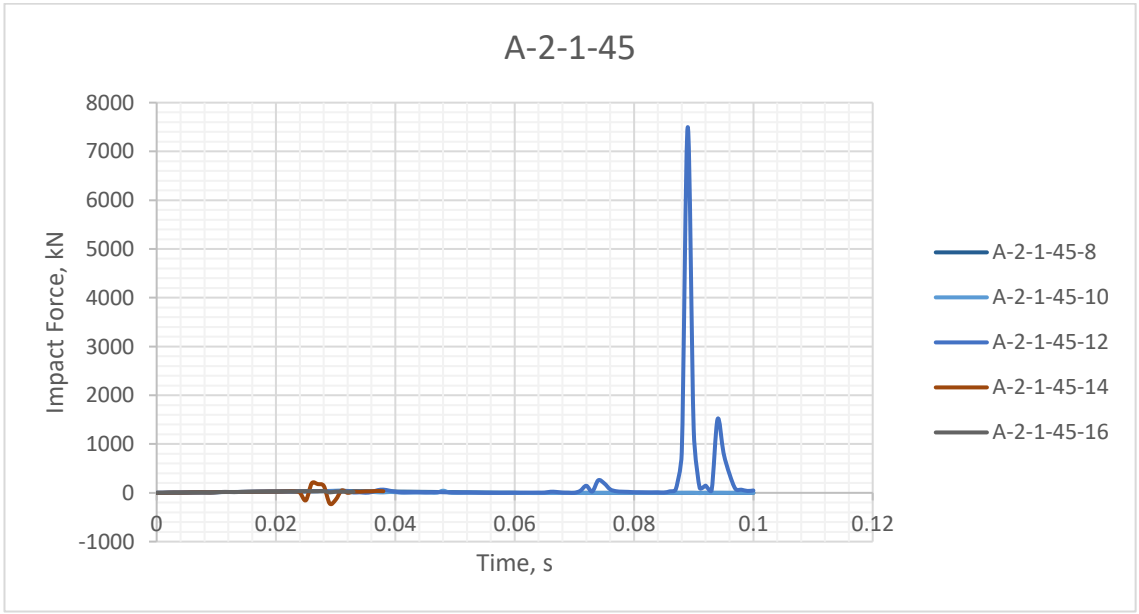
A-2-1-45
Impact Force, kN
Time, s
8000
7000
6000
5000
4000
3000
2000
1000
0
-1000
0
0.02
0.04
0.06
0.08
0.1
0.12
A-2-1-45-8
A-2-1-45-10
A-2-1-45-12
A-2-1-45-14
A-2-1-45-16

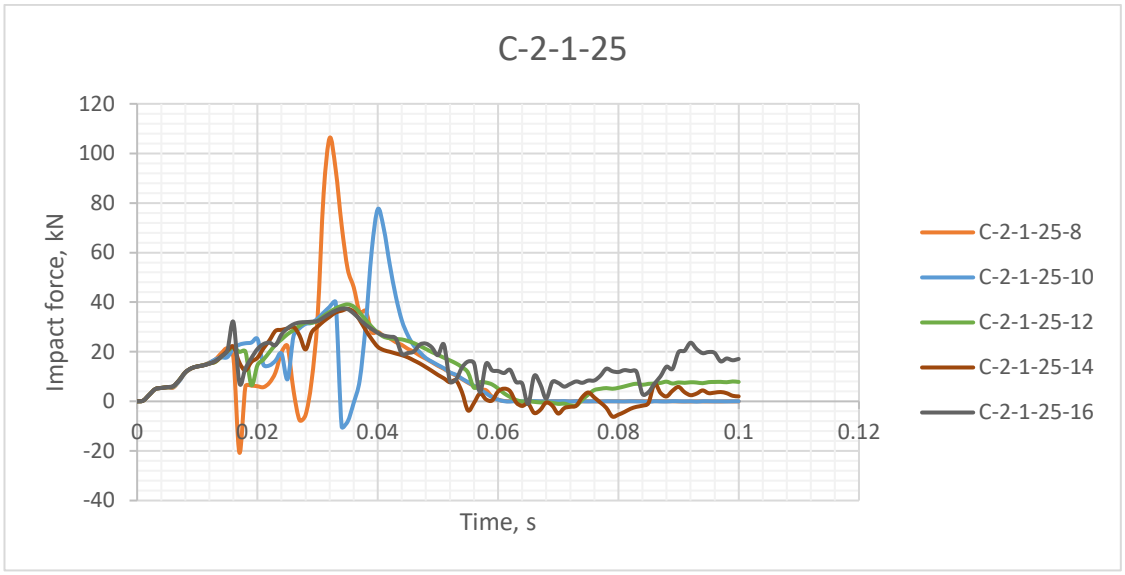
C-2-1-25
Impact force, kN
Time, s
120
100
80
60
40
20
0
-20
-40
0
0.02
0.04
0.06
0.08
0.1
0.12
C-2-1-25-8
C-2-1-25-10
C-2-1-25-12
C-2-1-25-14
C-2-1-25-16

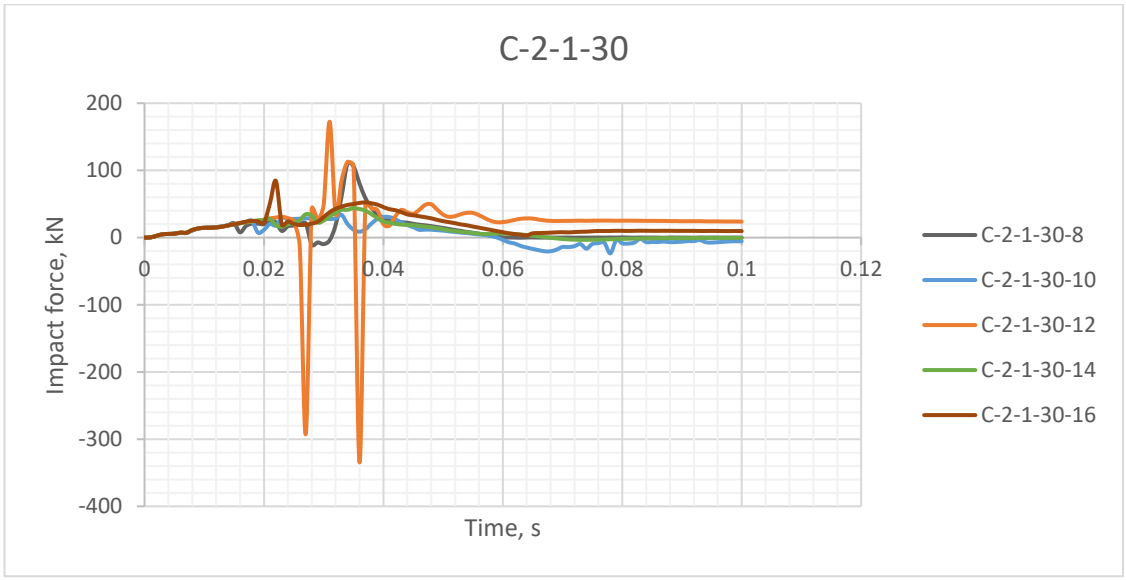
C-2-1-30
Impact force, kN
Time, s
200
100
0
-100
-200
-300
-400
0
0.02
0.04
0.06
0.08
0.1
0.12
C-2-1-30-8
C-2-1-30-10
C-2-1-30-12
C-2-1-30-14
C-2-1-30-16

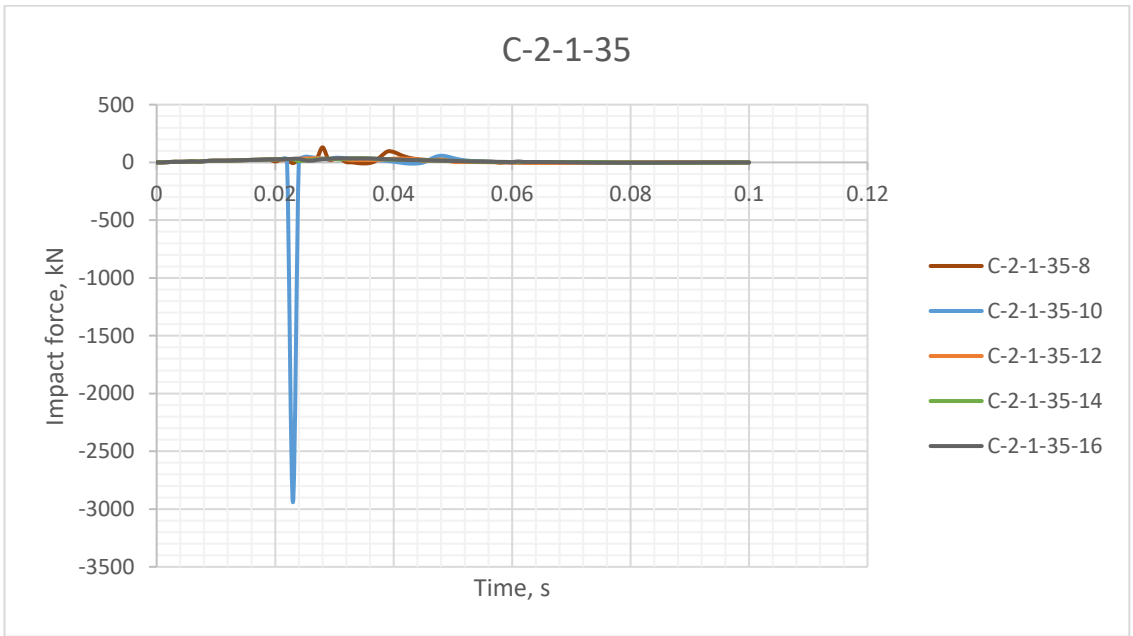
C-2-1-35
Impact force, kN
Time, s
500
0
-500
-1000
-1500
-2000
-2500
-3000
-3500
0
0.02
0.04
0.06
0.08
0.1
0.12
C-2-1-35-8
C-2-1-35-10
C-2-1-35-12
C-2-1-35-14
C-2-1-35-16

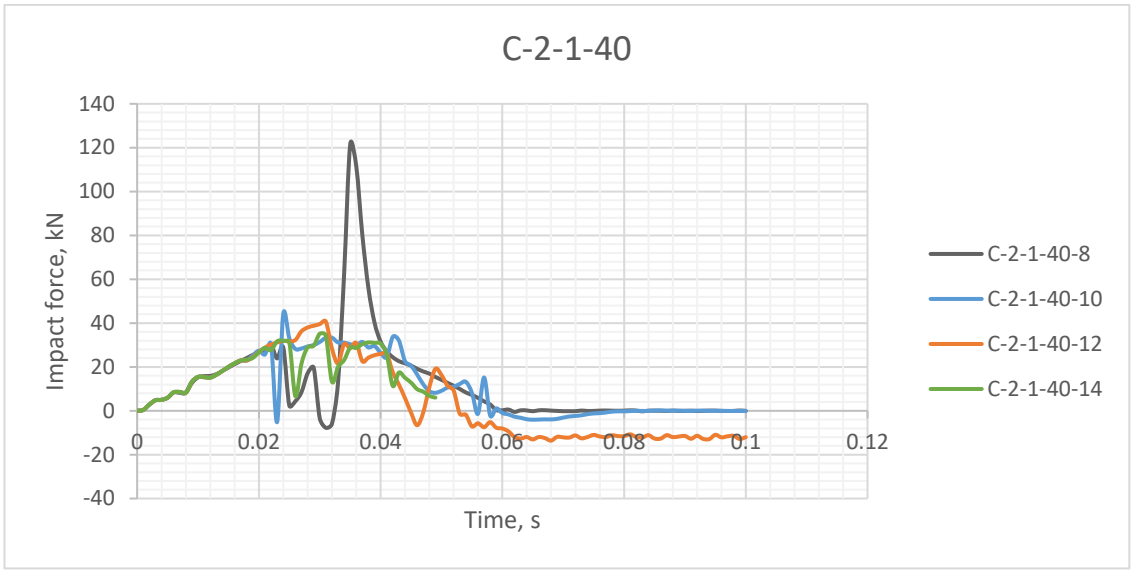
C-2-1-40
Impact force, kN
Time, s
140
120
100
80
60
40
20
0
-20
-40
0
0.02
0.04
0.06
0.08
0.1
0.12
C-2-1-40-8
C-2-1-40-10
C-2-1-40-12
C-2-1-40-14

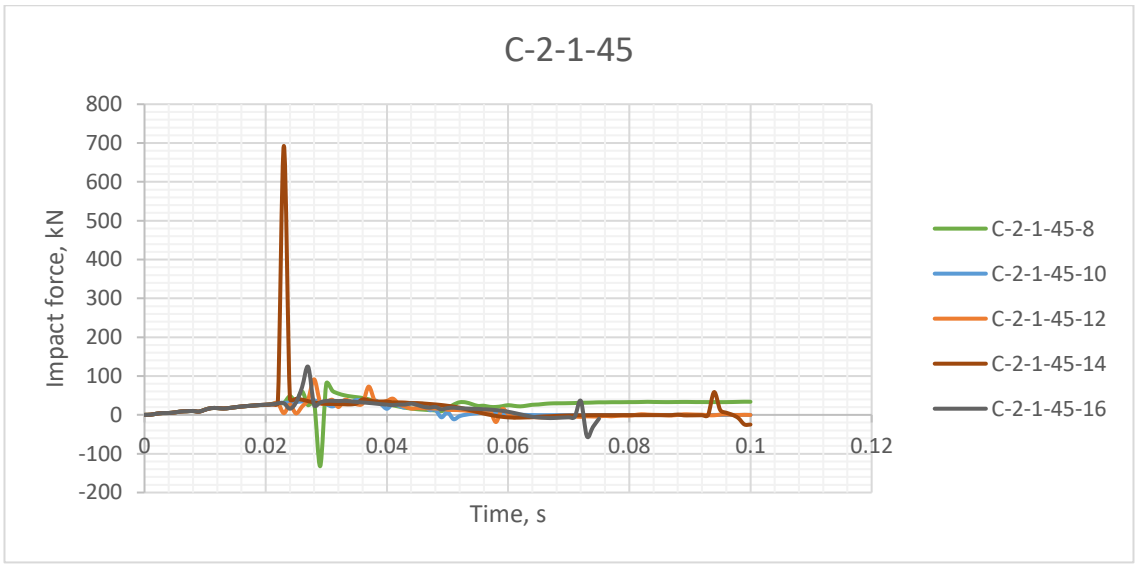
C-2-1-45
Impact force, kN
Time, s
800
700
600
500
400
300
200
100
0
-100
-200
0
0.02
0.04
0.06
0.08
0.1
0.12
C-2-1-45-8
C-2-1-45-10
C-2-1-45-12
C-2-1-45-14
C-2-1-45-16

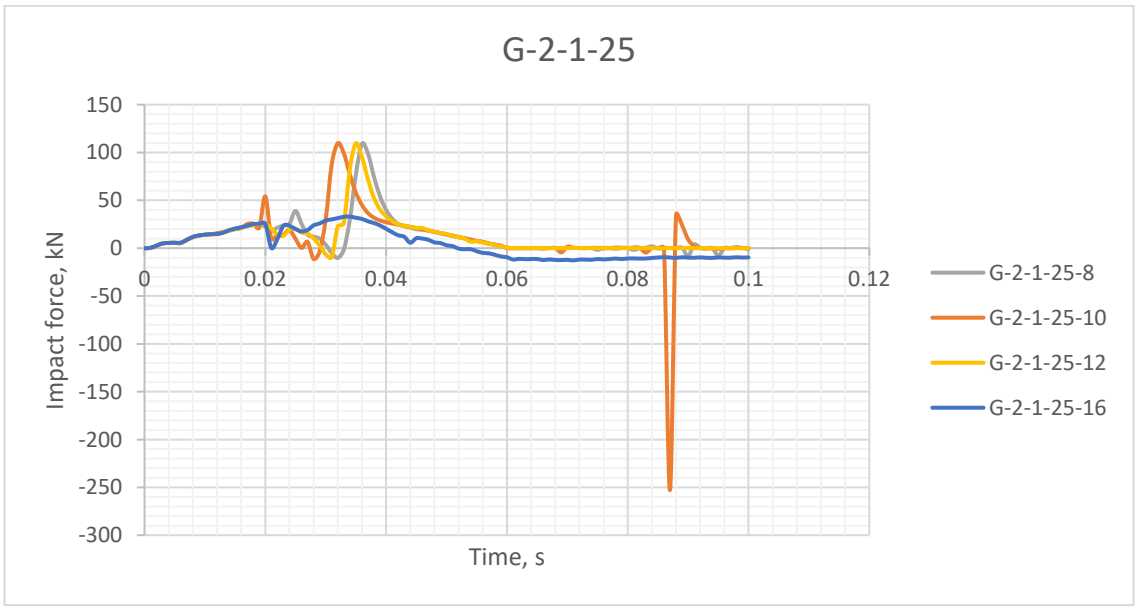
G-2-1-25
Impact force, kN
Time, s
150
100
50
0
-50
-100
-150
-200
-250
-300
0
0.02
0.04
0.06
0.08
0.1
0.12
G-2-1-25-8
G-2-1-25-10
G-2-1-25-12
G-2-1-25-16

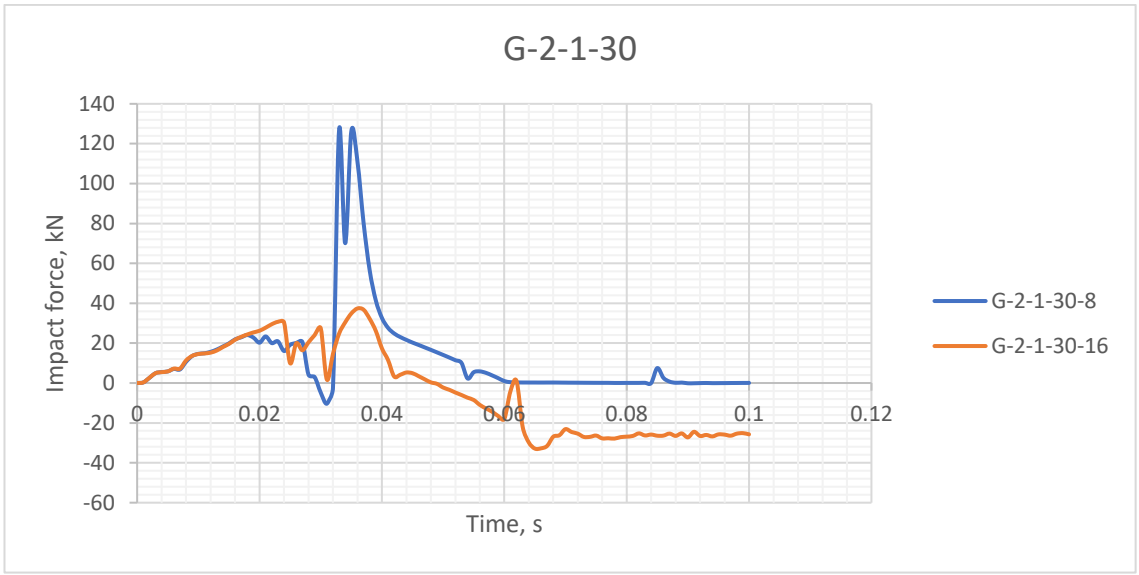
G-2-1-30
Impact force, kN
Time, s
140
120
100
80
60
40
20
0
-20
-40
-60
0
0.02
0.04
0.06
0.08
0.1
0.12
G-2-1-30-8
G-2-1-30-16

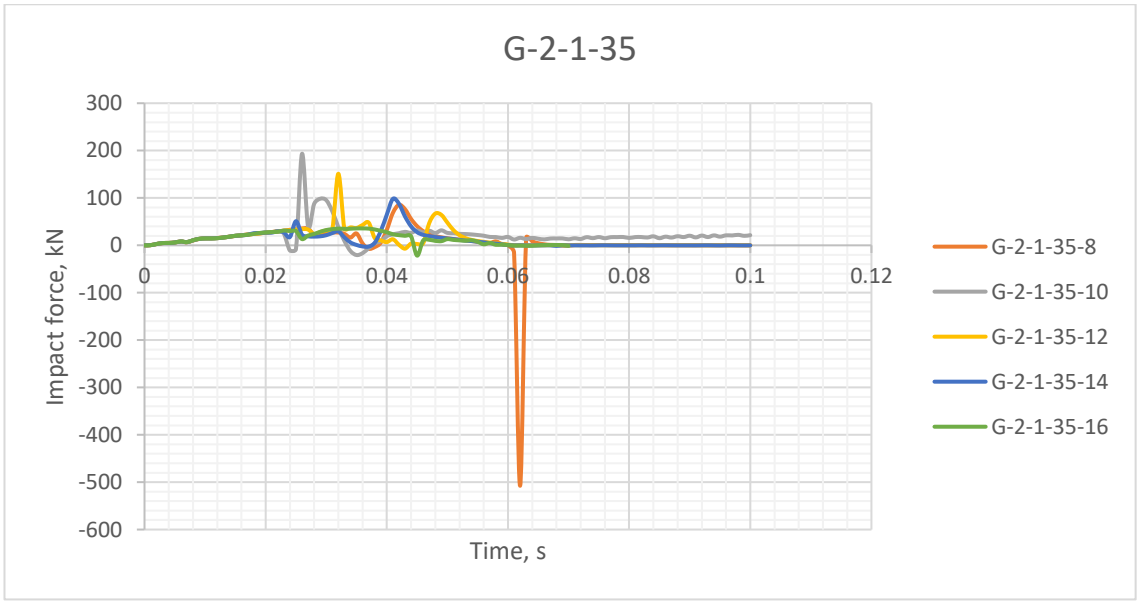
G-2-1-35
Impact force, kN
Time, s
300
200
100
0
-100
-200
-300
-400
-500
-600
0
0.02
0.04
0.06
0.08
0.1
0.12
G-2-1-35-8
G-2-1-35-10
G-2-1-35-12
G-2-1-35-14
G-2-1-35-16

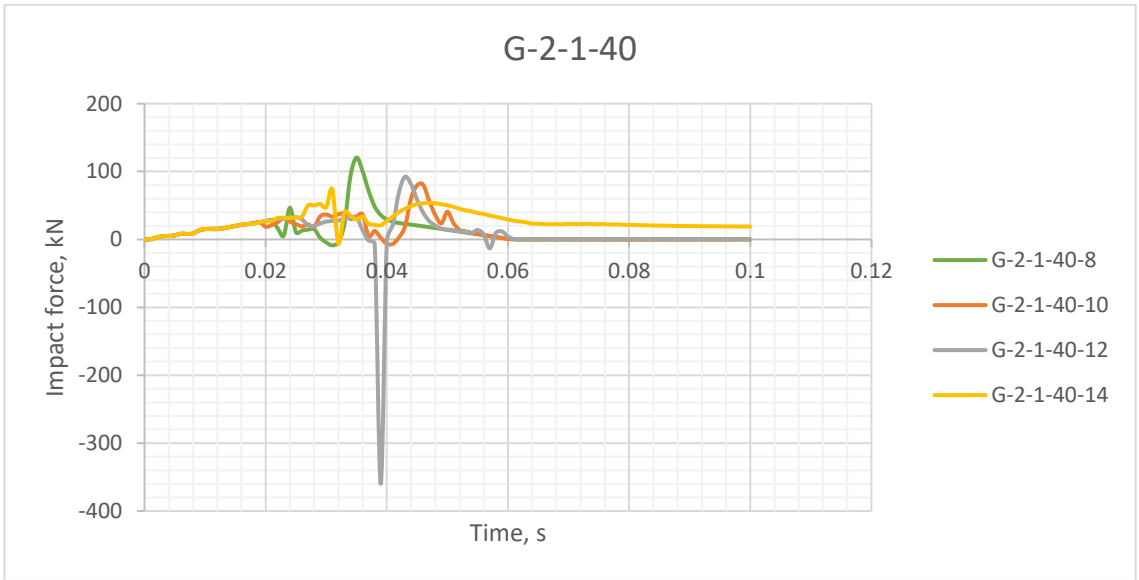
G-2-1-40
Impact force, kN
Time, s
200
100
0
-100
-200
-300
-400
0
0.02
0.04
0.06
0.08
0.1
0.12
G-2-1-40-8
G-2-1-40-10
G-2-1-40-12
G-2-1-40-14

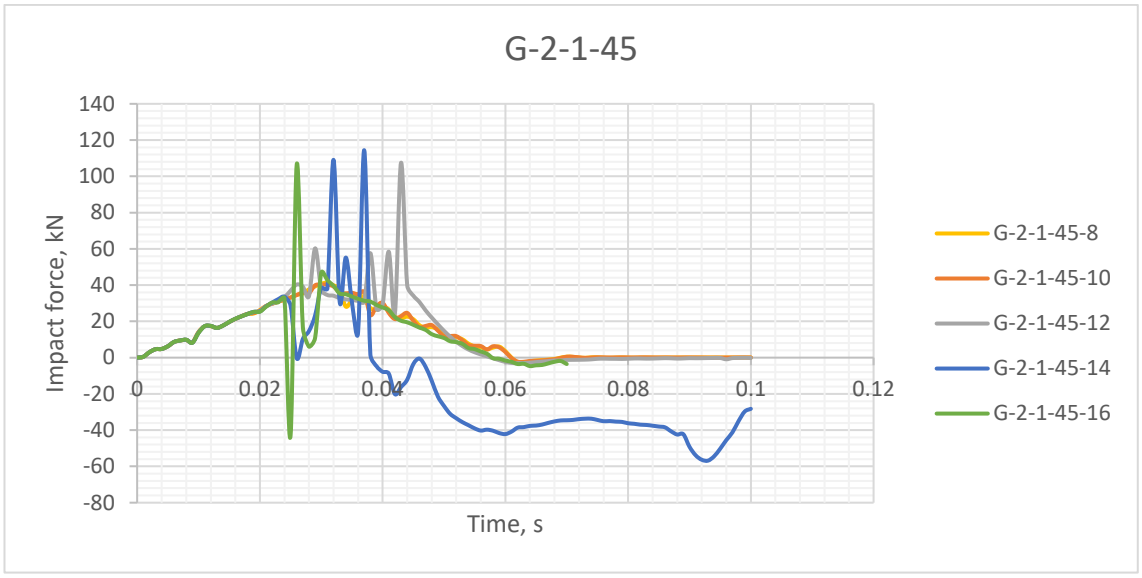

Figure 143: Reaction force time histories for AFRP, CFRP, GFRP RC beam models under 80 kN impact loading, ABAQUS.

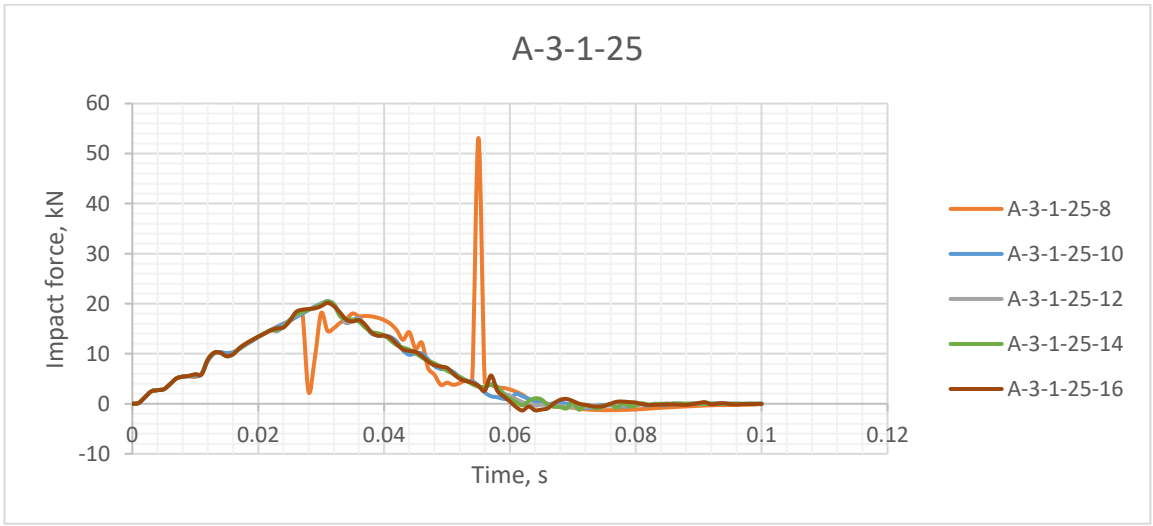

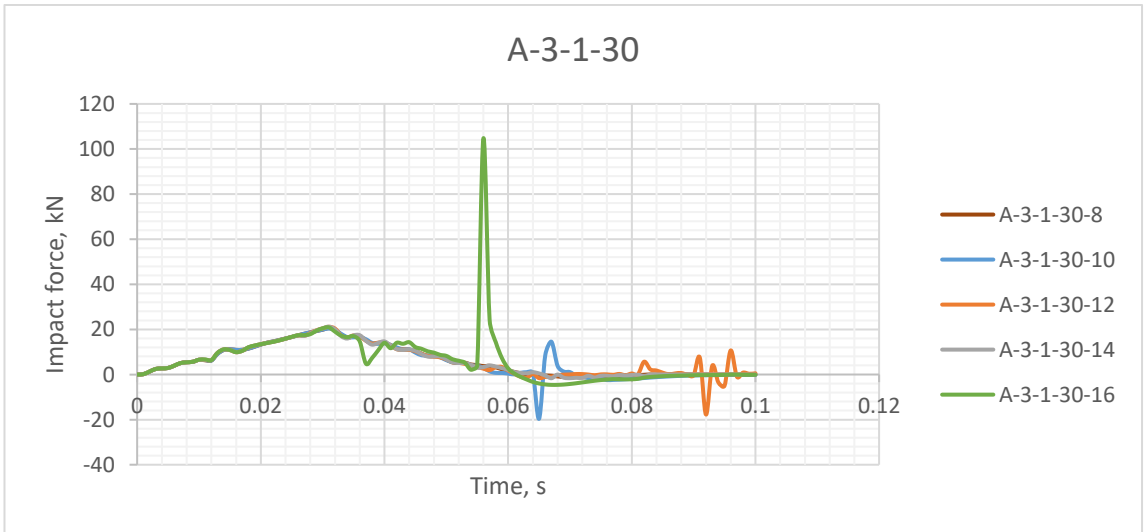

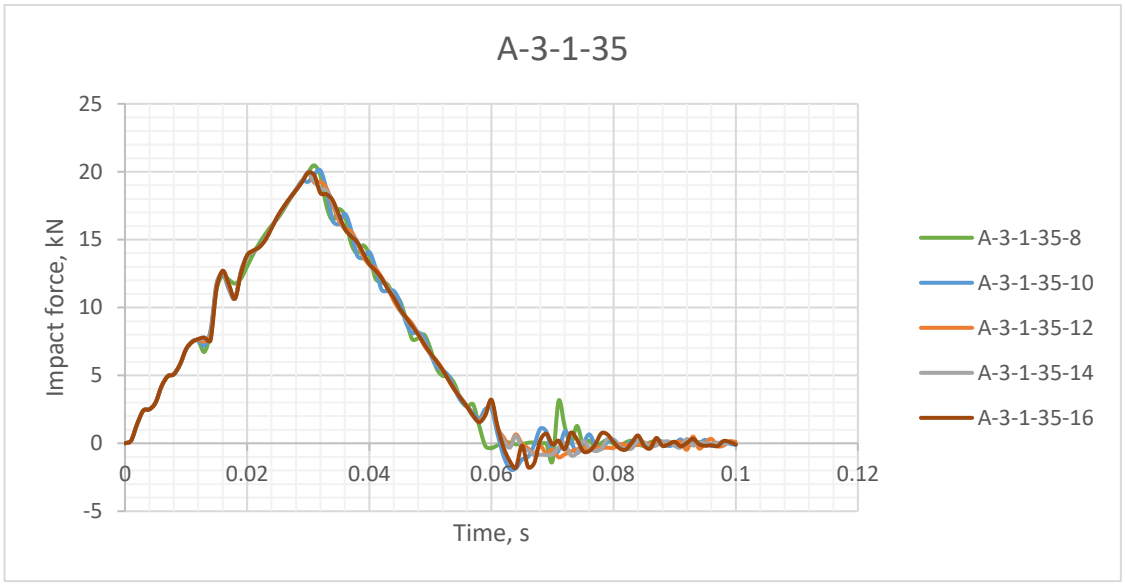
A-3-1-35
Impact force, kN
25
20
15
10
5
0
-5
0
0.02
0.04
0.06
0.08
0.1
0.12
Time, s
A-3-1-35-8
A-3-1-35-10
A-3-1-35-12
A-3-1-35-14
A-3-1-35-16

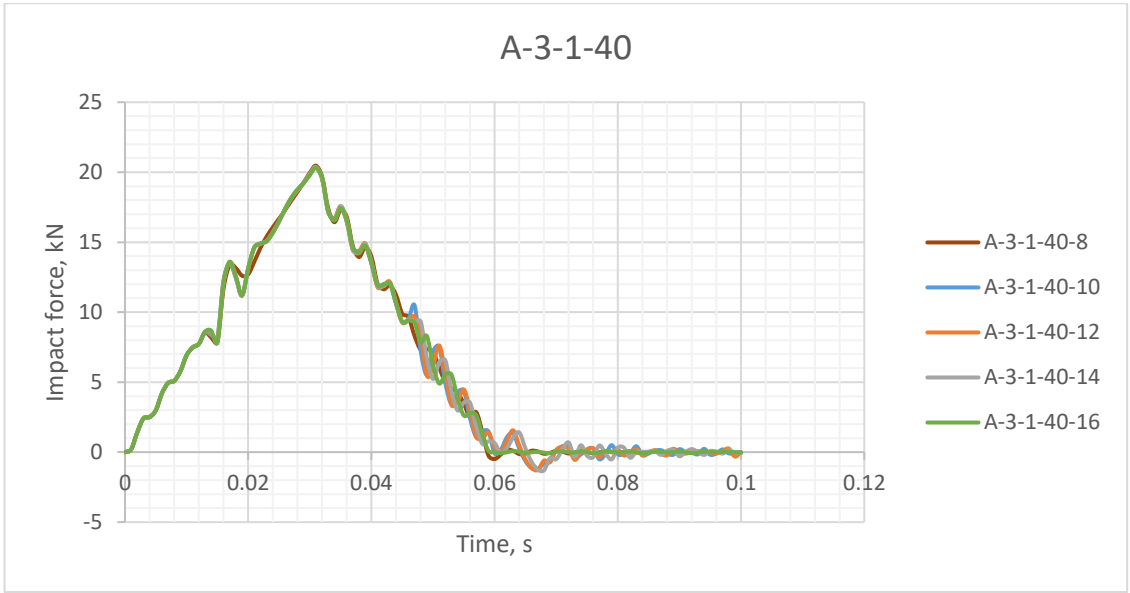
A-3-1-40
Impact force, kN
25
20
15
10
5
0
-5
0
0.02
0.04
0.06
0.08
0.1
0.12
Time, s
A-3-1-40-8
A-3-1-40-10
A-3-1-40-12
A-3-1-40-14
A-3-1-40-16

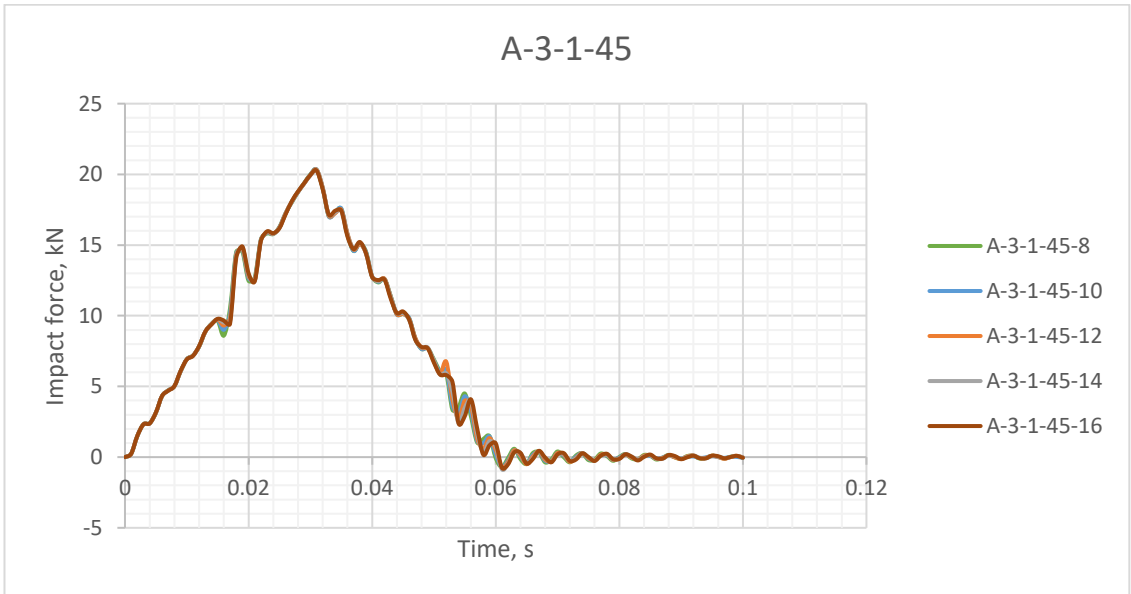
A-3-1-45
Impact force, kN
25
20
15
10
5
0
-5
0
0.02
0.04
0.06
0.08
0.1
0.12
Time, s
A-3-1-45-8
A-3-1-45-10
A-3-1-45-12
A-3-1-45-14
A-3-1-45-16

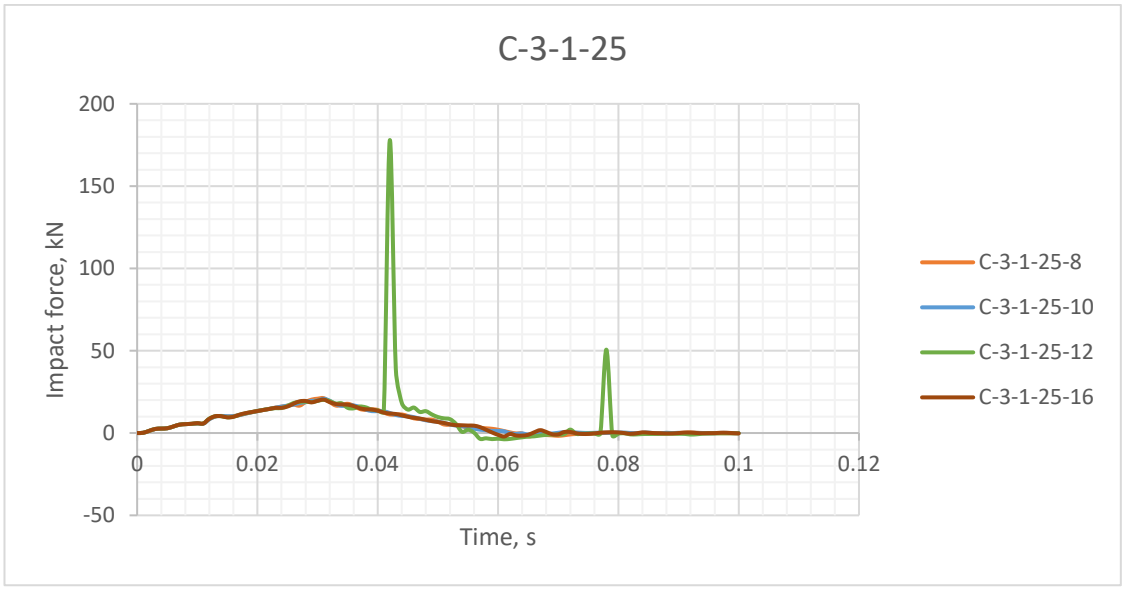
C-3-1-25
200
150
100
50
0
-50
Impact force, kN
0
0.02
0.04
0.06
0.08
0.1
0.12
Time, s
C-3-1-25-8
C-3-1-25-10
C-3-1-25-12
C-3-1-25-16

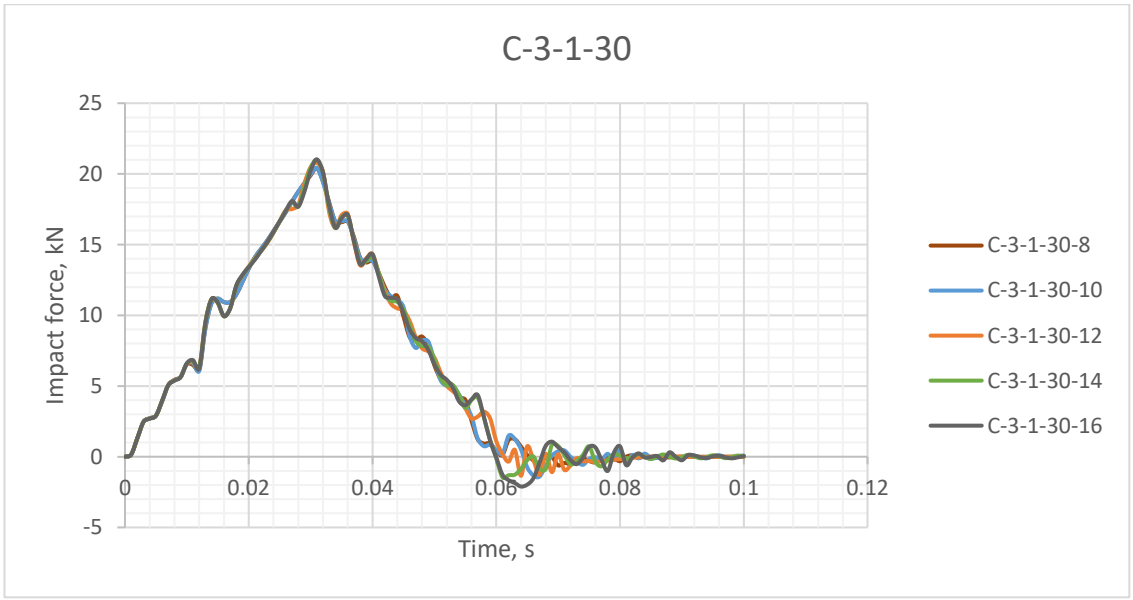
C-3-1-30
25
20
15
10
5
0
-5
Impact force, kN
0
0.02
0.04
0.06
0.08
0.1
0.12
Time, s
C-3-1-30-8
C-3-1-30-10
C-3-1-30-12
C-3-1-30-14
C-3-1-30-16

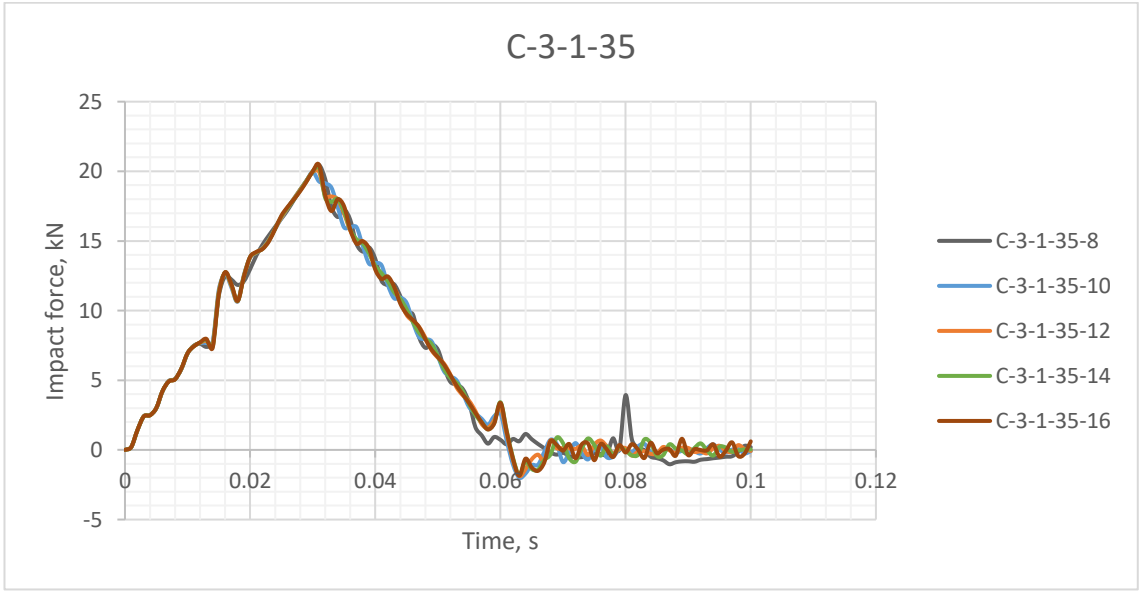
C-3-1-35
25
20
15
10
5
0
-5
Impact force, kN
0
0.02
0.04
0.06
0.08
0.1
0.12
Time, s
C-3-1-35-8
C-3-1-35-10
C-3-1-35-12
C-3-1-35-14
C-3-1-35-16

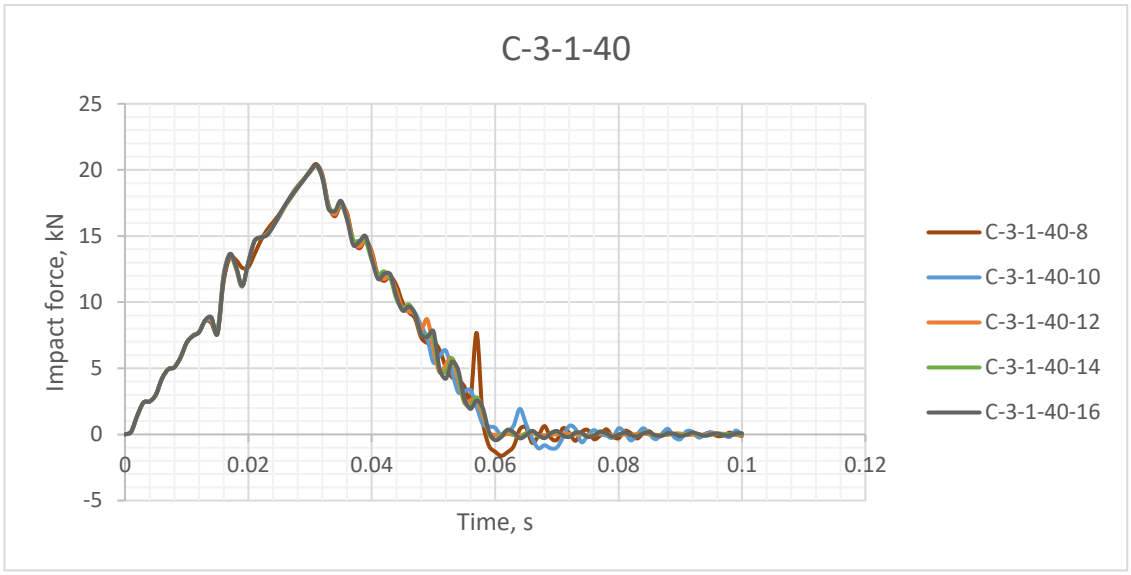
C-3-1-40
Impact force, kN
25
20
15
10
5
0
-5
0
0.02
0.04
0.06
0.08
0.1
0.12
Time, s
C-3-1-40-8
C-3-1-40-10
C-3-1-40-12
C-3-1-40-14
C-3-1-40-16

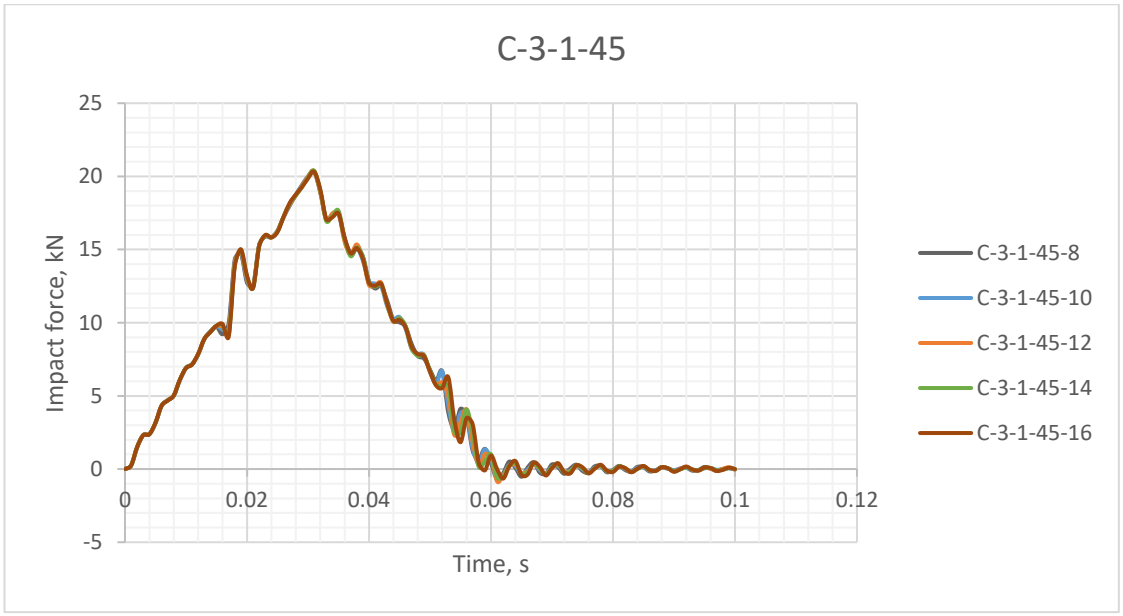
C-3-1-45
Impact force, kN
25
20
15
10
5
0
-5
0
0.02
0.04
0.06
0.08
0.1
0.12
Time, s
C-3-1-45-8
C-3-1-45-10
C-3-1-45-12
C-3-1-45-14
C-3-1-45-16

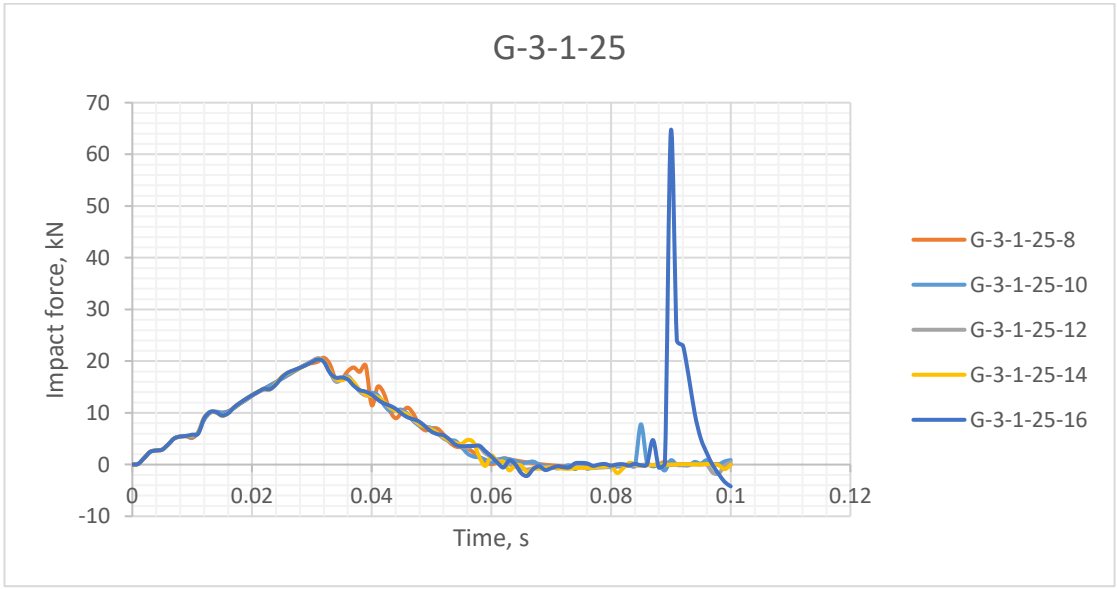
G-3-1-25
Impact force, kN
70
60
50
40
30
20
10
0
-10
0
0.02
0.04
0.06
0.08
0.1
0.12
Time, s
G-3-1-25-8
G-3-1-25-10
G-3-1-25-12
G-3-1-25-14
G-3-1-25-16

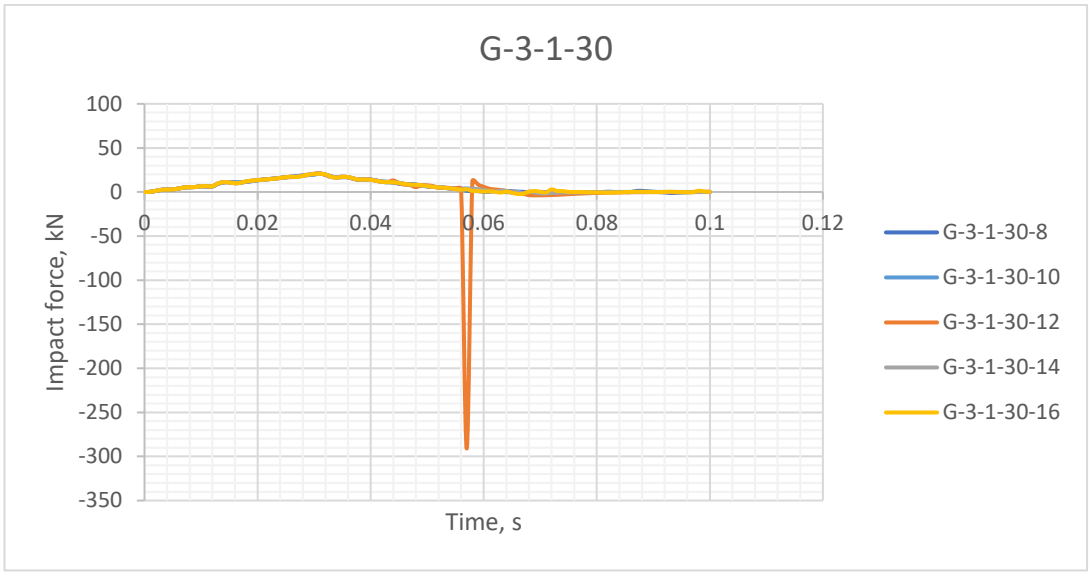
G-3-1-30
100
50
0
-50
-100
-150
-200
-250
-300
-350
0
0.02
0.04
0.06
0.08
0.1
0.12
Impact force, kN
Time, s
G-3-1-30-8
G-3-1-30-10
G-3-1-30-12
G-3-1-30-14
G-3-1-30-16

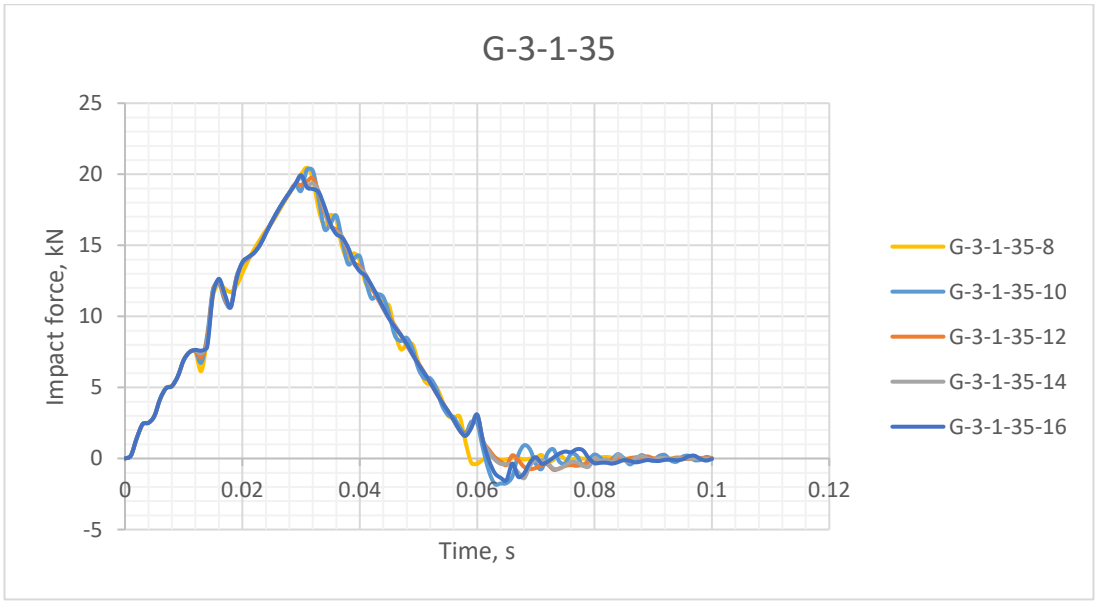
G-3-1-35
25
20
15
10
5
0
-5
0
0.02
0.04
0.06
0.08
0.1
0.12
Impact force, kN
Time, s
G-3-1-35-8
G-3-1-35-10
G-3-1-35-12
G-3-1-35-14
G-3-1-35-16

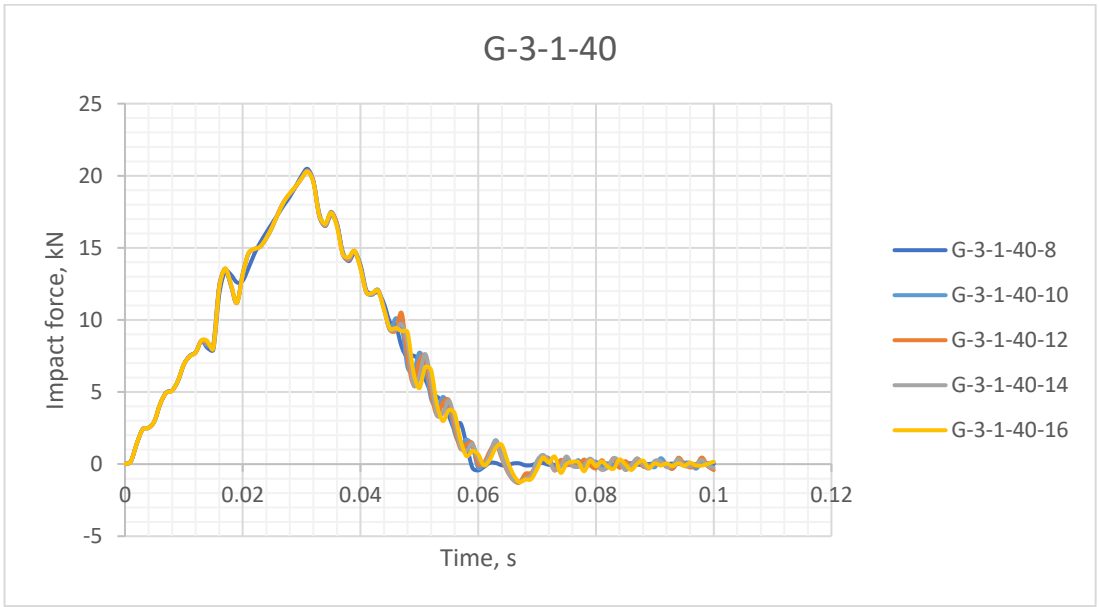
G-3-1-40
25
20
15
10
5
0
-5
0
0.02
0.04
0.06
0.08
0.1
0.12
Impact force, kN
Time, s
G-3-1-40-8
G-3-1-40-10
G-3-1-40-12
G-3-1-40-14
G-3-1-40-16

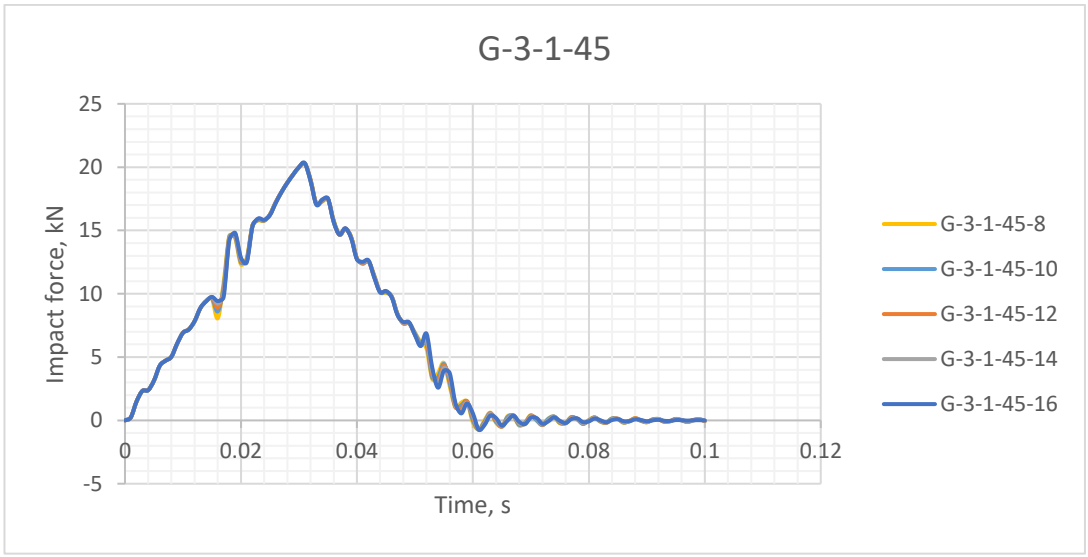

Figure 144: Reaction force time histories for AFRP, CFRP, GFRP RC beam models under 40 kN impact loading, ABAQUS.

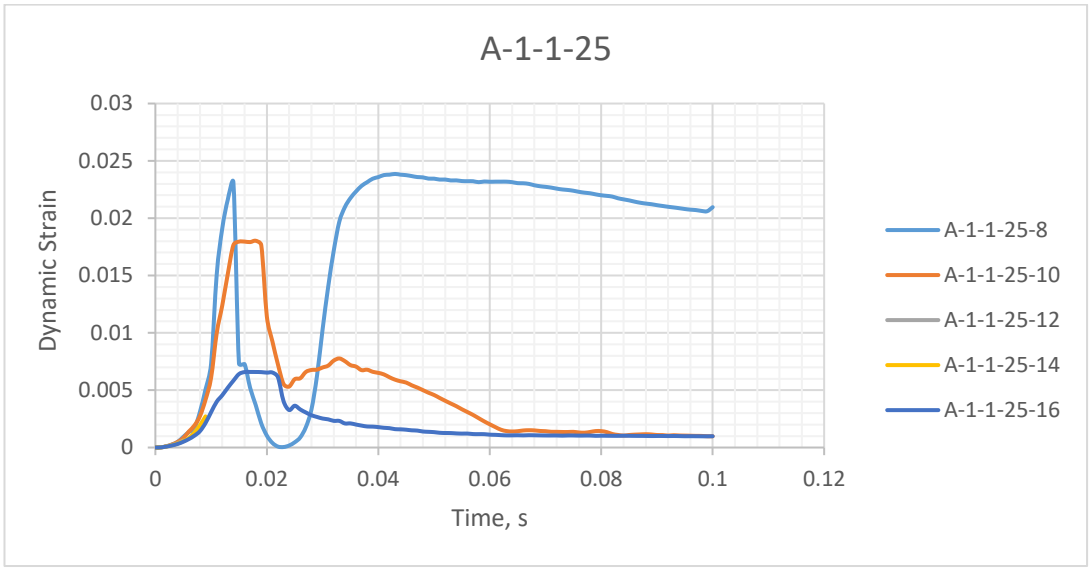

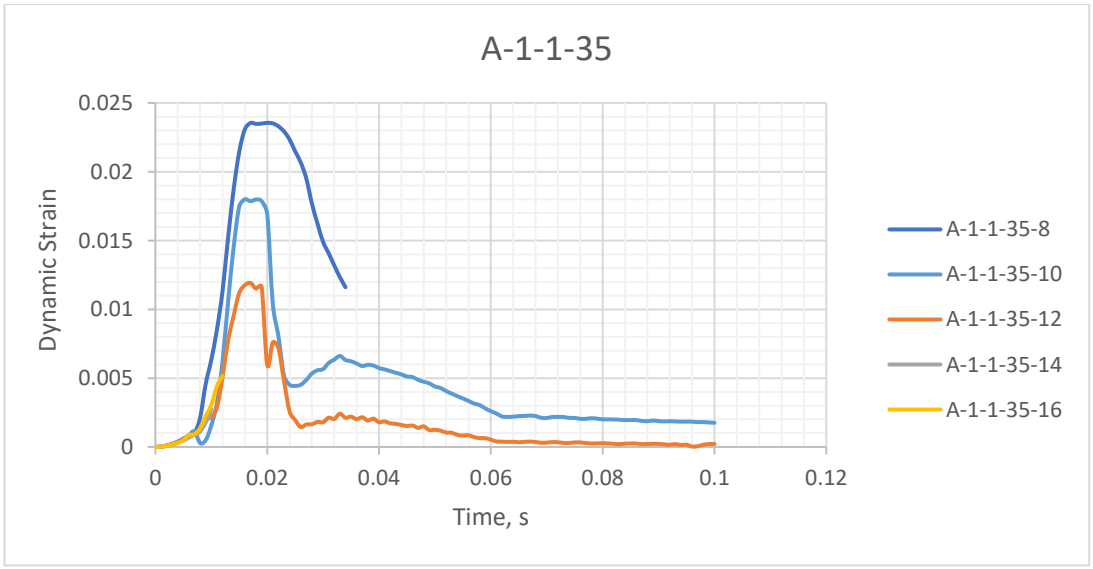

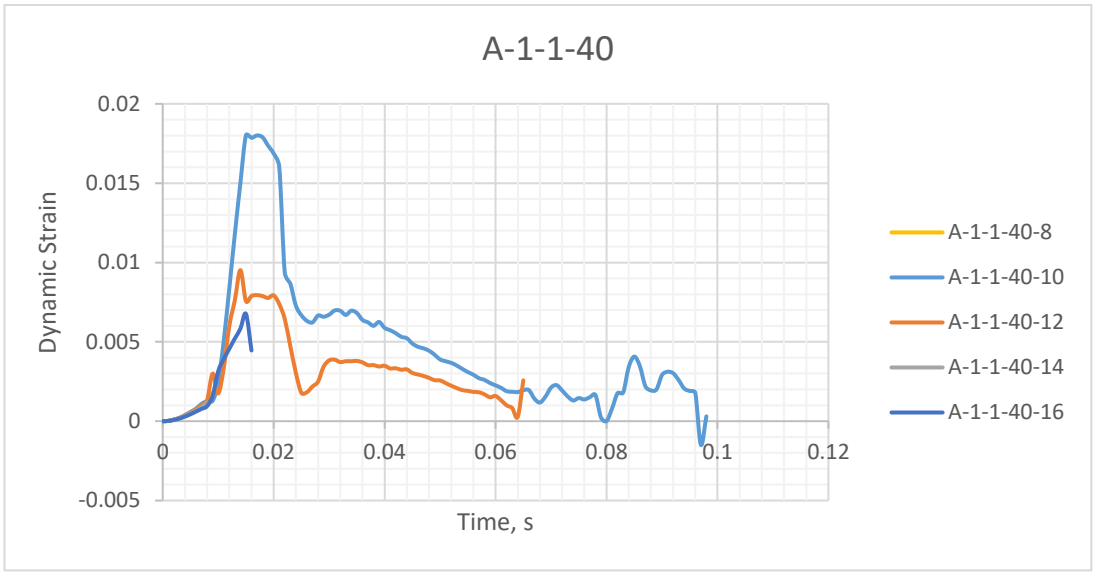
A-1-1-40
Dynamic Strain
0.02
0.015
0.01
0.005
0
-0.005
0
0.02
0.04
0.06
0.08
0.1
0.12
Time, s
A-1-1-40-8
A-1-1-40-10
A-1-1-40-12
A-1-1-40-14
A-1-1-40-16

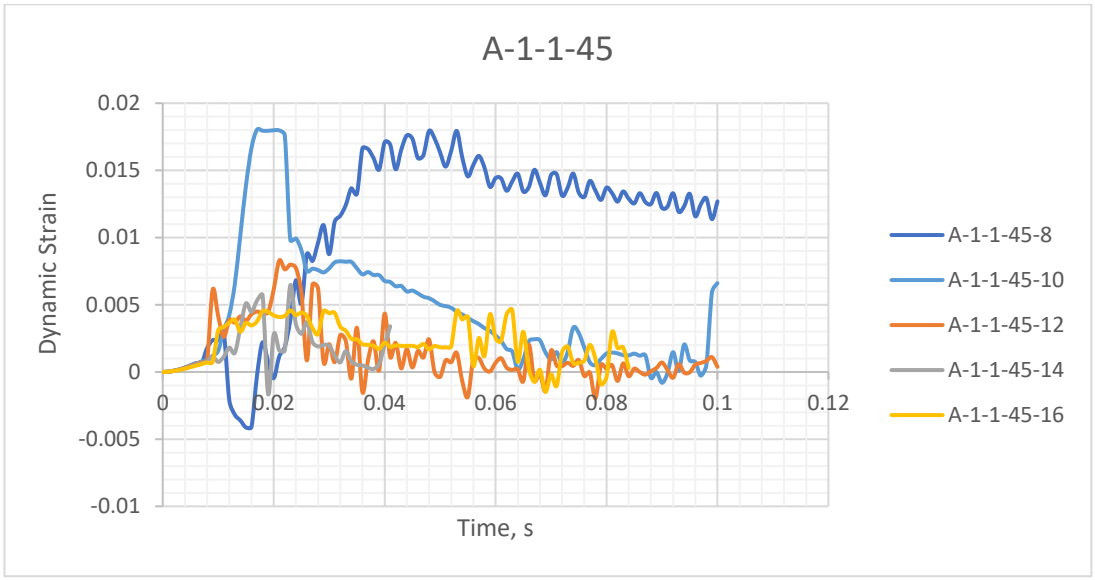
A-1-1-45
Dynamic Strain
0.02
0.015
0.01
0.005
0
-0.005
-0.01
0
0.02
0.04
0.06
0.08
0.1
0.12
Time, s
A-1-1-45-8
A-1-1-45-10
A-1-1-45-12
A-1-1-45-14
A-1-1-45-16

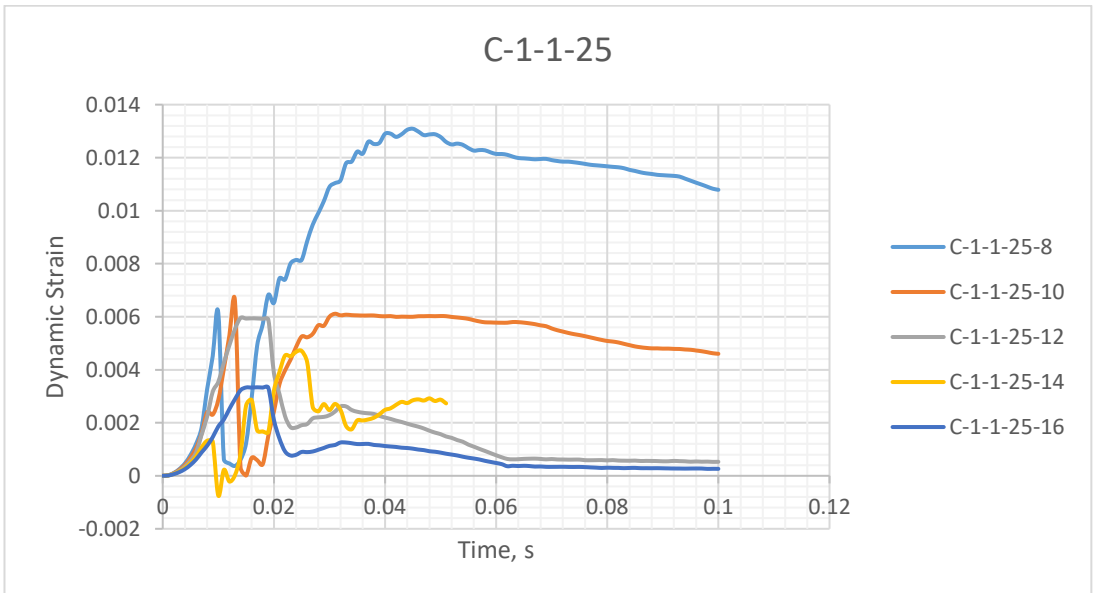
C-1-1-25
Dynamic Strain
0.014
0.012
0.01
0.008
0.006
0.004
0.002
0
-0.002
0
0.02
0.04
0.06
0.08
0.1
0.12
Time, s
C-1-1-25-8
C-1-1-25-10
C-1-1-25-12
C-1-1-25-14
C-1-1-25-16

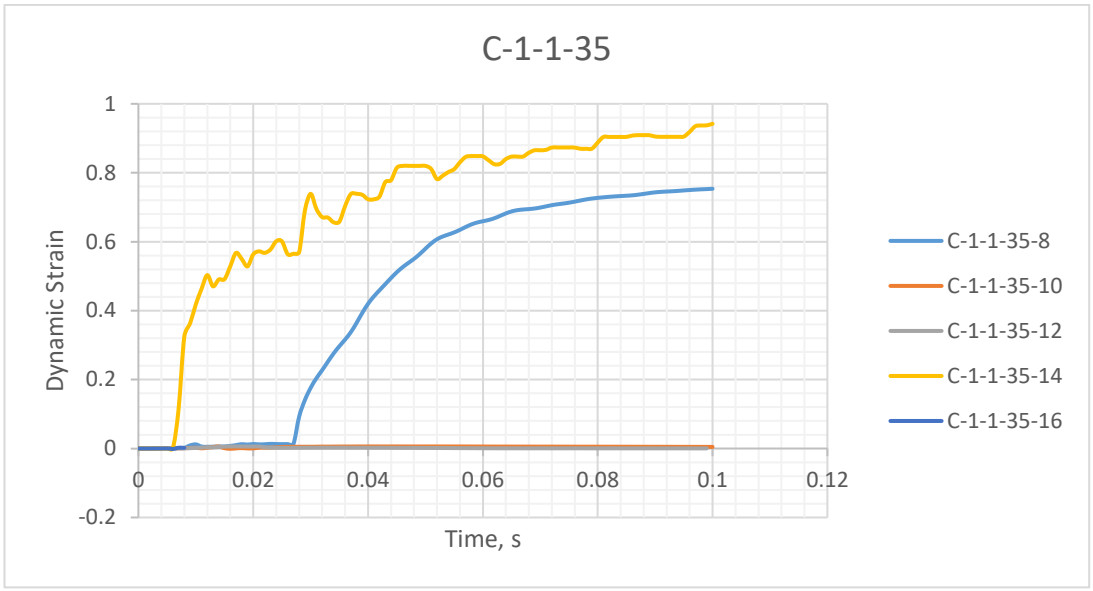
C-1-1-35
Dynamic Strain
Time, s
1
0.8
0.6
0.4
0.2
0
-0.2
0
0.02
0.04
0.06
0.08
0.1
0.12
C-1-1-35-8
C-1-1-35-10
C-1-1-35-12
C-1-1-35-14
C-1-1-35-16

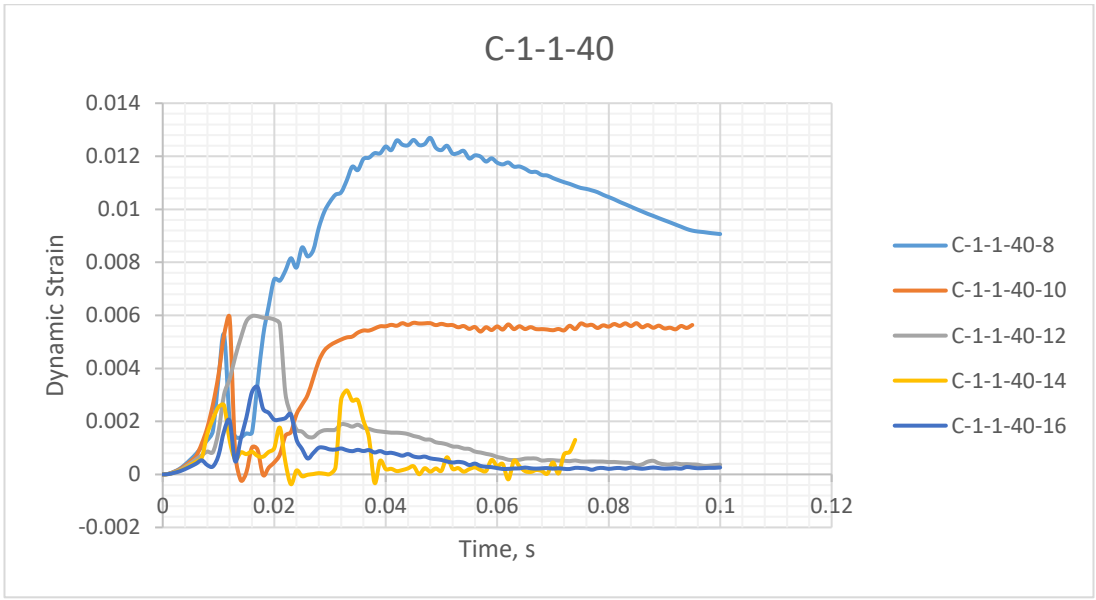
C-1-1-40
Dynamic Strain
Time, s
0.014
0.012
0.01
0.008
0.006
0.004
0.002
0
-0.002
0
0.02
0.04
0.06
0.08
0.1
0.12
C-1-1-40-8
C-1-1-40-10
C-1-1-40-12
C-1-1-40-14
C-1-1-40-16

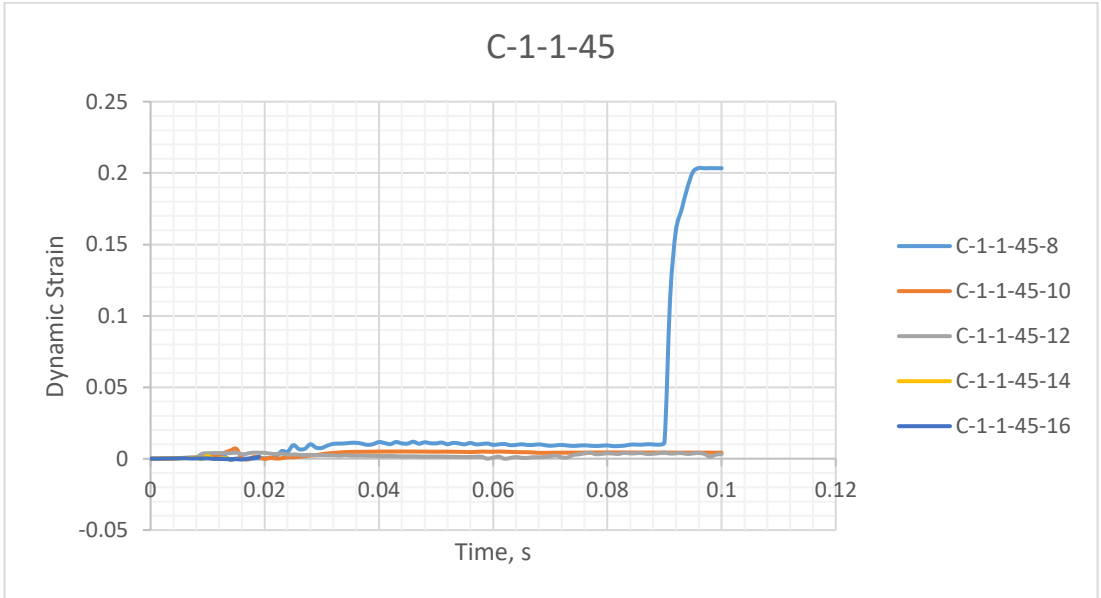
C-1-1-45
Dynamic Strain
Time, s
0.25
0.2
0.15
0.1
0.05
0
-0.05
0
0.02
0.04
0.06
0.08
0.1
0.12
C-1-1-45-8
C-1-1-45-10
C-1-1-45-12
C-1-1-45-14
C-1-1-45-16

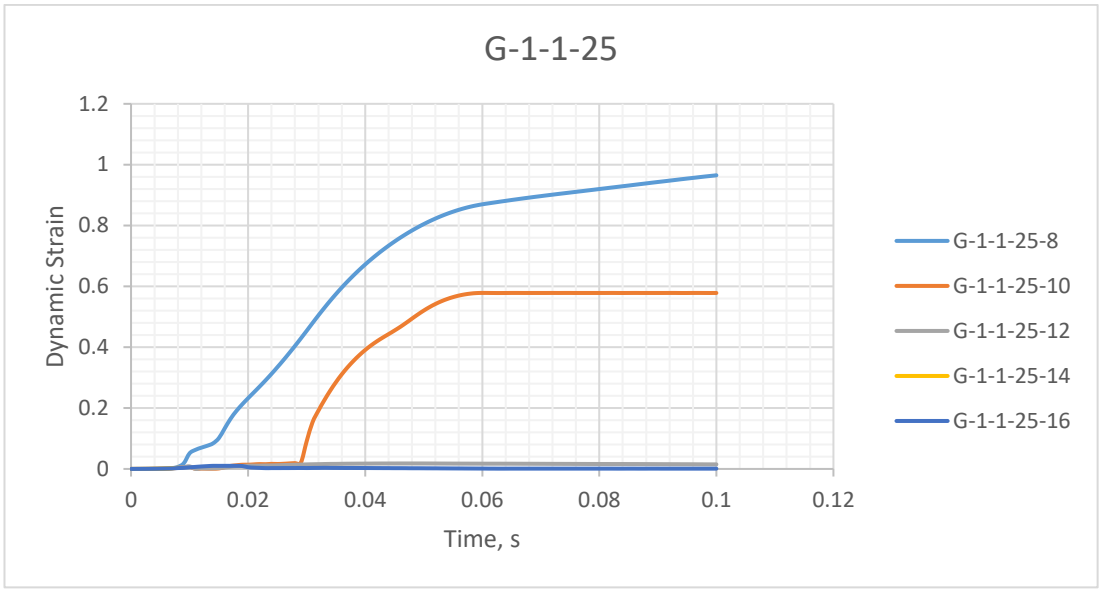
G-1-1-25
Dynamic Strain
Time, s
1.2
1
0.8
0.6
0.4
0.2
0
0
0.02
0.04
0.06
0.08
0.1
0.12
G-1-1-25-8
G-1-1-25-10
G-1-1-25-12
G-1-1-25-14
G-1-1-25-16

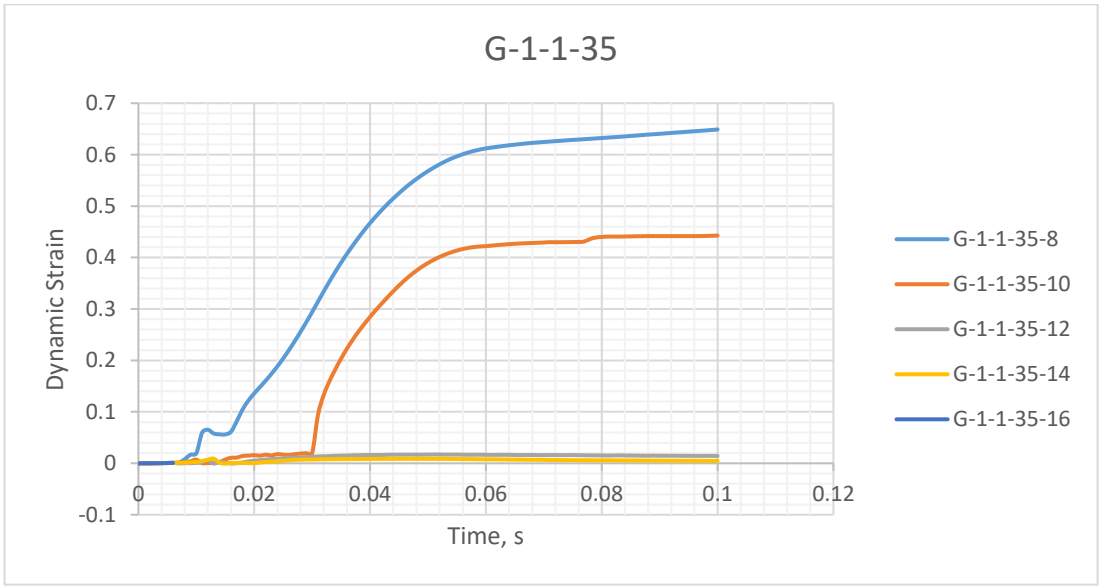
G-1-1-35
Dynamic Strain
Time, s
0.7
0.6
0.5
0.4
0.3
0.2
0.1
0
-0.1
0
0.02
0.04
0.06
0.08
0.1
0.12
G-1-1-35-8
G-1-1-35-10
G-1-1-35-12
G-1-1-35-14
G-1-1-35-16

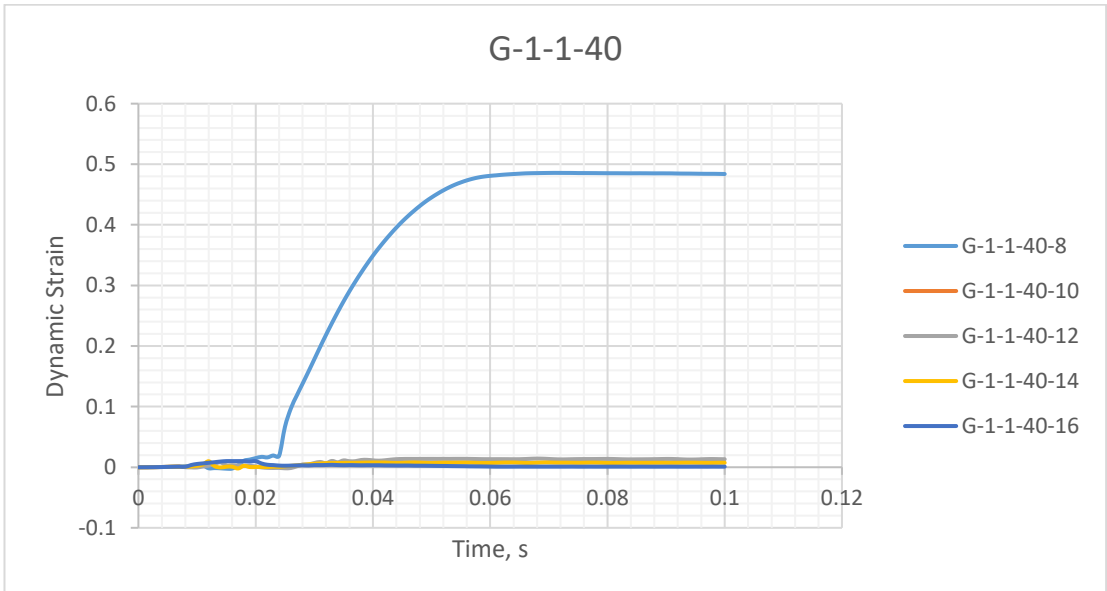
G-1-1-40
Dynamic Strain
Time, s
0.6
0.5
0.4
0.3
0.2
0.1
0
-0.1
0
0.02
0.04
0.06
0.08
0.1
0.12
G-1-1-40-8
G-1-1-40-10
G-1-1-40-12
G-1-1-40-14
G-1-1-40-16

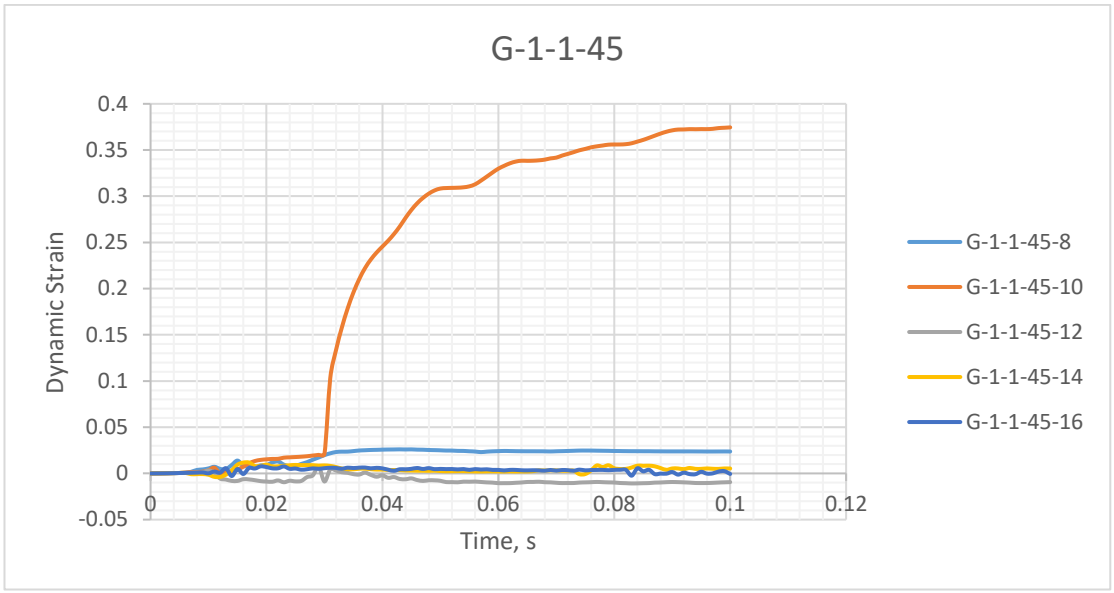

Figure 145: Dynamic strain time histories for AFRP, CFRP and GFRP RC beam models under 320 kN impact load

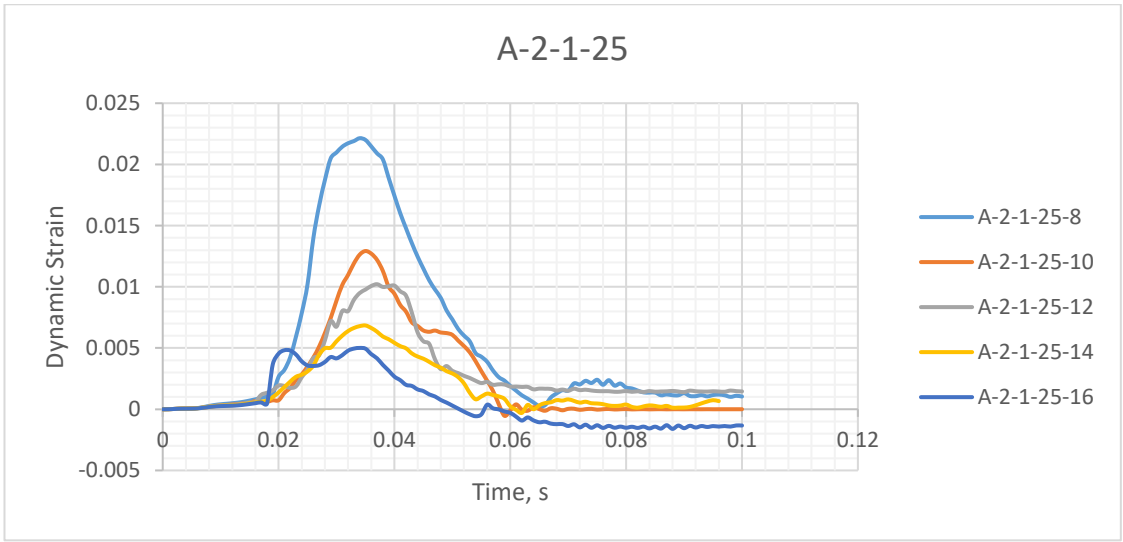

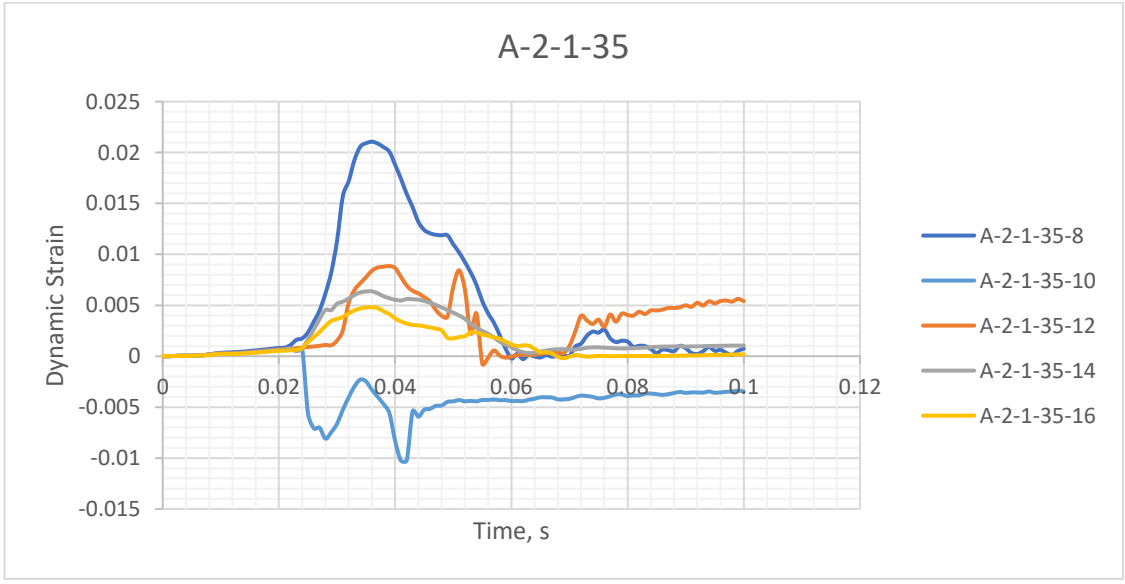

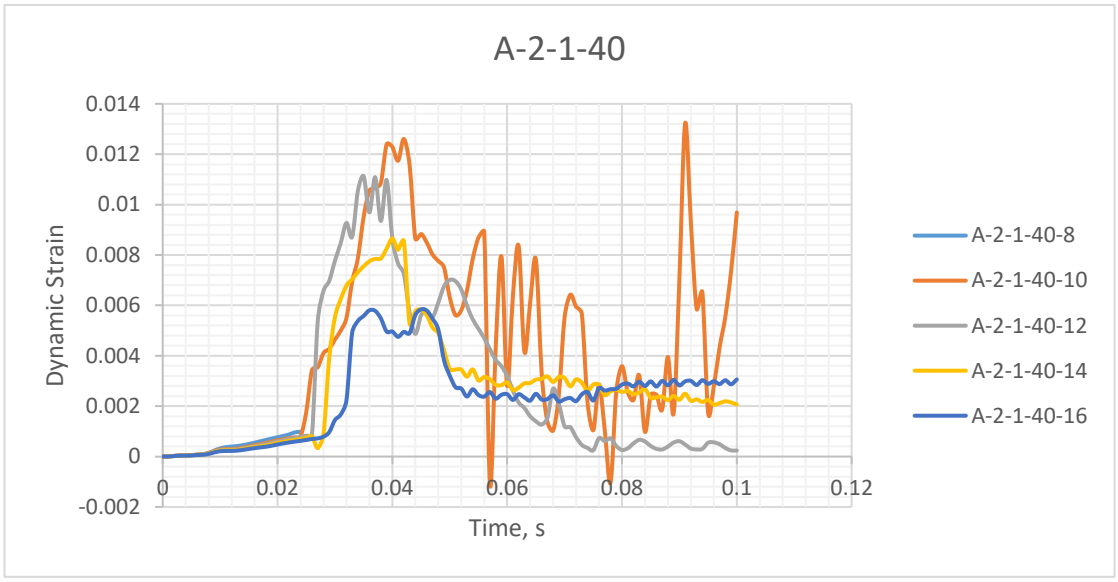
A-2-1-40
Dynamic Strain
Time, s
0.014
0.012
0.01
0.008
0.006
0.004
0.002
0
-0.002
0
0.02
0.04
0.06
0.08
0.1
0.12
A-2-1-40-8
A-2-1-40-10
A-2-1-40-12
A-2-1-40-14
A-2-1-40-16

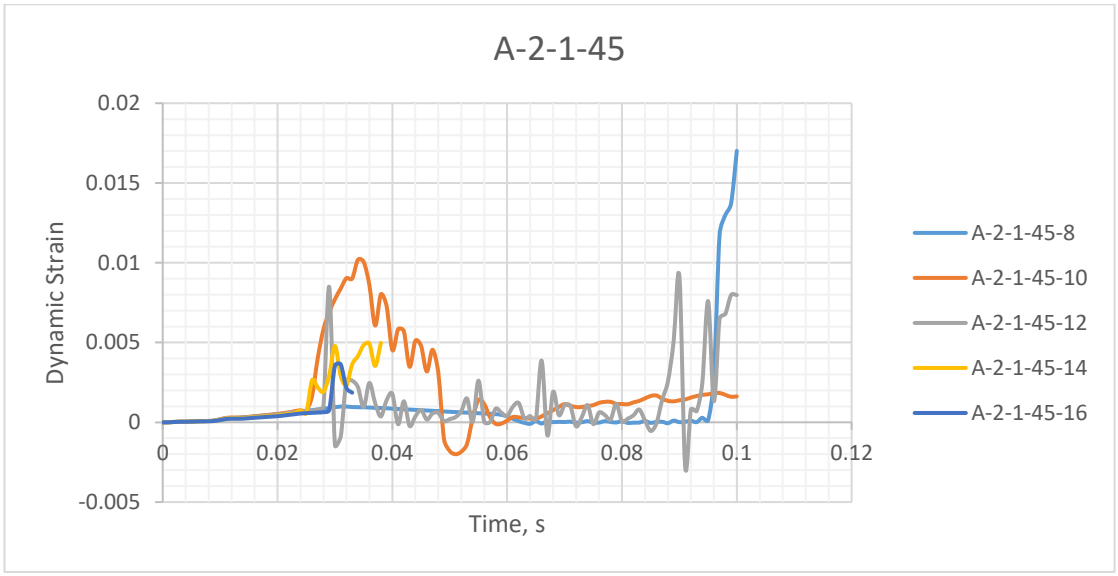
A-2-1-45
Dynamic Strain
Time, s
0.02
0.015
0.01
0.005
0
-0.005
0
0.02
0.04
0.06
0.08
0.1
0.12
A-2-1-45-8
A-2-1-45-10
A-2-1-45-12
A-2-1-45-14
A-2-1-45-16

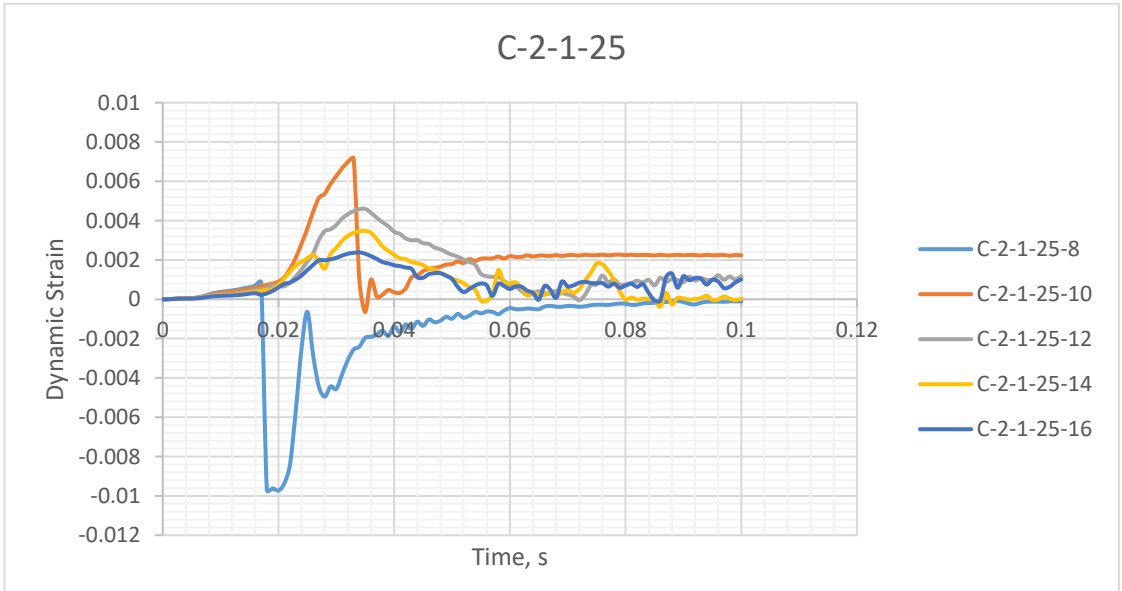
C-2-1-25
Dynamic Strain
Time, s
0.01
0.008
0.006
0.004
0.002
0
-0.002
-0.004
-0.006
-0.008
-0.01
-0.012
0
0.02
0.04
0.06
0.08
0.1
0.12
C-2-1-25-8
C-2-1-25-10
C-2-1-25-12
C-2-1-25-14
C-2-1-25-16

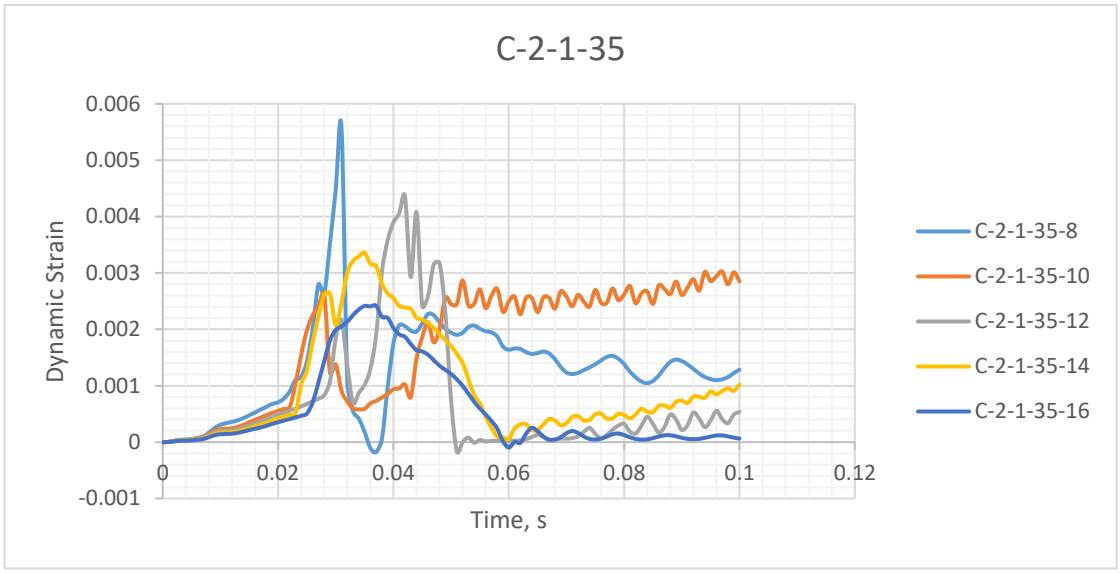
C-2-1-35
Dynamic Strain
0.006
0.005
0.004
0.003
0.002
0.001
0
-0.001
0
0.02
0.04
0.06
0.08
0.1
0.12
Time, s
C-2-1-35-8
C-2-1-35-10
C-2-1-35-12
C-2-1-35-14
C-2-1-35-16

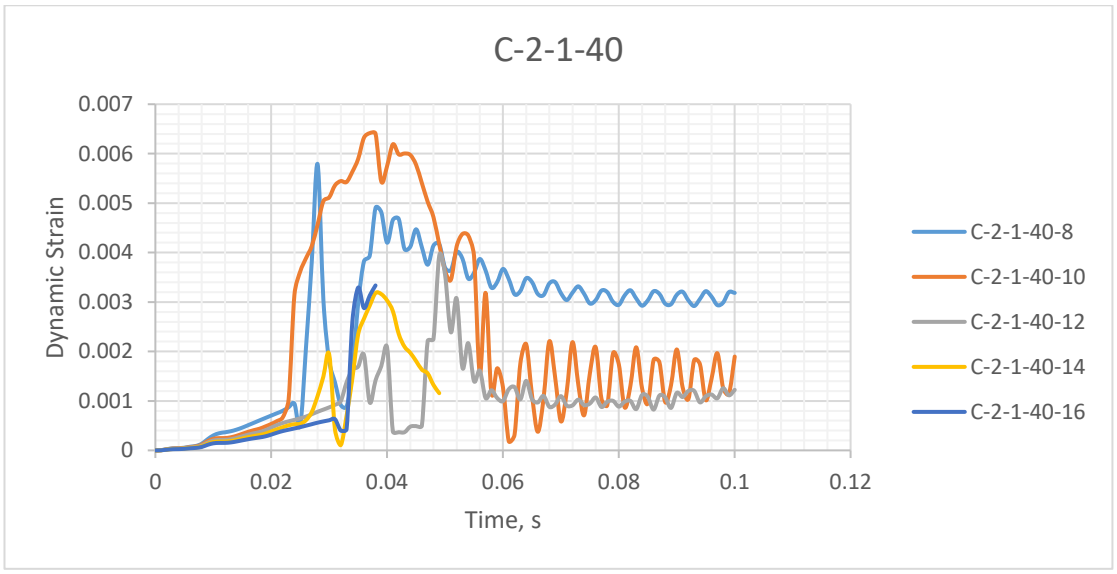
C-2-1-40
Dynamic Strain
0.007
0.006
0.005
0.004
0.003
0.002
0.001
0
0
0.02
0.04
0.06
0.08
0.1
0.12
Time, s
C-2-1-40-8
C-2-1-40-10
C-2-1-40-12
C-2-1-40-14
C-2-1-40-16

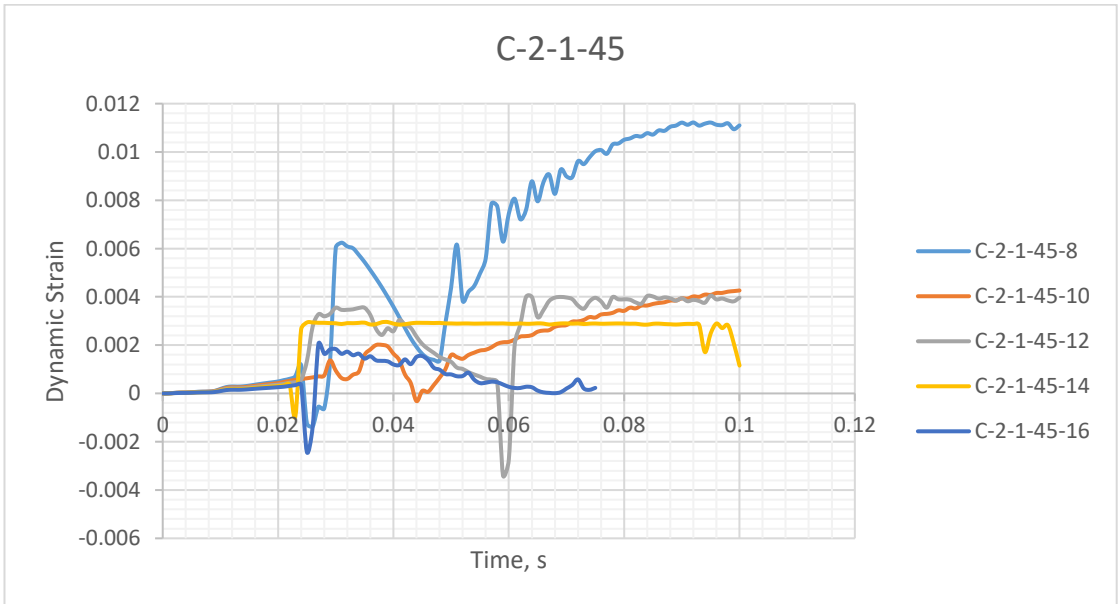
C-2-1-45
Dynamic Strain
0.012
0.01
0.008
0.006
0.004
0.002
0
-0.002
-0.004
-0.006
0
0.02
0.04
0.06
0.08
0.1
0.12
Time, s
C-2-1-45-8
C-2-1-45-10
C-2-1-45-12
C-2-1-45-14
C-2-1-45-16

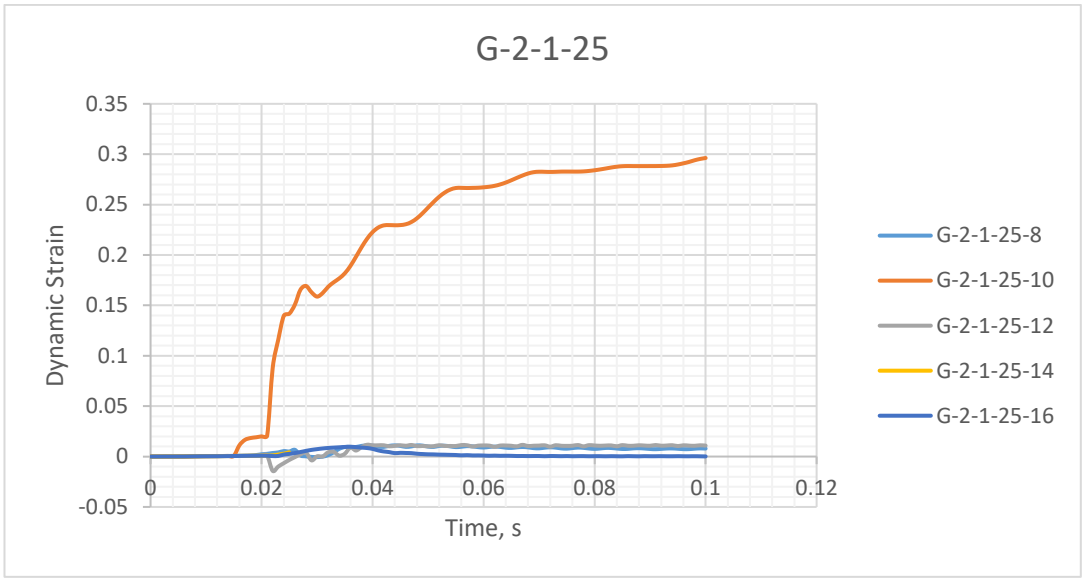
G-2-1-25
Dynamic Strain
Time, s
0.35
0.3
0.25
0.2
0.15
0.1
0.05
0
-0.05
0
0.02
0.04
0.06
0.08
0.1
0.12
G-2-1-25-8
G-2-1-25-10
G-2-1-25-12
G-2-1-25-14
G-2-1-25-16

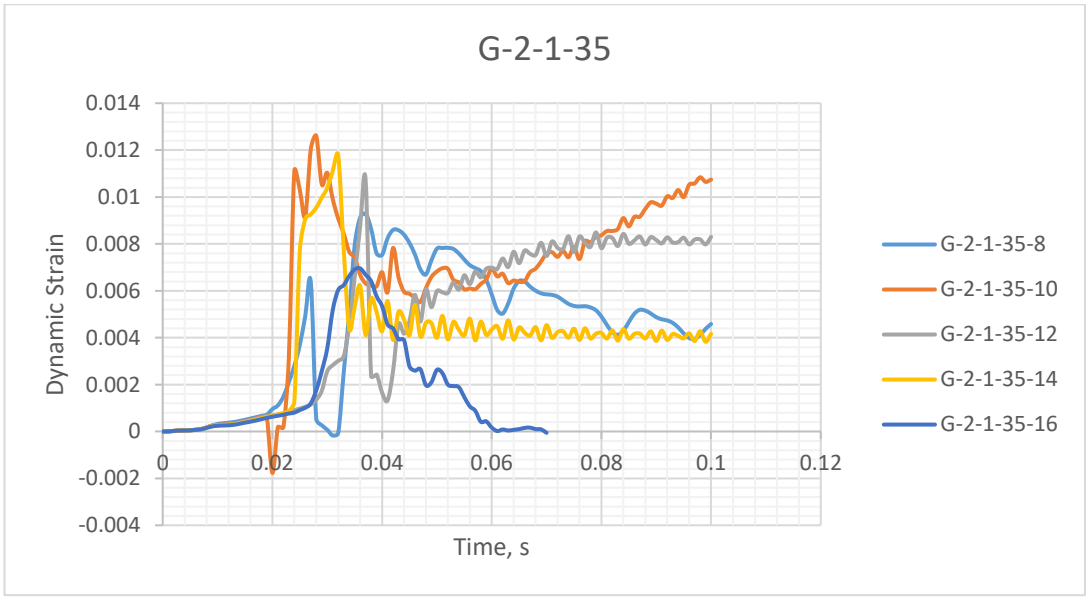
G-2-1-35
Dynamic Strain
Time, s
0.014
0.012
0.01
0.008
0.006
0.004
0.002
0
-0.002
-0.004
0
0.02
0.04
0.06
0.08
0.1
0.12
G-2-1-35-8
G-2-1-35-10
G-2-1-35-12
G-2-1-35-14
G-2-1-35-16

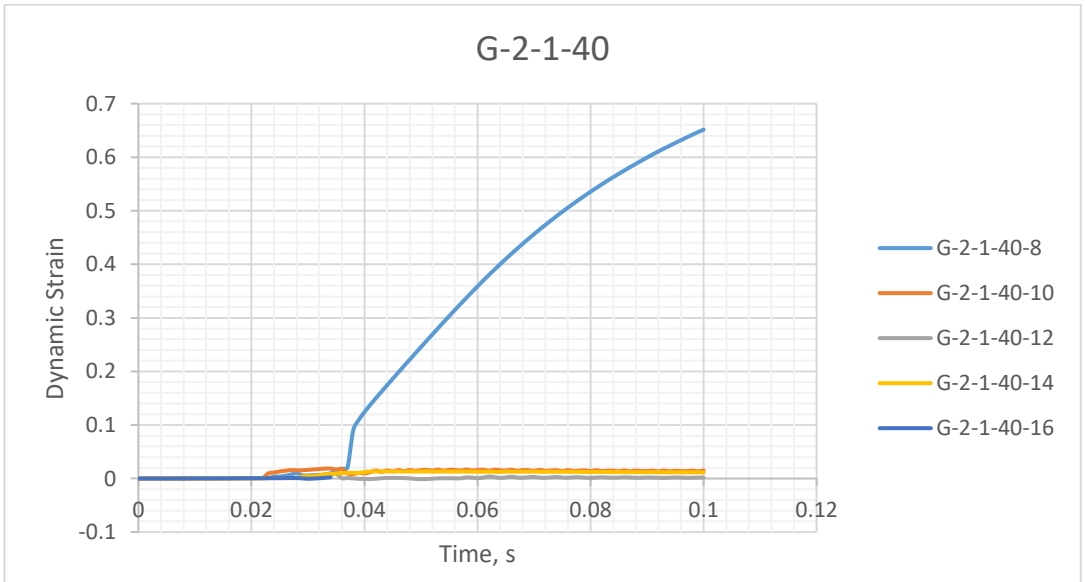
G-2-1-40
Dynamic Strain
Time, s
0.7
0.6
0.5
0.4
0.3
0.2
0.1
0
-0.1
0
0.02
0.04
0.06
0.08
0.1
0.12
G-2-1-40-8
G-2-1-40-10
G-2-1-40-12
G-2-1-40-14
G-2-1-40-16

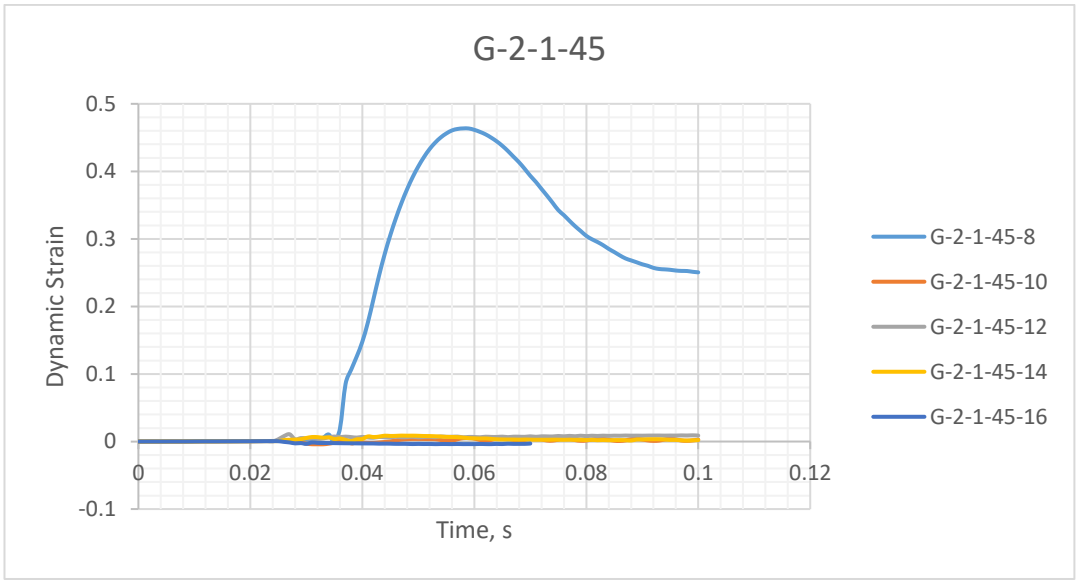

Figure 146: Dynamic strain time histories for AFRP, CFRP and GFRP RC beam models under 80 kN impact load.

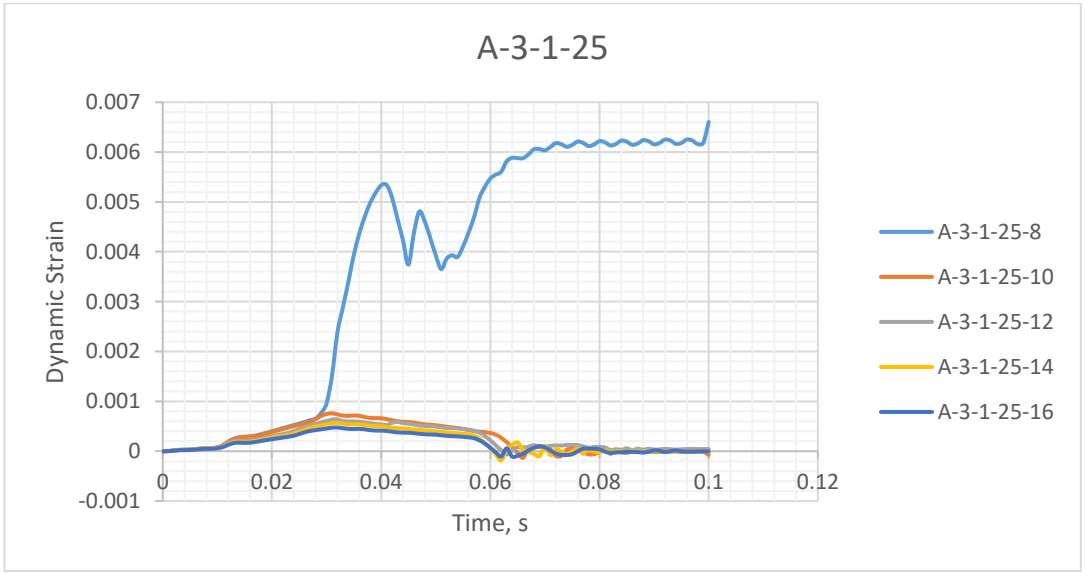

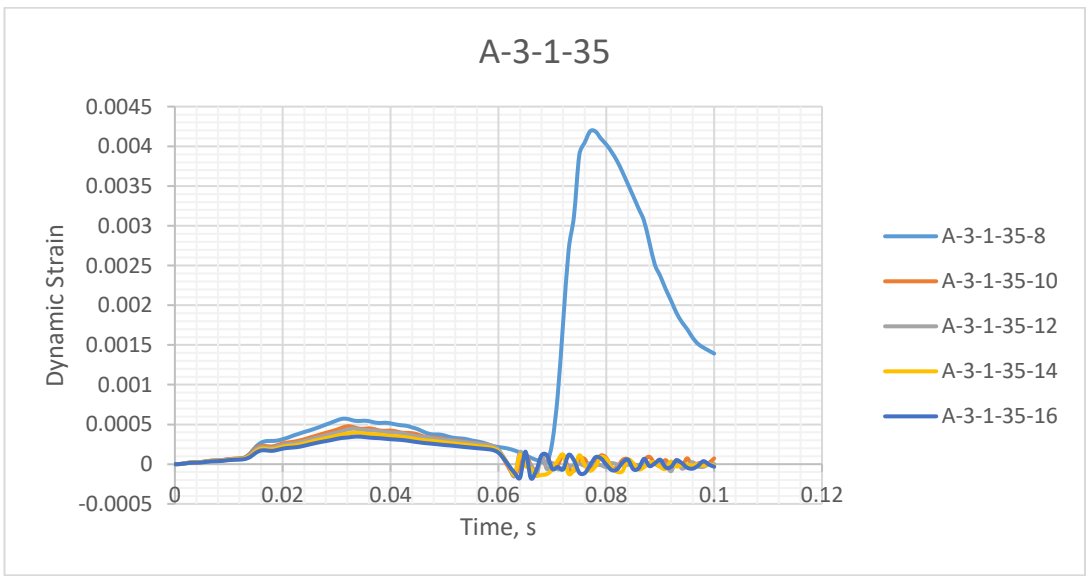

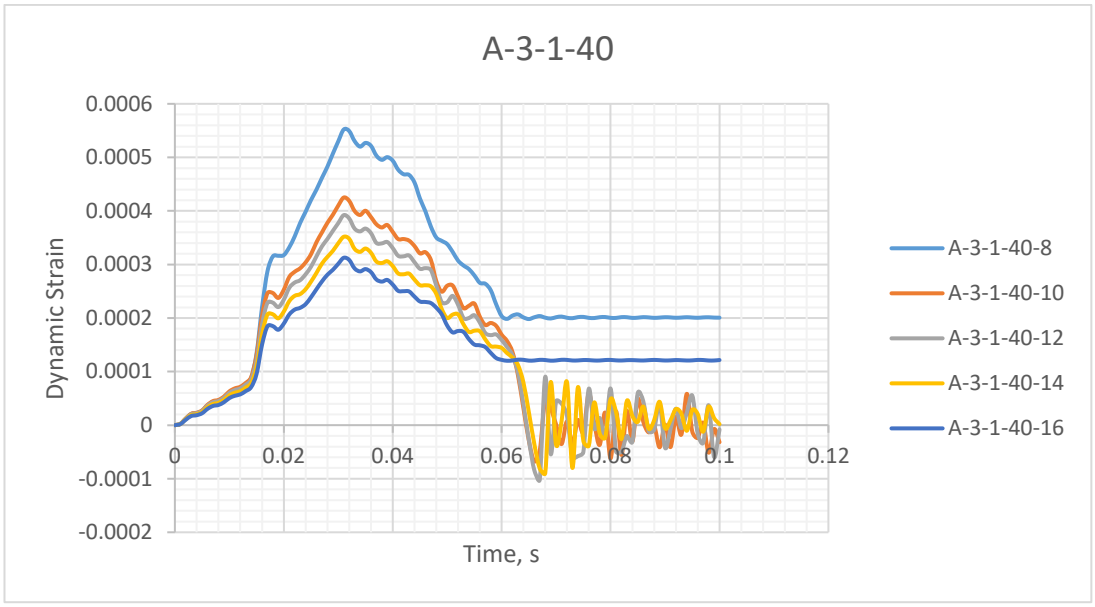
A-3-1-40
0.0006
0.0005
0.0004
0.0003
0.0002
0.0001
0
-0.0001
-0.0002
Dynamic Strain
0
0.02
0.04
0.06
0.08
0.1
0.12
Time, s
A-3-1-40-8
A-3-1-40-10
A-3-1-40-12
A-3-1-40-14
A-3-1-40-16

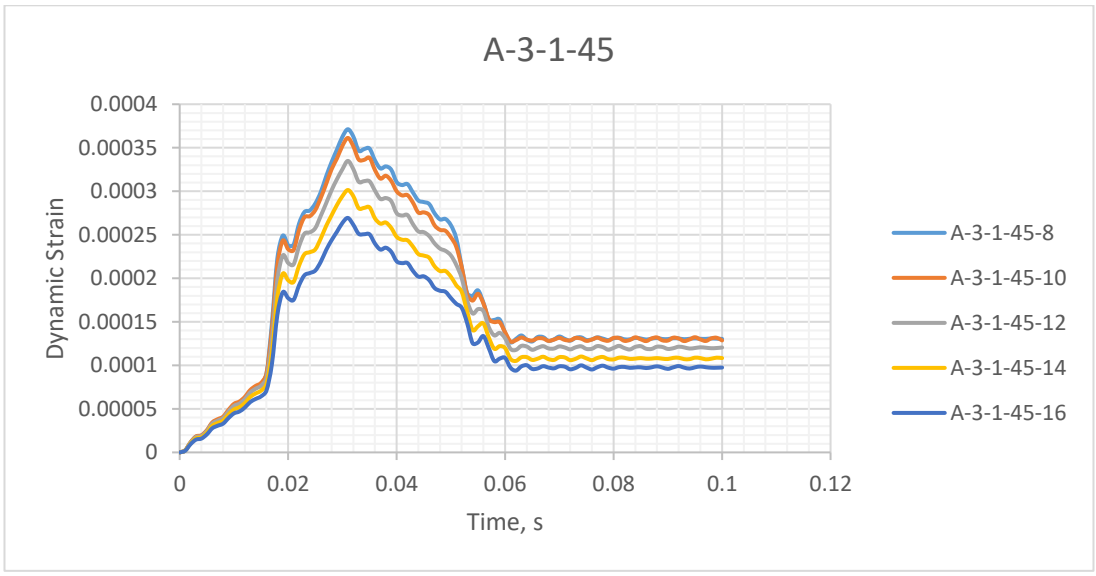
A-3-1-45
0.0004
0.00035
0.0003
0.00025
0.0002
0.00015
0.0001
0.00005
0
Dynamic Strain
0
0.02
0.04
0.06
0.08
0.1
0.12
Time, s
A-3-1-45-8
A-3-1-45-10
A-3-1-45-12
A-3-1-45-14
A-3-1-45-16

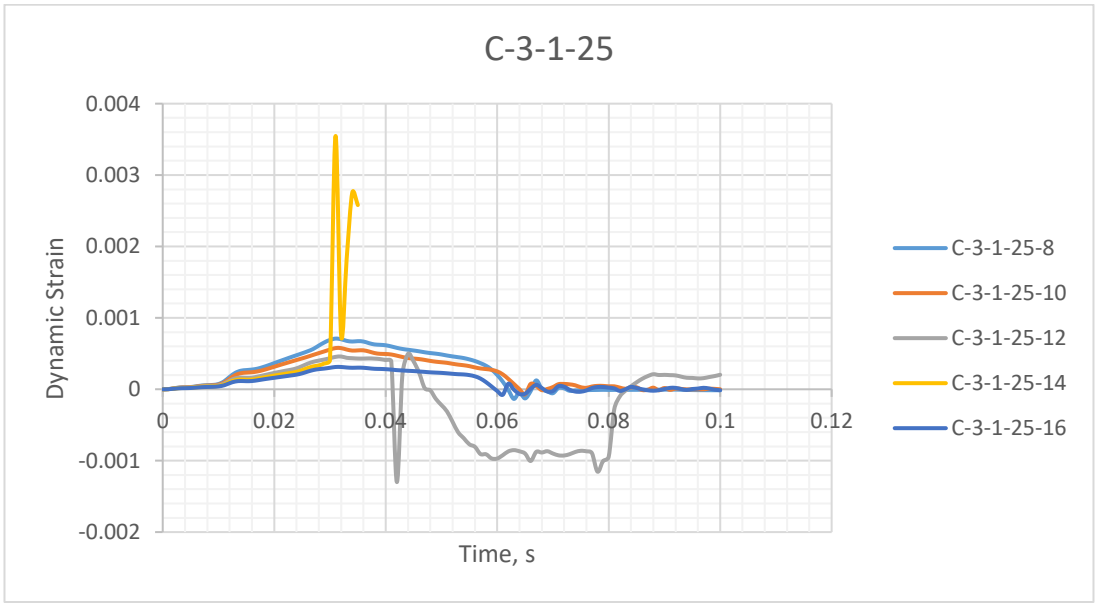
C-3-1-25
0.004
0.003
0.002
0.001
0
-0.001
-0.002
Dynamic Strain
0
0.02
0.04
0.06
0.08
0.1
0.12
Time, s
C-3-1-25-8
C-3-1-25-10
C-3-1-25-12
C-3-1-25-14
C-3-1-25-16

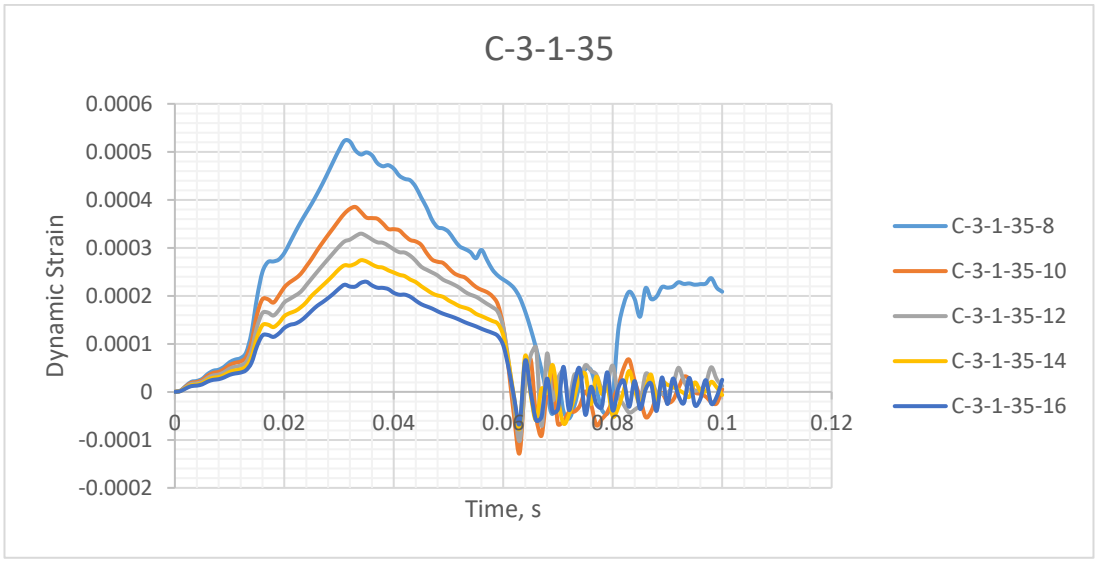
C-3-1-35
Dynamic Strain
0.0006
0.0005
0.0004
0.0003
0.0002
0.0001
0
-0.0001
-0.0002
0
0.02
0.04
0.06
0.08
0.1
0.12
Time, s
C-3-1-35-8
C-3-1-35-10
C-3-1-35-12
C-3-1-35-14
C-3-1-35-16

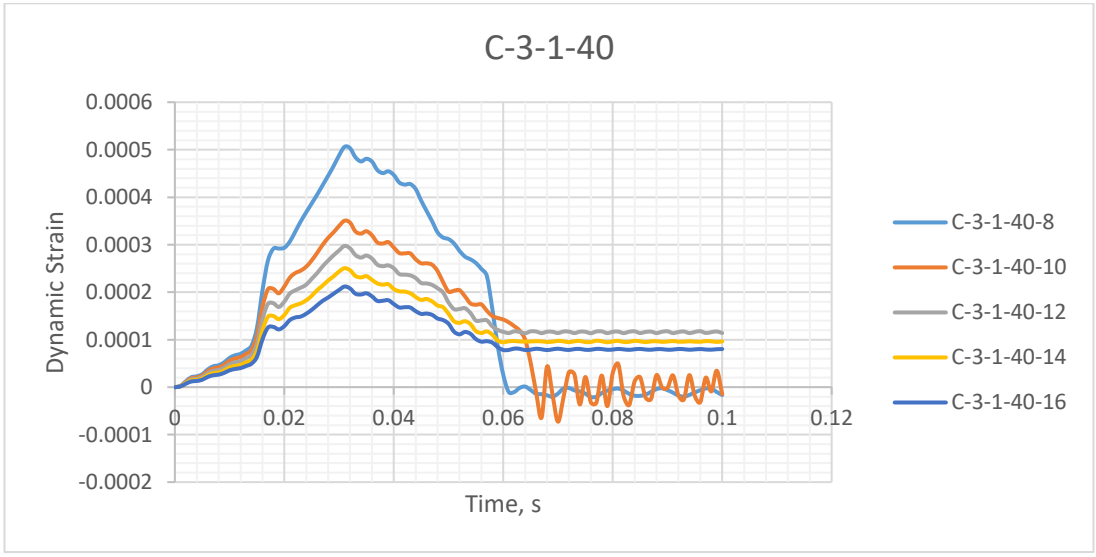
C-3-1-40
Dynamic Strain
0.0006
0.0005
0.0004
0.0003
0.0002
0.0001
0
-0.0001
-0.0002
0
0.02
0.04
0.06
0.08
0.1
0.12
Time, s
C-3-1-40-8
C-3-1-40-10
C-3-1-40-12
C-3-1-40-14
C-3-1-40-16

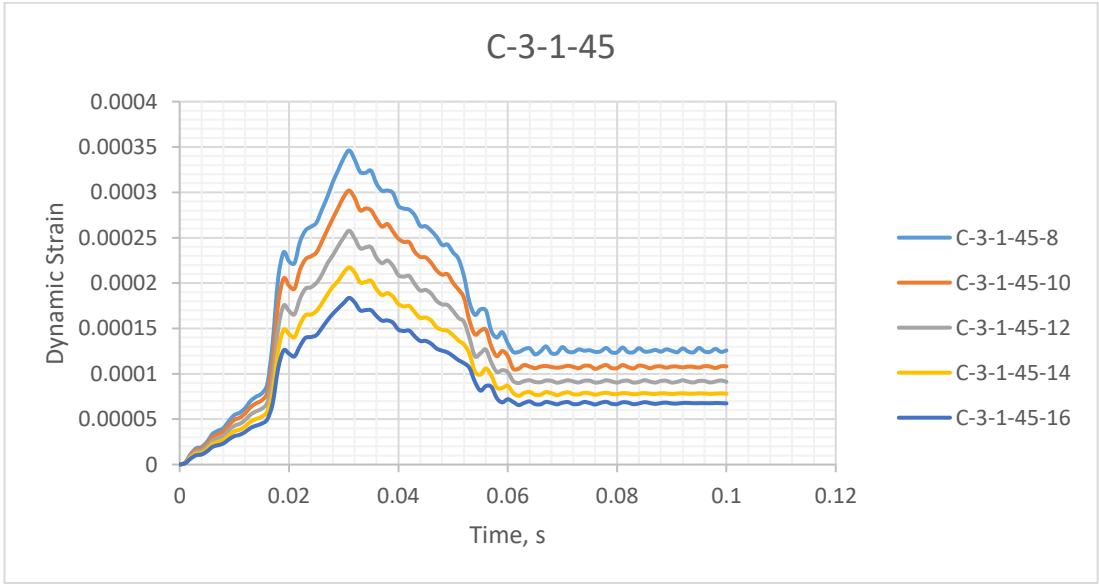
C-3-1-45
Dynamic Strain
0.0004
0.00035
0.0003
0.00025
0.0002
0.00015
0.0001
0.00005
0
0
0.02
0.04
0.06
0.08
0.1
0.12
Time, s
C-3-1-45-8
C-3-1-45-10
C-3-1-45-12
C-3-1-45-14
C-3-1-45-16

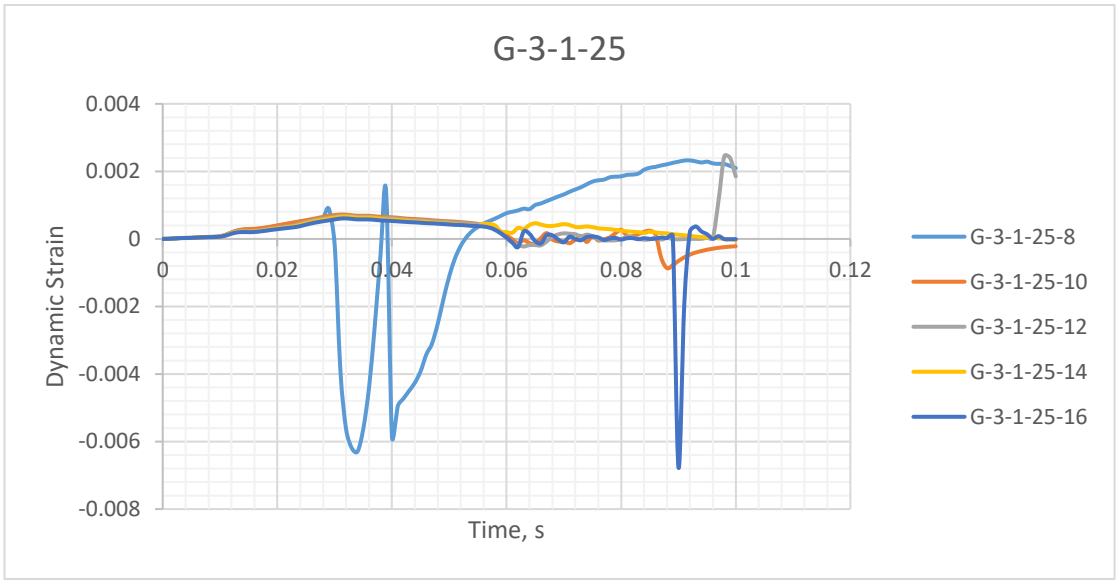
G-3-1-25
0.004
0.002
0
-0.002
-0.004
-0.006
-0.008
Dynamic Strain
0
0.02
0.04
0.06
0.08
0.1
0.12
Time, s
G-3-1-25-8
G-3-1-25-10
G-3-1-25-12
G-3-1-25-14
G-3-1-25-16

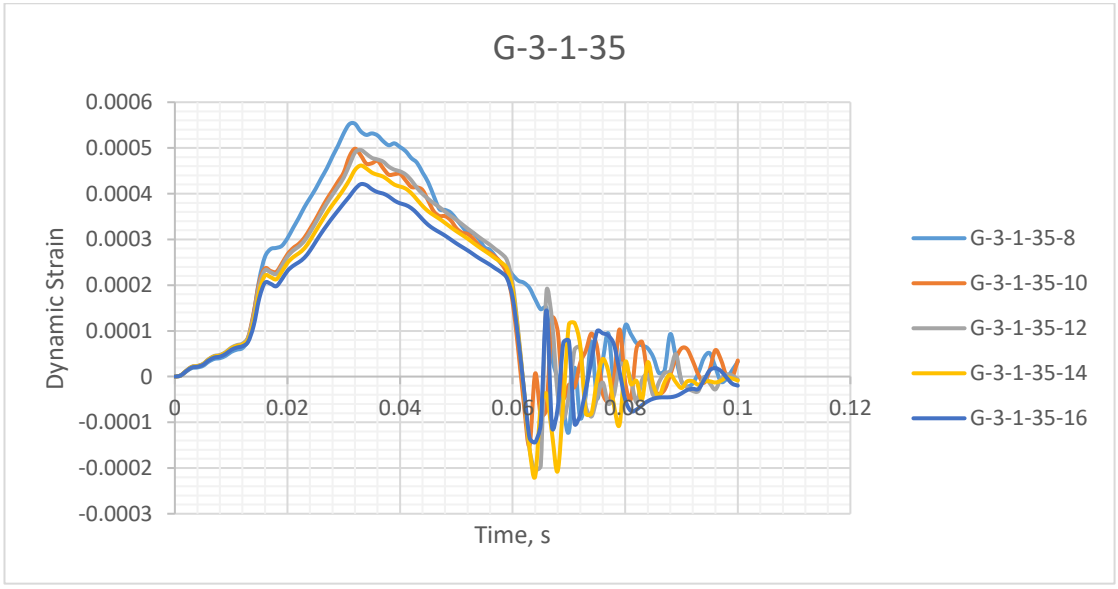
G-3-1-35
0.0006
0.0005
0.0004
0.0003
0.0002
0.0001
0
-0.0001
-0.0002
-0.0003
Dynamic Strain
0
0.02
0.04
0.06
0.08
0.1
0.12
Time, s
G-3-1-35-8
G-3-1-35-10
G-3-1-35-12
G-3-1-35-14
G-3-1-35-16

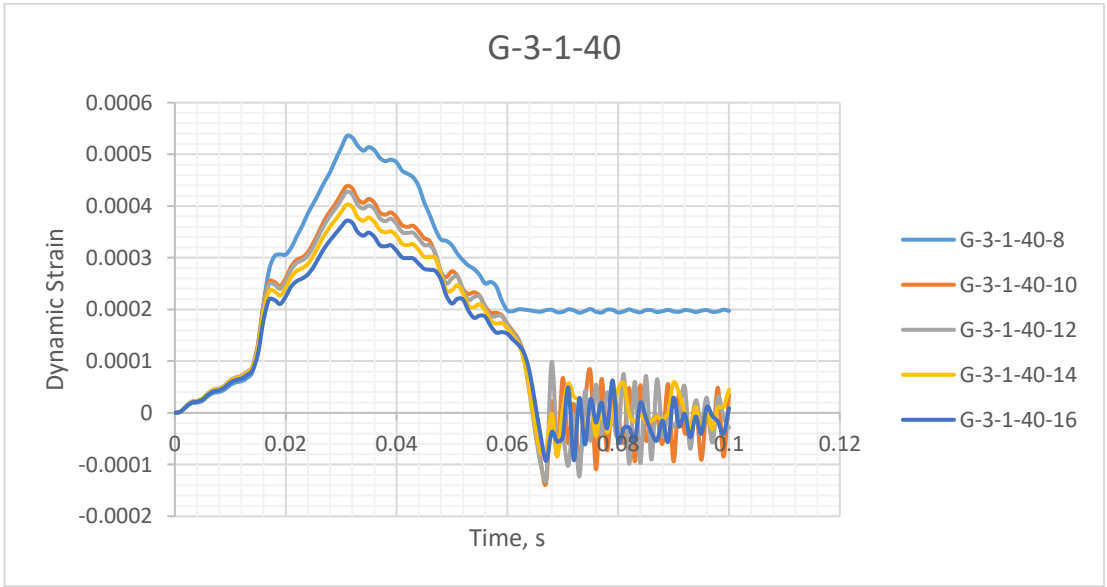
G-3-1-40
0.0006
0.0005
0.0004
0.0003
0.0002
0.0001
0
-0.0001
-0.0002
Dynamic Strain
0
0.02
0.04
0.06
0.08
0.1
0.12
Time, s
G-3-1-40-8
G-3-1-40-10
G-3-1-40-12
G-3-1-40-14
G-3-1-40-16

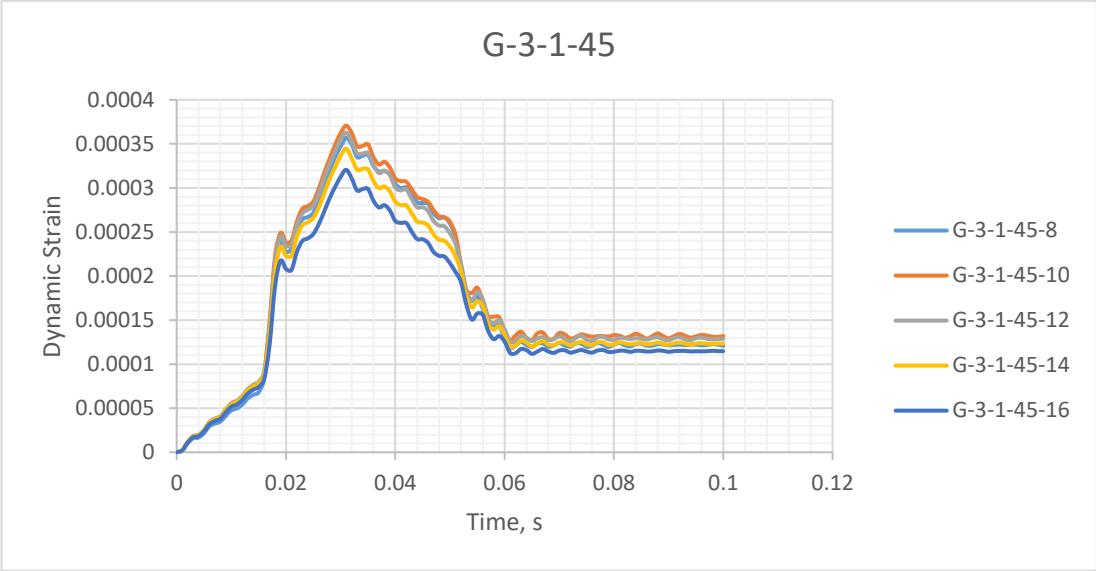

Figure 147: Dynamic strain time histories for AFRP, CFRP and GFRP RC beam models under 40 kN impact load.

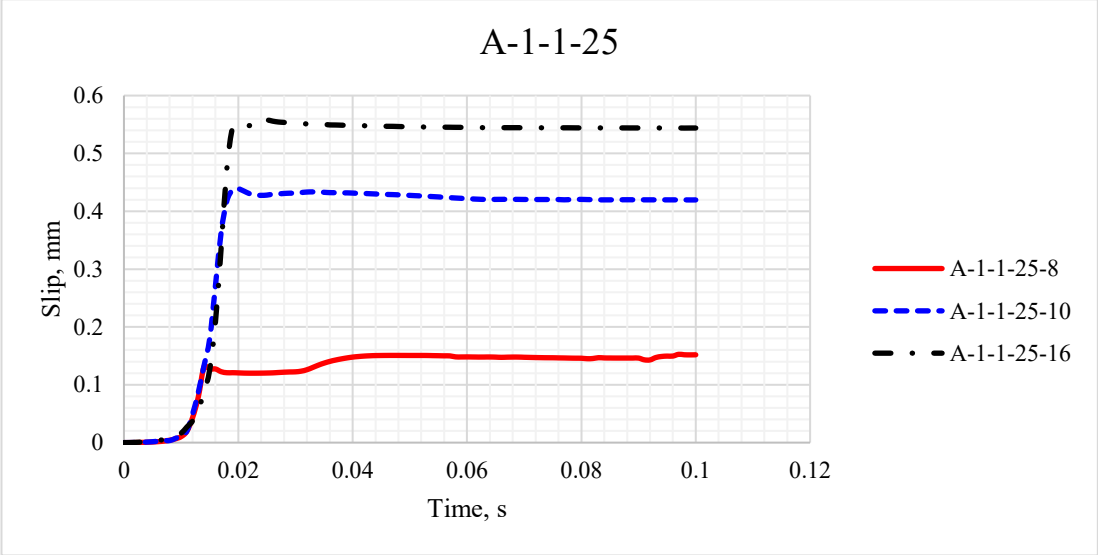

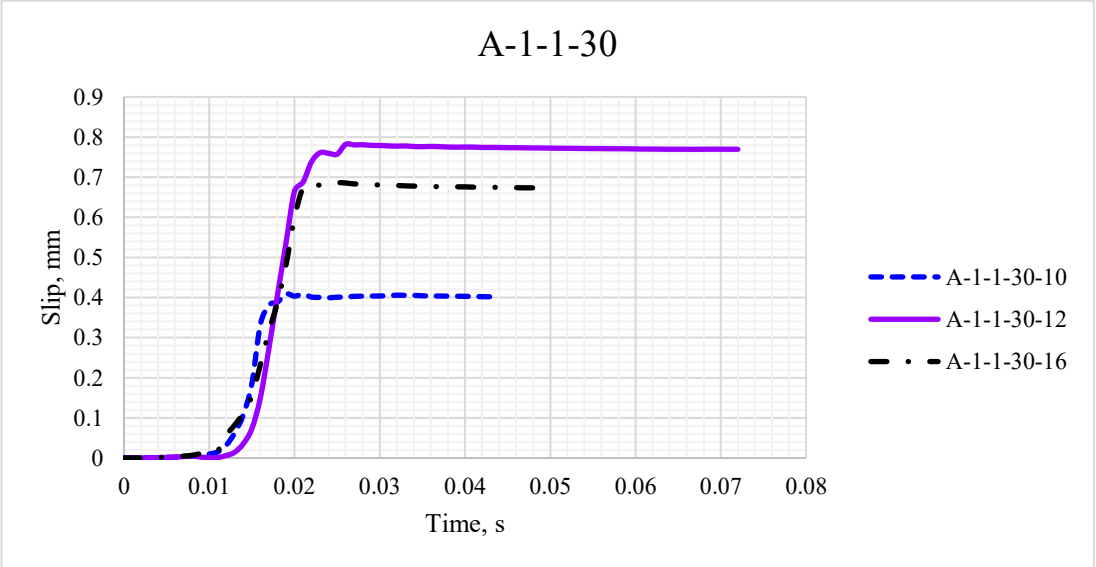

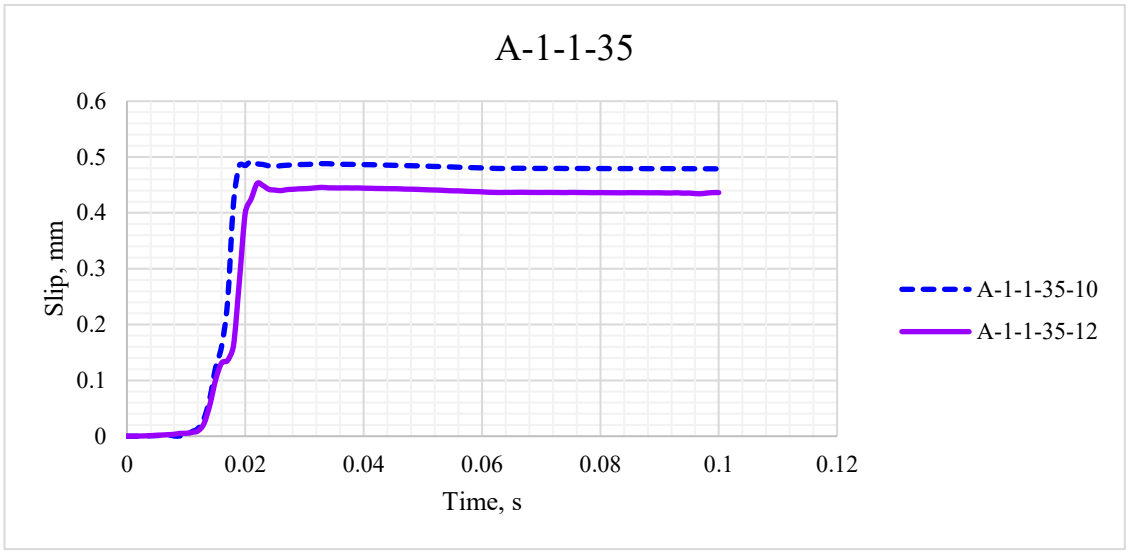
A-1-1-35
Slip, mm
0.6
0.5
0.4
0.3
0.2
0.1
0
0
0.02
0.04
0.06
0.08
0.1
0.12
Time, s
A-1-1-35-10
A-1-1-35-12

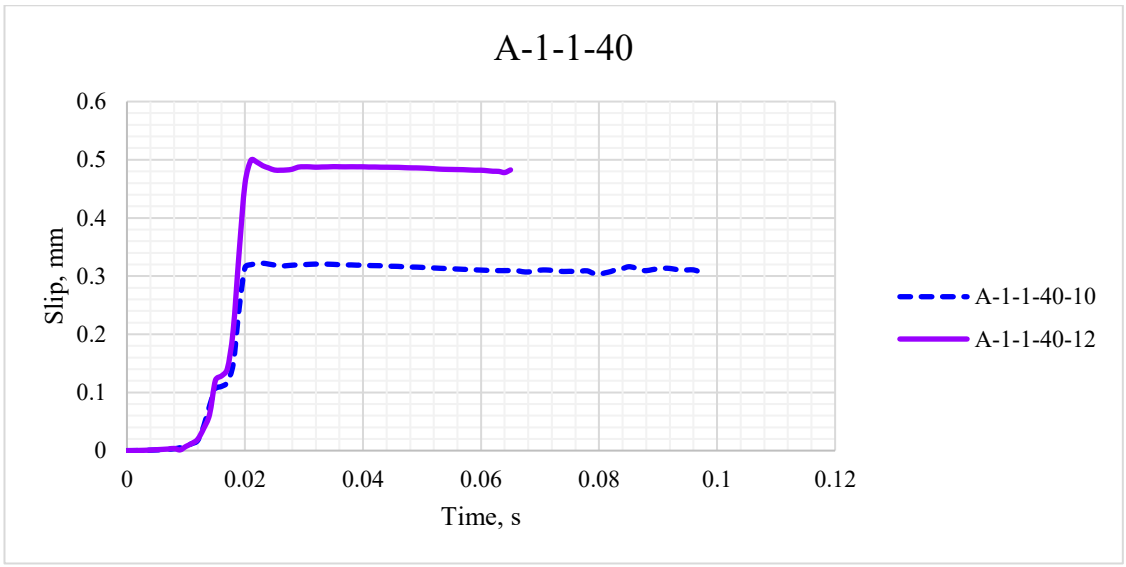
A-1-1-40
Slip, mm
0.6
0.5
0.4
0.3
0.2
0.1
0
0
0.02
0.04
0.06
0.08
0.1
0.12
Time, s
A-1-1-40-10
A-1-1-40-12

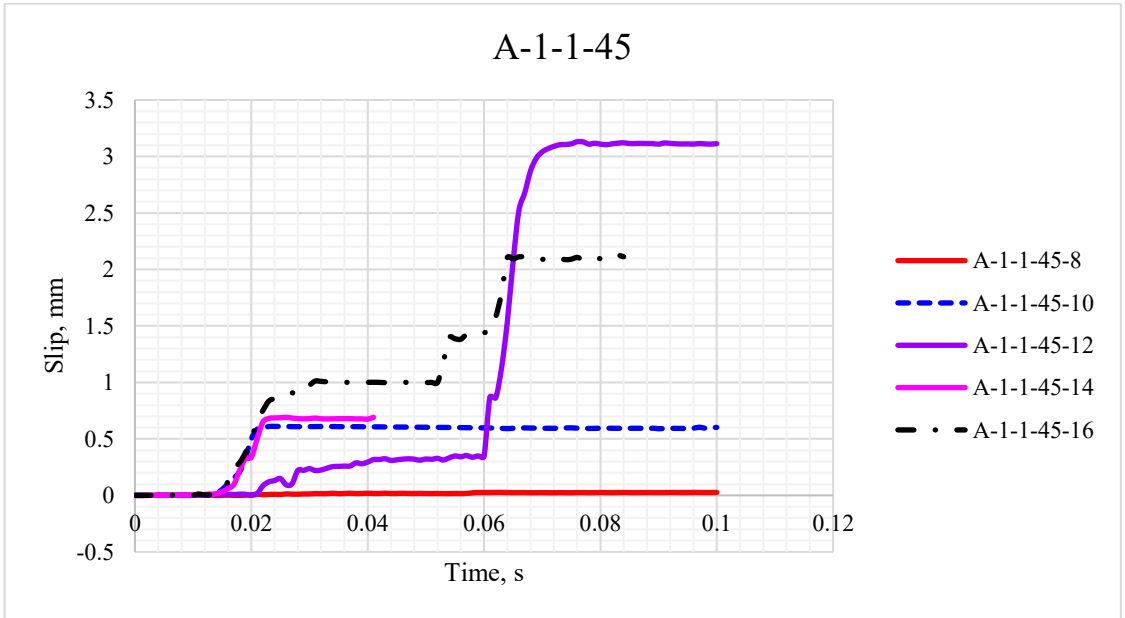
A-1-1-45
Slip, mm
3.5
3
2.5
2
1.5
1
0.5
0
-0.5
0
0.02
0.04
0.06
0.08
0.1
0.12
Time, s
A-1-1-45-8
A-1-1-45-10
A-1-1-45-12
A-1-1-45-14
A-1-1-45-16

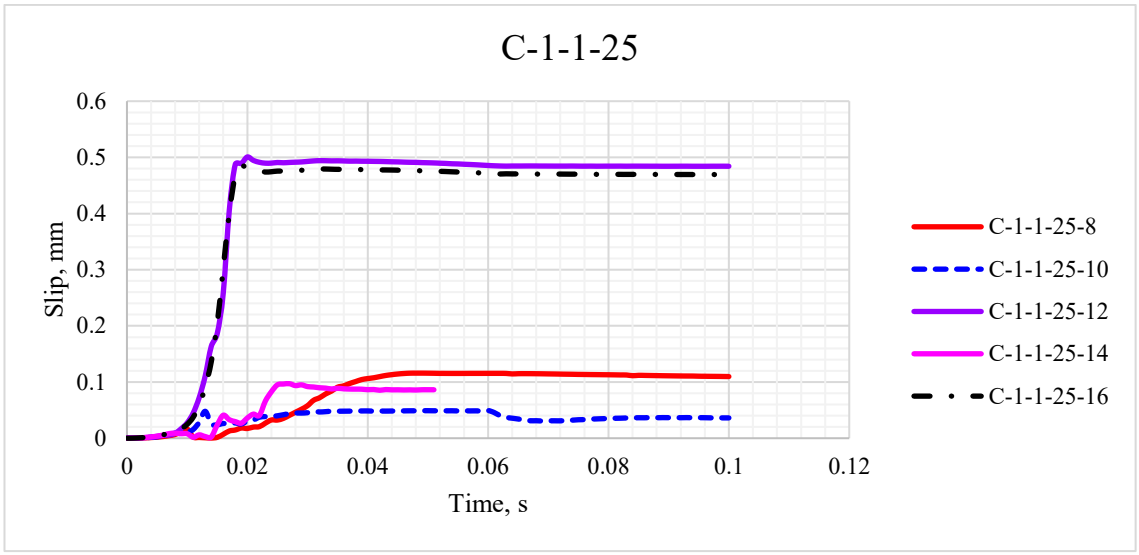
C-1-1-25
Slip, mm
0.6
0.5
0.4
0.3
0.2
0.1
0
0
0.02
0.04
0.06
0.08
0.1
0.12
Time, s
C-1-1-25-8
C-1-1-25-10
C-1-1-25-12
C-1-1-25-14
C-1-1-25-16

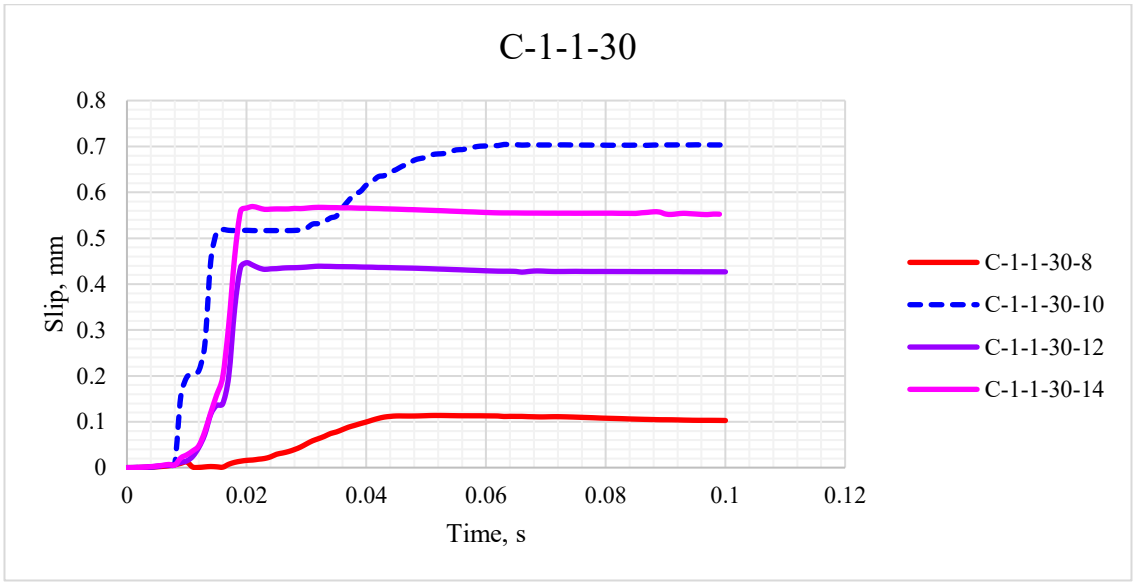
C-1-1-30
Slip, mm
0.8
0.7
0.6
0.5
0.4
0.3
0.2
0.1
0
0
0.02
0.04
0.06
0.08
0.1
0.12
Time, s
C-1-1-30-8
C-1-1-30-10
C-1-1-30-12
C-1-1-30-14

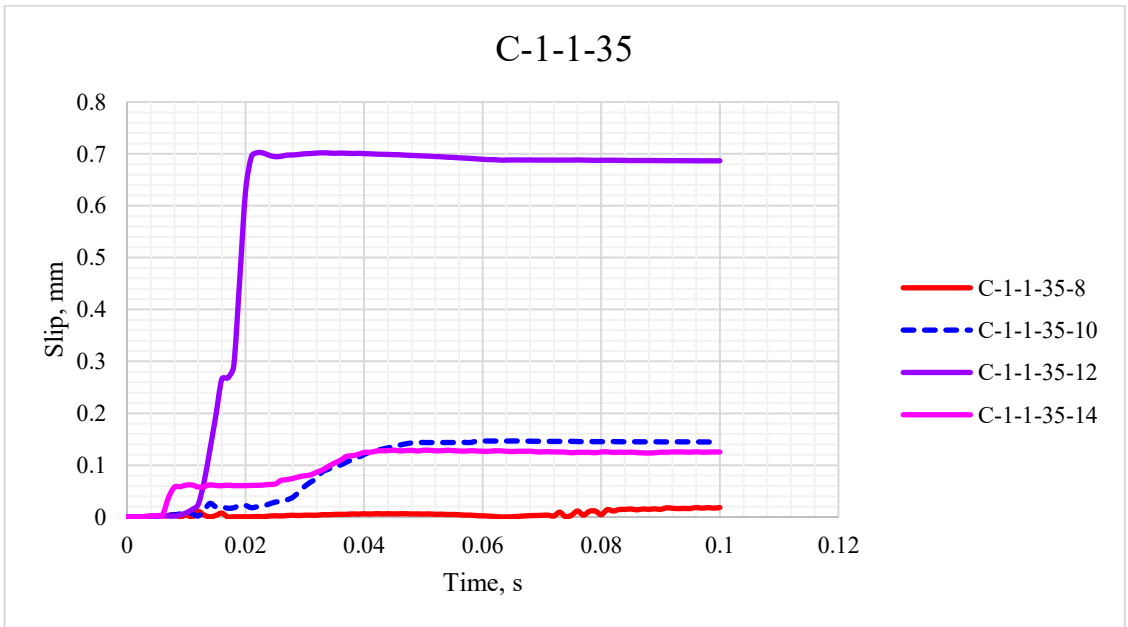
C-1-1-35
Slip, mm
0.8
0.7
0.6
0.5
0.4
0.3
0.2
0.1
0
0
0.02
0.04
0.06
0.08
0.1
0.12
Time, s
C-1-1-35-8
C-1-1-35-10
C-1-1-35-12
C-1-1-35-14

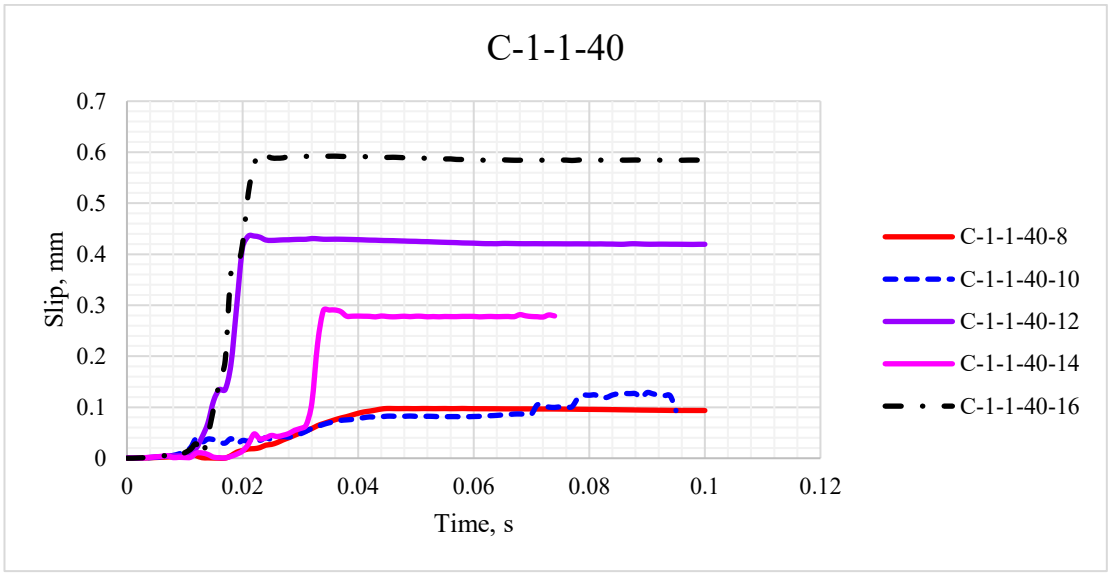
C-1-1-40
Slip, mm
Time, s
0
0.1
0.2
0.3
0.4
0.5
0.6
0.7
0.02
0.04
0.06
0.08
0.12
C-1-1-40-8
C-1-1-40-10
C-1-1-40-12
C-1-1-40-14
C-1-1-40-16

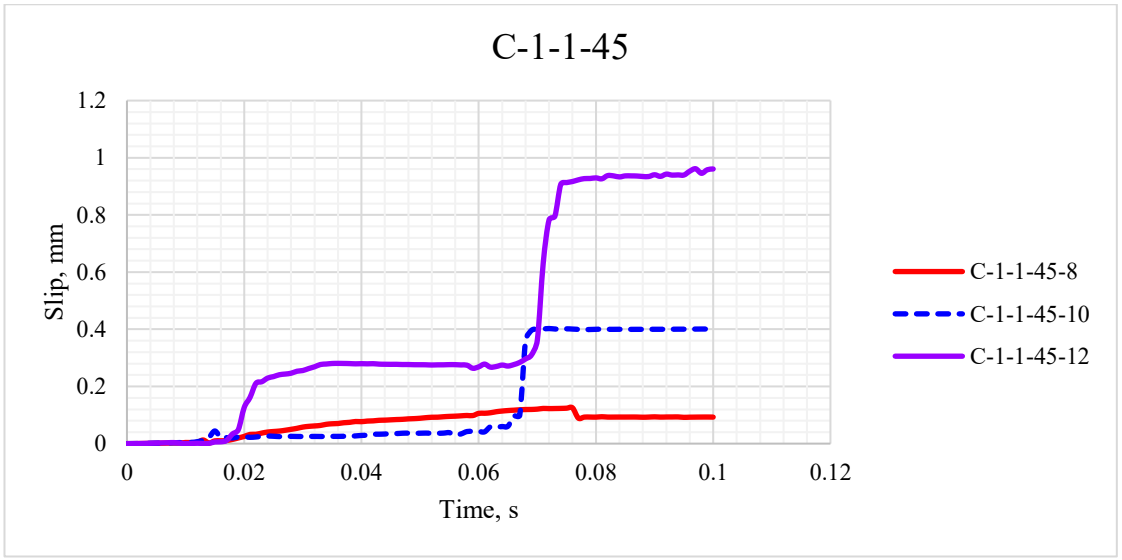
C-1-1-45
Slip, mm
Time, s
0
0.2
0.4
0.6
0.8
1
1.2
0.02
0.04
0.06
0.08
0.1
0.12
C-1-1-45-8
C-1-1-45-10
C-1-1-45-12

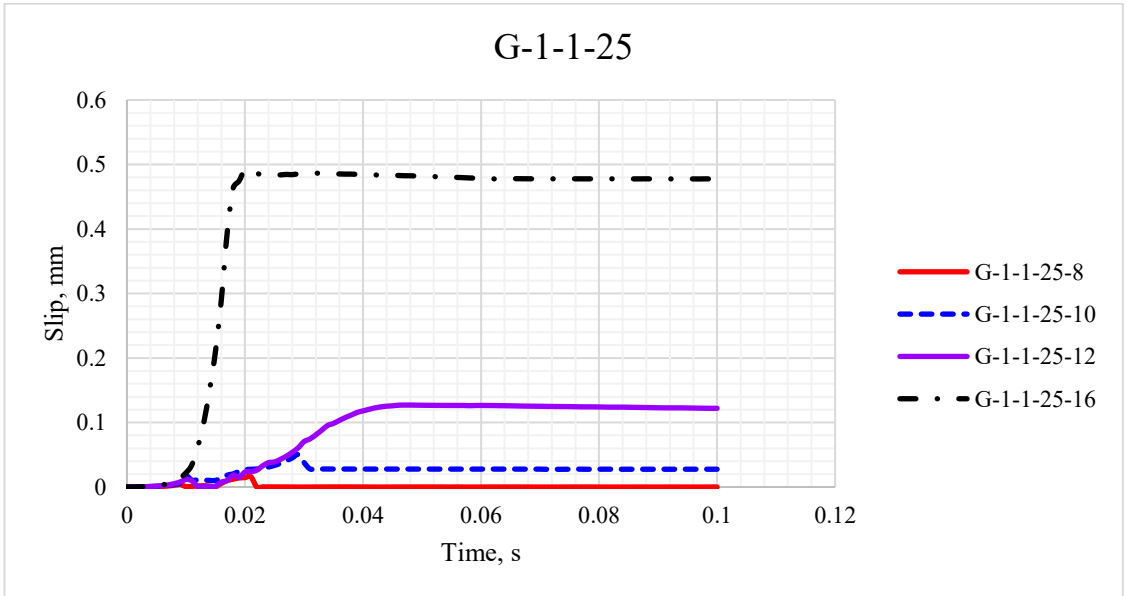
G-1-1-25
Slip, mm
Time, s
0
0.1
0.2
0.3
0.4
0.5
0.6
0.02
0.04
0.06
0.08
0.1
0.12
G-1-1-25-8
G-1-1-25-10
G-1-1-25-12
G-1-1-25-16

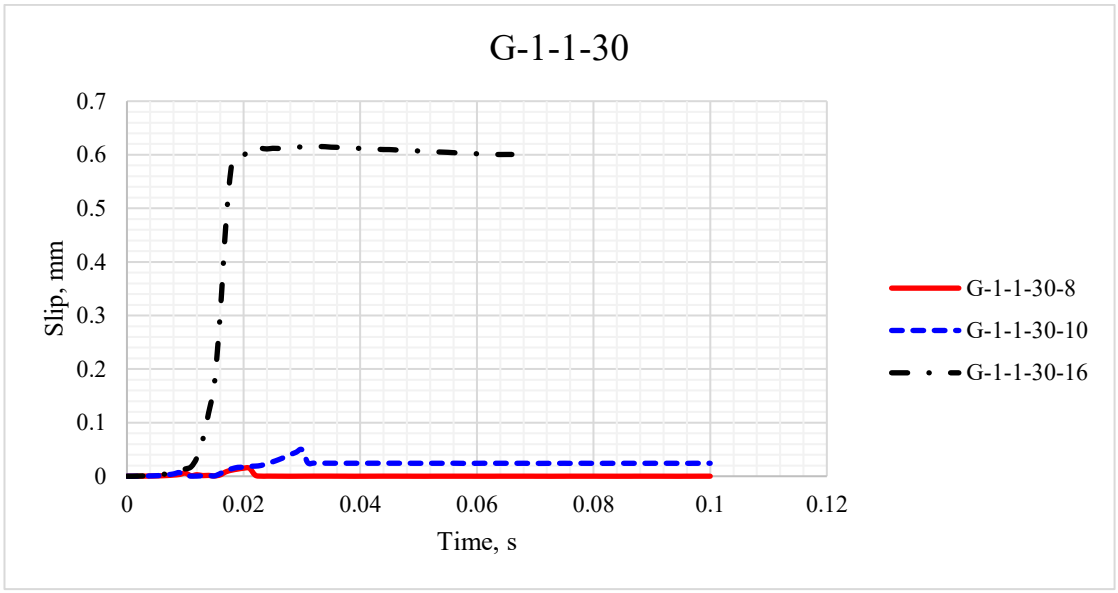
G-1-1-30
Slip, mm
Time, s
0.7
0.6
0.5
0.4
0.3
0.2
0.1
0
0
0.02
0.04
0.06
0.08
0.1
0.12
G-1-1-30-8
G-1-1-30-10
G-1-1-30-16

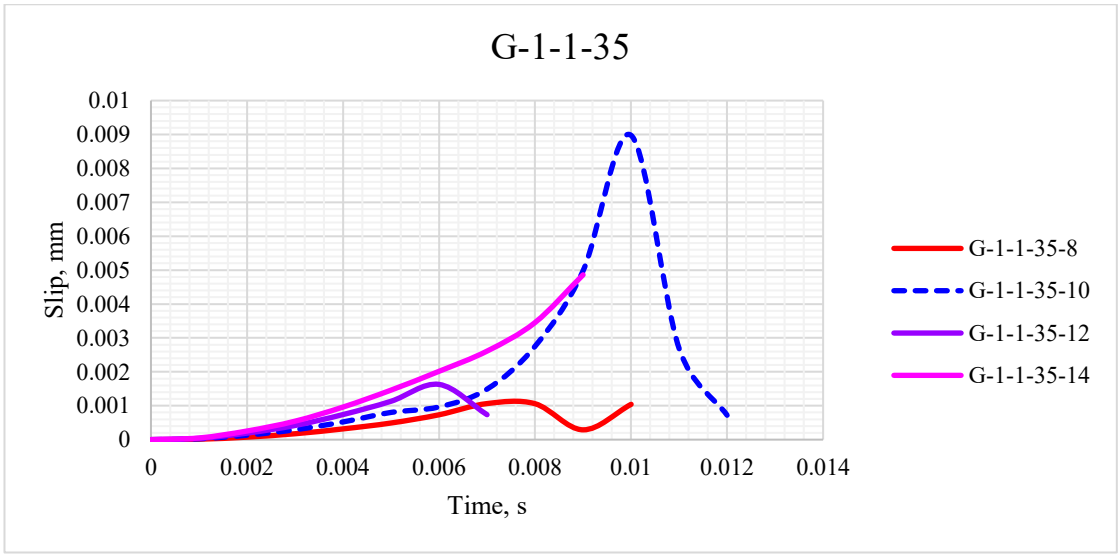
G-1-1-35
Slip, mm
Time, s
0.01
0.009
0.008
0.007
0.006
0.005
0.004
0.003
0.002
0.001
0
0
0.002
0.004
0.006
0.008
0.01
0.012
0.014
G-1-1-35-8
G-1-1-35-10
G-1-1-35-12
G-1-1-35-14

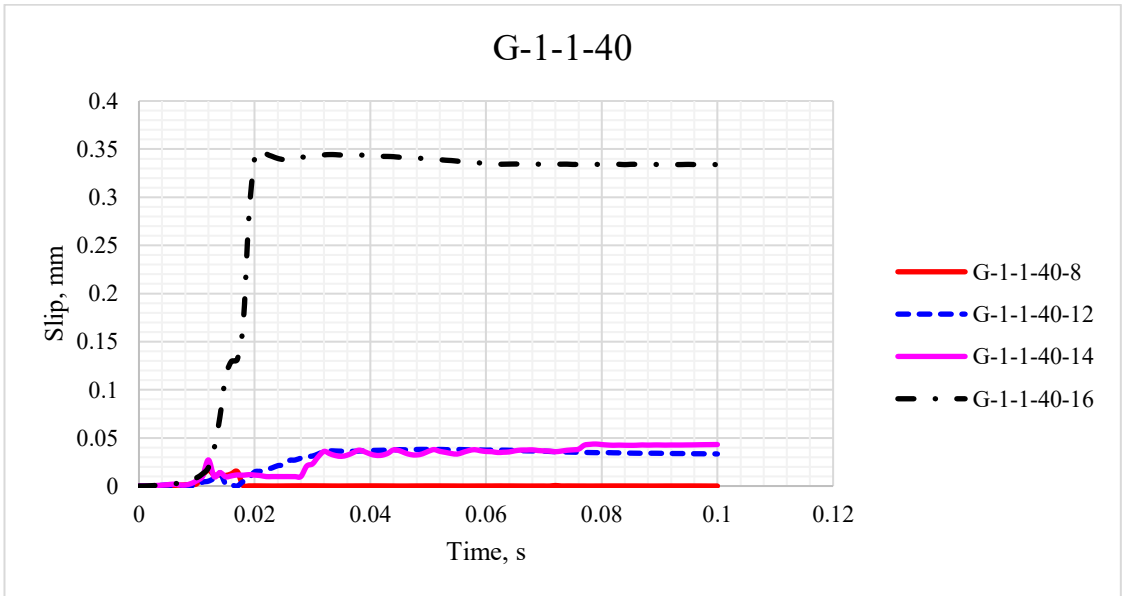
G-1-1-40
Slip, mm
Time, s
0.4
0.35
0.3
0.25
0.2
0.15
0.1
0.05
0
0
0.02
0.04
0.06
0.08
0.1
0.12
G-1-1-40-8
G-1-1-40-12
G-1-1-40-14
G-1-1-40-16

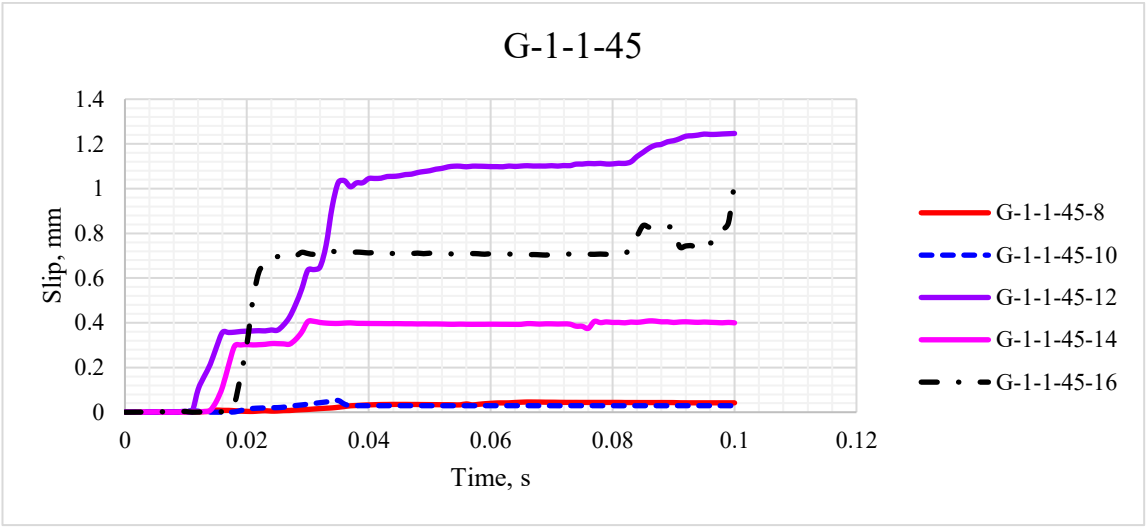

Figure 148: Slip- time histories for AFRP, CFRP, and GFRP RC models under 320 kN impact load- ABAQUS.

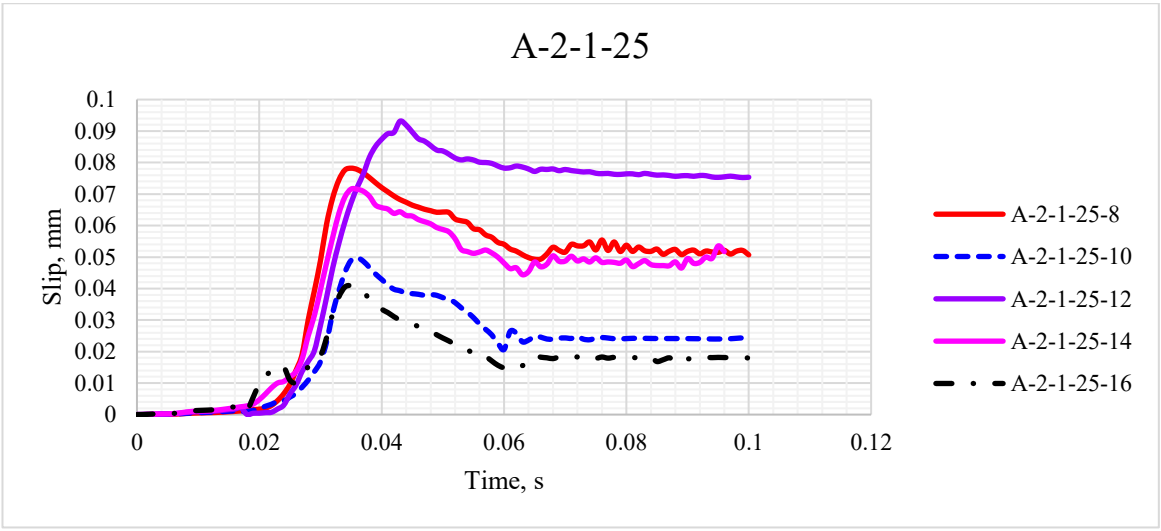

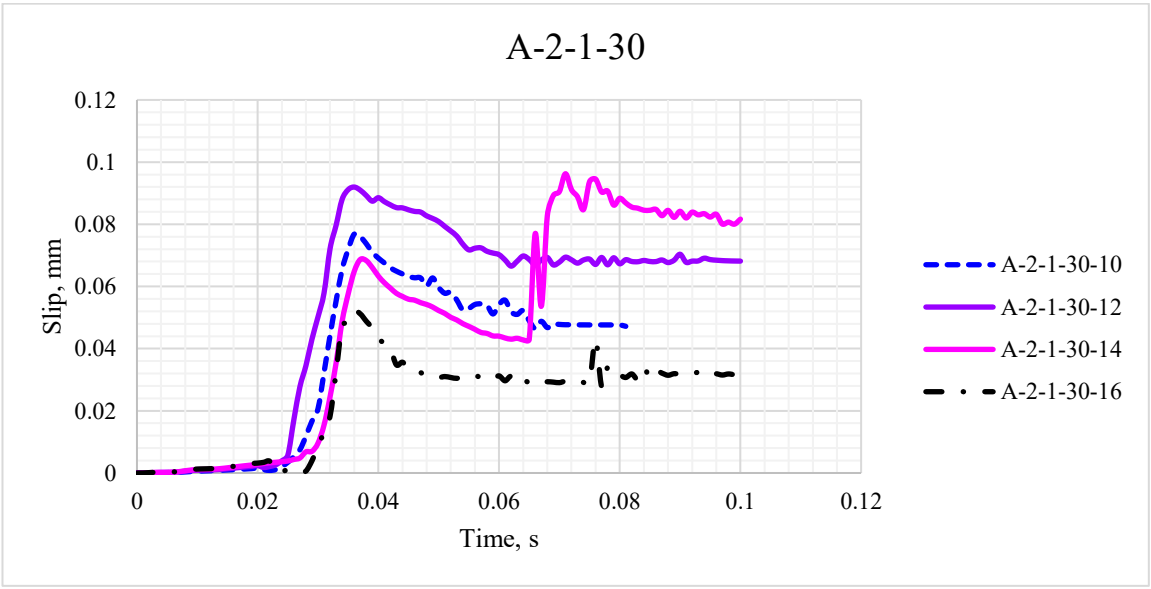

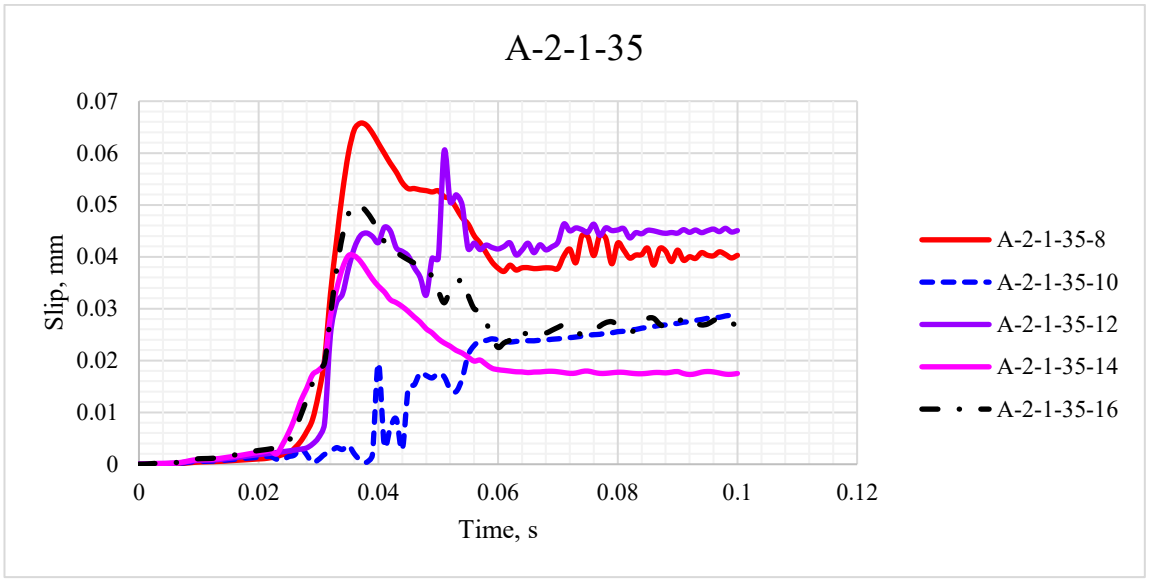
A-2-1-35
Slip, mm
0.07
0.06
0.05
0.04
0.03
0.02
0.01
0
0
0.02
0.04
0.06
0.08
0.1
0.12
Time, s
A-2-1-35-8
A-2-1-35-10
A-2-1-35-12
A-2-1-35-14
A-2-1-35-16

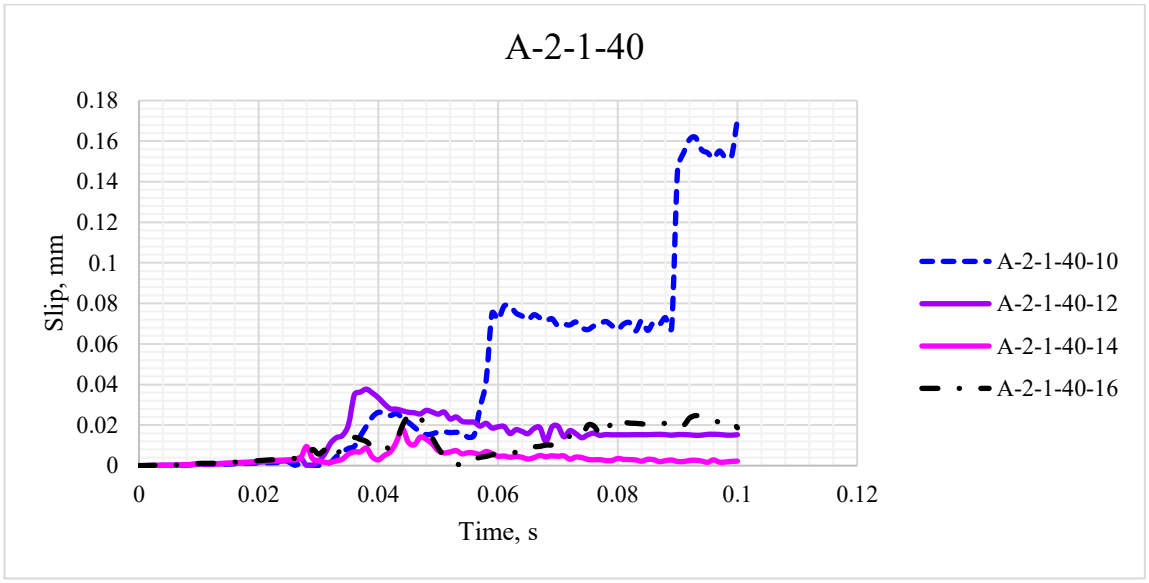
A-2-1-40
Slip, mm
0.18
0.16
0.14
0.12
0.1
0.08
0.06
0.04
0.02
0
0
0.02
0.04
0.06
0.08
0.1
0.12
Time, s
A-2-1-40-10
A-2-1-40-12
A-2-1-40-14
A-2-1-40-16

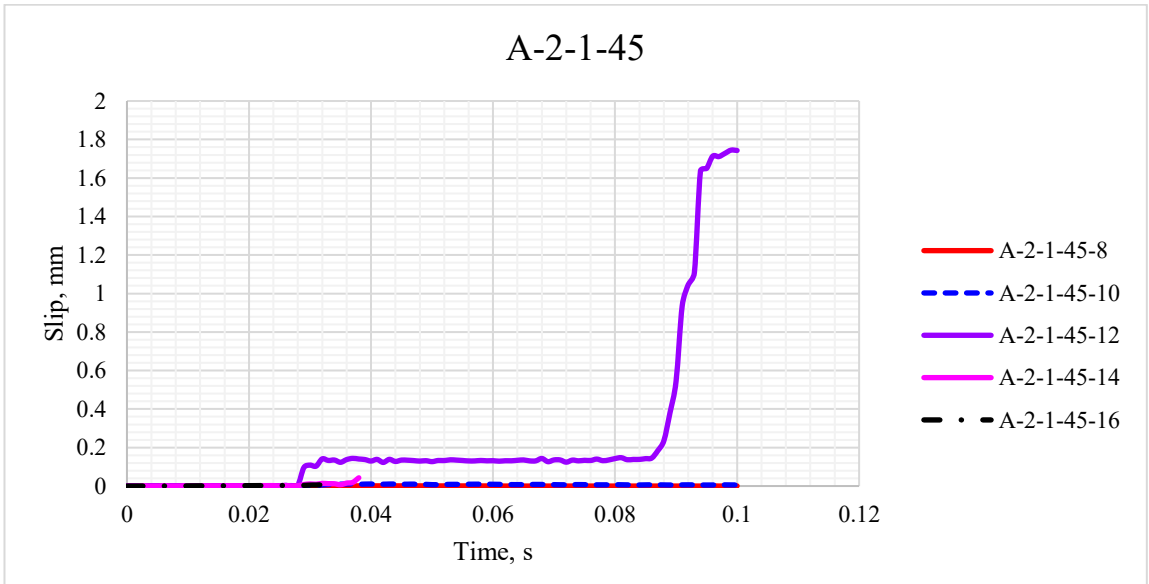
A-2-1-45
Slip, mm
2
1.8
1.6
1.4
1.2
1
0.8
0.6
0.4
0.2
0
0
0.02
0.04
0.06
0.08
0.1
0.12
Time, s
A-2-1-45-8
A-2-1-45-10
A-2-1-45-12
A-2-1-45-14
A-2-1-45-16

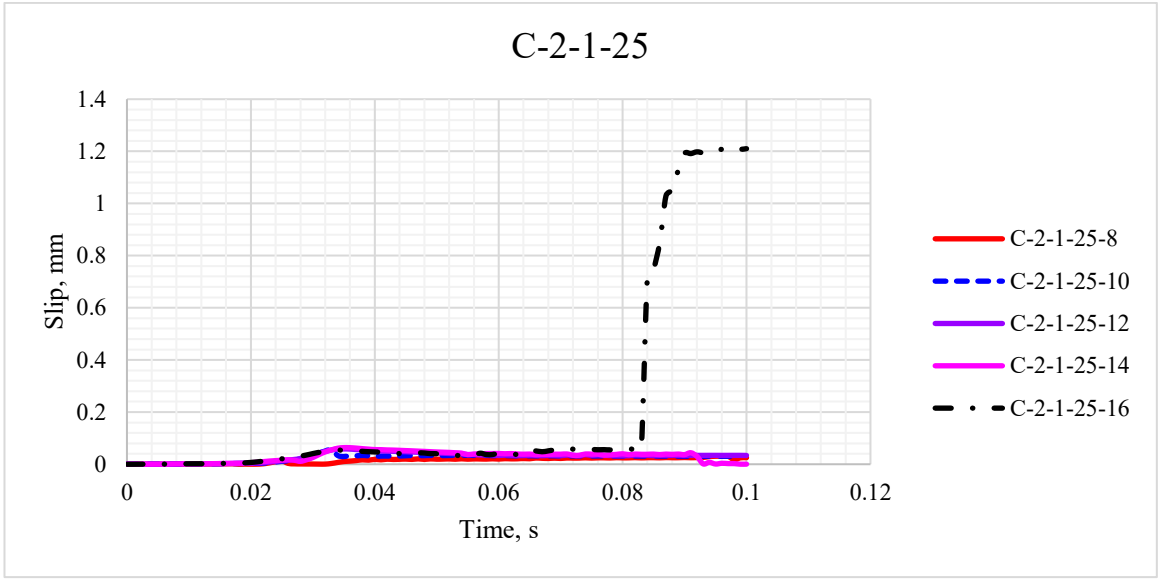
C-2-1-25
Slip, mm
Time, s
C-2-1-25-8
C-2-1-25-10
C-2-1-25-12
C-2-1-25-14
C-2-1-25-16

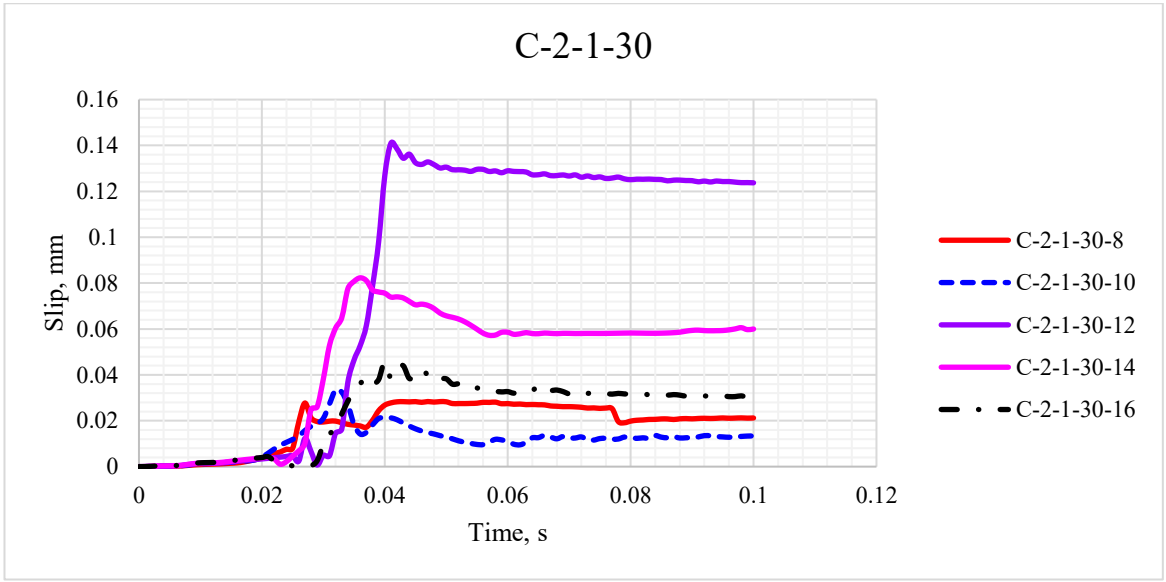
C-2-1-30
Slip, mm
Time, s
C-2-1-30-8
C-2-1-30-10
C-2-1-30-12
C-2-1-30-14
C-2-1-30-16

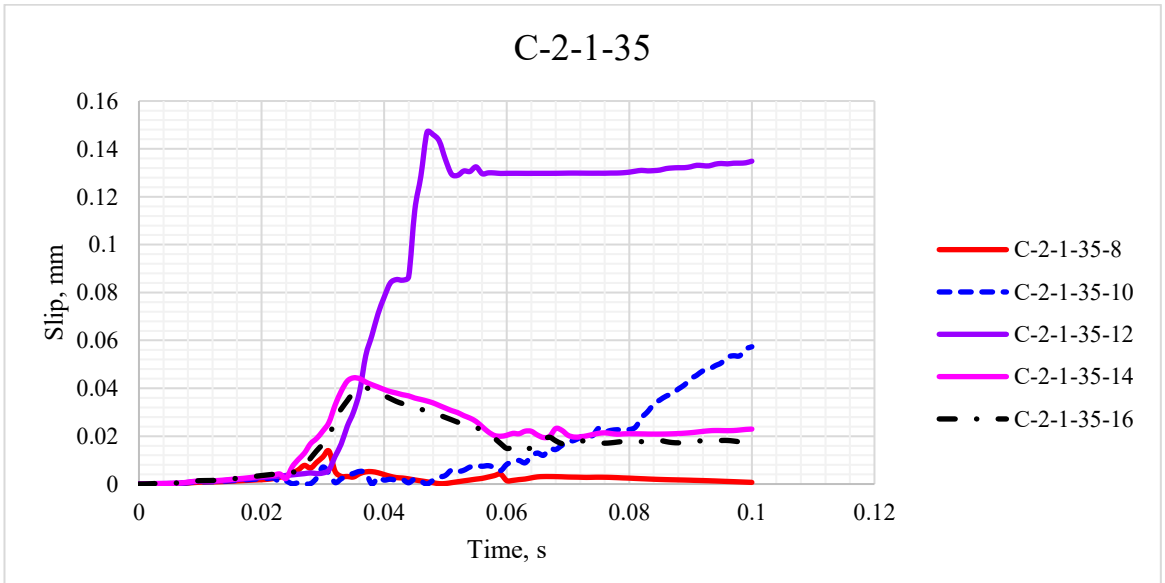
C-2-1-35
Slip, mm
Time, s
C-2-1-35-8
C-2-1-35-10
C-2-1-35-12
C-2-1-35-14
C-2-1-35-16

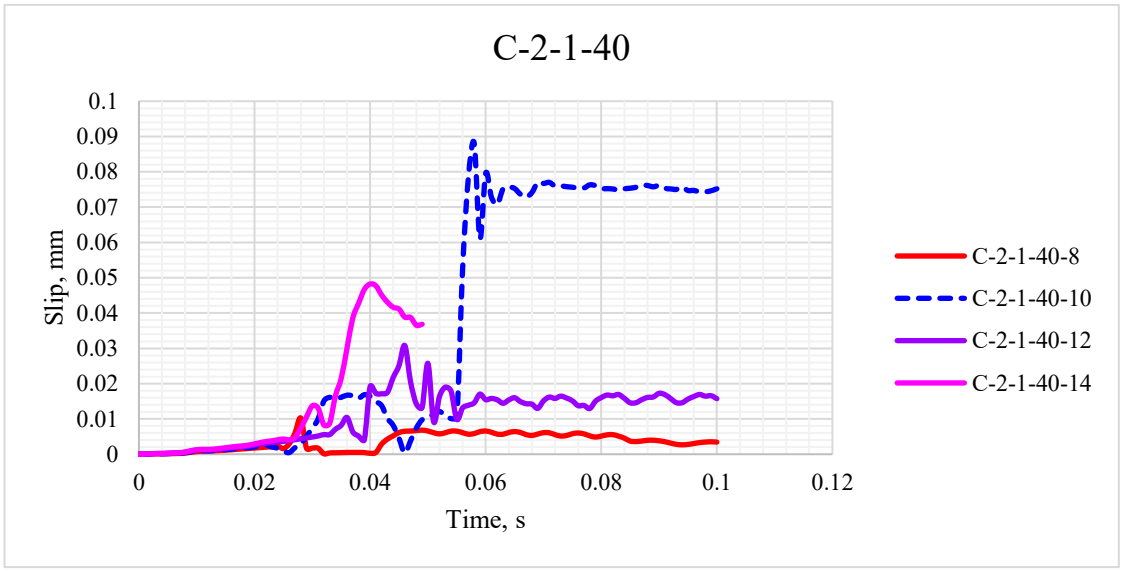
C-2-1-40
Slip, mm
0.1
0.09
0.08
0.07
0.06
0.05
0.04
0.03
0.02
0.01
0
0
0.02
0.04
0.06
0.08
0.1
0.12
Time, s
C-2-1-40-8
C-2-1-40-10
C-2-1-40-12
C-2-1-40-14

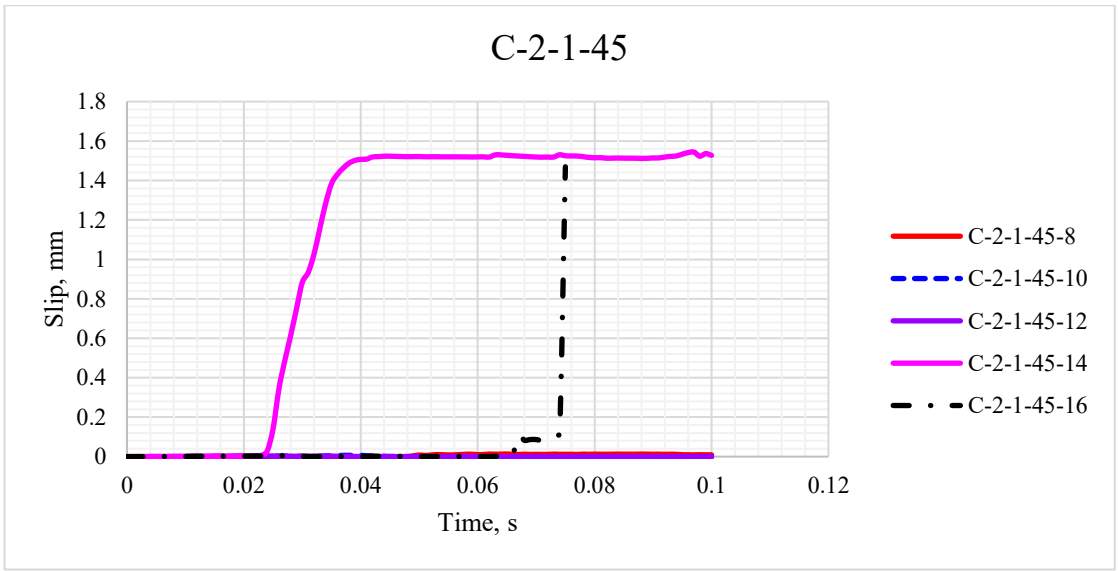
C-2-1-45
Slip, mm
1.8
1.6
1.4
1.2
1
0.8
0.6
0.4
0.2
0
0
0.02
0.04
0.06
0.08
0.1
0.12
Time, s
C-2-1-45-8
C-2-1-45-10
C-2-1-45-12
C-2-1-45-14
C-2-1-45-16

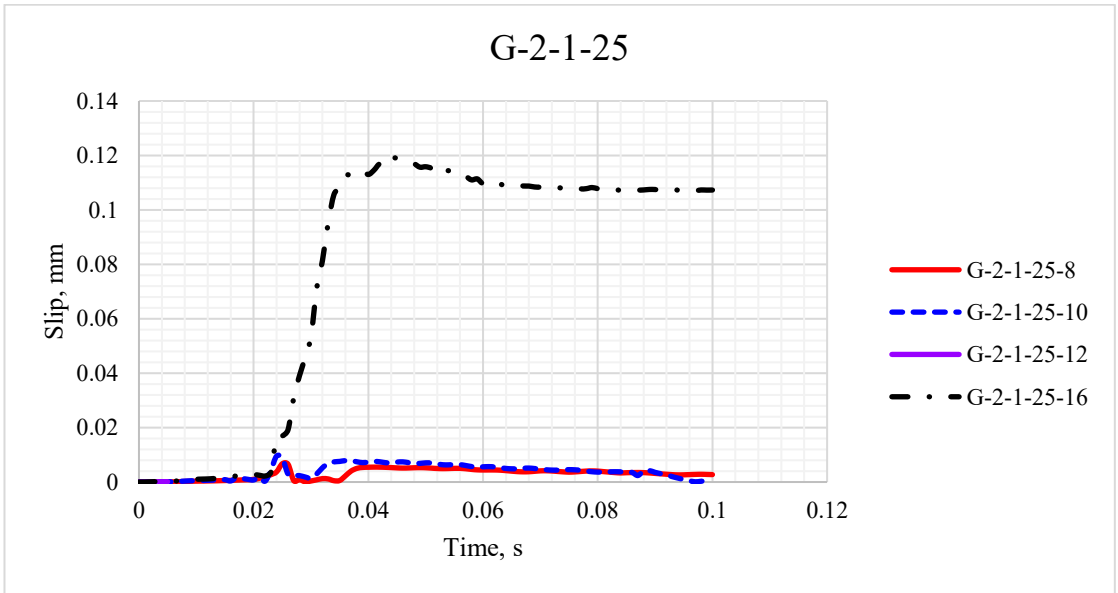
G-2-1-25
Slip, mm
0.14
0.12
0.1
0.08
0.06
0.04
0.02
0
0
0.02
0.04
0.06
0.08
0.1
0.12
Time, s
G-2-1-25-8
G-2-1-25-10
G-2-1-25-12
G-2-1-25-16

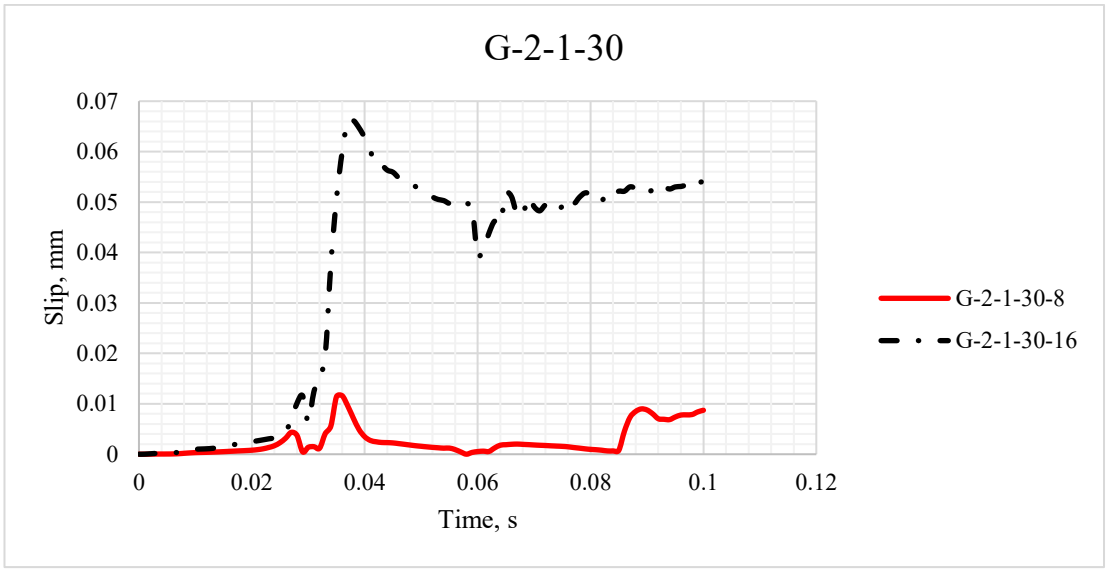
G-2-1-30
Slip, mm
0.07
0.06
0.05
0.04
0.03
0.02
0.01
0
0
0.02
0.04
0.06
0.08
0.1
0.12
Time, s
G-2-1-30-8
G-2-1-30-16

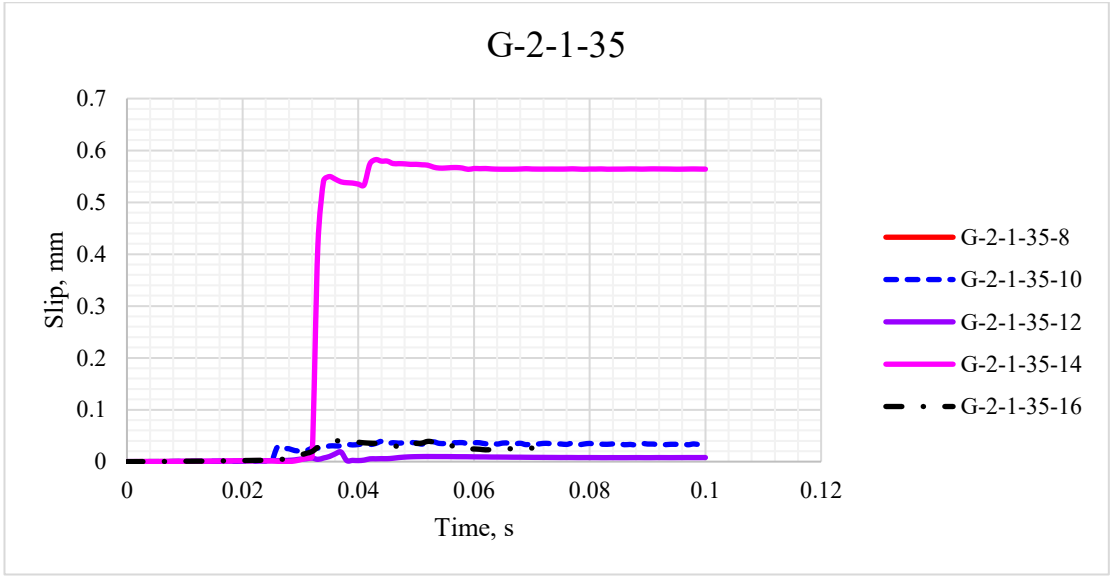
G-2-1-35
Slip, mm
0.7
0.6
0.5
0.4
0.3
0.2
0.1
0
0
0.02
0.04
0.06
0.08
0.1
0.12
Time, s
G-2-1-35-8
G-2-1-35-10
G-2-1-35-12
G-2-1-35-14
G-2-1-35-16

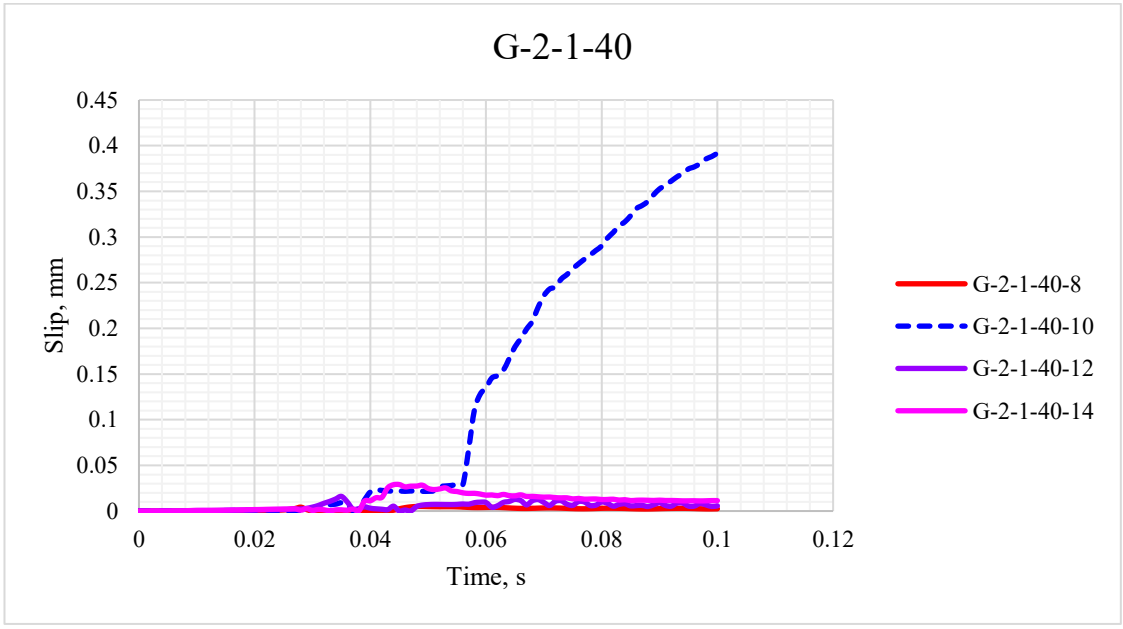
G-2-1-40
Slip, mm
0.45
0.4
0.35
0.3
0.25
0.2
0.15
0.1
0.05
0
0
0.02
0.04
0.06
0.08
0.1
0.12
Time, s
G-2-1-40-8
G-2-1-40-10
G-2-1-40-12
G-2-1-40-14

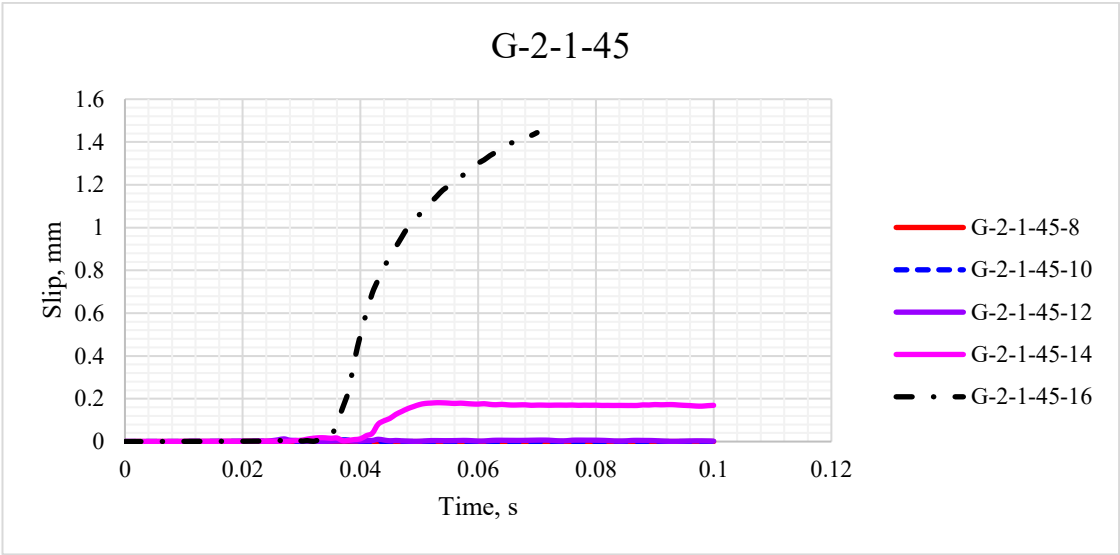

Figure 149: Slip- time histories for AFRP, CFRP, and GFRP RC models under 80 kN impact load- ABAQUS.

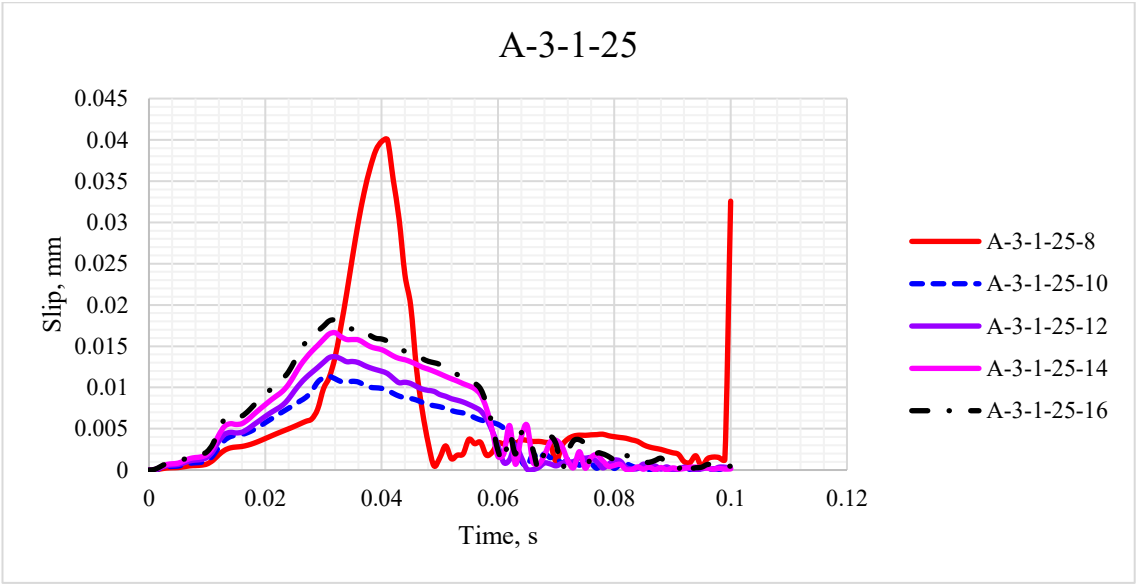

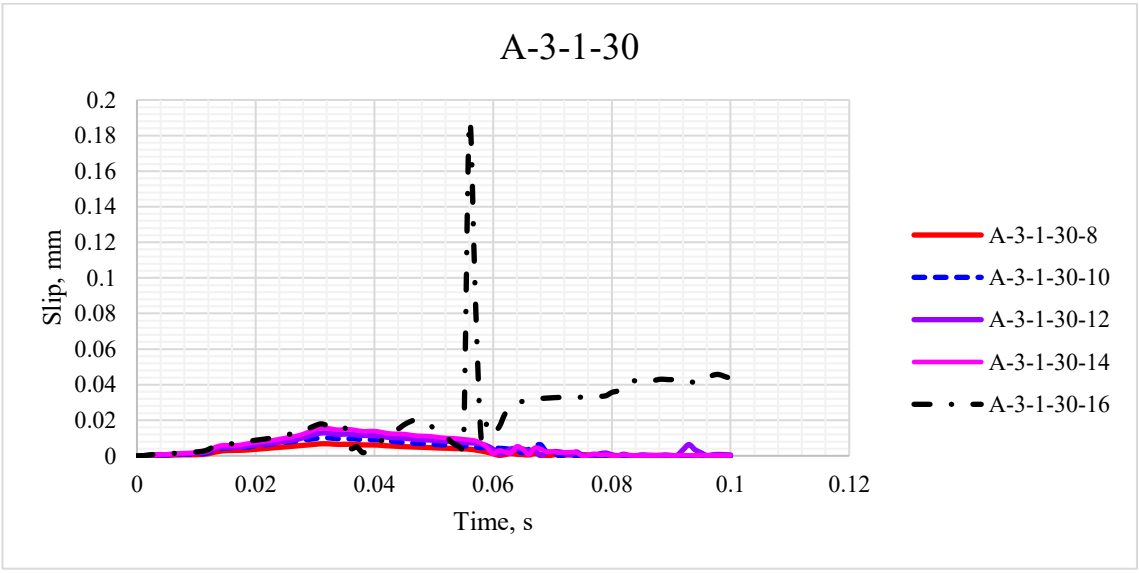

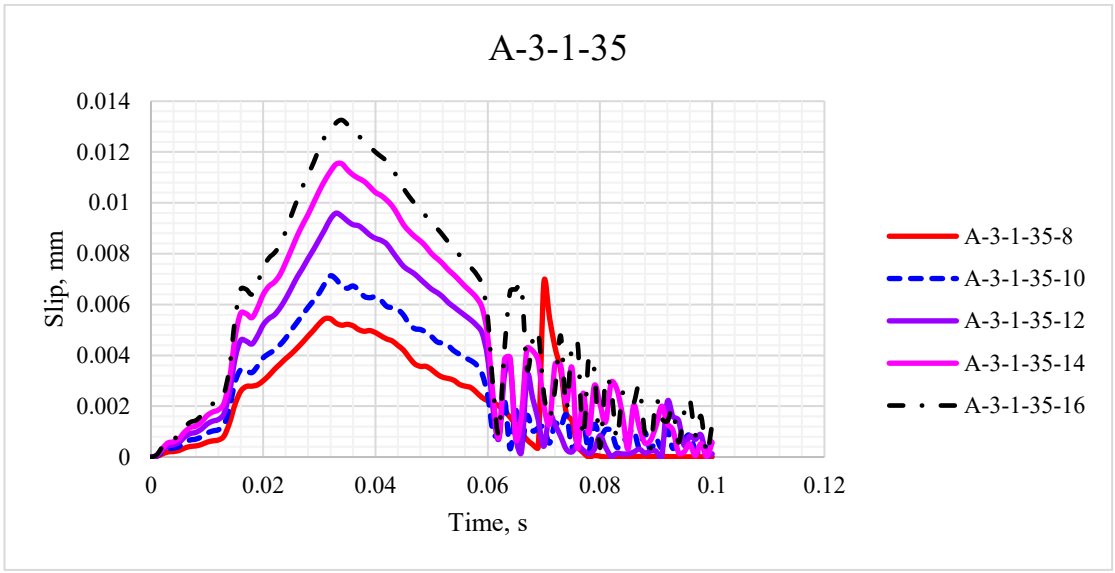
A-3-1-35
Slip, mm
0.014
0.012
0.01
0.008
0.006
0.004
0.002
0
0
0.02
0.04
0.06
0.08
0.1
0.12
Time, s
A-3-1-35-8
A-3-1-35-10
A-3-1-35-12
A-3-1-35-14
A-3-1-35-16

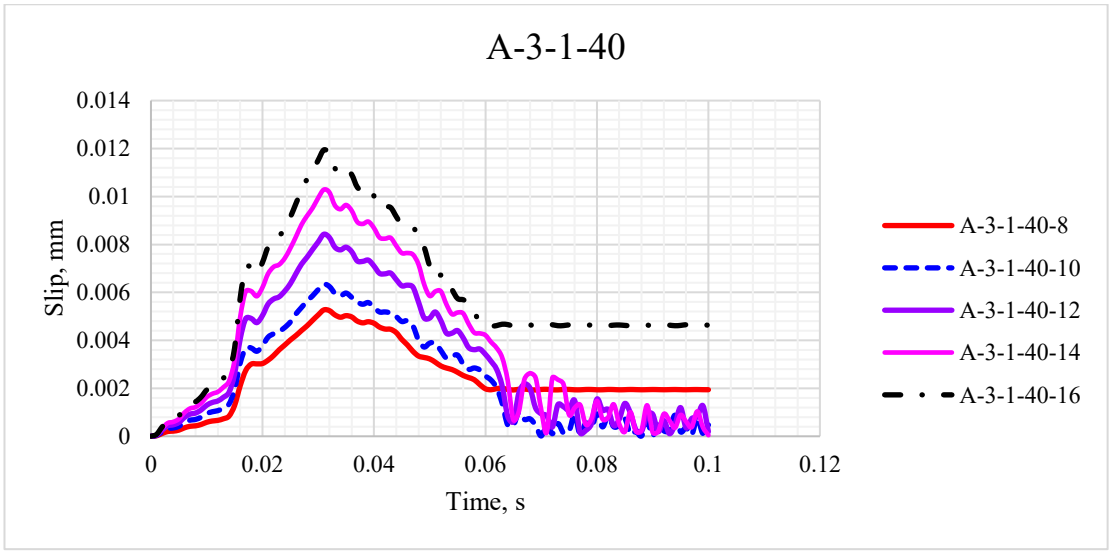
A-3-1-40
Slip, mm
0.014
0.012
0.01
0.008
0.006
0.004
0.002
0
0
0.02
0.04
0.06
0.08
0.1
0.12
Time, s
A-3-1-40-8
A-3-1-40-10
A-3-1-40-12
A-3-1-40-14
A-3-1-40-16

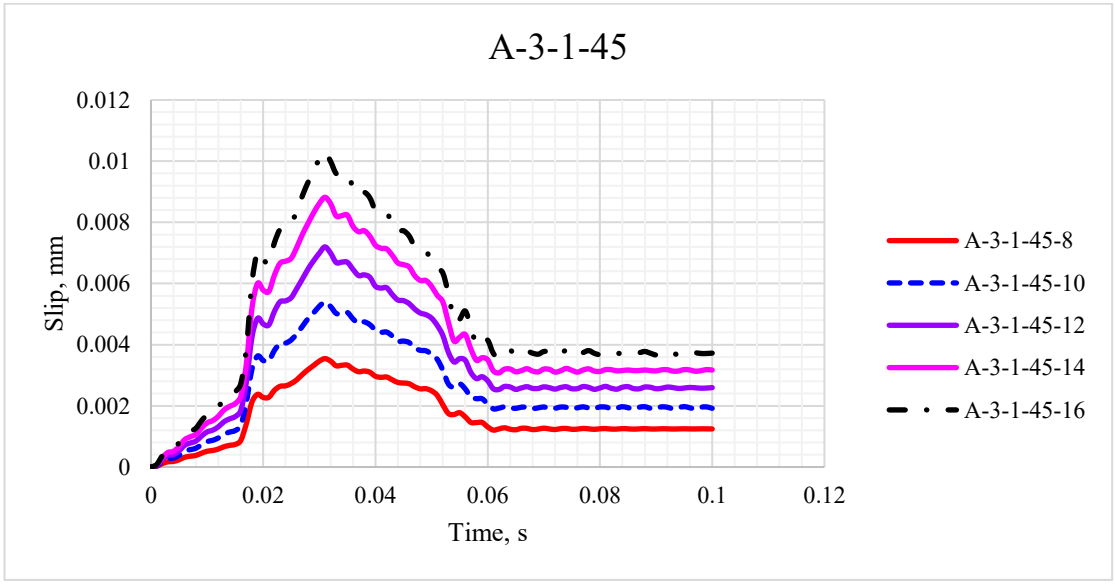
A-3-1-45
Slip, mm
0.012
0.01
0.008
0.006
0.004
0.002
0
0
0.02
0.04
0.06
0.08
0.1
0.12
Time, s
A-3-1-45-8
A-3-1-45-10
A-3-1-45-12
A-3-1-45-14
A-3-1-45-16

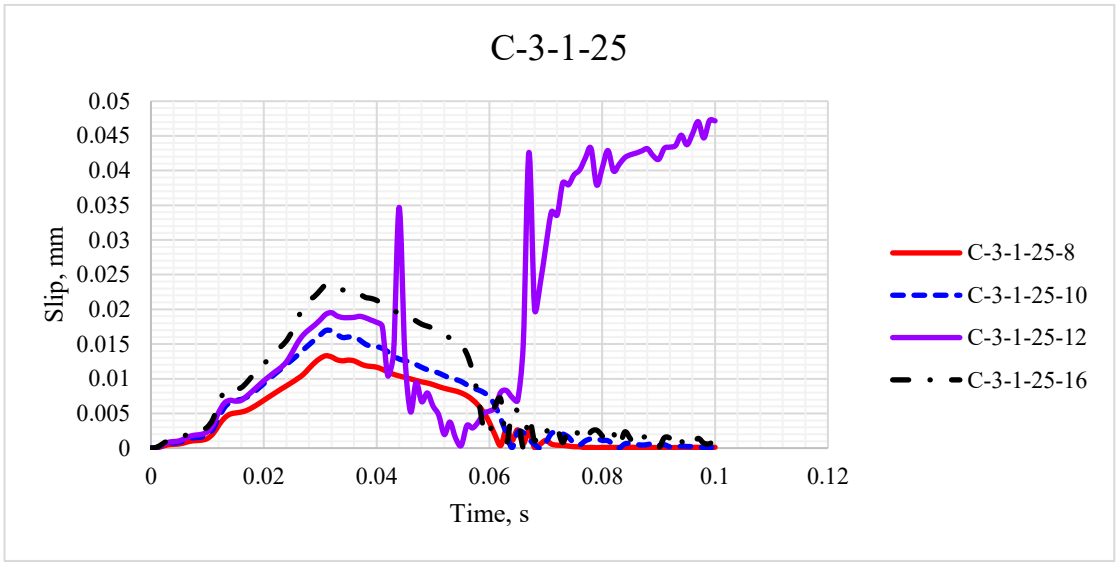
C-3-1-25
Slip, mm
0.05
0.045
0.04
0.035
0.03
0.025
0.02
0.015
0.01
0.005
0
0
0.02
0.04
0.06
0.08
0.1
0.12
Time, s
C-3-1-25-8
C-3-1-25-10
C-3-1-25-12
C-3-1-25-16

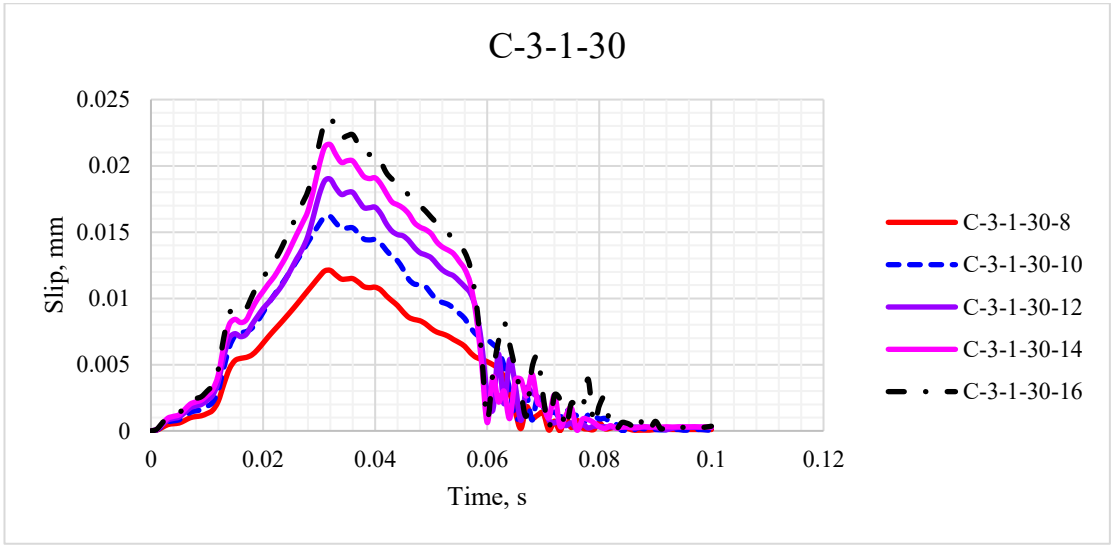
C-3-1-30
Slip, mm
0.025
0.02
0.015
0.01
0.005
0
0
0.02
0.04
0.06
0.08
0.1
0.12
Time, s
C-3-1-30-8
C-3-1-30-10
C-3-1-30-12
C-3-1-30-14
C-3-1-30-16

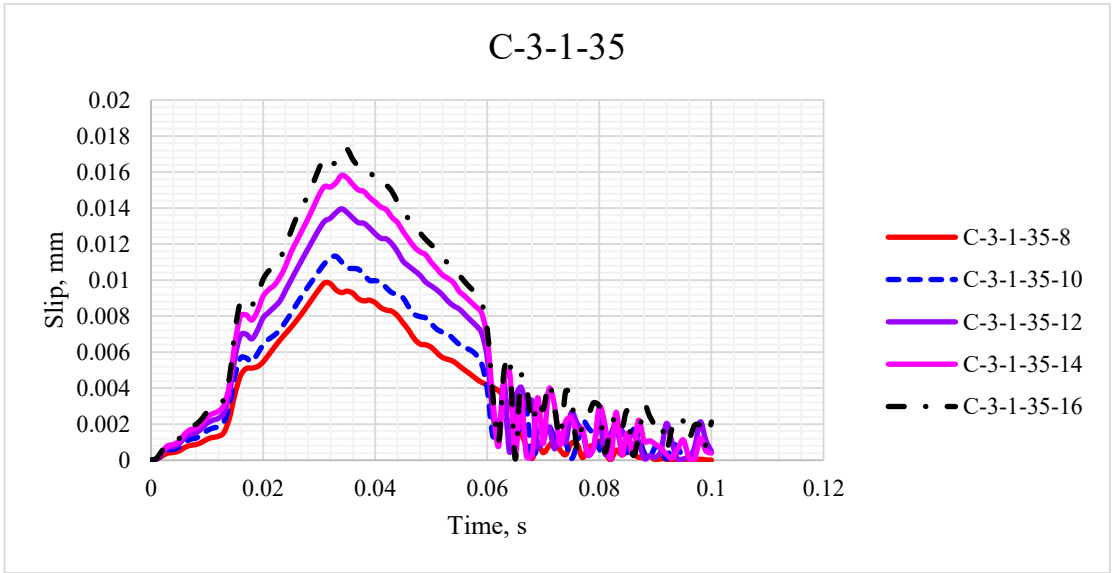
C-3-1-35
Slip, mm
0.02
0.018
0.016
0.014
0.012
0.01
0.008
0.006
0.004
0.002
0
0
0.02
0.04
0.06
0.08
0.1
0.12
Time, s
C-3-1-35-8
C-3-1-35-10
C-3-1-35-12
C-3-1-35-14
C-3-1-35-16

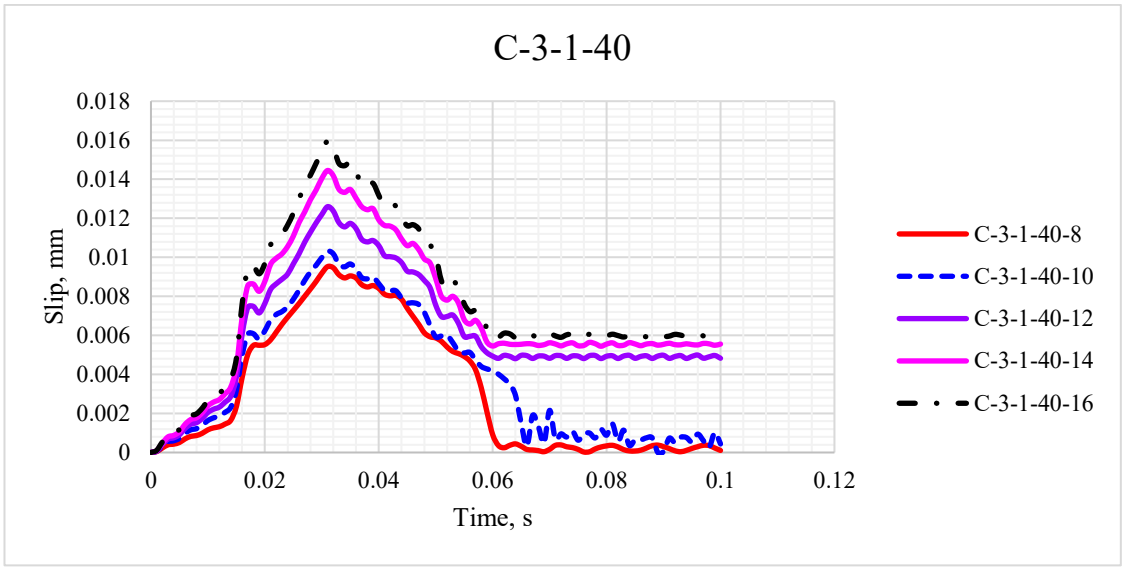
C-3-1-40
Slip, mm
0.018
0.016
0.014
0.012
0.01
0.008
0.006
0.004
0.002
0
0
0.02
0.04
0.06
0.08
0.1
0.12
Time, s
C-3-1-40-8
C-3-1-40-10
C-3-1-40-12
C-3-1-40-14
C-3-1-40-16

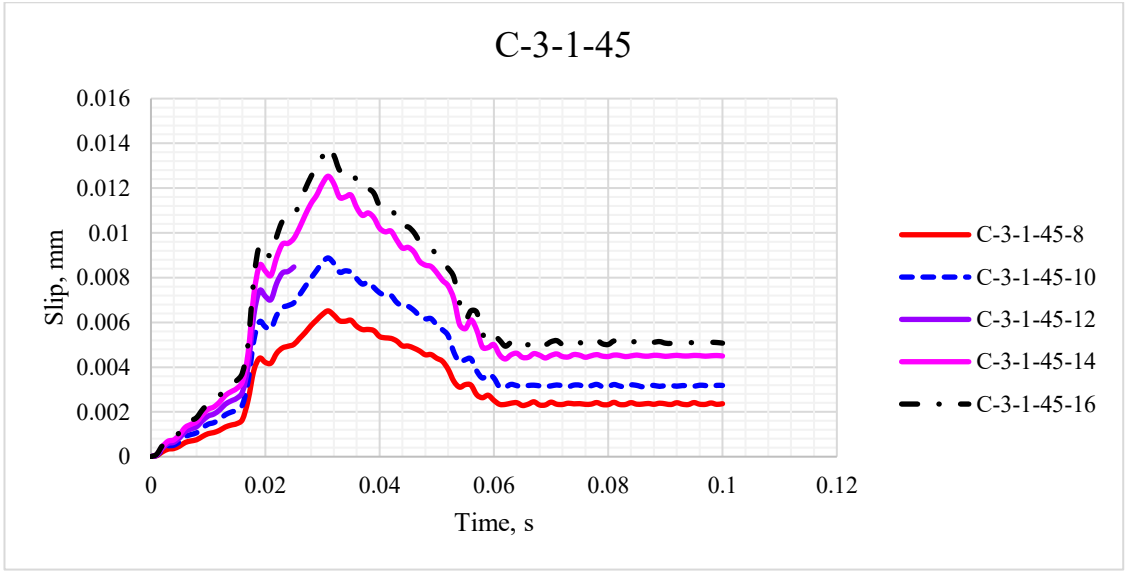
C-3-1-45
Slip, mm
0.016
0.014
0.012
0.01
0.008
0.006
0.004
0.002
0
0
0.02
0.04
0.06
0.08
0.1
0.12
Time, s
C-3-1-45-8
C-3-1-45-10
C-3-1-45-12
C-3-1-45-14
C-3-1-45-16

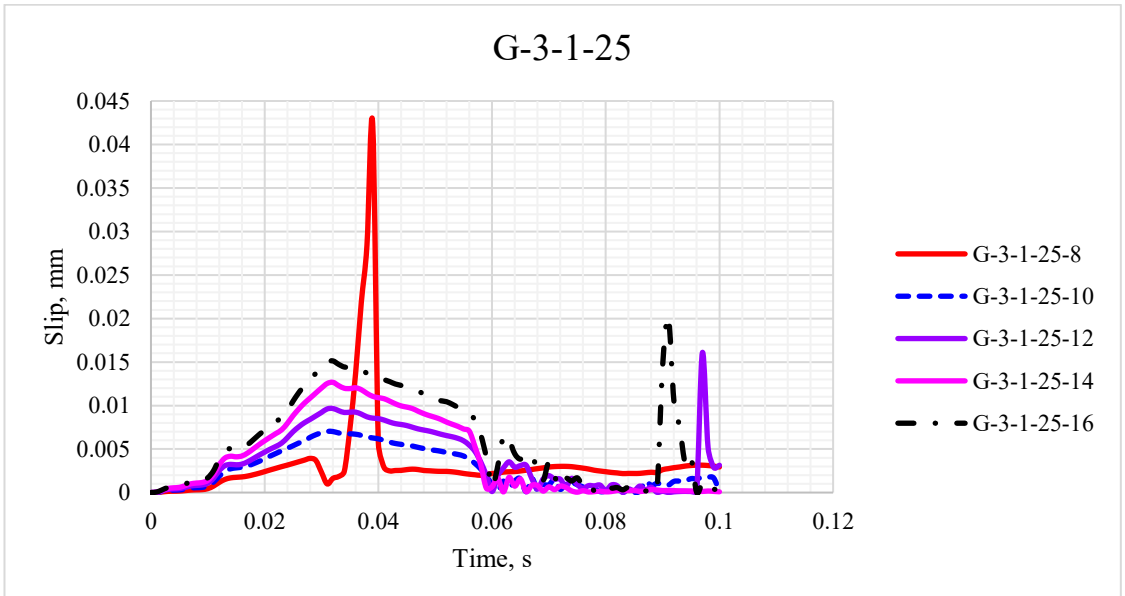
G-3-1-25
Slip, mm
0.045
0.04
0.035
0.03
0.025
0.02
0.015
0.01
0.005
0
0
0.02
0.04
0.06
0.08
0.1
0.12
Time, s
G-3-1-25-8
G-3-1-25-10
G-3-1-25-12
G-3-1-25-14
G-3-1-25-16

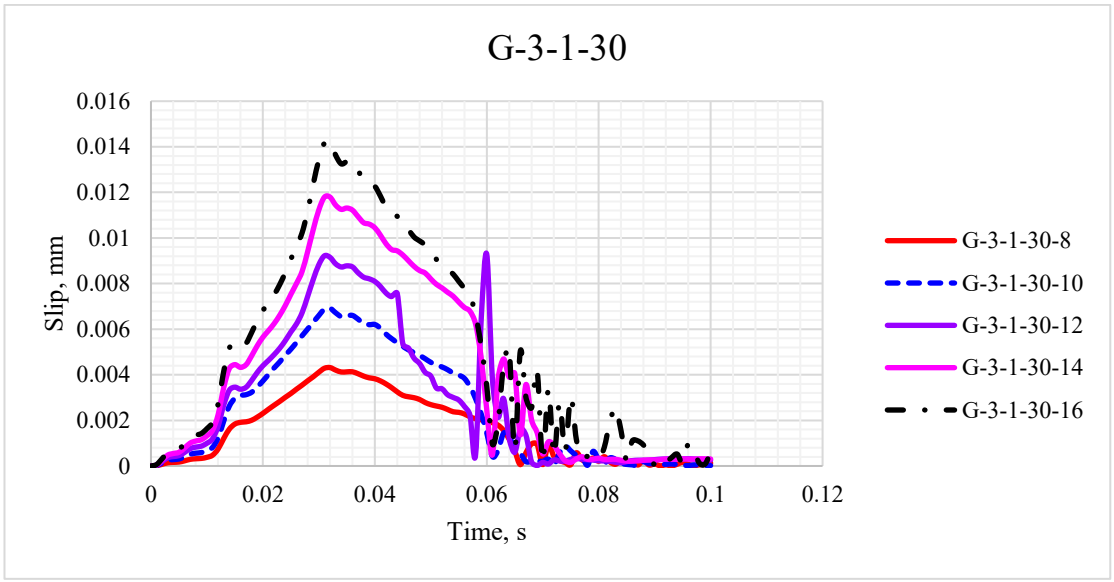
G-3-1-30
0.016
0.014
0.012
0.01
0.008
0.006
0.004
0.002
0
Slip, mm
0
0.02
0.04
0.06
0.08
0.1
0.12
Time, s
G-3-1-30-8
G-3-1-30-10
G-3-1-30-12
G-3-1-30-14
G-3-1-30-16

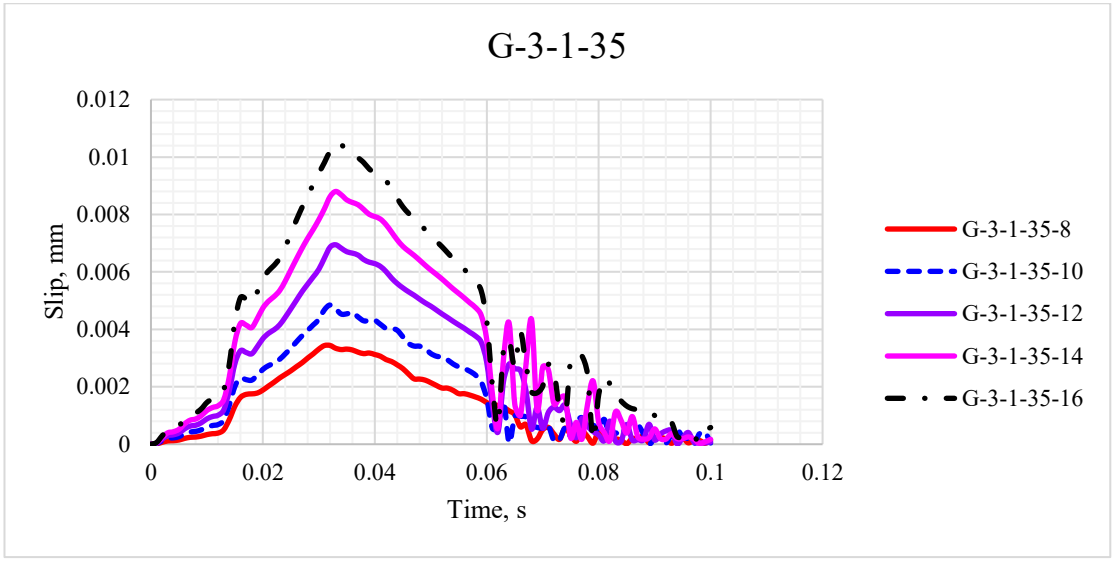
G-3-1-35
0.012
0.01
0.008
0.006
0.004
0.002
0
Slip, mm
0
0.02
0.04
0.06
0.08
0.1
0.12
Time, s
G-3-1-35-8
G-3-1-35-10
G-3-1-35-12
G-3-1-35-14
G-3-1-35-16

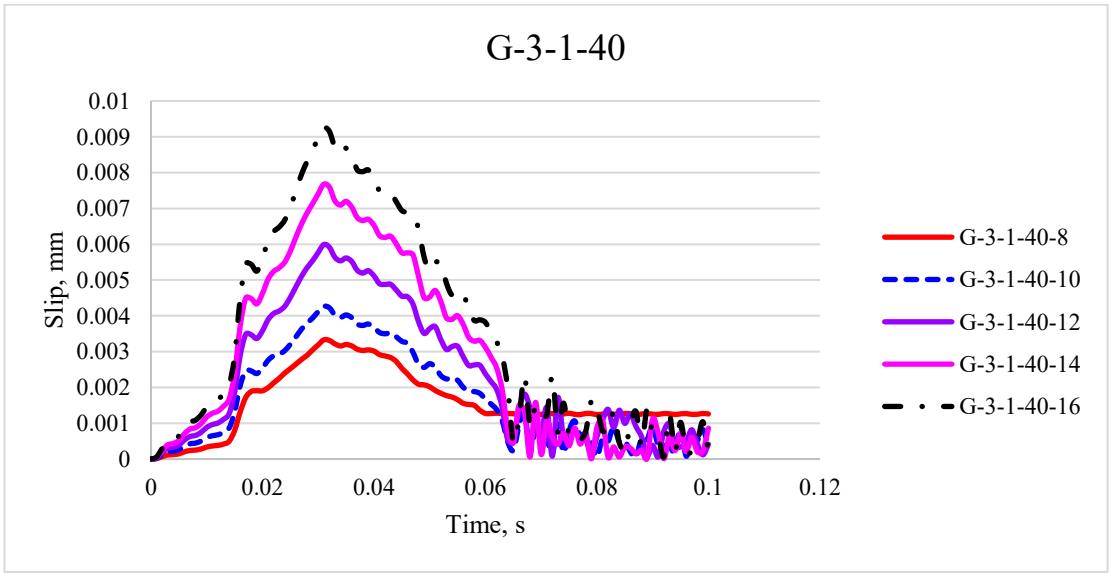
G-3-1-40
0.01
0.009
0.008
0.007
0.006
0.005
0.004
0.003
0.002
0.001
0
Slip, mm
0
0.02
0.04
0.06
0.08
0.1
0.12
Time, s
G-3-1-40-8
G-3-1-40-10
G-3-1-40-12
G-3-1-40-14
G-3-1-40-16

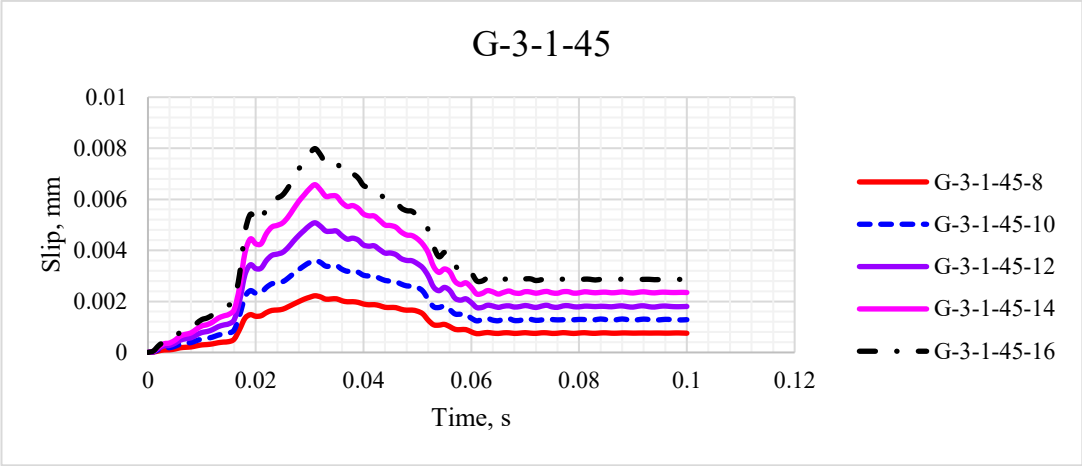

Figure 150: Slip- time histories for AFRP, CFRP, and GFRP RC models under 40 kN impact load- ABAQUS.

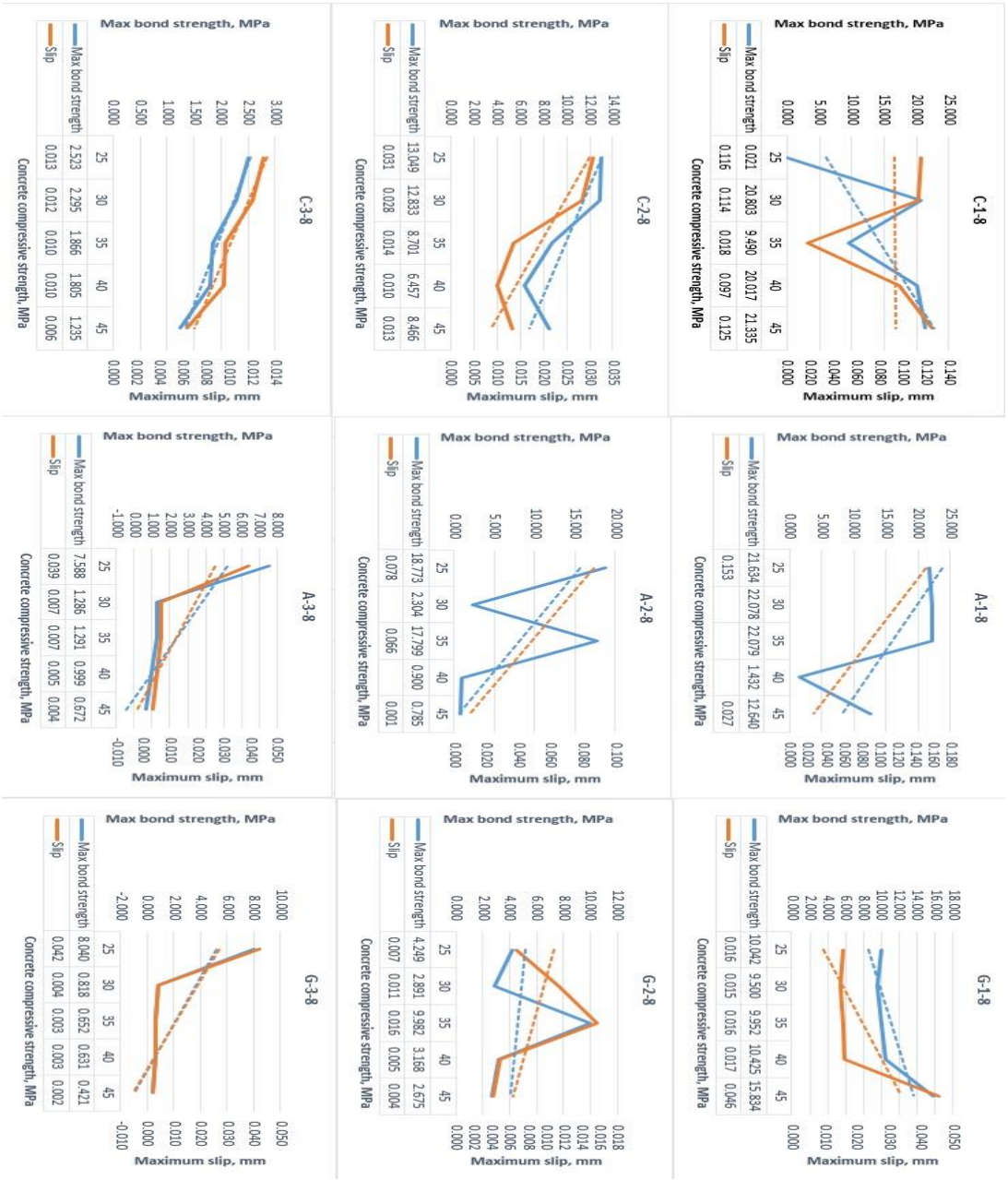

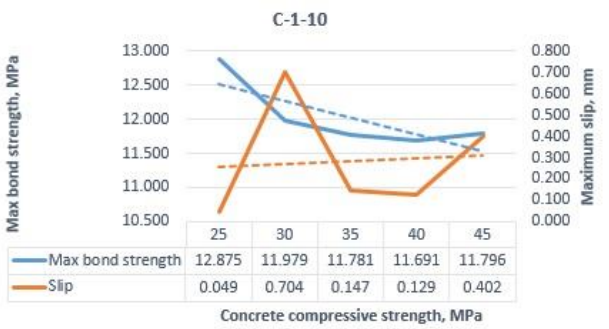
C-1-10
Max bond strength, MPa
Maximum slip, mm
13.000
12.500
12.000
11.500
11.000
10.500
0.800
0.700
0.600
0.500
0.400
0.300
0.200
0.100
0.000
25 30 35 40 45
Max bond strength 12.875 11.979 11.781 11.691 11.796
Slip 0.049 0.704 0.147 0.129 0.402
Concrete compressive strength, MPa

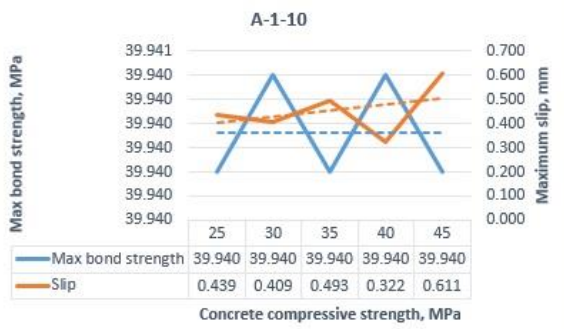
A-1-10
Max bond strength, MPa
Maximum slip, mm
39.941
39.940
0.700
0.600
0.500
0.400
0.300
0.200
0.100
0.000
25 30 35 40 45
Max bond strength 39.940 39.940 39.940 39.940 39.940
Slip 0.439 0.409 0.493 0.322 0.611
Concrete compressive strength, MPa

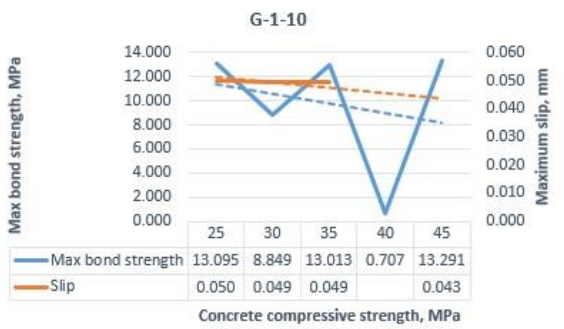
G-1-10
Max bond strength, MPa
Maximum slip, mm
14.000
12.000
10.000
8.000
6.000
4.000
2.000
0.000
0.060
0.050
0.040
0.030
0.020
0.010
0.000
25 30 35 40 45
Max bond strength 13.095 8.849 13.013 0.707 13.291
Slip 0.050 0.049 0.049 0.043
Concrete compressive strength, MPa

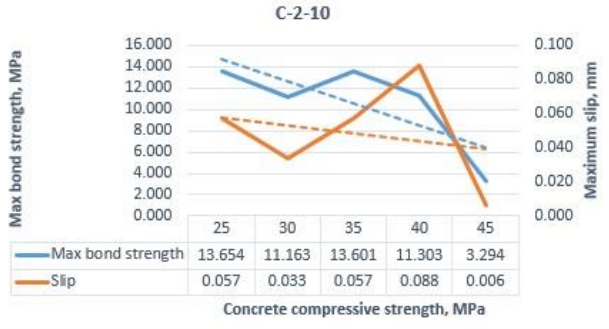
C-2-10
Max bond strength, MPa
Maximum slip, mm
16.000
14.000
12.000
10.000
8.000
6.000
4.000
2.000
0.000
0.100
0.080
0.060
0.040
0.020
0.000
25 30 35 40 45
Max bond strength 13.654 11.163 13.601 11.303 3.294
Slip 0.057 0.033 0.057 0.088 0.006
Concrete compressive strength, MPa

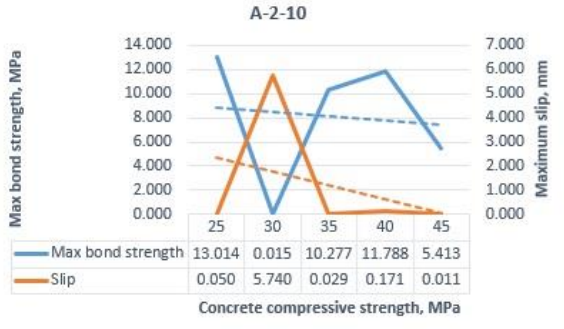
A-2-10
Max bond strength, MPa
Maximum slip, mm
14.000
12.000
10.000
8.000
6.000
4.000
2.000
0.000
7.000
6.000
5.000
4.000
3.000
2.000
1.000
0.000
25 30 35 40 45
Max bond strength 13.014 0.015 10.277 11.788 5.413
Slip 0.050 5.740 0.029 0.171 0.011
Concrete compressive strength, MPa

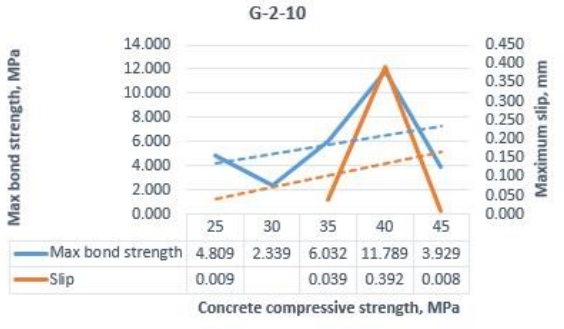
G-2-10
Max bond strength, MPa
Maximum slip, mm
14.000
12.000
10.000
8.000
6.000
4.000
2.000
0.000
0.450
0.400
0.350
0.300
0.250
0.200
0.150
0.100
0.050
0.000
25 30 35 40 45
Max bond strength 4.809 2.339 6.032 11.789 3.929
Slip 0.009 0.039 0.392 0.008
Concrete compressive strength, MPa

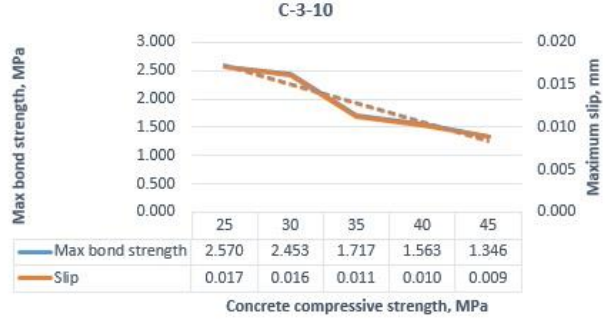
C-3-10
Max bond strength, MPa
Maximum slip, mm
3.000
2.500
2.000
1.500
1.000
0.500
0.000
0.020
0.015
0.010
0.005
0.000
25 30 35 40 45
Max bond strength 2.570 2.453 1.717 1.563 1.346
Slip 0.017 0.016 0.011 0.010 0.009
Concrete compressive strength, MPa

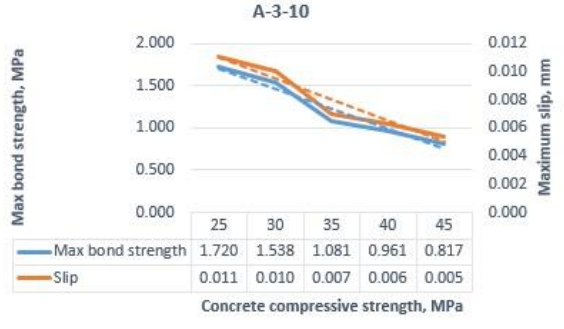
A-3-10
Max bond strength, MPa
Maximum slip, mm
2.000
1.500
1.000
0.500
0.000
0.012
0.010
0.008
0.006
0.004
0.002
0.000
25 30 35 40 45
Max bond strength 1.720 1.538 1.081 0.961 0.817
Slip 0.011 0.010 0.007 0.006 0.005
Concrete compressive strength, MPa

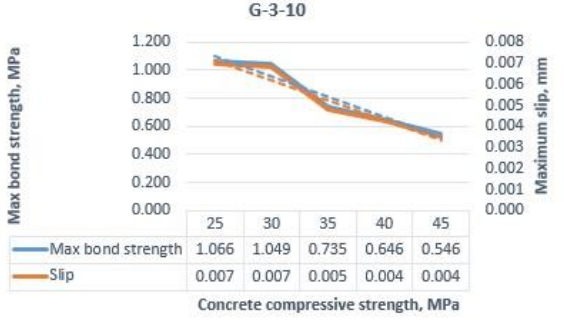
G-3-10
Max bond strength, MPa
Maximum slip, mm
1.200
1.000
0.800
0.600
0.400
0.200
0.000
0.008
0.007
0.006
0.005
0.004
0.003
0.002
0.001
0.000
25 30 35 40 45
Max bond strength 1.066 1.049 0.735 0.646 0.546
Slip 0.007 0.007 0.005 0.004 0.004
Concrete compressive strength, MPa

C-1-12

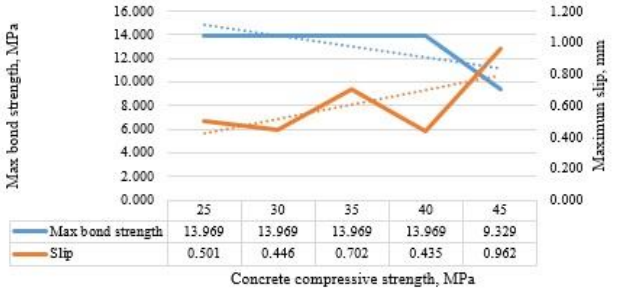

	25	30	35	40	45
Max bond strength	13.969	13.969	13.969	13.969	9.329
Slip	0.501	0.446	0.702	0.435	0.962

A-1-12

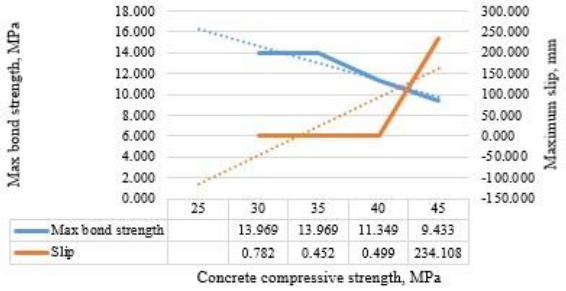

	25	30	35	40	45
Max bond strength		13.969	13.969	11.349	9.433
Slip		0.782	0.452	0.499	234.108

G-1-12

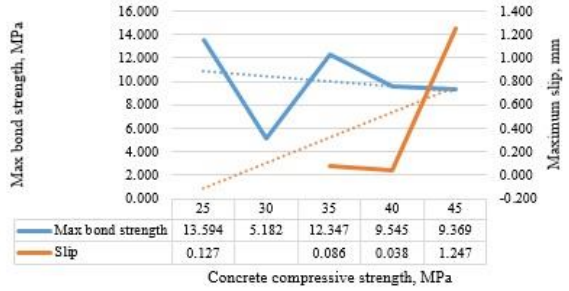

	25	30	35	40	45
Max bond strength	13.594	5.182	12.347	9.545	9.369
Slip	0.127		0.086	0.038	1.247

C-2-12

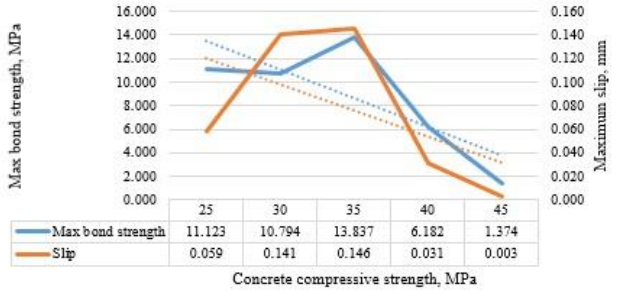

	25	30	35	40	45
Max bond strength	11.123	10.794	13.837	6.182	1.374
Slip	0.059	0.141	0.146	0.031	0.003

A-2-12

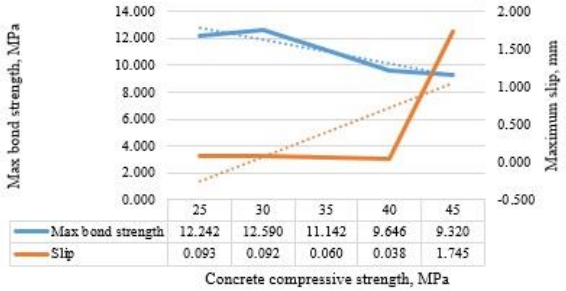

	25	30	35	40	45
Max bond strength	12.242	12.590	11.142	9.646	9.320
Slip	0.093	0.092	0.060	0.038	1.745

G-2-12

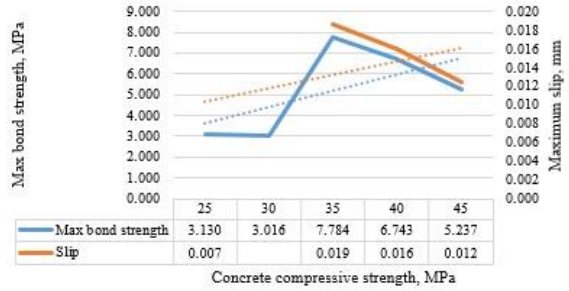

	25	30	35	40	45
Max bond strength	3.130	3.016	7.784	6.743	5.237
Slip	0.007		0.019	0.016	0.012

C-3-12

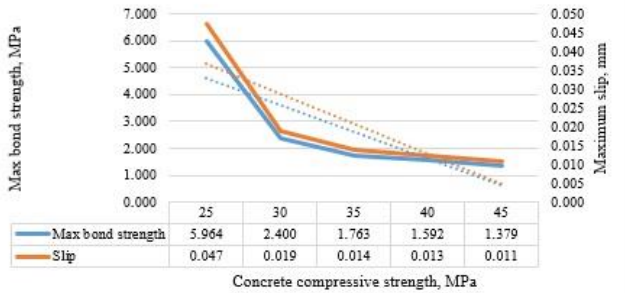

	25	30	35	40	45
Max bond strength	5.964	2.400	1.763	1.592	1.379
Slip	0.047	0.019	0.014	0.013	0.011

A-3-12

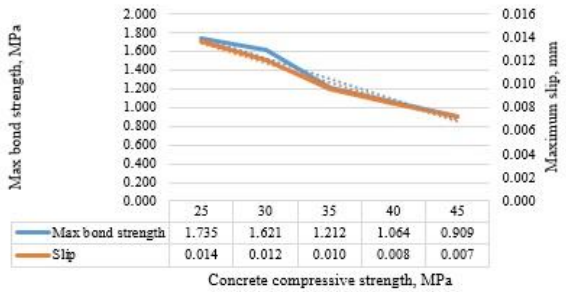

	25	30	35	40	45
Max bond strength	1.735	1.621	1.212	1.064	0.909
Slip	0.014	0.012	0.010	0.008	0.007

G-3-12

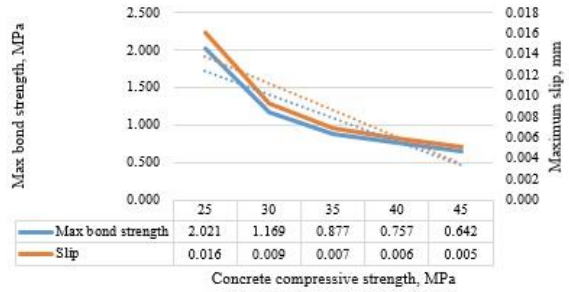

	25	30	35	40	45
Max bond strength	2.021	1.169	0.877	0.757	0.642
Slip	0.016	0.009	0.007	0.006	0.005

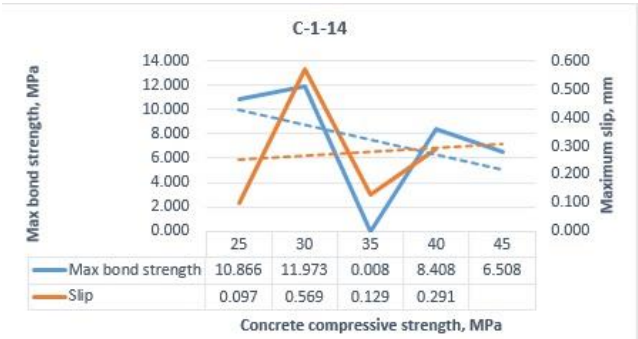

	25	30	35	40	45
Max bond strength	10.866	11.973	0.008	8.408	6.508
Slip	0.097	0.569	0.129	0.291	

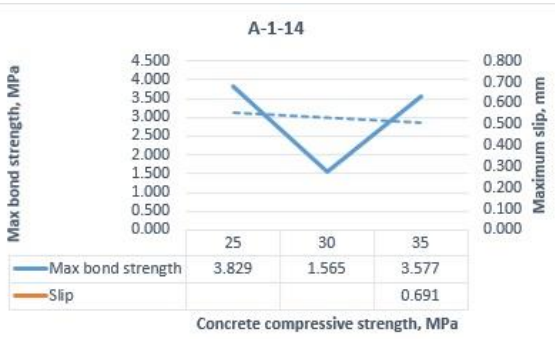

	25	30	35
Max bond strength	3.829	1.565	3.577
Slip			0.691

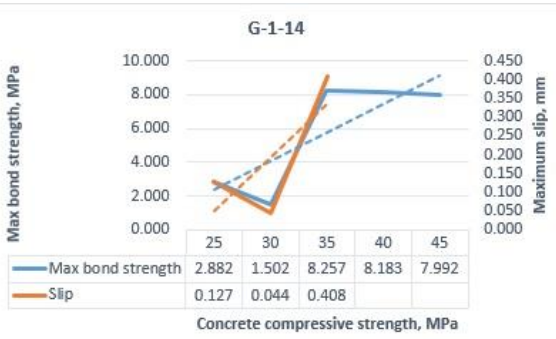

	25	30	35	40	45
Max bond strength	2.882	1.502	8.257	8.183	7.992
Slip	0.127	0.044	0.408		

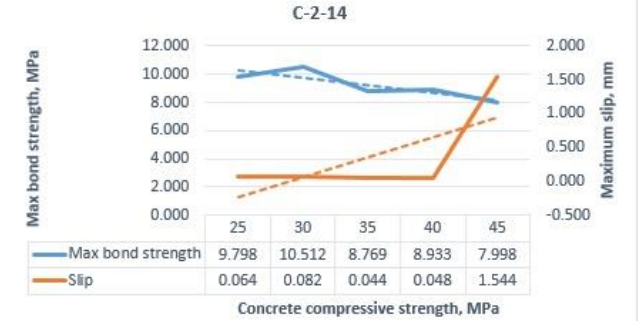

	25	30	35	40	45
Max bond strength	9.798	10.512	8.769	8.933	7.998
Slip	0.064	0.082	0.044	0.048	1.544

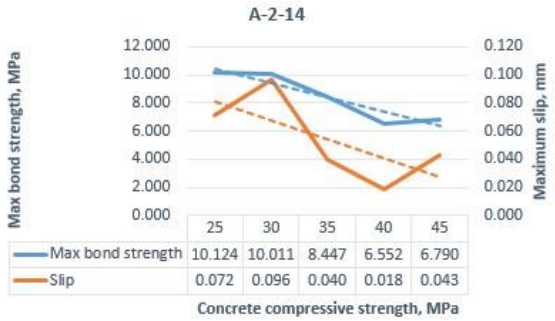

	25	30	35	40	45
Max bond strength	10.124	10.011	8.447	6.552	6.790
Slip	0.072	0.096	0.040	0.018	0.043

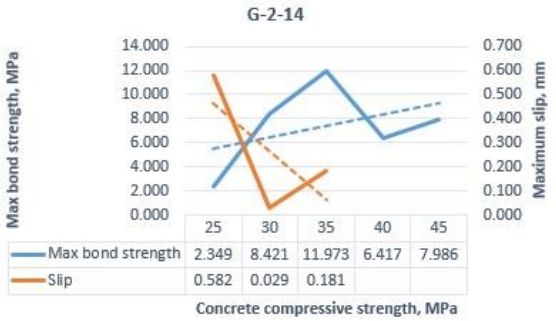

	25	30	35	40	45
Max bond strength	2.349	8.421	11.973	6.417	7.986
Slip	0.582	0.029	0.181		

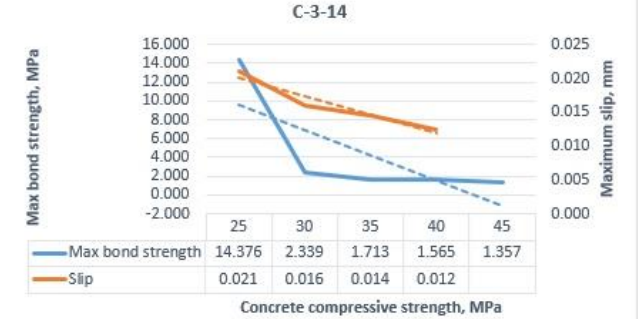

	25	30	35	40	45
Max bond strength	14.376	2.339	1.713	1.565	1.357
Slip	0.021	0.016	0.014	0.012	

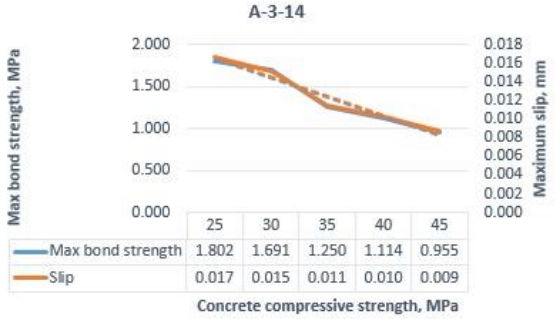

	25	30	35	40	45
Max bond strength	1.802	1.691	1.250	1.114	0.955
Slip	0.017	0.015	0.011	0.010	0.009

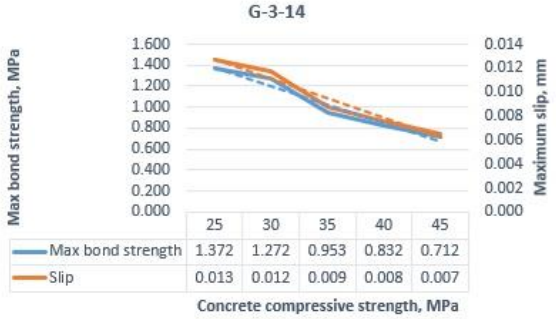

	25	30	35	40	45
Max bond strength	1.372	1.272	0.953	0.832	0.712
Slip	0.013	0.012	0.009	0.008	0.007

Figure 151: Maximum bond strength and maximum slip versus concrete compressive strength for models under three different impact loading.

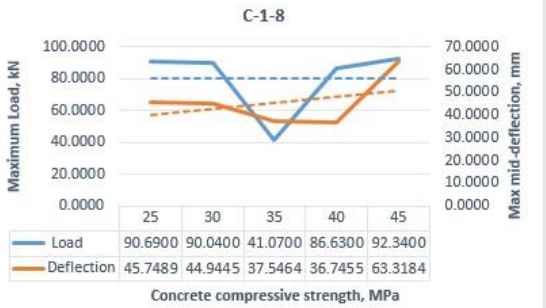

	25	30	35	40	45
Load	90.6900	90.0400	41.0700	86.6300	92.3400
Deflection	45.7489	44.9445	37.5464	36.7455	63.3184

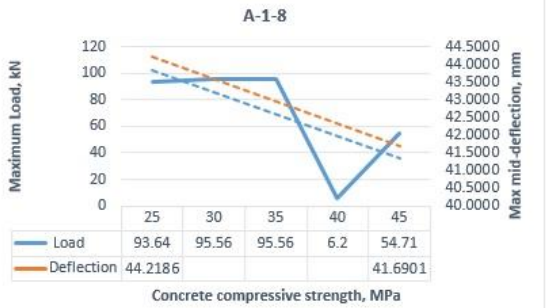

	25	30	35	40	45
Load	93.64	95.56	95.56	6.2	54.71
Deflection	44.2186				41.6901

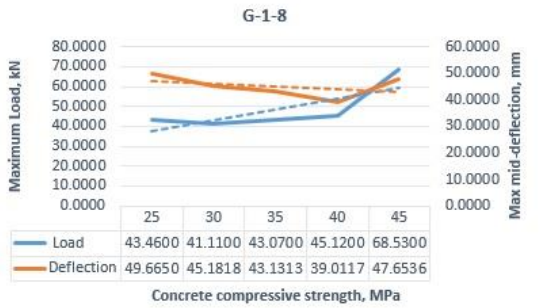

	25	30	35	40	45
Load	43.4600	41.1100	43.0700	45.1200	68.5300
Deflection	49.6650	45.1818	43.1313	39.0117	47.6536

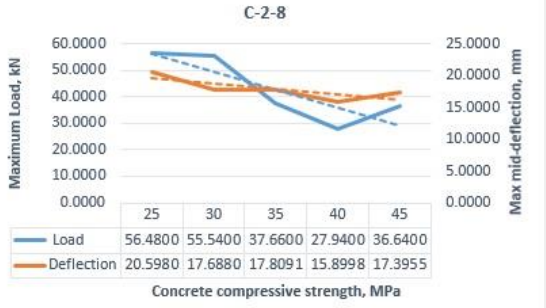

	25	30	35	40	45
Load	56.4800	55.5400	37.6600	27.9400	36.6400
Deflection	20.5980	17.6880	17.8091	15.8998	17.3955

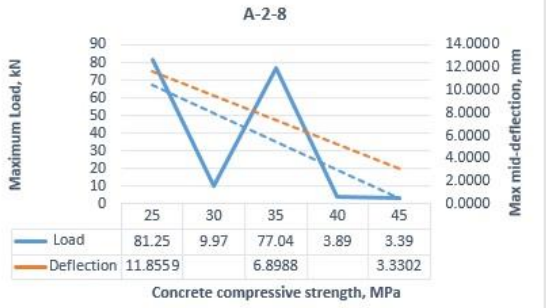

	25	30	35	40	45
Load	81.25	9.97	77.04	3.89	3.39
Deflection	11.8559		6.8988		3.3302

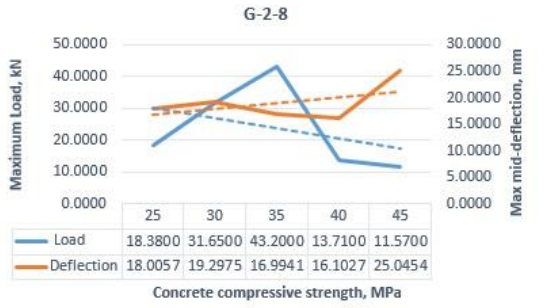

	25	30	35	40	45
Load	18.3800	31.6500	43.2000	13.7100	11.5700
Deflection	18.0057	19.2975	16.9941	16.1027	25.0454

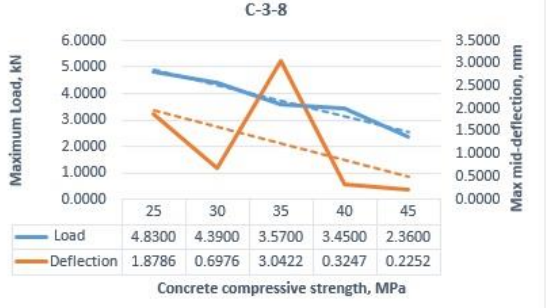

	25	30	35	40	45
Load	4.8300	4.3900	3.5700	3.4500	2.3600
Deflection	1.8786	0.6976	3.0422	0.3247	0.2252

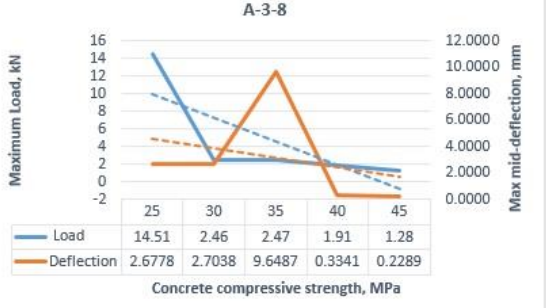

	25	30	35	40	45
Load	14.51	2.46	2.47	1.91	1.28
Deflection	2.6778	2.7038	9.6487	0.3341	0.2289

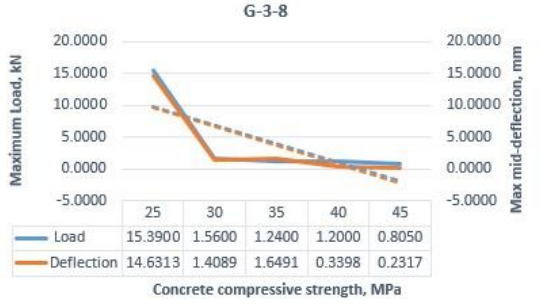

	25	30	35	40	45
Load	15.3900	1.5600	1.2400	1.2000	0.8050
Deflection	14.6313	1.4089	1.6491	0.3398	0.2317

C-1-10

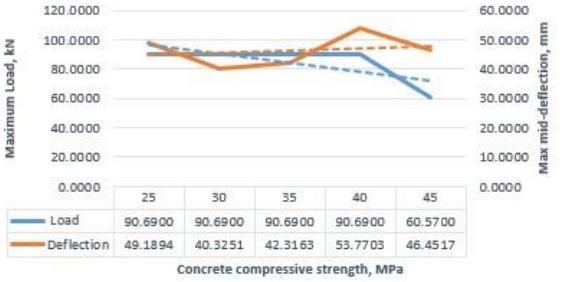

	25	30	35	40	45
Load	90.6900	90.6900	90.6900	90.6900	60.5700
Deflection	49.1894	40.3251	42.3163	53.7703	46.4517

Concrete compressive strength, MPa

A-1-10

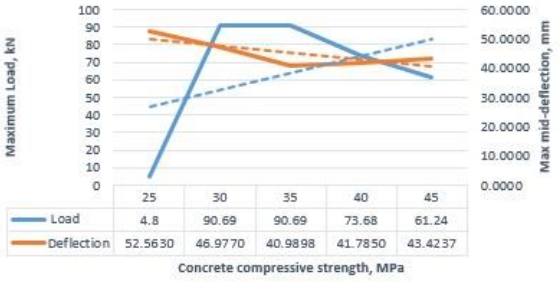

	25	30	35	40	45
Load	4.8	90.69	90.69	73.68	61.24
Deflection	52.5630	46.9770	40.9898	41.7850	43.4237

Concrete compressive strength, MPa

G-1-10

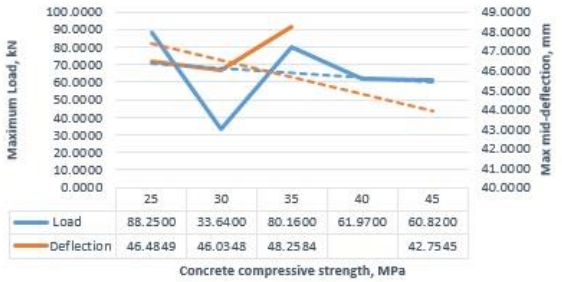

	25	30	35	40	45
Load	88.2500	33.6400	80.1600	61.9700	60.8200
Deflection	46.4849	46.0348	48.2584		42.7545

Concrete compressive strength, MPa

C-2-10

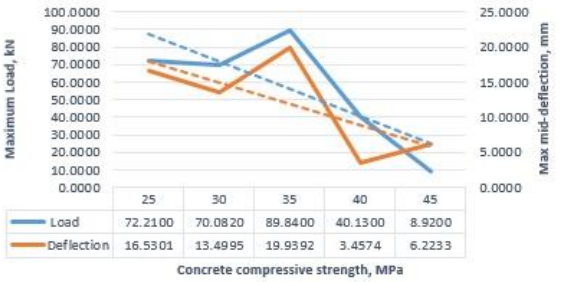

	25	30	35	40	45
Load	72.2100	70.0820	89.8400	40.1300	8.9200
Deflection	16.5301	13.4995	19.9392	3.4574	6.2233

Concrete compressive strength, MPa

A-2-10

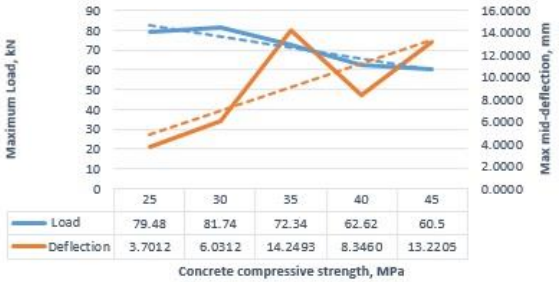

	25	30	35	40	45
Load	79.48	81.74	72.34	62.62	60.5
Deflection	3.7012	6.0312	14.2493	8.3460	13.2205

Concrete compressive strength, MPa

G-2-10

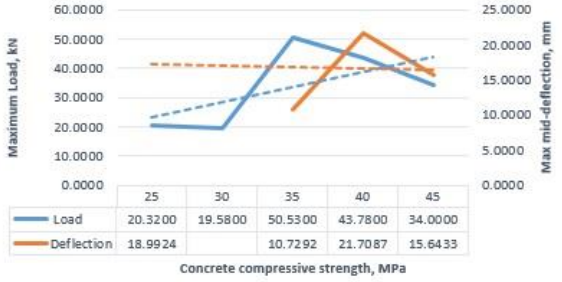

	25	30	35	40	45
Load	20.3200	19.5800	50.5300	43.7800	34.0000
Deflection	18.9924		10.7292	21.7087	15.6433

Concrete compressive strength, MPa

C-3-10

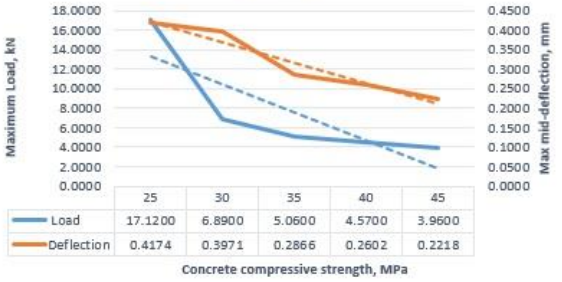

	25	30	35	40	45
Load	17.1200	6.8900	5.0600	4.5700	3.9600
Deflection	0.4174	0.3971	0.2866	0.2602	0.2218

Concrete compressive strength, MPa

A-3-10

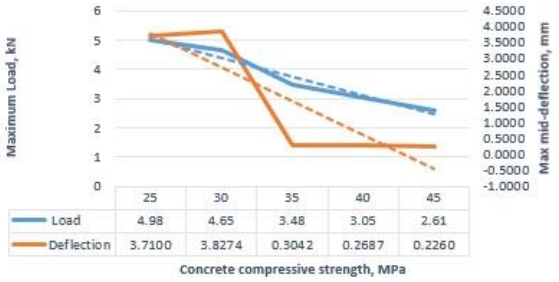

	25	30	35	40	45
Load	4.98	4.65	3.48	3.05	2.61
Deflection	3.7100	3.8274	0.3042	0.2687	0.2260

Concrete compressive strength, MPa

G-3-10

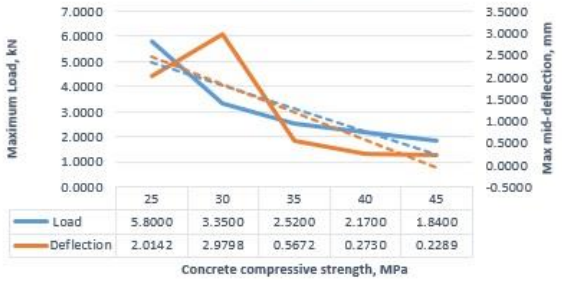

	25	30	35	40	45
Load	5.8000	3.3500	2.5200	2.1700	1.8400
Deflection	2.0142	2.9798	0.5672	0.2730	0.2289

Concrete compressive strength, MPa

C-1-12

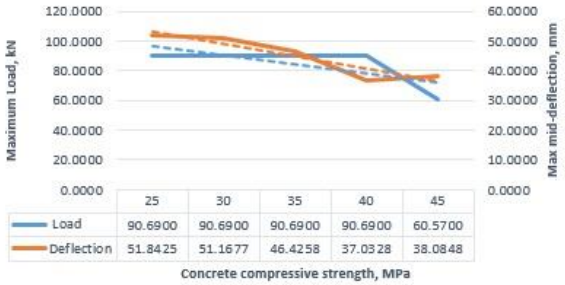

	25	30	35	40	45
Load	90.6900	90.6900	90.6900	90.6900	60.5700
Deflection	51.8425	51.1677	46.4258	37.0328	38.0848

A-1-12

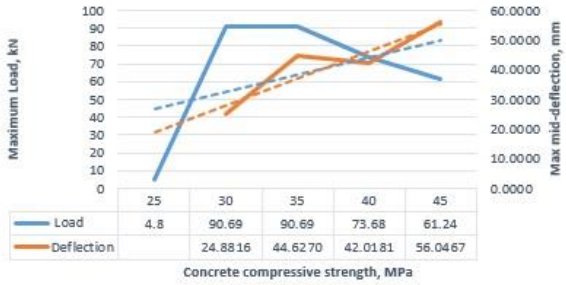

	25	30	35	40	45
Load	4.8	90.69	90.69	73.68	61.24
Deflection		24.8816	44.6270	42.0181	56.0467

G-1-12

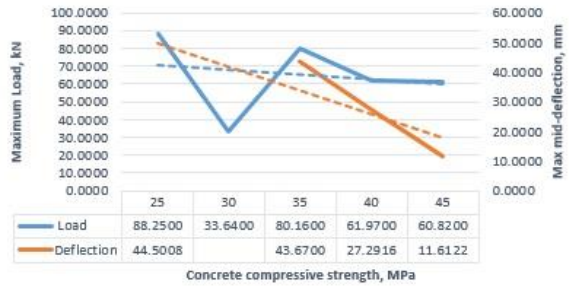

	25	30	35	40	45
Load	88.2500	33.6400	80.1600	61.9700	60.8200
Deflection	44.5008		43.6700	27.2916	11.6122

C-2-12

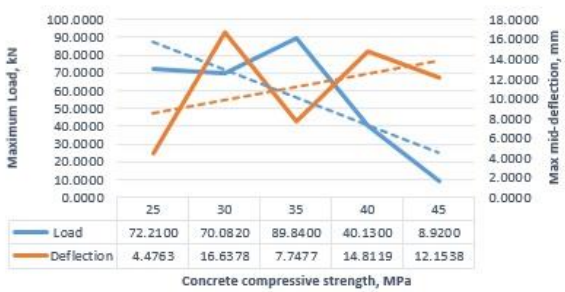

	25	30	35	40	45
Load	72.2100	70.0820	89.8400	40.1300	8.9200
Deflection	4.4763	16.6378	7.7477	14.8119	12.1538

A-2-12

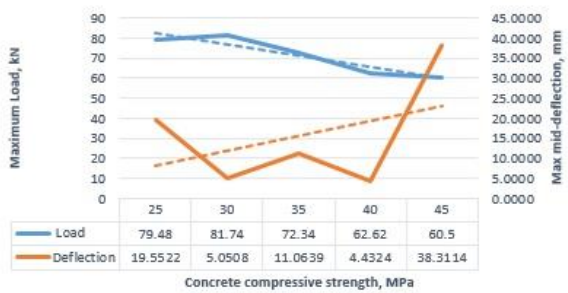

	25	30	35	40	45
Load	79.48	81.74	72.34	62.62	60.5
Deflection	19.5522	5.0508	11.0639	4.4324	38.3114

G-2-12

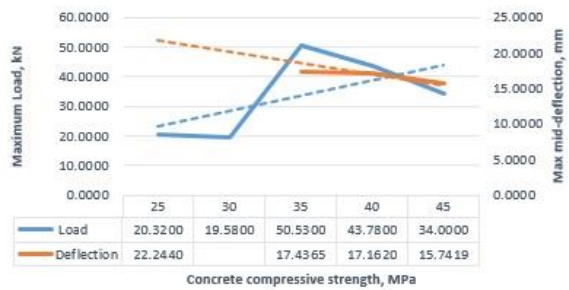

	25	30	35	40	45
Load	20.3200	19.5800	50.5300	43.7800	34.0000
Deflection	22.2440		17.4365	17.1620	15.7419

C-3-12

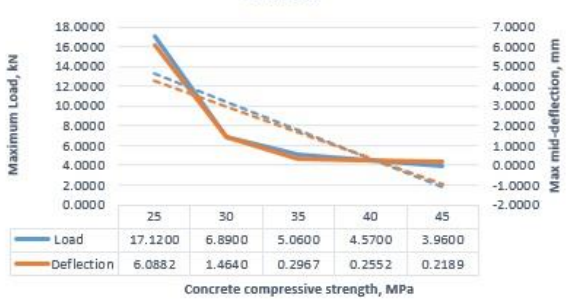

	25	30	35	40	45
Load	17.1200	6.8900	5.0600	4.5700	3.9600
Deflection	6.0882	1.4640	0.2967	0.2552	0.2189

A-3-12

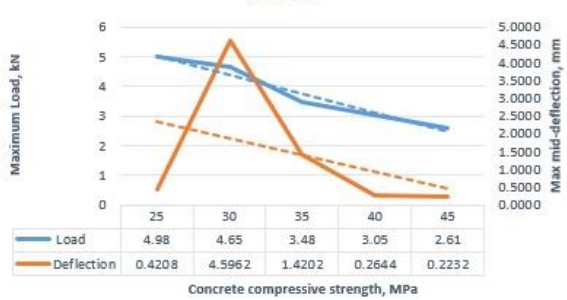

	25	30	35	40	45
Load	4.98	4.65	3.48	3.05	2.61
Deflection	0.4208	4.5962	1.4202	0.2644	0.2232

G-3-12

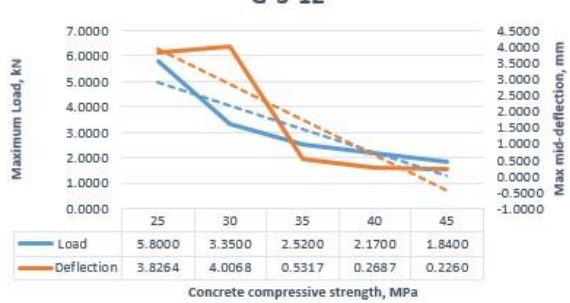

	25	30	35	40	45
Load	5.8000	3.3500	2.5200	2.1700	1.8400
Deflection	3.8264	4.0068	0.5317	0.2687	0.2260

C-1-14

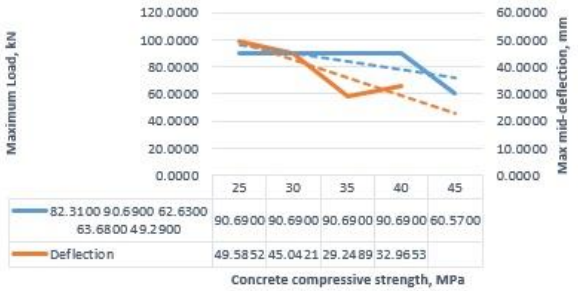

	25	30	35	40	45
82.3100 90.6900 62.6300 63.6800 49.2900	90.6900	90.6900	90.6900	90.6900	60.5700
Deflection	49.5852	45.0421	29.2489	32.9653	

A-1-14

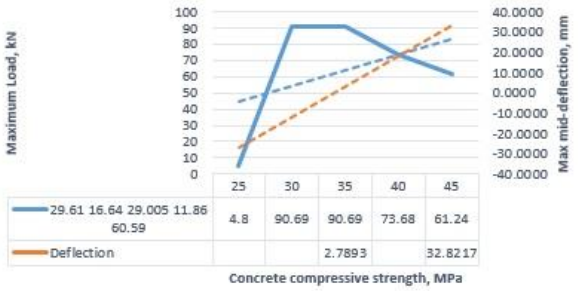

	25	30	35	40	45
29.61 16.64 29.005 11.86 60.59	4.8	90.69	90.69	73.68	61.24
Deflection			2.7893		32.8217

G-1-14

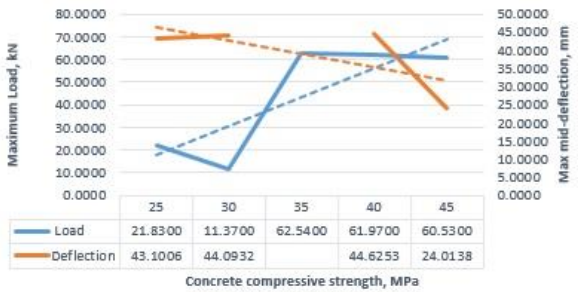

	25	30	35	40	45
Load	21.8300	11.3700	62.5400	61.9700	60.5300
Deflection	43.1006	44.0932		44.6253	24.0138

C-2-14

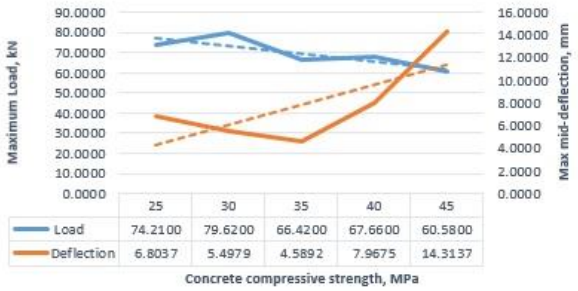

	25	30	35	40	45
Load	74.2100	79.6200	66.4200	67.6600	60.5800
Deflection	6.8037	5.4979	4.5892	7.9675	14.3137

A-2-14

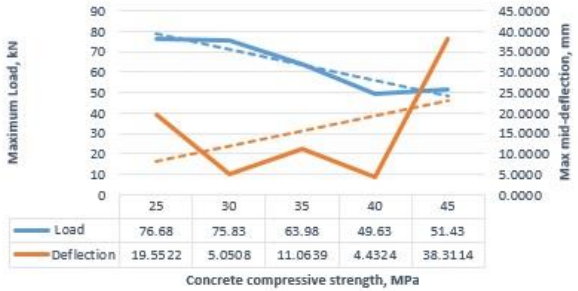

	25	30	35	40	45
Load	76.68	75.83	63.98	49.63	51.43
Deflection	19.5522	5.0508	11.0639	4.4324	38.3114

G-2-14

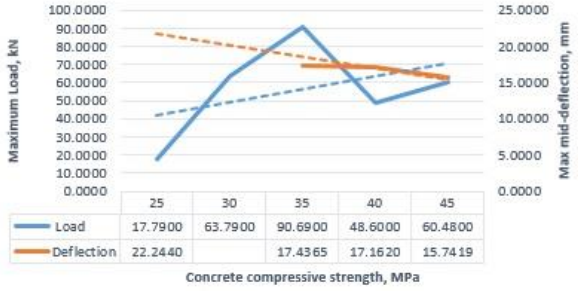

	25	30	35	40	45
Load	17.7900	63.7900	90.6900	48.6000	60.4800
Deflection	22.2440		17.4365	17.1620	15.7419

C-3-14

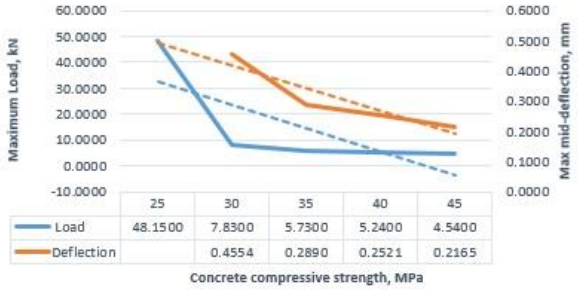

	25	30	35	40	45
Load	48.1500	7.8300	5.7300	5.2400	4.5400
Deflection		0.4554	0.2890	0.2521	0.2165

A-3-14

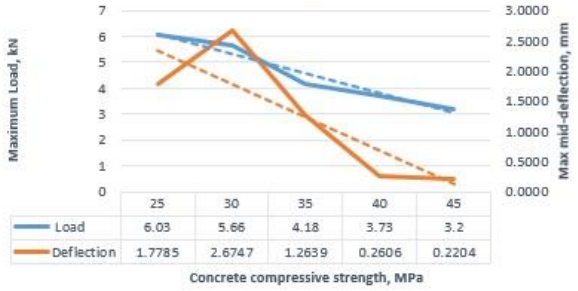

	25	30	35	40	45
Load	6.03	5.66	4.18	3.73	3.2
Deflection	1.7785	2.6747	1.2639	0.2606	0.2204

G-3-14

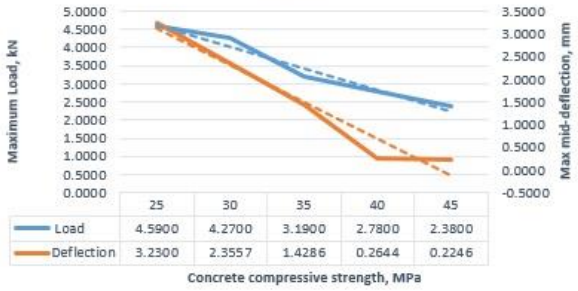

	25	30	35	40	45
Load	4.5900	4.2700	3.1900	2.7800	2.3800
Deflection	3.2300	2.3557	1.4286	0.2644	0.2246

Figure 152: Max load and Max mid-deflection relationship with respect to concrete compressive strength for CFRP, AFRP, and GFRP RC beams under impact loading.

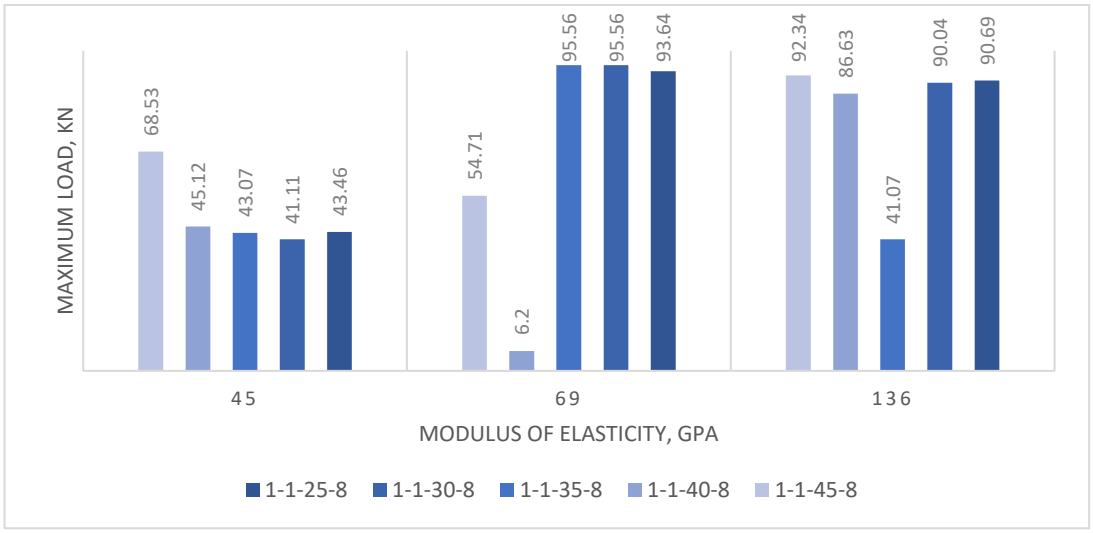
MAXIMUM LOAD, KN
68.53
45.12
43.07
41.11
43.46
54.71
6.2
95.56
95.56
93.64
92.34
86.63
41.07
90.04
90.69
45
69
136
MODULUS OF ELASTICITY, GPA
1-1-25-8
1-1-30-8
1-1-35-8
1-1-40-8
1-1-45-8

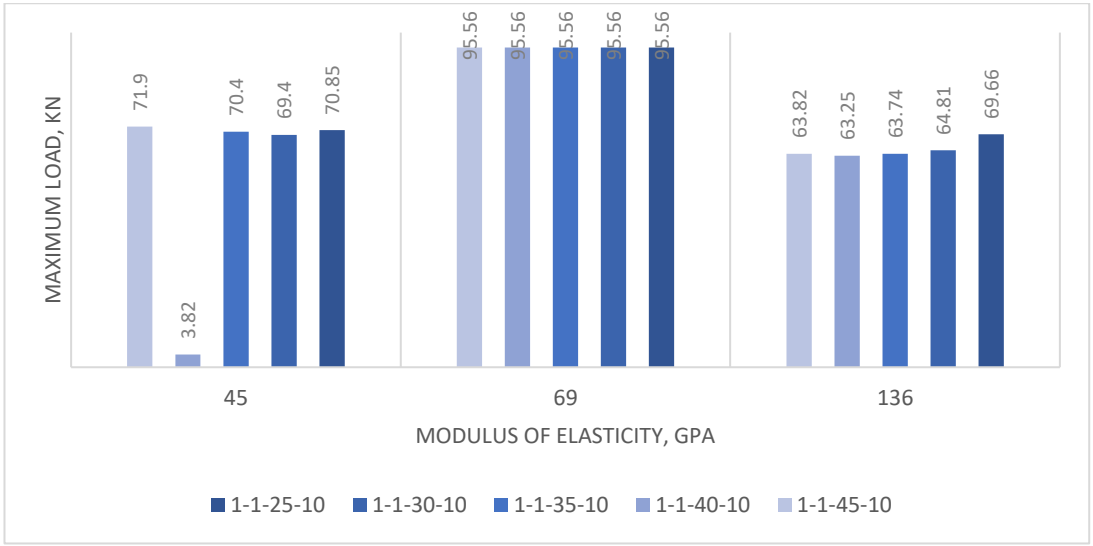
MAXIMUM LOAD, KN
71.9
3.82
70.4
69.4
70.85
95.56
95.56
95.56
95.56
95.56
63.82
63.25
63.74
64.81
69.66
45
69
136
MODULUS OF ELASTICITY, GPA
1-1-25-10
1-1-30-10
1-1-35-10
1-1-40-10
1-1-45-10

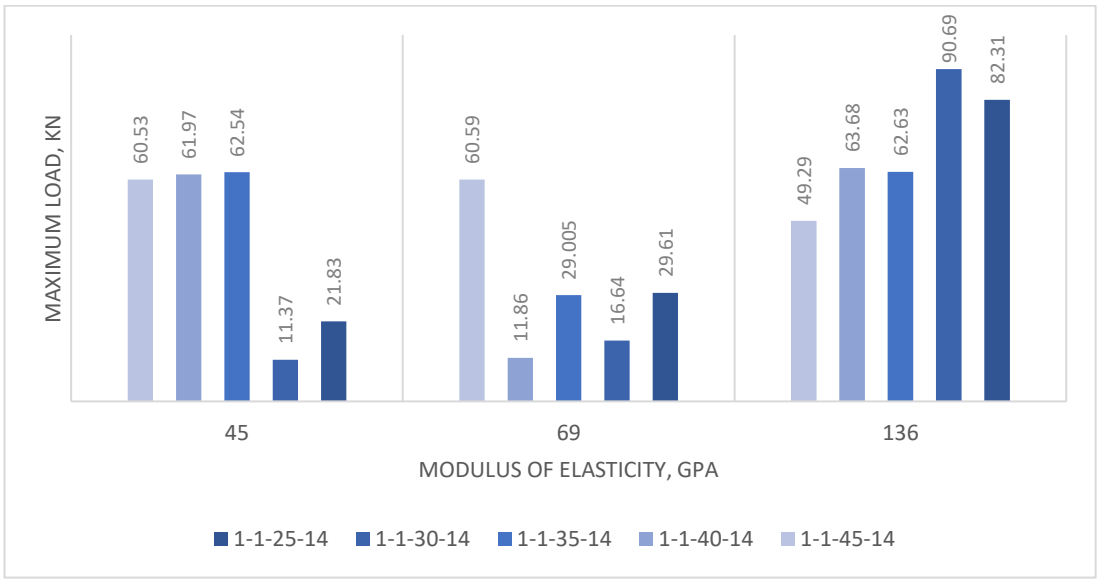
MAXIMUM LOAD, KN
60.53
61.97
62.54
11.37
21.83
60.59
11.86
29.005
16.64
29.61
49.29
63.68
62.63
90.69
82.31
45
69
136
MODULUS OF ELASTICITY, GPA
1-1-25-14
1-1-30-14
1-1-35-14
1-1-40-14
1-1-45-14

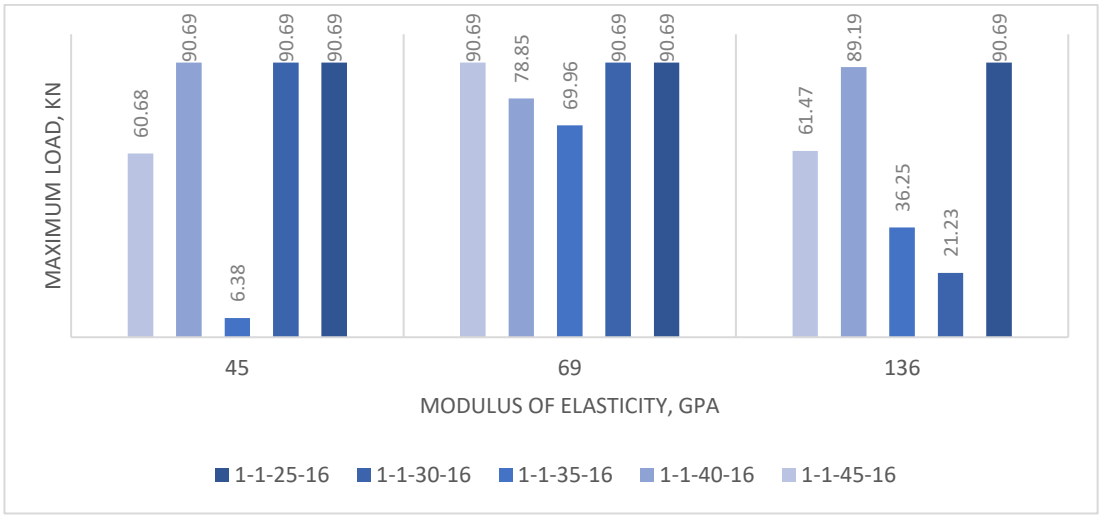

Figure 153: Effect of modulus of elasticity on maximum load under 320 kN impact loading.

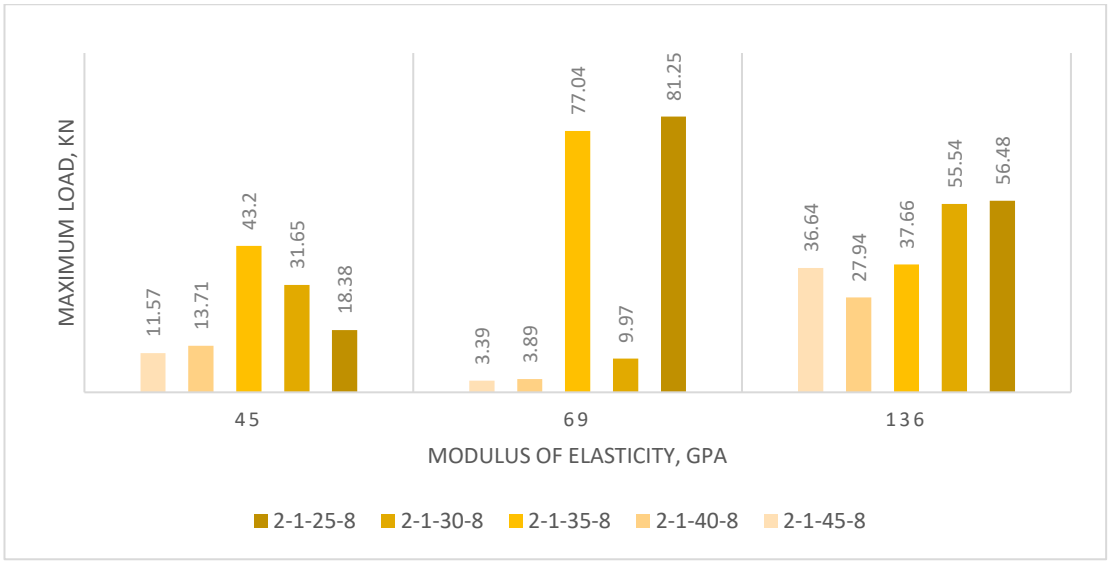

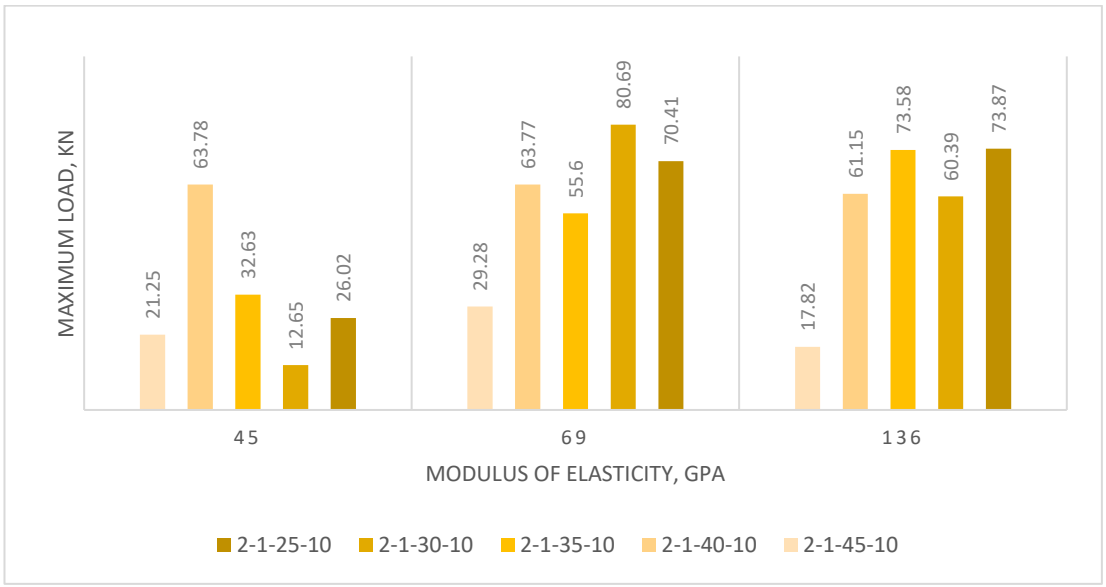

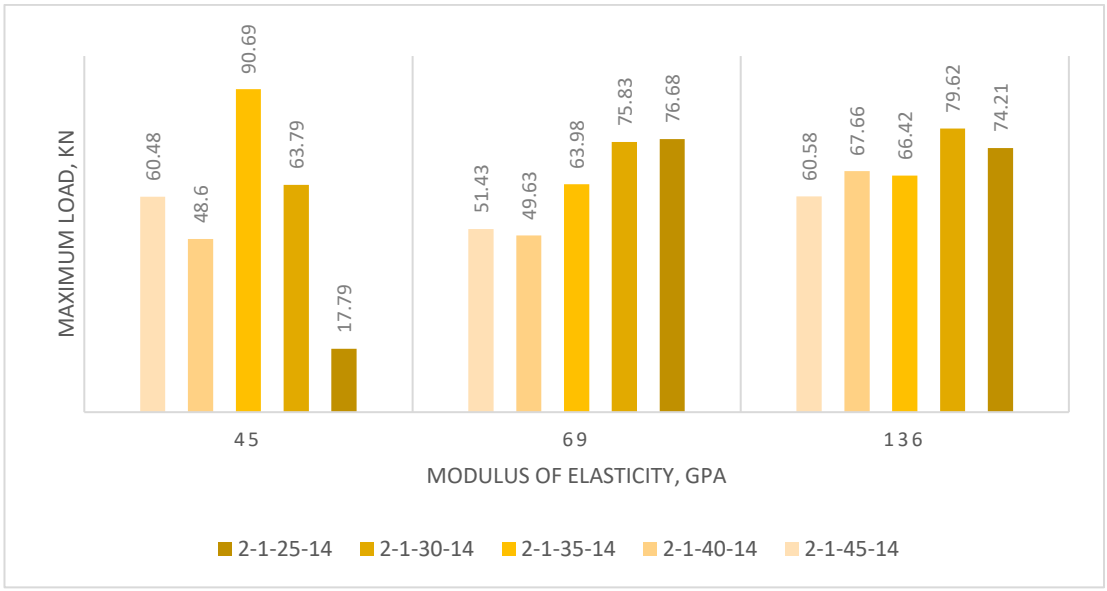

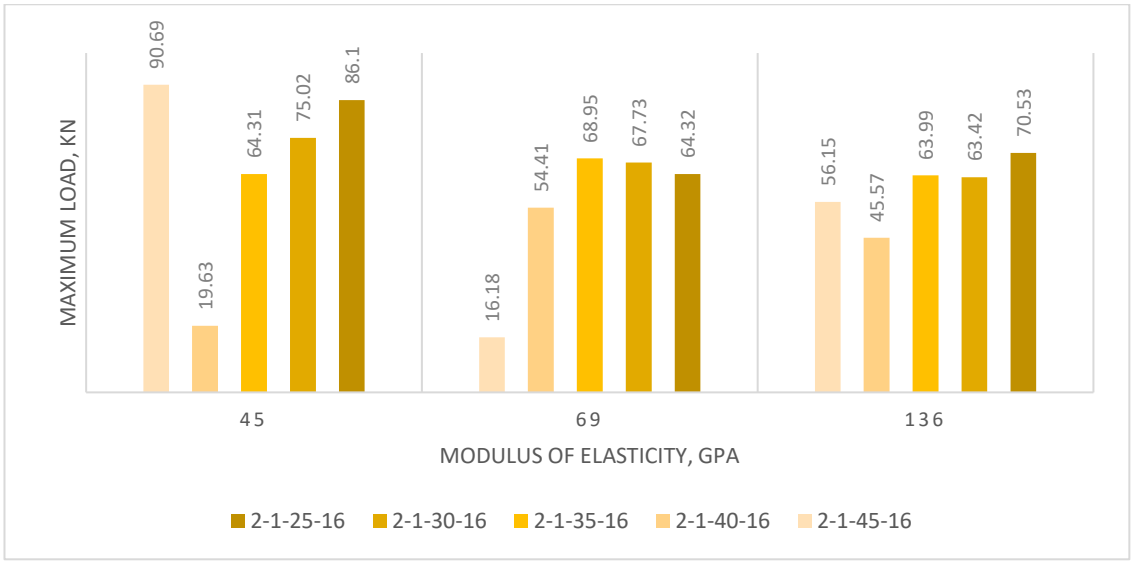

Figure 154: Effect of modulus of elasticity on maximum load under 80 kN impact loading.

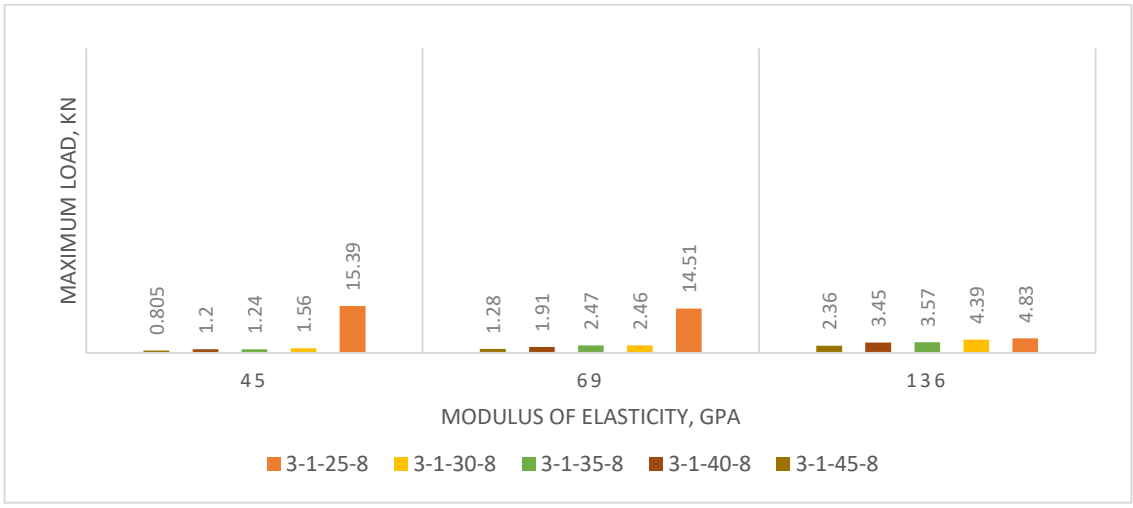

Figure 155: Effect of modulus of elasticity on maximum load under 40 kN impact loading.

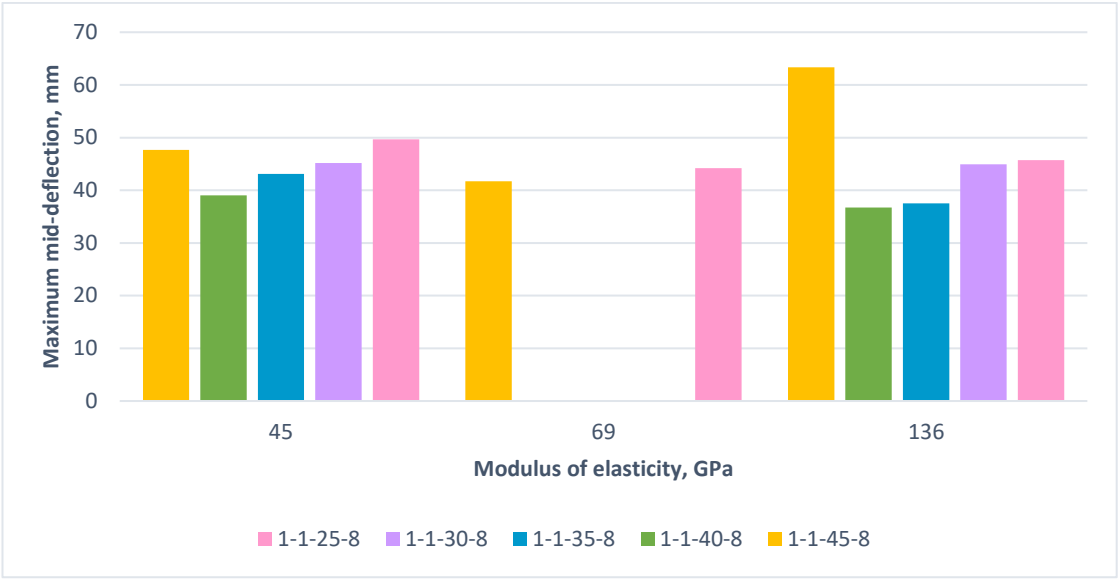
70
60
50
40
30
20
10
0
Maximum mid-deflection, mm
45
69
136
Modulus of elasticity, GPa
1-1-25-8
1-1-30-8
1-1-35-8
1-1-40-8
1-1-45-8

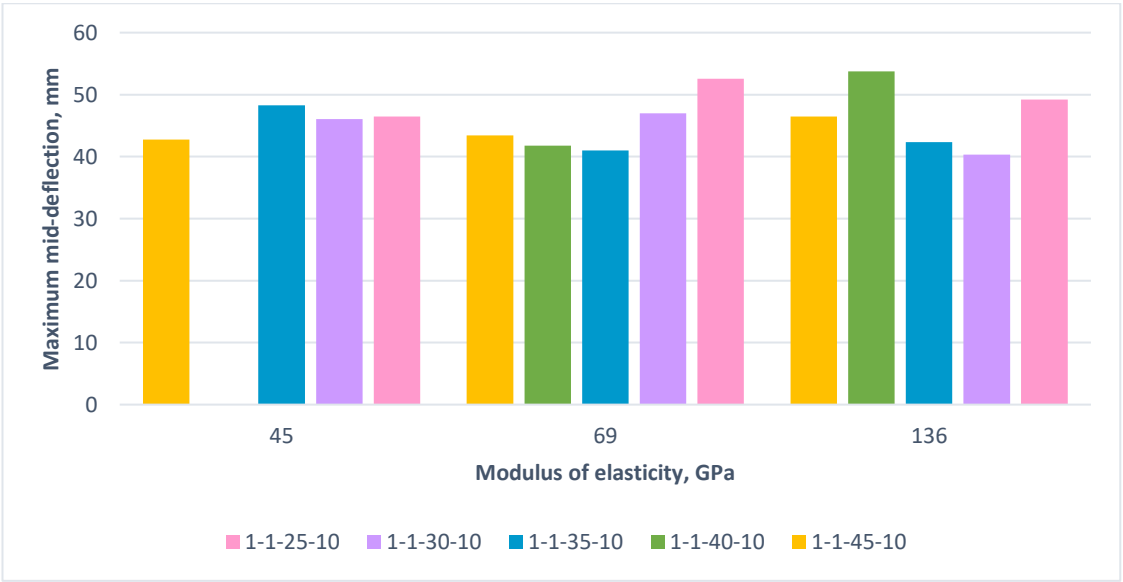
60
50
40
30
20
10
0
Maximum mid-deflection, mm
45
69
136
Modulus of elasticity, GPa
1-1-25-10
1-1-30-10
1-1-35-10
1-1-40-10
1-1-45-10

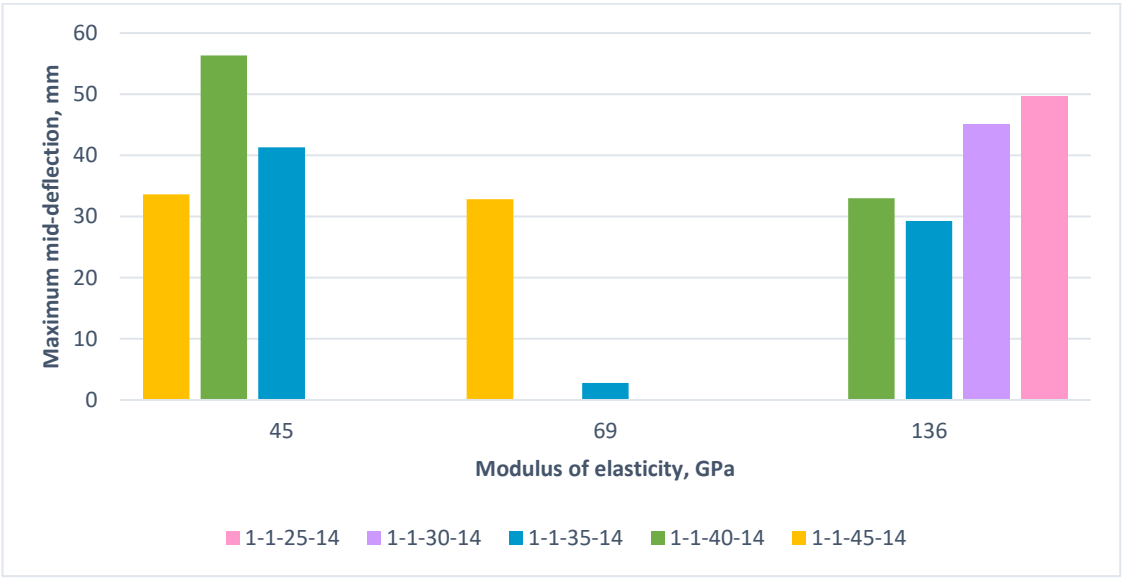
60
50
40
30
20
10
0
Maximum mid-deflection, mm
45
69
136
Modulus of elasticity, GPa
1-1-25-14
1-1-30-14
1-1-35-14
1-1-40-14
1-1-45-14

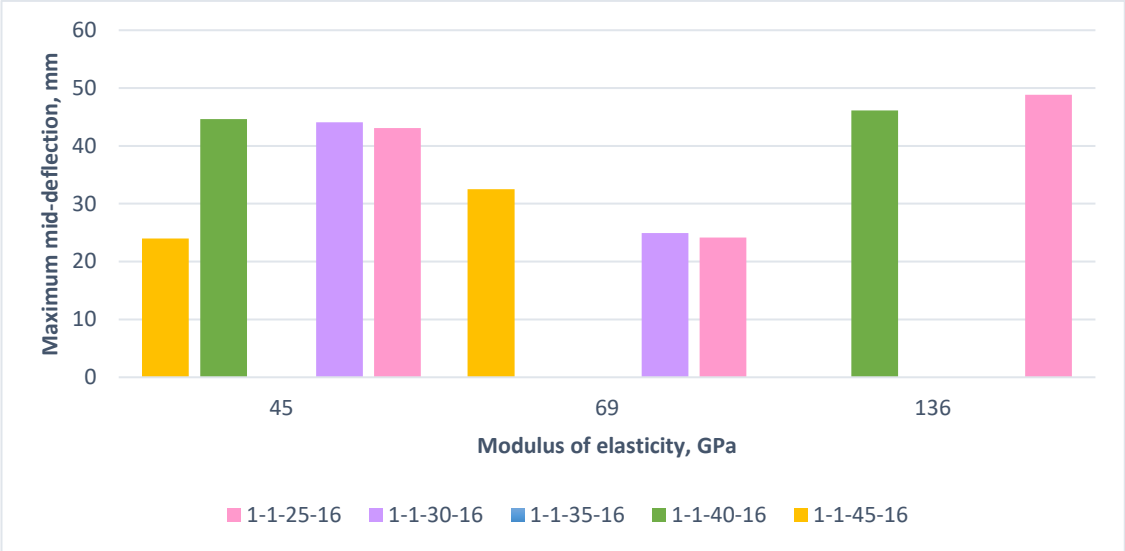

Figure 156: Effect of modulus of elasticity on maximum mid-deflection under 320 kN impact loading.

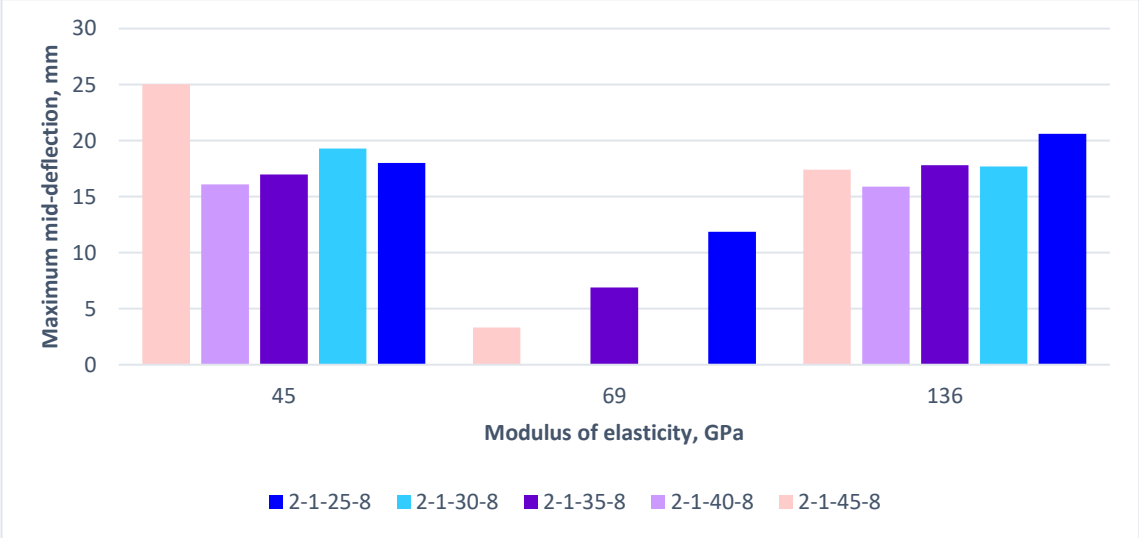

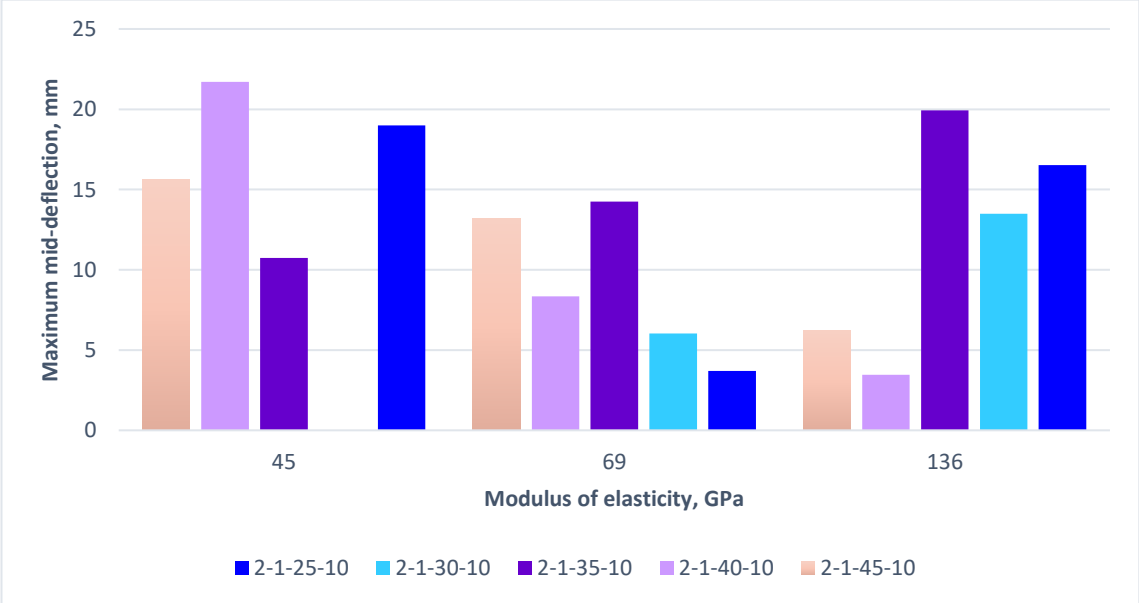

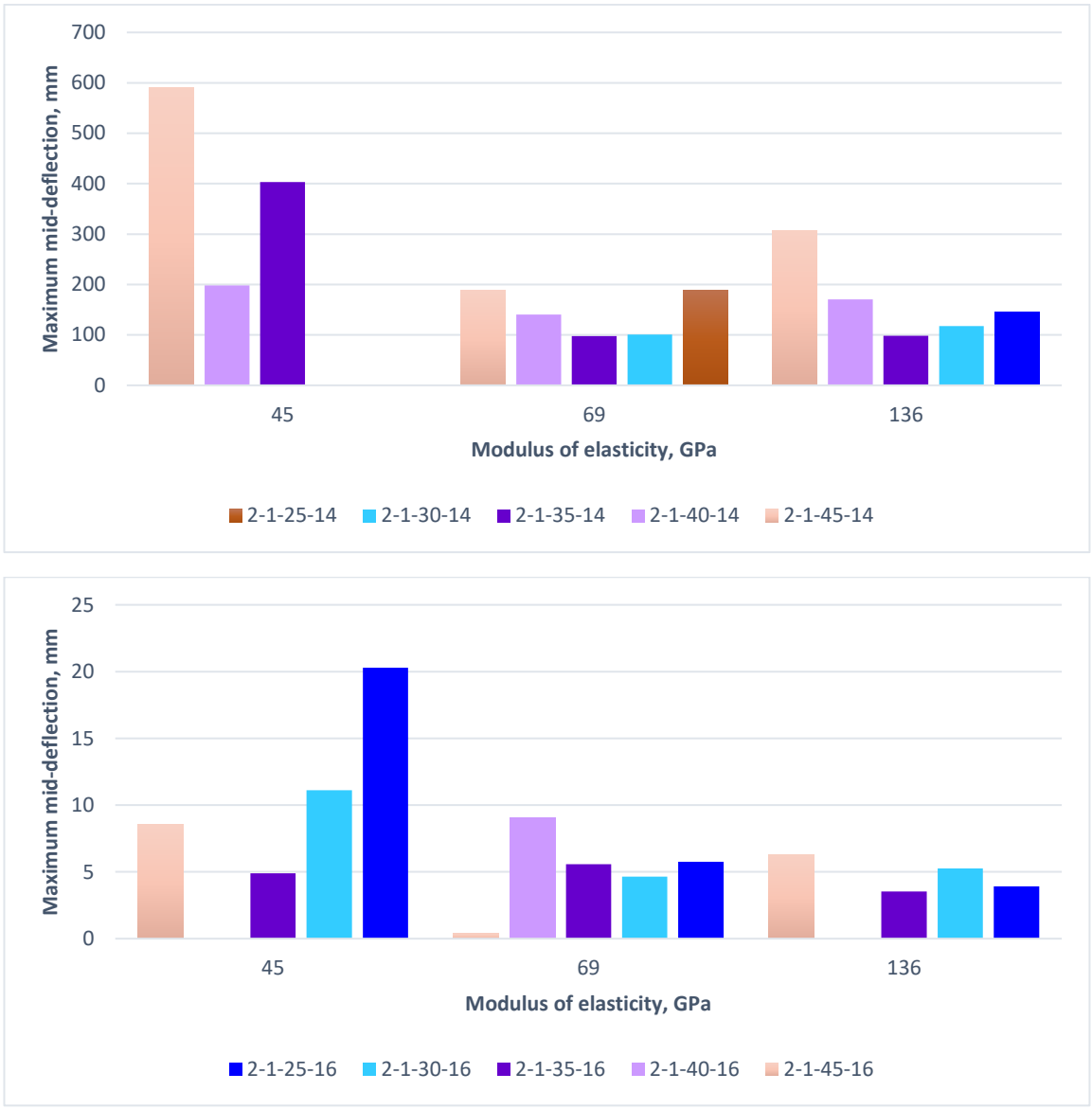

Figure 157: Effect of modulus of elasticity on maximum mid-deflection under 80 kN impact loading.

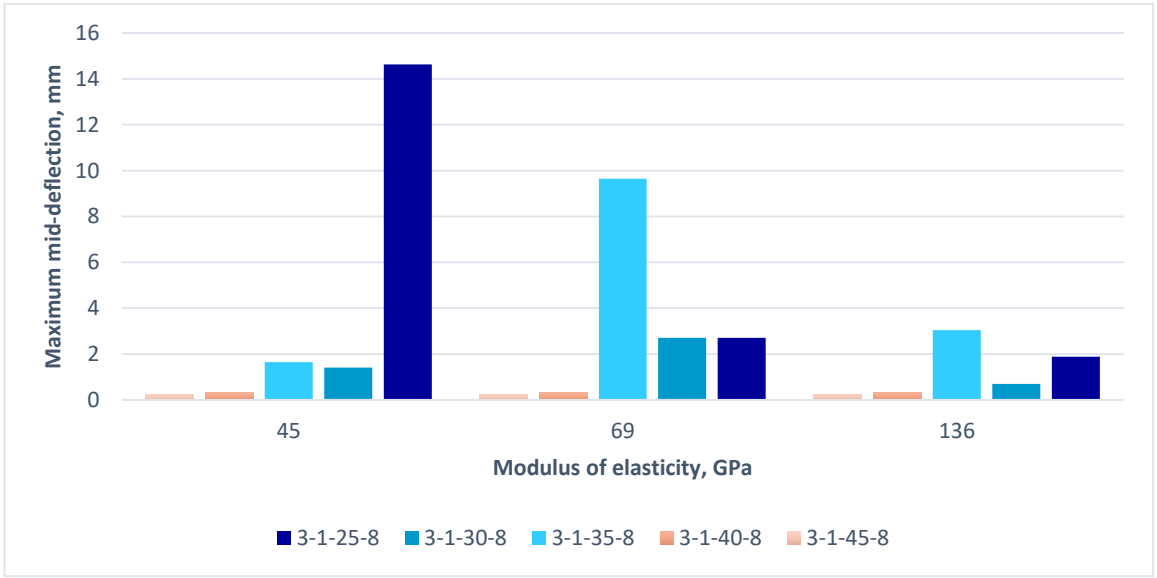

Figure 158: Effect of modulus of elasticity on maximum mid-deflection under 40 kN impact loading.

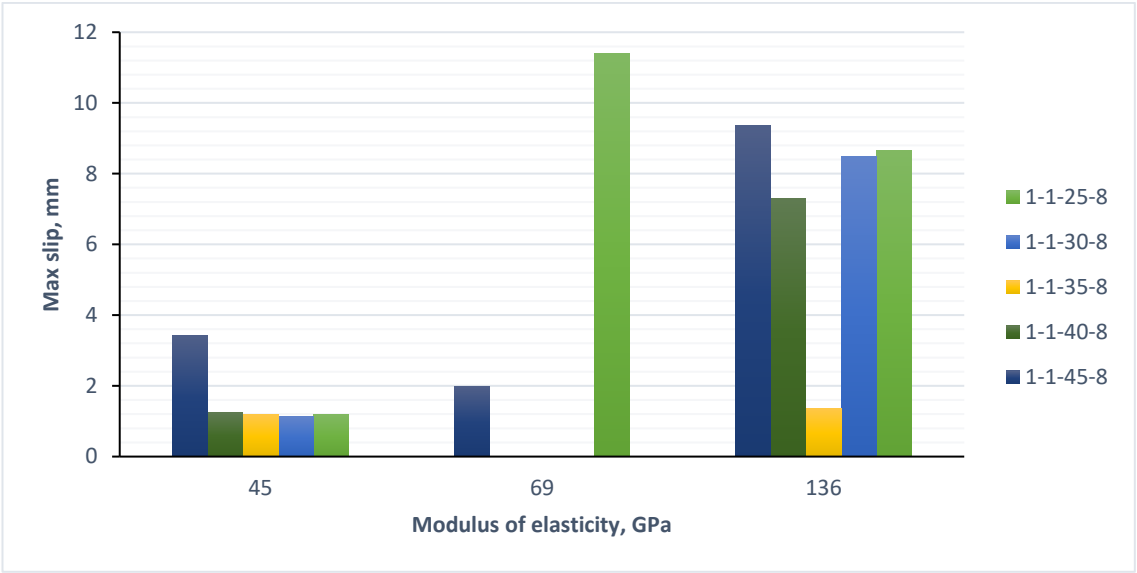
12
10
8
6
4
2
0
Max slip, mm
45
69
136
Modulus of elasticity, GPa
1-1-25-8
1-1-30-8
1-1-35-8
1-1-40-8
1-1-45-8

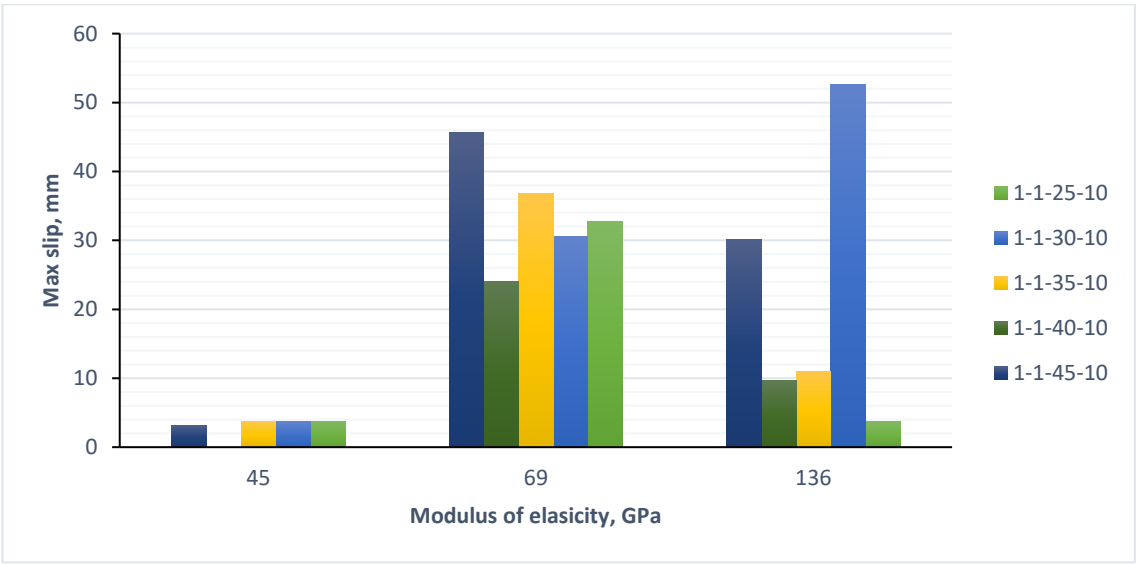
60
50
40
30
20
10
0
Max slip, mm
45
69
136
Modulus of elasicity, GPa
1-1-25-10
1-1-30-10
1-1-35-10
1-1-40-10
1-1-45-10

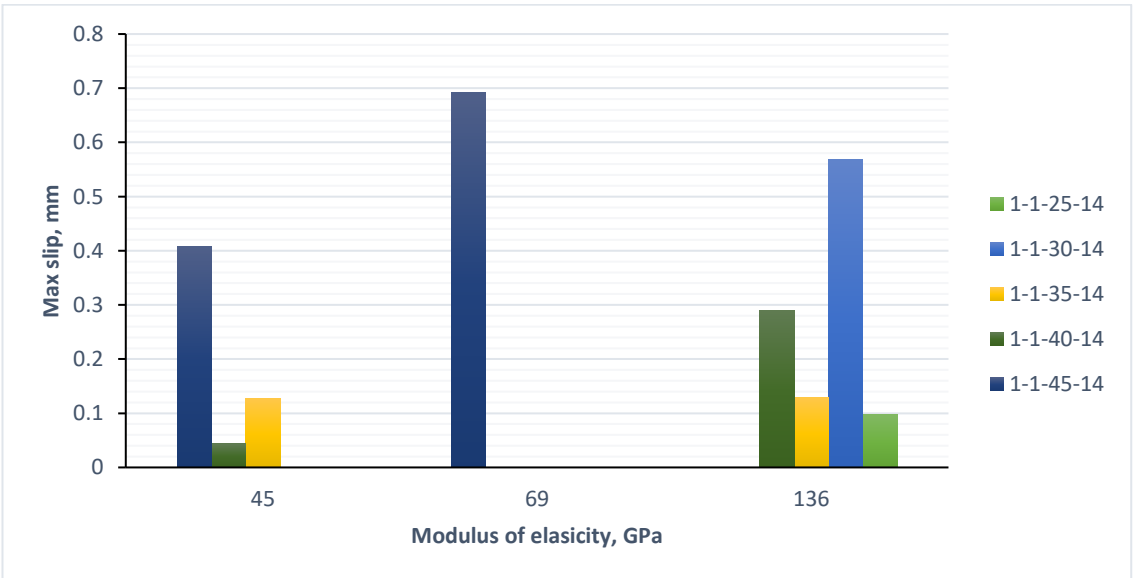
0.8
0.7
0.6
0.5
0.4
0.3
0.2
0.1
0
Max slip, mm
45
69
136
Modulus of elasicity, GPa
1-1-25-14
1-1-30-14
1-1-35-14
1-1-40-14
1-1-45-14

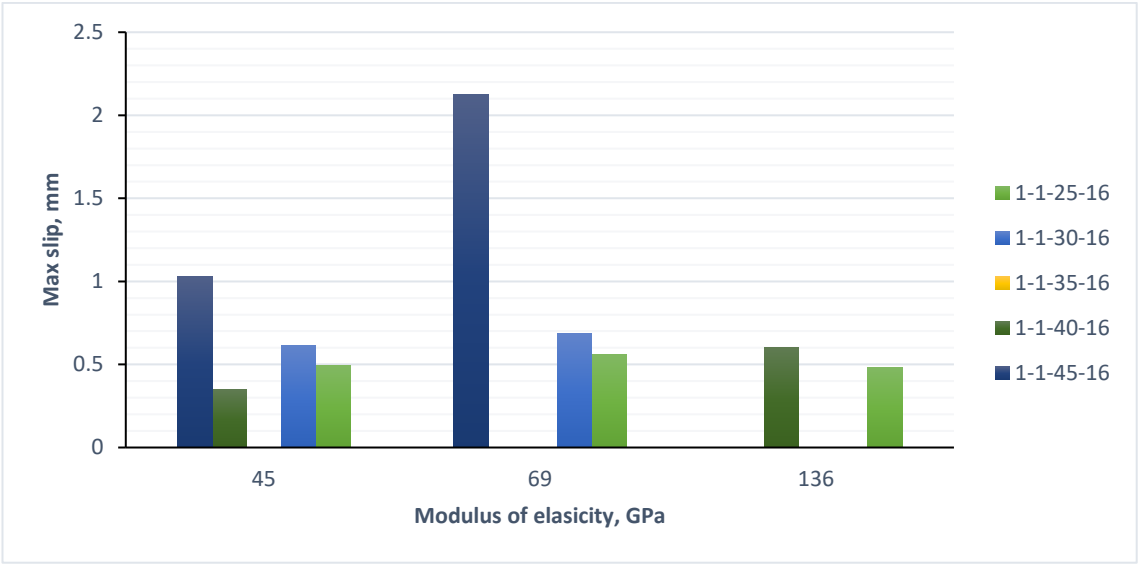

Figure 159: Effect of modulus of elasticity on maximum slip under 320 kN impact loading.

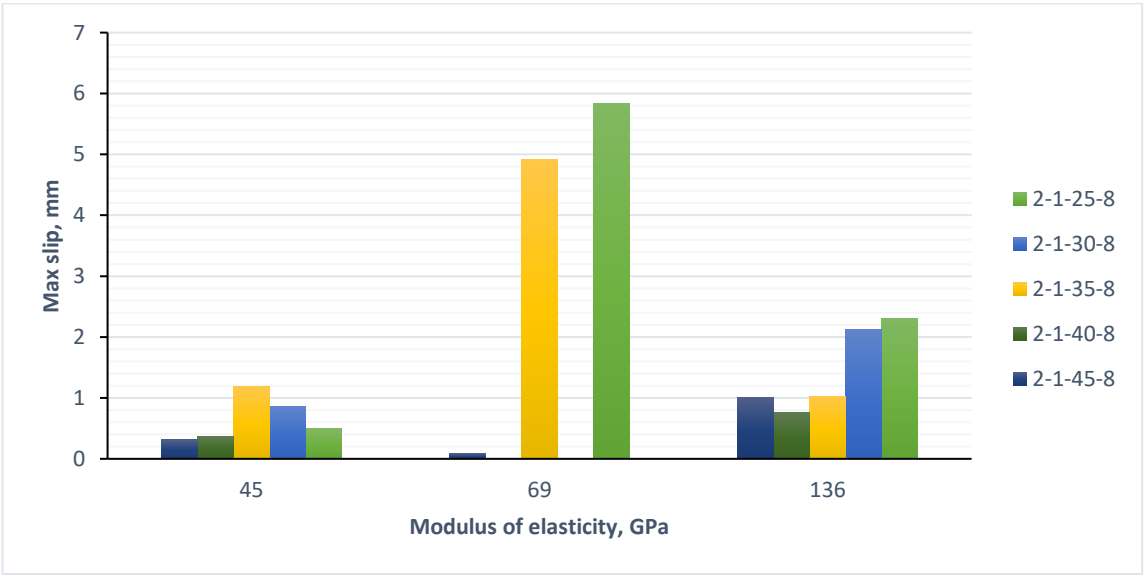

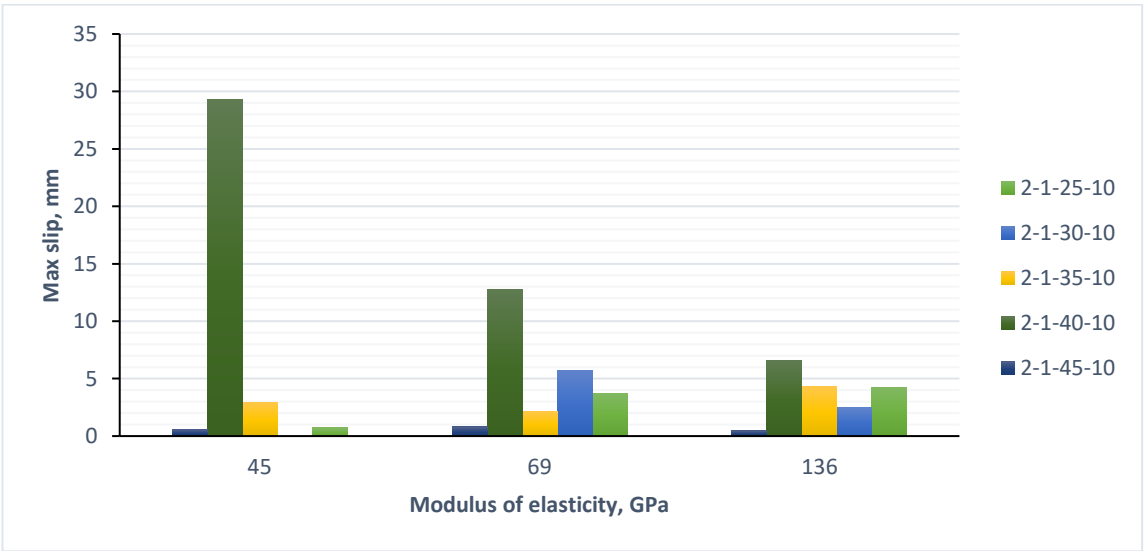

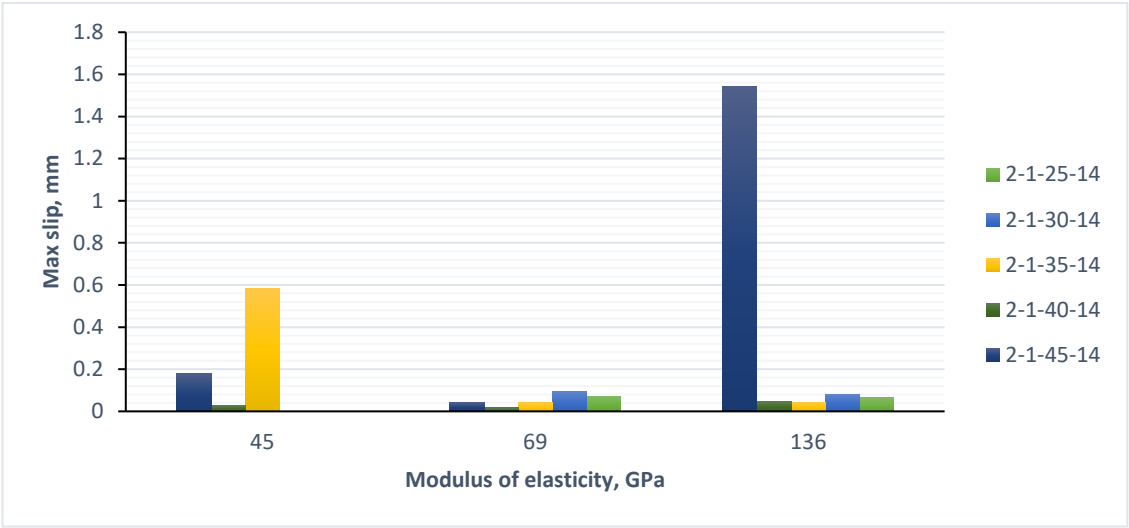

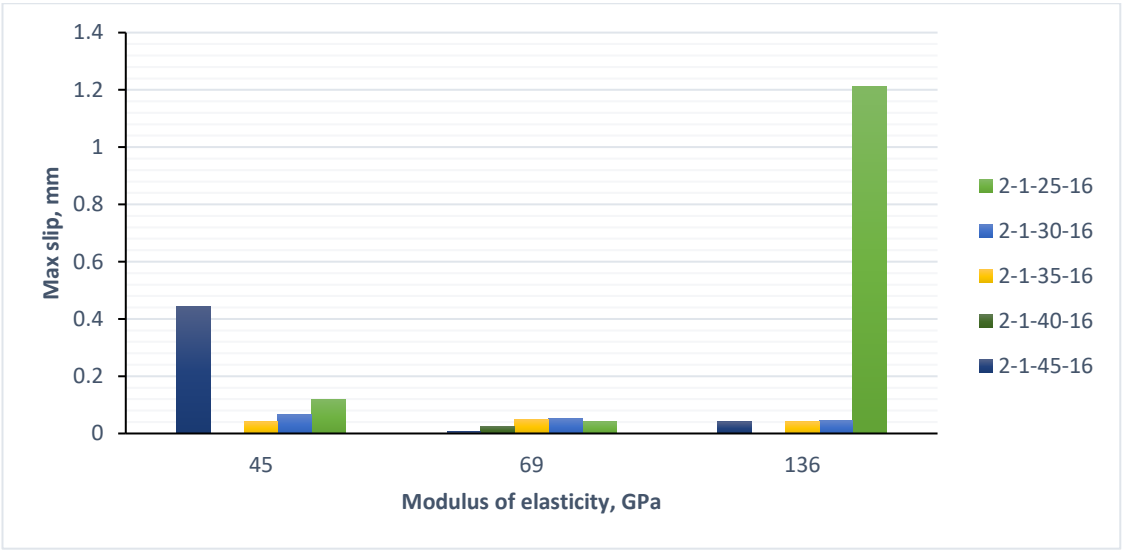

Figure 160: Effect of modulus of elasticity on maximum slip under 80 kN impact loading.

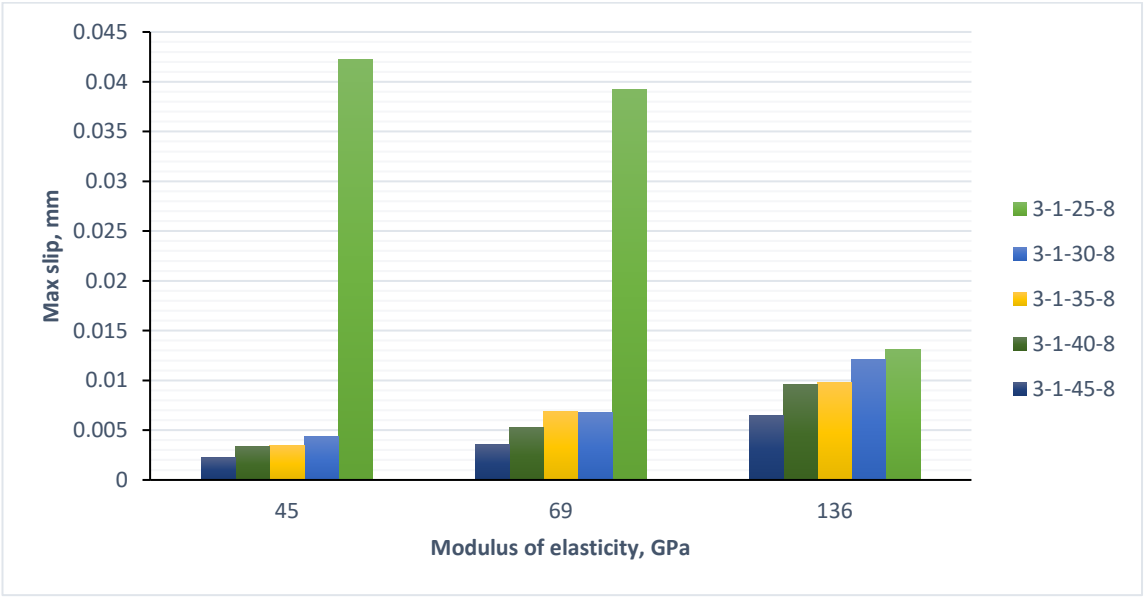

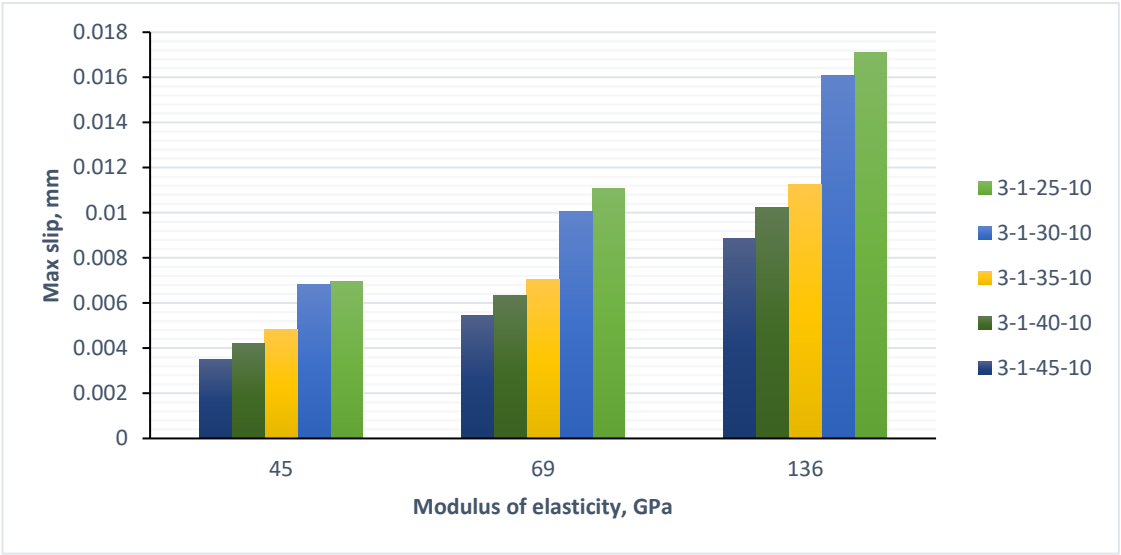

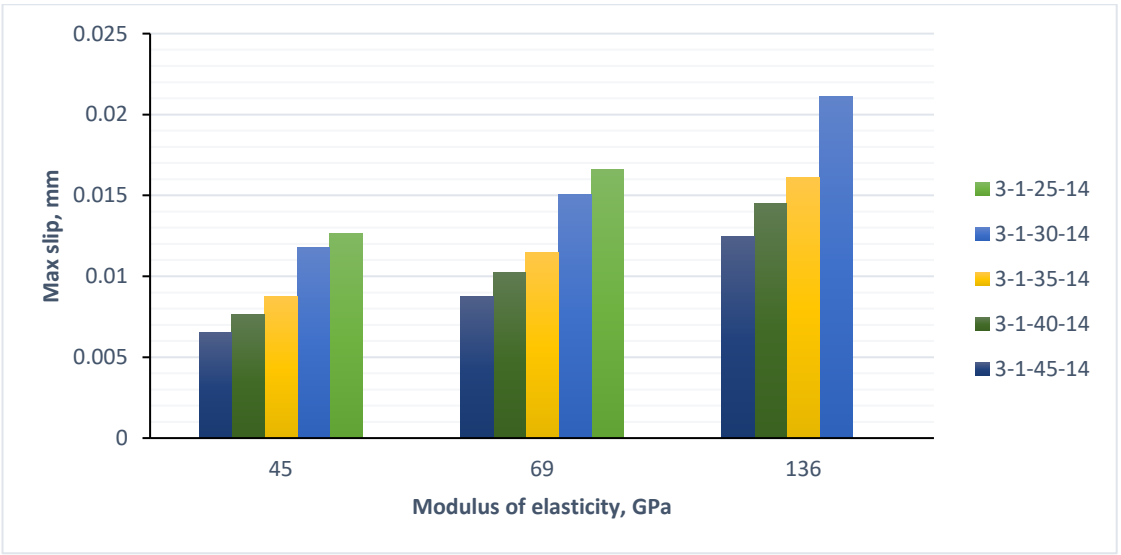

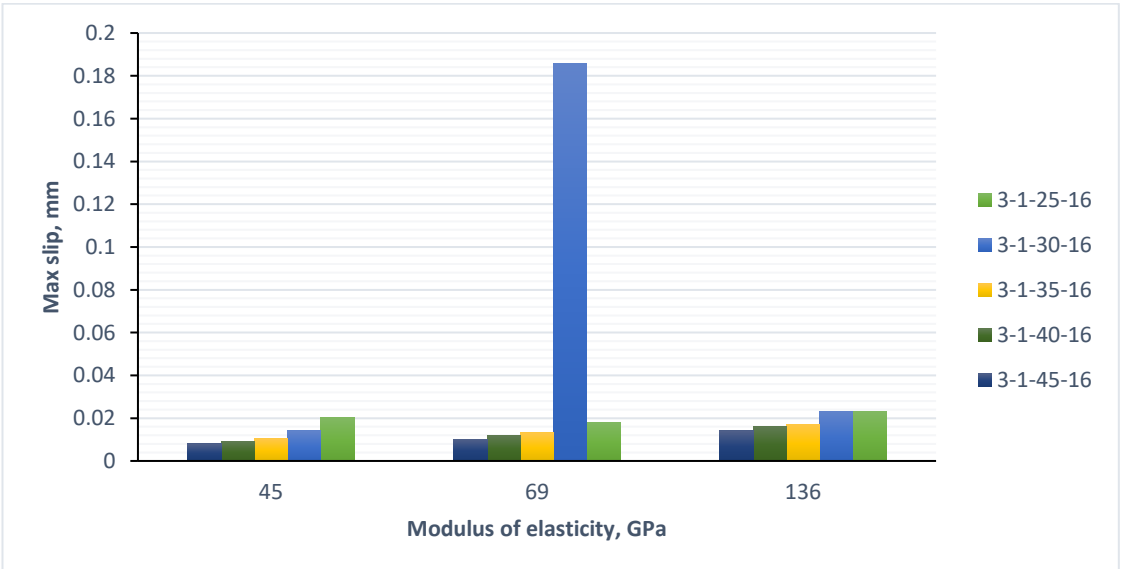

Figure 161: Effect of modulus of elasticity on maximum slip under 40 kN impact loading.

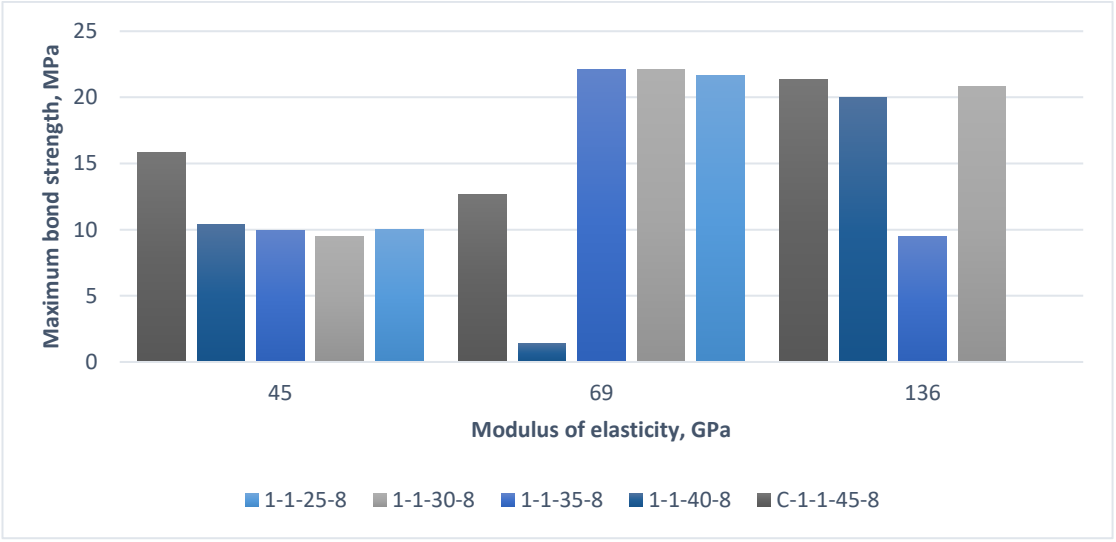
Maximum bond strength, MPa
25
20
15
10
5
0
45
69
136
Modulus of elasticity, GPa
1-1-25-8
1-1-30-8
1-1-35-8
1-1-40-8
C-1-1-45-8

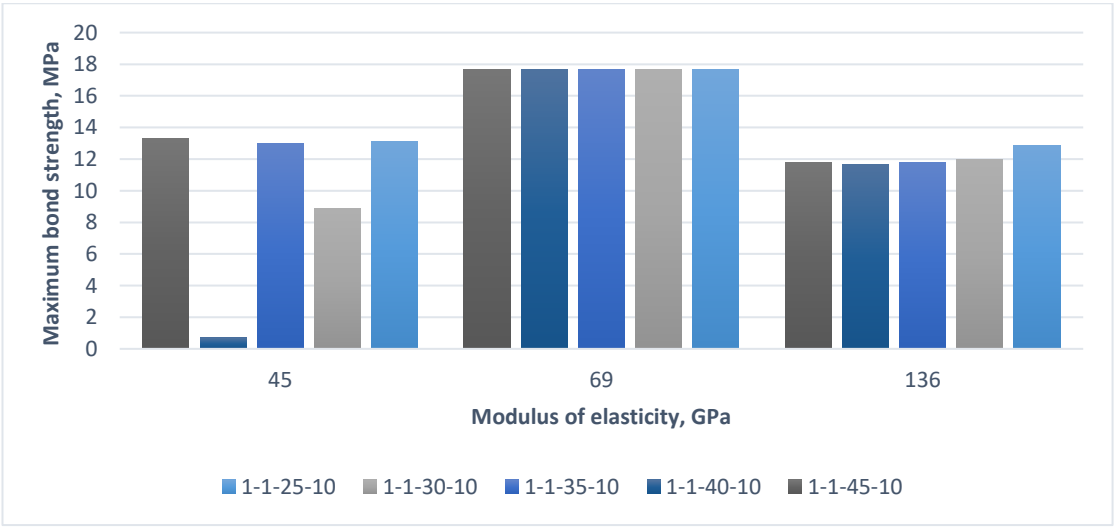
Maximum bond strength, MPa
20
18
16
14
12
10
8
6
4
2
0
45
69
136
Modulus of elasticity, GPa
1-1-25-10
1-1-30-10
1-1-35-10
1-1-40-10
1-1-45-10

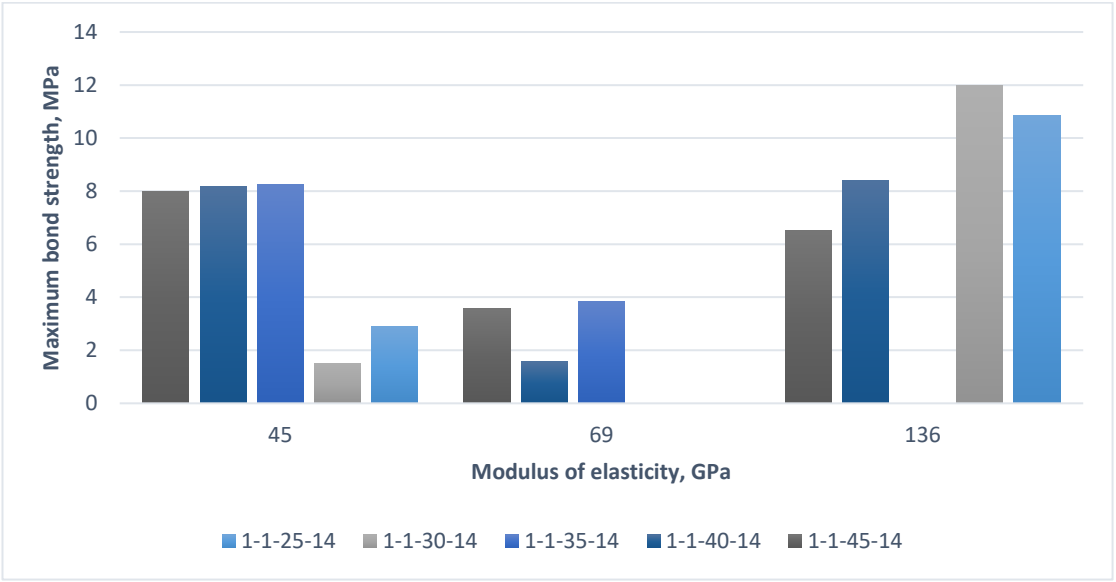
Maximum bond strength, MPa
14
12
10
8
6
4
2
0
45
69
136
Modulus of elasticity, GPa
1-1-25-14
1-1-30-14
1-1-35-14
1-1-40-14
1-1-45-14

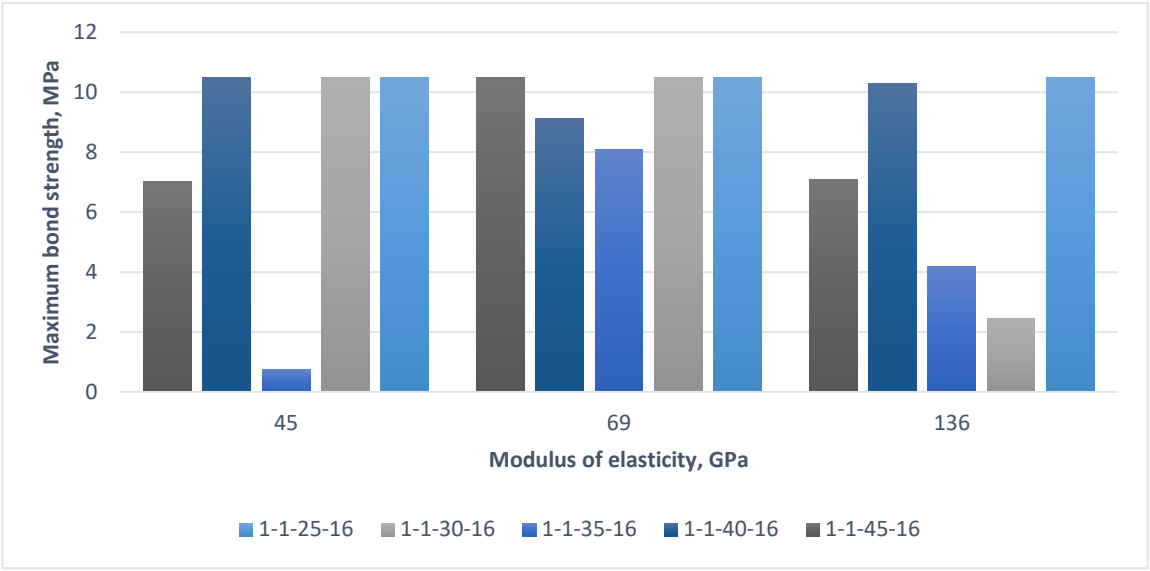

Figure 162: Effect of modulus of elasticity on maximum bond strength under 320 kN impact loading.

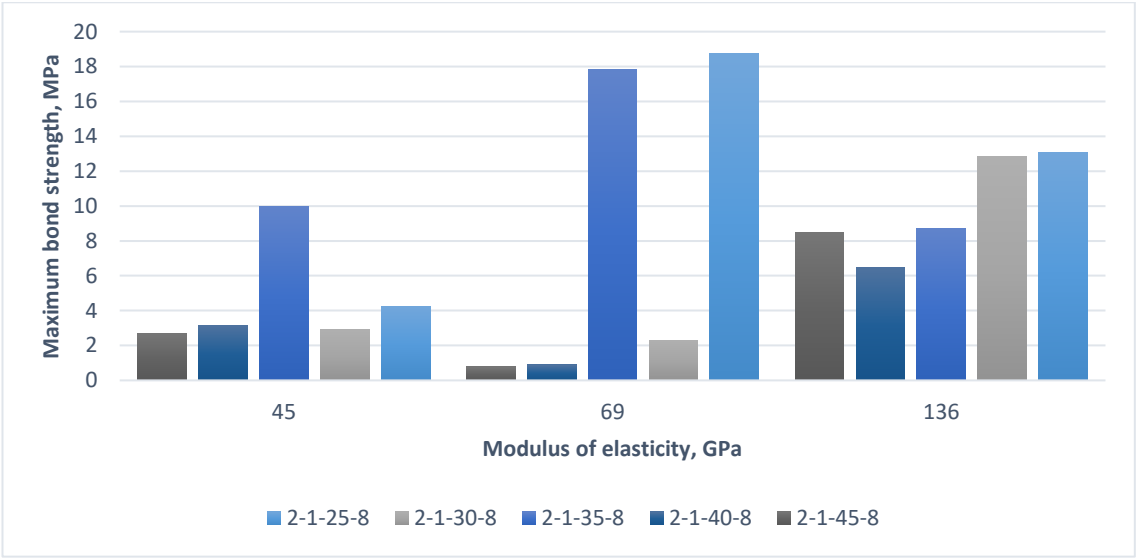

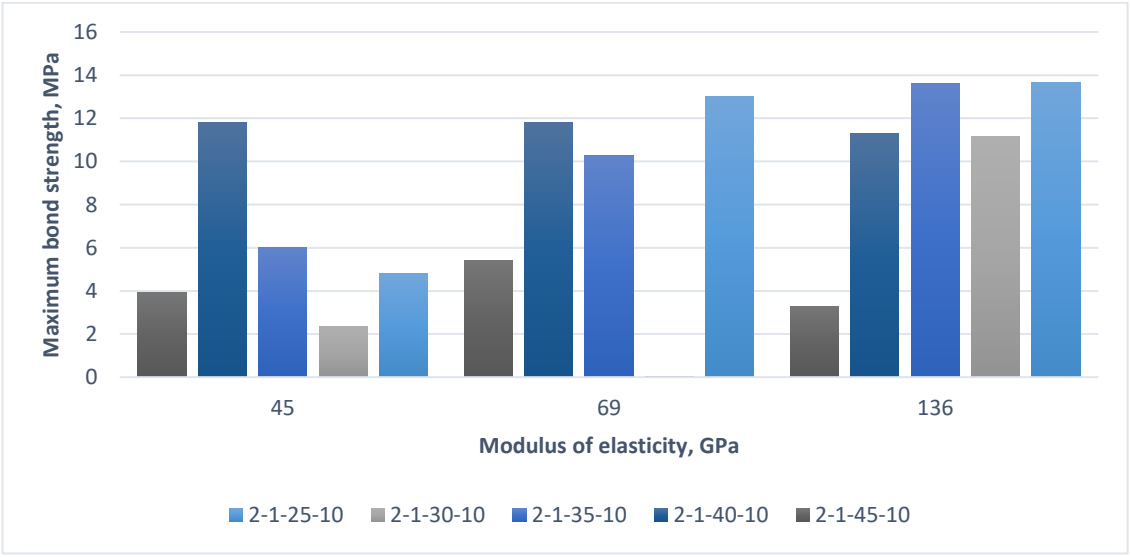

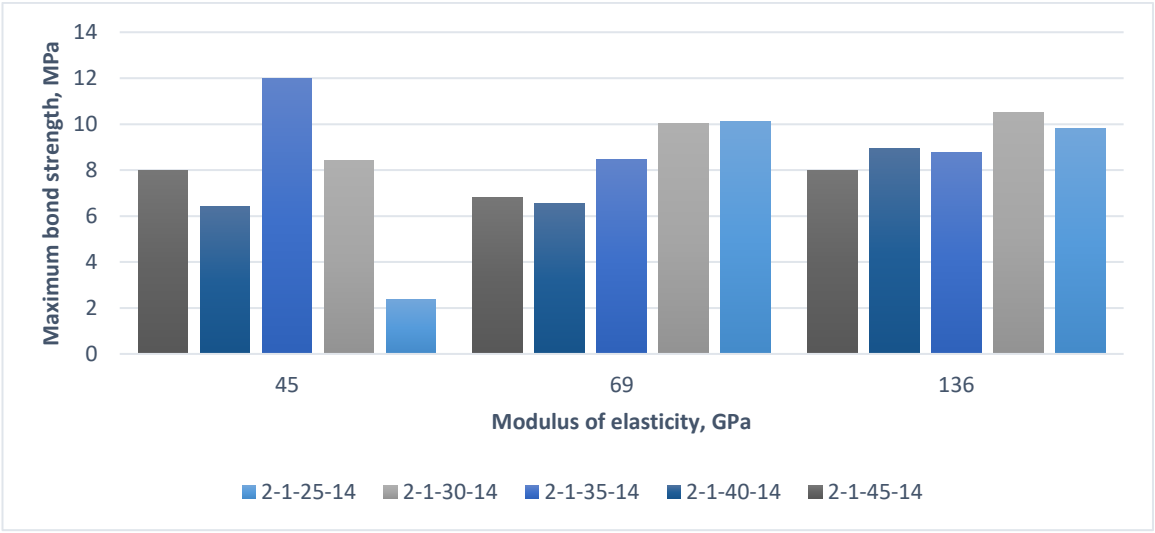

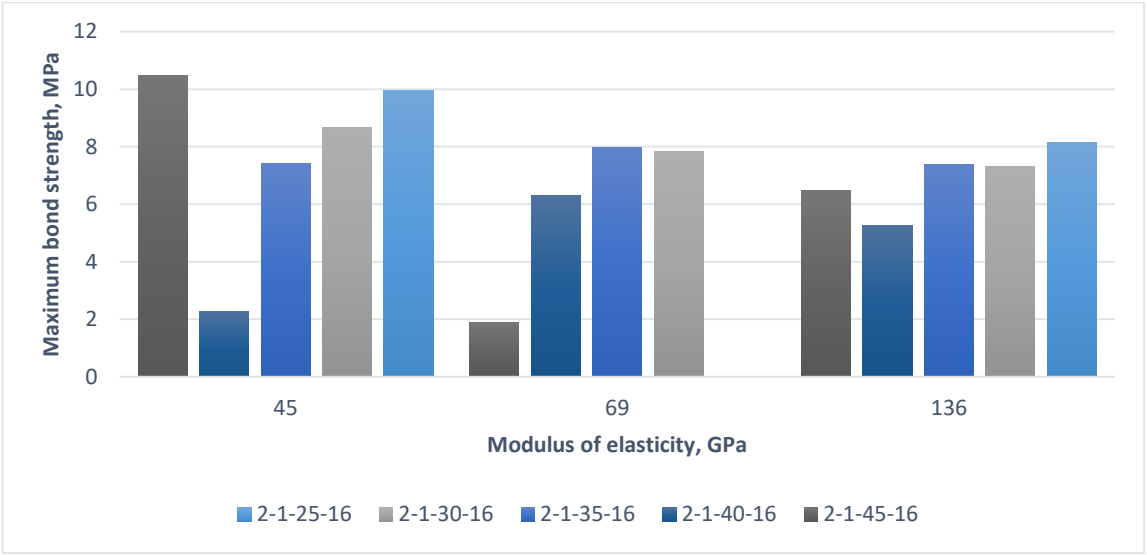

Figure 163: Effect of modulus of elasticity on maximum bond strength under 80 kN impact loading.

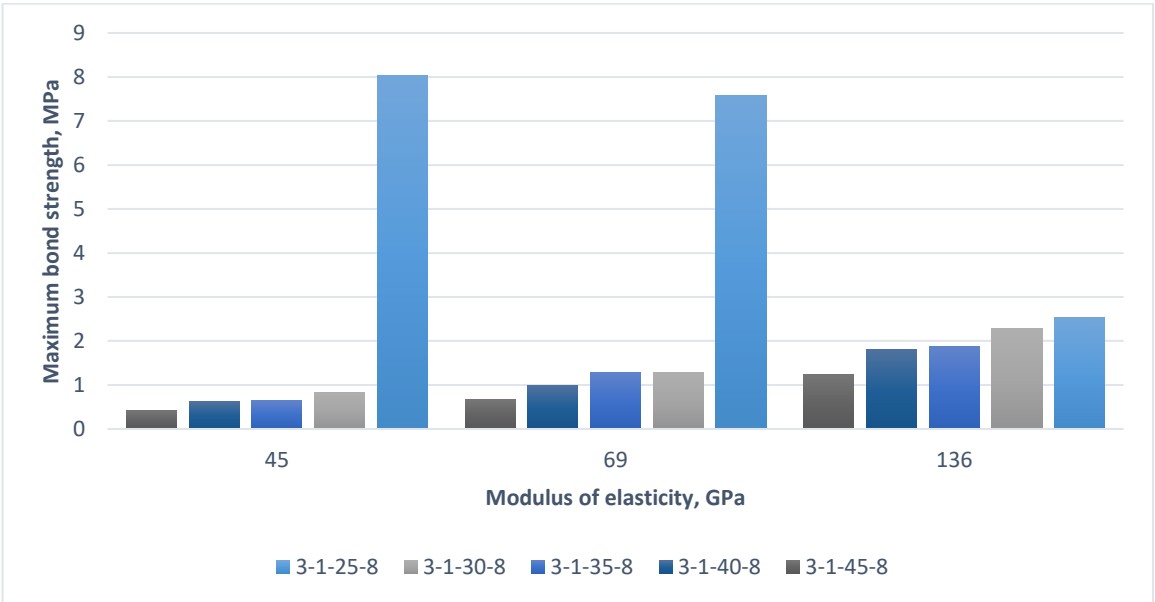

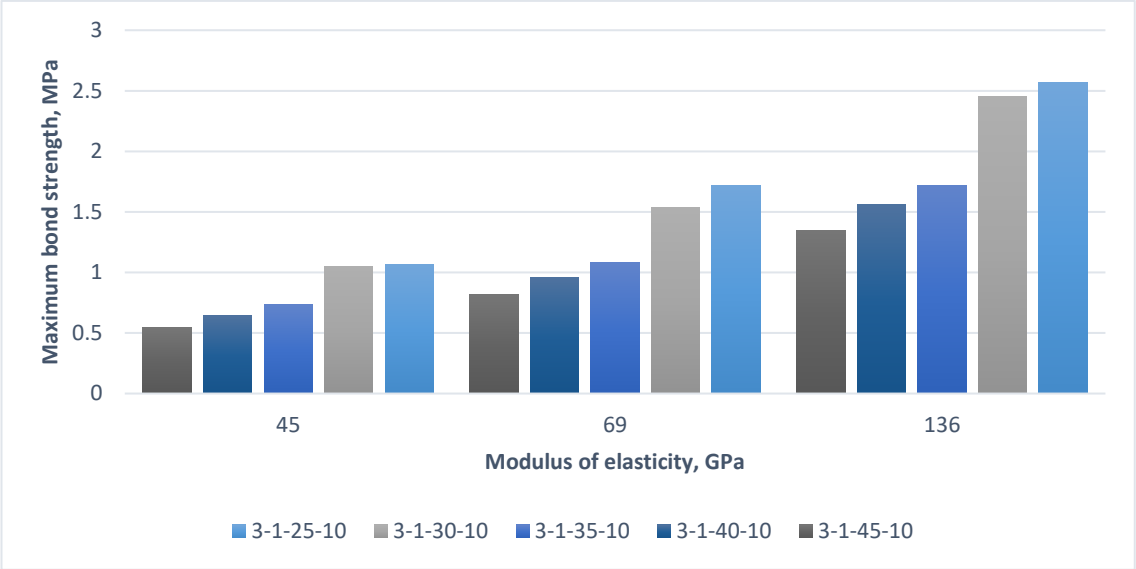

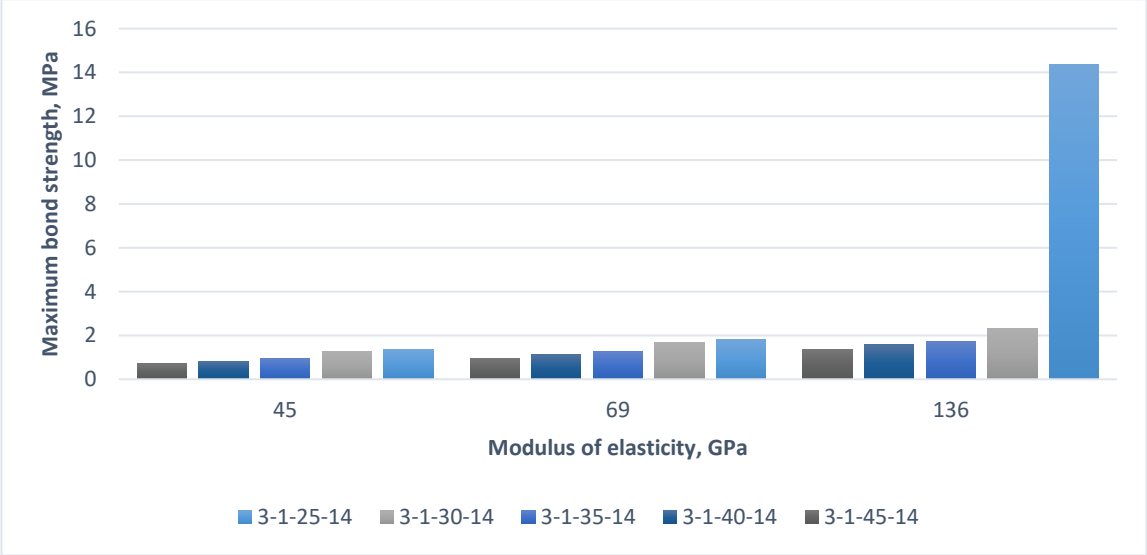

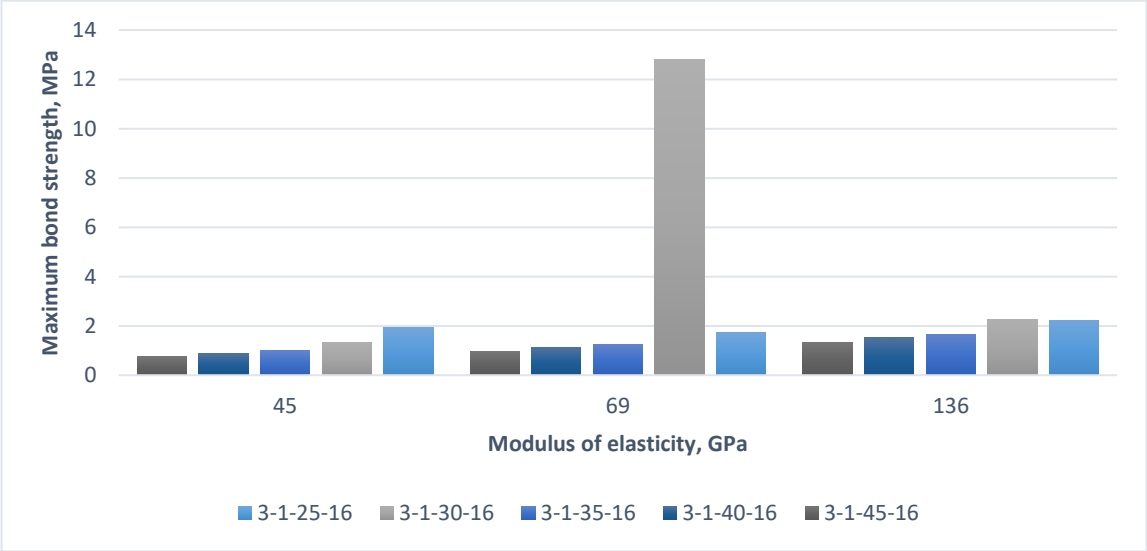

Figure 164: Effect of modulus of elasticity on maximum bond strength under 40 kN impact loading.

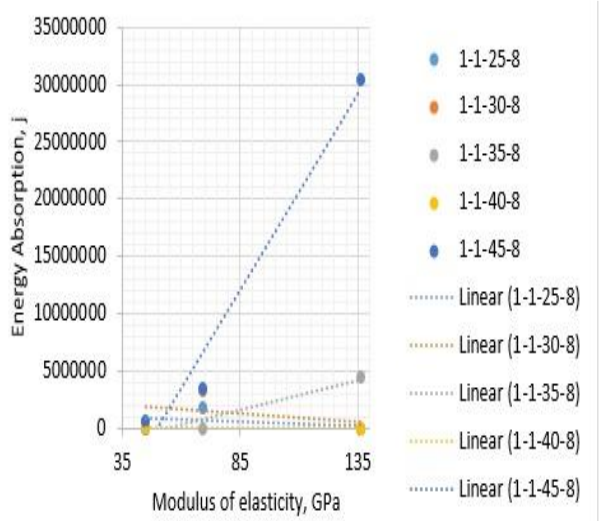
Energy Absorption, j
35000000
30000000
25000000
20000000
15000000
10000000
5000000
0
35
85
135
Modulus of elasticity, GPa
1-1-25-8
1-1-30-8
1-1-35-8
1-1-40-8
1-1-45-8
Linear (1-1-25-8)
Linear (1-1-30-8)
Linear (1-1-35-8)
Linear (1-1-40-8)
Linear (1-1-45-8)

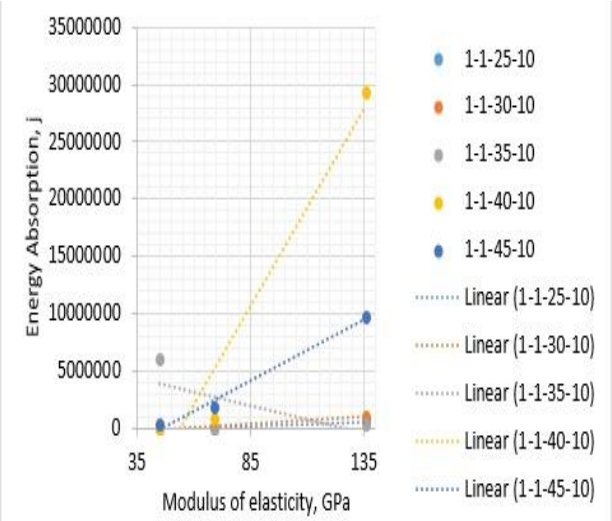
Energy Absorption, j
35000000
30000000
25000000
20000000
15000000
10000000
5000000
0
35
85
135
Modulus of elasticity, GPa
1-1-25-10
1-1-30-10
1-1-35-10
1-1-40-10
1-1-45-10
Linear (1-1-25-10)
Linear (1-1-30-10)
Linear (1-1-35-10)
Linear (1-1-40-10)
Linear (1-1-45-10)

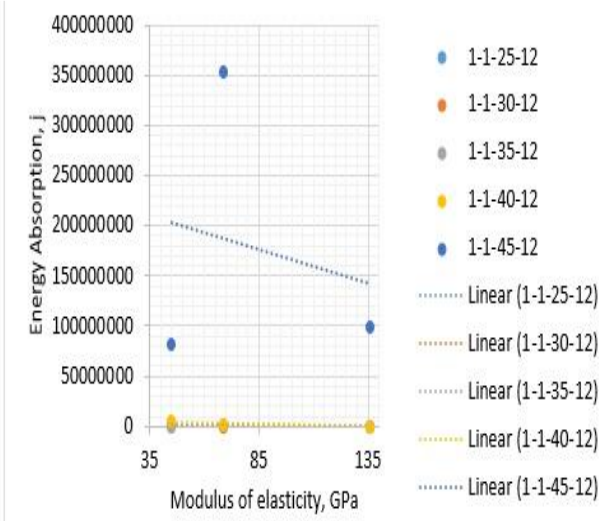
Energy Absorption, j
400000000
350000000
300000000
250000000
200000000
150000000
100000000
50000000
0
35
85
135
Modulus of elasticity, GPa
1-1-25-12
1-1-30-12
1-1-35-12
1-1-40-12
1-1-45-12
Linear (1-1-25-12)
Linear (1-1-30-12)
Linear (1-1-35-12)
Linear (1-1-40-12)
Linear (1-1-45-12)

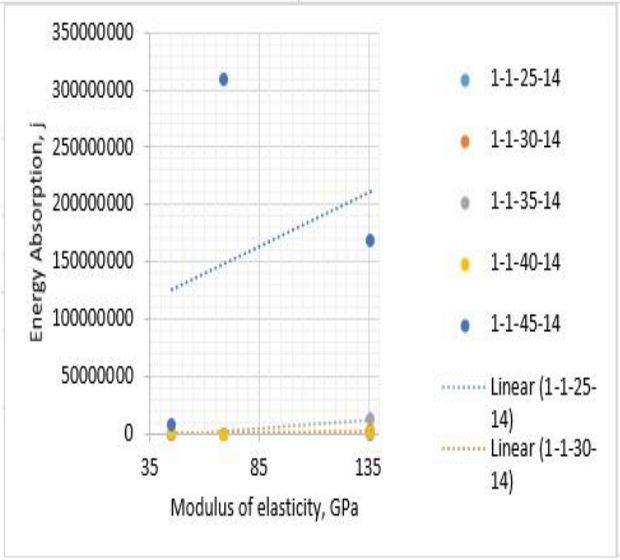
Energy Absorption, j
350000000
300000000
250000000
200000000
150000000
100000000
50000000
0
35
85
135
Modulus of elasticity, GPa
1-1-25-14
1-1-30-14
1-1-35-14
1-1-40-14
1-1-45-14
Linear (1-1-25-14)
Linear (1-1-30-14)

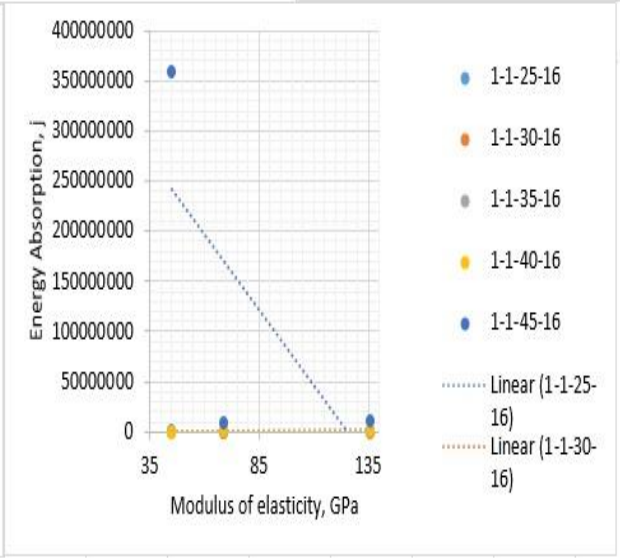
Energy Absorption, j
400000000
350000000
300000000
250000000
200000000
150000000
100000000
50000000
0
35
85
135
Modulus of elasticity, GPa
1-1-25-16
1-1-30-16
1-1-35-16
1-1-40-16
1-1-45-16
Linear (1-1-25-16)
Linear (1-1-30-16)

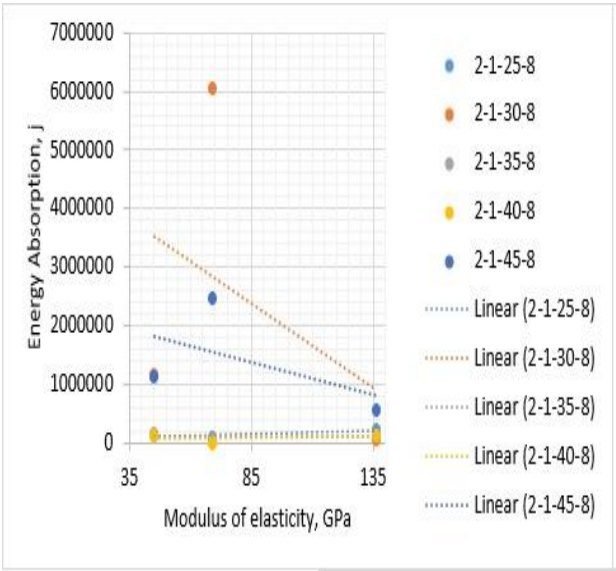
Energy Absorption, j
7000000
6000000
5000000
4000000
3000000
2000000
1000000
0
35
85
135
Modulus of elasticity, GPa
2-1-25-8
2-1-30-8
2-1-35-8
2-1-40-8
2-1-45-8
Linear (2-1-25-8)
Linear (2-1-30-8)
Linear (2-1-35-8)
Linear (2-1-40-8)
Linear (2-1-45-8)

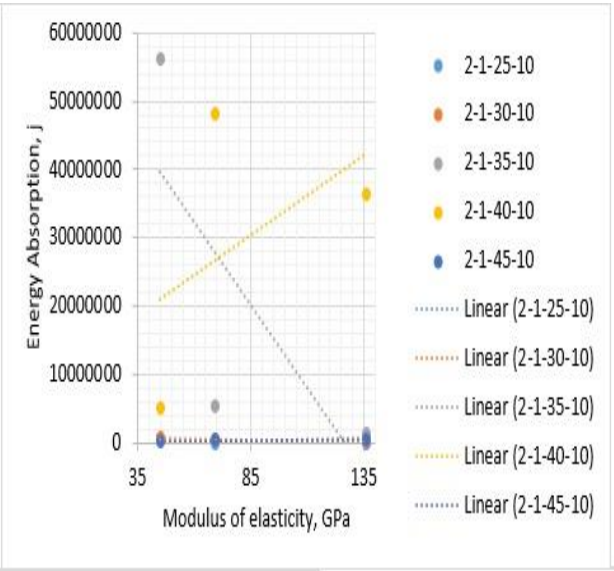
Energy Absorption, j
60000000
50000000
40000000
30000000
20000000
10000000
0
35
85
135
Modulus of elasticity, GPa
2-1-25-10
2-1-30-10
2-1-35-10
2-1-40-10
2-1-45-10
Linear (2-1-25-10)
Linear (2-1-30-10)
Linear (2-1-35-10)
Linear (2-1-40-10)
Linear (2-1-45-10)

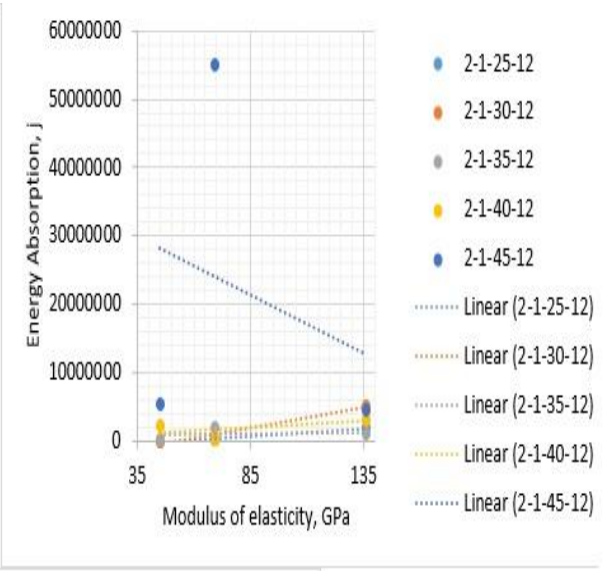
Energy Absorption, j
60000000
50000000
40000000
30000000
20000000
10000000
0
35
85
135
Modulus of elasticity, GPa
2-1-25-12
2-1-30-12
2-1-35-12
2-1-40-12
2-1-45-12
Linear (2-1-25-12)
Linear (2-1-30-12)
Linear (2-1-35-12)
Linear (2-1-40-12)
Linear (2-1-45-12)

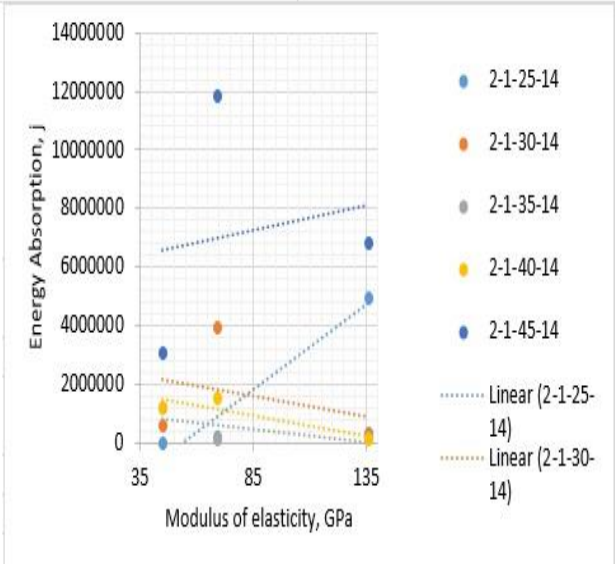
Energy Absorption, j
14000000
12000000
10000000
8000000
6000000
4000000
2000000
0
35
85
135
Modulus of elasticity, GPa
2-1-25-14
2-1-30-14
2-1-35-14
2-1-40-14
2-1-45-14
Linear (2-1-25-14)
Linear (2-1-30-14)

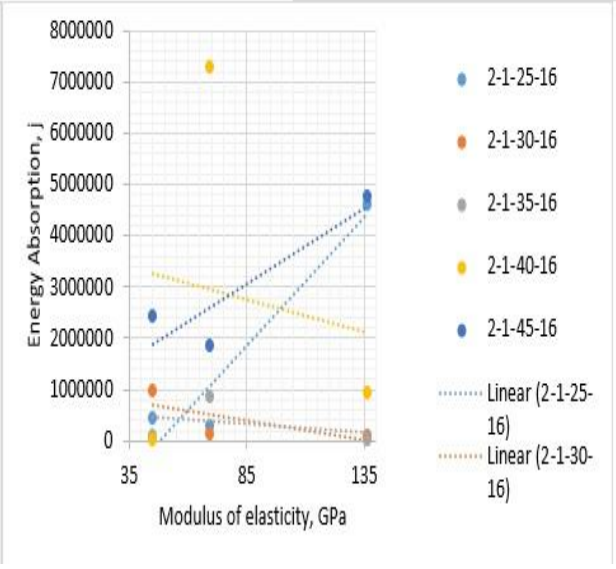
Energy Absorption, j
8000000
7000000
6000000
5000000
4000000
3000000
2000000
1000000
0
35
85
135
Modulus of elasticity, GPa
2-1-25-16
2-1-30-16
2-1-35-16
2-1-40-16
2-1-45-16
Linear (2-1-25-16)
Linear (2-1-30-16)

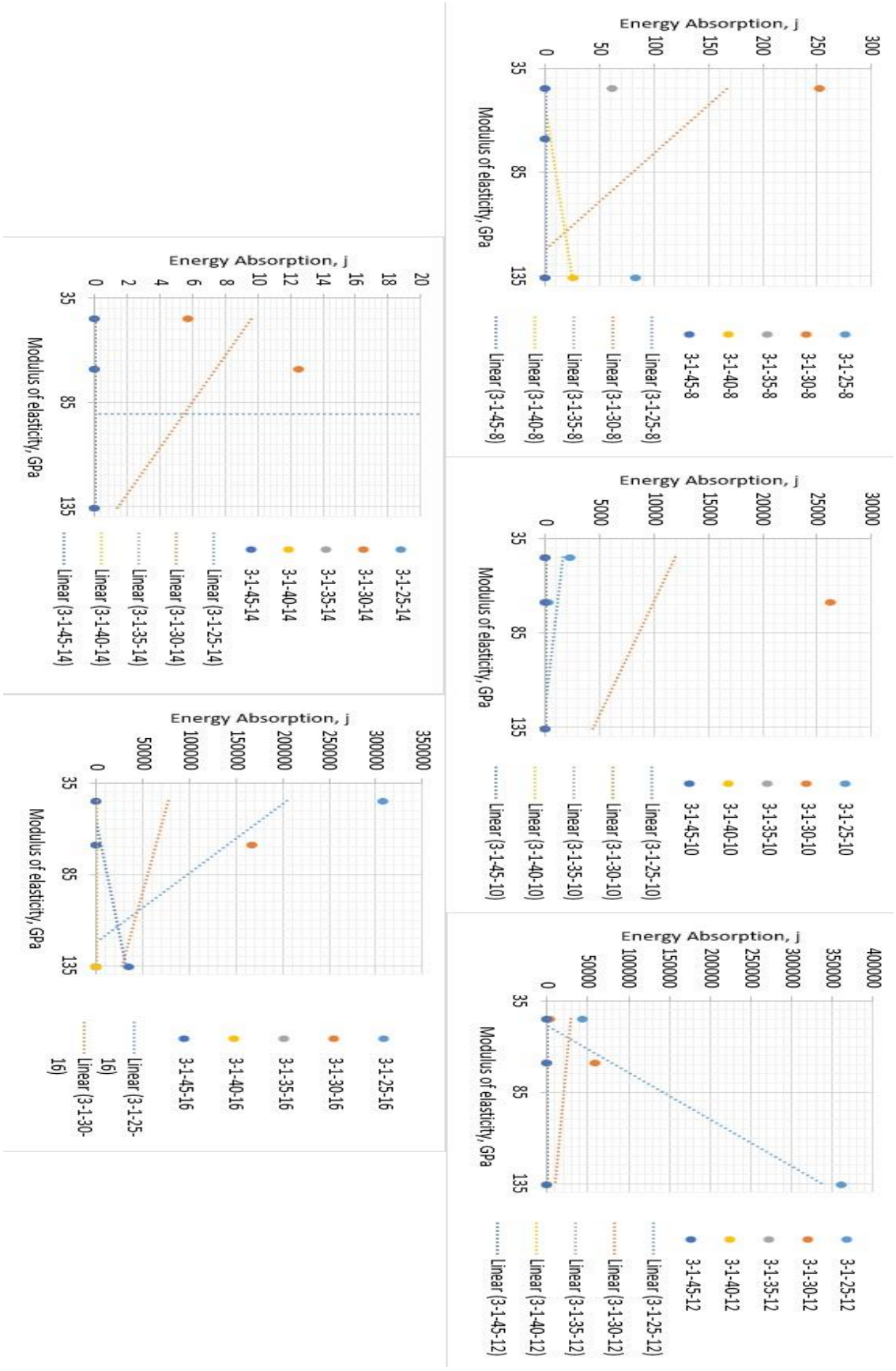

Figure 165: Effect of modulus of elasticity on energy absorption of models under three impact loading.

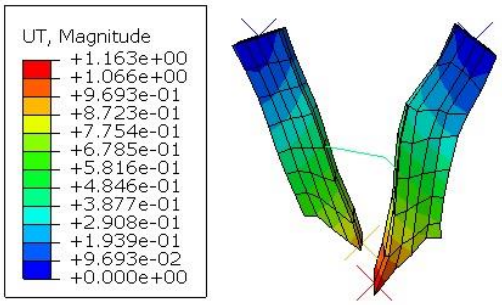

A-1-1-25-8

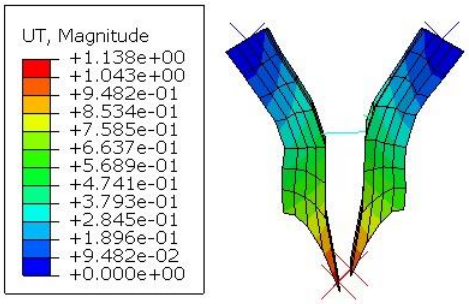

A-1-1-25-10

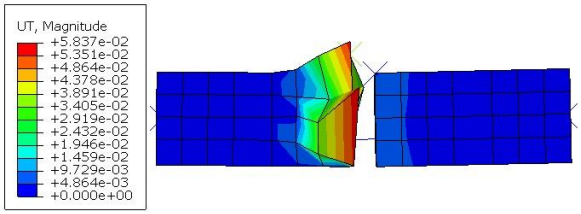

A-1-1-25-12

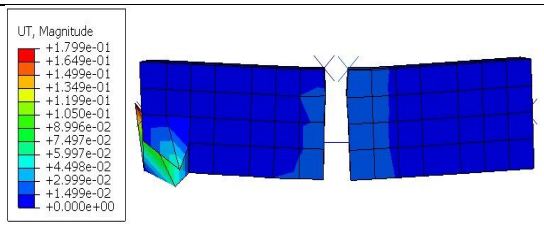

A-1-1-25-14

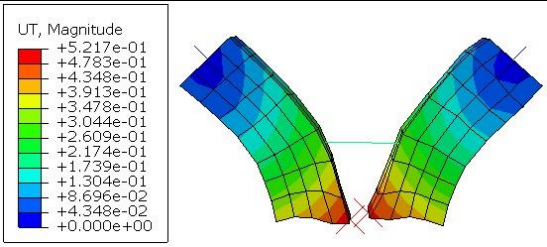

A-1-1-25-16

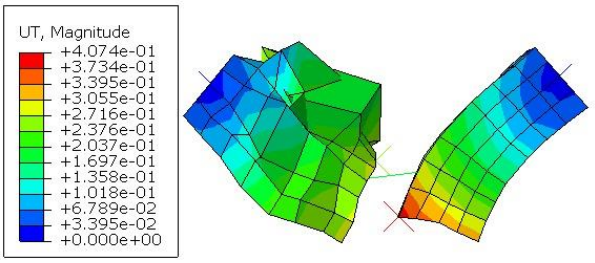

A-1-1-30-8

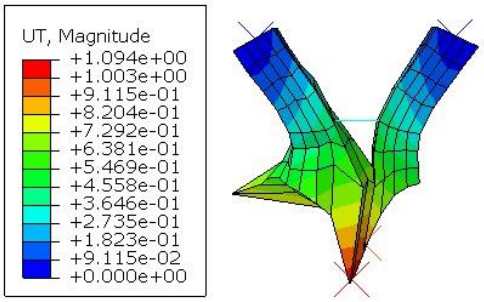

A-1-1-30-10

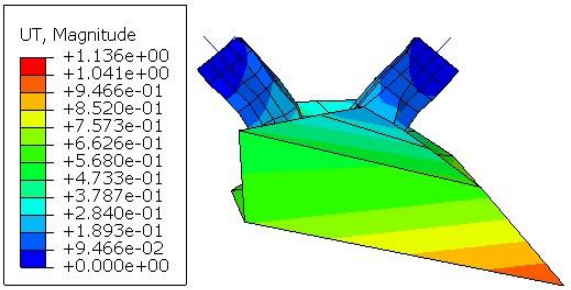

A-1-1-30-12

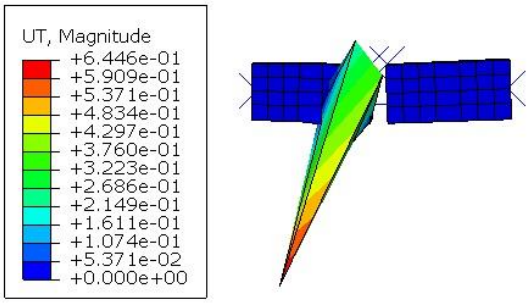

A-1-1-30-14

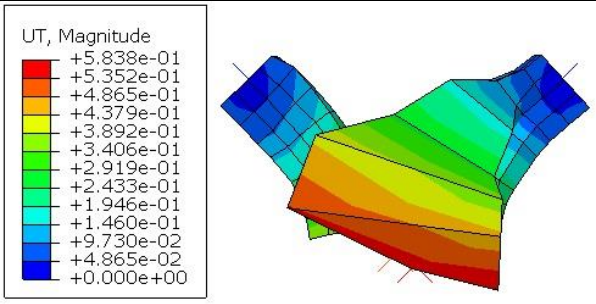

A-1-1-30-16

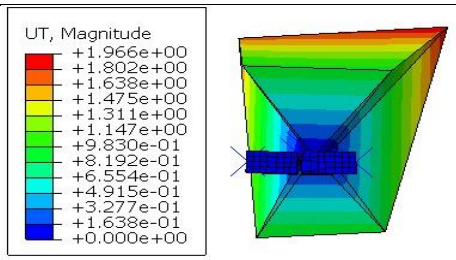

A-1-1-35-8

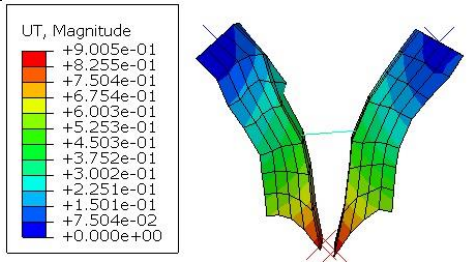

A-1-1-35-10

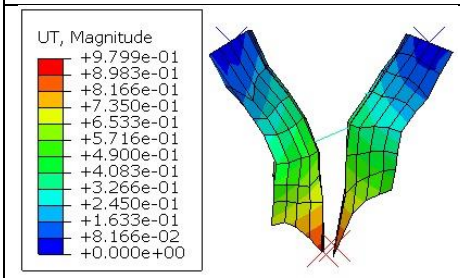

A-1-1-35-12

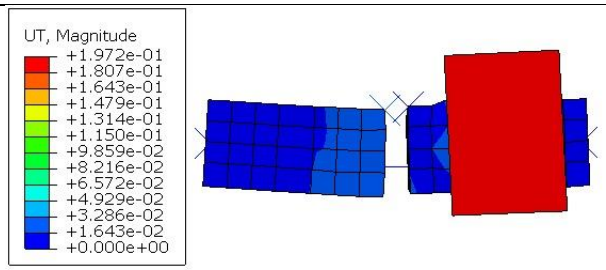

A-1-1-35-14

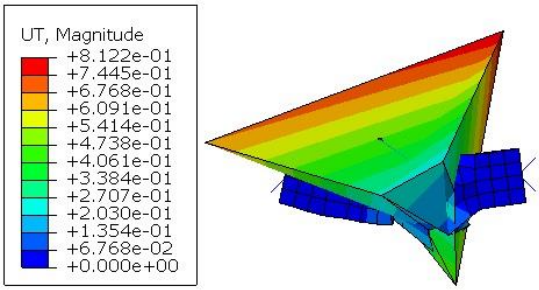

A-1-1-35-16

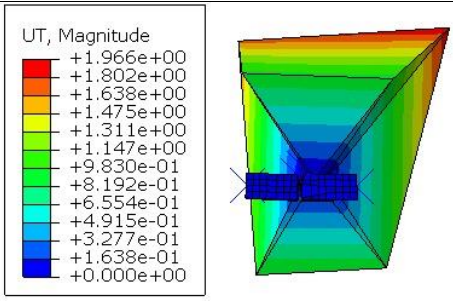

A-1-1-40-8

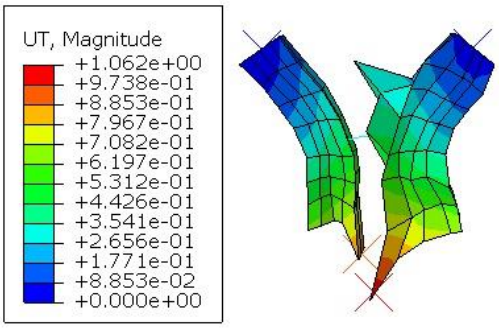

A-1-1-40-10

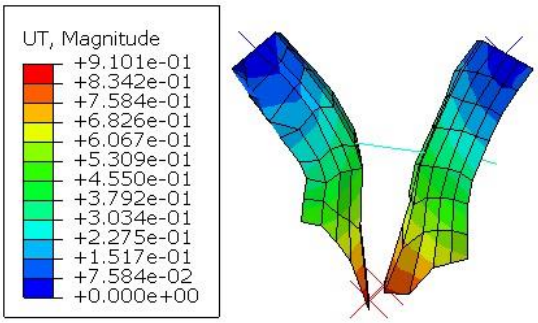

A-1-1-40-12

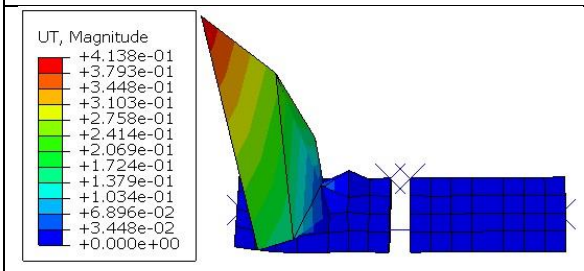

A-1-1-40-14

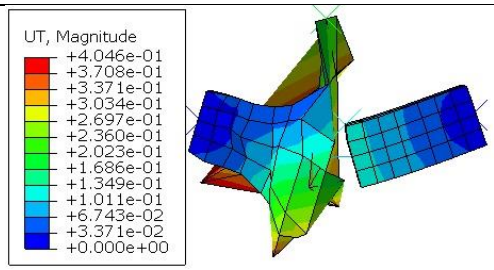

A-1-1-40-16

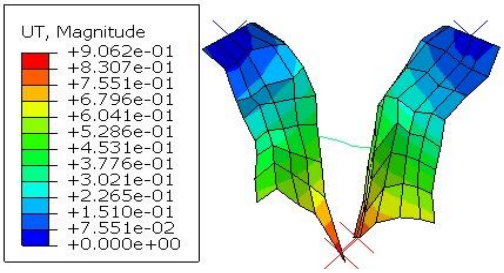

A-1-1-45-8

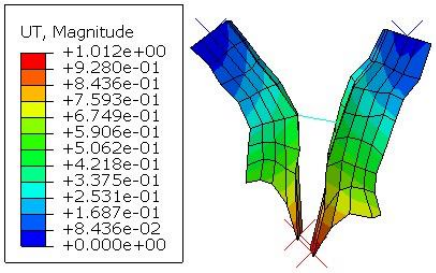

A-1-1-45-10

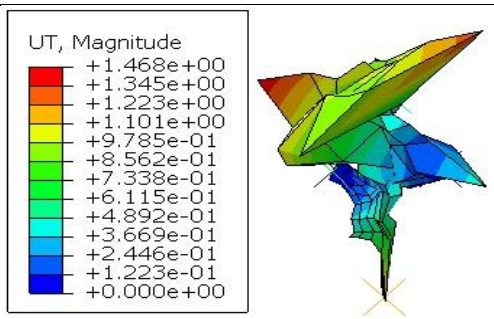

A-1-1-45-12

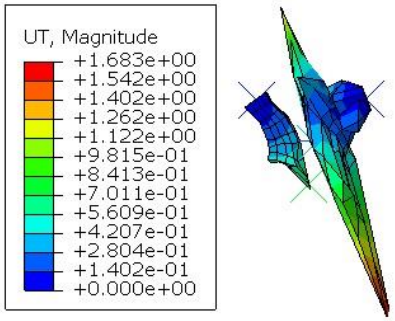

A-1-1-45-14

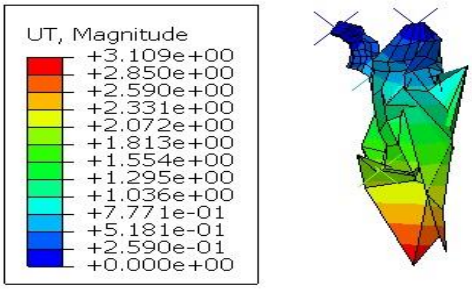

A-1-1-45-16

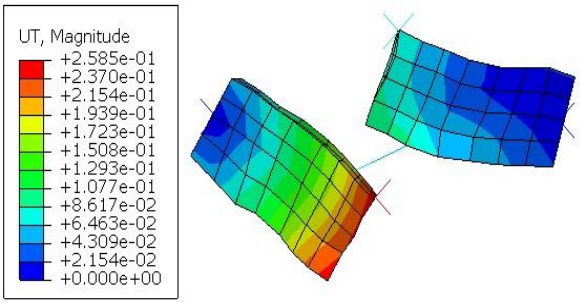

A-2-1-25-8

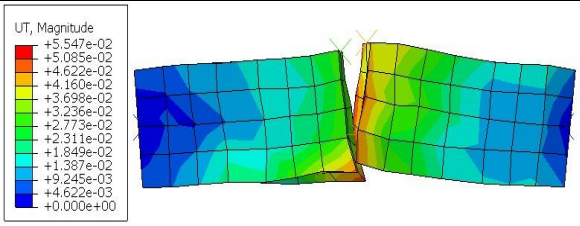

A-2-1-25-10

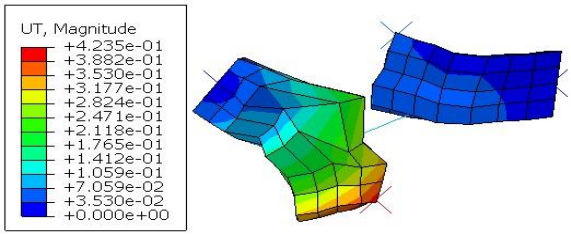

A-2-1-25-12

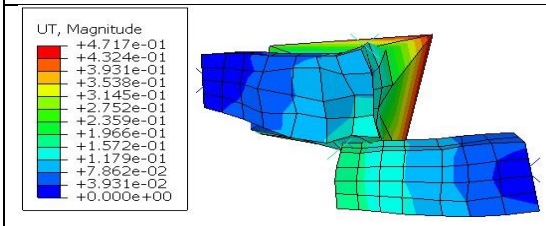

A-2-1-25-14

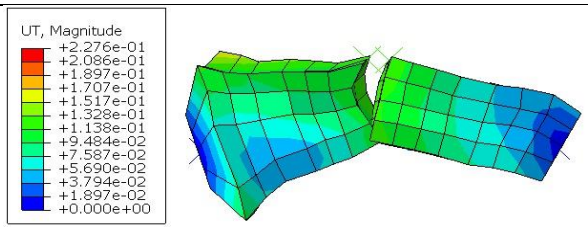

A-2-1-25-16

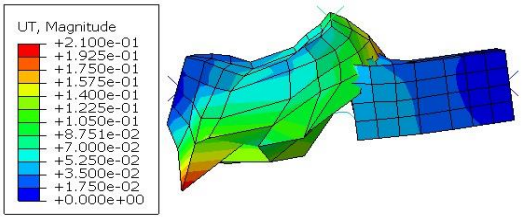

A-2-1-30-8

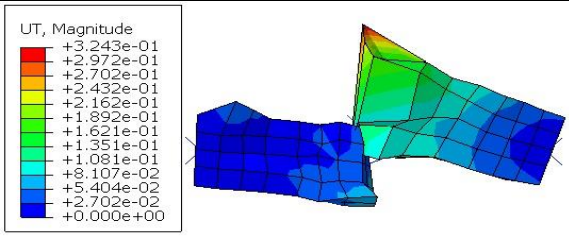

A-2-1-30-10

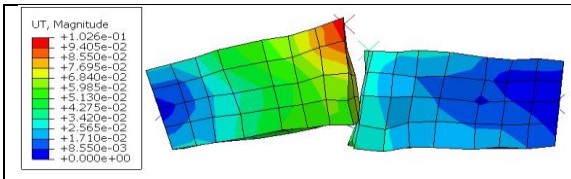

A-2-1-30-12

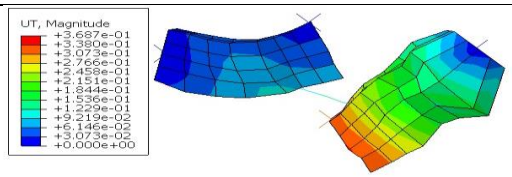

A-2-1-30-14

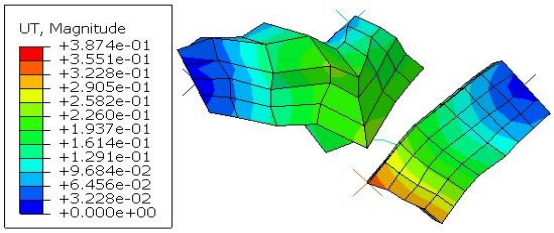

A-2-1-30-16

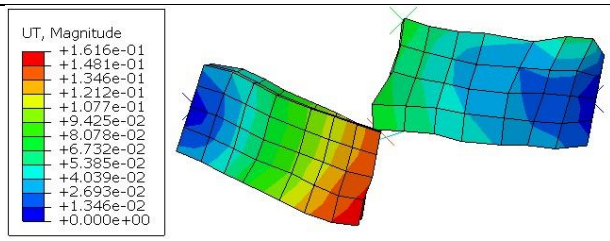

A-2-1-35-8

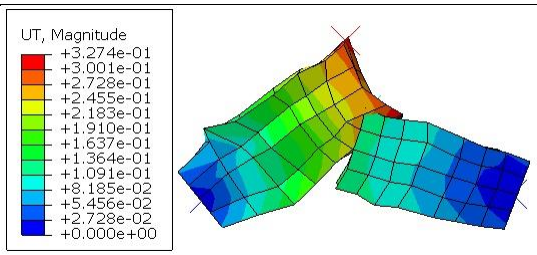

A-2-1-35-10

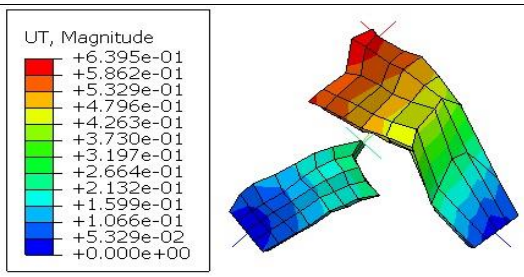

A-2-1-35-12

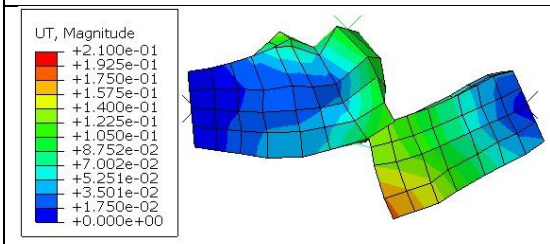

A-2-1-35-14

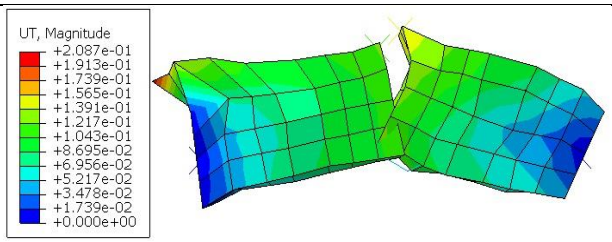

A-2-1-35-16

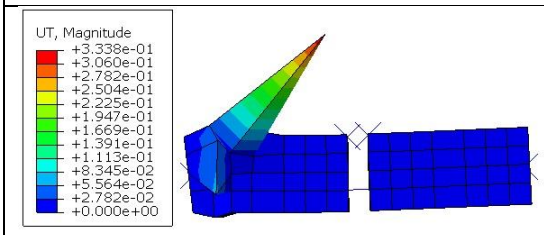

A-2-1-40-8

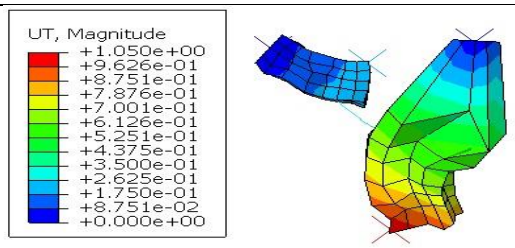

A-2-1-40-10

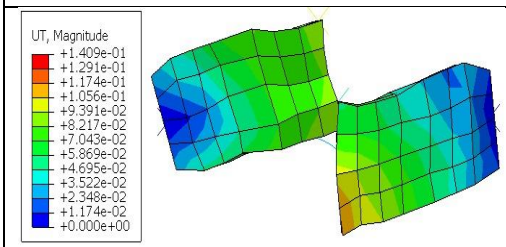

A-2-1-40-12

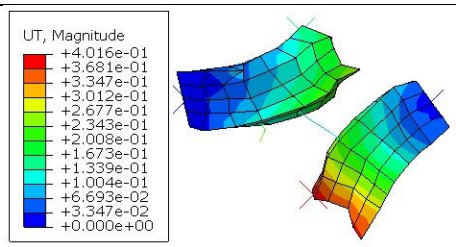

A-2-1-40-14

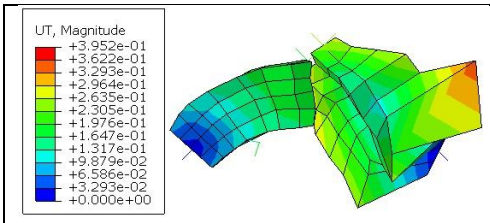

A-2-1-40-16

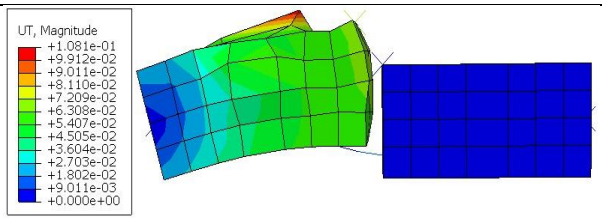

A-2-1-45-8

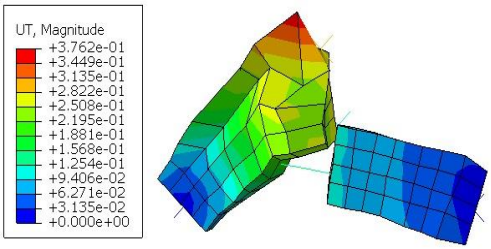

A-2-1-45-10

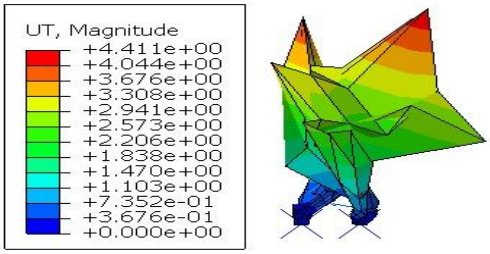

A-2-1-45-12

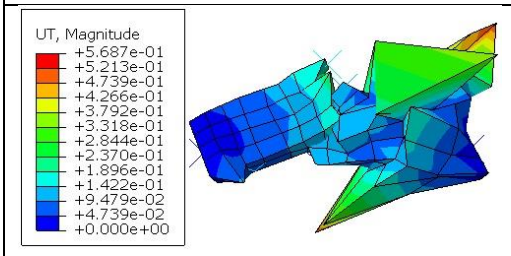

A-2-1-45-14

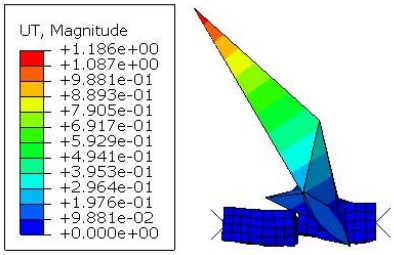

A-2-1-45-16

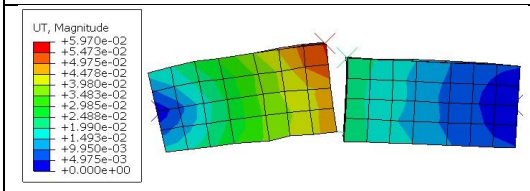

A-3-1-25-8

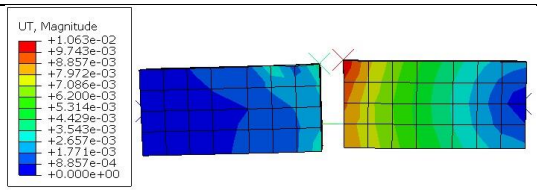

A-3-1-25-10

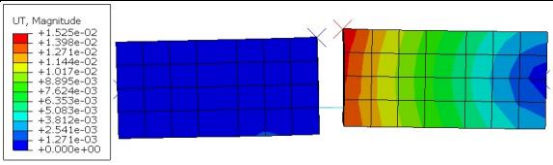

A-3-1-25-12

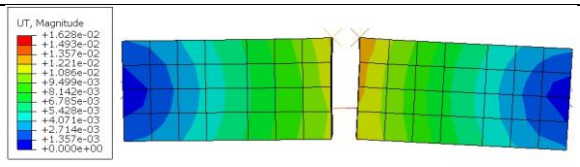

A-3-1-25-14

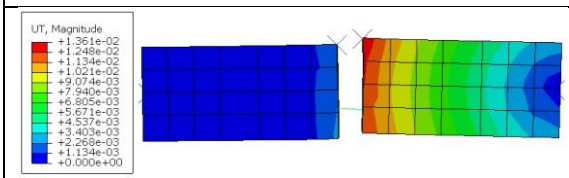

A-3-1-25-16

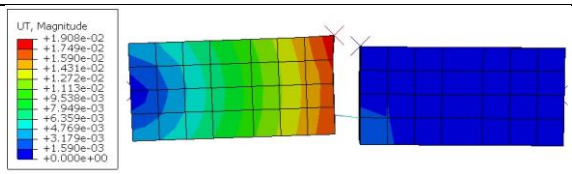

A-3-1-30-8

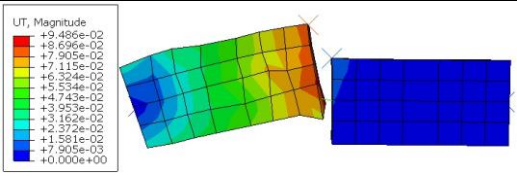

A-3-1-30-10

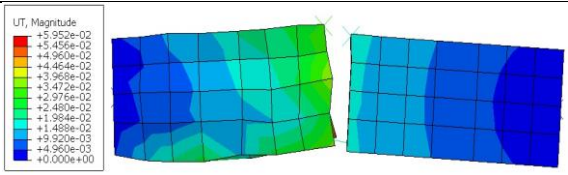

A-3-1-30-12

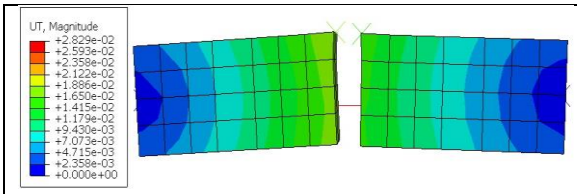

A-3-1-30-14

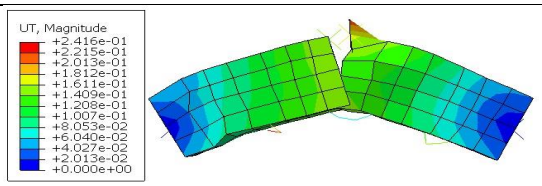

A-3-1-30-16

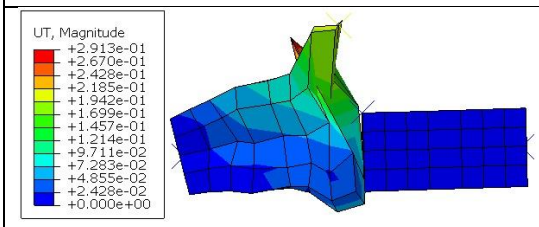

A-3-1-35-8

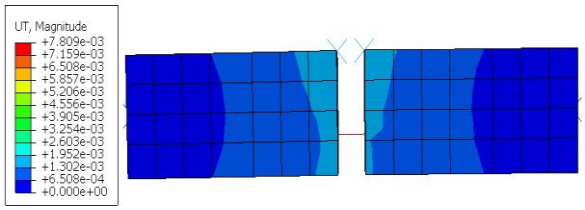

A-3-1-35-10

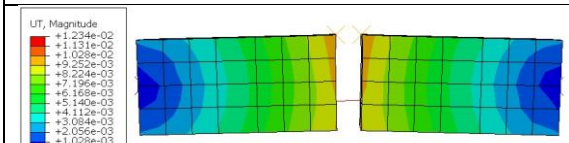

A-3-1-35-12

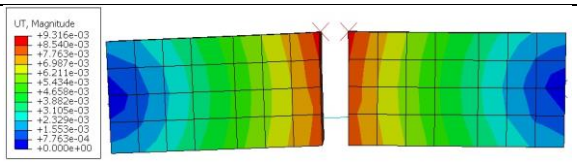

A-3-1-35-14

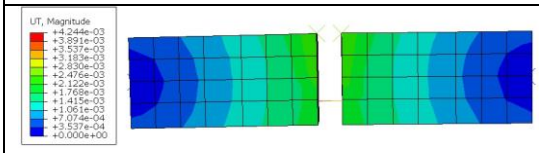

A-3-1-35-16

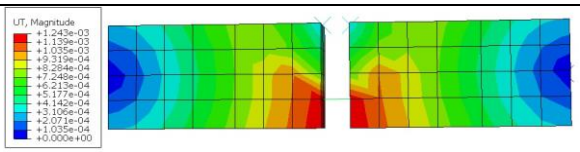

A-3-1-40-8

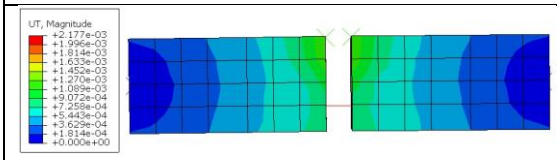

A-3-1-40-10

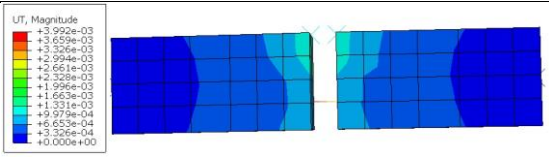

A-3-1-40-12

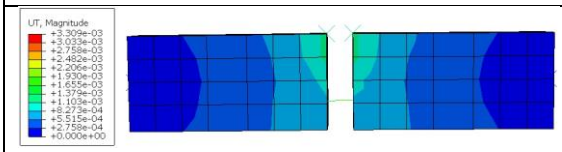

A-3-1-40-14

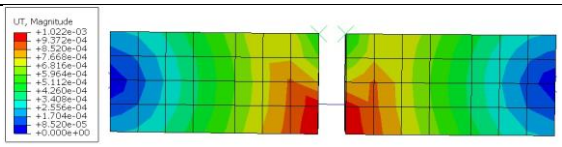

A-3-1-40-16

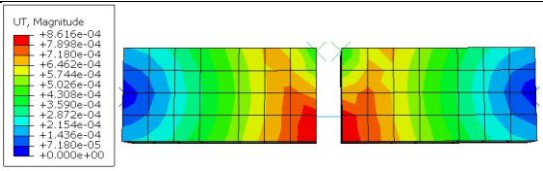

A-3-1-45-8

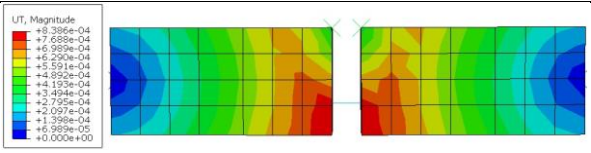

A-3-1-45-10

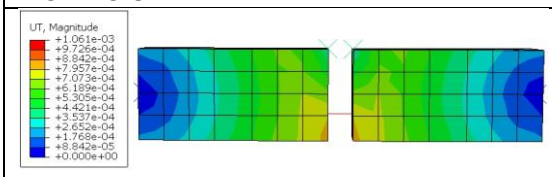

A-3-1-45-12

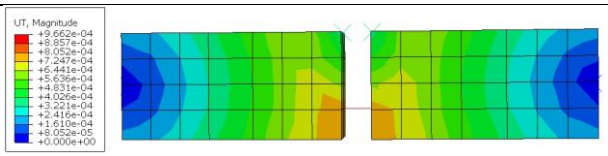

A-3-1-45-14

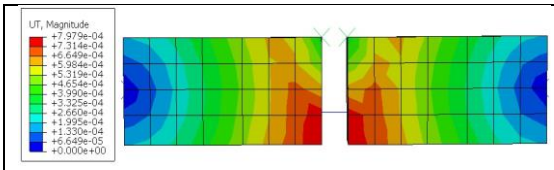

A-3-1-45-16

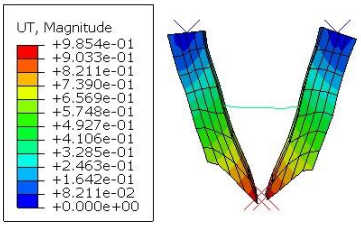

C-1-1-25-8

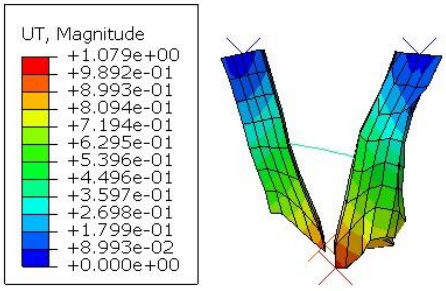

C-1-1-25-10

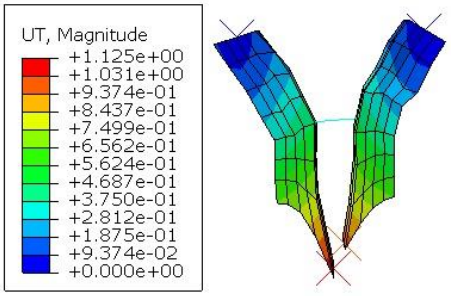

C-1-1-25-12

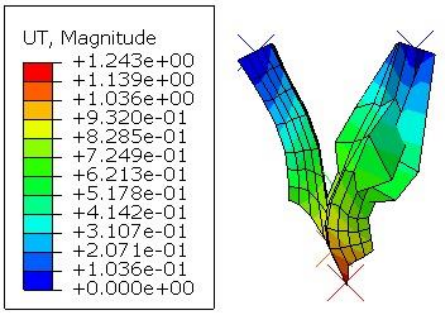

C-1-1-25-14

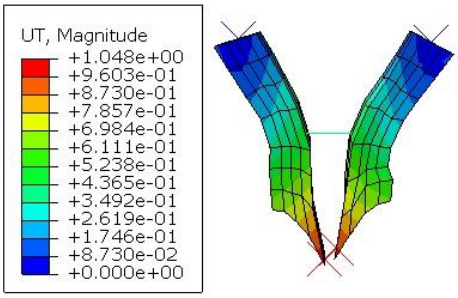

C-1-1-25-16

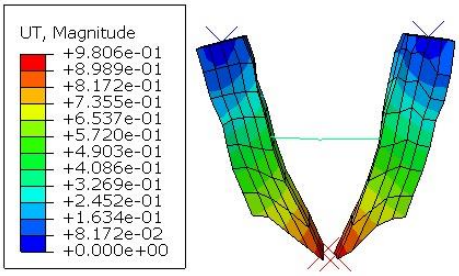

C-1-1-30-8

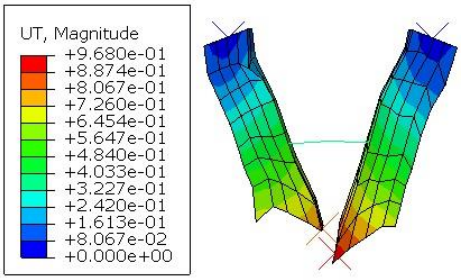

C-1-1-30-10

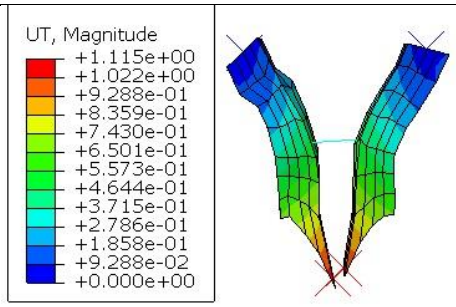

C-1-1-30-12

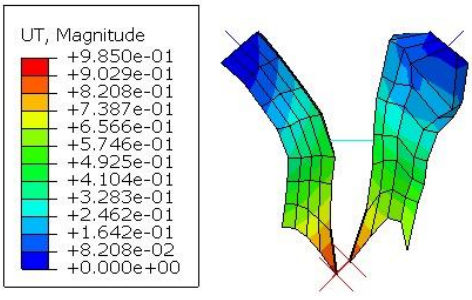

C-1-1-30-14

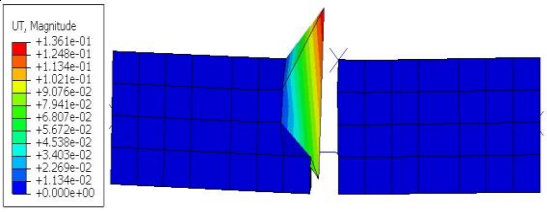

C-1-1-30-16

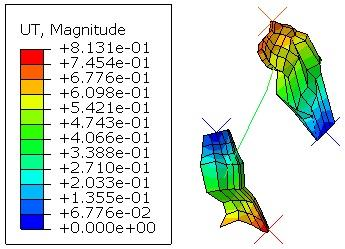

C-1-1-35-8

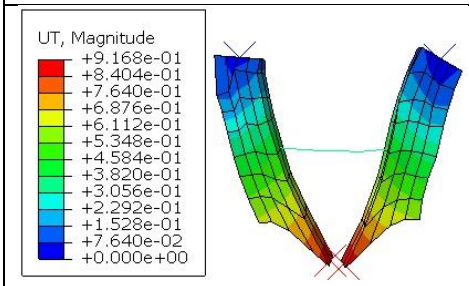

C-1-1-35-10

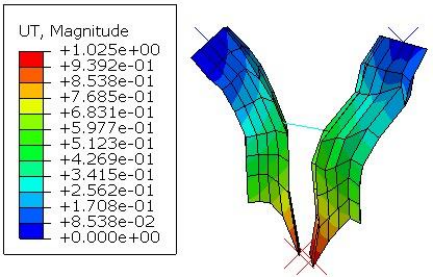

C-1-1-35-12

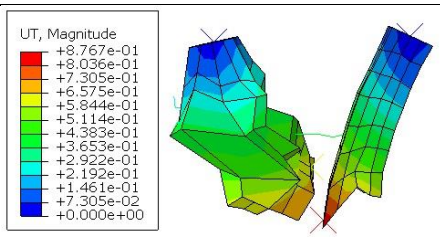

C-1-1-35-14

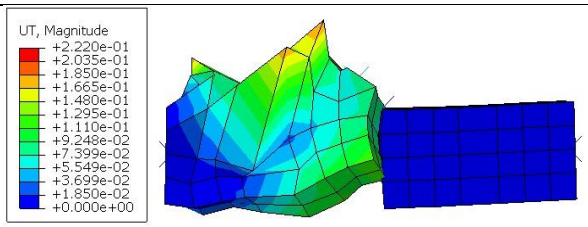

C-1-1-35-16

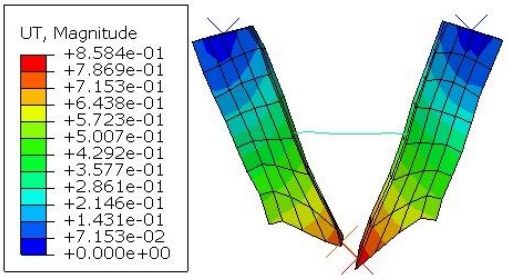

C-1-1-40-8

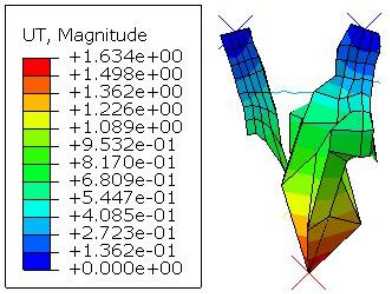

C-1-1-40-10

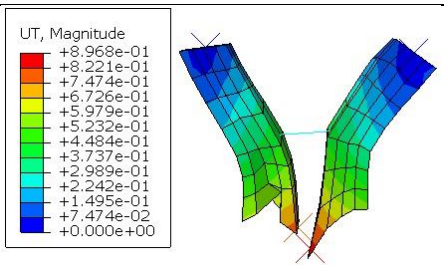

C-1-1-40-12

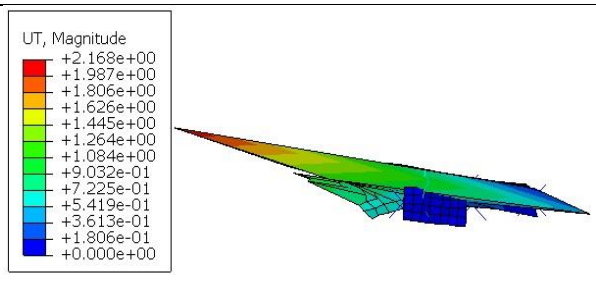

C-1-1-40-14

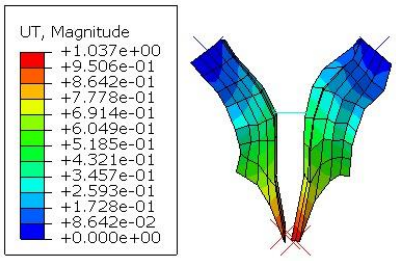

C-1-1-40-16

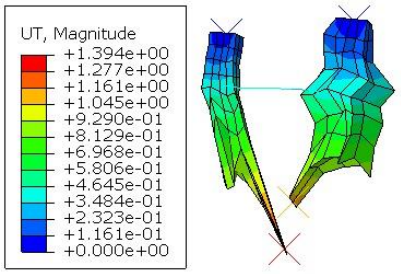

C-1-1-45-8

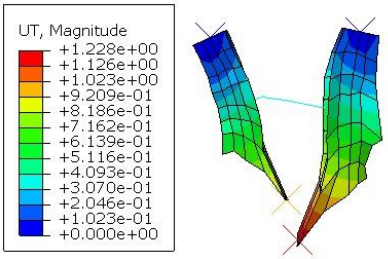

C-1-1-45-10

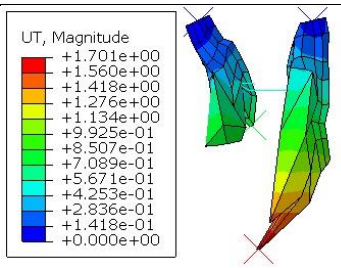

C-1-1-45-12

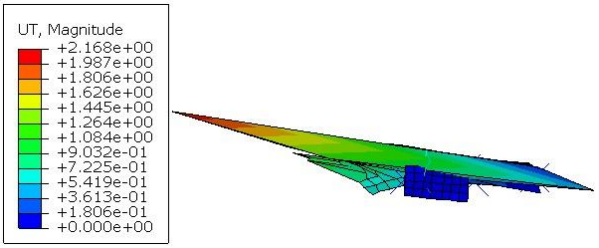

C-1-1-45-14

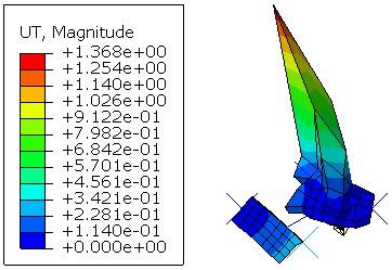

C-1-1-45-16

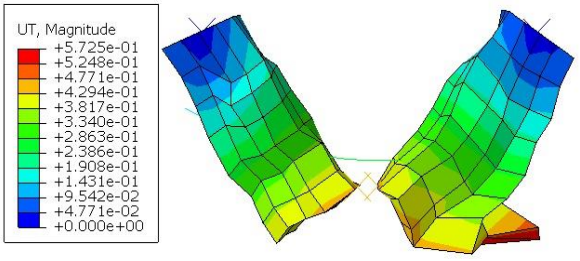

C-2-1-25-8

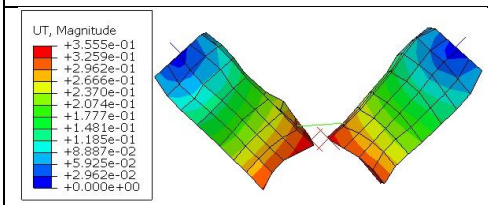

C-2-1-25-10

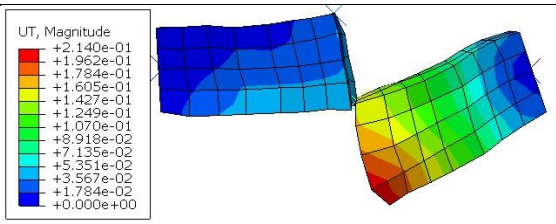

C-2-1-25-12

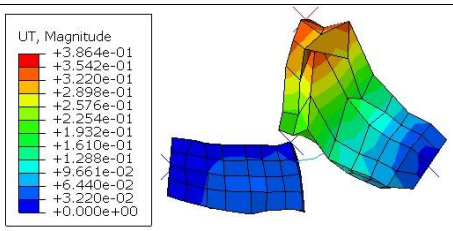

C-2-1-25-14

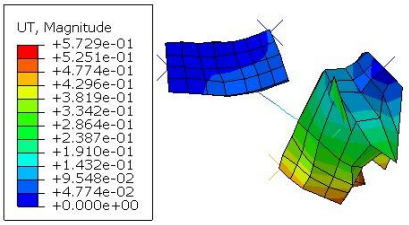

C-2-1-25-16

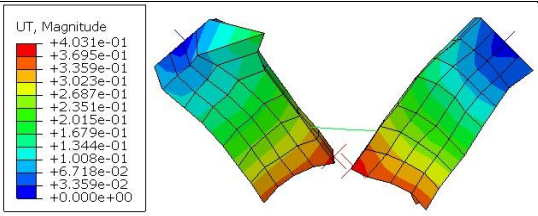

C-2-1-30-8

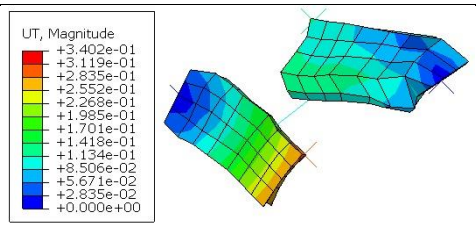

C-2-1-30-10

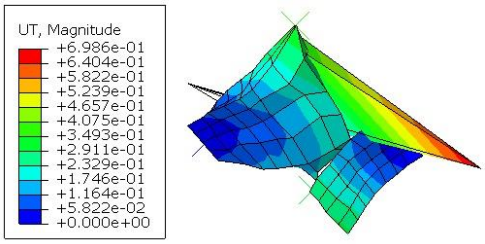

C-2-1-30-12

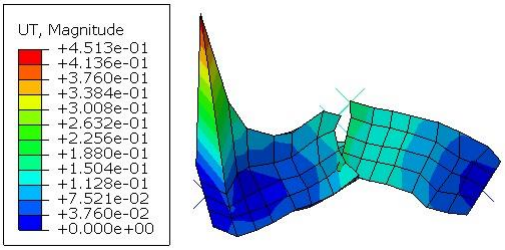

C-2-1-30-14

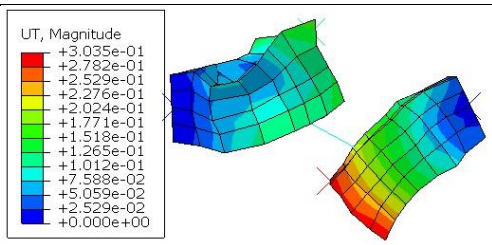

C-2-1-30-16

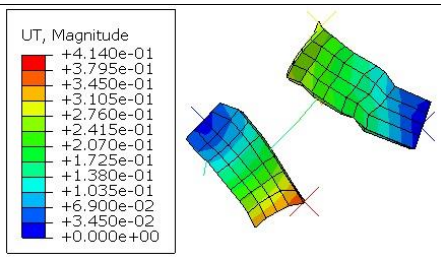

C-2-1-35-8

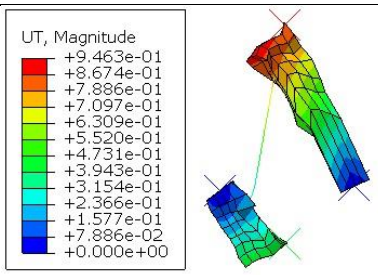

C-2-1-35-10

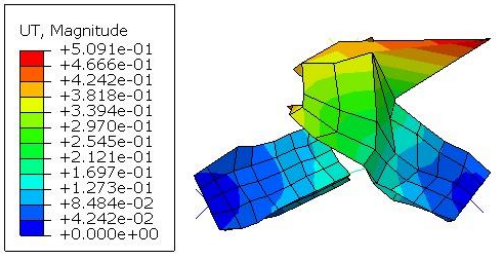

C-2-1-35-12

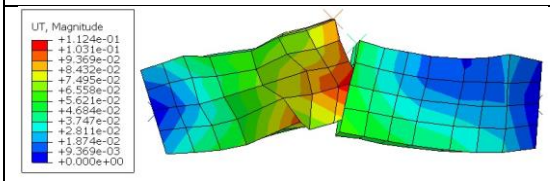

C-2-1-35-14

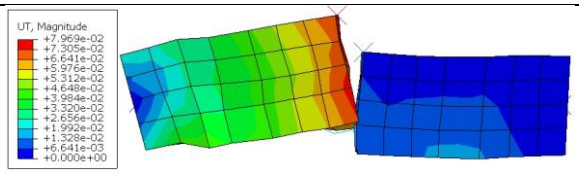

C-2-1-35-16

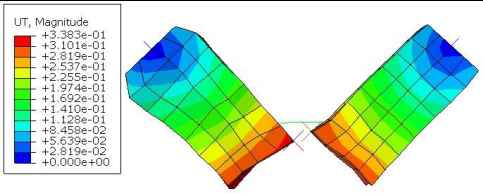

C-2-1-40-8

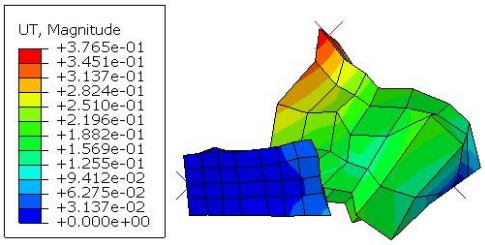

C-2-1-40-10

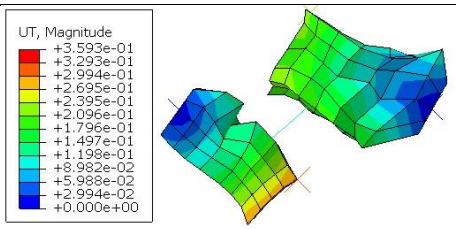

C-2-1-40-12

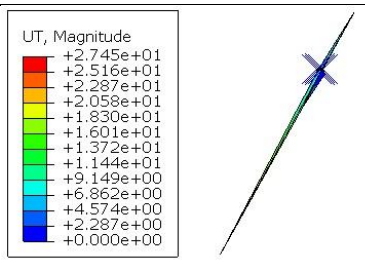

C-2-1-40-14

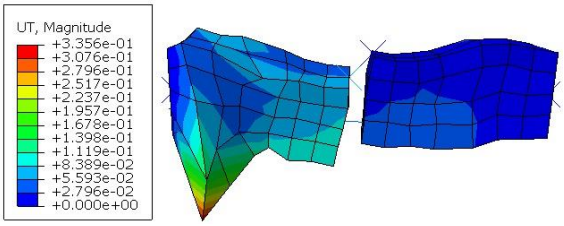

C-2-1-40-16

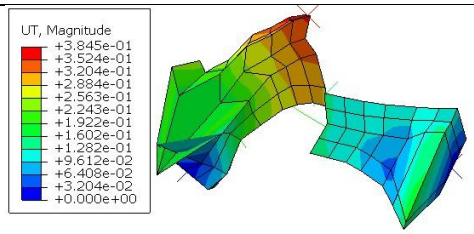

C-2-1-45-8

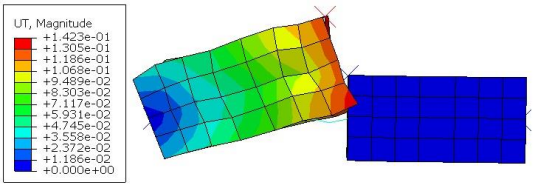

C-2-1-45-10

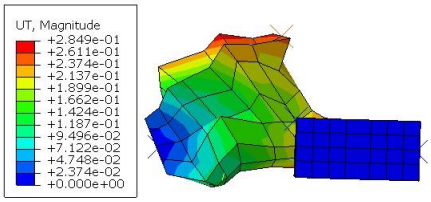

C-2-1-45-12

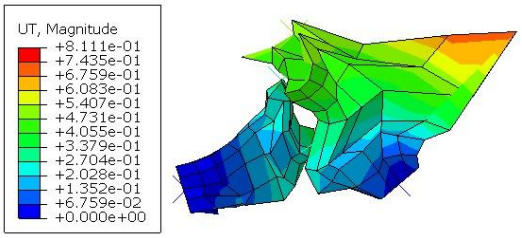

C-2-1-45-14

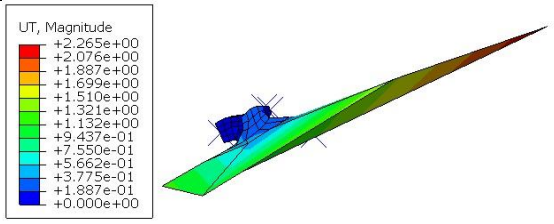

C-2-1-45-16

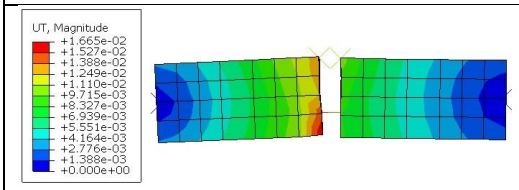

C-3-1-25-8

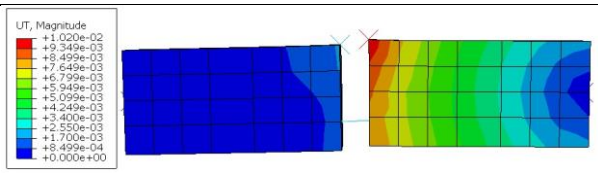

C-3-1-25-10

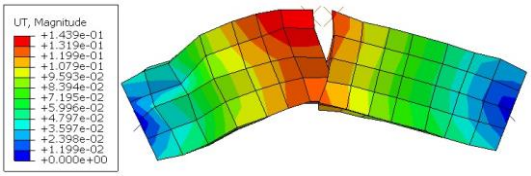

C-3-1-25-12

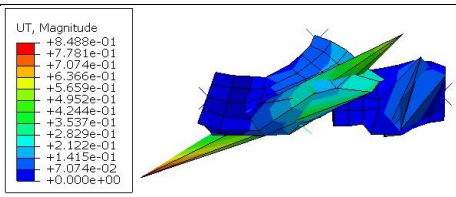

C-3-1-25-14

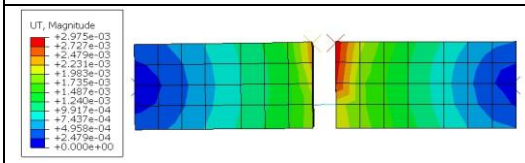

C-3-1-25-16

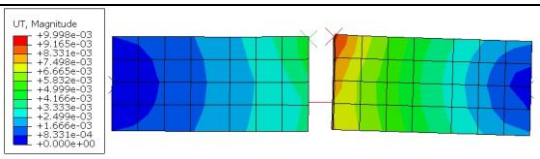

C-3-1-30-8

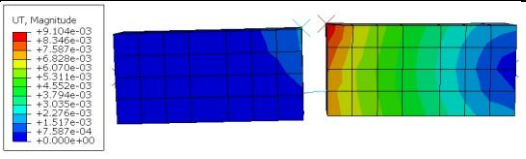

C-3-1-30-10

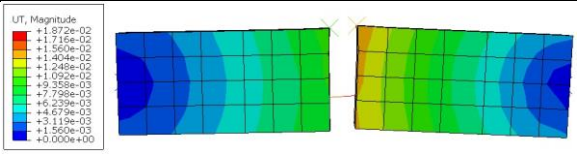

C-3-1-30-12

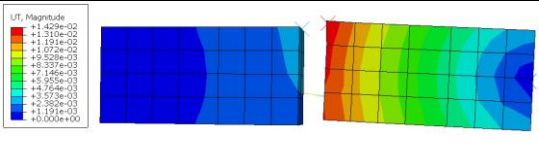

C-3-1-30-14

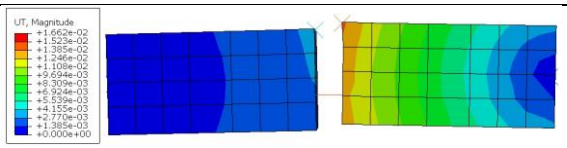

C-3-1-30-16

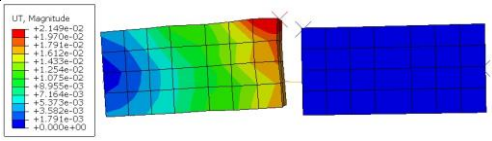
C-3-1-35-8

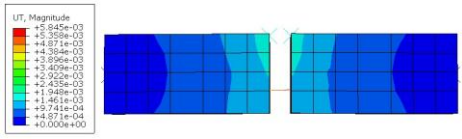
C-3-1-35-10

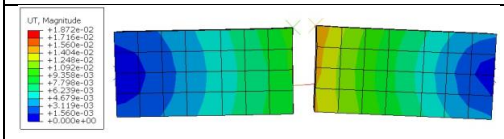
C-3-1-35-12

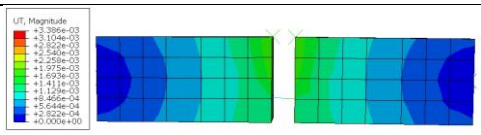
C-3-1-35-14

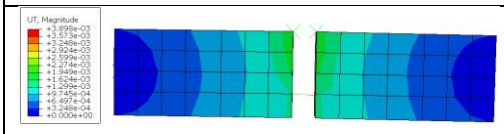
C-3-1-35-16

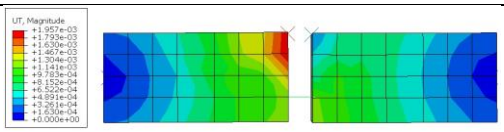
C-3-1-40-8

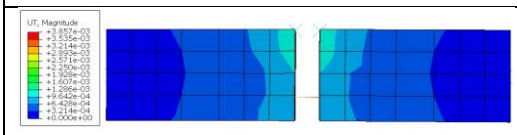
C-3-1-40-10

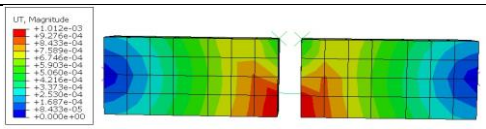
C-3-1-40-12

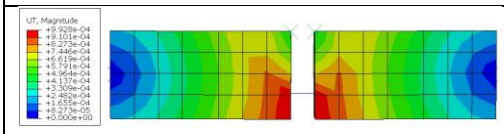
C-3-1-40-14

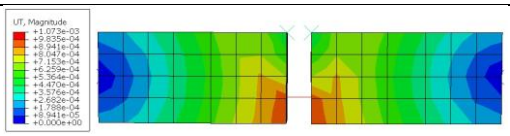
C-3-1-40-16

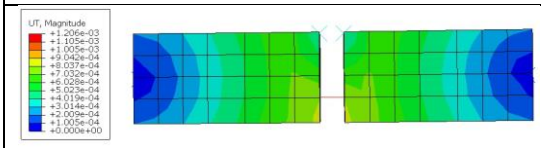
C-3-1-45-8

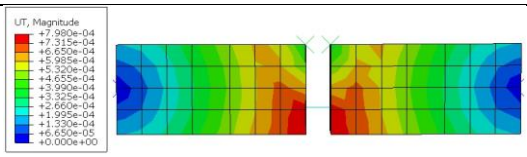
C-3-1-45-10

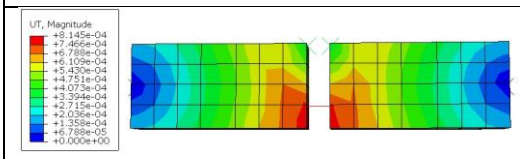
C-3-1-45-12

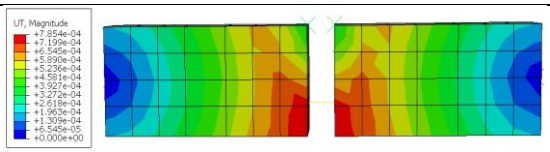
C-3-1-45-14

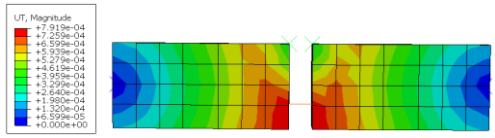
C-3-1-45-16

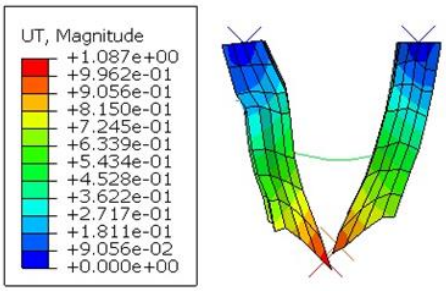

G-1-1-25-8

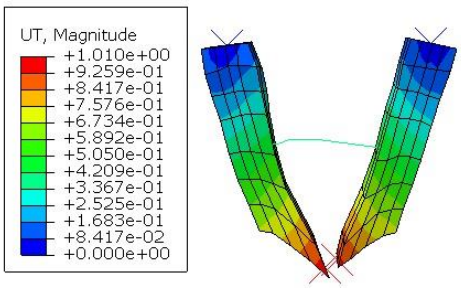

G-1-1-25-10

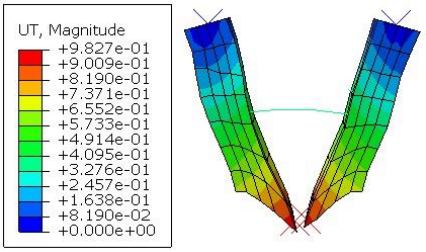

G-1-1-25-12

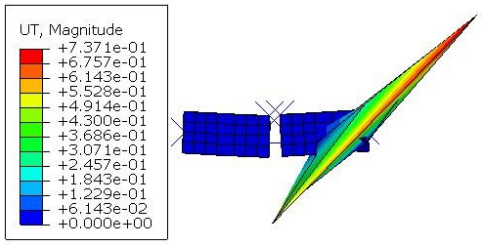

G-1-1-25-14

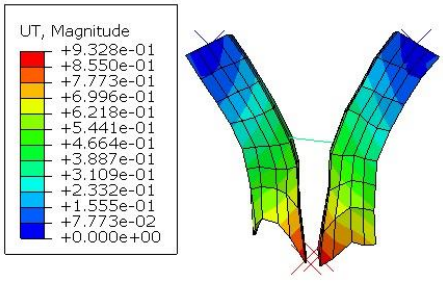

G-1-1-25-16

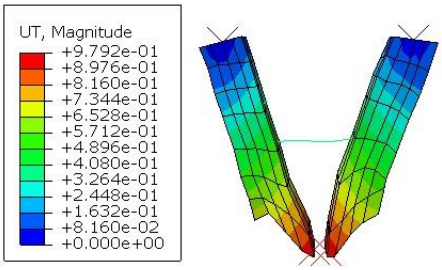

G-1-1-30-8

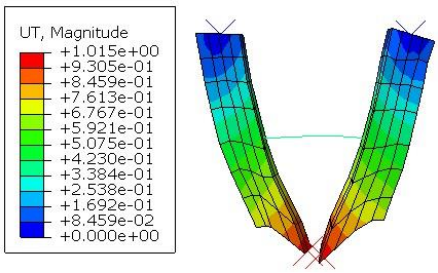

G-1-1-30-10

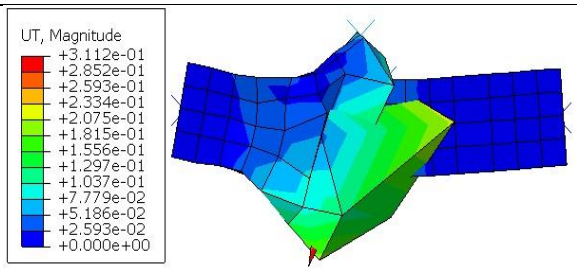

G-1-1-30-12

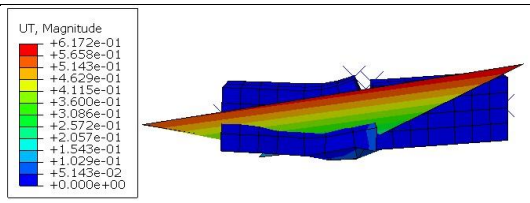

G-1-1-30-14

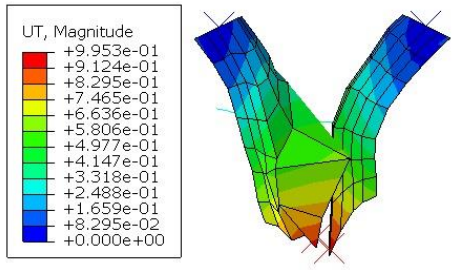

G-1-1-30-16

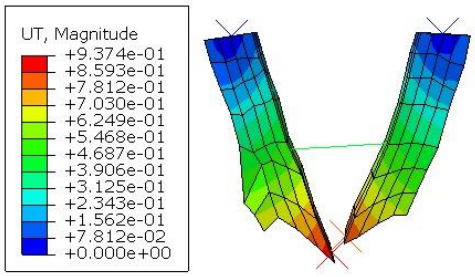

G-1-1-35-8

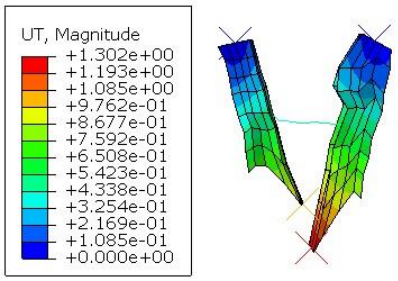

G-1-1-35-10

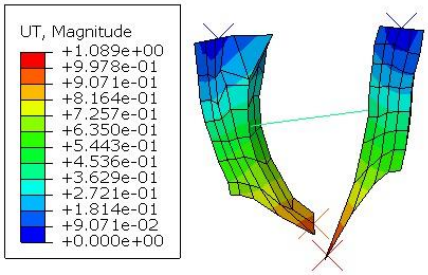

G-1-1-35-12

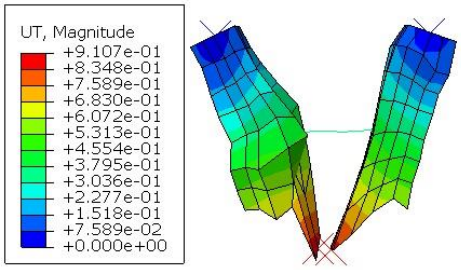

G-1-1-35-14

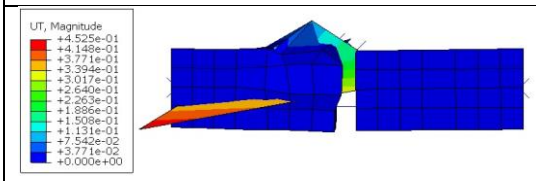

G-1-1-35-16

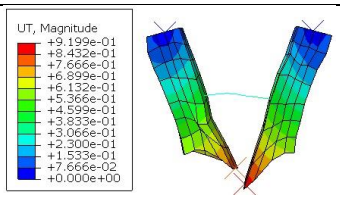

G-1-1-40-8

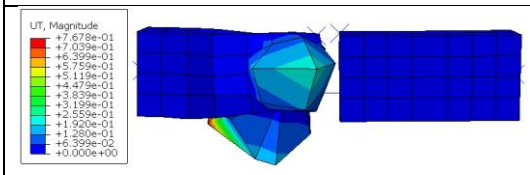

G-1-1-40-10

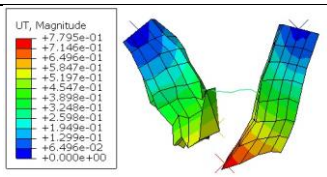

G-1-1-40-12

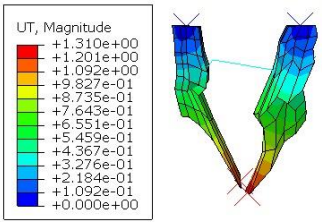

G-1-1-40-14

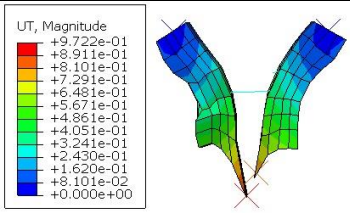

G-1-1-40-16

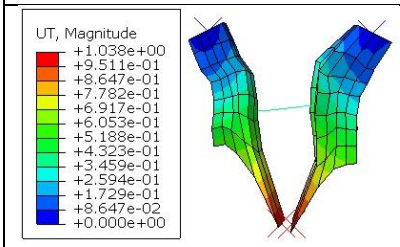

G-1-1-45-8

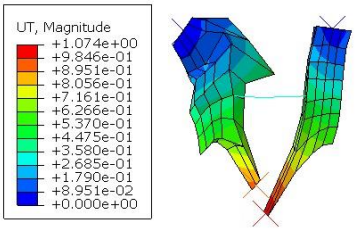

G-1-1-45-10

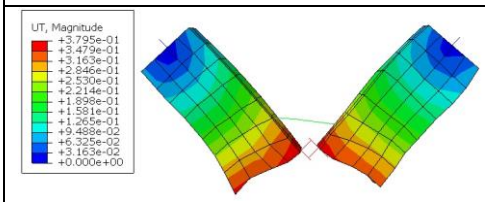

G-2-1-25-8

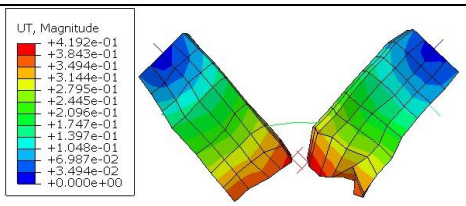

G-2-1-25-10

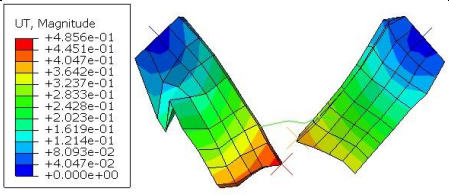

G-2-1-25-12

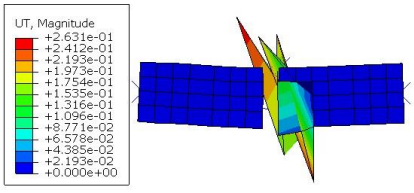

G-2-1-25-14

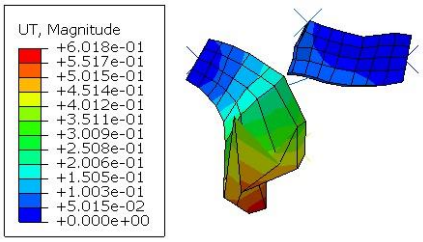

G-2-1-25-16

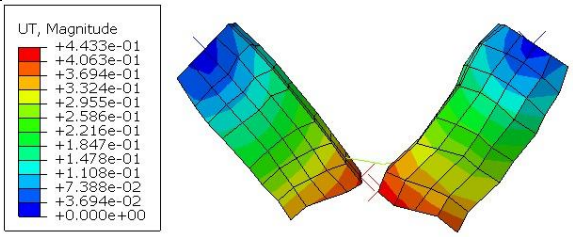

G-2-1-30-8

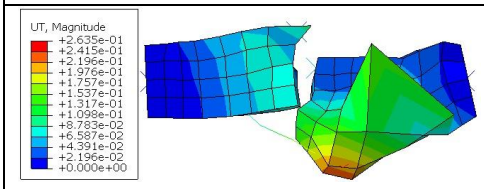

G-2-1-30-10

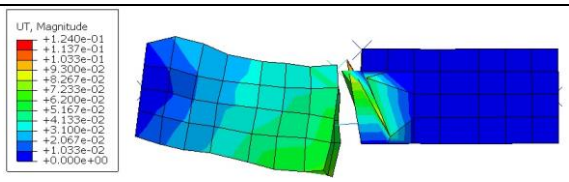

G-2-1-30-12

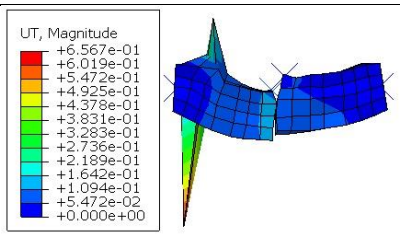

G-2-1-30-14

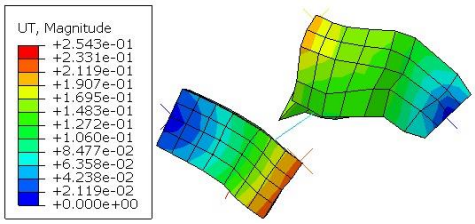

G-2-1-30-16

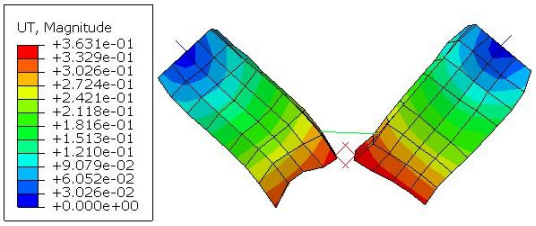

G-2-1-35-8

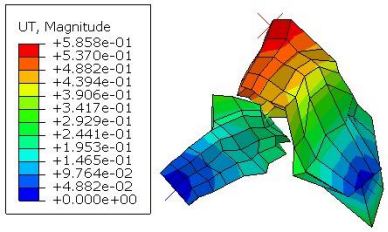

G-2-1-35-10

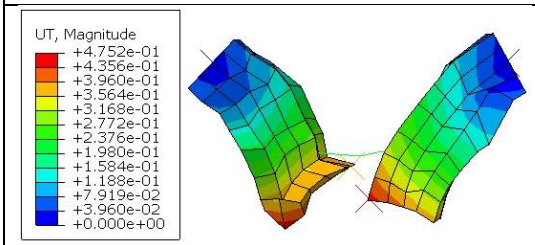

G-2-1-35-12

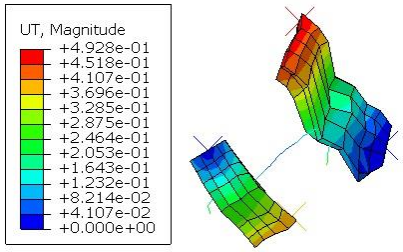

G-2-1-35-14

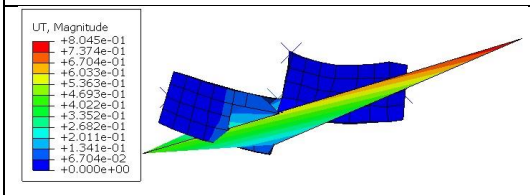

G-2-1-35-16

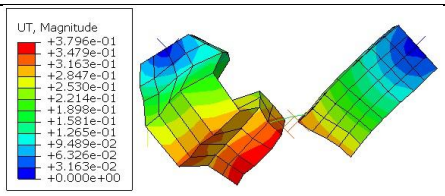

G-2-1-40-8

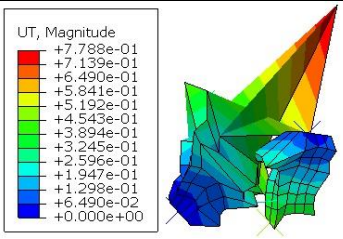

G-2-1-40-10

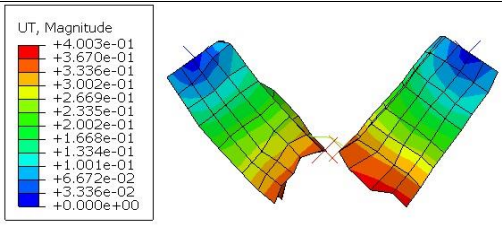

G-2-1-40-12

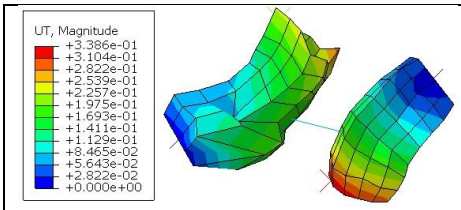

G-2-1-40-14

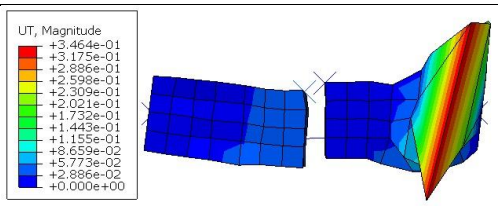

G-2-1-40-16

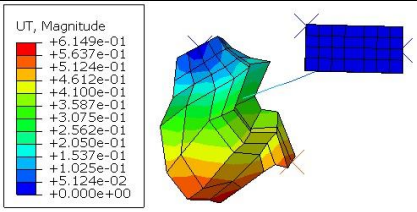

G-2-1-45-8

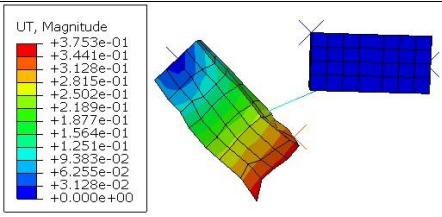

G-2-1-45-10

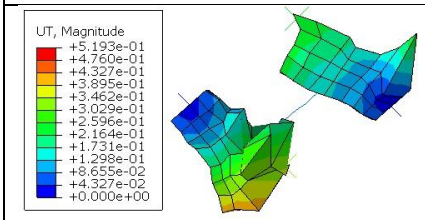

G-2-1-45-12

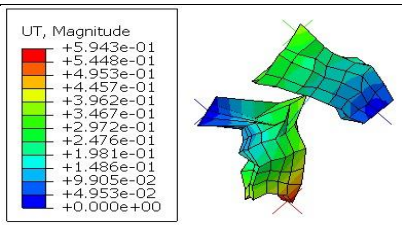

G-2-1-45-14

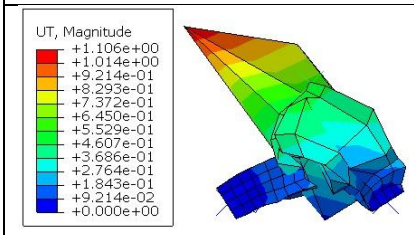

G-2-1-45-16

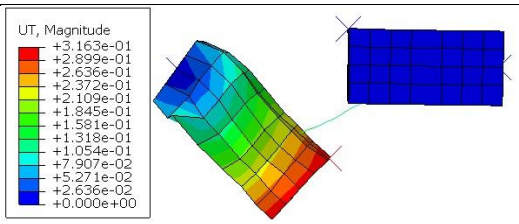

G-3-1-25-8

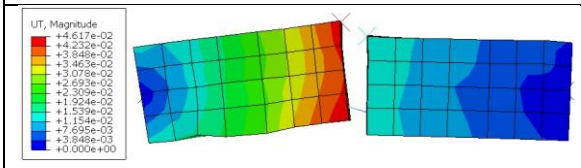

G-3-1-25-10

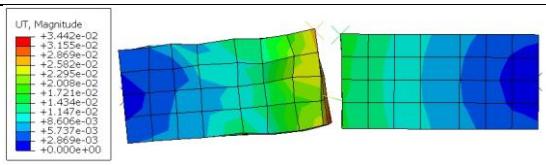

G-3-1-25-12

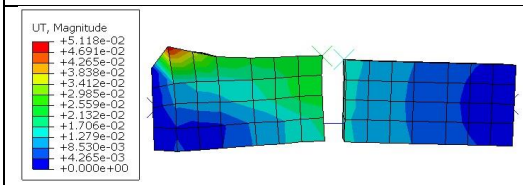

G-3-1-25-14

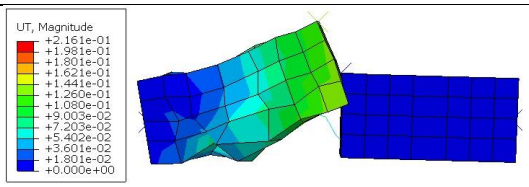

G-3-1-25-16

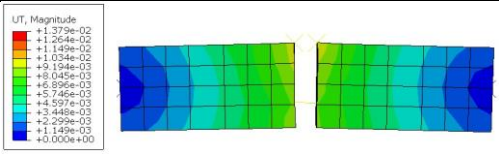

G-3-1-30-8

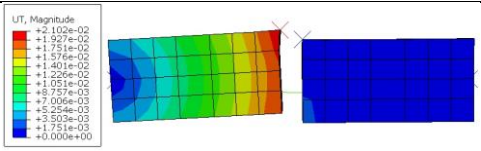

G-3-1-30-10

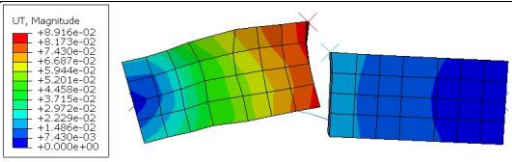

G-3-1-30-12

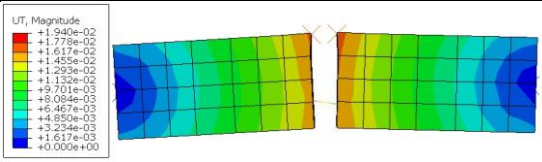

G-3-1-30-14

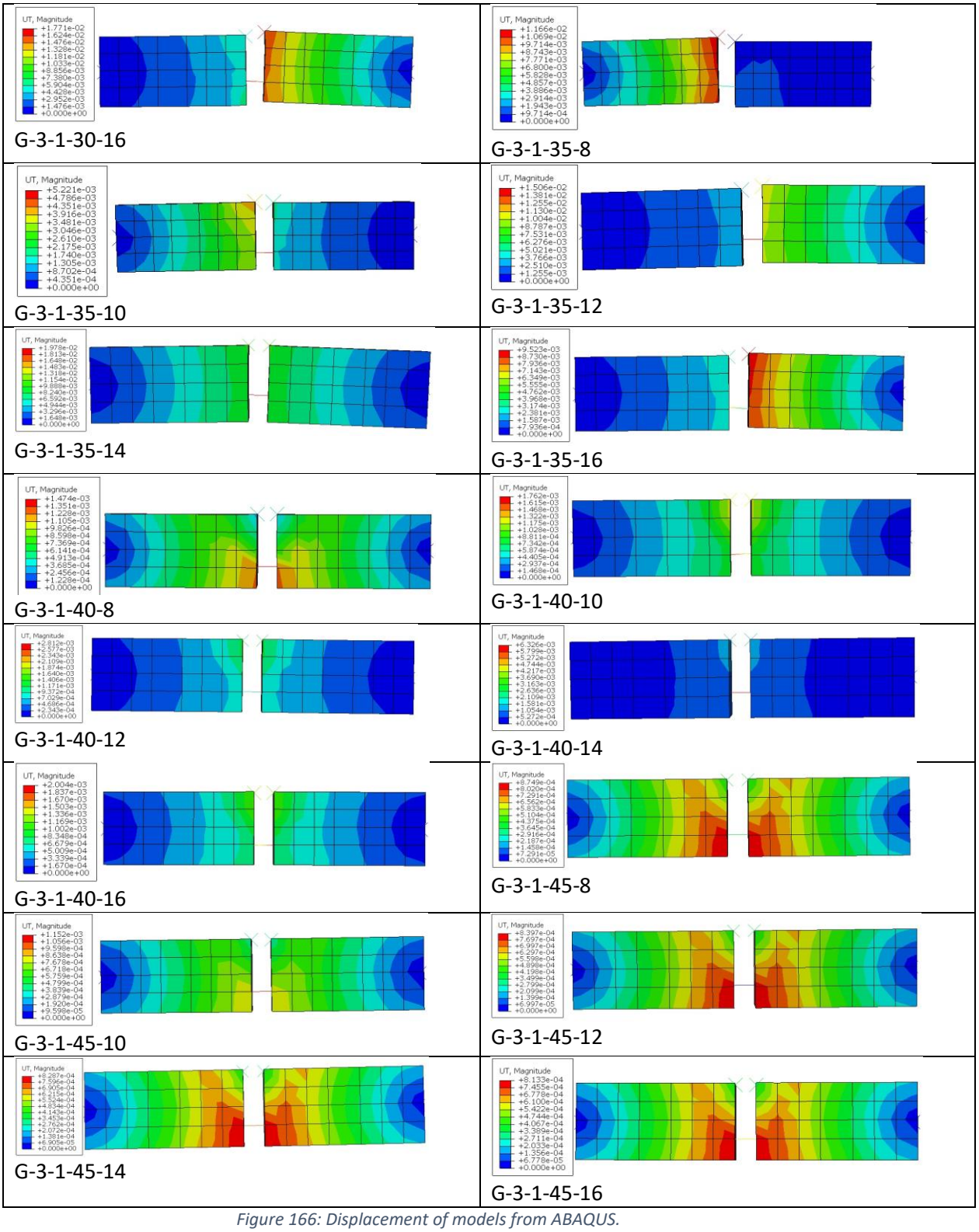

Figure 166: Displacement of models from ABAQUS.

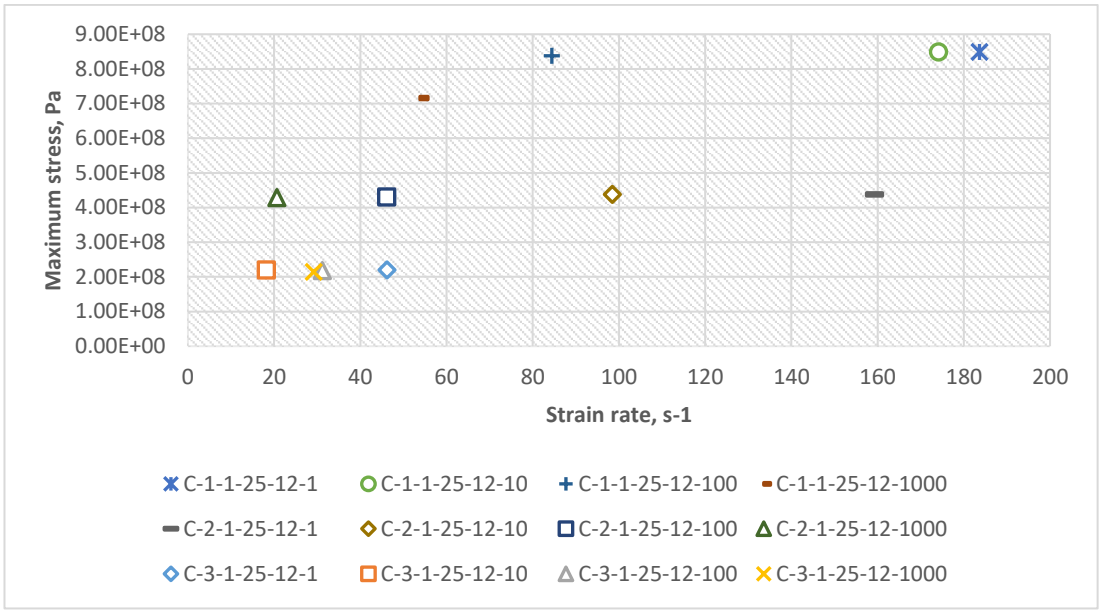
9.00E+08
8.00E+08
7.00E+08
6.00E+08
5.00E+08
4.00E+08
3.00E+08
2.00E+08
1.00E+08
0.00E+00
Maximum stress, Pa
0
20
40
60
80
100
120
140
160
180
200
Strain rate, s-1
C-1-1-25-12-1
C-1-1-25-12-10
C-1-1-25-12-100
C-1-1-25-12-1000
C-2-1-25-12-1
C-2-1-25-12-10
C-2-1-25-12-100
C-2-1-25-12-1000
C-3-1-25-12-1
C-3-1-25-12-10
C-3-1-25-12-100
C-3-1-25-12-1000

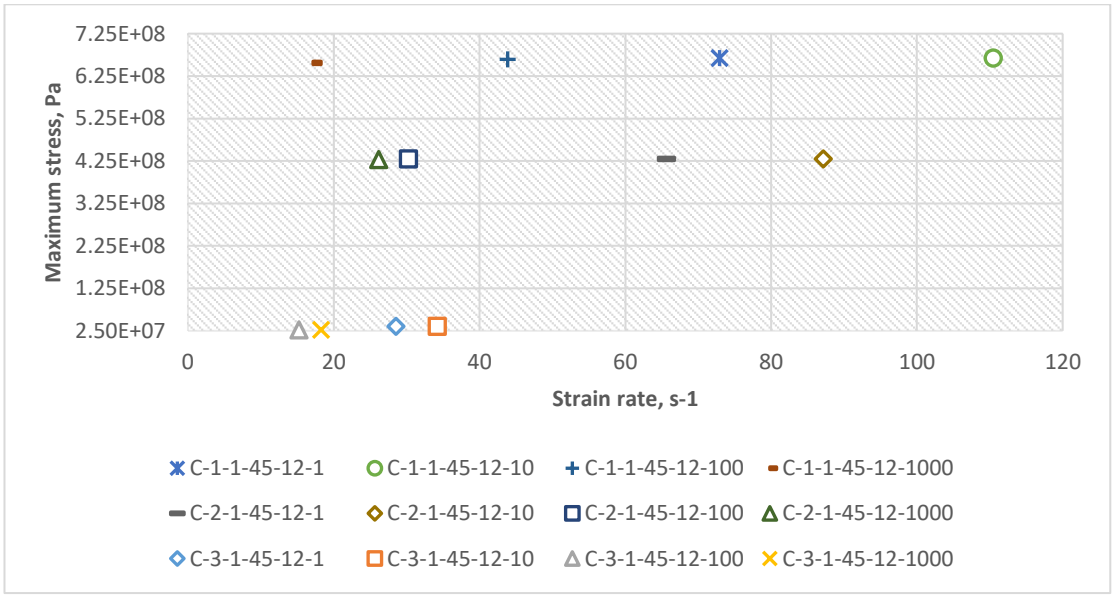
7.25E+08
6.25E+08
5.25E+08
4.25E+08
3.25E+08
2.25E+08
1.25E+08
2.50E+07
Maximum stress, Pa
0
20
40
60
80
100
120
Strain rate, s-1
C-1-1-45-12-1
C-1-1-45-12-10
C-1-1-45-12-100
C-1-1-45-12-1000
C-2-1-45-12-1
C-2-1-45-12-10
C-2-1-45-12-100
C-2-1-45-12-1000
C-3-1-45-12-1
C-3-1-45-12-10
C-3-1-45-12-100
C-3-1-45-12-1000

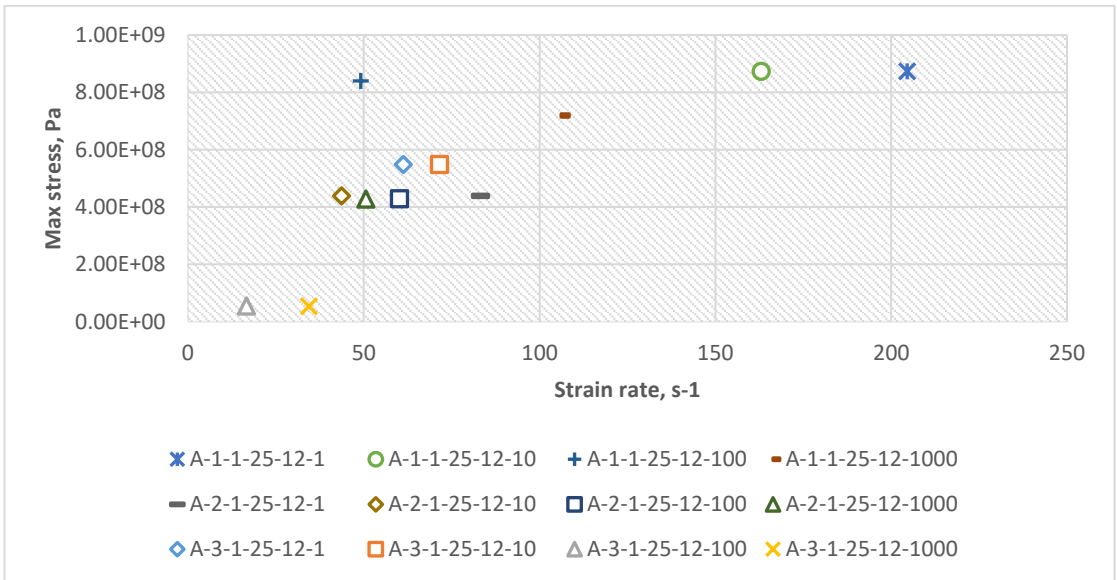
1.00E+09
8.00E+08
6.00E+08
4.00E+08
2.00E+08
0.00E+00
Max stress, Pa
0
50
100
150
200
250
Strain rate, s-1
A-1-1-25-12-1
A-1-1-25-12-10
A-1-1-25-12-100
A-1-1-25-12-1000
A-2-1-25-12-1
A-2-1-25-12-10
A-2-1-25-12-100
A-2-1-25-12-1000
A-3-1-25-12-1
A-3-1-25-12-10
A-3-1-25-12-100
A-3-1-25-12-1000

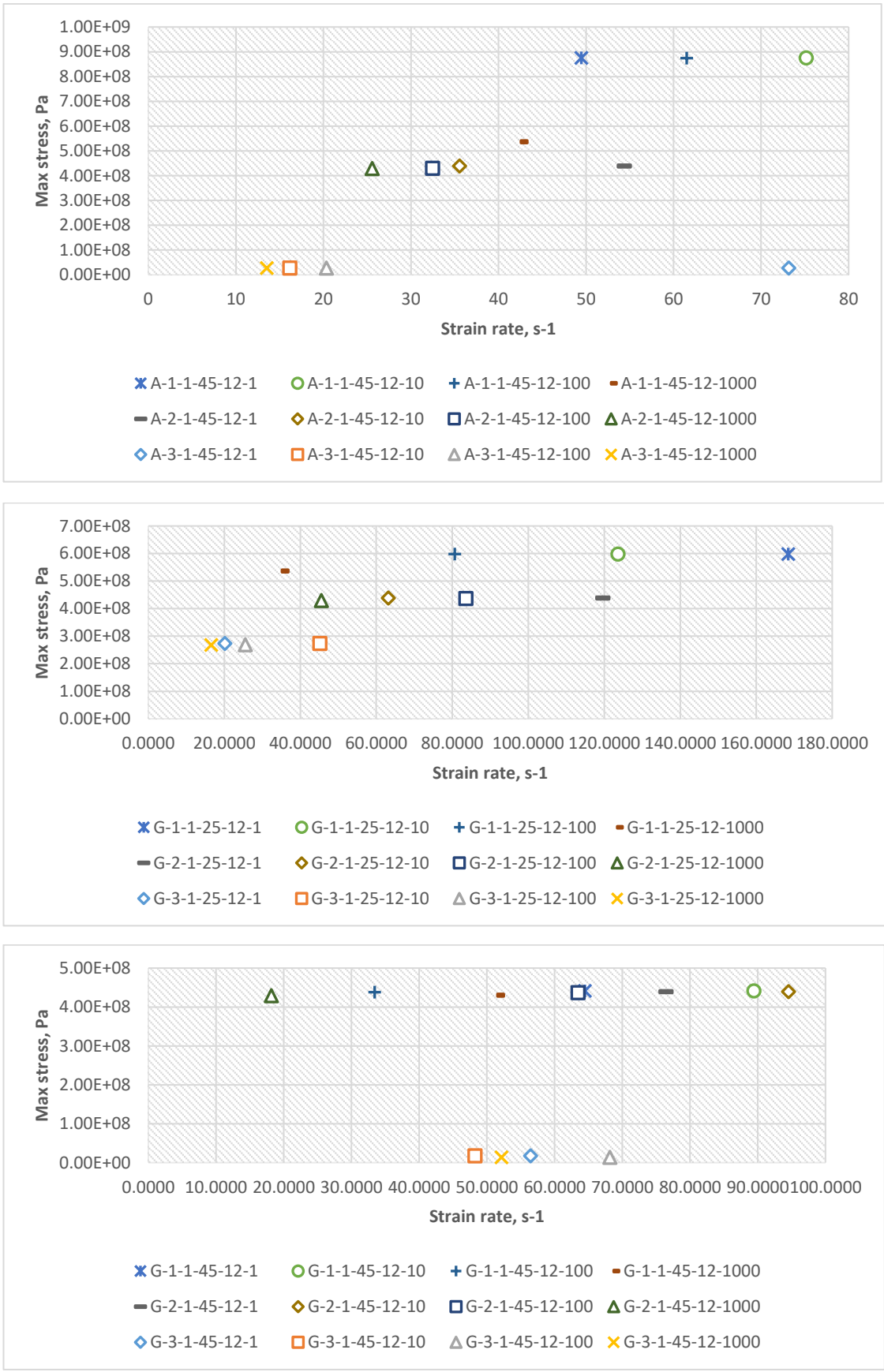

Figure 167: Peak stress as a function of strain rate.

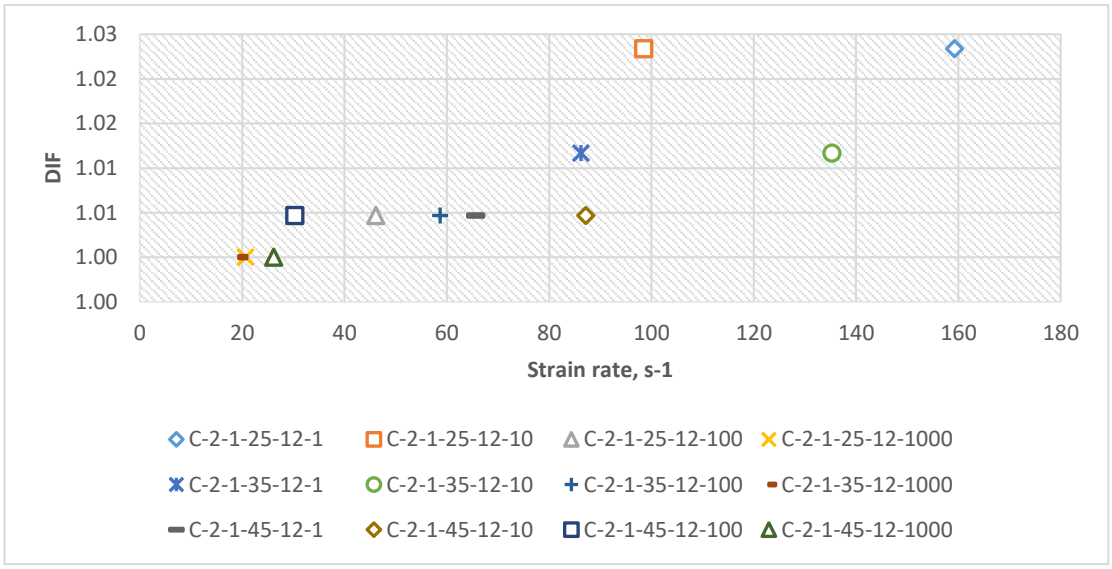
1.03
1.02
1.02
1.01
1.01
1.00
1.00
DIF
0
20
40
60
80
100
120
140
160
180
Strain rate, s-1
C-2-1-25-12-1
C-2-1-25-12-10
C-2-1-25-12-100
C-2-1-25-12-1000
C-2-1-35-12-1
C-2-1-35-12-10
C-2-1-35-12-100
C-2-1-35-12-1000
C-2-1-45-12-1
C-2-1-45-12-10
C-2-1-45-12-100
C-2-1-45-12-1000

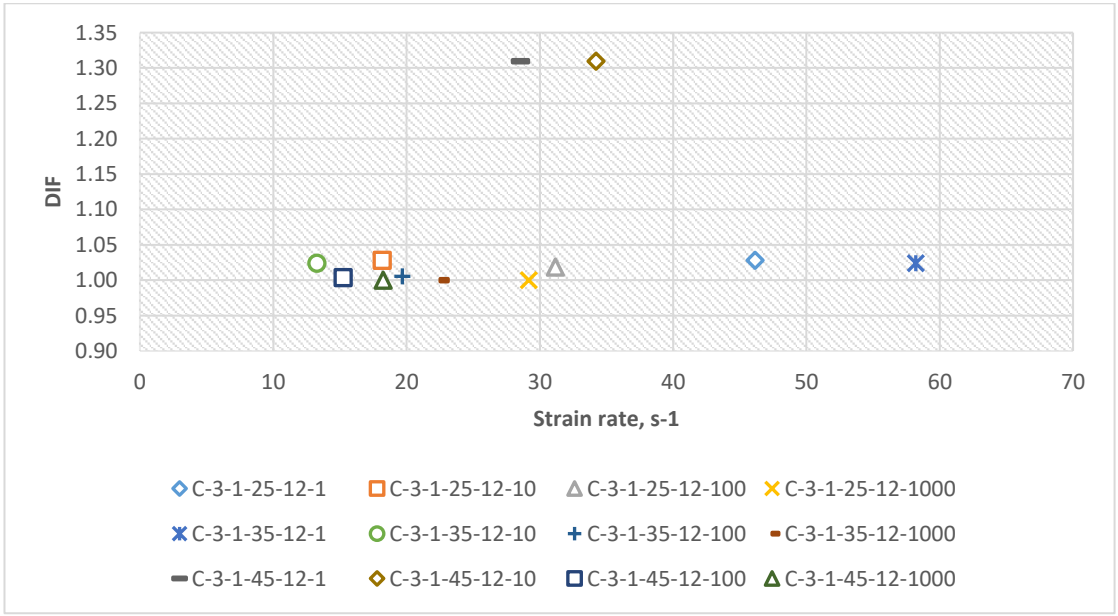
1.35
1.30
1.25
1.20
1.15
1.10
1.05
1.00
0.95
0.90
DIF
0
10
20
30
40
50
60
70
Strain rate, s-1
C-3-1-25-12-1
C-3-1-25-12-10
C-3-1-25-12-100
C-3-1-25-12-1000
C-3-1-35-12-1
C-3-1-35-12-10
C-3-1-35-12-100
C-3-1-35-12-1000
C-3-1-45-12-1
C-3-1-45-12-10
C-3-1-45-12-100
C-3-1-45-12-1000

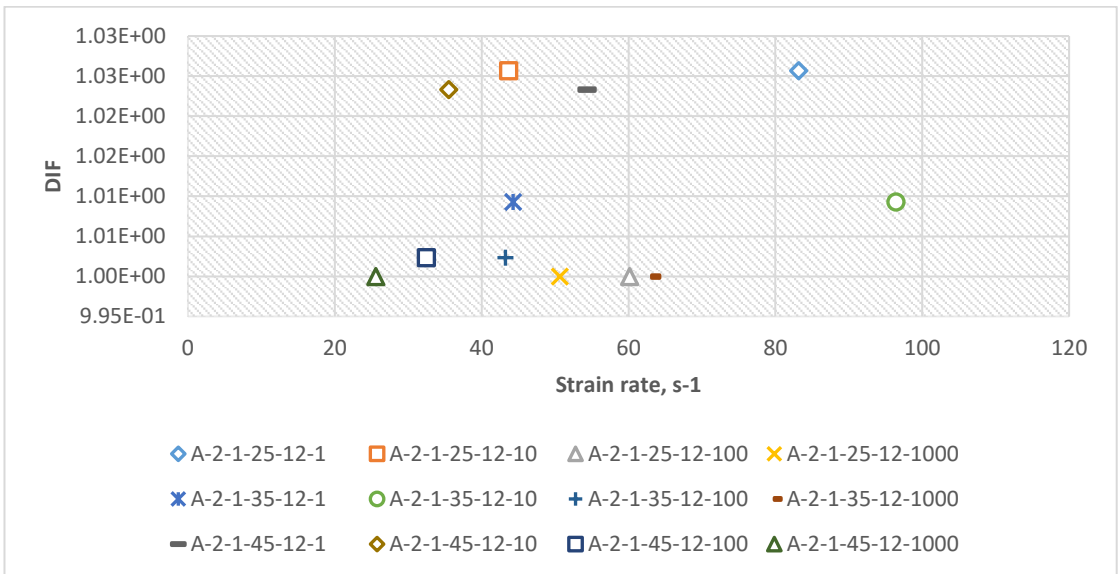
1.03E+00
1.03E+00
1.02E+00
1.02E+00
1.01E+00
1.01E+00
1.00E+00
9.95E-01
DIF
0
20
40
60
80
100
120
Strain rate, s-1
A-2-1-25-12-1
A-2-1-25-12-10
A-2-1-25-12-100
A-2-1-25-12-1000
A-2-1-35-12-1
A-2-1-35-12-10
A-2-1-35-12-100
A-2-1-35-12-1000
A-2-1-45-12-1
A-2-1-45-12-10
A-2-1-45-12-100
A-2-1-45-12-1000

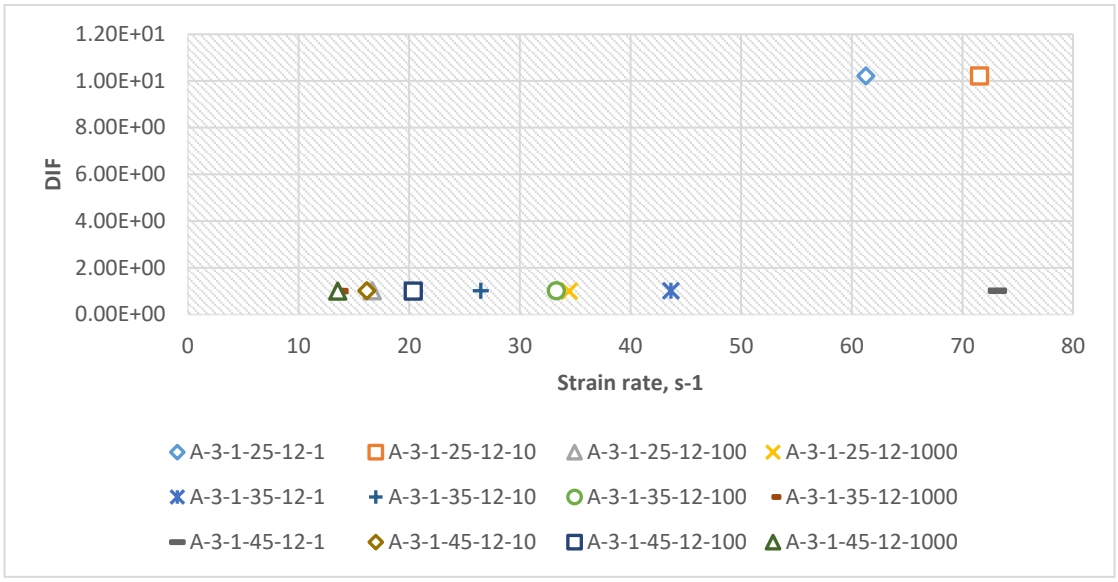

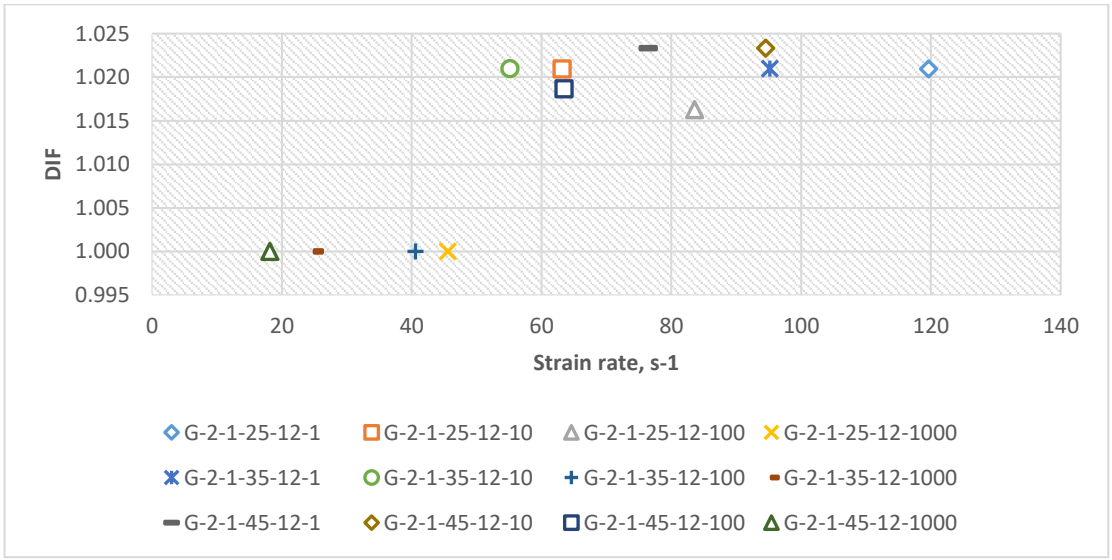

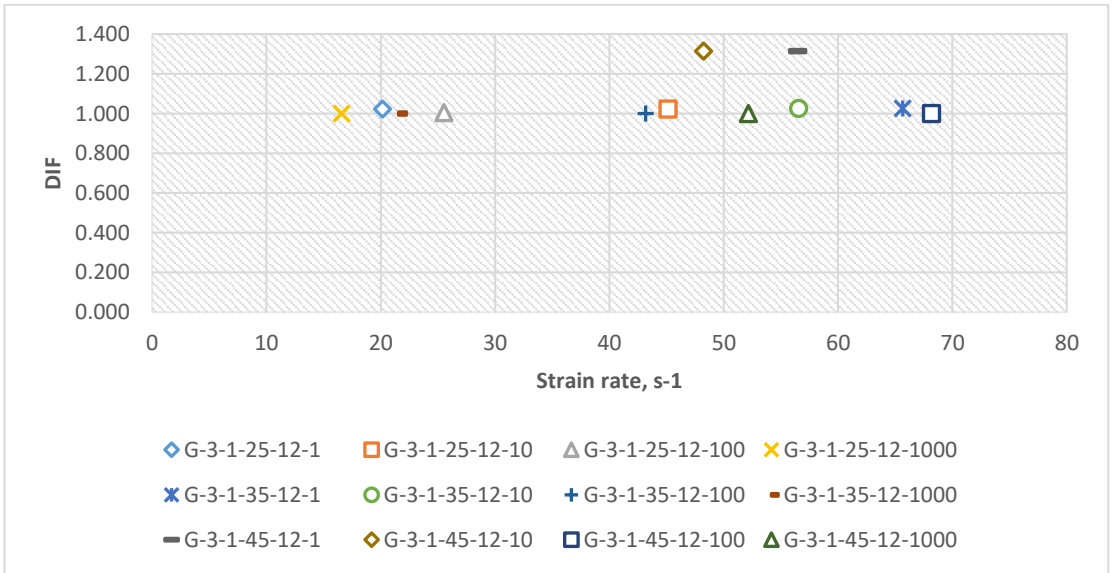

Figure 168: DIF as a function of strain rate.